UNIVERSITAT POLITÈCNICA DE CATALUNYA BARCELONATECH

Multi-level-objective design optimization of permanent magnet synchronous wind generator and solar photovoltaic system for an urban environment application

Pedram Asef

Ph.D. Dissertation

Topic: Multi-Level-Objective Design Optimization of Permanent Magnet Synchronous Wind Generator and Solar Photovoltaic System for an Urban Environment Application

Ph.D. Degree Candidate: Pedram Asef

Major: Electrical Engineering

Supervisor: Prof. Dr. Roman Bargallo Perpina

Co-advisors:

Dr. Andrew C. Lapthorn

Dr. M. R. Barzegaran

Department: Electrical Engineering

East Barcelona School of Engineering (EEBE)

Universitat Politècnica de Catalunya-BarcelonaTech

Autumn 2018

Abstract

This Ph.D. thesis illustrates a novel study on the analytical and numerical design optimization of radial-flux permanent magnet synchronous wind generators (PMSGs) for small power generation in an urban area, in which an outer rotor topology with a closed-slot stator is employed. The electromagnetic advantages of a double-layer fractional concentration non-overlapping winding configuration are discussed. The analytical behavior of a PMSG is studied in detail; especially for magnetic flux density distribution, time and space harmonics, flux linkages, back-EMF, cogging torque, torque, output power, efficiency, and iron losses computation. The electromagnetic behavior of PMSGs are evaluated when a number of various Halbach array magnetization topologies are presented to maximize the generator's performance. In addition, the thermal behavior of the PMSG is improved using an innovative natural air-cooling system for rated speed and higher to decrease the machine's heat mainly at the stator teeth. The analytical investigation is verified via 2-D and 3-D finite element analysis along with a good experimental agreement.

Design optimization of electrical machines plays the deterministic role in performance improvements such as the magnetization pattern, output power, and efficiency maximization, as well as losses and material cost minimization. This dissertation proposes a novel multi-objective design optimization technique using a dual-level response surface methodology (D-RSM) and Booth's algorithm (coupled to a memetic algorithm known as simulated annealing) to maximize the output power and minimize material cost through sizing optimization. Additionally, the efficiency maximization by D-RSM is investigated while the PMSG and drive system are on duty as the whole. It is shown that a better fit is available when utilizing modern design functions such as mixed-resolution central composite (MR-CCD) and mixed-resolution robust (MR-RD), due to controllable and uncontrollable design treatments, and also a Window-Zoom-in approach. The proposed design optimization was verified by an experimental investigation. Additionally, there are several novel studies on vibro-acoustic design optimization of the PMSGs with considering variable speed analysis and natural frequencies using two techniques to minimize the magnetic noise and vibrations.

Photovoltaic system design optimization considered of 3-D modeling of an innovative application-oriented urban environment structure, a smart tree for small power generation. The horizon shading is modeled as a broken line superimposed onto the sun path diagram, which can hold any number of height/azimuth points in this original study. The horizon profile is designed for a specific location on the Barcelona coast in Spain and the meteorological data regarding the location of the project was also considered. Furthermore, the input weather data is observed and stored for the whole year (in 2016). These data include, ambient temperature, module's temperature (open and closed circuits tests), and shading average rate. A novel Pareto-based 3-D analysis was used to identify complete and partial shading of the photovoltaic system. A significant parameter for a photovoltaic (PV) module operation is the nominal operating cell temperature (NOCT). In this research, a glass/glass module has been referenced to the environment based on IEC61215 via a closed-circuit and a resistive load to ensure the module operates at the maximum power point. The proposed technique in this comparative study attempts to minimize the losses in a certain area with improved output energy without compromising the overall efficiency of the system. A Maximum Power Point Track (MPPT) controller is enhanced by utilizing an advanced perturb & observe (P&O) algorithm to maintain the PV operating point at its maximum output under different temperatures and insolation. The most cost-effective design of the PV module is achieved via optimizing installation parameters such as tilt angle, pitch, and shading to improve the energy yield. The variation of un-replicated factorials using a Window-Zoom-in approach is examined to determine the parameter settings and to check the suitability of the design. An experimental investigation was carried out to verify the 3-D shading analysis and NOCT technique for an open-circuit and grid-connected PV module.

Keywords: Analysis of Variance, Acoustics, Booth's Algorithm, Bertottie's Equation, Design Optimization, Design of Experiment, Electromagnetic Evaluation, Eddy-Currents, Finite Element Analysis, Flux Weakening, Halbach Array, Heat Transfer, IEM-Formula, Iron Losses, Lumped Circuit Model, Magnetic Field Density, Multiple Magnetic Antennae, Magnetic Noise, Permanent Magnet Synchronous Generator, Photovoltaic System, Partial Shading Analysis, Pareto Optimization, Response Surface Method, Resistance Consideration, Simulated Annealing Method, Sensitivity Analysis, Solar Energy, Stress Calculation, Sizing Optimization, Smart Tree, Vibrations, Wind Energy, Window-Zoom-in Approach, and 3-D Printer.

Resumen

Optimización Multi Nivel de un Generador Eólico Síncrono de Imanes Permanentes y de un Sistema Solar Fotovoltáico para una aplicación en un Entorno Urbano.

Esta tesis muestra un novedoso estudio referente al diseño optimizado de forma analítica y numérica de un generador síncrono de imanes permanentes (PMSGs) para una aplicación de microgeneración eólica en un entorno urbano, donde se ha escogido una topología de rotor exterior con un estator de ranuras cerradas. Las ventajas electromagnéticas de los arrollamientos fraccionarios de doble capa, con bobinas concentradas se discuten ampliamente en la parte inicial del diseño del mismo, así como las características de distribución de la inducción, los armónicos espaciales y temporales, la fem generada, el par de cogging así como las características de salida (par, potencia generada, la eficiencia y la distribución y cálculo de las pérdidas en el hierro que son analizadas detalladamente) Posteriormente se evalúan diferentes configuraciones de estructuras de imanes con magnetización Halbach con el fin de maximizar las prestaciones del generador. Adicionalmente se analiza la distribución de temperaturas y su mejora mediante el uso de un novedoso diseño mediante el uso de ventilación natural para velocidades próximas a la nominal y superiores con el fin de disminuir la temperatura de la máquina, principalmente en el diente estatórico. El cálculo analítico se completa mediante simulaciones 2D y 3D utilizando el método de los elementos finitos así como mediante diversas experiencias que validan los modelos y aproximaciones realizadas.

Posteriormente se desarrollan algoritmos de optimización aplicados a variables tales como el tipo de magnetización, la potencia de salida, la eficiencia así como la minimización de las pérdidas y el coste de los materiales empleados. En la tesis se proponen un nuevo diseño optimizado basado en una metodología multinivel usando la metodología de superficie de respuesta (D-RSM) y un algoritmo de Booth (maximizando la potencia de salida y minimizando el coste de material empleado) Adicionalmente se investiga la maximización de la eficiencia del generador trabajando conjuntamente con el circuito de salida acoplado. El algoritmo utilizado queda validado mediante la experimentación desarrollada conjuntamente con el mismo.

Adicionalmente, se han realizado diversos estudios vibroacústicos trabajando a velocidad variable usando dos técnicas diferentes para reducir el ruido generado y las vibraciones producidas.

Posteriormente se considera un sistema fotovoltaico orientado a aplicaciones urbanas que hemos llamado “Smart tree for small power generation” y que consiste en un poste con un generador eólico en la parte superior juntamente con uno o más paneles fotovoltaicos. Este sistema se ha modelado usando metodologías en 3D. Se ha considerado el efecto de las sombras proyectadas por los diversos elementos usando datos meteorológicos y de irradiación solar de la propia ciudad de Barcelona. Usando una metodología basada en un análisis 3D y Pareto se consigue identificar completamente el sistema fotovoltaico; para este sistema se considera la temperatura de la célula fotovoltaica y la carga conectada con el fin de generar un algoritmo de control que permita obtener el punto de trabajo de máxima potencia (MPPT) comprobándose posteriormente el funcionamiento del algoritmo para diversas situaciones de funcionamiento del sistema.

Palabras clave: Análisis de Variancia, Acustica, Algoritmo de Booth, Ecuación de Bertotti, Diseño Optimizado, Diseño de Experimentos, Evaluación Electromagnética, Corrientes de Foucault, Análisis por elementos finitos, Debilitamiento de campo, Matriz Halbach, Transferencia de calor, Fórmula IEM, Perdidas en el hierro, Modelo circuital concentrado, Inducción, Antena magnética múltiple, Ruido magnético, Generador Síncrono de Imanes permanentes, Sistema Fotovoltaico, Análisis de sombreado parcial, Optimización de Pareto, Método de Superficie de Respuesta, Resistencia, Método de Simulación del Recocido, Análisis de sensibilidad, Energía Solar, Calculo de esfuerzos, Optimización del Tamaño, Smart Tree, Vibraciones, Energía Eólica, Aproximación de Ventana, Impresión 3D.

Resum

Optimització Multi Nivell d'un Generador Eòlic Síncron amb Imants Permanents i del Sistema Solar Fotovoltaic associat per a una aplicació en un paratge urbà.

LA tesis desenvolupa un nou estudi per al disseny optimitzat, analític i numèric, d'un generador síncron d'imants permanents (PMSGs) per a una aplicació de microgeneració eòlica en aplicacions urbanes, on s'ha escollit una configuració amb rotor exterior i estator amb ranures tancades.

Es discuteixen de forma extensa els avantatges electromagnètics dels bobinats fraccionaris de doble capa així com les característiques resultats vers la distribució de les induccions, els harmònics espacials i temporals, la fem generada, el parell de cogging i les característiques de sortida (parell, potencia, eficiència i pèrdues) Tanmateix s'afegeix l'estudi de diferents estructures Halbach per als imants permanents a fi i efecte de maximitzar les característiques del generador. Tot seguit s'analitza la distribució de temperatures i la seva reducció mitjançant la utilització d'una nova metodologia basada en la ventilació natural. Els càlculs analítics es complementen mitjançant anàlisi en 2 i 3 dimensions utilitzant elements finits i diverses experiències que validen els models i aproximacions emprades.

Una vegada fixada la geometria inicial es desenvolupen algoritmes d'optimització per a diverses variables (tipus de magnetització dels imants, potencia de sortida, eficiència, minimització de pèrdues i cost dels materials) La tesi planteja una optimització multinivell emprant la metodologia de superfície de resposta i un algoritme de Booth; a més, es realitza la optimització considerant el circuit de sortida. L'algoritme resta validat per la experimentació realitzada.

Finalment, s'han considerat diversos estudis vibroacústic treballant a velocitat variable, emprant dues tècniques diferents per a reduir el soroll i les vibracions desenvolupades.

Per a finalitzar l'estudi es considera un sistema format per una turbina eòlica instal·lada sobre un pal de llum autònom, els panells fotovoltaics corresponents i el sistema de càrrega. Per a modelitzar l'efecte de l'ombrejat s'ha emprat un model en 3D i les dades del temps i d'irradiació solar de la ciutat de Barcelona. El model s'ha identificat completament i s'ha generat un algoritme de control que considera, a més, l'efecte de la temperatura de la cèl·lula fotovoltaica y la càrrega connectada al sistema per tal d'aconseguir el seguiment del punt de màxima potencia.

Paraules clau: Anàlisi de Variància, Acústica, Algoritme de Booth, Equació de Bertotti, Disseny Optimitzat, Disseny d'experiments, Avaluació Electromagnètica, Corrents de Foucault, Anàlisi per elements finits, Debilitament de camp, Matriu Halbach, Transferència de calor, Fórmula IEM, Pèrdues en el ferro, Model circuital concentrat, Inducció, Antena magnètica múltiple, Soroll magnètic, Generador Síncron d'Imants permanents, Sistema Fotovoltaic, Anàlisi d'ombrejat parcial, Optimització de Pareto, Mètode de Superfície de Resposta, Resistència, Mètode de Simulació del Recuit, Anàlisi de sensibilitat, Energia Solar, Càlcul d'esforços, Optimització de mida, Smart Tree, Vibracions, Energia Eòlica, Aproximació de finestra, Impressió 3D.

Preface

The research presented in the dissertation has been carried out at the Electrical Machines Lab, Department of Electrical Engineering, Polytechnic University of Catalonia-BarcelonaTech, between September 2015 to September 2018. It is a project focused on Design and Optimization of Electrical Machine and its Drive for high-performance applications due to the huge demand, approximately 46% of all global electricity consumption which accounts for the largest share of electricity use by nearly 19% of the world's demand in industrial and residential terms. Therefore, a very small improvement in terms of the energy efficiency as well as the drive systems can be significant for the energy conservation, environment and sustainable development of the world.

To achieve the best design objectives in order to investigate and develop new concepts of Electrical Machines based on the wind energy system application, where higher electromagnetic-based performance at lower cost has been targeted, and thus, this thesis dealt with a number of optimization methods and techniques to reach this goal in close cooperation with academic and industrial partners. Dr. M. R. Barzegaran from the Lamar University (USA), Dr. Andrew C. Lapthorn from the University of Canterbury (New Zealand), Dr. Lean Le Besnerais from EOMYS Engineering (France), Dr. Jianning Dong from the Delft University of Technology (Netherlands), and Prof. Dr. Osama A. Mohammed from the Florida International University (USA).

During the investigation process, a number of new machine concepts and remarkable advances in both analytical and numerical parts have been recognized. In particular, a few studies by Prof. K. Hameyer from RWTH Aachen University, in which he has investigated a novel analytical model, known as IEM-Formula. Prof. Q. Li from the Chinese Academy of Sciences have studied new analytical techniques respect to iron losses computation advances, where he has evaluated iron loss during flux weakening condition by taking into account the resistance consideration of the stator. In addition to recent analytical improvements, there are also valuable works have done in the area of optimization. For example, robust design optimization based on response surface methodology by Dr. X. K. Gao, in which he has defined a new design function which also consists of noises, known as mixed-resolution central composite design (MR-CCD) in order to offer smaller error in comparison to other conventional design functions. Furthermore, the vibro-acoustic design optimization section is based on a semi-analytical model by Prof. Z. Q. Zhu from The University of Sheffield (UK), and Dr. Jean L. Besnerais who has proposed a variable speed analysis with considering natural frequencies for the first time.

According to the defined urban-based application of this project, solar photovoltaic module advances, integrated with wind generator have been studied to serve renewable energy sustainability under 2030 European Union targets by at least a 27% share of renewable energy consumption.

The thesis consists of eight main chapters, their contents are briefly described here.

Chapter 1 introduces the layout of the research based on the recent studies, as well as defines the objectives and the main contributions of the work.

Chapter 2 deals with steady-state and transient electromagnetic computations of the wind generator for a variable-range speed analysis, where a number of hot advances are applied. For instance, use of Halbach array magnetization topologies which have brought remarkable results.

Chapter 3 contains a full discussion of iron loss calculations in both analytical and numerical terms. In this section, there are a number of novel techniques used to enhance the accuracy of each component of iron loss individually.

Chapter 4 discusses the thermal analysis of the studied wind generator and also proposed a new technique of cooling system which can be used for any permanent magnet synchronous machines (PMSMs) to remove heat from the stator core. Moreover, several remarkable mechanical considerations have been discussed in this chapter. Furthermore, variable speed vibro-acoustic analysis of PMSMs, where the impact of various minimization techniques on noise, vibration, as well as sound power for double-layer fractional-slot concentrated winding has been studied.

Chapter 5 presents all the steps for the multi-level-objective optimization of the wind generator using numerical optimization methods (coupled with memetic algorithm such as simulated annealing). This section includes most of the contribution of the research, and thus, a number of novel optimization techniques have been proposed.

Chapter 6 verifies all the numerical and analytical findings of the thesis via experimental investigation regarding the machine design and optimization.

Chapter 7 reports some of the studies that have been done on solar photovoltaic modules based on recent advances. This section also proposes a new prediction technique with considering the nominal operating cell temperature and partial shading analysis.

At last, a brief conclusion on all objectives and findings has been given in chapter 8. Also, this chapter discusses some future perspectives of the research, in which discovered a number of considerable ideas to enhance power generation using new topology, where a US patent is in processing to be submitted. Finally, all the useful references (chaptered-based) that were used in order to develop this research is given in chapter 9.

Acknowledgement

It is a great pleasure to express my wholehearted gratitude to who agreed to be my supervisor, Prof. Dr. Ramon Bargallo Perpiña. His rich experience in the field of machine design optimization has been extremely valuable to me. Without his admonishment and patience, encouragement and intuition during the past three years, this research proposal would not have been possible. I feel very proud of having his name as my Ph.D. supervisor undoubtedly and I will never forget his kindness and humility.

I want to thank Dr. M. R. Barzegaran (co-advisor), Director of Lamar Renewable Energy and Microgrid (LAREM) at the Department of Electrical Engineering of Lamar University in Texas, USA. He has been knowledgeable, respectful, and always pleased to review my project's studies. I appreciate his gratitude for hosting me during the last one year (2017) to work with his research team. Additionally, I thank the Texas State Center of Port Management (USA) as one of the main founders of this project.

My sincere appreciation to my co-advisor, Dr. Andrew Craig Lapthorn from the Department of Electrical and Computer Engineering of the University of Canterbury in Christchurch, New Zealand. He has been always there to help me within the last two years in terms of technical, research reports, and articles. I will not forget his continuously valuable contributions even during his overseas trips.

I wish to express my gratitude to my beloved family and fiancée for their love, faithful encouragement, as well as unfailing support during these three years, while I had hard times.

Last but not least, I would like to express my appreciation to all the people and friends who have been helping and advising me to reach this position such as, Dr. Jianning Dong from TU Delft (Netherlands), Dr. Helena Martin from UPC (Spain), Dr. Jean Le Besnerais from EOMYS Engineering (France), Prof. Dr. Ronghai Qu from Huazhong University of Science and Technology (China), Dr. Dave Staton from Motor Design Ltd (UK), Daniela Mewes from KTH Royal Institute of Technology (Sweden), Núria Góngora Mora from UTGAEIB-UPC (Spain), Payam Niknejad from LU (USA), Tanushree Agarwal from LU (USA), and Karson Riggs (USA).

I would like to express my deep appreciation to the Polytechnic University of Catalonia BarcelonaTech for catering all I need to study and work.

Contents

.

List of Symbols

A	The cross-sectional area (mm^2)
A_z	The magnetic vector potential in z-direction ($V \cdot s \cdot m^{-1}$)
J_{PM}	The magnitude of the equivalent current density in the magnet boundaries (A/mm^2)
B_m	Maximum magnitude of magnetic flux density (T)
B_{rad}, B_{tan}	Radial and tangential components of the magnetic flux density (T)
H	The magnetic field intensity (A/m)
ω_b	The Base speed for control targets (rad/s)
λ_d, λ_q	The d- and q-axis magnetic flux density (T)
ω_{max}	The maximum rotational speed (rad/s)
β	The current angle (°)
θ_m	The permanent magnet arc angle (°)
θ_x	The auxiliary variable angle (°)
B_{gm}	The top face air-gap flux density in the magnet (T)
B_{g1}	The fundamental air-gap flux density (T)
E	The induced back-EMF (v)
E_1	The fundamental back-EMF of phase A (v)
e_a, e_b, e_c	The instantaneous EMF of each phase A, B, C (v)
e_{a1}	The EMF of phase A (v)
v_D, i_D, R_D	The diode forward voltage drop (V), dioide current (A), and dioide resistant (Ohms)
Z	The internal impedance (siemens)
E_{pk}	The peak internal EMF (V)
σ_{air}, σ_{PM}	The conductivity of the air, and permanent magnet (S/m
σ_{copper}	The conductivity of the copper (S/m)
I_s	The stator winding current (A)
V_s	The terminal voltage (v)
I_{sm}	The maximum stator current (A)
V_{sm}	The maximum terminal voltage (v)
R_{sy}	The magnetic reluctance of the stator yoke (H^{-1})
R_{st}	The magnetic reluctance of the stator tooth (H^{-1})
R_g	The magnetic reluctance of the air-gap (H^{-1})
R_{sy}	The magnetic reluctance of the rotor yoke (H^{-1})
F_{st}	The MMF source due to the stator currents (A)
F_{PM}	The MMF source due to the permanent magnets (A)
P, P_s	The active and apparent powers (W and V.A)
P_{in}, P_{out}	The input and output powers (W)
Φ	The magnetic flux matrix (Wb)

$\Re$	The magnetic reluctance matrix (H^{-1})
F	The sourse matrix of MMF due to the stator currents and permanent magnets (A)
l_i	The length of a particular part of the machine that is modelled by a reluctance element (m)
μ_0, μ_r	The permeability of the vaccum and the relative permeability ($H.\ m^{-1}$)
S_i	The cross-sectional area of part in a reluctance element (m^2)
θ	Electrical space angle (°)
p	Pole-pair number
n	Rotational speed (rpm)
f	Frequency (Hz)
I	The current in a coil turn (A)
l_{PM}	The thickness of the magnet (mm)
Q^*	The number of slots in a symmetrical base-winding
p^*	The number of poles in a symmetrical base-winding
t^*	The number of base-windings in the stator winding
α_s	The angle between two spokes (°)
α	The electric angle between adjacent slots (°)
$< n(\theta_s) >$	The average of the turn function in winding
F_a, F_b, F_c	The MMF of each phase currents a,b, and c (A)
L_{aa}, L_{ab}	The self-inductance and mutual inductance (mH)
$L_{s\sigma}, L_{end}$	The slot and end leakage inductances (mH)
L_{gap}, L_h	The air-gap and harmonic leakage inductances (mH)
l_{Cu}	The total length of the coil (mm)
T	The temperature (°C)
χ	The skin effect length (mm)
d_w	The diameter of single wire (mm)
L_s	The total inductance of stator winding (mH)
h_s	The slot height (mm)
h_0	The slot opening height (mm)
h_3	The length between the end tooth and inner stator face (mm)
b_s	The slot opening length (mm)
b_0	The slot width of the statore core (mm)
w_s	The equivalent slot width (mm)
X_d, X_q	The d- and q-axis reactances (ohms)
u_d, u_q	The d- and q-axis voltages (v)
q	The slot per pole per phase
P_{Cu}	The Joule loss in the stator winding (W)
k_{W1}	The fundamental winding factor

η_v	The angle in voltage vector map of winding
v	The fundamental harmonic
$K_{s(rms)}$	The surface current density in the stator winding (A/mm^2)
k_1	The factor that is derived by the amplitude of the air-gap flux density
$\Im_p$	The MMF of one pole of a complete two pole magnetic circuit (A)
L_d	d-axis inductance (mH)
L_q	q-axis inductance (mH)
ω_{vs}	The generic vth MMF harmonic in the stator reference frame
ω_{rv}	The MMF speed with respect to the rotor
f_{rv}	The frequency of the rotating MMF harmonics at the rotor (Hz)
C	Final cost of the machine ($)
T_r	Rated torque (N.m)
T_e	Electromagnetic torque (N.m)
$CPSR$	Constant power speed range (W)
λ_m	Flux linkage (mVs)
$P_{opt.}$	Optimized output power (W)
C_0	Initial cost of the machine ($)
$i_{d,i}$, $i_{q,i}$	Peak direct and transverse axis currents for ith operating point (A)
L_m	Thickness of permanent magnet (mm)
D_{ro}/ D_{ri}	Outer/ and inner diameter of rotor core (mm)
D_{so}/ D_{si}	Outer/ and inner diameter of stator core (mm)
A_{slot}	Cross-sectional area of a stator slot (mm^2)
P_{arc}	Permanent magnet's arc (°e)
α_p	Ratio of pole-arc to pole-pitch
n_0	Minimum speed (rpm)
P_r	Rated power (W)
n_r	Rated speed (rpm)
S_w	Slot-width (mm)
y_{ij}	Linear statistic model objective (means model)
y_i	Objective of second-order model of ith level
$\hat{y}_i$	Predicted value by the fitted model in the ith observation
$\hat{y}$	The fitted second-order polynomial observation
$\bar{y}$	Mean value of y_i
S_a	The probability of acceptance through SA
J_c	Current density (A/mm^2)
SSR	Random regression (error) sum of squares
l_s	Active stack stator length

ζ_{min}	Non-normalized minimum value of *i*th treatment
ζ_{max}	Non-normalized maximum value of *i*th treatment
SST	Total reformed sum of squares
m	Stator number of phases
N_s	Number of turns per phase
N	Number of turns per coil
$2p$	Number of poles
Q_s	Total number of the stator slots
$W_{ph\text{-}s}$	Width of phase separator (excluding legs)
$L_{a\text{-}pm}$	Air-gap between PMs (mm)
δ_g	Air-gap length (mm)
δ_{st}	Under-cut angle of the stator tooth-top (º)
ε_{ij}	Random error component
R^2	A statistic to express the proportion of the variation of y_i by fitted-model and FEA data for mean of $\bar{y}$
$\%\eta$	Percentage of the efficiency
x_i	Normalized *i*th controllable treatment
z_i	Normalized *i*th noise treatment
$\beth_i$	An individualized parameter to *i*th treatment
μ	Frequent parameter to any treatment (overall mean)
$\{v\}$	The velocity vector for mass transport of heat
D_{sh}	Shaft diameter (mm)
S_d	Effective slot-depth (mm)
α_p	Ratio of pole-arc to pole-pitch
n_m	Minimum speed (rpm)
$\{L\}$	The vector operator
t	The time (s)
Q	The heat source rate per unit volume (W/m^3)
ρ	The mass density (kg/m^3)
W_c	Coenergy (J)
Ψ	Flux linkage (mVs)
A	Cross-sectional area of a counter (mm^2)
l_i	The initial segment number per pole
P_{EM}	Electromagnetic output power (W)
R_0, R_1	Inner and outer radius of magnet segment (mm)
M_r, M_θ	The radial and tangential component of the airgap magnetic flux density (T)
W_p	The pole-pitch
$W_{n,pa}$	The pole-arc of the nth magnet pole

$\left\|B_{radial}^{1}\right\|$	The fundamental amplitude of the radial component of air-gap flux density (T)
B_{radial}^{h}	The *i*th harmonic amplitude of the radial component of air-gap flux density (T)
$W_{\text{ph-s}}$	Width of phase separator (excluding legs) in (mm)
$L_{\text{a-pm}}$	Airgap between PMs (mm)
A_1, A_2	The distance between PMs, and the width segment (mm)
u_{n}	The nodal voltage vector
E_{p}	Peak back-EMF per phase (v)
Ω_i	Speed operating point (rpm)
R^2	A statistic to express the proportion of the variation of y_{i} by fitted model and FEA data for mean of y
z_{i}	Normalized *i*th uncontrollable variable
x_{i}	Normalized *i*th controllable variable
F_{r}	Radial component of the electromagnetic force (N)
F_{c}	Centrifugal force (N)
F_{t}	Tangential component of the electromagnetic force (N)
$L_{\text{p,max}}$	A-weighted maximum sound power (magnetic noise) in (dBA)
Z_0	The air acoustic impedance (ohm^{-1})
S_{c}	The PMSG frame area (m^2)
σ_{m}	The modal radiation factor
f_0	The breathing model natural frequency (Hz)
K_{fs}	The stator stacking factor
p_r, p_Θ	The stator and rotor winding harmonic magnetic field (T)
$F_{\text{x}}, F_{\text{y}}$	*x*-axis and *y*-axis components of total electromagnetic force (N)
μ_{PM}	The permeability of permanent magnet
μ_{air}	The permeability of air (H/m)
S	The heat transfer area (mm^2)
x	The distance where the heat is conducted (mm)
k_{k} or k	The thermal conductivity of the material (W/m.K)
h_c	The convective heat transfer constant
ΔT	The difference between surface and fluid temperatures (°C)
R_{c}	The resistance due to convective heat transfer (Ω)
Q	The heat source (J)
ρ	The density of the material used (kg/m^3)
C	The heat capacitance (J/ K)
c	The specific heat (J/ g.m. °C)
$\{L\}$	The vector operator
|D|	The magnitude of temperature (°C)
$\{V\}$	The velocity vector for conductivity matrix (m/s)

E_1, E_2	Modulus of elasticity of the rotor, and the driven wheel (Pa)
E_{sh}	Modulus of elasticity of the shaft (Pa)
ρ_1, ρ_2	Mean specific mass density of the rotor, and the driven wheel (kg/ m^3)
w_1, w_2	Width of the disk rotor, and the driven wheel (m)
a_1, a_2	Location of the rotor from the left end of shaft, and location of the driven wheel from the left end of shaft (m)
L	Length of the shaft (m)
g	Acceleration of gravity (m/s^2)
n_{cr}	The critical value of the Dunkerley and Rayleigh-Ritz method (1/s)
L_p	The sound pressure level (Pa)
L_w	The sound power level (dBA)
D_f	The directivity factor
Z_0	The air acoustic impedance (siemens)
S_c	The electric machine frame area (mm^2)
$L_{\omega,max}$	The maximum sound power (dBA)
$L_{p,max}$	The maximum sound power level (dBA)
σ_m	The modal radiation factor
h_f	The frame width (mm)
f_0	The breathing natural frequency (Hz)
ρ_s	The stator stack mass (kg)
Δ_m	The increasing mass due to the winding and teeth (kg)
a	The stator mean radius (mm)
r	The radius of the rotor (mm)
A_{slot}, A_{gap}, A_m	The magnetic vectors potential of slot, airgap, and magnet boundaries
J_{slot}	The current density in the slot (A/mm^2)
Δ	The offset in the tangential direction
M	The magnetization vector (A/m)
Λ	The air-gap permeance per unit area ($1/\Omega$)
S_i	The sensitivity of the objective function
P_{abs}	The absolute values power in the machine (W)
β_{ii}, β_{ij}	Pure quadratic coefficients in main diagonal and, off-diagonal elements
η, η'	The pure and ture response of the quadratic model
ε_{exp}	The experimental or noise error of the quadratic model
σ^2	The quadratic model variance
α	The distance among each controllable design variable in MR-CCD
k	The number of controllable variables
P_{Cu}, P_{copper}	The copper loss (W)
P_{iron}, P_{fe}	The iron loss (W)
k_R	The factor of square of the frequency and normal to the slot leakage flux direction

φ_z	The operation point of the rectifier system
$E_{G,t}$	The global irradiance onto the PV module (W/m^2)
$E_{Dir,t}$	The direct component of the solar irradiance onto the horizontal plane (W/m^2)
$E_{Diff,t}$	The diffuse component of the solar irradiance onto the horizontal plane (W/m^2)
$E_{Ref,t}$	The reflected radiation from the ground (W/m^2)
I_{ph}	The photo current (A)
I_b	The bypass diode current (A)
I_0	The inverse saturation current (A)
R_s	The total series resistance of the solar panel (Ω)
V_p	The voltage drop due to the partial shading (V)
I_{Sat}	The saturation current of the solar panel (A)
I_{Rp1}	The current passes the area S1 which is shaded (A)
T_n	The temperature measured on each segment by an infrared camera (°C)
E_n	The global radiation onto segment area (V)
C_s	The material and technology-dependent constant
R_L	The output load resistance of DC-DC converter
S_L	The slope of the load line
d, d'	The linear control variable between output voltage V_{out} and PV voltage V_{pv}; the duty cycle of the converter
V_{mpp}	The maximum power point voltage (V)
K_{oc}	The open circuit coefficient
V_{oc}	The open circuit voltage (V)
P_{eff} (z)	The PV array effective output energy, where z is the duty ration of the DC-DC converter
P_{lossm}	The total minimum power loss (W)
$\Delta\eta_{rel}$	The relative efficiency deviation
T_2	The cell temperature (°C)
G	The solar irradiance (W/mm^2)
I_{sc}	The short circuit current (A)
V_s	The voltage of the string including the cell (V)
I_s	The current of the string including the cell (A)
r_s	The Spearman's ρ correlation coefficient

List of Tables

- **Chapter 1**

- **Chapter 2**

- **Chapter 3**

- **Chapter 4**

- **Chapter 5**

List of Figures

- **Chapter 1**

- **Chapter 2**

1. Introduction

Renewable energy and technology development play a significant role in power generation today, in which wind and solar are the main resources. Globally, the number of installations of wind turbines and photovoltaic (PV) systems have dramatically grown lately. This research illustrates a new sustainable energy application in the field of electrical wind generator design optimization and aid of PV modules for an innovative stand-alone power system application which generates a small power range. Additionally, the CO_2 emissions reduction by the assist of the proposed innovative smart tree is sufficiently important to be discussed.

- Wind energy

Regarding Table 1.1, the wind energy scenarios are worldwide determined for a significant development up to 2050. Hence the wind energy industry grows its dimension through improvements and innovations. Therefore, the renewable energy solutions have aimed to decrease consumption of fossil fuels via the wind and solar sources, and energy efficiency improvements techniques.

Table 1.1 Global wind energy scenarios road map.

GLOBAL		2007	2015	2020	2030	2040	2050
Reference scenario	electricity generation(TW/a)	173	677	1,009	1,536	2,034	2,516
	installed capacity(GW)	95	293	417	595	739	883
Energy [r]evolution scenario	electricity generation(TW/a)	173	941	2,168	4,539	6,674	8,474
	installed capacity(GW)	95	407	878	1,733	2,409	2,943
advanced energy [r]evolution scenario	electricity generation(TW/a)	173	1,166	2,849	5,872	8,481	10,841
	installed capacity(GW)	95	494	1,140	2,241	3,054	3,754

Regarding the objective of the project, power generation via the wind energy production over the Metropolitan Area of Barcelona (AMB in Catalan) is carried out to build an optimal small wind generator either as self-user or to be connected to the smart grid.

As a smart tree requires a specific location with good wind, following reports are given to verify the location of the project, the coast of Barcelona city. The supported location near the shore at Sirena (41°20'28.29"N, 2° 9'57.99"E, H = 10, Port of Barcelona) can be shown [1] through the wind speed histogram and the wind rose observation. Fig. 1 presents the strength and direction of wind onto the proposed given location.

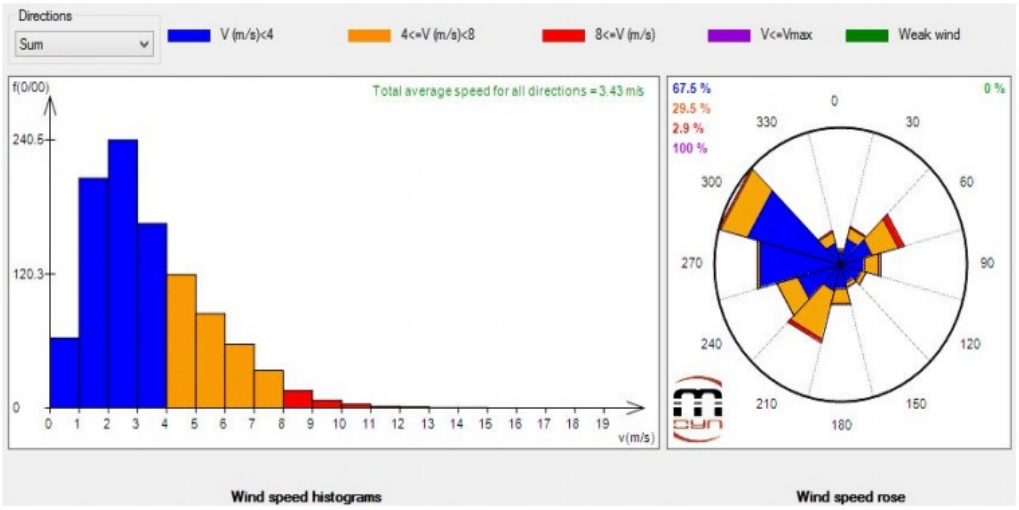

Fig. 1.1 Wind Rose and histogram of the wind reference at Sirena (Barcelona). Data source: Port of Barcelona.

As shown in Fig. 1.1, approximately 67.5% of the wind speed is under 4 m/s, almost 29.5% between 4 to 8 m/s, and about 2.9% more than 8 m/s have been stored. Moreover, 3.43 m/s has been recorded as total average speed for all the directions. Mean annual wind speed and mean annual energy production for a 1 kW wind turbine are computed on various mappings at 10 m, 20 m, 30 m, 40 m and 50 m above the ground with a horizontal resolution of 10 m. Fig. 1.2-a presents that along the beach of Barcelona,

the mean annual speed of 3.0 to 3.5 m/s has been reached due to that fact the mean annual energy generation is between 250 to 500 MWh/year (Fig. 1.2-b) [1][2]. Also, the red star marker represents the project's location with average 3 m/s and 0.35 MWh/year.

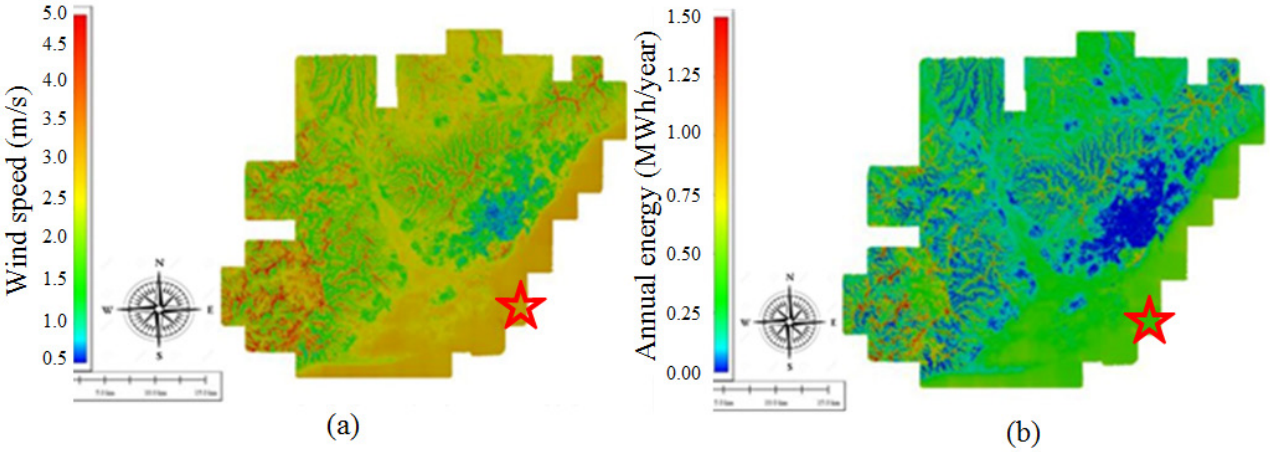

Fig. 1.2 Wind speed demonstration of Barcelona, a) Mean annual wind speed, and b) mean annual energy production Atlas at 20 m high.

Table 1.2 indicates that there are two important locations to build-up our 5 kW wind turbine in the city of Barcelona. One, in the Observatori Fabra station nearby Tibidabo park), and in El Prat de Llobregat station (red star's location), where acquires almost the same range of required speed of wind (3.0 m/s) for the generator to produce output power of 1.5 kW as the same results along the coast of Barcelona based on Fig. 1.2.

Table 1.2 Comparison between computed mean speed and measured mean speed.

Station	Height	Mean Speed Measured	Mean Speed Computed	Difference
El Prat de Llobregat	10 m	3.0 m/s	2.6 m/s	0.4 m/s
Barcelona - Zona Universitaria	10 m	2.1 m/s	2.1 m/s	0.0 m/s
Barcelona - el Raval	30 m	2.0 m/s	1.7 m/s	0.3 m/s
Vallirana	10 m	1.9 m/s	2.5 m/s	-0.6 m/s
Castellbisbal	10 m	2.4 m/s	2.2 m/s	0.2 m/s
Badalona - Museu	33 m	2.7 m/s	2.8 m/s	-0.1 m/s
Barcelona - Observatori Fabra	10 m	4.7 m/s	4.3 m/s	0.4 m/s

- Solar Energy

Barcelona city proves to be one of the most successful solar powered cities in the world recently. It is a city of "firsts" on the solar energy front. The city has several characteristics which make it a prime location for solar power. The city has considerable potential to generate electricity by the PVs. Fig. 1.3 illustrates the average annual sum of solar irradiation capacity in Spain. The direct normal irradiance of the Barcelona city can be approximately estimated by 1700 kWh/m^2 which is shown in Fig. 1.3-a. In addition, the average annual sum of global horizontal irradiation is almost 1650 kWh/m^2 in Barcelona. Furthermore, the annual sun horizon and height of the sun in Barcelona city can be seen in Fig. 1.4-a-b (the azimuth between -30 to 30˚).

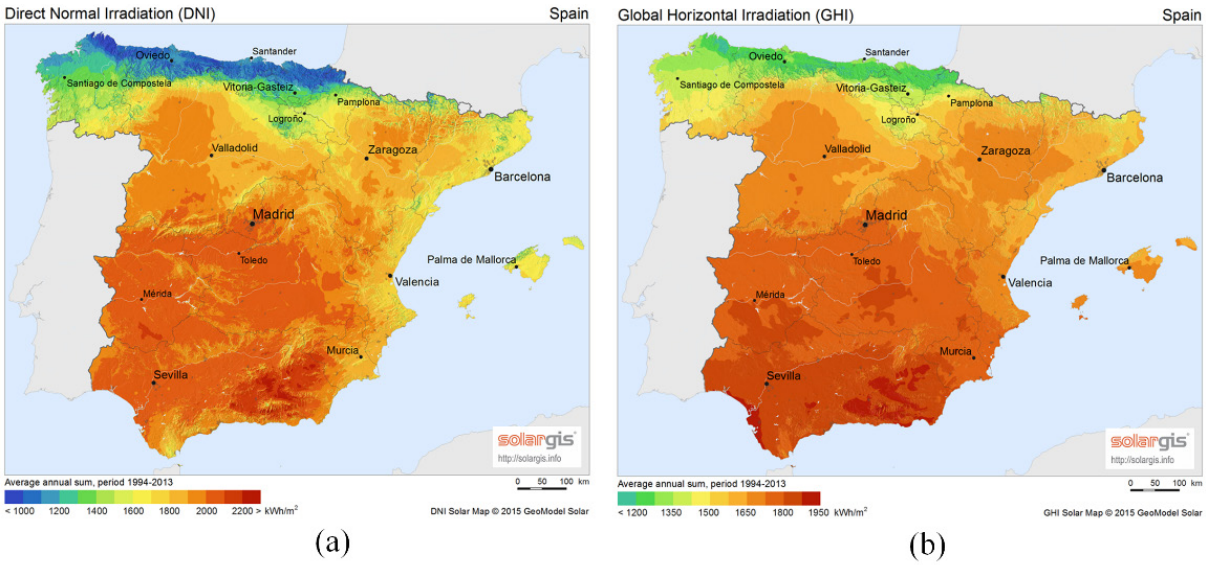

Fig. 1.3 Average annual sum of solar irradiation of Spain, a) direct normal irradiation, and b) global horizontal irradiation.

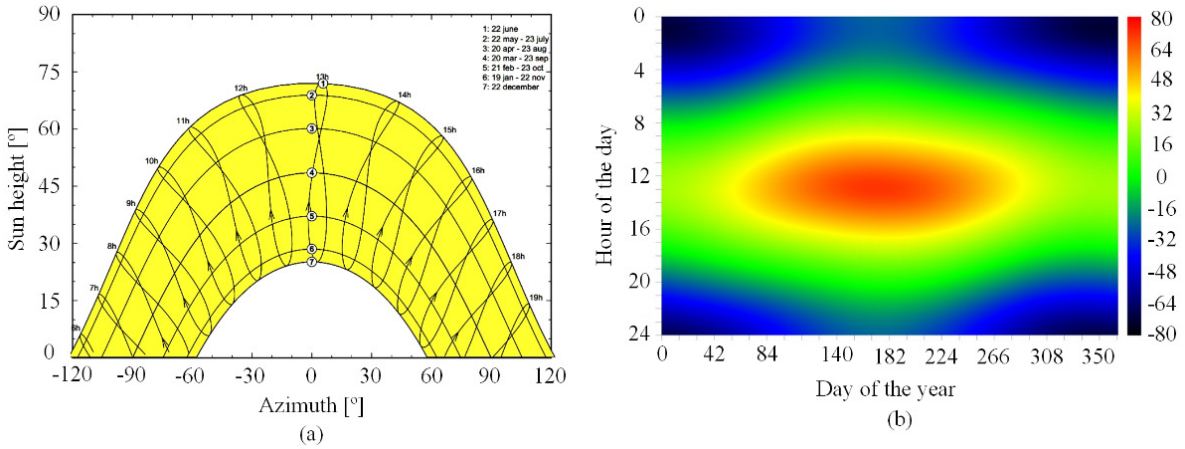

Fig. 1.4 Annual sun horizon and height in Barcelona, a) sun horizon, and b) sun height.

The design and optimization of wind generator and PV system for the small range of power generation are utilized in a new application as smart tree, in which both sustainable energy resources (wind and solar) are considered base on the specific climate, horizon, and weather conditions at the coast of Barcelona city in Spain. The application demonstration of the smart tree is introduced in the next section.

The dissertation consists of nine main chapters, in which chapters two, three, four, and five dealt directly with the permanent magnet synchronous wind generator (PMSG). In section two, basic design's electromagnetic-based significant parameters, constraints, and goals are calculated (post-process) along with 2-D and 3-D finite element analysis verifications. A deep novel study is done in iron losses computation using frequency and time domains of PMSG used in section three. Also, thermal and mechanical design aspects of PMSG is fully studied (in section five). In section six, a considerable research contribution is successfully reached in the area of design optimization of PMSG base on the findings of previous chapters. Finally, an experimental investigation is reported to verify a number of analytical, and numerical calculations of the proposed PMSG. Whereas, an application-oriented complex design optimization is studied for the photovoltaic system design optimization of the smart tree in section seven. At last, the major outcomes of the research are completely highlighted to present the work's achievement of the project. Additionally, a short discussion is given to bold the future research development of the study in section nine.

1.1 Renewable Energy Systems

Due to higher energy efficiency in renewable energy (RE) systems, the increasing global of RE in the developing countries was impactful during the last decades. In a climatically sustainable way, use of RE is the only solution theoretically to provide the needed energy demand of the world. The today's energy supply relies dominantly on fossil fuel-based energies. The reason for it

is because of their ready availability, in which the energy can be used wherever customer demand will be. However, the availability of the most RE sources fluctuates. Therefore, the availability of RE supply has to be improved to be fully available in any form of energy, where large energy storage systems can significantly help.

Solar energy as the largest resource by 1.08×10^{18} kWh (annually) which means approximately ten thousand times larger than the annual global primary energy demand itself. There are two major ways to use solar energy, direct or indirect. The direct implementation of solar energy requires technologies:

- Solar thermal power plants
- Photovoltaics, solar cells for electricity generation (which is utilized in this research)
- Photolysis systems for fuel production
- Passive solar heating systems
- solar collectors for water heating

Solar photovoltaic (PV) power generated the capacity of 4,669 MW by 2016 in Spain. In 2017, the country was awarded 3,909 MW out of 3000 MW based on 2020 roadmap of RE's development.
Indirect use of solar energy is based on natural processes of solar energy transform into other types which can be listed as:

- Wind (which mainly the focus of this dissertation as primary RE resource)
- Evaporation, precipitation, water flow (e.g. Hydro-electric power)
- Wave movements
- Ocean currents
- Melting of snow
- Biomass production
- Heating of Earth's surface and the atmosphere

More than a century ago, wind power was a dominant energy supply for many countries. In the market, the earliest wind generators in order to transform wind energy into electricity type of energy were known in the early 1980s in Denmark and the US. In Spain, the total installed wind generator power capacity is considerably under development, in which the wind power generation has surpassed all other electricity sources in Spain. By the year 2015, the country was ranked the fifth biggest producer of wind power with 23,031 MW in the world, providing 19% of the electricity consumed in the country via wind power energy. Table 1.1.1 illustrates the installed wind power capacity of Spain from 2008 to 2015. Hence, the country has a remarkable potential to develop RE power generation, therefore, the influence of application along with technology development can be carried out for future RE-based investigations. Base on the range of power and level of noise, the investigation can be recognized as urban and non-urban environment projects, where the investigated project of this study dealt with small power generation and very low level of noise production to be considered an urban environment project in the city of Barcelona.

Table 1.1.1 Installed wind power capacity development between 2008 to 2015 throughout Spain.

Rank	Region	2008	2009	2010	2015
1	Castile and León	3,334.04	3,882.72	4,803.82	5,560.01
2	Castile-La Mancha	3,415.61	3,669.61	3,709.19	3,806.54
3	Andalusia	1,794.99	2,840.07	2,979.33	3,337.73
4	Galicia	3,145.24	3,231.81	3,289.33	3,314.12
5	Aragon	1,749.31	1,753.81	1,764.01	1,893.31
6	Catalonia	420.44	524.54	851.41	1,267.05
7	Valencian Community	710.34	986.99	986.99	1,118.59
8	Navarre	958.77	961.77	968.37	1,003.92
9	Asturias	304.30	355.95	355.95	518.45
10	La Rioja	446.62	446.62	446.62	446.62
11	Murcia	152.31	152.31	189.91	261.96
12	Canary Islands	134.09	138.34	138.92	165.11
13	Basque Country	152.77	152.77	153.25	153.25
14	Cantabria	17.85	17.85	35.30	38.30
15	Balearic Islands	3.65	3.65	3.65	3.68
Total (MW)		16 740.32	19 148.80	20 676.05	22,988.00

1.2 State of art on Permanent Magnet Synchronous Generators (PMSGs)

The history of PM machines began by J. Henry, H. Pixii, and W. Ricthie in the 19th century and the overbearing concept was leading permanent magnets (PMs) instead of the electromagnetic excitation into the machine to gain efficiency. However, the output power has strongly restricted because of the poor quality of hard magnetic materials then. In 1934, a needful invention in order to improve the hard-magnetic materials characteristics has been done by Bell Telephone Laboratories and afterward an industrial basis by the availability of Alinco provided the first PM material has industrially produced. Therefore, Alinco due to their high flux density and notable energy production has hastily injected to power applications such as electric machines. However, their low coercive force caused their use to the relatively constant current application [3-4].

In 1951, a significant industrial-oriented contribution of the design of PM alternators where the design of stator and rotor, and specific design and operation aspects of Alinco PM machines have been discussed by R. M. Saunder and R. H. Weakley [3][5].

In the mid-1950's, hard ferrite (ceramic) has found its way into countless applications (such as electric machines) and reputed as an expensive class of permanent magnet materials. Their high coercive force able them to withstand the conventional levels of armature reaction without any risk of demagnetization and many automotive motors have intensively and cursory been converted ferrite excitation [5] [6].

In the 60's, development of rare-earth PMs has successfully rolled into PM excitation applications. The first publications on hard ferrite magnets and also explicating electrical apparatus by D. J. Hanrahan and D. S. Toffolo during 1960 decade although hard ferrite magnets have been introduced about 10 years before [3] [7-9].

In the early 1970s, the early rare-earth PM has developed by Albert Gale and Dilip K. Das of Raytheon Corporation with an alloy of Samarium and Cobalt (known as SamCo). Their flux density as high as the Alinco class with a higher coercive force than the ferrite class which outcomes in energy density that has never been seen. However, the high cost of them has been seen as the main disadvantage [3][5][9].

In 1982 by General Motors and Sumitomo Special Metals, the second generation of rare-earth PMs which was made of Neodymium Iron and Boron (known as NdFeB) was developed. Their better magnetic characteristics and also less expensive than SamCo have interestingly rolled them into PM machines due to offered potential to compete with conventional motors in the industry. By Fig. 1.2.1, the energy production through its evolution during the 20th century and flux density of discussed materials have been shown in [3] [5] [7] [11].

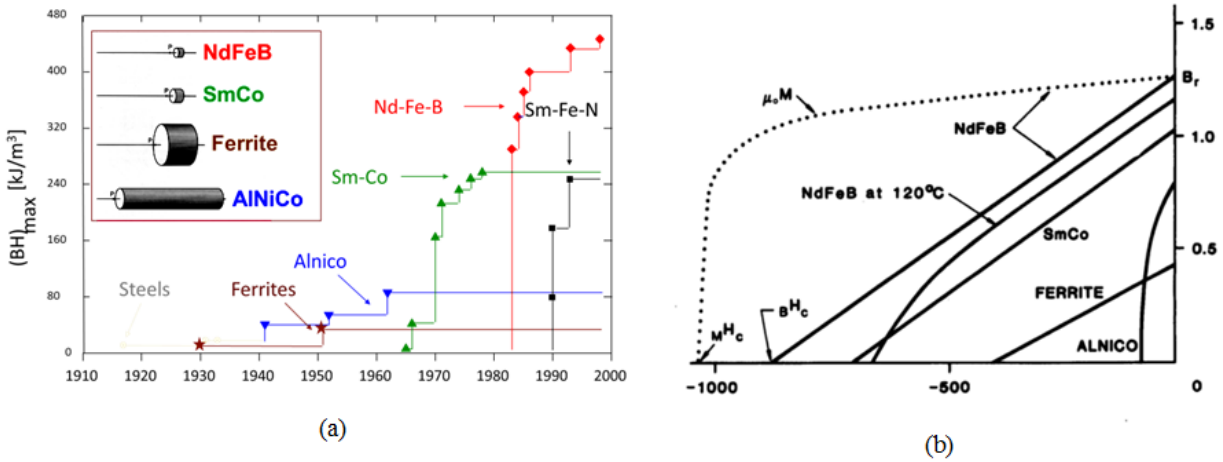

Fig. 1.2.1 Magnetic characteristics of discussed materials by their a) energy production, and b) magnetic flux density.

Regarding the emergence of modern ferrites and NdFeB magnets, PM machines are being increasingly employed where high efficiency, simplification of construction and maintenance, as well as more significantly, losses are of concern. However, gaining high efficiency needs a proper design, the efficiency of a PM generator is higher than any other kind of rotating generators. In fact, the field ohmic losses of wound field or synchronous generators are eliminated while PMs have used into the design. In addition, the lower armature current than excitation current which drawn from the energy source via induction or reluctance generators [3] [5] [8] [12].

In terms of simplification of construction and maintenance, the simplified assembly process yields greater capability in order to automate assembly methodologies. Materiality, the multi-stage procedure of the wound field coils, insulation damage to the coils and field coil insulation failures (which lead emergency repairs) of other types of rotating generators yield more complexity and maintenance costs than PM generators [8].

Indeed, since PM generators employed the PMs for providing excitation current (uses to magnetize the iron parts), a considerable reduction of the stator current can be achieved thereby perfectly decreasing the losses as an important concern. In

PM synchronous generators, the flexibility has offered to designer through the use of PMs which has led to the development of different types and class of PMSG rotor configurations [3][8].

In 1949, rotor configuration background started with classical type (which included salient poles, laminated pole shoes, and a cage winding) when the first successful construction of a PM rotor for small synchronous machines rated at high frequencies was patented by F.W. Merrill (US patent 2543639) for General Electric. It is a four-pole motor similar to the two-pole machine shown in Fig. 1.2.2. In addition, the laminated external ring has deep narrow slots between each of the PM poles Fig. 1.2.2. The machine is self-starting because of cage rotor winding. The leakage flux generates by the PMs can be adjusted by changing the width of the narrow slots. The Alnico class of PM is protected against demagnetization due to the armature flux in starting and reversal goes via the laminated rings and narrow slots eliminating the PM. The PM is mounted on the shaft with the assist of an aluminum or zinc alloy sleeve. The thickness of the laminated rotor ring is chosen such that its magnetic flux density is almost 1.5 T when the rotor and stator are assembled while magnetic flux density in the rotor teeth can be up to 2 T [7].

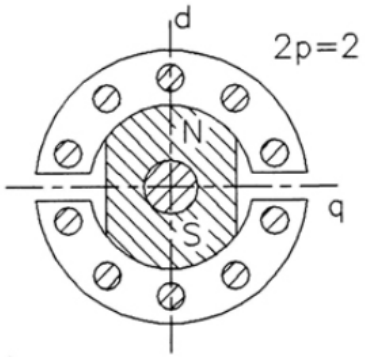

Fig. 1.2.2 classical rotor configurations for PM synchronous generators.

Latterly, the surface-mounted magnet (known as SPMSM) machines that magnetize PMs radially or sometimes circumferentially that can be seen in Fig. 1.2.3-a. An external high conductivity non-ferromagnetic cylinder is sometimes employed which protects the PMs against the demagnetizing action of armature reaction and centrifugal forces, also provides an asynchronous starting torque and operates as a damper. If rare-earth PMs are used, the synchronous reactance's in the *d*- and *q*-axis are practically the same. This type of rotor configuration has gradually been employed for wind generator applications. Additionally, many different types of rotor configurations have been designed for various desired electromagnetic performance and applications presented in Fig. 1.2.3-b-c-d-e-f-g-h-k. In contrast of the rotor topology of SPMSM (Fig. 1.2.3-a), Buried PM configuration types (Fig. 1.2.3-b-c) offer smaller air-gap flux density than the remanence magnetization, simple generator construction, small armature reaction flux, and damper in form of conducting sleeve [8] [11].

Base on demand of the application, various topologies in terms of exterior/ or interior rotor, distributed/ or concentrated winding, radial/ or axial flux, double rotor/ or stator, and single layer/ or double layer concentrated winding have been recently studied.

Today, the only aspect to use geared-drive is when the application needs a low rotating speed (1000 to 3000 rpm) a high torque. However, electric machines designers offered another alternative into the market recently which calls direct-drive that carries many advantages over geared-drive which can be shortlisted as higher reliability, less maintenance, higher efficiency, less use of active materials, and less noise [5] [12]. Fig. 1.2.4 illustrates the load to converter block diagram as the whole, where conventional geared-drive (Fig. 1.2.4-a) is compared to the direct-driven system (Fig. 1.2.4-b).

1.3 Survey of Solar Photovoltaic Modules

The word of photovoltaic (PV) is made up two words from Greek-Italian languages which means the direct conversion of sunlight to electricity. In 1954, Bell Laboratories has been produced the first solar cell with five percent efficiency based on Shockley invention on the p-n junction model. By the years, researchers have improved the efficiency (approximately 25 percent) and also have reduced the cost. Though knowing that PV systems are able to provide the entire electricity demand of each country in the world. In the 1990s, tens of thousands of grid-connected systems were installed in mainly Germany and Japan. In terms of materials used, later work on Se, Cu-Cu_2O, PbS, TlzS, AgzS, and many other materials known as photoconductors or phosphors showed which the photovoltaic influence is very common in some specific type of material. Afterward, a photovoltaic effect has been discovered in material such as silicon, GaAs and other material and its usefulness for technical applications such as solar energy was later developed.

Today, there are about six different types of solar PV modules in the market as:

- Crystalline Silicon
- Monocrystalline
- Polycrystalline
- String Ribbon
- Thin-Film Solar Panels
- Building Integrated Photovoltaics

Crystalline Silicon (c-Si), almost 90% of the World's photovoltaics today are based on some variation of silicon. [13-14] In 2011, approximately 95% of all shipments by U.S. manufacturers to the residential sector have been crystalline silicon solar panels [14]. The silicon employed in the PV takes many forms. The significant difference is the purity of the silicon. However, silicon purity means, the more perfectly aligned the silicon molecules are, the better the solar cell will be at converting solar energy into electricity. The efficiency of solar panels goes hand in hand with purity, but the processes used to improve the purity of silicon are costly. Hence, efficiency enhancement should not be the major objective. While cost and space-efficiency are also important factors. They have laboratory energy conversion efficiencies over 25% for single-crystal cells as well as more than 20% for multi-crystalline cells. But, industrially produced solar modules currently achieve efficiencies ranging between 18% to 22% under standard test conditions (STC).

Monocrystalline Silicon, this type of solar cells is made out of silicon ingots, which are cylindrical in shape. To optimize performance and lower costs of a single monocrystalline solar cell, four sides are cut out of the cylindrical ingots to make silicon wafers. The difference in the way mono- and polycrystalline solar panels look is that polycrystalline solar cells seem perfectly rectangular with no rounded edges. This type can be popular because of the following advantages, (1) Monocrystalline solar panels have the highest efficiency rates because they are made out of the highest-grade silicon. The efficiency rates of monocrystalline solar panels are normally about 15-20% [13-14]. (2) Monocrystalline silicon solar panels are space-efficient. Since these solar panels yield the highest power outputs, they also require the least amount of space compared to any other types. Monocrystalline solar panels produce up to four times the amount of electricity as thin-film solar panels. (3) Longevity, these solar panels lifetime is the longest, and because of this fact, most solar panel manufacturers put a 25-year warranty on their monocrystalline solar panels. (4) Tend to perform better than similarly rated polycrystalline solar panels at low-light conditions. Additionally, they have several disadvantages which can be given as (1) Monocrystalline solar panels are the most expensive. (2) In case the solar panel is partially covered with shade (shading issue), dirt or snow, the entire circuit can break down. (3) The Czochralski process is used to produce monocrystalline silicon which results in large cylindrical ingots. Four sides are cut out of the ingots to make silicon wafers. Therefore, a considerable amount of the original silicon ends up as waste. (4) Monocrystalline solar panels tend to be more efficient in warm weather. Performance suffers as temperature goes up, however less so than polycrystalline solar panels.

Polycrystalline (p-Si), the first solar panels based on polycrystalline silicon which have been introduced to the market in 1981. Unlike Monocrystalline-based solar panels, polycrystalline solar panels do not need the Czochralski process. Raw silicon is melted and poured into a square mold, which is cooled and cut into perfectly square wafers. The following two major advantages can be addressed, (1) the process used to make polycrystalline silicon is simpler and cost less. The amount of waste silicon is less compared to monocrystalline. (2) Polycrystalline solar panels approaching to be considered slightly lower heat tolerance than monocrystalline solar panels. In high-temperature applications, they perform slightly worse than monocrystalline solar panels technically, in which heat affects the performance of solar panels and shorten their lifespans. In addition, they have a number of disadvantages which are: (1) their efficiency of is normally 13-16%. Due to of lower silicon purity, polycrystalline solar panels are not quite as efficient as monocrystalline solar panels. (2) Lower space-efficiency. Typically, they need to cover a larger surface for output the same electrical power as you would with a monocrystalline silicon solar panel. Although, this does not mean every monocrystalline solar panel perform better than those based on polycrystalline silicon. (3) Monocrystalline and thin-film solar panels have more aesthetically pleasing since they offer a more uniform look compared to the speckled blue color of polycrystalline silicon [14].

String Ribbon, they are also produced out of polycrystalline silicon. String Ribbon is the name of a manufacturing technology which produces a form of polycrystalline silicon. Temperature-resistant wires are pulled by molten silicon, which results in very thin silicon ribbons. Solar panels made with this technology seems like traditional polycrystalline solar panels. The dominant advantage of them is because they are cheaper in material cost, the manufacturing of String Ribbon solar panels only uses half the amount silicon as monocrystalline manufacturing. However, (1) manufacturing of String Ribbon solar panels is considerably more energy extensive and more expensive. (2) Low efficiency about 13-14%. In research laboratories, researchers have been claimed the efficiency of String Ribbon solar cells as high as 18.3%, they reached [13-14]. (3) The lowest space-efficiency of any of the main types of crystalline-based solar panels.

Thin-Film Solar Cells (TFSC) or Photovoltaic Cells (TFPV), the first type of solar panel which has bypassed one or several thin substrates of PV materials to one layer in terms of production. There are four different kinds of TFSCs base on their characteristics which are known as:

- Amorphous silicon (a-Si), for low power applications, for example, pocket calculators
- Cadmium telluride (CdTe), which is the most cost-efficiency type
- Copper indium gallium selenide (CIS/CIGS), the most efficient (normally 10 to 12%)
- Organic photovoltaic cells (OPC)

Regarding efficiency, different kind of TFSC technology provides between 7 to 13% module efficiency which is expected to reach around 10 to 16% in the future. They have a number of advantages as, (1) potentially cheaper to manufacture than crystalline-based solar cells because of the simplicity of mass-production. (2) More flexible (physically) which makes many more possible new applications. (3) Better performance during high temperatures and shading. (4) In projects where the choice of PV module has no impact on the space used, they are more applicable. Moreover, like other types of solar panels, there are a number of disadvantages as well such as, (1) needs more space than other types to generate the same amount of power. (2) Higher PV equipment costs. (3) Faster degrade, in comparison with other typical types such as Monocrystalline silicon and polycrystalline PV modules.

1.4 Objectives and Main Contributions

The overall objectives of the research project are mainly analytical and numerical-based studies which considerably affect the performance of AC PMSG. The attention was focused to maximize the output power and efficiency via enhancing the electromagnetic performance of the machine that resulted in the machine's losses reduction through both analytical and finite element analysis (FEA), along with experimental verifications. Additionally, the mentioned improvements are carried out using well-known optimization methodologies. To achieve these goals, the foundations of these models are illustrated and verified in this thesis. Therefore, the main objectives of the design optimization of PMSG are listed as:

1) Define and build a parametric model of 5 kW wind generator using double-layer fractional-slot concentrated winding (FSCW) with outer-rotor, closed-slot topology.
2) MMF harmonic analysis is done to find out the most suitable slot/ pole combination for non-overlapping double layer FSCW.
3) Develop tools and models to investigate the performance of such machines at no-load and load conditions.
4) Evaluate 3-D and 2-D electromagnetic performance of PMSG through steady-state and transient analysis using FEA.
5) Investigate the impact of different Halbach array magnetization topologies in the magnetic flux density distribution and load identification.
6) Analytical Iron loss computation development, where the proposed models are verified by FEA.
7) Finding the most sensitive design parameters via local and global sensitivity analysis.
8) Programming a multi-objective scheme based on dual-response surface optimization method (DRSM) coupled with Booth's algorithm using simulated annealing (BA-SA) method to improve output power and minimize the cost of material used.
9) Global sizing multi-objective optimization using DRSM with mixed-resolution central composite design (MR-CCD) to maximize the efficiency.
10) Study and develop the thermal lumped circuit of the generator for steady-state analysis.
11) Vibro-acoustic optimization using a skewing technique.
12) Simulate transient behavior of thermal distribution in the model.
13) Validate each achieved objective through experimental measurements on a full-scale prototype.
14) Future research disclosure regarding our findings, in which a considerable improvement is studied.

The investigation has resulted in the following main contributions:

1) The influence of coil conductor turns and their connections on the electromagnetic behavior of the generator
2) Definition and evaluation of different Halbach-based magnetization patterns in the generator's major outputs such as torque, power, etc. These findings are considered to be used in daily engineering calculation routines.
3) Load identification of a full-scale generator, where different patterns of magnetization are carried out.
4) Analytical development of IEM-Formula to compute iron loss with high accuracy, where the outcome of the research can be highly cited in the future.

5) An advanced time domain iron loss computation with consideration of bulk conductivity is proposed. This methodology brings the most accurate iron loss computations and predictions. The findings of this research are achieved for the first time.
6) Power maximization using DRSM which is coupled with BA-SA to reduce the cost of the generator. The work has been successfully done with a significant outcome, where the accuracy of different design functions (such as FFD, BBD, CCD, and mixed resolution robust design (MR-RD)) are compared and finally the most accurate ones are reported. Also, the FEA-based achievements were tested experimentally.
7) Global sizing optimization using DRSM based on MR-CCD is carried out to enhance the efficiency map of the generator, in which FEA and experimental measurements verify the findings. The improvement is highly considered effective and the scenario to reach the target can be used by engineers.
8) Discovered an innovative natural air-cooling system model for the temperature distribution reduction in the stator core.
9) Minimized the audible magnetic noise (sound power) using optimal skewing angle and pole number techniques, where the radial velocity, vibration, and modal structure contributions to the sound power and pressure were studied. A remarkable finding regarding the skew slice number and its effect on the magnetic noise radiation.
10) US Patent on the novel structure (as part of the future investigation of the thesis).

The solar photovoltaic module research with a number of objectives and main contributions also can be listed as given:

1) Definition and description of the solar PV module based on its characteristics such as V-I and P-V curves.
2) Implementing an MPPT controller based on an advanced perturb & observe (P&O) algorithm.
3) Providing experimental measurements of the weather and horizon conditions on the coast of Barcelona city as valuable input data.
4) 3-D modeling of the solar PV module using PVsys and PV*Sol software.
5) Evaluate the nominal operating cell temperature (NOCT) for a 60-cell module.
6) Studying the impact of shading effect (partial and complete) on the module's output.
7) Influence of the shading effects on the load.
8) Output power maximization based on the module losses is defined to be maximized using a Pareto-optimization.

The main contributions of the solar PV system investigation can be summarized in:

1) Impact of shading effects of 20% to 100% was examined on the I-V and P-V curves.
2) Used advanced MPPT controller has resulted in power maximization significantly.
3) Based on our findings, the NOCT investigation proves that cell temperature varies 5 ˚C lower due to having an open-circuit test, in contrast with the grid-connected temperature distribution.
4) Effective output power also was optimized using a Pareto-based design optimization.

1.5 List of Utilized Materials

A short list of material used is provided, in which the research dealt with the wind generator design, solar photovoltaic (PV) systems, and power electronics. The consumed materials are classified into three clusters:

- Wind Permanent Magnet Synchronous Generator (PMSG)

Low-voltage PMSG used mainly for small-scale wind power generation applications have been employed as a workhorse for recent years. This section presents the material used to manufacture such a generator, illustrated by a prototype successfully built. The prototype has a 36 slots/40 poles machine. The rated power is 5 kW.

1) Lamination steel of M400-50A.
2) Stator coils, copper strands.
3) Insulation for the winding of the stator cores, Plastic strips which protect the PD-protection and ease the coil insertion.
4) Permanent magnet (PM), NdFeB.
5) Ferrite Magnet FB14H.
6) Resistance temperature detectors (RTDs).
7) Search-coils for flux measurement.

8) Six temperature sensors in the stator winding, stator and rotor cores, PM, and bearings.
9) Magnetic Antennae (including 3-D printed structure from polymer material).
10) Encoder.
11) DC motor as Load.
12) Torque/ speed transducer.
13) 3-phase inverter.
14) IGBT pack & driver.
15) dSPACE 1104.
16) Laboratory desktop computer.
17) Yakogawa WT 3000.
18) Voltage and current circuit measurements.
19) Switches.

- Solar PV system

1) Solar PV module 60 cells, 150 W, 12 V, Monocrystalline panel.
2) Infrared (IR) thermo-camera.
3) Ohmic load.
4) Analog to digital converter.
5) DC-DC Buck converter (SEMITEACH B6U+E1CIF+B6CI converter with IGBT switches).
6) NTC sensors.
7) Maximum power point tracking (MPPT) controller.
8) Laptop to store experimental data.
9) DC motor of 250 W (MotorSolver DCMOT8077).

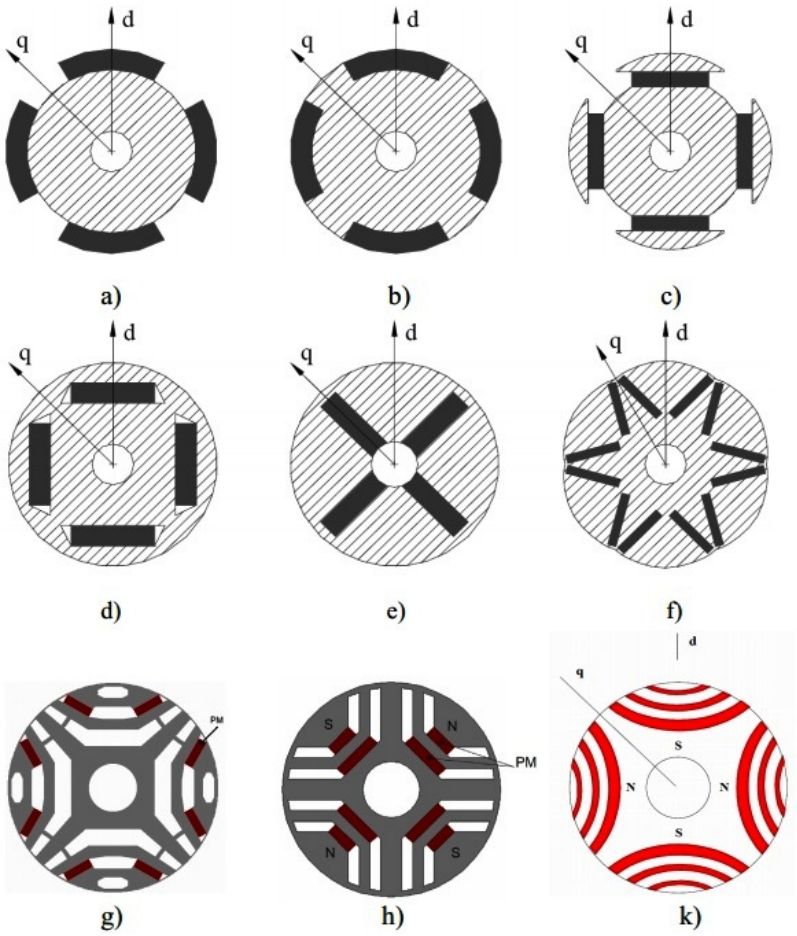

Fig. 1.2.3 Rotor configurations for PM synchronous machines: a) SPM), b) IPM, c), d), e) rotor with buried (spoke) magnets symmetrically distributed, f) V-shape buried magnets asymmetrically distributed, g), h), k) PM assisted synchronous reluctance machines [11].

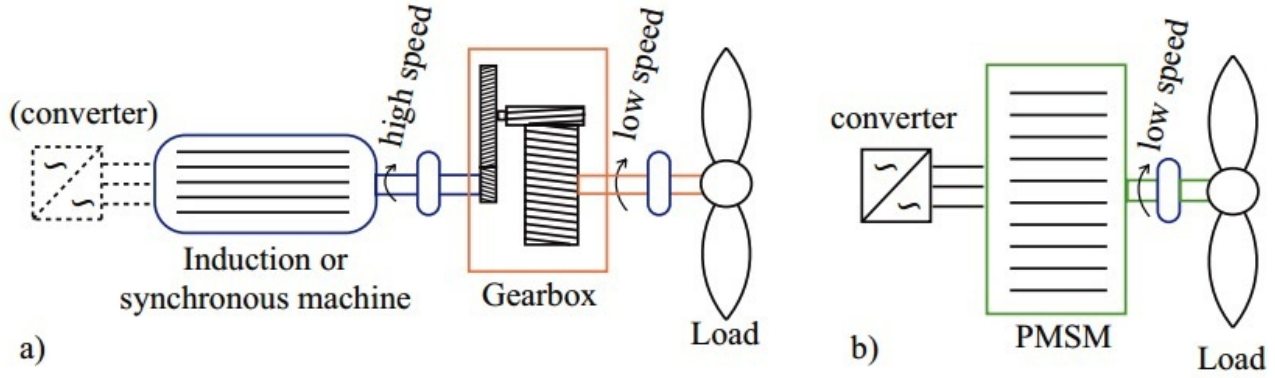

Fig. 1.2.4 Load to converter block diagram as whole, a) geared-drive and b) direct-drive [12].

1.6 Publications

1) Pedram Asef, Ramon B. Perpina, M. R. Barzegaran, and Andrew Lapthorn "*A 3-D Pareto-Based Shading Analysis on Solar Photovoltaic System Design Optimization in Urban Environment*," ***IEEE Trans. On Sustainable Energy***, Status: DOI: 10.1109/TSTE.2018.2849370, **published in early access format**, Jun. 2018.

2) Pedram Asef, Ramon Bargallo Perpina, M. R. Barzegaran, Andrew Lapthorn, and Daniela Mewes "*Multi-objective Design Optimization Using Dual-Level Response Surface Methodology and Booth's Algorithm for Permanent Magnet Synchronous Generators*". ***IEEE Trans. on Energy Conversion***, Vol 32, No. 2, pp. 652 - 659 DOI: 10.1109/TEC.2017.2777397**,** 2018.

3) Pedram Asef, Ramon Bargallo Perpina, and M. R. Barzegaran, "*Global Sizing Optimization Using Dual-Level Response Surface Methodology for Surface Mounted Pole Synchronous Machines*," pp. 1-8. ***IET Electric Power Application***, DOI: 10.1049/iet-epa.2017.0810, Vol. 12, No. 5, pp. 684 - 692, 2018.

4) Pedram Asef, Ramon Bargallo Perpina, and M. R. Barzegaran, "*An innovative of Natural Air Cooling System Technique for the Exterior Rotor PM Synchronous Machine*". ***Electric Power Research Systems, Elsevier Journal***, DOI: https://doi.org/10.1016/j.epsr.2017.07.0, pp. 1 – 8**,** 2018.

5) Pedram Asef, Ramon Bargallo Perpina, M. R. Barzegaran, Andrew Lapthorn, and Daniela Mewes, "*Load Identification of Different Halbach-Array Topologies on the PM Synchronous Generators Using the Coupled Field-Circuit FE Methodology*" ***Electric Power Research Systems, Elsevier Journal***, DOI: https://doi.org/10.1016/j.epsr.2017.08.0, pp. 1 – 8, 2018.

6) Pedram Asef, Ramon Bargallo, M. R. Barzegaran, J. Dong, A. Lapthorn, and O. A. Mohammed, "*An Advanced Quasi-FEA Technique on Iron Losses Prediction for Permanent Magnet Synchronous Machines*," ***Progress in Electromagnetics Research (PIER) Journal***, Vol. 81, pp. 101-113, March 2018.

7) Pedram Asef, Ramon Bargallo Perpina, and M. R. Barzegaran, "*Electromagnetic-based Calculations of Different Halbach-Array topologies on the Exterior Rotor PM Synchronous Machines*". pp. 1 - 8. ***Springer Journal of Electrical Engineering***, type: Scientific paper. DOI: **doi.org/10.1007/s00202-017-0656-6**, 13/11/2017.

8) Pedram Asef, Ramon Bargallo Perpina, S. Moazemie, and Andrew Lapthorn, "*Mechanical Rotor Shape Multi-Objective Design Optimization for Double-Stator Permanent Magnet Synchronous Motors*". pp. 1 - 8. ***IEEE Trans. On Energy Conversion***, type: Scientific paper, status: **accepted to be published**, 2018.

9) Pedram Asef, *et al*. "*Global Benefits of Open Research*" Chapter Book, ISBN 978-3-03897-009-5 (Pbk); ISBN 978-3-03897-010-1 (PDF), DOI: https://doi.org/10.3390/books978-3-03897-010-1, MDPI, Switzerland, Nov. 2018.

10) Pedram Asef, Ramon Bargallo Perpina, and Andrew Lapthorn, "*A Time Domain Rotational Iron Losses Computation with Bulk Conductivity Consideration for Permanent Magnet Synchronous Machines*," ***IET Electric Power Application***, pp. 1-8, Status: **accepted to be published**, 2018.

11) Pedram Asef, Ramon Bargallo Perpina, and Andrew Lapthorn, "*Magnetic Noise Minimization using Skewing Technique by Multi-Slice Subdomain Modeling for Permanent Magnet Synchronous Generators*". pp. 1 - 8. ***Journal of Sound and Vibration***, type: Scientific paper, status: **under review**, 2018.

12) Pedram Asef, Ramon Bargallo, and Andrew Lapthorn, "*Optimal Pole Number for Magnetic Noise Reduction in Variable Speed Permanent Magnet Synchronous Machines with Fractional-Slot Concentrated Windings*". pp. 1 - 8. ***IEEE Trans. on Transportation Electrification***, type: Scientific paper, status: **under review**, 2018.

13) Pedram Asef, Payam Niknejad, M. R. Barzegaran, Ramon Bargallo, and Andrew Lapthorn, "*Correlation of Solar Power Prediction Considering the Nominal Operating Cell Temperature under Partial Shading Effect*". pp. 1 - 8. ***IEEE Trans. on Engineering Management***, type: Scientific paper, status: **under review**, 2018.

14) Pedram Asef, Ramon Bargallo, and Andrew Lapthorn, "*IEM-Formula Development on Iron Loss Prediction During the Flux Weakening for Permanent Magnet Synchronous Machines*," ***MDPI-Machines Journal***, status: **published**, DOI: 10.3390/machines5040030, Vol. 5, No. 4, 2017.

15) T. Agarwal, P. Niknejad, P. Asef, and M. R. Barzegaran, "*A Time Sensitive Networking-Enabled Wide Area Monitoring System for Microgrid*," ***Sustainable Energy, Grids and Networks***, status: **under review**, 2018.

16) Pedram Asef, and Ramon Bargallo Perpina, "*Design of High-Speed PM Synchronous Motor—Thermal and Mechanical Analyzes Study for Aerospace Retraction Wheel Motor Application*", ***Journal of Energy and Power Engineering***, Vol. 10, DOI: 10.17265/1934-8975/2016.04.007, ISSN 1934-8975, USA, 30/04/2016. Status: **Published,** 2016.

17) Pedram Asef, and Ramon Bargallo Perpina, "*Losses calculation of an Aerospace Retraction Wheel Motor with regarding to Electromagnetic-field analysis investigation*". 10 - 3, ***Journal of Energy and Power Engineering***, DOI:10.17265/1934-8975/2016.03.006, ISSN 1934-8975, USA, 20/03/2016, status: **Published,** 2016.

18) Pedram Asef, Ramon Bargallo Perpina, B. Tisgua, and A. Babaiean, "*An Alternative Organic Growth through Acquisitions Investigation on Wind Energy*". pp. 1 - 4. ***Elsevier Energy Journal***, 15/12/2016. Type: Scientific paper Format: **Journal**. ***Elsevier Journal, Energy Procedia***, 115 (2017), pp. 298-307, status: **Published**, DOI: https://doi.org/10.1016/j.egypro.2017.05.027, 2017.

2. Electromagnetic-based Design of Polyphase PMSG

In general, the polyphase synchronous machine has a number of coils that are wounded around the periphery of the stator, and they have been connected as a winding of the proper number of phases (which is selected $m = 3$ in this research) and the number of poles. The number of poles is determined through both parameters, supply frequency and the nominal speed of rotor rotation. In fact, these parameters have such a relationship as given:

$$f = \frac{np}{120} = \frac{\omega_m p}{4\pi} \tag{2-1}$$

where f, n, p, and ω_m are frequency (Hz), rotational speed (rev/min or rpm), pole-pair number, and angular velocity (in rad/sec). In the stator (or armature) winding the supplied excitation current flows through coils which are displaced in time corresponding to 120 degrees for a three-phase (m=3) system. Hence, a magneto-motive force (known as MMF) produces a flux density in the airgap for each phase winding, in which the magnitude of each phase (A, B, or C) flux density pulsates with time along the axis of the particular phase winding. A sinusoidal distribution in space of each of the phase flux density waves is the primary objective of the magnetic circuit design in the electrical machine. The phase waves combine to form a net flux density in the airgap by $B(\theta, t)$ that is defined as:

$$B(\theta, t) = \frac{m}{2} B_m \cos(\theta \pm \omega t) \tag{2-2}$$

where θ, t, B_m, and m are the electrical space angle (in degree), time (s), the maximum magnitude of flux density waveform (T), and phase number, respectively. The resulting average output torque is valuable only when both stator and rotor fields are stationary toward each other.

In overall, the electromagnetic performance of the PMSG relies on a number of parameters such as armature inductances, slot leakage, harmonics on the distributed flux, field winding, leakage flux, back electromotive force (EMF), equivalent circuit, average output electromagnetic torque, torque ripples, cogging torque, output power, impact of inverter, and etc. These electromagnetic-based factors are considered to be discussed in this chapter.

2.1 Surface Mounted Permanent Magnet Synchronous Generator (PMSG) and its Features

The early attempts to design permanent magnets machines mainly was focused on the electromagnetic excitation replacement with the alternative permanent magnet instead of direct current via slip rings or via shaft mounted brushless exciter with rotating ac to dc converter. Also, they are known as a source of magnetic field to increase the efficiency of the electromagnetic behavior of the system. On the other hand, the material invention (rare-earth magnets) could reserve a high flux density and considerable energy product which tend them to be utilized in many applications nowadays such as power generation, electric vehicle, aerospace, and etc. Simply, PMSGs with an appropriate design offers the following main advantages in comparison to any other type of machines:

1) High efficiency
2) Simple construction and maintenance
3) Reasonable High-power production (to weight and size ratios)
4) High dynamic behavior
5) Shape optimization flexibility

In fact, the field ohmic losses of wound field direct current (DC) or synchronous machines are significantly decreased by using permanent magnets. In addition, the armature current is lower than the excitation current drawn from the energy source using induction and reluctance machines at the same rated speed and power. It is worthy to mention that, more than half the electrical energy is consumed via electrical drives in another type of machines such as induction and reluctance in comparison to permanent magnet synchronous machines (PMSMs). Whereas the automated assembly techniques are applied in the industries, thus PMSMs because of their simpler structure are more beneficial for the investments these days. From efficiency/lower running cost point of view, this type of machines is economically beneficial especially in the low-speed applications (such as small-scale wind turbine), in which field ohmic losses plays a large part of the total losses. Even though permanent magnets are known as the major cost of PMSMs, they are also under production due to their preferable over electromagnetic excitation for high-speed applications by Mega-watt range today. The resulting high energy densities of the rare-earth magnets (such as NdFeB) have direct affect the field

loss (originated in the stator) reduction which reduces the heat from the stator core. Therefore, the need for a cooling system is decreased in many applications such as automotive. Due to higher-level of magnetic flux density and also the lower inertia of PMSMs. They can be utilized in servo applications, positioning machines, automation, robotics, and etc. On the other hand, like any device, there are a few drawbacks which can be summarized as:

1) Expensive permanent magnet
2) Demagnetization issues
3) Temperature dependency
4) Loss of field control

Because of the material advantages, many manufacturers are today evolved to produce the permanent magnets (mainly in China by approximately global 75% ferrite magnet and 80% NdFeB), which can be available at a lower price in the future. Theoretically, a safe behavior can be provided by magnets at any operation point on the linear part of their B-H curve. However, the magnetic flux density reduction is a sign of either a partial or large irreversible demagnetization. As the third disadvantage, in case the temperature of the magnet goes beyond the magnet maximum temperature, the magnetic flux density will be affected. To keep the magnet under protection, a careful choice of magnet type and design of the PMSM and also inverter is a plus.

As the evaluation of permanent magnet materials has significantly influenced the PMSMs investment and production, Fig. 2.1 presents the trend of the innovation based on the type and maximum energy product (which is known as one of the important magnetic characteristics of magnet materials). This graph illustrates that modern NdFeB magnets produce over 400 kJ/m^3.

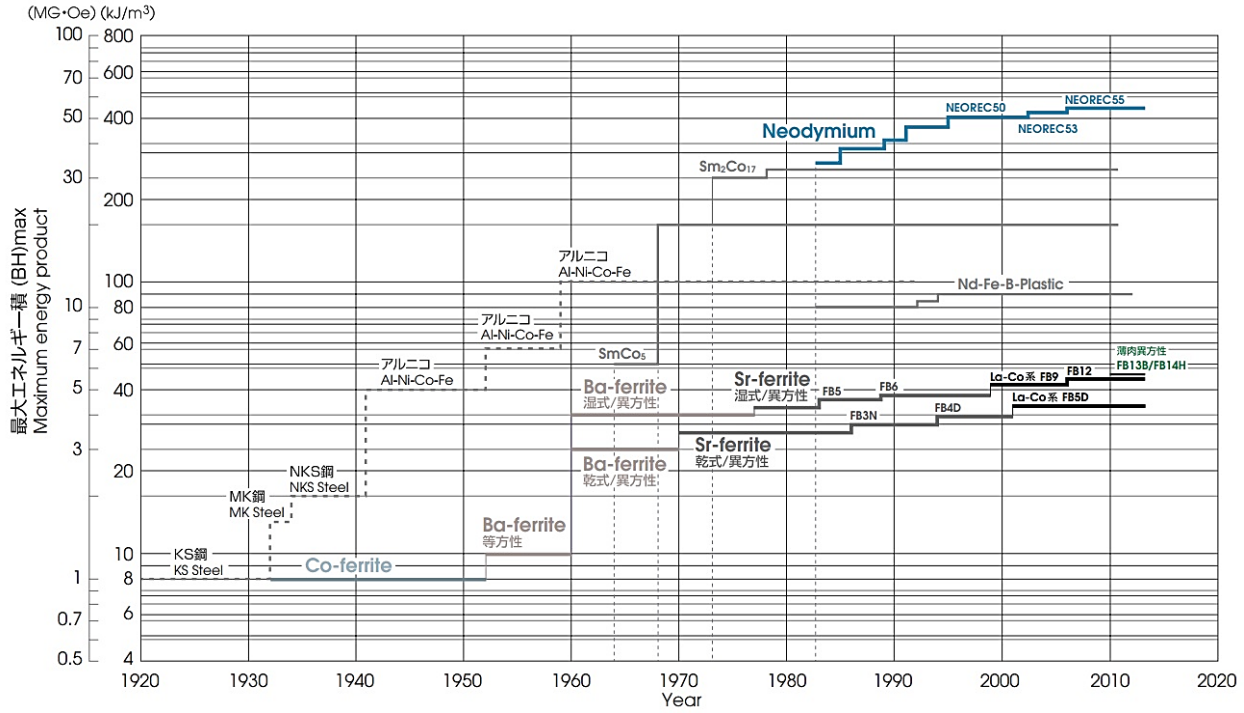

Fig. 2.1.1 Permanent magnet evaluation map from TDK Co.

To avoid any performance fault during the design procedure, the following design constraints have to be satisfied:

- Advanced efficiency calculation

The efficiency value is valuable when all loss terms are considered such as copper loss of windings and field, iron core loss, stray load loss, friction and windage loss, and exciter loss (in case the machine's shaft is driven).

- Unbalanced voltages test

This test allows the designer to ensure the designed machine performance under non-ideal condition. For instance, the supplied voltages are unbalanced which causes negative sequence currents. A torque opposite to load torque and also induce voltages by resulting heavy currents on the damper windings. Normally, voltage unbalanced is known in percent by (maximum voltage deviation from average/average voltage)*100. It is worthy to mention that the operation of PMSM under 5% voltage unbalance test is highly recommended.

- Torque locked rotor test

This test ensures that when the PMSM is supplied by nominal values of voltage and frequency, the torque bumps (pull in and out) should not be less than 100 and 175 (in percent of nominal full-load torque values), respectively. Under rotational speed between 500 to 1800 rpm for machines with the rated power of 111855 W with a power factor of 0.8. A complete rating values discussion can be found in the following of table 2-1. Where index a, b, and c are presenting values of torque applied to salient pole machines, Values of normal WK^2 of load, and rated excitation current applied, respectively. On the other hand, the effect of unbalance voltage results in the locked-rotor torque reduction.

Table 2.1.1 The locked-rotor test characteristics of synchronous machines (presented in [1])

			Torque[a] in percent of rated full-load torque		
Speed (rpm)	Horsepower	Power factor	Locked rotor	Pull-in[bc]	Pull-out
500 to 1800	200 and below	1.0	100	100	150
	150 and below	0.8	100	100	175
	250 to 1000	1.0	60	60	150
	200 to 1000	0.8	60	60	175
	1250 and larger	1.0	40	60	150
		0.8	40	60	175
450 and below	All ratings	1.0	40	30	150
		0.8	40	30	200

- Terminal voltage reduction

During starting time, basically, the peak current is flown through supply and the end-winding in order to tolerate the forces because of a large current. There are two common techniques to deal with the terminal voltage. One, using impedance in series with the machine during the start sequence. Second, the use of an autotransformer. It should be mentioned that the autotransformer utilization is much costlier than the series impedance technique. However, the autotransformer technique has considerable advantages such as removing (at a synchronous speed) the field discharge resistor circuit affects the field winding which giving motion relative to the rotating magnetic field of the armature. In other words, this technique is controllable via slip frequency (as the relay to find out a speed near synchronous speed).

2.1.1 Magnetic equivalent circuit of outer rotor PMSG

It is important to know the analytics behind the magnetic characteristics of the electrical machines for any further investigation, especially in optimization processing. However, 3-D computation model the flux densities in different parts of the machine is much more accurate. For instance, references [2-3] have proposed a non-linear reluctance network which provides the magnetic characteristics with a very small error. In this thesis, as the reluctance network is not compatible with the FE-method in terms of accuracy, thus, it is only used for the preliminary fast estimations. To understand the fundamental elements of the magnetic equivalent circuit of an outer rotor, closed-slot, PMSG, Fig. 2.1.1.1 presented a part of the non-linear reluctance network which we applied to PMSG modeling for the stator and rotor magnetic characteristics. In this graph, R_{sy} is the reluctance of the stator yoke, R_{st} is the reluctance of the stator tooth, R_{so} is the reluctance of slot opening which is zero in the used closed-slot topology, R_g is the reluctance of air-gap which it is a sum of reluctances of the physical air-gap, R_{ry} is the reluctance of the rotor yoke which is normally not large in this type of topology, F_{st} is the MMF source due to the stator currents only, F_{PM} is the MMF source due to the permanent magnet. The non-linear reluctance network can be defined iteratively as:

$$\Phi = \Re^{-1} F \tag{2-3}$$

where Φ is the magnetic flux matrix in Weber, $\Re$ is the reluctance matrix, F is the source matrix of MMF originated from the PMs and the stator phase currents ($F = F_{st}+F_{PM}$).

The reluctance matrix can be given as:

$$\Re_i = \frac{l_i}{\mu_0 \mu_r S_i} \tag{2-4}$$

where l_i, μ_0, μ_r, S_i are the length of a particular part of the PMSG modeled by a reluctance element, the permeability of vacuum, the relative permeability of the reluctance element material, and the cross-sectional area of a particular part of the PMSG with a reluctance element.

The produced total MMF due to each stator phase current and permanent magnets can be calculated using:

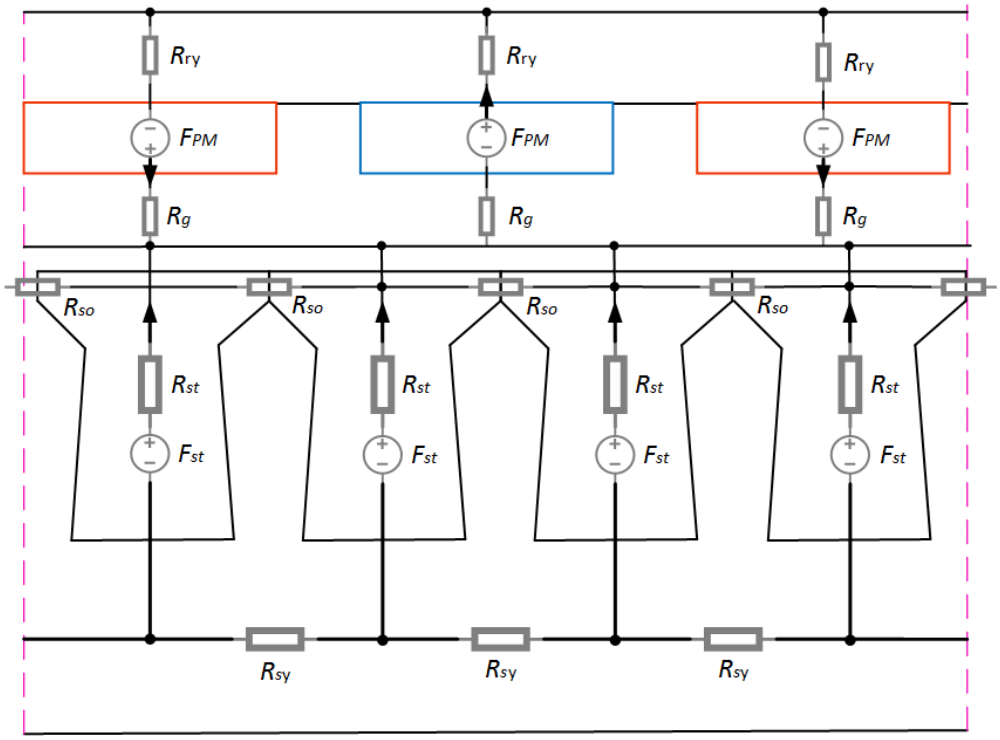

Fig. 2.1.1.1 Reluctance network over a pole-pair magnet.

$$F = F_{I,ph} + F_{PM} = N_s I + \frac{B_r l_{PM}}{\mu_0 \mu_{r,PM}} \tag{2-5}$$

where N_s, I, l_{PM} are the number of coil turns in a slot, the current via one coils turn, the thickness of the magnets.

Finally, the magnetic flux density can be solved for the particular reluctance element as:

$$B_i = \frac{\Phi_i}{S_i} \tag{2-6}$$

2.2 Winding Configuration

Since the 2000s, the researchers are developing the *m*-phase winding including of identically designed phase coils which are notched in equally along the periphery of the stator core in mostly two configuration types [4], which are commonly used for all the categories of AC machines:

- Distributed type, where the phase coils have placed into slots in the inner surface of the cylindrical stator iron.

- Overlapping type.

The stator core design consists of slots number and its shape, in which an integral value of slots-per-phase-per-pole, that is known as variable q should be defined in order to clarify the mechanical position relationship between rotor poles and stator slots at each second in time. When $q = 1$, integral-slot distributed winding is called. On the other hand, concentrated windings without any overlap of coils in the end-turn or end-winding region offer a shorter end-winding in comparison to distributed windings which technically reduces winding loss and machine's weight and also more economically. During the concentrated winding design, if the only q becomes a fraction which often known as a ratio of whole numbers, the winding topology called fractional-slot concentrated winding (FSCW). To improve low constant-power-speed-range (SPSR) characteristic of surface PMSMs because of low phase inductance (mainly at high-speed applications), PM machine flux weakening is the opportunity they provide for significantly increasing the stator inductance values by factors exceeding 5:1 [5-6].

In this study, we have used double-layer FSCW, in which one of the coil sides of each coil is in the upper layer of the slot, and the other coil side is in the bottom layer. All the coils have been rolled via an equal span. By double-layer FSCW, reaching higher winding factors with higher torque density is possible, in where weight and size are critical design parameters. It has been reported that selection of pole and slot numbers must be chosen very carefully as long as the parasitic effects occur with a certain number of combinations. These parasitic effects include cogging torque, radial magnetic forces, and alternating magnetic fields with high frequency. Based on Vogt (1996) method, a few definitions can determine whether the winding should be a 1st grade or a 2nd-grade winding (please see Table 2.2.1). These definitions are given below [7-8].

$$q = \frac{Q_s}{2p.m} = \frac{36}{40 \times 3} = \frac{3}{10} = \frac{z}{n} \tag{2-7}$$

where Q_s, $2p$, and m are the stator slot number, pole numbers, and phase number.

Table. 2.2.1 Winding definitions by Vogts' method.

Vogts' method	**1st grade**	**2nd grade**	**2nd grade**
Denominator, n	odd	Even (10)	Even (10)
t	$^{p}/_{n}$	$^{2p}/_{n} = 4$	$^{2p}/_{n} = 4$
Layer	One/ or two	One	Two
Q^*	$^{Q_s}/_{t}$	$2 \times {}^{Q_s}/_{t} = 18$	$^{Q_s}/_{t} = 9$
P^*	n	$n = 10$	$^{n}/_{2} = 5$
t^*	1	2	1

Q^* is the number of slots in a symmetrical base-winding, p^* is the number of poles in a symmetrical base-winding, and t^* is the number of base-windings in the stator winding. Base windings have the same induced voltage, phase shift angle and they may be paralleled if needed.

Fig. 2-2-2 presents the stator winding layout for all 36 slots. Fig. 2-2-2-a illustrates each phase by individual color (green, blue, and red), and thus, every phase consists of 9 coils which are grouped into 3, and each group (i.e. A_1, A_2, A_3) is displaced by 120˚e (electrical degrees) from each other, the same for other phases (B and C). It is worthy to mention that 1 and -1 at the top of each coil indicate the electrical current direction. Fig. 2-2-2-b illustrates the complete voltage vector diagram of the stator core, in which the slot numbers are shown in order to specify the voltage vector of each specific notched-in-coil. Fig. 2-2-2-b illustrates a voltage vector diagram (or star of the slot) for the surface PMSG with 36 slots and 40 poles, where electromotive force (EMF) and the fundamental winding factors have been calculated. Specification of the star of slots is given as:

- The number of slots ($Q_s = 36$) gives the number of spokes, as 36.
- The number of the periodicities t of the generator is $t = GCD\ (36, 20) = 4$.
- The number of spokes per cycle equals $Q_s \,.\, t^{-1} = 9$.
- The angle between two spokes $\alpha_s = 2\pi.\ Q_s \,.\, t^{-1} = 2\pi/9$.
- The electric angle between adjacent slots equals to $\alpha = 2\pi p.\ Q_s^{-1} = 10\pi/9$.

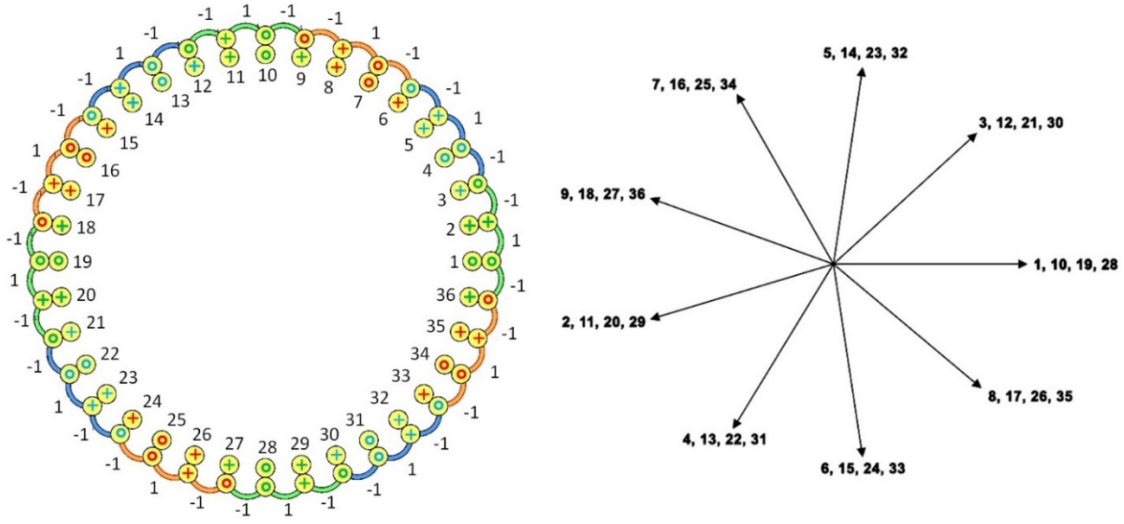

(a) (b)

Fig. 2.2.1 Stator winding arrangement, (a) 3-phase connections diagram, and (b) complete voltage vector diagram.

To verify the coils configuration which satisfies all winding assumptions, these coils, and their associated phase B and C counterparts have been presented in Table. 2. The coil offset of K_0 = 6 slots has been chosen to place the corresponding coils of phase B and C.

Fig. 2-2-3-a illustrates three-dimensional view of side-by-side notched-in-coil into the slots of the stator core, in which closed slot opening can be seen. In term of model and manufacture, the closed-slot fashion has been embedded to gain lower cogging torque and being able to fill the stator slots completely which leads to better performance.

The winding function of each phase can be given as the difference between the turn function and the average value of the turn function $-< n_{a,b,c}(\theta_s) >$:

$$N_a(\theta_s) = n_a(\theta_s) - < n_a(\theta_s) >$$

$$N_b(\theta_s) = n_b(\theta_s) - < n_b(\theta_s) > \quad (2\text{-}8)$$

$$N_c(\theta_s) = n_c(\theta_s) - < n_c(\theta_s) >$$

Table. 2.2.2 Winding layout of a 2nd grade with two-layers for 2p=40, and m = 3.

Phase A	Current direction	Phase B	Current direction	Phase C	Current direction
1 to 2	1	7 to 8	1	4 to 5	1
10 to 11	1	16 to 17	1	13 to 14	1
19 to 20	1	25 to 26	1	22 to 23	1
28 to 29	1	34 to 35	1	31 to 32	1
2 to 3	-1	6 to 7	-1	3 to 4	-1
9 to 10	-1	8 to 9	-1	5 to 6	-1
11 to 12	-1	15 to 16	-1	12 to 13	-1
18 to 19	-1	17 to 18	-1	14 to 15	-1
20 to 21	-1	24 to 25	-1	21 to 22	-1
27 to 28	-1	26 to 27	-1	23 to 24	-1
29 to 30	-1	33 to 34	-1	30 to 31	-1
36 to 1	-1	35 to 36	-1	32 to 33	-1

The winding function defines the regions, in which the flux has been produced through one unit of the current in the turns. Based on Eq. (2-8), the average of the turn function can be calculated [6] as:

$$< n(\theta_s) >= \frac{1}{2\pi} \int_0^{2\pi} n(\theta_s)\, d\theta_s \tag{2-9}$$

$$N(\theta_s) >= n(\theta) - < n(\theta) > \quad where: \; n(\theta) = \sum n(\theta_i) \tag{2-10}$$

According to [1] [10-12], the MMF of each (a, b, c) phase only as result of the current of the phase in any point in the air-gap is related to the winding function of the phase as given below:

$$\begin{aligned} F_a(\theta_s) &= N_a(\theta_s).i_a \\ F_b(\theta_s) &= N_b(\theta_s).i_b \\ F_c(\theta_s) &= N_c(\theta_s).i_c \end{aligned} \tag{2-11}$$

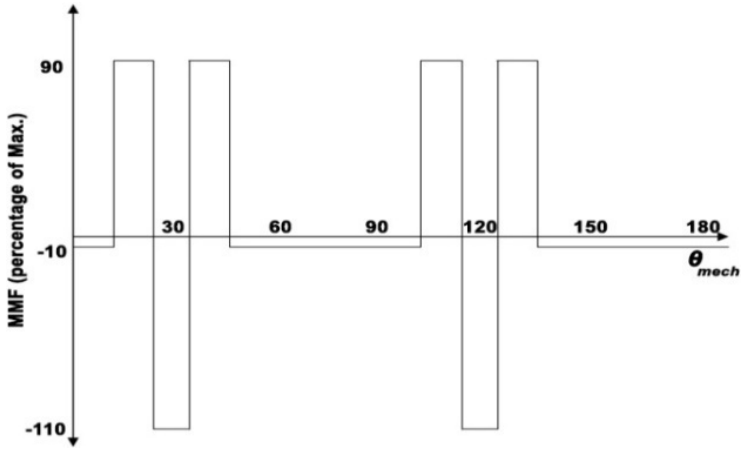

Fig. 2.2.2 MMF of the SPM generator based on q = 0.3.

2.2.1 Inductances of stator winding

The total inductance of stator winding (L_s) depends on the type of winding used offer various values for each type of inductances which are known as:

- The self-inductance (L_{aa})
- The mutual inductance (L_{ab})
- The slot leakage inductance ($L_{s\sigma}$)
- The end leakage inductance (L_{end})
- The Air-gap leakage inductance (L_{gap})
- The harmonic leakage inductance (L_h)

The magnetic energy memory of the phase winding can be estimated through the self-inductance L_{aa}. When PMSG is under normal operation condition, the magnetic energy is stored in the generated magnetic field of coils of the phase winding, in which L_{aa} of phase A is a constant. This component of inductance can be calculated by [13-18]:

$$L_{aa} = \frac{\psi_{aa}}{i_{aa}} = \frac{\mu_0 l_s r_s}{l_g} \frac{\int_0^{2\pi} N_a(\theta_s) F_{sa}(\theta_s) d\theta_s}{i_a} = \frac{\mu_0 l_s r_s}{l_g} \int_0^{2\pi} N_a^2(\theta_s) d\theta_s \quad (2\text{-}12)$$

l_s and l_g are effective stack and airgap lengths. Assuming that L_{aa} (phase A) is a constant, when the current of phase A to the flux of phase A linking coils in phase B, the mutual inductance L_{ab} has been produced which can be written as [7] [13]:

$$L_{ab} = \frac{\psi_{ba}}{i_{aa}} = \frac{\mu_0 l_s r_s}{l_g} \frac{\int_0^{2\pi} N_b(\theta_s) F_{sa}(\theta_s) d\theta_s}{i_a} = \frac{\mu_0 l_s r_s}{l_g} \int_0^{2\pi} N_a(\theta_s) N_b(\theta_s) d\theta \quad (2\text{-}13)$$

The slot leakage inductance per phase in a double-layer FSCW is calculated using:

$$L_{slot} = \frac{Q_s 4 N_c^2 l_s P_{slot}}{3} \quad (2\text{-}14)$$

It is important to mention that the specific slot permeance P_{slot} depends on the slot shape type. In this study, the slot type is presented in Fig. 2.2.1.1. Based on the geometrical parameters shown in Fig. 2.2.1.1, P_{slot} can be defined as [13-14]:

$$P_s = \mu_0 \left[\frac{h_s}{3 w_s} + \frac{h_1}{(w_{s2} + w_{s3})/2} + \frac{h_0}{b_s} \right] \quad (2\text{-}15)$$

μ_0 is vacuum permeability which is $4\pi \times 10^{-7}$ H.m^{-1}, h_s is the slot height that equals h_1+h_2. Ws is the equivalent slot width which can be calculated by:

$$w_s = \frac{w_{s1} + w_{s2}}{2} \quad (2\text{-}16)$$

h_0 is the slot opening height, and b_s is the slot opening which is zero in this research (closed-slot topology).

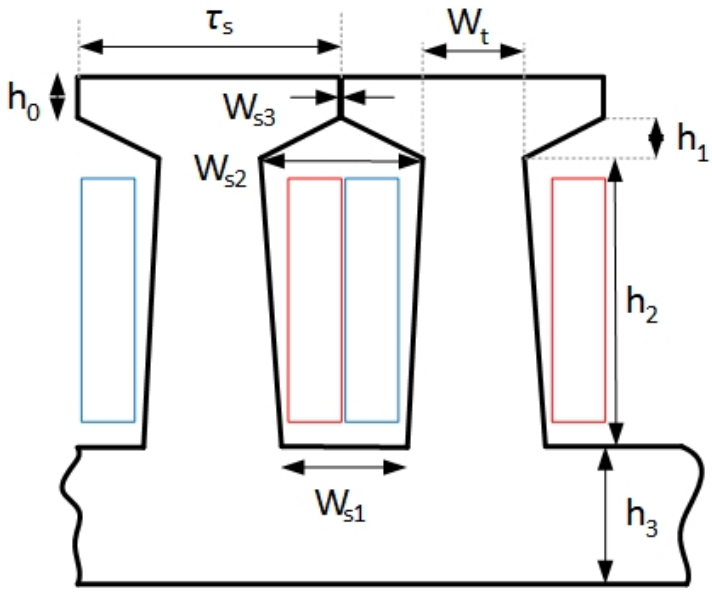

Fig. 2.2.1.1 Geometrical-based dimensions of the stator core including slot.

The end leakage inductance for phase winding [7] [16] which highly depends on the end leakage flux can be estimated using the following:

$$L_{end} = \frac{N_{coil} N_c^2 \mu_0 \tau_s}{6} \ln\left(\frac{\pi \tau_s^2 / 4}{h_s w_s / 2}\right) \quad (2\text{-}17)$$

therefore, the total leakage inductance relies on both mentioned components $L_{s\sigma} = L_{\text{slot}} + L_{\text{end}}$.

The air-gap leakage inductance is calculated based on the Richter method [19-20] as:

$$L_{gap} = \frac{\mu_0}{\pi} \frac{m}{\delta} D_\delta L_i \left[\frac{N_{ph}}{p}\right]^2 \sigma_\delta \quad (2\text{-}18)$$

In references [19-20], the factor σ_δ has been calculated from the winding harmonics as follows:

$$\sigma_\delta = \sum_{v=-\infty}^{v=+\infty} \left(\frac{\xi}{v_{\xi_1}}\right)^2, \quad v \neq 1 \quad (2\text{-}19)$$

Based on the phasor diagram and the assumption which the stator self-inductance and mutual-inductance are either fixed or vary sinusoidally via the position of the rotor ($2\theta_{er}$). In fact, the PM flux-linkages $\Psi_{PM_{a,b,c}}(\theta_{er})$ (these parameters are computed using steady-state finite element analysis (FEA) method, which fully discussed in section 2.3.2) at the stator phases also vary sinusoidally, that is presented in Fig. 2.2.1.2 However by θ_{er} rotor position. Final harmonics at $\Psi_{PM_{a,b,c}}(\theta_{er})$ can be also treated in the *d-q* system.

To predict the behavior of the SPMSG through its d-q model by below expressions [1] [14] [21-23]:

$$I_d(\gamma) = I.\sin(\gamma), \qquad I_q(\gamma) = I.\cos(\gamma) \quad (2\text{-}20)$$

and the outcome vector of current is:

$$I(\gamma) = \sqrt{I_d(\gamma)^2 + I_q(\gamma)^2} \quad (2\text{-}21)$$

in addition, reactance which needs inductances in the d-q plane can be given:

$$X_d(I) = \omega.L_d(I), \qquad X_q(I) = \omega.L_q(I) \quad (2\text{-}22)$$

where:

$$L_d = L_{ls} + \frac{3}{2}(L_0 - |L_2|), \qquad L_q = L_{sl} + \frac{3}{2}(L_0 + |L_2|) \quad (2\text{-}23)$$

Through FEA, a variation of inductances and currents at d-q model can be seen in Fig. 2.2.1.3-a-b, as the d-q inductances should be nearly equal for such a topology and winding configuration, Fig. 2.2.1.3-a has a good agreement with Fig. 2.2.1.3-b.

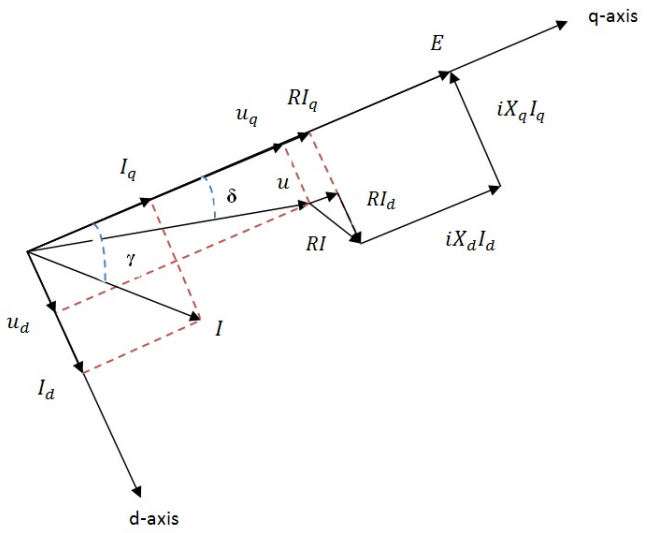

Fig. 2.2.1.2 Phasor diagram of surface PMSG with γ-angle = π/4.

As the resulted harmonics are supposed to cause time pulsations in the torque with sinusoidal currents in speed and frequency $\omega_1 = \omega_r$, [23] it can be written as:

$$\left|L_{abc}(\theta_{er})\right| = \begin{vmatrix} L_{sl}+L_0+L_2\cos(2\theta_{er}), & L_{ab}+L_2\cos\left(2\theta_{er}+2\pi/3\right), & L_{ab}+L_2cos(2\theta_{er}-2\pi/3) \\ L_{ab}+L_2\cos\left(2\theta_{er}+2\pi/3\right), & L_{sl}+L_0+L_2\cos\left(2\theta_{er}-2\pi/3\right), & L_{ab}+L_2cos(2\theta_{er}) \\ L_{ab}+L_2\cos\left(2\theta_{er}-2\pi/3\right), & L_{ab}+L_2\cos(2\theta_{er}), & L_{sl}+L_0+L_2cos(2\theta_{er}+2\pi/3) \end{vmatrix} \quad (2\text{-}24)$$

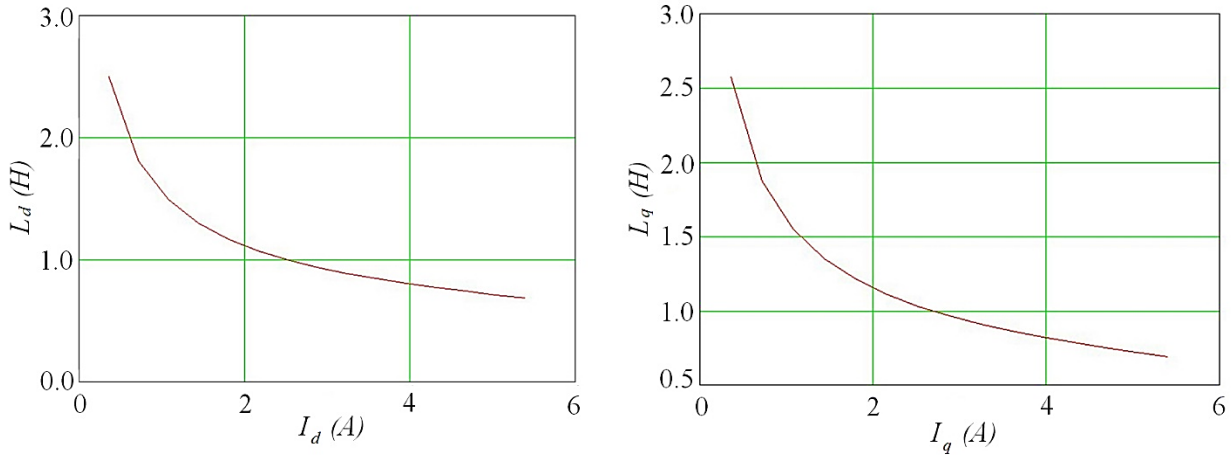

Fig. 2.2.1.3 The variation of inductances L_d and L_q versus currents in the d-q plane, a) L_d versus I_d, and b) L_q versus I_q.

The voltage in d-q model can be given as:

$$u_d(I,\gamma) = X_d(I).I_d(\gamma) - R.I_d(\gamma) \quad (2\text{-}25)$$

$$u_q(I,\gamma) = X_q(I).I_q(\gamma) - R.I_q(\gamma) \quad (2\text{-}26)$$

Finally, the outcome vector of voltage is:

$$u(\gamma,I) = \sqrt{u_d(I,\gamma)^2 + u_q(I,\gamma)^2} \quad (2\text{-}27)$$

Therefore, as an acceptable agreement between both L_d and L_q, Fig. 2.2.1.4 presents the interpolation of both inductances, in which an ignorable difference between them which verifies the design topology.

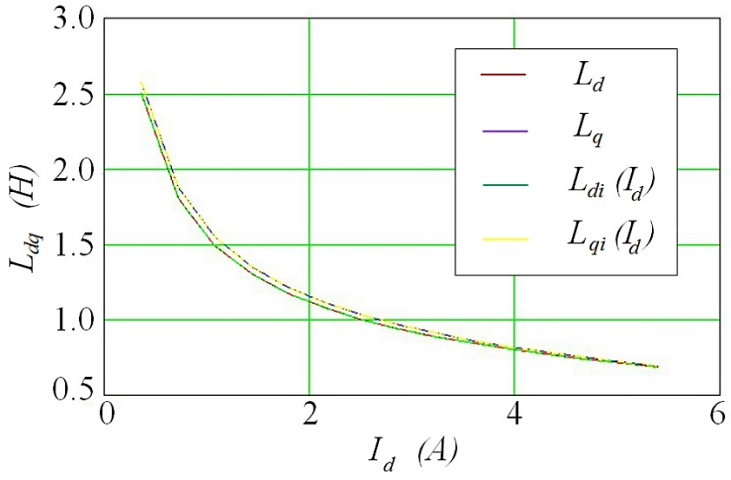

Fig. 2.2.1.4 The interpolation of inductances L_d and L_q in the d-q plane.

2.2.2 Winding factor

The stator winding factor of PMSMs is studied for the fractional-slot concentrated windings (FSCW) with $q < 1$ which depends on the slot/ pole numbers. The fundamental winding factor (k_{w1}) can be reported in Table 2.2.2.1. The q value is a fraction of the number of slot per pole per phase, as well as the periodic/ or antiperiodic indicates the winding distribution. As the electromagnetic torque is a significant product of PMSMs is proportional to the value of k_{w1}, therefore, a higher fundamental k_{w1}, when other sub-harmonics are as low as possible is preferred. It is worthy to mention that to enhance small k_{w1} in the special machines, higher current or coil turns are required which makes the machine more expensive. To define the winding factor analytically, based on [7] [24-26], the winding factor has resulted from the pitch factor, distribution factor, and the skewing factor. Based on Vogt [26], the 2nd –grade two-layer winding has the following winding factor when the equal zone widths exist:

$$\xi_v = \sin\left(\frac{v}{p}\frac{\pi}{2}\right)\frac{\sin\left(\frac{v}{p}\frac{\pi}{m2}\right)}{nq\sin\left(\frac{v}{p}\frac{\pi}{2nmq}\right)}\cos\left(\frac{v}{p}\frac{\eta_v}{2}\right) \tag{2-28}$$

where η_v is an angle in voltage vector map of winding. Based on [24-25], the harmonics (only if n is even, and thus $p^* = n / 2$) can be calculated from:

$$\frac{v}{p} = \pm\frac{1}{n}(2mg+2), \qquad g = 0, \pm1, \pm2, \pm3, \ldots \tag{2-29}$$

The sign ± makes the equation yield positive for the fundamental harmonic ($v = +1$). Note that FSCW with $q \notin N$ always produces integer order harmonics consists of even and odd numbers, as well as also sub-harmonics $v < 1$.

Table 2.2.2.1 Double-layer FSCW layout and factors.

Slot/ pole number		Slots/poles combination	q	Winding layout	Periodic number of winding	t	k_{w1} (pu)
1	36/20	9/5	3/5	…'CA'AB'BA'AB'BC'CB'BC'…	12	2	0.735246
2	36/24	3/2	1/2	…'CA'AB'BC'…	12	12	0.866025
3	36/30	6/5	2/5	…'AA'AB'BB'BC'CC'CA'…	6	3	0.933013
4	36/40	9/10	3/10	…'BA'AA'AA'AC'CC'CC'CB'BB'BB'…	4	4	0.945214
5	36/42	6/7	2/7	…'BA'AA'AC'CC'CB'BB'…	6	3	0.933013

As presented in Table 2.2.2.1, the winding factor of different five slot/pole combinations, where each of those machines (1-5) have shown various winding layout and fundamental winding factor. Machine No. 4 with 40 slots, 40 poles have the highest k_{w1} = 0.945214, and apparently the best combination. Highest k_{w1} brings the greatest electromagnetic forces (EMFs) and finally the highest average electromagnetic torque. Machine No. 1 has the minimum k_{w1}, which meant the lowest production of EMFs and torque. It should be mentioned that all five machines have periodic winding distribution, and also assumed to be equal in the winding turns and magnet volume for an identical comparison.

Fig. 2.2.2.1 illustrates the winding factor evaluation of all studied machines with double-layer FSCW winding in a constant range of harmonic orders, where the machine (1) with 36 slots and 20 poles for a range of harmonic order is presented in Fig. 2.2.2.1, machine (2) with 36 slots and 24 poles is performed better by k_{w1} = 0.866025 and 12 periodic number of winding. Fig. 2.2.2.1-c reported the machine (3) with 36 slots and 30 poles by the peak winding factor of 0.933013 which is higher than the other two machines. Machine (4) with 36 slots and 40 poles has shown the greatest winding factor (0.945214) by four periodic number of distributed windings that can be seen in Fig. 2.2.2.1-d. Machine (5) with 36 slots and 42 poles has indicated a lower peak winding factor through 6 periodic number of winding for a range of harmonic orders which is depicted in Fig. 2.2.2.1-e.

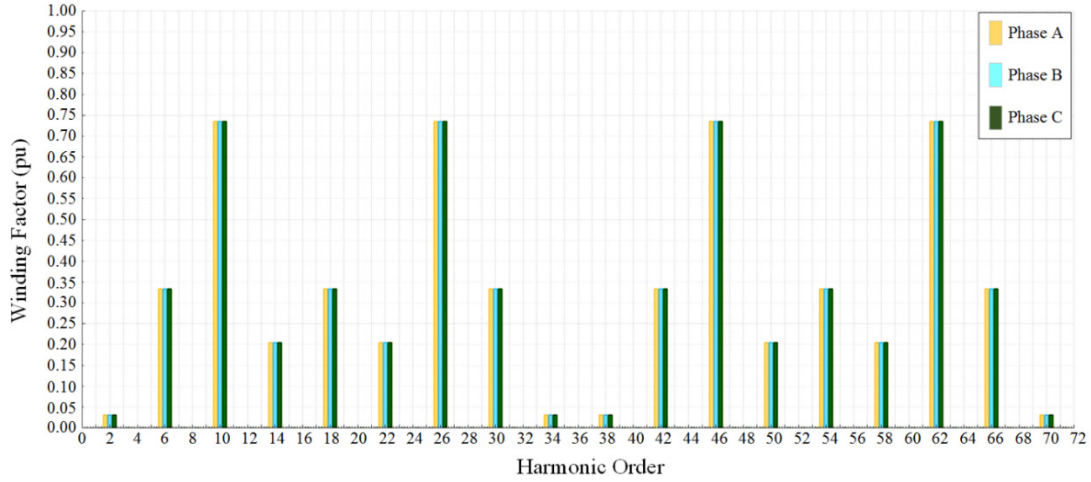

(a)

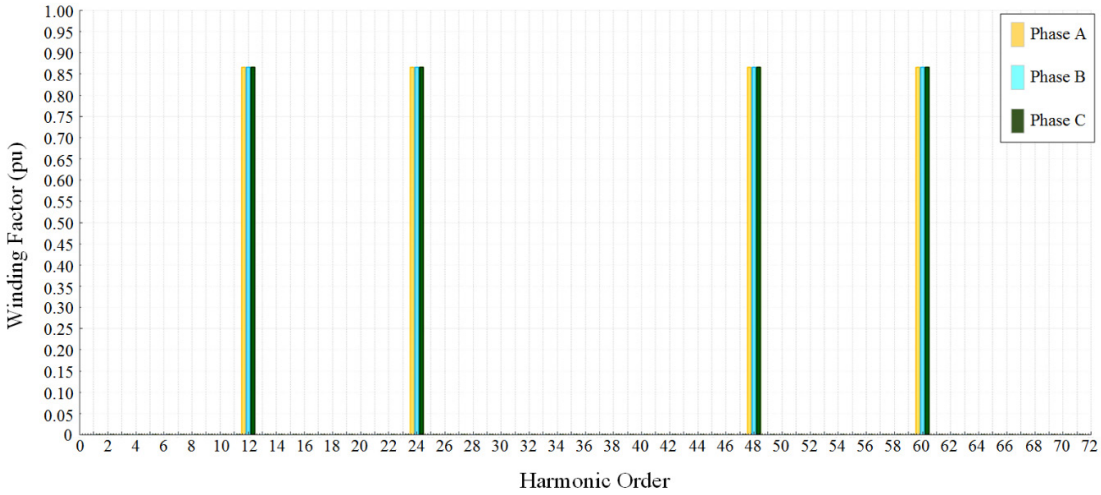

(b)

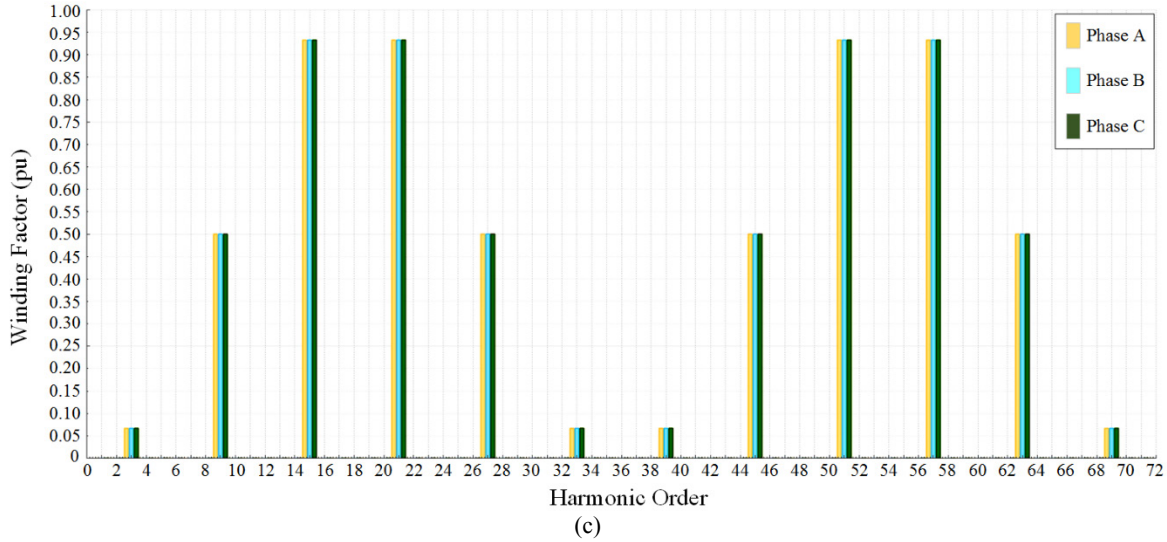

(c)

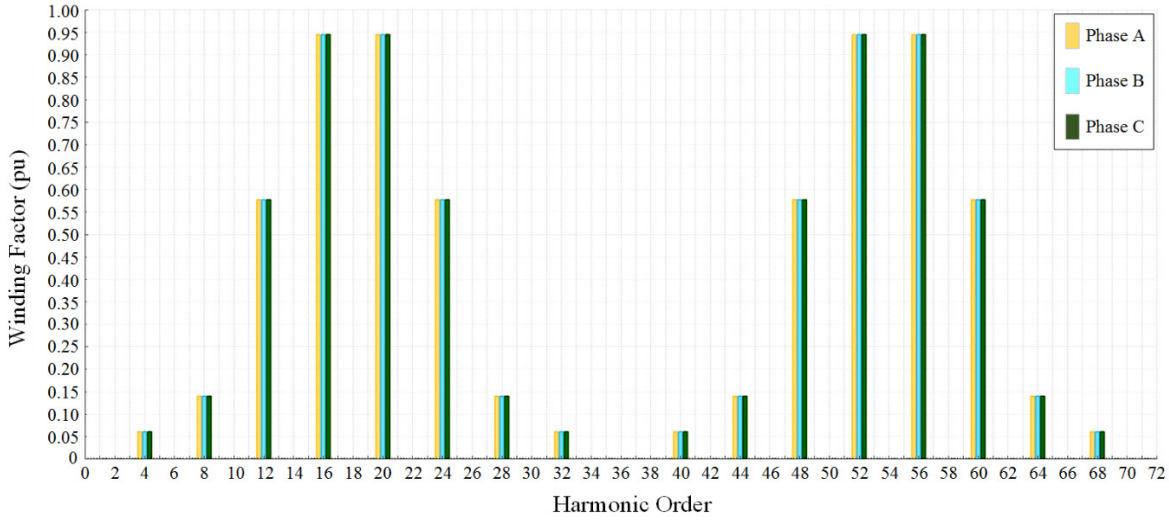

(d)

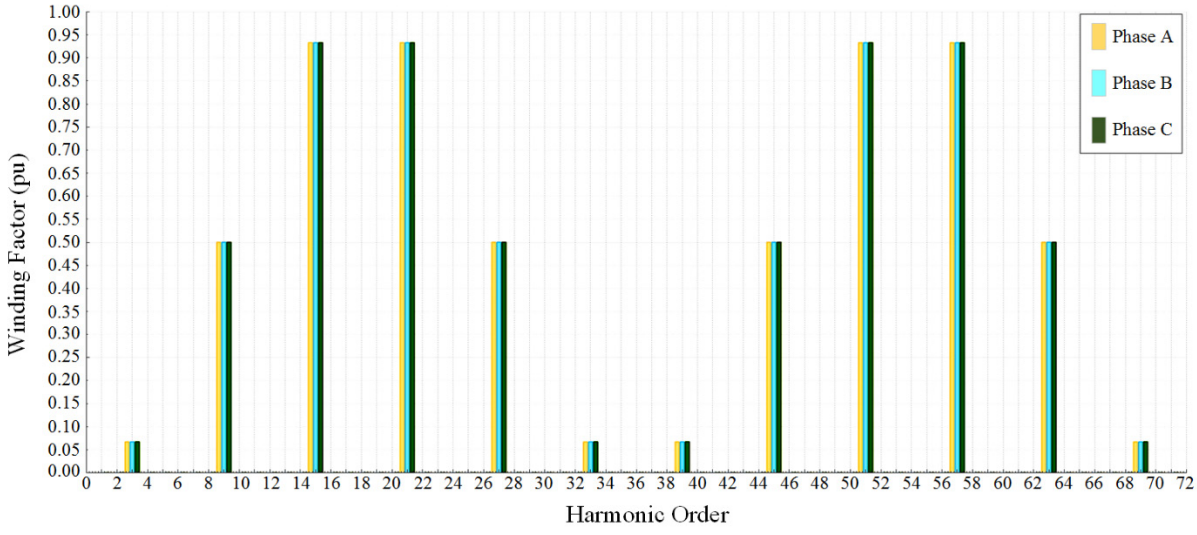

(e)

Fig. 2.2.2.1 The winding factor evaluation for a range of harmonic order, a) machine (1), b) machine (2), c) machine (3), d) machine (4), and e) machine (5).

2.2.3 MMF Computations and Choice of Electric Loading

Basically, the operation of AC machines is tied to the MMF production and its effect on the other parts of the machine. First, the stator winding MMF magnetizes the whole machine through the magnetizing inductance. Secondly, the MMF seeks to synthesize a sinusoidally distributed rotating magnetic flux density between stator and rotor core (air-gap) in order to induce a sinusoidal current in the rotor core, and afterward generate an appropriate, non-fluctuating electromagnetic torque. It is worthy to mention that an ideal sinusoidal magnetic flux density only can be generated if a sinusoidal MMF exists [14].

For full pitch windings, where the fundamental pitch factor k_{y1} equals to one, the magnetic flux density curve form is intrinsically proportional to the MMF at every point in the air-gap. The MMF of one pole of a complete two-pole magnetic circuit can be calculated from [14]:

$$\Im_p = \left(\frac{4}{\pi}\right)\left(\frac{N_t I}{2}\right)\left[\sin\theta + \frac{1}{3}\sin 3\theta + \frac{1}{5}\sin 5\theta + \ldots\right] \tag{2-30}$$

According to [1] [11] [27-28], the MMF of each phase (a, b, c) simply is the result of a current of the phase in any point in the air-gap is related to the winding function of the phase as given:

$$\begin{aligned} \Im_a(\theta) &= N_a(\theta).i_a \\ \Im_b(\theta) &= N_b(\theta).i_b \\ \Im_c(\theta) &= N_c(\theta).i_c \end{aligned} \tag{2-31}$$

As it is obvious the winding function can be regarded as the MMF (which can be seen in Fig. 2.2.3.1) because of a unit current. Moreover, the total MMF at the air-gap is the sum of the MMF distributions of all phases. In this study, it is assumed that the length of the air-gap along the surface of the armature is constant.

Choice of electric loading relies on the electric circuits, however, the saturation phenomena of magnetic circuits in terms of the losses associated with the conductors play a significant role to improve the electric loading of PMSMs. For machines using air cooling system, the nominal value of electric loading is between 15 to 35 ampere-conductors per millimeter (A/mm). For machines with a small number of poles and small diameter, the electric loading choice has to be a smaller value. For machines with a larger number of poles, low voltage, and low frequency, electric loading may be increased up to 20% which is targeting the studied machines in this research with 40 poles. For water-cooled machines, a value of electric loading as high as 150 A/mm may be used [1] [14]. To modify the electric loading of a synchronous machine, power rating, speed, and frequency variables are very well known, besides, the following limitations may be considered:

- Voltage rating

Essentially the stator slots are occupied more by air than copper conductors. The slot fill factor consideration, in which the amount of copper cross-sectional area as per unit of the available cross-sectional area of a stator slot is normally in the range of 0.2 to 0.4. It is worthy to mention that by reducing the available conductor area, the voltage rating of PMSM increases, and thus, the ground wall and coil separator insulations increases. Note that, to slip the coils into the slots, the conductors must be insulated between strands, separate coils with regarding the ground [14].

- Current density constraint

To determine a proper value of the surface current density $K_{s(RMS)}$ in the stator winding, the steady-state value should be limited via the ability of the cooling system which removes the heat produced in the stator core (including windings). When the stator winding consists of N_s series connected turns, hence, the fundamental linear current density for all three phases (m = 3) [14] can be calculated through:

$$K_{s(RMS)} = \frac{6}{\sqrt{2}\pi}\left(\frac{k_1 N_s}{D_{is}} I_s\right) \tag{2-32}$$

k_1 is a factor which has derived from the amplitude of the air-gap flux density. D_{is} is the inner diameter of the stator core. ls is the stack length.

- Representative Values of current density

This consideration also should be considered if $K_{s(RMS)}$ is for open drip proof as well as enclosed fan cooled machines. As the studied machine dealt with none of them [14], therefore, this consideration is not accounted for the design.

In this section, the MMF computation (green curve) is studied for all studied machines from the previous section which are basically different in slot/ pole combinations. Fig. 2.2.3.1 illustrates the variation of MMF and electric loading for each specific slot/ pole combination. Fig. 2.2.3.1-a presents the semi-sinusoidal MMF curve with the peak of 2 A and also peak electric loading value of 4500 A/m for the machine (1) with 36 slots and 20 poles. Machine (2) with 36 slots and 24 poles have shown a not preferable shape of MMF which is smooth with the peak-to-peak value of 6 A and 4500 A/m peak value for electric loading, can be seen in Fig. 2.2.3.1-b. Fig. 2.2.3.1-c presents the variation of MMF and electric loading for the machine (3), 36 slots and 30 poles, with a better sinusoidal MMF waveform, as well as the electric loading. Fig. 2.2.3.1-d depicts the smoothest sinusoidal MMF waveform which belongs to machine (4), 36 slots and 40 poles. Machine (5) with 36 slots and 42 poles have also offered an acceptable sinusoidal MMF along with its electric loading shape and value.

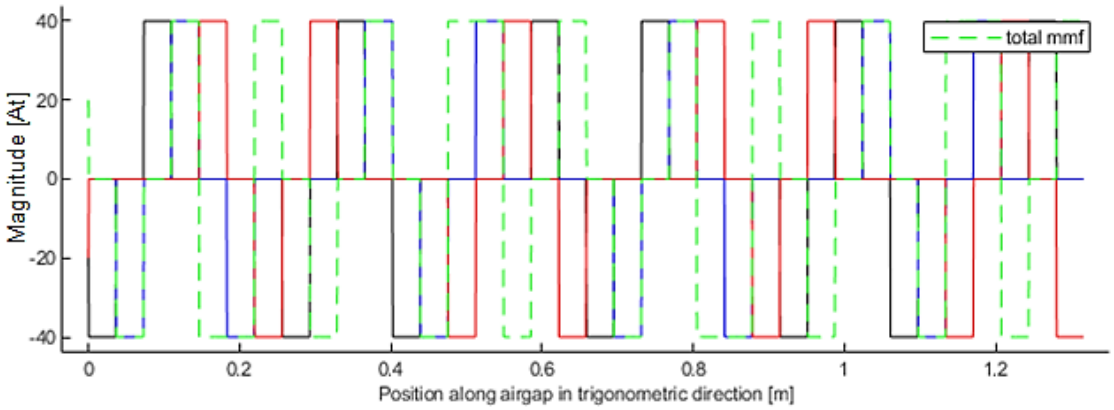

(a)

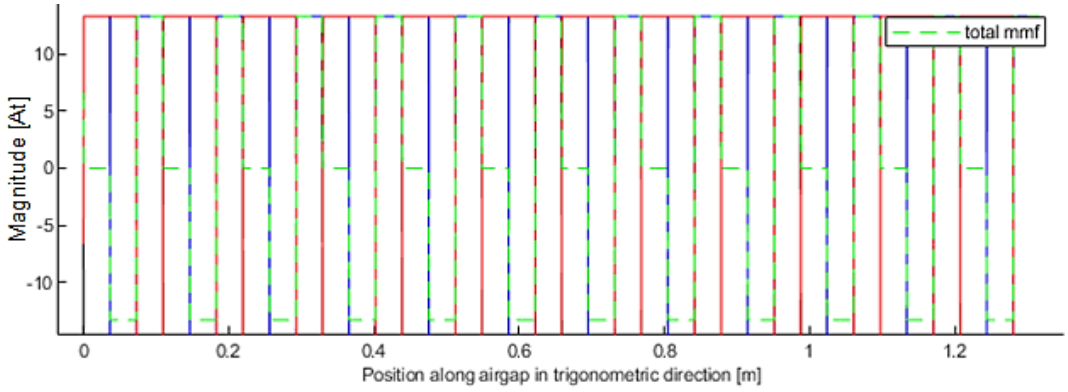

(b)

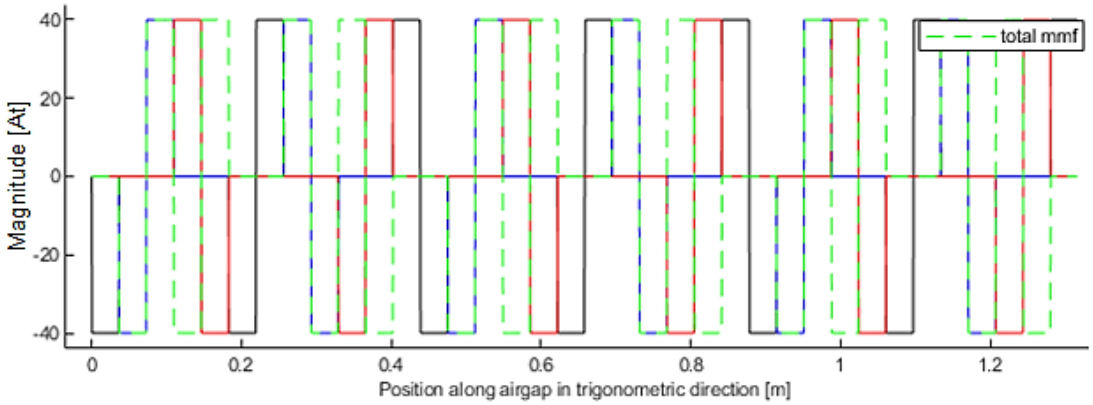

(c)

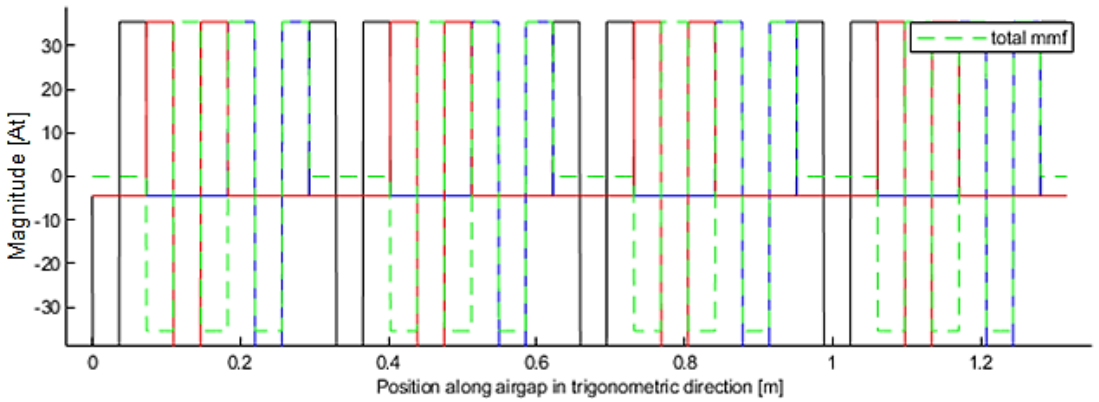

(d)

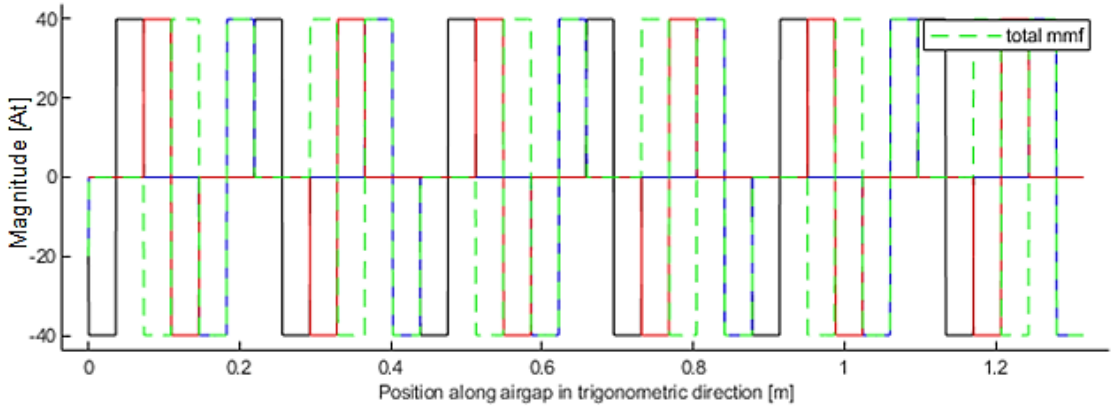

(e)

Fig. 2.2.3.1 Variation of MMF (phase A) of the studied machines with: a) 36 slots and 20 poles, b) 36 slots and 24 poles, c) 36 slots and 30 poles, d) 36 slots and 40 poles, and e) 36 slots and 42 poles.

2.2.4 MMF Harmonic Analysis

Because of the discrete position of the coil within the slots, there are space harmonics in the MMF distribution. Let v be the order of the MMF harmonic, according to for the two-pole MMF harmonic, also called the fundamental harmonic. Thus, the order of the main harmonics is $v = p$, where p is the number of pole pairs [29-30]. The number v is considered without a sign. It can be the only positive integer. The main harmonic is that harmonic whose order is the same of the number of the pole pairs p. Only this main harmonic is synchronous with respect to the rotor. Conversely, all harmonics of different order are asynchronous with the rotor. Therefore, since they cause a time–varying magnetic field, they induce currents in the rotor, which is mainly one of the most significant reasons that induced eddy-current losses (mostly in the rotor) can be increased along with permeance variation and PWM harmonics [1]. Synthesis of different slot/pole combinations regarding the dimensions and acceptable winding factor can be chosen in the design of FSCWs.

Next, to harmonics of higher order (fundamental) there are also lower order harmonics, which known as sub-harmonics. Fig. 2.2.4.1 illustrates the MMF behavior in the air-gap, which is enlarged for a better understanding in this graph. When the fundamental or main harmonics $v_3 = p$ are synchronous with the rotor speed, where the sub-harmonic $v_1 < p$ occurs when the speed is greater than rotor speed. Whereas, the speed is lower than rotor speed, positive or negative harmonic of $v_2 > p$ [31] can appear as shown in the figure.

The MMF harmonics rotate in the air-gap with various speeds. The mechanical speed of the generic v-th MMF harmonic in the stator reference frame can be calculated from [31-32]:

$$\omega_{vs} = \frac{\omega}{sign \ . \ v} \tag{2-33}$$

where *sign* is the sign function, and *sign* = +1 if the v–th harmonic rotates in the same direction of the rotor, on the other hand, *sign* = −1 if the v–th harmonic rotates in the opposite direction. The sign function is defined in [31-32]; harmonics that correspond to the values of:

$$v = 1 + 3k, \qquad where: k = 0, 1, 2, \ldots \tag{2-34}$$

have the positive sign, while the harmonics that correspond to the value of [4-5]:

$$v = 2 + 3k, \qquad where: k = 0, 1, 2, \ldots \tag{2-35}$$

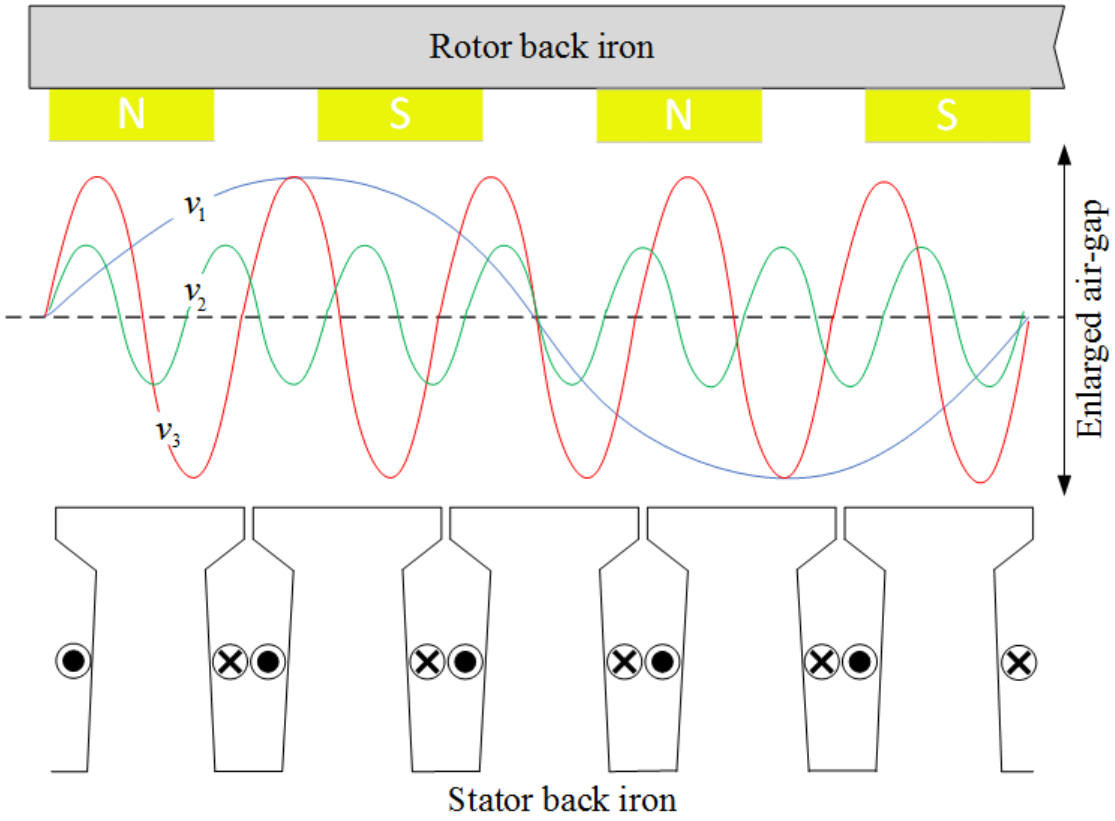

Fig. 2.2.4.1 MMF harmonics speed with respect to the rotor speed.

where k value is always a positive integer.

Under the condition of having the same sign but opposite to that of the previous series. A positive sign is conventionally assigned to the series containing the main harmonic ($v = p$). The MMF speed with respect to the rotor is computed as [31-32]:

$$\omega_{rv} = 2\pi f \left(\frac{sign}{v} - \frac{1}{p} \right) \tag{2-36}$$

The rotating MMF harmonics induce in the rotor an EMF at the frequency f_{rv}. Such a frequency can be expressed as a function of the harmonic order ν as [31-32]:

$$f_{rv} = v \frac{\omega_{rv}}{2\pi} = f \left| sign - \frac{v}{p} \right| \tag{2-37}$$

The MMF harmonic was computed for all studied five machines in order to find out more about the chosen winding configuration at last. Fig. 2.2.4.2 illustrates MMF harmonic content analysis, in which total harmonic distortion (THD) also is calculated for a better understanding of the amplitude of each individual harmonic order. Fig. 2.2.4.2-a presents the MMF harmonic content for the machine (1) with 36 slots and 20 poles. This machine by the largest fundamental harmonic of 2.52 A produces the lowest THD of 49.27%. In contrast to machine (1), machine (2) with 36 slots and 24 poles has brought lower fundamental harmonic of 2.48 A, but also larger THD of 55.69% which can be seen in Fig. 2.2.4.2-b. Machine (3) with 36 slots

and 30 poles have shown (in Fig. 2.2.4.2-c) even lower fundamental harmonic (2.14 A), and larger THD of 76.49%. Fig. 2.2.4.2-d indicates the harmonic content for the machine (4) with 36 slots and 40 poles by the lowest fundamental harmonic of 2.03 A and THD of 73.17%. It is worthy to mention that, the greatest winding factor is not always bringing the lowest THD as it has occurred in the machine (4). Fig. 2.2.4.2-e depicts the machine (5) with 36 slots and 42 poles, in which the fundamental harmonic is 2.14 A (similar to machine (3)) and THD of 70.02%. As the star diagram of the machine (3) and (5) are similar, and thus, the distribution of harmonic contents is quite the same, but various amplitudes.

Fig. 2.2.4.3 presents the produced MMF at t = 0s in the stator (red) and rotor (blue) cores, in which the dashed sinusoidal curves are fundamental. The rotor MMF consists of some ripples at the peak value approximately 7880 At.

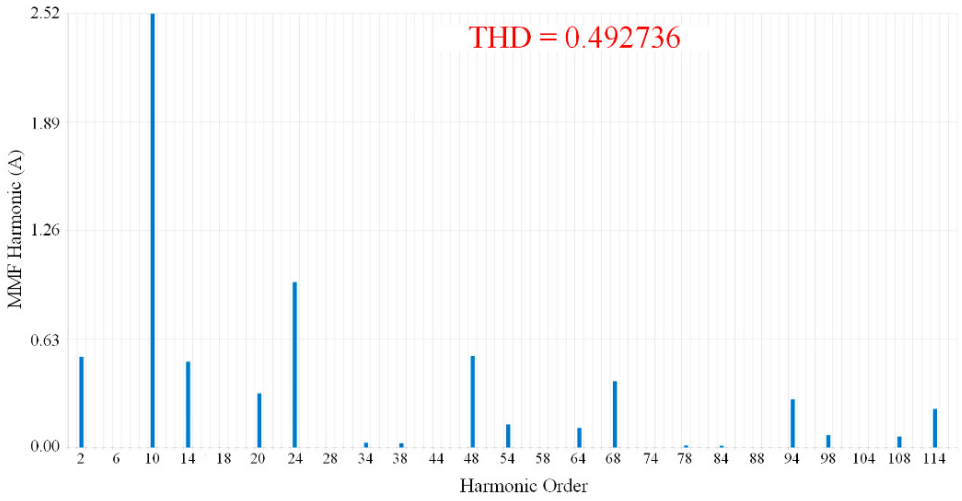

(a)

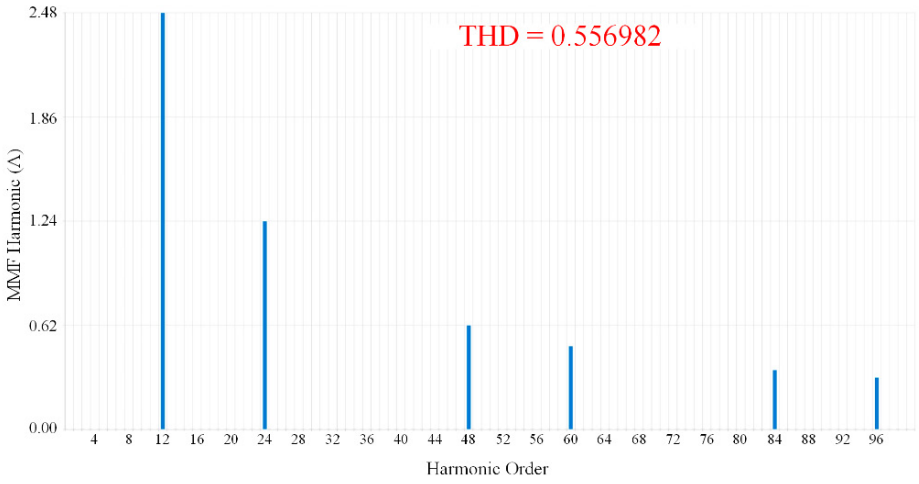

(b)

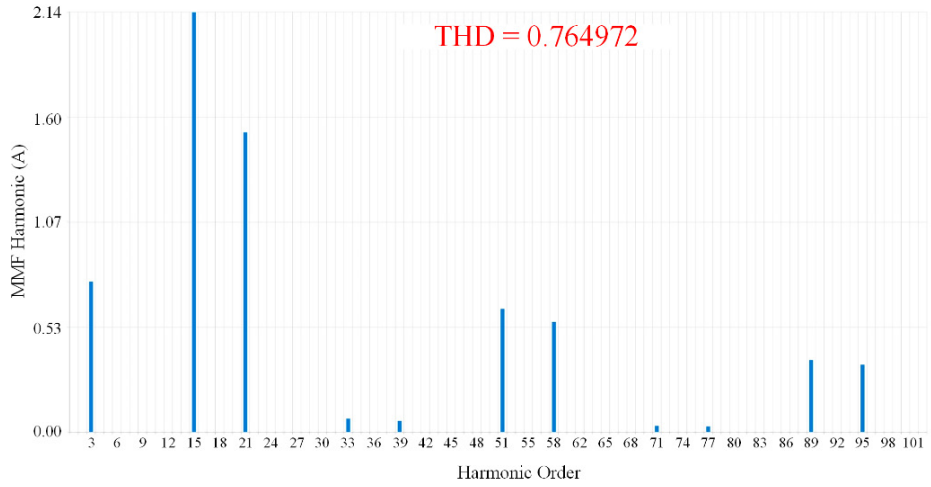

(c)

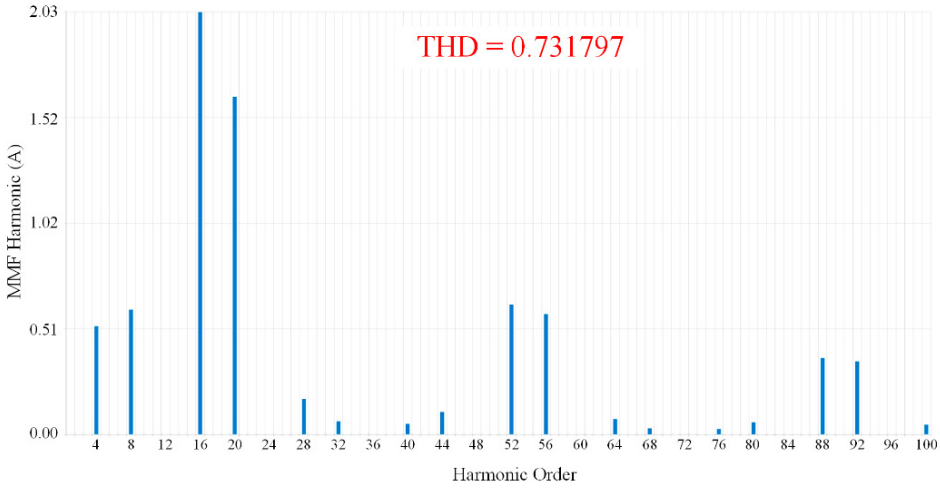

(d)

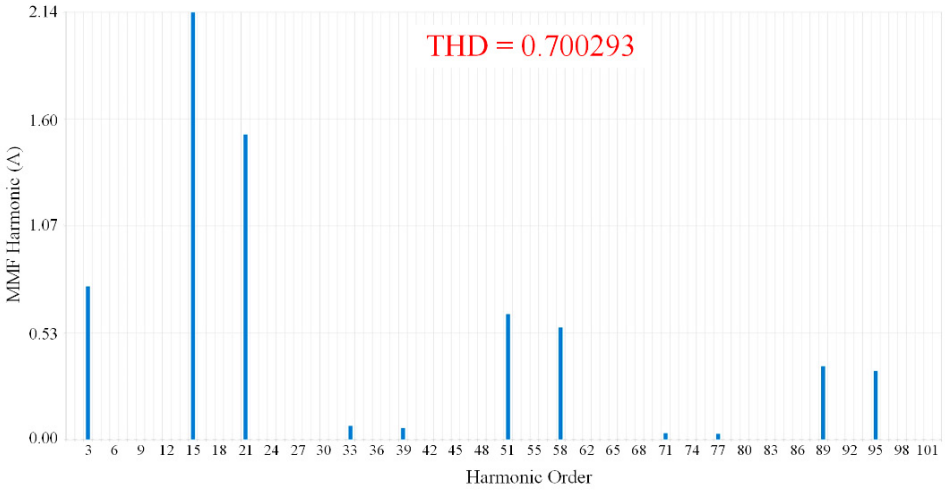

(e)

Fig. 2.2.4.2 Evaluation of MMF harmonic analysis for various slot/ pole combinations, where a) 36 slots and 20 poles, b) 36 slots and 24 poles, c) 36 slots and 30 poles, d) 36 slots and 40 poles, and e) 36 slots and 42 poles.

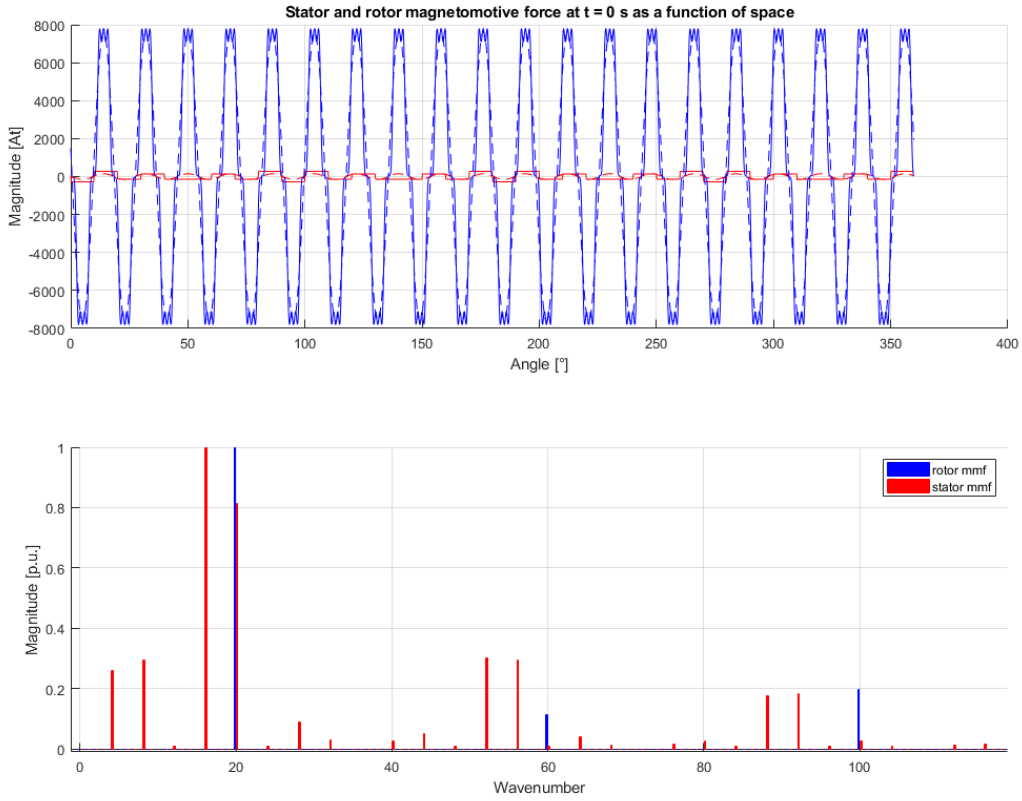

Fig. 2.2.4.3 Stator and rotor MMF at $t = 0$ s as function of space for exiting wave number per unit.

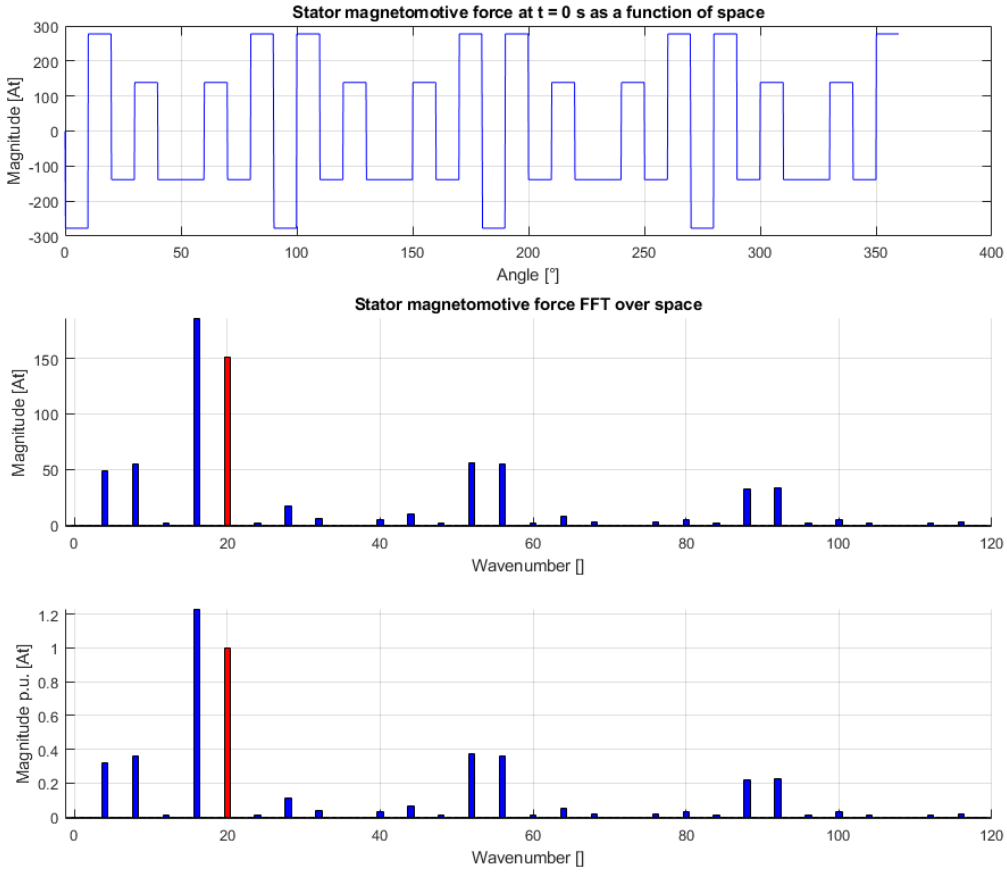

Fig. 2.2.4.4 Stator MMF at $t = 0$ s as function of space for exiting A.t unit and per unit wave number.

Fig. 2.2.4.4 illustrates only the stator MMF at t = 0s while it is not well shown in Fig. 2.2.4.3 due to the large gap between peak values in the stator and rotor MMFs. Fig. 2.2.4.5 depicts the total air-gap MMF at t = 0s with its harmonics.

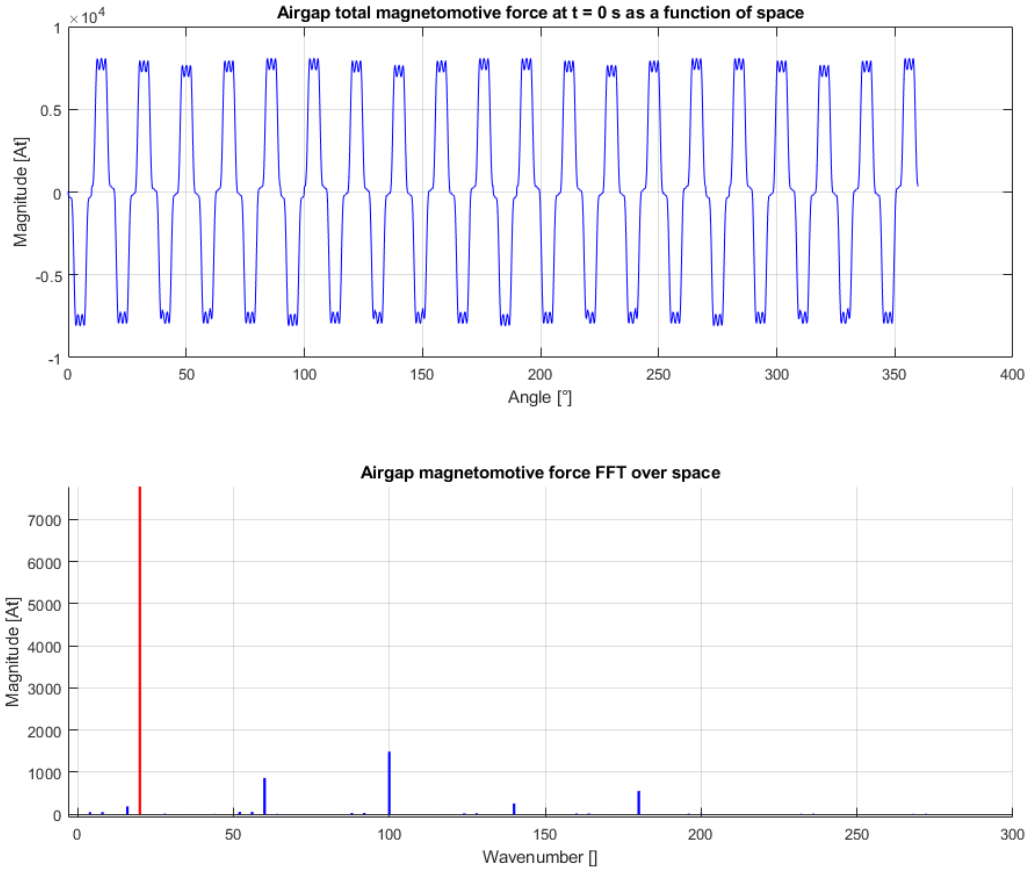

Fig. 2.2.4.5 Total air-gap MMF at t = 0s as function of space with the number of waves.

2.2.5 Permeance of the stator and rotor

In the electrical machine design, the permeance is not easy to be calculated. When the flux density varies over the cross-sectional area, we can define the permeance as [14]:

$$d\Phi = NIdp \tag{2-38}$$

where ϕ is the flux in a magnetic circuit, and base on Ampere's law $F = NI$, in which N is the number of turns per coil and I is current that passes the coil. As we know [14]:

$$dp = \frac{\mu dA}{l} \tag{2-39}$$

Therefore, the total permeance can be computed using [14]:

$$p = \int_0^A \mu \frac{dA}{l} \tag{2-40}$$

where l is the length of the magnetic path which equals to $2\pi R$ and often it is a function of A which is a cross-sectional area by $h.d$x.

Fig. 2.2.5.1 illustrates the permeance, stator, and rotor MMF waveforms at t = 0 versus angle between 0 to 1.5 rad. It can be seen that the rotor slot centers as dashed lines on the produced MMF curves to understand in what angle of rotor slot centers, how

much is the MMF has been produced, where one p. u. have been shown at 0.25 rad and 1.5 rad for the stator. The rotor MMF with more sinusoidal shape provides the peak value (1 p. u.) at each rotor slot center.

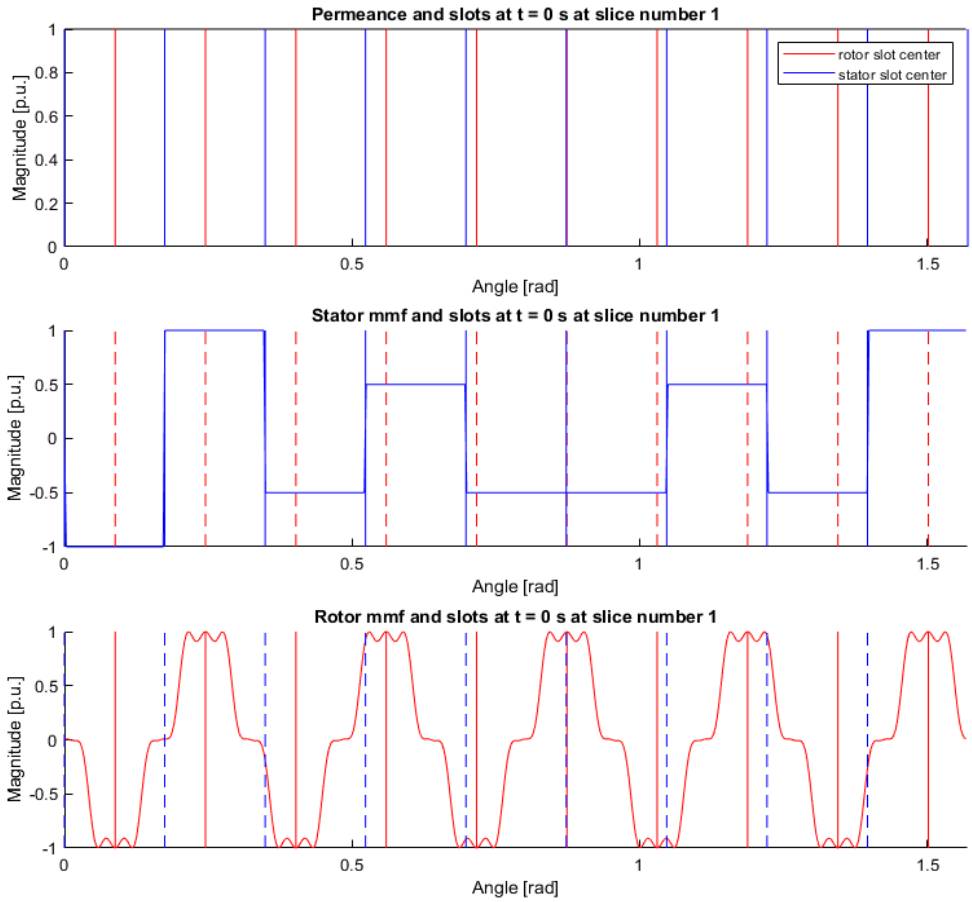

Fig. 2.2.5.1 Permenace, and stator and rotor MMF waveforms at t = 0s versus angle.

2.3 Steady-state 2-D electromagnetic finite element analysis (FEA)

Finite element analysis (FEA) known as a complex methodology, in which non-linear material characteristics normally are obtained. This methodology deals with the discretization of the machine cross-section into much smaller areas (triangular shape) which is known as finite elements in 2-D computations. The 2-D FE computations are in two popular categories, either time-independent (steady-state) or time-step-based which are called transient analysis. FEA application for machine design can be summarized in three tasks as:

1. Preprocessing stage
2. Field-based solution
3. Post-processing stage

2-D non-linear magnetic vector potential can be defined as [1] [33-34]:

$$\frac{\partial}{\partial x}\left(\frac{1}{\mu}\frac{\partial A_z(x,y)}{\partial x}\right)+\frac{\partial}{\partial y}\left(\frac{1}{\mu}\frac{\partial A_z(x,y)}{\partial y}\right)=-J_c-J_{PM} \tag{2-41}$$

where A_z is the magnetic vector potential in z-direction which can be calculated during post processing stage, J_c is the current density, J_{PM} is the magnitude of the equivalent current density in the magnet boundaries, μ is the permeability of the medium. It is worthy to mention that μ can be easily calculated from $\mu = \mu_r . \mu_0$ [H/m], in which μ_r is the relative permeability, and μ_0 is the permeability of free space (vacuum) that is $4\pi\times10^{-7}$ [H/m].

The 2-D FEA-based machine modeling within preprocessing can be summarized as follows:

- The 2-D generator symmetric model (in one direction) based on the estimated rated values from analytical specifications is drawn in an x-y reference plane. In the z-direction, the end effects are neglected, as well as, the copper windings with strings coils are modeled a single rectangular conductor. For instance, if each coil consists of $N = 80$ turns in one layer of the slot, it is typically modeled as a rectangular with respect to slot fill factor. For no-load condition, the magnetic properties of the stator winding are the ambient air and the conductivity of the copper σ is manually set to zero. Based on Maxwell's equations, the magnetic field is modeled as follows:

$$\begin{aligned} \overline{B} &= \mu \overline{H} \\ \sigma_{air} &= 0 \\ \sigma_{copper} &= \sigma_{air} \end{aligned} \tag{2-42}$$

where H is the magnetic field intensity based on A/m in the steel lamination which is modeled as the function of magnetic flux density B. Moreover, the permanent magnets (PMs) are modeled as excitation sources respect to Maxwell's equations, in which the magnetic flux density and conductivity can be assumed as follow [34], if only the Eddy currents in the block of PM is ignored:

$$\begin{aligned} \overline{B} &= \mu_0 . \mu_{rec} . \overline{H} + \overline{B}_r \\ \sigma_{PM} &= 0 \end{aligned} \tag{2-43}$$

where B_r is the remanent flux density vector which theoretically gives direction to B of the excitation sources. Therefore, the modeled generator with a radial outward magnetization vector in the x-y reference plane can be defined as [1] [33-35]:

$$\begin{bmatrix} B_{r,x} \\ B_{r,y} \end{bmatrix} = \begin{bmatrix} B_{r(120)} \cdot \dfrac{x}{\sqrt{x^2 + y^2}} \\ B_{r(120)} \cdot \dfrac{y}{\sqrt{x^2 + y^2}} \end{bmatrix} \tag{2-44}$$

- Settings of the subdomains, when the 2-D model is drawn based on the above assumptions and design constraints, besides, the properties of the geometry such as material coefficients (which involves curve fitting of the soft and hard magnetic materials) and excitation sources are required to be modified for various subdomain within the model.

- Boundary condition setting is a need to allow the FEM software to simply recognize the range of area which is assumed to be computed. In addition, the stationary and rotary parts must be defined by different boundary setup based on Maxwell's boundary definitions. This boundary setting becomes very practical while either a segment of the machine (i.e. a quarter or half) or a moving boundary is targeted to be simulated due to the simulation time reduction.

- Prior to electromagnetic computation, a fine meshing is required because the accuracy of FEA depends on how good each block of the generator has meshed especially stator tooth. The robustness of any FE analysis results relies on the fitness of the generated mesh in the pre-calculation stage of the analysis. Modeling errors in this stage can be listed as [35]:

    1) Improper geometric description (if an axial symmetry and/ or rotational symmetry has been accounted without considering that an anti-symmetric load).
    2) A poor definition of the used materials, for instance, the limit of Poisson's ratio at isotropic materials.
    3) Bad Improper definition of the load that is not recommended to simplify complex load states or several loads with one load.
    4) A wrong boundary expresses.
    5) Choosing a wrong kind of analysis (depends on the case).
    6) Singularity concept existing in the model, which leads the points in the model where values tend toward an infinite value; FE model where the infinite density and gravity are equivalent to an infinite stress in a sharp corner. Singularities due to an accuracy problem in the model that implies a problem of visualization because singularities extend the range of stresses.

Field solution based on the discretized partial differential equation carries out specialized mathematical algorithms which have been developed over many years. Basically, the discretization transforms the partial differential equation into many simultaneous non-linear algebraic equations consist of the unknown node potentials, hence, iteration is needed. Thus, the Newton-Raphson, as well as conjugate-gradient, are often applied [36]. As the results from the filed solution are the magnetic vector, therefore, post-processing task which is normally the engineer's work provides the remarkable values to examine if either the machine is designed proper or not.

During post-processing, a number of main quantities should be calculated based on the result from field solution such as leakage magnetic flux, leakage permeances, magnetic flux density, BH curve of the PMs in order to the impact of demagnetization, back-EMF, Lorentz force, and electromagnetic torque through Maxwell stress tensor method as given [21] [36]:

$$T_e(\theta) = \frac{1}{\mu}\left[\int_L r.B_{rad.}.B_{\tan.}dL\right]\times l_s \tag{2-45}$$

where μ is the permeability of the medium, L is integration contour, r is the radius, l_s is the stack length, $B_{rad.}$ and $B_{tan.}$ are radial and tangential components of the magnetic flux density.

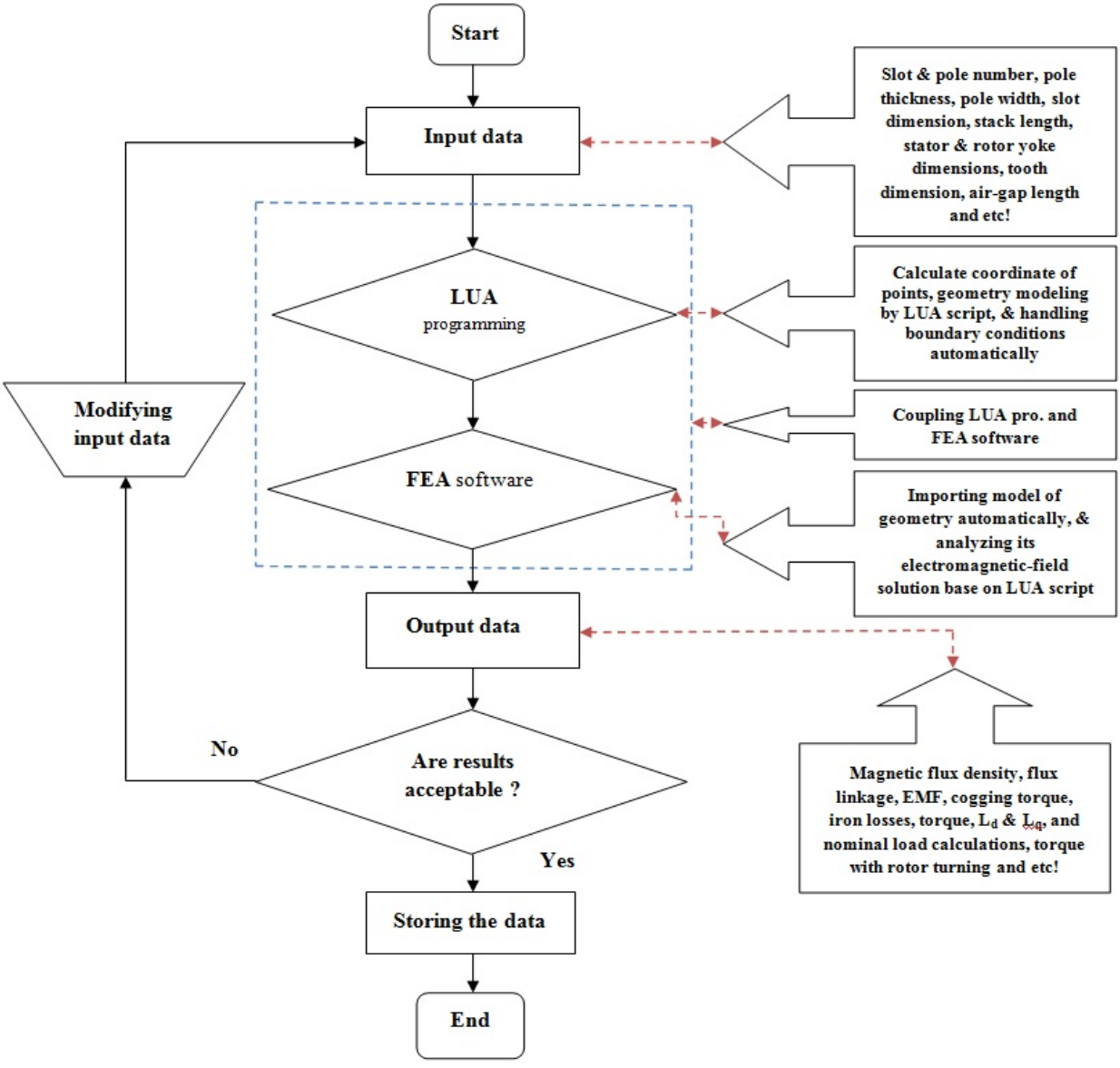

Fig. 2.3.1 Flow chart for pre-FEA analysis of PMSG including rotor motion.

The analytical model of PMSG (as initial design) has been verified using 2-D FEA-based design, where the generator is fed by inverters. To avoid cost, the power rating of inverter often is matching the power rating of the machine, where the current and voltage constraints because power rating limitation causes the stator winding current (I_s) and terminal voltage (V_s) are limited as given [1] [33]:

$$I_s = \sqrt{I_d^2 + I_q^2} \le I_{sm} \tag{2-46}$$

$$V_s = \omega_s . \sqrt{\lambda_d^2 + \lambda_q^2} \le V_{sm} \tag{2-47}$$

The limited terminal voltage can be rewritten as:

$$\sqrt{(L_d I_d + \lambda_m)^2 + (L_q I_q)^2} \le \frac{V_{sm}}{\omega_s} \tag{2-48}$$

In steady-state, the maximum stator current I_{sm} is the continues stator winding current rating, and the maximum terminal voltage V_{sm} is also the maximum reachable output voltage from the inverter respect to the dc-link voltage.

For non-linear material, μ is a function of the magnetic flux density. In Fig. 2.3.1, the proposed electromagnetic-based computation process to design and electromagnetic-field FE analysis for PMSG is shown. As presented in the core of the proposed flow chart employing FEA software is linked to LUA programming software. Capable initial data has been achieved after a couple of times of simulation in order to calculate the coordinates of points. Thus, the geometry modeling has automatically made through a combination of LUA script and user-interface of FEA software to obtain the program as much as possible flexible. After that, LUA scripts have been run firstly by generating a verifiable mesh and afterward the electromagnetic-field analysis including rotor motion with boundary conditions. With respect to this trend of calculation, time-consuming of the entire simulation has remarkably been reduced.

Fig. 2.3.2 illustrates the static polar view of the generated air-gap radial permeance, MMF, and radial flux density of the studied generator with 36 slots/ 40 poles, where the rotor motion is in a clockwise direction.

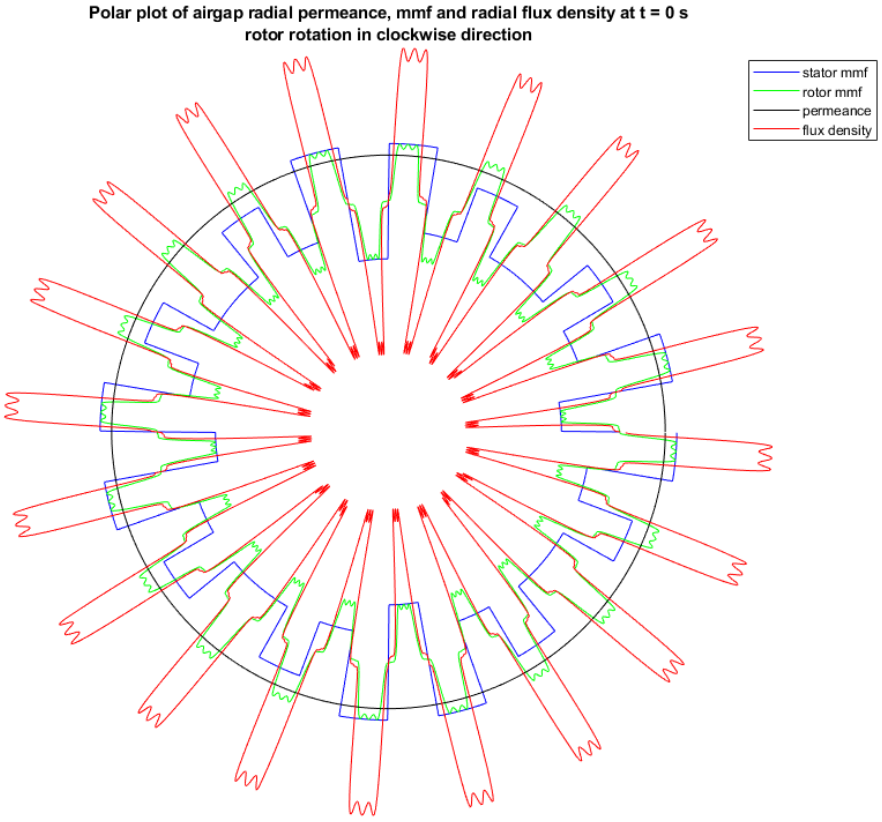

Fig. 2.3.2 Polar plot of air-gap radial permeance, MMF, and radial flux density at t = 0s.

2.3.1 Variable-Speed-Range Analysis Restrictions

The profile of torque and power in electrical machines (presented in Fig. 2.3.1.1) has such a variation. For a variable-speed AC drive fed from a voltage source and PWM controlled inverter, the area is divided into two sub-areas by base speed ω_b (where the rated voltage limit has been achieved), therefore, the left side region as function of speed from ω_0 to ω_b belongs to torque constant operation and the right side area based on rotational speed of ω_b to ω_{max} is when a constant power is achievable. However, the influence of flux weakening must be considered carefully, and thus, because the back EMF is proportional to speed, the flux weakening requires to be carried out in case the back EMF must be remained constant [37-40].

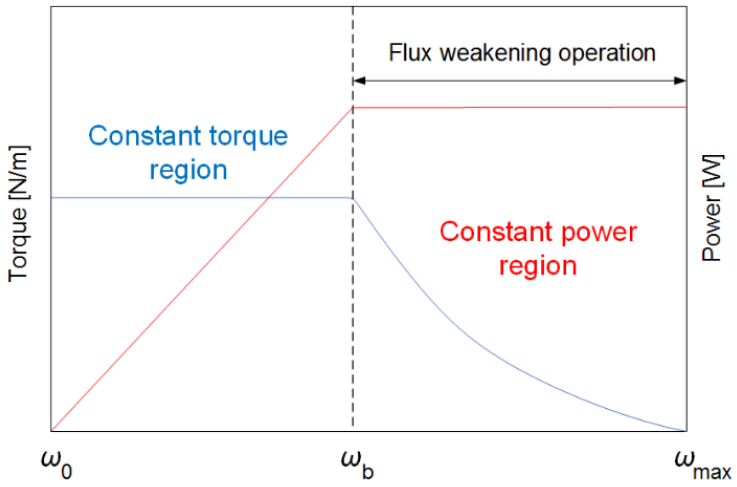

Fig. 2.3.1.1 Typical torque-power-speed profile characteristics for variable speed AC drives.

2.3.1.1 Current and Voltage

As the stator current is limited to a rated value I_{sm} in order to ensure a reliable thermal loading in PMSG. By defining a multi-modes control law as a function of speed, the torque-power-speed characteristics also have been computed (which will be demonstrated in the next section) [23] [36] as follow:

$$I_{dk} = \frac{\lambda_m}{L_{din}(I_n)} \tag{2-49}$$

$$I_{dn} = L_{din}(I_n), \quad L_{qn} = L_{qin}(I_n) \tag{2-50}$$

$$V_d^2 + V_q^2 < V_{\max} \tag{2-51}$$

The voltage limit can be rewritten as:

$$(\lambda_m + L_d I_d)^2 + L_q I_q^2 \le \left(\frac{V_{\max}}{\omega}\right)^2 \tag{2-52}$$

Note that, if I_{dk} has become smaller than I_n, then the maximum speed will be infinite.

Table. 2.3.1.1.1 Multi-modes approach for torque-power-speed profile computation.

Mode	Definitions	Note
Mode 1	$I_{d0} = 0,\ \ I_{q0} = \sqrt{(I_n^2 - I_{d0}^2)}$ $\omega_b = \dfrac{U_n}{\sqrt{(L_{qn}.I_{q0})^2 + (\lambda_m + L_{dn}.I_{d0})^2}}$	From ω_0 to ω_b, I_d will be zero. Only current is limited.
Mode 2	$I_{d2}(\omega) = \dfrac{1}{2.L_{dn}.\lambda_m}\left[\left(\dfrac{V_n}{\omega}\right)^2 - \lambda_m^2 - (L_{dn}.I_n)^2\right]$ $I_{q2}(\omega) = \sqrt{(I_n^2 - I_{d2}(\omega)^2)}$	From ω_b to I_{dk}, current and voltage are limited.
Mode 3	$I_{d3}(\omega) = -I_{dk},\ \ I_{q30} = \sqrt{I_n^2 - I_{dk}^2}$ $\omega_{max} = \dfrac{U_n}{\sqrt{(\lambda_m - L_{dn}.I_{dk})^2 + (L_{qn}.I_{q30})^2}}$ $I_{q3}(\omega) = \dfrac{\sqrt{\left(\dfrac{V_n}{\omega}\right)^2 - (\lambda_m - L_{dn}.I_{dk})^2}}{I_{qn}}$	From ω_b to ω_{max}. When I_d equals to I_{dk}.

Thereafter, if-loops can be defined to evaluate the defined multi-modes current and voltage limitation approach as the function of speed by:

$$I_d(\omega) = \begin{vmatrix} I_{d0} \ \ if \ \ \omega \le \omega_b \\ I_{d2}(\omega) \ if \ \ \omega_b < \omega \le \omega_{\max} \\ I_{d3}(\omega) \ \ otherwise \end{vmatrix}, \qquad I_q(\omega) = \begin{vmatrix} I_{q0} \ \ if \ \ \omega \le \omega_b \\ I_{q2}(\omega) \ if \ \ \omega_b < \omega \le \omega_{\max} \\ I_{q3}(\omega) \ \ otherwise \end{vmatrix} \tag{2-53}$$

where total current as the function of speed is:

$$I(\omega) = \sqrt{I_d(\omega)^2 + I_q(\omega)^2} \tag{2-54}$$

and voltage which is also individually graphed by Fig. 2.3.1.1.1:

$$V(\omega) = \omega.\sqrt{(L_{qn}.I_q(\omega))^2 + (\lambda_m + L_{dn}.I_d(\omega))^2} \tag{2-55}$$

Fig. 2.3.1.1.1 depicts the variation of limited resultant current (blue curve) by 3 A peak value, and voltage with red curve by 243 V over the variable-speed-range, where a wide flux weakening region is considered.

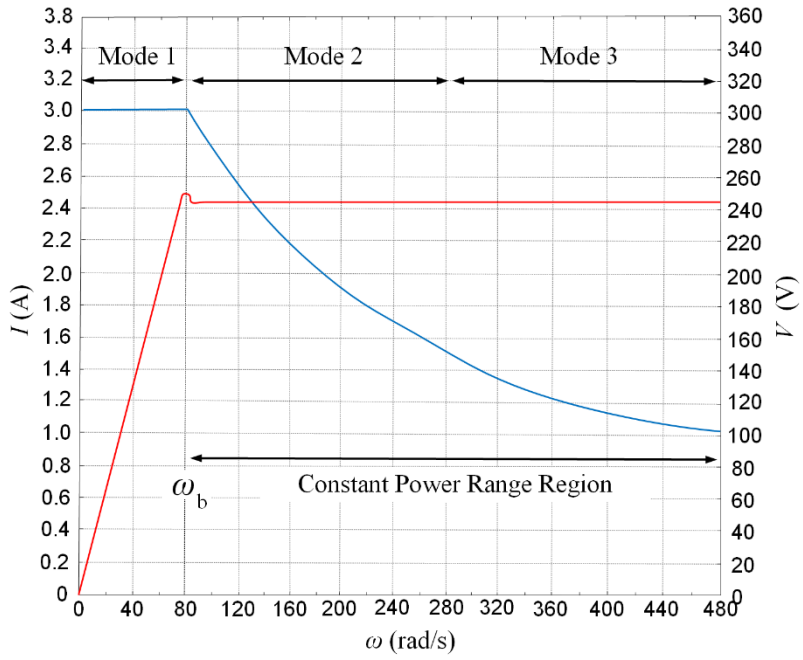

Fig. 2.3.1.1.1 Current and voltage limitations based on ω_b.

2.3.1.2 Constant Torque-Power-Speed Computation

The maximum torque of PMSG can be extracted within a certain range of speed from the current vector I_{Tm} [23] which can be carried out from:

$$T = \frac{3p}{2}\left(\lambda_m I_q + (L_d - L_q) I_d I_q\right) \tag{2-56}$$

$$\vec{I}_{T_m} = I_{rated} \angle \beta_{T_m} \tag{2-57}$$

where β_{Tm} is the resultant current angle, in which the maximum torque can be produced, the angle can be calculated using as follow [41]:

$$\beta_{T_m} = \arcsin\left(\frac{-\lambda_m + \sqrt{\lambda_m^2 + 8(L_q^2 + L_d^2)^2 I_{rated}}}{4(L_q - L_d) I_{rated}}\right) \tag{2-58}$$

As the stator current is limited to a rated value I_{rated} in order to ensure a reliable thermal loading in PMSG. Based on the defined multi-modes control law as a function of speed, the torque-power-speed characteristics also have been computed [23] as given:

$$T\left(I_d, I_q\right) = 3 \times 2p \times (\lambda_m . I_q) \tag{2-59}$$

$$\left(I_d, I_q, \omega\right) = T\left(I_d, I_q\right) . \omega / 2p \tag{2-60}$$

Therefore, I_{rated} at maximum angle generates a constant torque and consequently a magnetic flux λ_{Tm} which are calculable using the following equations [23] [41]:

$$T_m = \frac{3p}{2} I_{rated}\left(\lambda_m \sin\beta_{T_m} + (L_d - L_q) I_{rated} \cos(\beta_{T_m}) \sin(\beta_{T_m})\right) \tag{2-61}$$

where:

$$\lambda_{T_m} = \sqrt{\left(\lambda_m + L_d I_{rated} \cos(\beta_{T_m})\right)^2 + \left(L_q I_{rated} \sin(\beta_{T_m})\right)^2} \tag{2-62}$$

While the voltage increases linearly, the power also raises until the base speed. The maximum constant power over speed range ω_b to ω_{max} can be calculated from:

$$P = T_m \omega_b \tag{2-63}$$

where the base speed is [41]:

$$\omega_b = \frac{V_{max}}{\lambda_{T_m}} \tag{2-64}$$

Fig. 2.3.1.2.1 presents how the constant torque region (CTR) and power regions are provided based on the above definitions between speeds of 40 to 520 rad/s. The red curve represents the power variation by a maximum value of 601 W, as well as the blue curve indicates the torque variation by 131.2 N.m (peak value). Note that a wide constant power region is needed as the machine is operating in the application of wind power generation.

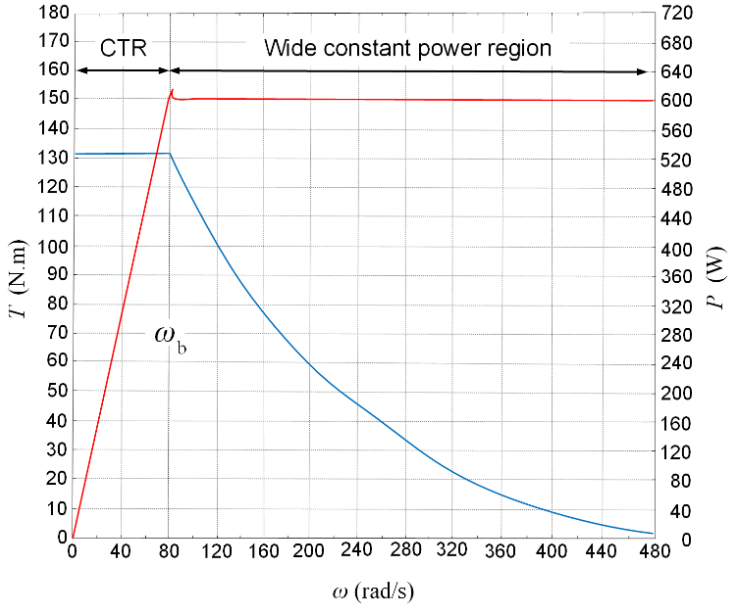

Fig. 2.3.1.2.1 Torque and power variable speed range profile.

2.3.1.3 Flux Weakening Region

When the current angle β_i exceeds the maximum current value of β_{max}, the demagnetizing current -I_d increases, and thus, it weakens the magnetic flux produced by PMs. Hence, the d-axis magnetic flux λ_d decreases. Similarly, in the q-axis, the stator winding current reduces which downgrades the q-axis magnetic flux λ_q. As a result, λ_i (β_i) becomes smaller than [1] [14] [23] [41]:

$$\lambda_{max}(\beta_{max}) = \sqrt{\left(\lambda_d\right)^2 + \left(\lambda_q\right)^2} \tag{2-65}$$

The rotational speed respect to the following equation will raise because the maximum voltage remained changeless [41-42]:

$$\omega = \frac{V_{\max}}{\lambda} \tag{2-66}$$

The maximum speed attainable depends on the flux weakening capability of the machine. The total flux linkage stays at its minimum value due to the stator winding current is applied to [41-42]:

$$\begin{cases} I_d = -I_{rated} \\ I_q = 0 \end{cases} \tag{2-67}$$

Therefore, the maximum rotational speed is restricted by [41]:

$$\omega_{\max} = \frac{V_{\max}}{\lambda_{\max} - L_d I_{rated}} \tag{2-68}$$

In the flux weakening capability study, another question is that at what range of speed the machine produces the rated power. The answer is constant power speed range (CPSR) as given [41-42]:

$$CPSR = \frac{\omega_2}{\omega_1} \tag{2-69}$$

As the power capability can be predicted based on $\lambda_{\max}$, L_d, as well as L_q, therefore, the maximum magnetic flux can be [41]:

$$\lambda_{\max} = L_d I_{rated} \tag{2-79}$$

Fig. 2.3.1.3.1 illustrates CPSR where the rated power 438 W respect to power curve (shown in red color), besides, the rated power and voltage (in blue) are reachable for a certain range of speed between ω_1 and ω_2.

By increasing the current angle β beyond 180˚-α_m/2, the effective air-gap flux density decrease, and consequently the speed can be higher up to infinite. For maximum torque, the maximum frequency, in where zero torque has been reported without leakage inductance consideration, can be defined as base frequency as follow [14]:

$$\frac{\omega_{e,\max}}{\omega_{e,base}} = \frac{1}{2\sin\left(\frac{\alpha_m}{2}\right) - 1} \tag{2-80}$$

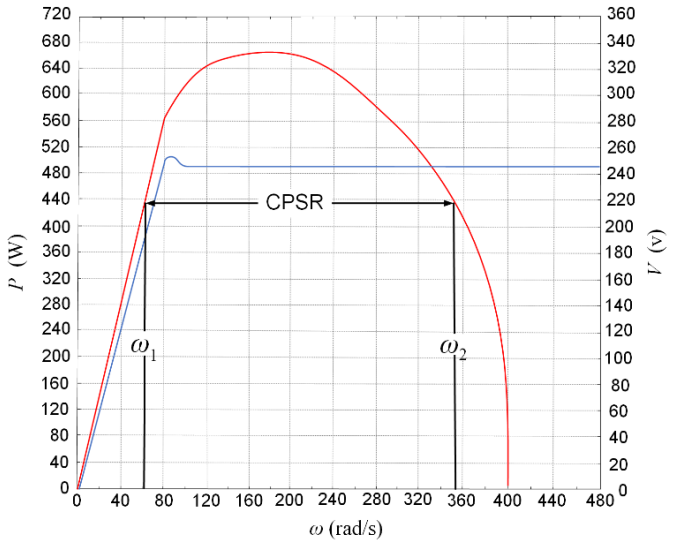

Fig. 2.3.1.3.1 CPSR and voltage variation under optimum current angel.

2.3.2 Radial and Tangential Magnetic Flux Density Calculations

In 1973, the influence of installing magnetic blocks in a certain order was discovered by Mallinson [23] to achieve higher airgap flux density for the very first time. This study relies on a permanent magnet synchronous AC generator with exterior rotor topology applied to a wind turbine. The initial design parameters are given in Table 2.3.2.1.

By simplifying the distribution of air-gap flux density, afterward, the analytical modeling [43] of it can be done as presented in Fig. 2.3.2.1.

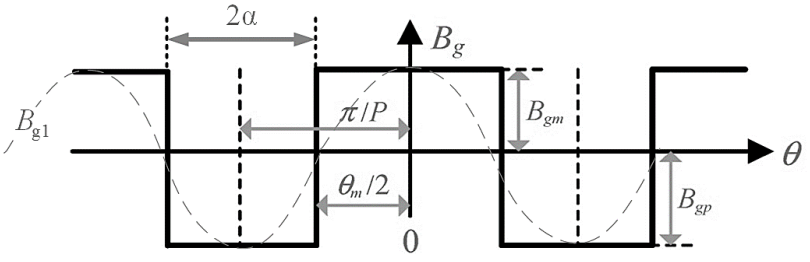

Fig. 2.3.2.1 Simplified shape of magnetic air-gap flux density distribution.

As the PM arc α_p is a significant parameter in the air-gap flux density, as given:

$$\alpha_p = \frac{\theta_m P}{2\pi} \tag{2-81}$$

where P is the number of pole pair and θ_m is the PM-arc angle. The Fourier series expansion of B_g can be calculated as:

$$B_g = \sum_i B_{gi} \cos(ip\theta) \tag{2-82}$$

Respect to Fig. 2.3.2.1, the air-gap flux density above in the PM pole B_{gm}, as well as iron pole B_{gp} are defined [43]:

$$B_{gm} = \frac{B_r}{1+\mu_{rm}(\frac{g}{h_m(1-\alpha_p)}} \tag{2-83}$$

$$B_{gp} = \frac{\alpha_p}{1-\alpha_p} B_{gm} = \frac{\alpha_p B_r}{1-\alpha_p+\mu_{rm}\left(\frac{g}{h_m}\right)} \tag{2-84}$$

The amplitude of fundamental air-gap flux density B_{g1} based on the above equations [43] can be expressed as:

$$B_{g1} = \frac{2p}{\pi}\left[\int_0^{\theta_m/2} B_{gm}\cos(p\theta)d\theta - \int_{\theta_m/2}^{\pi/p} B_{gp}\cos(p\theta)d\theta\right] \tag{2-85}$$

Additionally, the relationship between fundamental B_{g1} and air-gap flux density B_g can be written as:

$$B_{g1} = \frac{2\sqrt{2}}{\pi} B_g \sin\alpha \tag{2-86}$$

The stator contains 36 segmented teeth with closed slot modulation in order to reduce the amplitude of cogging torque significantly (which will be discussed fully in section 2.3.4). A 2-D FE model is simulated to examine magnetic flux distribution. The mesh is automatically generated (Fig. 2.3.2.2-a), and the magnetic field distribution versus rotor position of a PMSG with

radial orientation is presented in Fig. 2.3.2.2-b. The dips in the magnetic flux density in different points occur due to the slot opening of the stator lamination, in which the reluctance is much higher, and thus, the magnetic flux density is lower.

Fig. 2.3.2.3 illustrates the magnetic flux density B computation using 2-D FEA, in which the magnitude of B with a peak value of 1.39 T is shown in Fig. 2.3.2.3-a for a full mechanical rotation, besides, the radial component of B has presented (in Fig. 2.3.2.3-b) a good sinusoidal performance. Fig. 2.3.2.3-c indicates the tangential component of B by the peak value of 0.34 T.

Table 2.3.2.1 Initial design values of the machine geometry.

Variable	Value	Unit
D_{ro}/ D_{ri}	460/430	mm
D_{so}/ D_{si}	419/228	mm
l_s	100	mm
A_{slot}	802.7	mm^2
L_m	8	mm
δ_g	0.6	mm
S_w	15	mm
A_{PM}	100	°e
S_d	50	mm
Q_s	36	
α_p	0.55	
$2P$	40	
m	3	

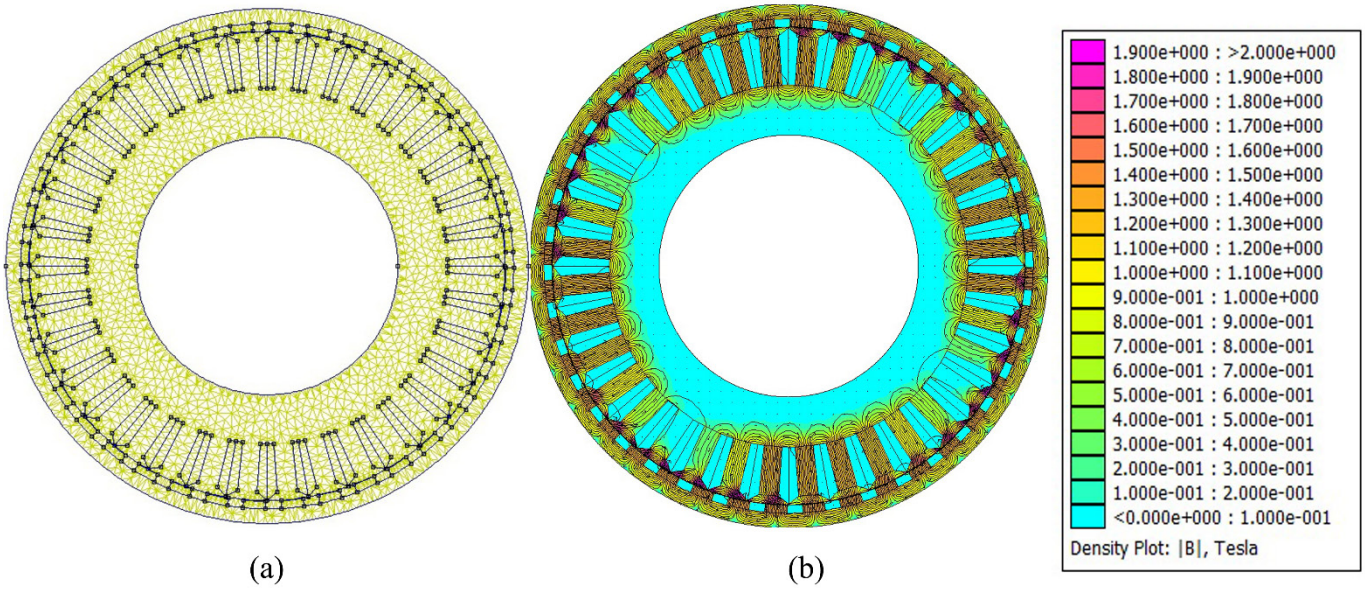

Fig. 2.3.2.2 FE-based schematic of the PMSG, a) generated mesh, and b) magnetic-field distribution.

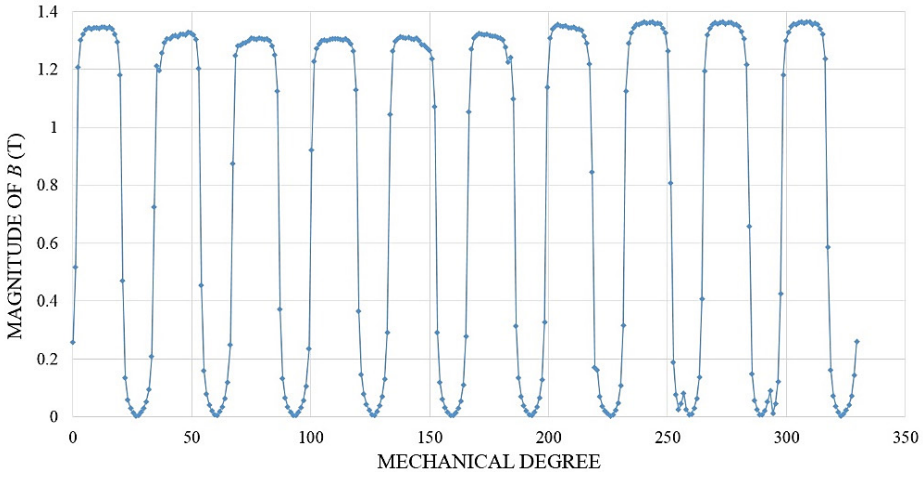

(a)

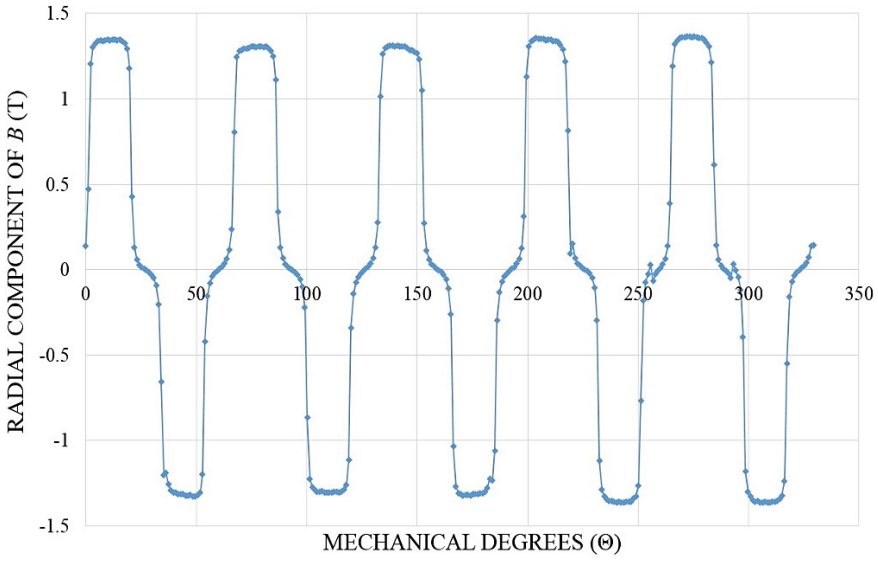

(b)

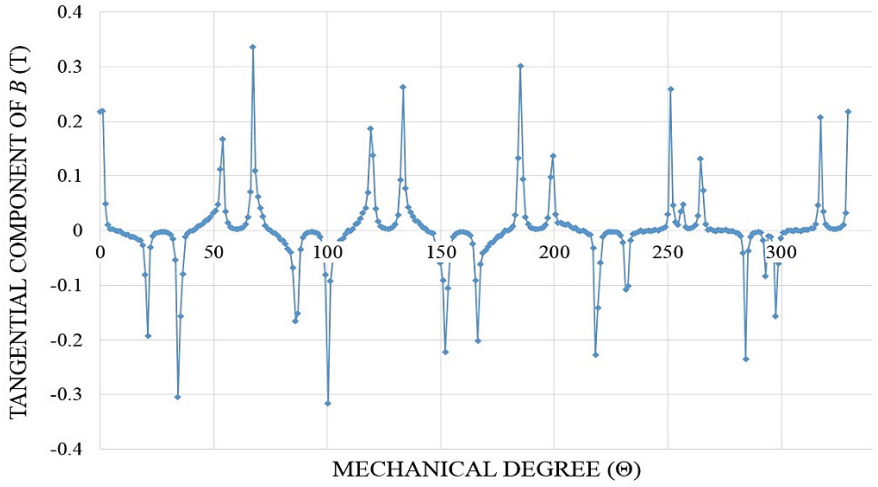

(c)

Fig. 2.3.2.3 Magnetic flux density components demonstration versus mechanical degree, a) magnitude of flux density, b) radial component of flux density, and c) tangential component of flux density.

2.3.3 Flux Linkage, Back-EMF, Cogging Torque, and Torque Calculations

- **Flux linkage calculation**

There are much research have done recently regarding flux linkage computation, the researchers [45] have proposed a novel scheme to identify the whole flux linkage map of PMSMs under uncertain circuit resistance and inverter nonlinearity. In another work [46], a novel analysis and design technique using the newly adopted synthetic flux linkage for PMSMs has been proposed.

Prior to the identification of the flux linkage profile, the RMS value of total voltage per phase for rotating flux is [23] needed to be known by:

$$E = N_c.\frac{\sqrt{2}D_{is}L}{p}\hat{B}_{g1}\omega_s = 4.44f.N_c.\phi \tag{2-87}$$

where N_c is the number of turns per phase in equivalent full pitch winding which can be calculated from:

$$N_c = k_\omega.N_{ph} \tag{2-88}$$

N_{ph} is the number of turns per phase in an actual winding, k_ω is the winding factor (which are calculated in section 2.2.2). D_{is} is the inner diameter of the stator. ω_s is the frequency which equals basically to $2\pi f$. ϕ is the maximum magnetic flux which passes through one full pitch coil [23] [45-46] as given:

$$\phi = \frac{2D_{is}L}{p}\hat{B}_{g1} \tag{2-89}$$

By knowing all the above parameters, the stator flux linkage λ_m can be defined [45-46] as:

$$\lambda_m = \frac{\sqrt{2}E}{\omega_s} = \frac{2D_{is}L}{p}\hat{B}_{g1}.k_\omega.N_{ph} \tag{2-90}$$

According to Faraday's induction law, the air-gap back-EMF of an electrical machine has to be induced at the magnetizing inductance L_m of the machine as a result of a propagating fundamental component of air-gap flux density. Due to a spatial slotting, the permeance harmonics induce EMF components at the fundamental frequency of the fractional 2nd-grade winding. To calculate the EMF of each phase, first of all, the flux linkage for each phase as given [1]:

$$\psi_{a1,m} = \iint_S n_a(\theta_s).B_{g1}(\theta_s,\theta_m)\,dA = l_s.r_s\int_0^{2\pi} n_a(\theta_s).B_{g1}(\theta_s,\theta_m)\,d\theta_s \tag{2-91}$$

$$\psi_{b1,m} = \iint_S n_b(\theta_s).B_{g1}(\theta_s,\theta_m)\,dA = l_s.r_s\int_0^{2\pi} n_b(\theta_s).B_{g1}(\theta_s,\theta_m)\,d\theta_s \tag{2-92}$$

$$\psi_{c1,m} = \iint_S n_c(\theta_s).B_{g1}(\theta_s,\theta_m)\,dA = l_s.r_s\int_0^{2\pi} n_c(\theta_s).B_{g1}(\theta_s,\theta_m)\,d\theta_s \tag{2-93}$$

Regarding the above equations, the flux linkage waveforms of the three phases are presented in Fig. 2.3.3.1-a, besides, the harmonic spectrum of the total flux linkage is shown in Fig. 2.3.3.1-b, where the highest harmonic order of 3 and 7 must be considered [44].

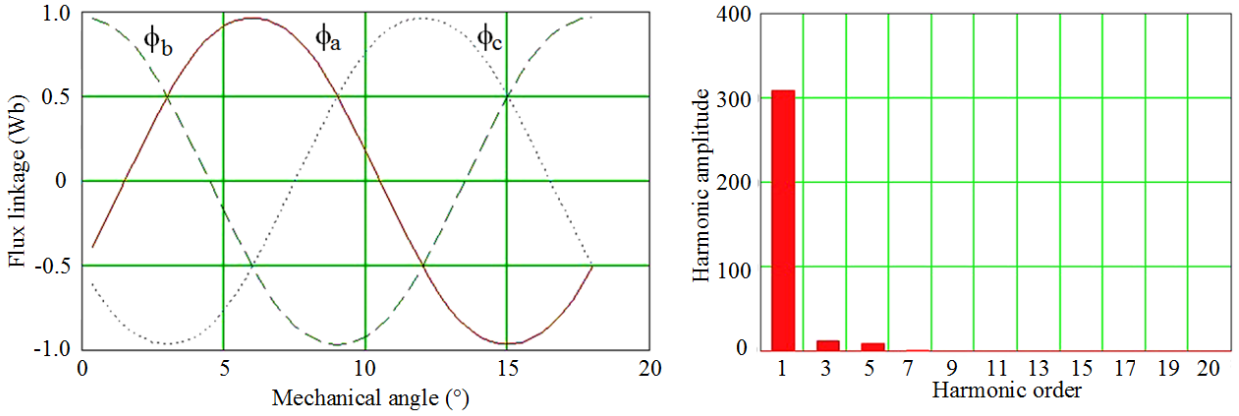

(a) (b)

Fig. 2.3.3.1 Flux linkage waveforms, a) for each phase, b) total harmonic contents.

- **Back-EMF calculation**

The impact of back-EMF in the rest of the machine's performance is a need to be examined. The researchers have worked the influence of speed ripple on the waveforms of back-EMF [47], the impact of a speed ripple on the back-EMF can become significant in some applications. In reference [48], they propose the optimization of the shape and size of a ferrite magnet and the arrangements necessary to reduce torque ripple and maximize back-EMF in a permanent-magnet-assisted synchronous reluctance motor. In another work [49], the researchers have developed a real-time method to detect the dynamic eccentricity of a rotor in a PM motor by monitoring a fault detection signal induced in an additional winding, without performing any further post-processing, even under a nonstationary rotational speed. After deriving a mathematical equation of the back-EMF induced in a tooth-coil winding, they proposed a fault detection signal, which is the back EMF in an additional winding divided by the rotational speed, when the additional winding is wound around the teeth corresponding to an even number of pole pitches.

The induced back-EMF E by the fractional-slot PMSG [1] [47-48] can be calculated from:

$$E = 2\pi \frac{N_{ph}\xi_1 f_s B_{PM1}}{\sqrt{2}} \tag{2-94}$$

where f_s is the frequency of stator field, ξ_1 is the fundamental harmonic of winding factor, and B_{PM1} is the fundamental air-gap flux density because of only PMs which can also analytically be solved using the approach used in [49]. The EMF of each phase (graphed by Fig. 2.3.3.2) can be calculated based on Faraday's law [1] by below equations:

$$e_{a1} = -d\psi_{a1,m}/dt \tag{2-95}$$

$$e_{b1} = -d\psi_{b1,m}/dt \tag{2-96}$$

$$e_{c1} = -d\psi_{c1,m}/dt \tag{2-97}$$

Fig. 2.3.3.2-a presents the variation of each phase back-EMF by the peak-to-peak value of 2 V, which is quite sinusoidal with a very small harmonic content, where the fundamental sinusoidal back-EMF curve (ideal) of phase A is compared to actual back-EMF of phase A in Fig. 2.3.3.2-b.

Fig. 2.3.3.3 illustrates the harmonic content of back-EMF, in which after the fundamental harmonic by 308 V, the 3rd and 5th harmonics are the most important harmonic orders. Mechanical restrictions and design considerations cause some harmonics in the flux and back-EMF of PMSMs. The back-EMF harmonics can be measured on the machine terminals if no stator current is present and the neutral point is accessible. The measured harmonics can then be consisting of a mathematical model of the machine. This measurement is typically done for a constant speed.

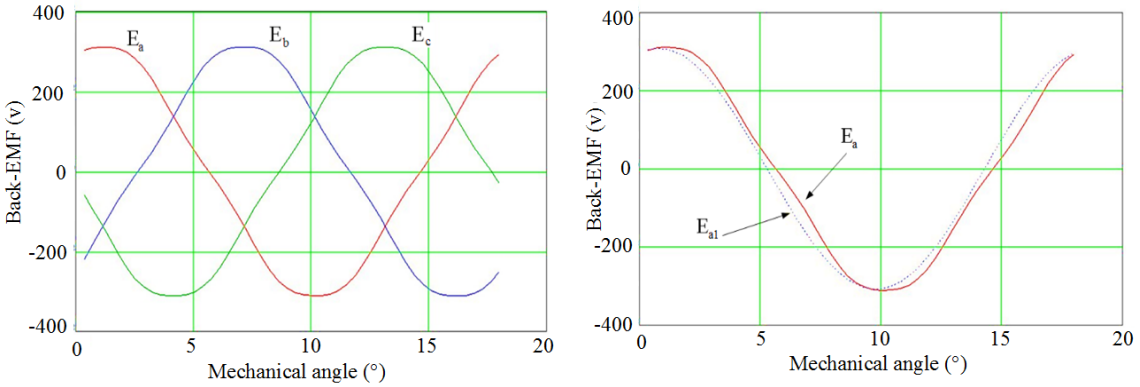

Fig. 2.3.3.2 Back-EMF waveforms per phase, a) three phase back-EMF, and b) actual phase A back-EMF B_a vs. fundamental value.

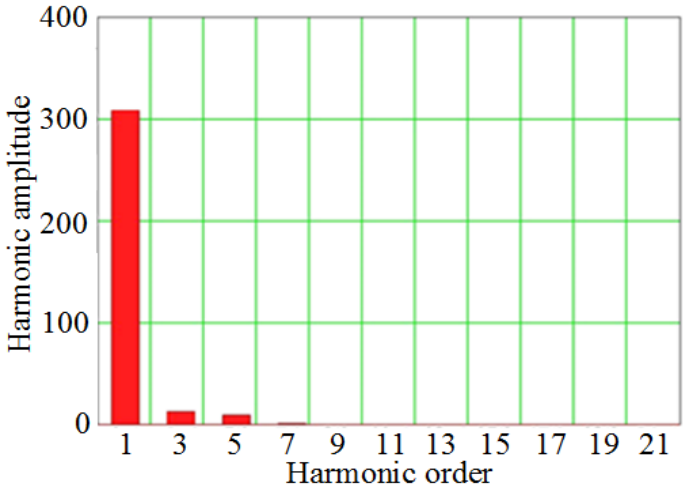

Fig. 2.3.3.3 Total harmonic content of Back-EMF of the studied PMSG.

- **Cogging torque calculation**

According to [1], cogging torque depends on the variation of the magnetic reluctance of the stator teeth when the rotor rotates. There are a few techniques to reduce the cogging torque. For instance, by skewing the stator slots or the rotor magnets by one slot pitch. In another study [50], researchers have pointed the magnet width w_m for equal tooth and slot widths, in which w_m has to be related to slot pitch by:

$$w_m \approx (m + 0.14)\tau_s \tag{2-98}$$

where m is an integer number of teeth under one pole.

There are a number of investigations [51-54] to reduce the maximum cogging torque without skewing the stator due to constriction difficulties. Either the pole-arc coefficient or the ratio of the slot opening to slot pitch can be optimized using numerical and analytical methods.

Based on the analytical Fourier series analysis using the Maxwell stress tensor method, the cogging torque of the surface PMSG [50-55] [17] can be defined as:

$$T_c(\theta_r) = \frac{\partial W_{airgap}(\theta_r)}{\partial \theta_r} = \frac{1}{4\mu_0} l_s (r_s^2 - r_m^2) \sum_{n=1}^{\infty} nNB_{nN}^2 \lambda_{nN}^2 \sin(nN\theta_r) \tag{2-99}$$

where N is the least common multiple (LCM) of $2p$ and Q_s, B_{nN}^2 and λ_{nN}^2 are the Fourier coefficient of $B_{mag}^2(\theta_s,\theta_r,r_{gav})$ and $\lambda_{ag}^2(\theta_s,r_{gav})$, respectively, for a period of 2π/N. θ_s is the angle [mech rad] along the stator periphery, and θ_r is the rotation angle [mech rad] of the rotor. $r_{gav} = r_g = (r_s + r_m)/2$. where r_s is the inner radius of the stator bore [m]. r_g shows the airgap radius [m]. r_m is the outer radius of the magnets [m]. Also, n index denotes the nth harmonic component. λ_{ag} is a relative permeance function (details can be found in [17]). W_{airgap} is the energy in the airgap in [J], μ_0 is the permeability in the air-gap, R_{is} is the inner radius of the stator, and α is the mechanical angle along the circumferential direction [50-53]. To calculate $B_{ab1,2}$, the following equations help:

$$B_{ab1,2} = \overline{B}_{r1}(z,\theta)\lambda(\theta) \tag{2-100}$$

$$\lambda(\theta) = \frac{R_{is} - R_{or}}{R_{is} - R_{or} + \pi R_{is}\left(\frac{b_0}{(2-\theta)/2}\right)} \tag{2-101}$$

where λ(θ) is the relative permeance of the slots, Ror is the outer radius of the rotor, b_0 is the slot width of the stator which can be given:

$$b_0 = \frac{(1-\delta_s)\pi}{Q} \tag{2-102}$$

Fig. 2.3.3.5 illustrates the cogging torque variation for the studied generator with 36 slots and 40 poles, where the average cogging torque equals to 0.334 N.m. Although, the cogging torque at the rated speed of 150 rpm seems small, in the section of optimization a Hlabach array-based technique will be discussed, where the cogging torque will be minimized.

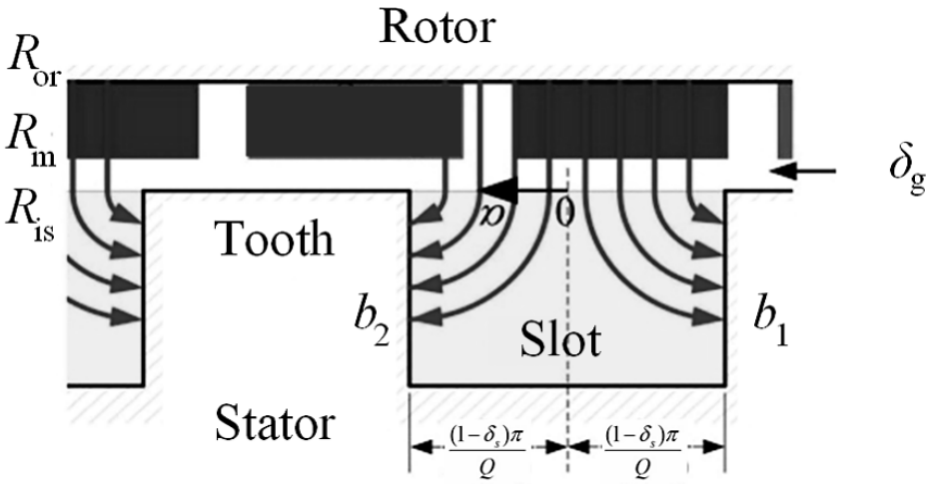

Fig. 2.3.3.4 2-D slotted stator model for the studied PMSG.

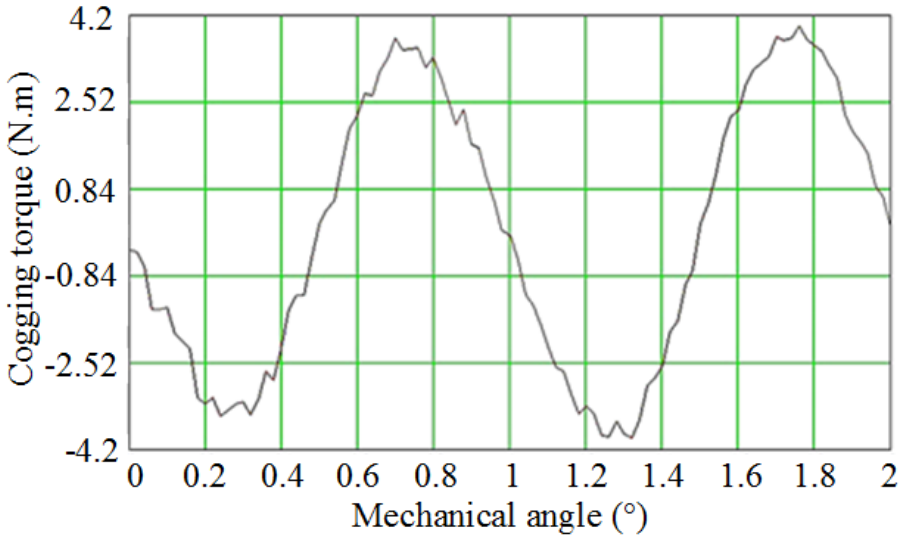

Fig. 2.3.3.5 Cogging torque variation for the studied PMSG.

- **Torque calculation**

As the development of advanced industrial products and technologies, the requirements for PMSMs with high torque density are increasing. Therefore, there are many investigations have done respect to torque improvement. For example, in reference [55], the researchers have proposed a new type of PMSM, named All-Harmonic-Torque PMSM (AHT-PMSM), which could use all harmonics of the magnetomotive force (MMF) generated by permanent magnets and armature currents to enhance the electromagnetic torque. Finally, it is demonstrated that the theoretical average electromagnetic torque of AHT-PMSM is improved by 23% comparing to that of the normal sinusoidal PMSM when they are with the same structure sizes and armature MMFs. In another works [56-60], research activities in novel theories and methods for improving the torque performance of the PMSM.

By defining the flux linkage in the d-q plane as follow:

$$\Psi_d = \Psi_{PM1} + L_d i_{d,} \tag{2-103}$$

$$\Psi_q = L_q i_q \tag{2-104}$$

$$\overline{\Psi}_s = \Psi_d + j\Psi_q \tag{2-105}$$

The torque can be obtained from power balance as given:

$$\Psi_{a,b,c} = \left|L_{a,b,c}(\theta_{er})\right|.\left|i_{a,b,c}\right| + \Psi_{PM_{a,b,c}}(\theta_{er}) \tag{2-106}$$

And therefore, the electromagnetic torque can be calculated using:

$$T_e = P_{abs}.\frac{P_e}{\omega_r} = \frac{3}{2}P_{abs}.Re\left(j\overline{\Psi}_s\overline{i^*}_s\right) = \frac{3}{2}P_{abs}\left(\Psi_d i_q - \Psi_q i_d\right) = \frac{3}{2}P_{abs}(\Psi_{PM1} + \left(L_d - L_q\right)i_d)i_q \tag{2-107}$$

Also, the electromagnetic torque can be calculated based on inductances and induced back-EMF as:

$$T_e = \frac{mp}{\omega_s^2}\left[\frac{E_{PM}U}{L_d}\sin(\delta_a) + \frac{U^2}{2}\left(\frac{1}{L_q} - \frac{1}{L_d}\right)\sin(2\delta_a)\right] \tag{2-108}$$

In this particular generator $L_d = L_q$, and thus, the maximum torque can be reached with a load angle of $\delta_a = 90^\circ$.

Fig. 2.3.3.6 presents the torque variation at the rated speed of 150 rpm for the studied PMSG with 36 slots and 40 poles. This graph indicates the torque turning which means the rotor is in the rotation, therefore, the torque is calculated at each degree of rotor rotation. The torque ripple of 6.75% has been calculated, where the average torque value is 350.715 N.m.

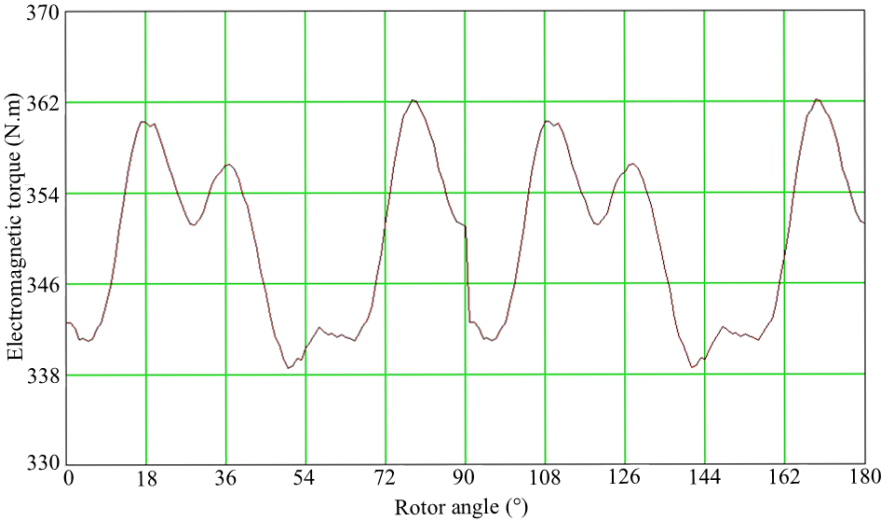

Fig. 2.3.3.6 Electromagnetic torque variation for the studied PMSG.

2.3.4 Phase Resistance and Joule Loss Calculations

There are two types of resistance in the stator of a PMSG regarding the passing current, as shown:

- Phase DC-resistance
- Phase AC-resistance

In low-speed PMSGs, the Joule loss often seems more critical than iron and mechanical losses, therefore, the machine phase resistance calculation is a need in order to provide a proper Joule loss estimation. Respect to the datasheet of each copper wire or conductor there is temperature dependency and the operation temperature of the winding which are important parameters. For the phase DC-resistance computation [14] [61], the following equation can be used:

$$R_{ph,DC} = \frac{l_{Cu}(1+k_{Cu}(T-20))}{\sigma_{Cu}.S_{Cu}.a} \tag{2-109}$$

where l_{Cu} is the total length of the phase coil, k_{Cu} is the temperature coefficient of copper resistivity which is $k_{Cu} = 3.8\times10^{-3}$ ˚C^{-1}. T is the average temperature of the coil in ˚C, σ_{Cu} is the electric conductivity of the copper at 20 ˚C temperature, and a is the number of parallel branches.

As the studied PMSG deals with AC current, it should be mentioned that the resulted resistance is often larger than phase DC-resistance due to the skin effect and proximity effect. Moreover, the eddy currents are also larger because of the slot leakage fluxes. For phase AC-resistance phase, as the shape of coils is circular with 1 mm diameter, therefore, there are no skin effects while χ =10 mm, as given:

$$d = 1mm <<< \chi = 10mm \tag{2-110}$$

where y is the depth of the slot, d_w is the diameter of single either wire or conductor, χ is the skin depth of the conductor or wire in free space which can be expressed as [62]:

$$\chi = \sqrt{\frac{2}{\omega\mu\sigma_{Cu}}} \tag{2-111}$$

where ω is the angular frequency.

According to [14], the total length of the phase coil l_{Cu} can be calculated as follow:

$$l_{Cu} = 2N_{ph}(l_s + (0.083p + 1.217)\tau_{p,ave} + 0.02m) \quad (2\text{-}112)$$

While the skin effect raises with the height of conductor, there is a subdividing technique, in which the conductor is segmented into subunits called "strand". Based on [14], the eddy currents in the stator coil can be significantly decreased via subdividing technique. The mean length of the coil can be calculated using:

$$l_{Cu} = 2l_s + 4l_{e2} + 4l_{e3} \quad (2\text{-}113)$$

where l_s is the length of the stator stack, l_{e2} is the straight extension of the coils beyond the stack, and l_{e3} is the diagonal portion of the end winding which can be calculated through:

$$l_{e3} = \frac{p\tau_{p,ave}}{2} \frac{\tau_{s,ave}}{\sqrt{\tau_{s,ave}^2 - (b_c + t_e)^2}} \quad (2\text{-}114)$$

where p is the slot pitch, $\tau_{p,ave}$ is the pole pitch measured from the slot radial midpoint, $\tau_{s,ave}$ is the slot pitch measured from the radial midpoint of the slots, and t_e is the spacing between coils.

After calculation of both phase current and phase resistance, the Joule loss at the stator winding can be defined as [1] [61-62]]:

$$P_{Cu} = mR_{ph}I_{ph}^2 \quad (2\text{-}115)$$

where m is the phase number, and I_{ph} is the RMS value of the phase current.

2.3.5 Electromagnetic Power and Efficiency Calculations

As lots of studies have done in order to minimize the machine's losses such as iron loss, Eddy current loss, Joule loss, mechanical loss, saturation loss, etc in order to maximize output power and efficiency. In [37] and [63], we have developed a new multi-objective optimization method based on dual response surface methodology and Booth's algorithm for sizing to maximize the output power of the generator which will be fully discussed in chapter 5. In another work [64], the researchers have proposed a new loss minimization control algorithm for inverter-fed PMSMs which allows for the reduction of the power losses of the electric drive without penalty on its dynamic performance, is studied. As result, in small motors enhancement, up to 3.5% of the efficiency can be reached in comparison with the PMSM drive equipped with a more traditional control strategy. In reference [65], a study on high-efficiency performance in an interior permanent-magnet synchronous motor (IPMSM) with a constant amount of PM. Based on a provided conventional single-layer IPMSM, a double-layer IPM rotor design has been proposed for improving motor efficiency performance under the same output torque performance. With the help of an introduced optimization approach, the design of the experiment, combined with the response surface methodology, an optimum design of the double-layer IPMSM model, is determined efficiently. Although, all above studies have very close and accurate sight of power and efficiency, they are very time-consuming for the first calculations. To provide a fast estimation of these two main parameters, the following expressions are presented.

By defining the instantaneous electromagnetic power [14] as given:

$$p_e(t) = e_a i_a + e_b i_b + e_c i_c \quad (2\text{-}116)$$

where e_a, e_b, and e_c present the instantaneous EMF of phase a, b, and c, respectively.

For calculating the electromagnetic power of the PMSMs, the general equation [14] can be expressed as:

$$P_e = m.E_1.I_1.\cos(\gamma) = m.E_1.I_1.\sin(\beta) \quad (2\text{-}117)$$

m is the number of phases, E_1 is the fundamental EMF of phase a, I_1 is the fundamental RMS current of the stator, γ is the electrical angle between the fundamental EMF E_1 and I_1, and β is the angular displacement between the fields generated through the PMs and the stator current.

As we have calculated the electromagnetic torque based on d-q plane currents, therefore, we can also calculate electromagnetic power as a function of torque and I_q because of voltage and current limitations, the power prediction is closer to practical value for the studied PMSG.

$$P_e(I_d, I_q, \omega) = T_e(I_d, I_q)\frac{\omega}{p} \tag{2-118}$$

where ω is angular speed, T_e is the electromagnetic torque, and p is the pole-pair number which is 20 in this study.

The energy efficiency of the PMSG can be predicted using the following expression:

$$\%\eta = \frac{\left|3\left(E_1 I_q + X_d - X_q I_d I_q\right) - P_{Cu}\right|}{\left|3\left(EI_q + X_d - X_q I_d I_q\right) - P_{Cu}\right| + \left|P_{Fe}\right| + \left|P_{mech}\right| + P_{Cu}} \times 100 \tag{2-119}$$

where X_d and X_q are the d-q plane reactance which can be calculated from:

$$X_d = \omega\frac{L_d}{1000}, \qquad X_q = \omega\frac{L_q}{1000} \tag{2-120}$$

Fig. 2.3.5.1-a presents an acceptable curve of output power calculated using above analytical expressions, where peak power can be reached by 1510 W at the rated speed of 150 rpm, and the amplitude of current phase A equals to 3A. Fig. 2.3.5.1-b indicates that a good efficiency over 95% around rated speed can be highlighted, in which it decreases over this speed gradually.

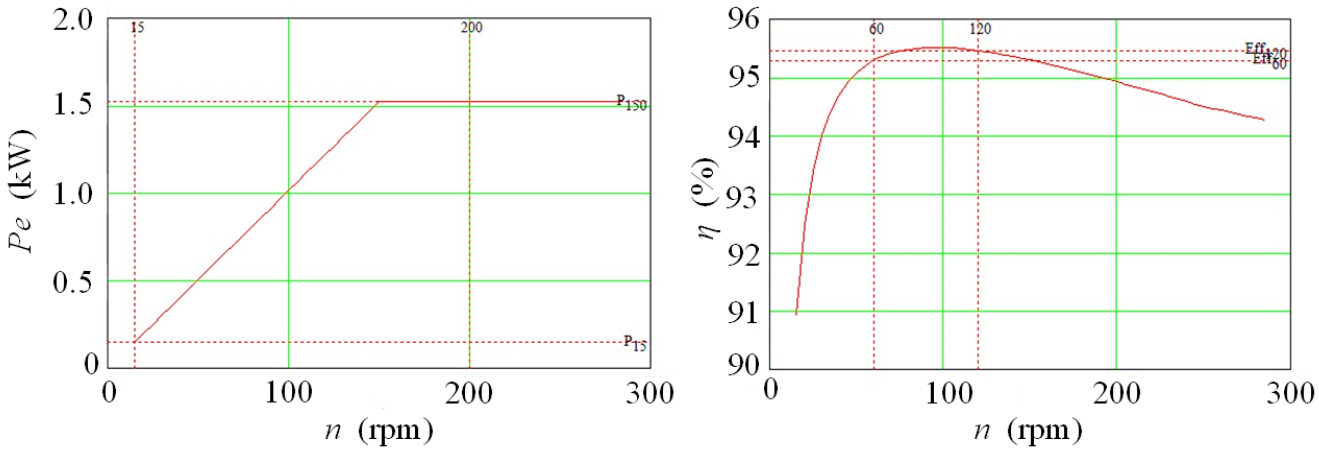

Fig. 2.3.5.1 Fast estimation evaluation versus speed, a) output power, and b) efficiency.

2.3.6 Optimum γ- angle Calculation

The expressions use the generator convention, as it delivers electrical power to the grid there is a positive gamma angle which requires a number of basic parameters as a function of this angle to be calculated [1]:

$$I_d(\gamma) = I.\sin(\gamma), \qquad I_q(\gamma) = I.\cos(\gamma) \tag{2-121}$$

where I is RMS value which is 2.121 A. The voltage equations based on d-q plane are given:

$$U_d(\gamma, I) = X_q(I).I_q(\gamma) - R.I_d(\gamma), \qquad U_q(\gamma, I) = X_d(I).I_d(\gamma) - R.I_q(\gamma) \tag{2-122}$$

where electrical reactance can be calculated from:

$$X_d(I) = \omega.L_d(I), \qquad X_q(I) = \omega.L_q(I) \tag{2-123}$$

Therefore, the internal power and Joule losses can be simply defined as [62]:

$$P_i(\gamma, I) = 3\left[E.I_q(\gamma) + (X_d(I) - X_q(I)).I_d(\gamma)I_q(\gamma) \right] \tag{2-124}$$

$$P_{Cu}(I) = 3RI^2 \tag{2-125}$$

where E as terminal voltage equal to $E = \lambda\omega$. Once the total generated power is known using [1] [62]:

$$P_{abs}(\gamma, I) = P_i(\gamma, I) + P_{mech} + P_{Fe} + P_{Cu}(I) \tag{2-126}$$

The efficiency of the generator as a function of gamma angle and total current can be written as [1] [62]:

$$\%\eta = \frac{P_i(\gamma, I) - P_{Cu}(I)}{P_{abs}(\gamma, I)} \times 100 \tag{2-127}$$

The initial gamma angle can be calculated by:

$$\gamma_0 = root\left(P_i(\gamma, I), \gamma, 0, \pi \right) = 1.571 \tag{2-128}$$

By Differentiation the power and root of it, the optimum gamma angle can be calculated as follow:

$$P_{der}(\gamma, I) = \frac{d}{d\gamma}\left[P(\gamma, I) \right] = \frac{d}{d\gamma}\left[P_i(\gamma, I) - P_{Cu} \right] \tag{2-129}$$

$$\gamma_{opt} = root\left(P_{der}(\gamma, I), \gamma, -\pi, \pi \right) = 0 \tag{2-130}$$

And for the maximum efficiency:

$$\begin{aligned} d\eta(\gamma, I) &= \frac{d}{d\gamma}\eta(\gamma, I) \\ \gamma_{opt} &= root(d\eta(\gamma, I), \gamma, 0, \gamma_0) = 0 \end{aligned} \tag{2-131}$$

where $-\pi$ to π are real numbers. Root searches for a root on the interval $-\pi \le x \le \pi$. To evaluate root with the symbolic equal sign. As a result of optimum angle calculation, we assume to extract the maximum power using this angle rather than any other angles, as follow:

$$P_{\max} = P\left(\gamma_{opt}, I \right) = 578.329 \quad W \tag{2-132}$$

$$\eta_{\max} = \eta(\gamma_{opt}, I) \tag{2-133}$$

Fig. 2.3.6.1 presents the impact of optimum gamma angle on the main outputs which are power and efficiency. The power variation proofs that the maximum power can be generated at 0 degrees of gamma angle which is shown in Fig. 2.3.6.1-a. Fig. 2.3.6.1-b indicates that also at this degree that maximum possible efficiency by 89% can be provided. It should be mention that these calculations are done for minimum speed rotation of 15 rpm.

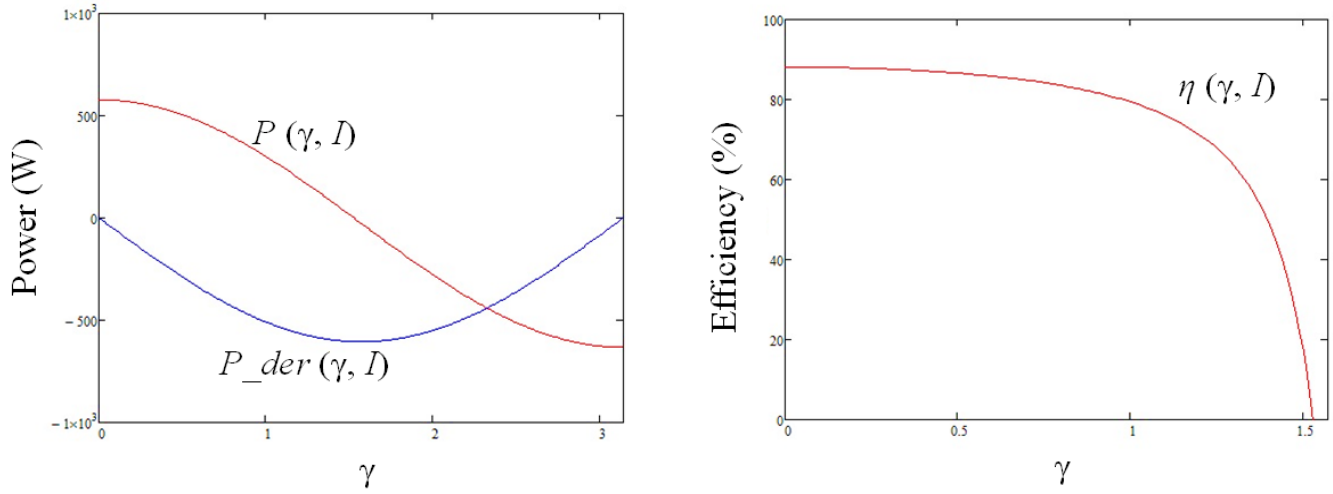

Fig. 2.3.6.1 Gamma angle evaluation at n = 15 rpm: a) power, and b) efficiency of the studied PMSG.

2.4 Three-Dimensional (3-D) Transient Electromagnetic FEA Method

Driven by the development of powerful and inexpensive computers, the field of computer-aided engineering emerged and has been offered tools and insights in complex engineering process which were only possible to achieve through costly experiment investigations. As modeling of electrical engineering problems leads frequently to nonlinear ordinary as well as partial differential equations, and thus, the most precise method to solve these equations is known as 3-D FEA. How to build a 3-D FE model and what to consider respect the type of simulation and application can be all found in the following worthy books [67-68].

A three-dimensional (3-D) finite element analysis (FEA) modeling known as the most accurate model due to a number of practical considerations such as the end effects of windings and magnetic which are not taken into account during 2-D FEA modeling. Although, 3-D FEA modeling is much more time-consuming in comparison with a 2-D model in both static (multiple rotor positions) and transient computations, the researchers often sacrifice time and complexity in order to provide solid results which are normally verified with a very small error by experimental tests. For doing this, a powerful computer is needed to especially simulate the full 3-D model, however, a new technique which uses a quarter of the model also is very precise and much less time-consuming. It is worthy to mention that this method is not popular for optimization computations today as a large number of iterations are required, and again timely process [37].

In this thesis, the design parameters of the studied PMSG is illustrated in Table 2.3.2.1 with a fixed current density, in which the maximum outer diameter is 460 mm with the stack length of 100 mm for a small standalone wind turbine. The primary dimensions are set based on the weight restriction of the tower. Also, the combination of 36 slots/ 40 poles with air-gap of 0.6 mm is chosen due to the acceptable electromagnetic outcome especially in cogging torque and back-EMF from double-layer fractional concentrated winding. Additionally, we have computed 3-D FEA using ANSYS Maxwell and JMAG software with a quarter of the full model. For transient calculations, a coupled-field circuit has been linked to the generator. Fig. 2.4.1 presents the built generator in the FE-package, where a quarter of the machine is shown. To execute the transient study, a coupled three-phase full rectifier load system has been linked to the generator which is illustrated in Fig. 2.4.2, in which we can test the performance under no-load- partial, and full load conditions as a function of time. This figure shows a 3-D FE model coupled with a variable-speed field-circuit PMSG finite element time-stepped model. It supplies power for an uncontrolled three-phase full rectifier load system which is shown as a whole in order to calculate the magnetic flux distribution and corresponding performance via a parameterized model [37] [69-70].

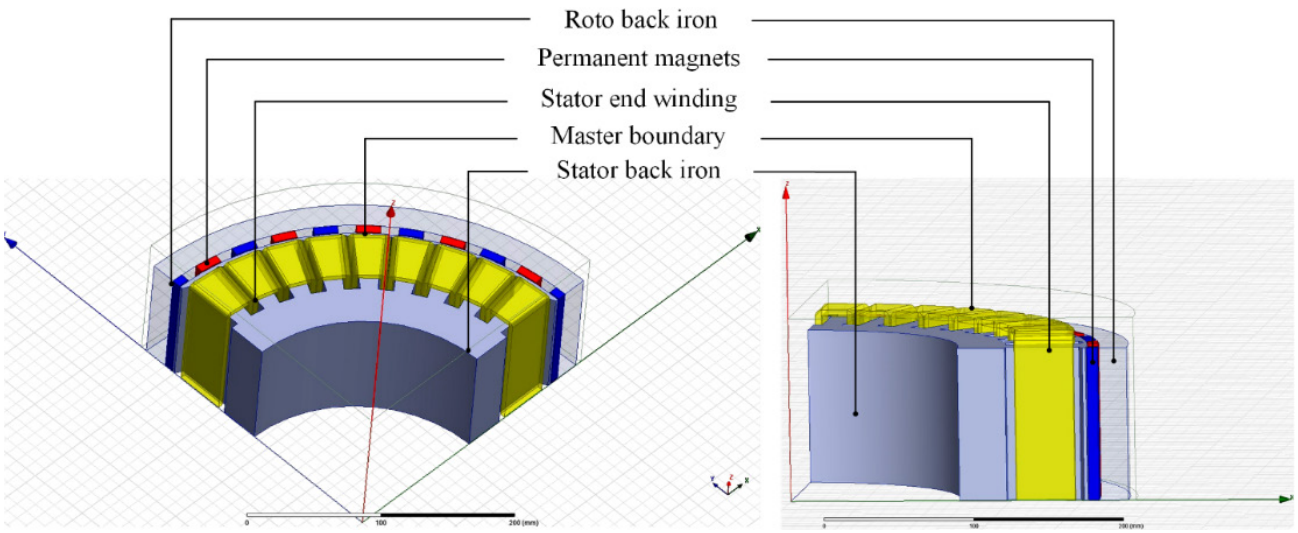

(a) (b)

Fig. 2.4.1 3-D view of the generator in ANSYS Maxwell environment, where: a) front view, and b) side view.

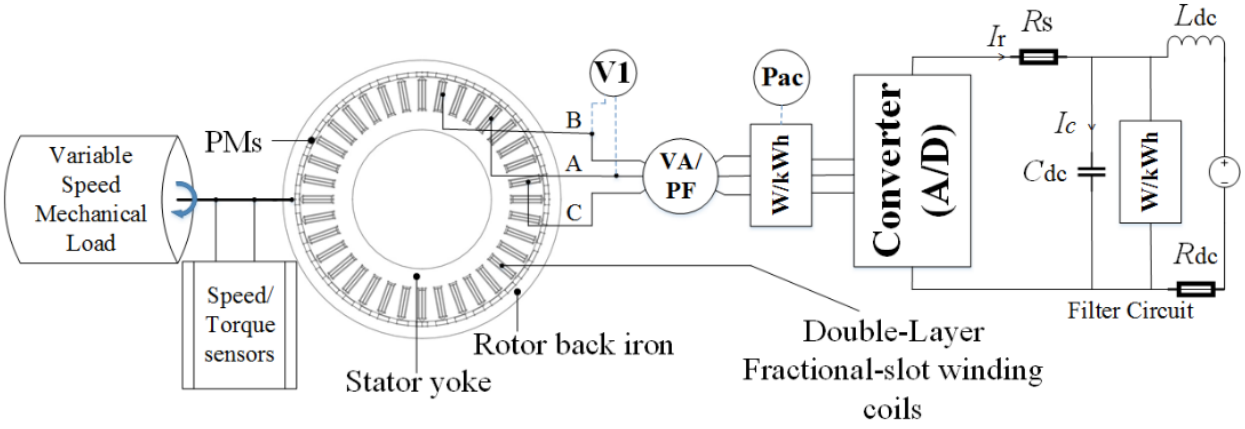

Fig. 2.4.2 A coupled three-phase full rectifier load system during test bench.

2.4.1 Time-depended Magnetic Flux Density Distribution

In this section, the 3-D FEA model of the generator has been successfully simulated, where the distribution of the magnetic flux density as a function of time in PMSG has been studied. In Fig. 2.4.1.1, the 3-D model has meshed with details presented in this graph, where 544289 elements and 163013 nodes have been generated. During 3-D FEA modeling, the continuity-periodic boundary conditions have been set, where we defined the vector magnetic potential of the source boundary A_{src} and the destination boundary A_{dst} as equal ($A_{src} = A_{dst}$). According to [70], the Arbitrary Lagrangian-Eulerian method, the generated meshes of the rotor motion are considered to be not deformed. Therefore, the dynamic part (rotor) slides over the stator as they have been coupled together through the symmetrical identity pairs. For transient (time-stepping) settings, basically, the simulations are either time-interval-based or by a number of defined time steps. The time length depends often on the time cycle of the fundamental back-EMF (internal voltage). For transient computations, the solver based on the Newton-Raphson method with Jacobian matrix has been updated at every single iteration [37] [70-71].

Fig. 2.4.1.2 depicts the no-load magnetic flux density distribution of the studied model under different times with a rated speed of 150 rpm, which are shown in Fig. 2.4.1.2-a-b-c-d-e-f-g-h-i-j-k, respectively. It is important to mention that the highest magnetic flux density has been recorded in the slot tips, where closed-slot topology used by approximately 2.0 T. In this time-depended graph, we focused on the hot spots (marked red circles), in which the highest magnetic flux density emerged in order to prevent any saturation problem. The FEA software package of ANSYS Maxwell has been used to provide these results [70-71].

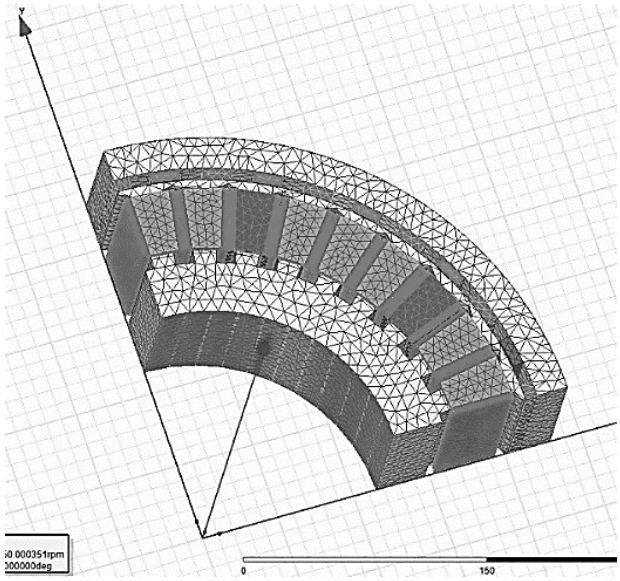

Fig. 2.4.1.1 Meshed 3-D model with a quarter of full generator.

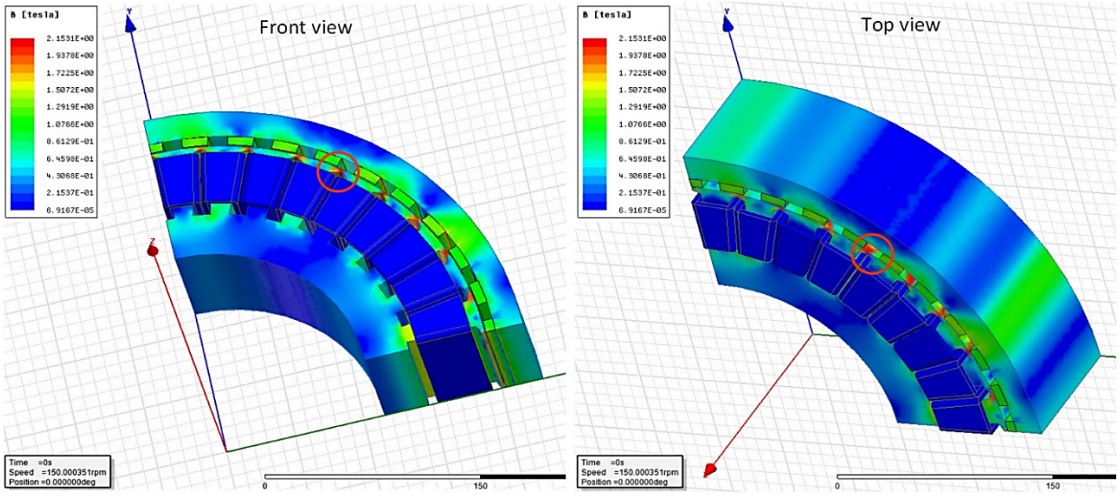

(a)

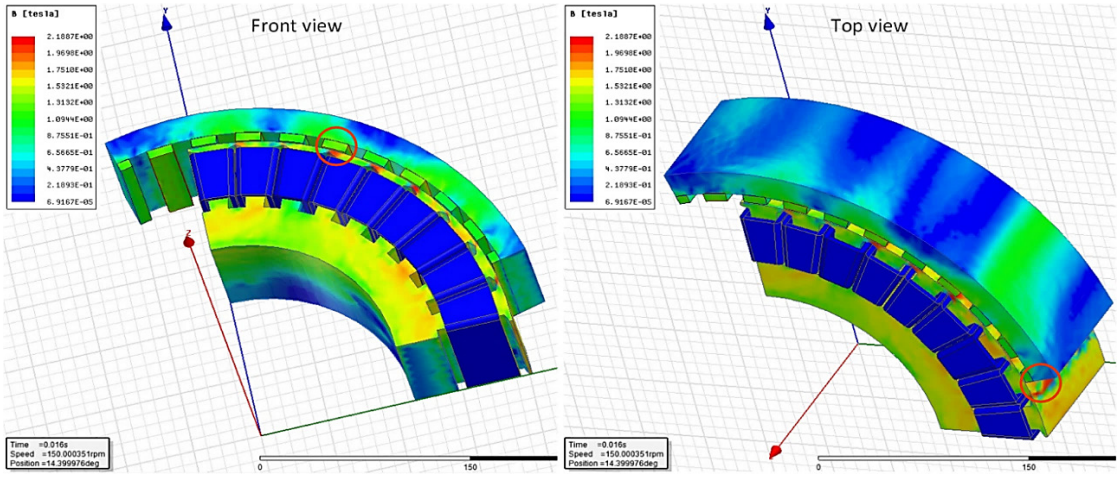

(b)

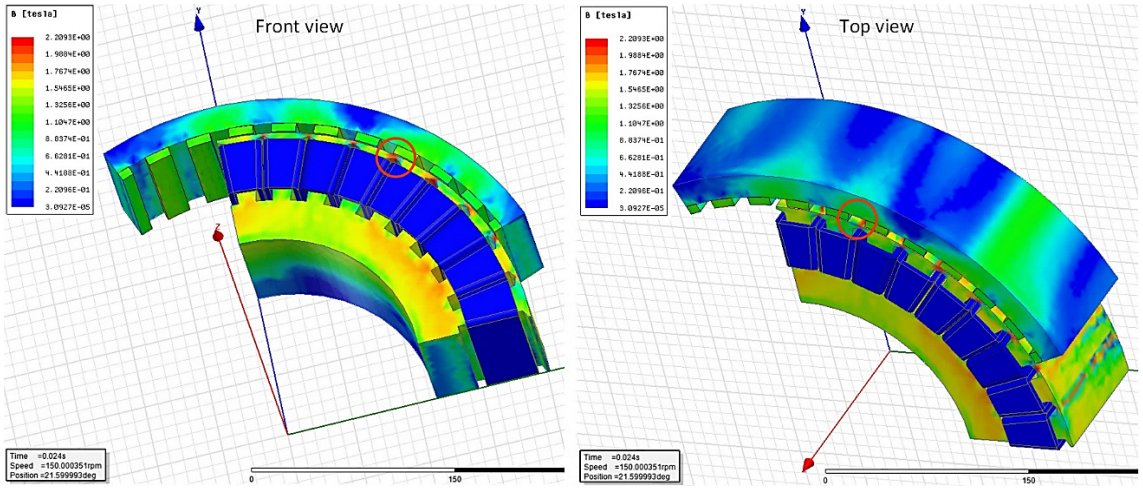
B [tesla]
2.2093E+00
1.9884E+00
1.7674E+00
1.5465E+00
1.3256E+00
1.1047E+00
8.8374E-01
6.6281E-01
4.4188E-01
2.2096E-01
3.0927E-05
Front view
Top view
Time =0.024s
Speed =150.000351rpm
Position =21.599993deg
0
150

(c)

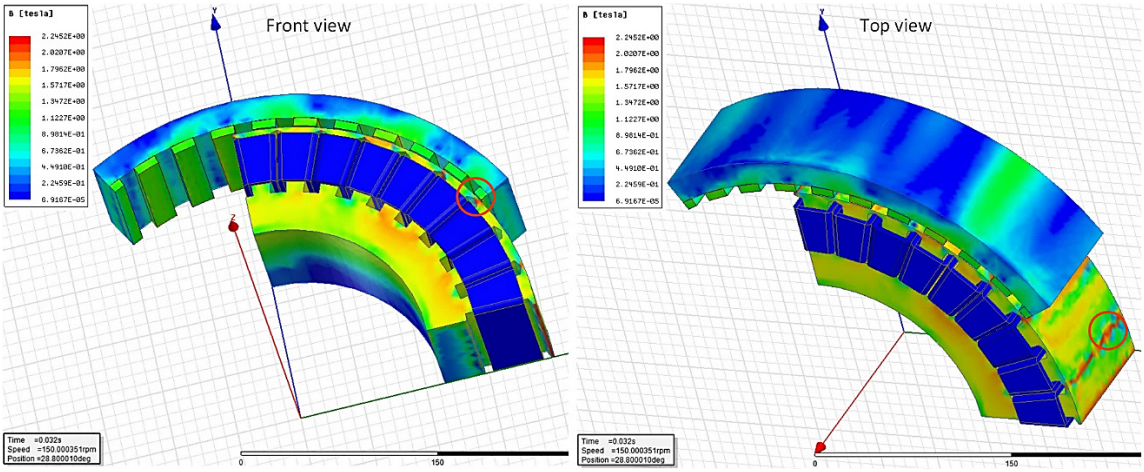
B [tesla]
2.2452E+00
2.0207E+00
1.7962E+00
1.5717E+00
1.3472E+00
1.1227E+00
8.9814E-01
6.7362E-01
4.4910E-01
2.2459E-01
6.9167E-05
Front view
Top view
Time =0.032s
Speed =150.000351rpm
Position =28.800010deg
0
150

(d)

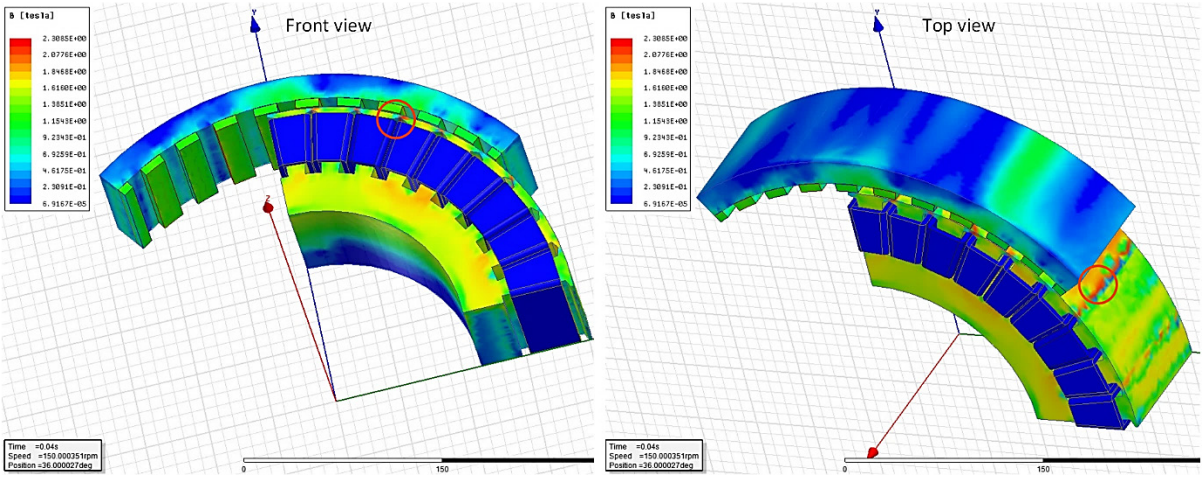
B [tesla]
2.3085E+00
2.0776E+00
1.8468E+00
1.6160E+00
1.3851E+00
1.1543E+00
9.2343E-01
6.9255E-01
4.6175E-01
2.3091E-01
6.9167E-05
Front view
Top view
Time =0.04s
Speed =150.000351rpm
Position =36.000027deg
0
150

(e)

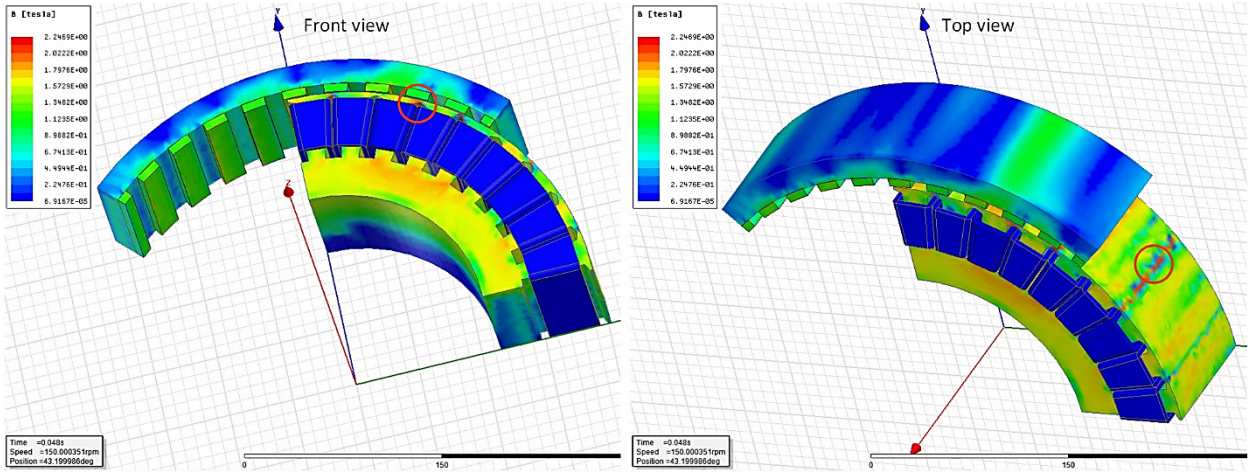
B [tesla]
Front view
Top view
Time =0.048s
Speed =150.000351rpm
Position =43.199986deg

(f)

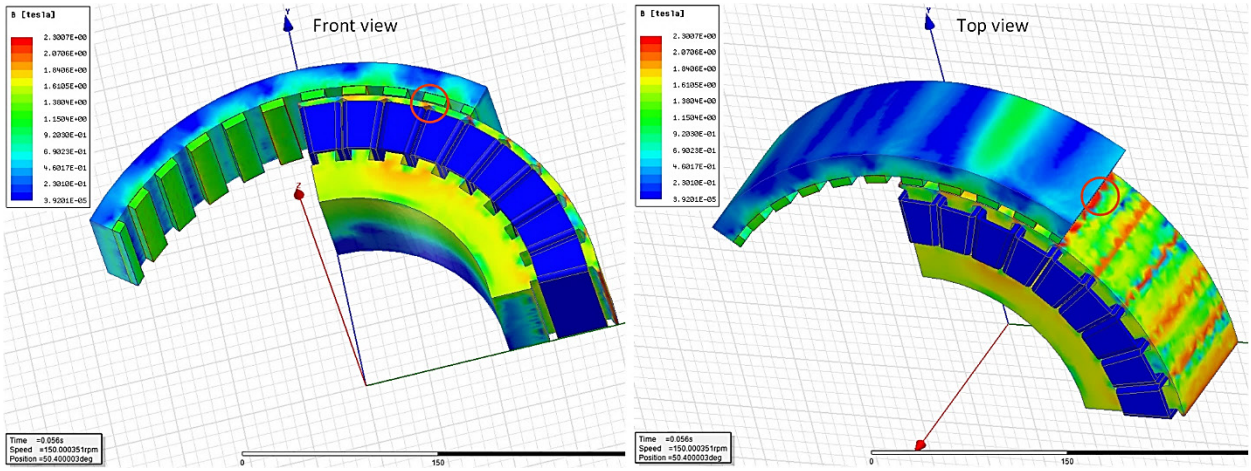
B [tesla]
Front view
Top view
Time =0.056s
Speed =150.000351rpm
Position =50.400003deg

(g)

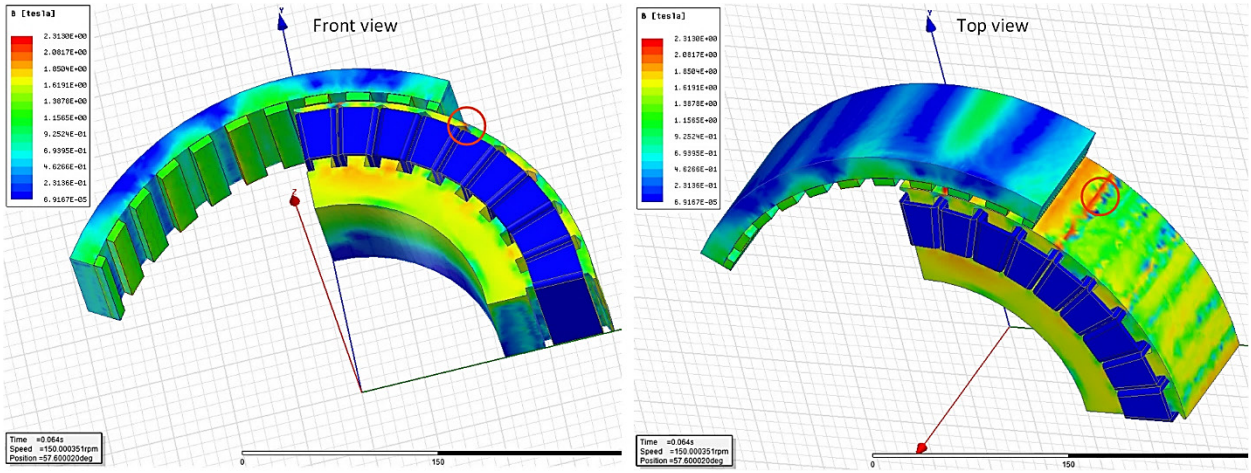
B [tesla]
Front view
Top view
Time =0.064s
Speed =150.000351rpm
Position =57.600020deg

(h)

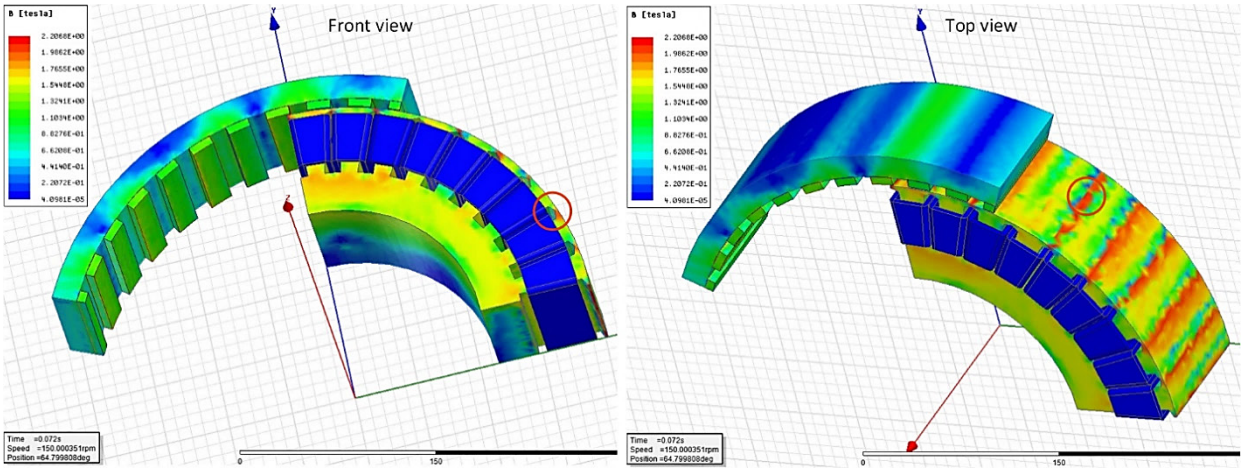

(i)

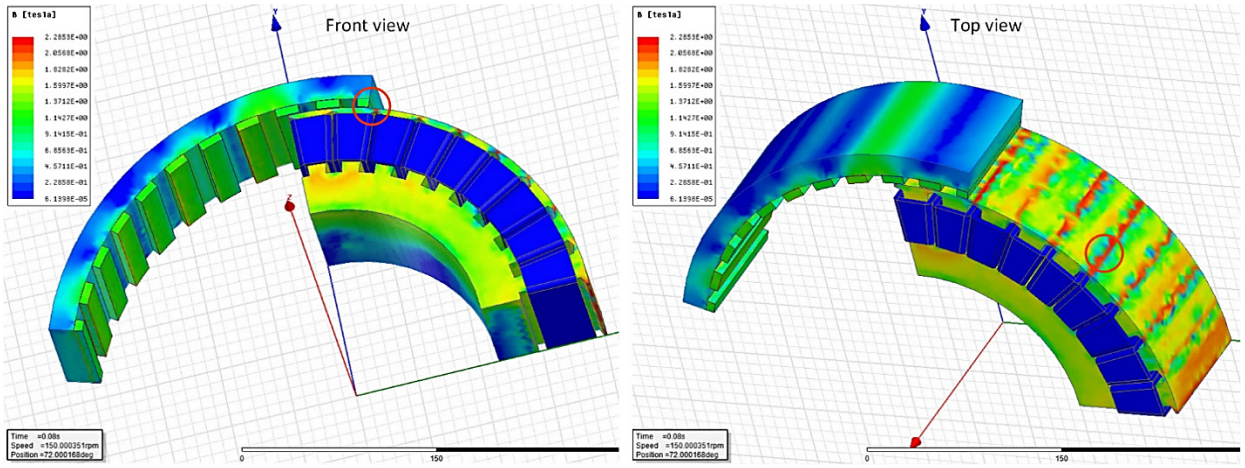

(j)

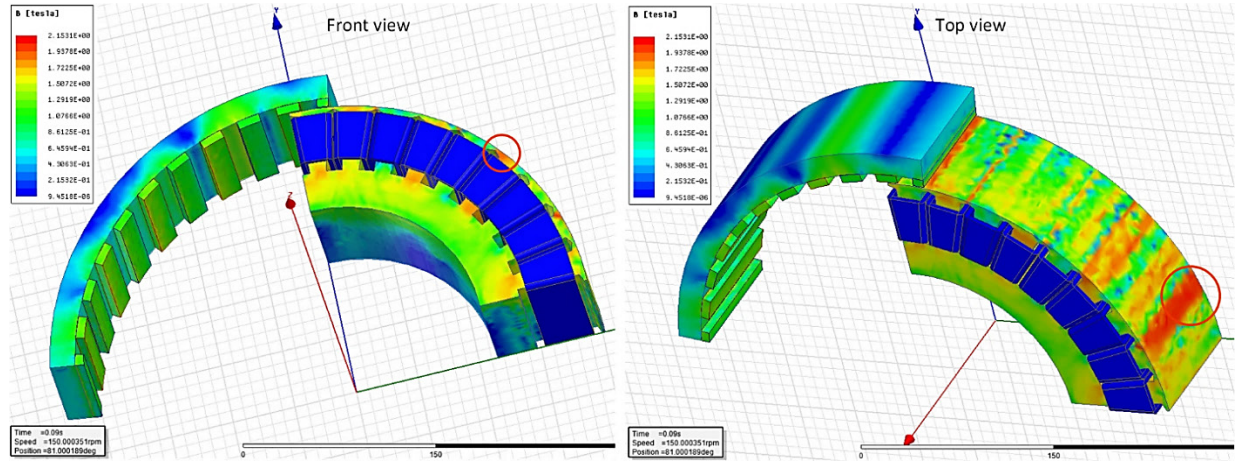

(k)

Fig. 2.4.1.2 Transient no-load magnetic flux density distribution of the 3-D model with 36 slots/ 40 poles at rated speed of 150 rpm using FEA, at: a) t = 0s, b) t = 0.016 s, c) t = 0.024 s, d) t = 0.032 s, e) t = 0.04 s, f) t = 0.48 s, g) t = 0.056 s, h) t = 0.64 s, i) t = 0.072 s, j) t = 0.08 s, and k) t = 0.09 s.

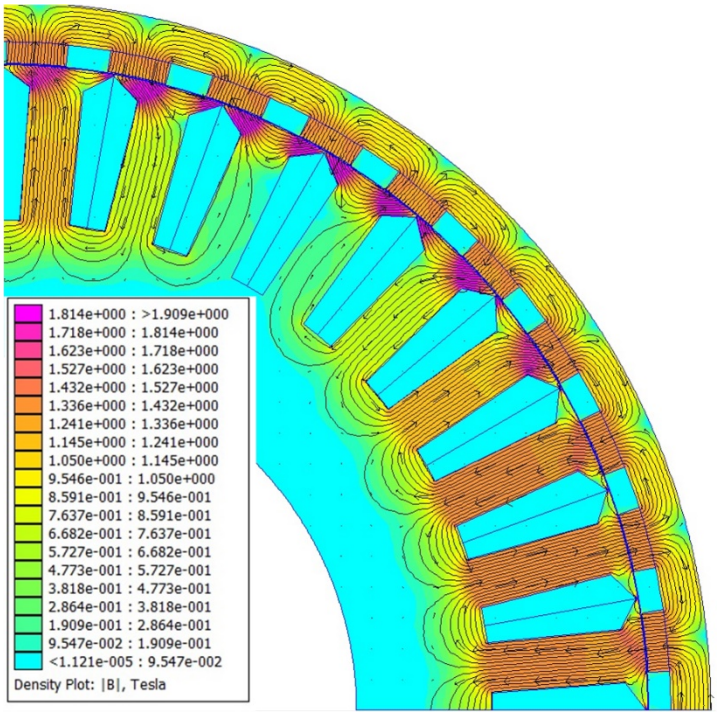

Fig. 2.4.1.3 No-load magnetic flux demonstration at rated speed of 150 rpm.

To evaluate the 3-D model the fluxes magnetization orientations throughout the model, the following Fig. 2.4.1.3 presented the magnetic flux distribution in the 3-D model which is shown in front view.

Fig. 2.4.1.4 presents the air-gap radial flux density as a function of time and angle for the rotor (Fig. 2.4.1.4-a), and the stator core (Fig. 2.4.1.4-b). As shown the magnitude of the rotor air-gap flux density by 0.9 T has a dominant behavior in comparison to the radial air-gap flux density at stator core which is about 0.3 T.

Fig. 2.4.1.5 illustrates the 2-D plot of the radial flux density at rotor (when the rotor motion angle is fixed in 0˚) as a function of time (Fig. 2.4.1.5-a), and also through FFT analysis over the curve, the existing harmonic contents have been presented in Fig. 2.4.1.5-b with the fundamental value of 0.846 T.

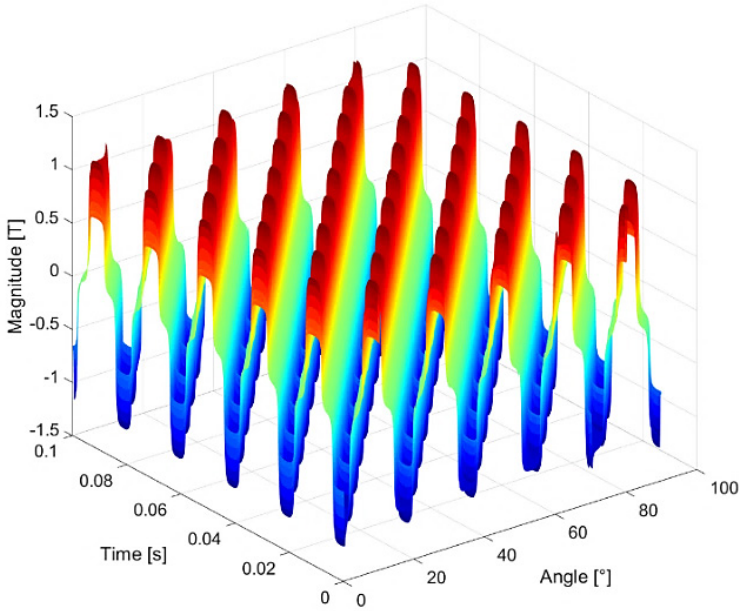

Fig. 2.4.1.4 Computed air-gap rotor radial magnetic flux density as function of time and angle.

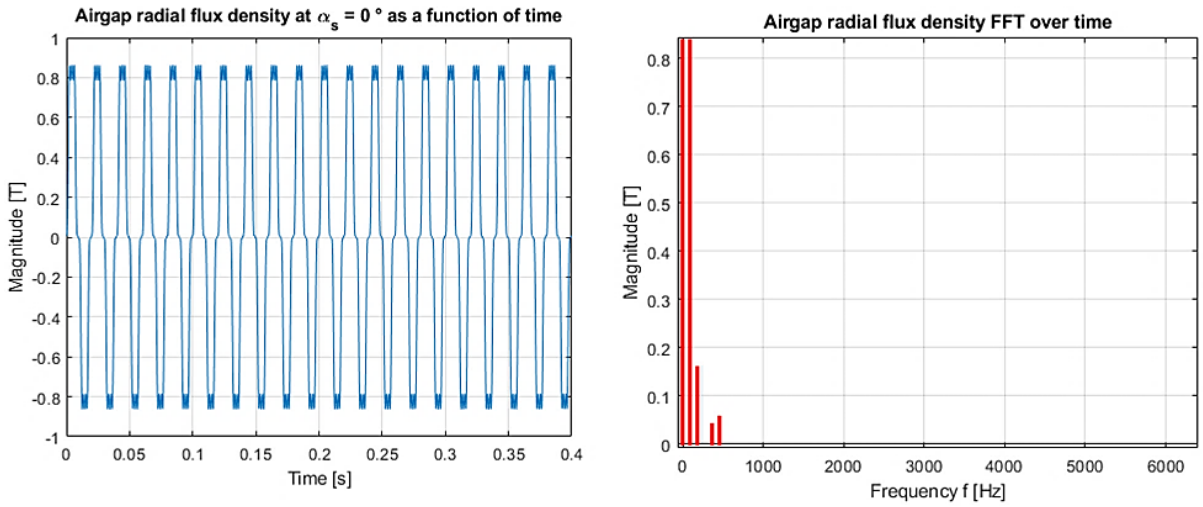

(a) (b)

Fig. 2.4.1.5 Computed rotor air-gap radial magnetic flux density: a) as function of time, and b) frequency.

2.4.2 No-load Air-gap Stator and Rotor MMF

During transient computation, one of the first or major machine computations which should be studied is the air-gap stator and rotor MMFs as a function of time and space, and their corresponding harmonics via FFT analysis. Due to the air-gap MMF quality, other main parameters have various behavior such as torque, torque ripple, flux density, etc. Fig. 2.4.2.1 illustrates the variation of no-load air-gap MMF of the stator as the function of time, where the waveform consists of three major loops of instability (which are marked by red arrows) before it becomes stable at 0.225 s. Fig. 2.4.2.2 presents the no-load air-gap MMF produced in the rotor as a function of time, in which a considerable sinusoidal MMF waveform exists with small unwanted ripples on peak values. Moreover, the time harmonics have been calculated by FFT, where the fundamental harmonic order has 7500 At.

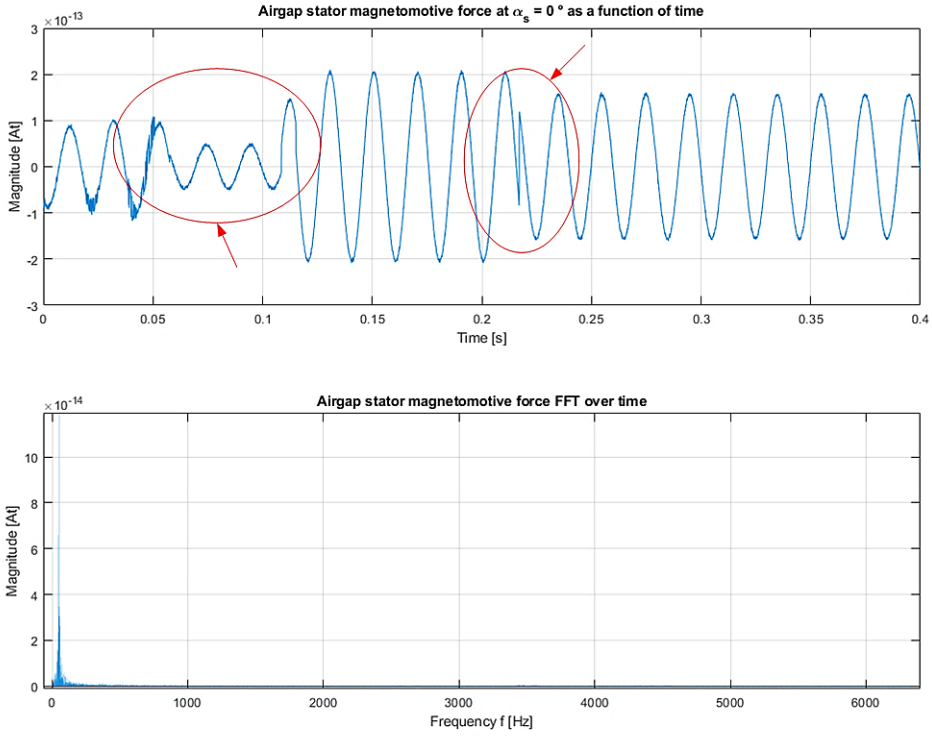

Fig. 2.4.2.1 Time-depended no-load air-gap MMF on the stator with existing harmonics using FFT over a range of frequencies.

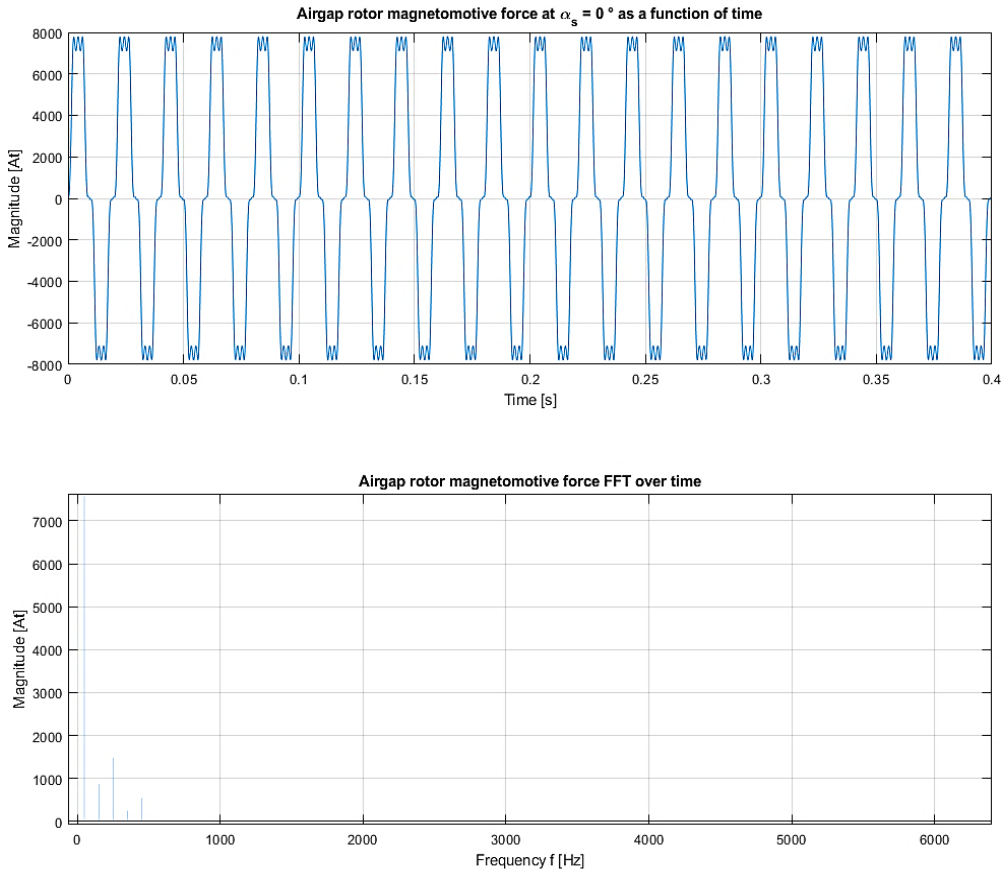

Fig. 2.4.2.2 No-load air-gap MMF variation of the rotor along with harmonics at various operation frequency.

2.4.3 No-load Air-gap Flux Density

In surface PMSGs, the permanent magnets play a major role on the radial air-gap flux density production. There are a number of studies regarding this computation. A 3-D analytical study of the magnetic field using integral transformation method is presented. Although, the model requires numerical iterations to compute the coefficients in the solution equations, which considerably increase the complexity of the model [72]. In other recent work [73], the researchers have investigated a fast-analytical method to compute the radial air-gap flux density distribution, where they result are verified using 3-D FEA along with experimental tests.

Fig. 2.4.3.1 presents the air-gap radial flux density as a function of time and angle for the rotor (Fig. 2.4.3.1-a), and the stator core (Fig. 2.4.3.1-b). As shown the magnitude of the rotor air-gap flux density by 0.9 T has a dominant behavior in comparison to the radial air-gap flux density at stator core which is about 0.3 T.

Fig. 2.4.3.2 illustrates the 2-D plot of the radial flux density at rotor (when the rotor motion angle is fixed in 0˚) as a function of time (Fig. 2.4.3.2-a), and also through FFT analysis over the curve, the existing harmonic contents have been presented in Fig. 2.4.3.2-b with the fundamental value of 0.846 T.

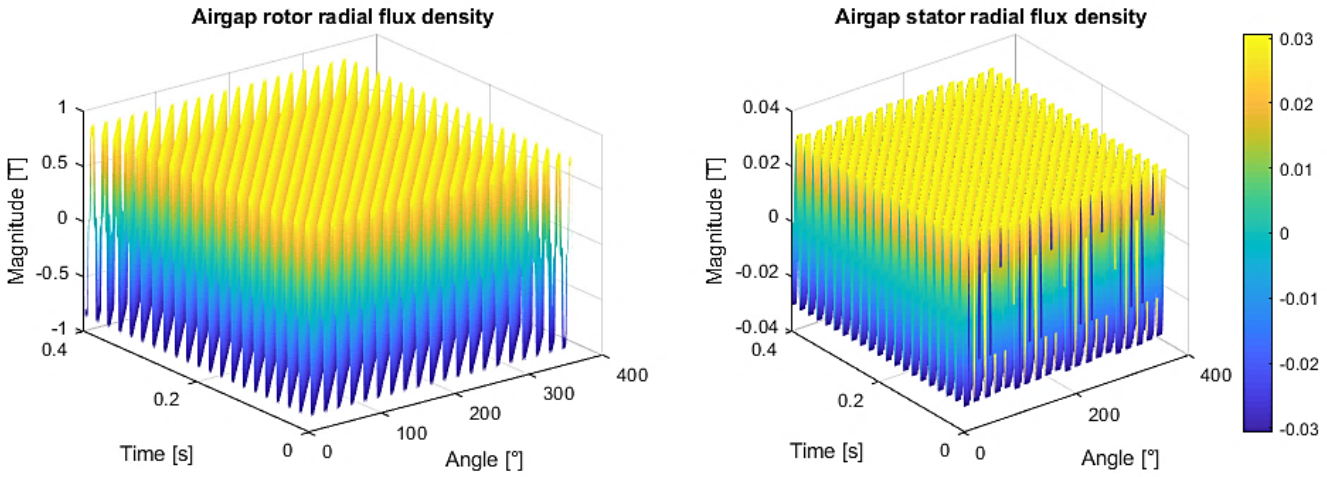

(a) (b)

Fig. 2.4.3.1 Computed air-gap radial magnetic flux density as function of time and angle for: a) rotor, and b) stator.

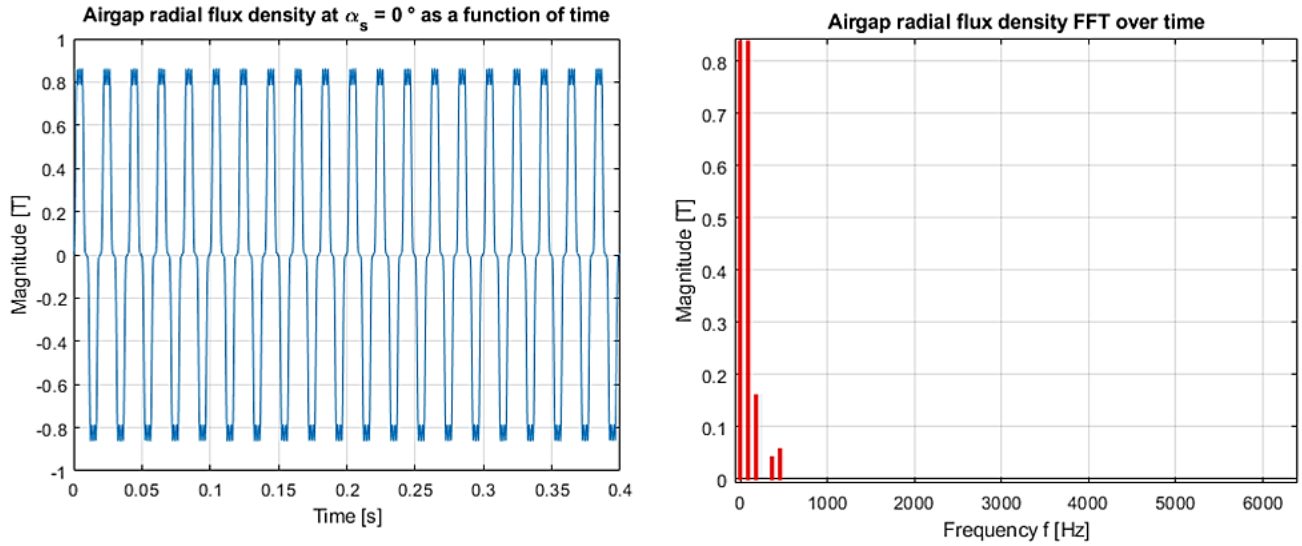

(a) (b)

Fig. 2.4.3.2 Computed rotor air-gap radial magnetic flux density: a) as function of time, and b) frequency.

2.4.4 Main Electrical Performance Characteristics under Dynamic Condition

The electrical machine's performance under a dynamic time-stepping condition is required to evaluate the output quality of the designed machine when the load is in-the-loop. Due to various effects of the load on the output of the machine, and also coupled-field-circuit FE modeling itself, we have provided the setting of this computation in this section. To reduce the design costs, the inverter can be replaced by a full-bridge diode rectifier followed by a DC–DC single switch converter (which is a simplistic but useful idealistic analysis for reaching the objectives of this research) [68] [74-75] instead of using a pulse width modulation (PWM) converter acting as a controlled rectifier. The studied coupled-field-circuit FE model that is used has been presented in Fig. 2.4.2. There are many remarkable publications in this area such as:

Lacchetti *et. al* [77], analyzes some operational issues of three-phase PMSG connected to a diode rectifier. This configuration coupled to a single-switch DC–DC converter has been used in small-scale wind energy conversion systems, and in energy harvesting systems to reduce costs. Weiming *et. al* [79], discusses an equivalent circuit model of a synchronous generator with a diode-bridge rectifier and back-electromotive force (EMF) load has been presented in the paper. The principle of harmonic balance has been applied, which makes it possible to construct a state-space mathematical model for the system. The criterion of stability is obtained for the system under small disturbances. Additionally, it is shown that the system's stability can effectively be improved

by installing a short-circuited quadrature-axis winding on the machine rotor. Wang *et. al* [79], the performance of an axial flux (PMSG) feeding an isolated rectifier load is studied using a coupled-circuit, time-stepping, 2-D finite-element analysis. The short-circuit performance has also been investigated. The second-order serendipity quadrilateral elements have been used in the analysis to obtain the accurate results of the analysis. Non-linearities in the field and electric circuit are taken into consideration. With the strong nonlinear diode parts existing in the external circuit, the special interpolating algorithm has been used for the motion interface between the stator and rotor to overcome the non-convergence problem in the computation. The algorithm has been validated by comparison with conventional algorithm for an AFPMSG feeding with a rectifier resistive load.

A flowchart based on the proceedings of the paper has been presented as Fig. 2.4.4.1. This demonstrates how the entire study has been developed from the initial input design data (such as slot/ pole number, the pole thickness of the magnet, pole-width, slot type and dimension, stack length, air-gap length, and etc.) of each model which was then defined in the algorithm. Following this, the calculation of coordinate points and geometry modeling was performed by the LUA program with automatic handling of boundary conditions, required key parameters have been computed by the 2-D FEA solver. Additionally, the time-stepped (transient) analysis was performed using the FE field analysis data and the circuit data (including external and the rectifier load) [68] [80] simultaneously in order to calculate the P_0 and η. The larger DQ-axis inductances are caused by the larger coercivity (A/m) produced by the FE model [81].

In this research, there are two main concerns to be defined and calculated analytically prior to the numerical-based computations. One, the combined moment of inertia of PMSG model, second, the Three-phase uncontrolled full rectifier load behavior.

- The combined moment of inertia of PMSG model:

The combined moment of inertia (also known as combined angular mass) is a mechanical design parameter that has to be calculated accurately. It is necessary for the load identification which determines the required torque for a desired angular acceleration about a rotational axis. This depends on the body's mass distribution as well as the axis chosen, with larger moments needing more torque to transform the body's rotation. Basically, the moment of inertia relies on the radiuses, used material, and related density [77]. Therefore, the combined moment of inertia is calculated based on Fig. 2.4.4.2 for each individual geometry and corresponding regions through the below equation:

$$\tilde{I} = \sum_{n=1}^{3} [\int_{Q} r^2 dm] \tag{2-153}$$

where $\tilde{I}$ is integrated over the entire mass (Q) of the machine that consists of three regions of the SPMSG. The rotor back iron, the PMs, and the stator yoke are region 1, 2, and 3, respectively. The conventional parallel topology (CPT), 2-segmented, modified-2-segmented, and 4-segmented are 0.786, 0.8185, 0.8157, and 0.8146 (kg.m^2), respectively. As mechanical properties of the material applied are important to be known for this calculation, Table. 2.4.4.1 presents the density of the used material in each part of PMSG.

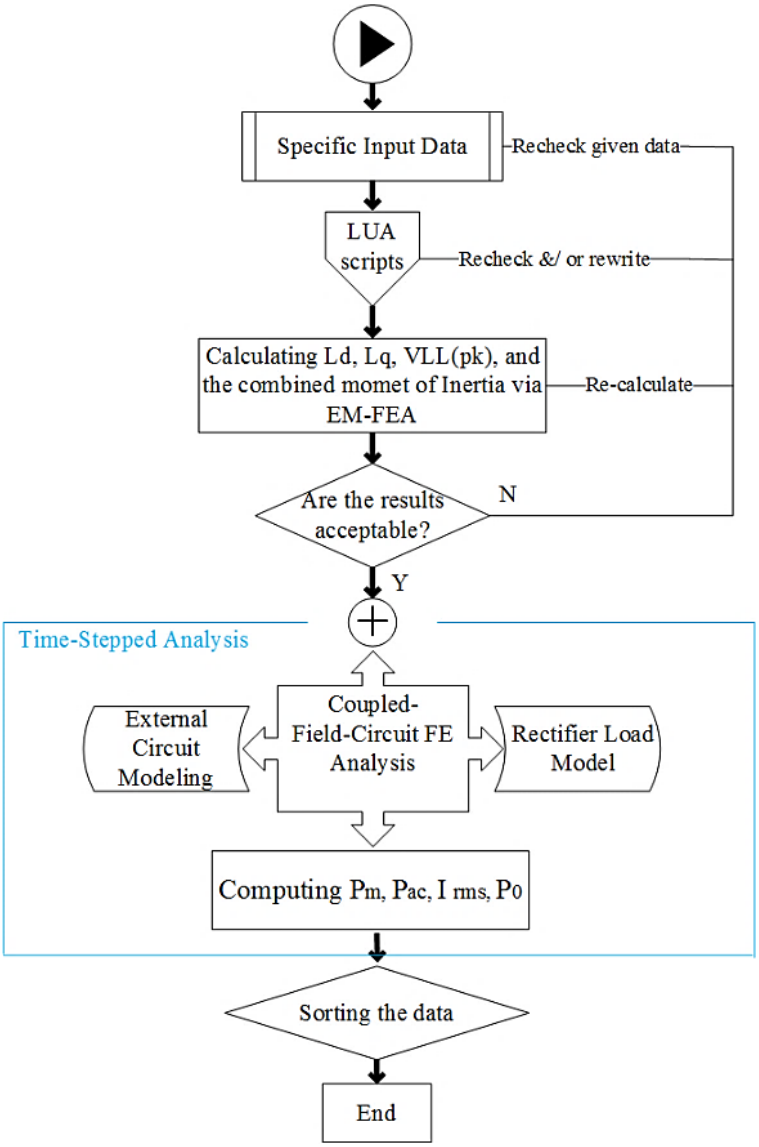

Fig. 2.4.4.1 The simplified procedure of the used methodology.

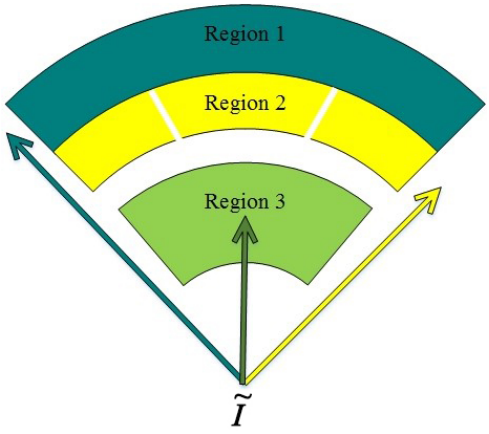

Fig. 2.4.4.2 The region definition with the related radiuses.

Table 2.4.4.1. The density of the used materials.

Parts	Rotor back iron	PMs	EPOXY-KLEBER 8601	Stator yoke	Coils
Density	7800	7600	1.31	7800	8890
Unit	*kg/m^3*	*kg/m^3*	*g/cm^3*	*kg/m^3*	*kg/m^3*

Through FEA, we have the moment of Inertial/ density as below (x^2+y^2) by planar coordination under below data from each part of the PMSG:

PMs = (6.27668e-006)*(7600 kg/m^3) = 0.0477 [kg.m^2]

Rotor = (2.28354e-005)*(7800 kg/m^3) = 0.178113 [kg.m^2]

Stator = (4.7403e-005)*(7800 kg/m^3) = 0.3697434 [kg.m^2]

Coil = (2.13765e-005)*(8890 kg/m^3) = 0.19004 [kg.m^2]

$$\tilde{I} = \sum_{n=1}^{4}[\int_{Q} r^2 dm] = 0.0477 + 0.178113 + 0.3697434 + 0.19004 = 0.786 \quad [kg.m^2] \tag{2-154}$$

- The three-phase uncontrolled full rectifier load behavior:

Based on the steady-state analytical model that is developed in [77], and [79], the behavior of the rectifier in Fig. 2.4.4.1 can be studied through a constant voltage V_0, and series of connected resistances and inductances as:

$$e_k(t) = \hat{V}.\sin(\omega t - (k-1).\frac{2\pi}{3}), k = 1,2,3 \tag{2-155}$$

where $\hat{V}$ stands for the amplitude of the phase voltage and ω is the angular frequency. The diode forward voltage drop is v_D due to the diode current i_D, which is modeled via a threshold voltage V_D, and a resistance R_D.

$$v_D(i_D) = V_D + R_D i_D \tag{2-156}$$

where $i_D > 0$. Since the DC load caters an adequate inductance, the load DC current I_{dc} will remain ripple-free and constant. The rectified voltage that is the yield of three-phase diode rectifier includes the generated ripples by the rectifier [82].

In this modeling system, two key parameters referred to as the *m*-ratio and φ_z can be addressed as follows:

$$m = \frac{V_0 + 2V_D}{E_{pk}}, \cos(\varphi_z) = \frac{R + R_D}{Z} \tag{2-157}$$

where *Z* stands for the modulus of the internal impedance that consists of R_D which further consists of the incremental resistance of the diodes by:

$$Z = \sqrt{(R + R_D)^2 + (\omega L)^2} \tag{2-158}$$

The peak value of the internal EMF E_{pk} is, which can be seen in Fig. 2.4.4.3 along with its harmonic contents:

$$E_{pk} = \omega k_\omega N \varphi \tag{2-159}$$

where k_ω, *N*, and φ are the winding factor for the fundamental harmonic, the number of turns in series per phase, the peak magnet flux, and ω is the stator angular frequency. Additionally, the average DC current, as well as the AC RMS current, can be expressed as:

$$I_0 = \frac{E_{pk}}{Z} I_0^*(\theta_x, m, \varphi_z) \tag{2-160}$$

θ_x is an auxiliary variable angle that is integrated via an additional constraint equation which is:

$$F(\theta_x, m, \varphi_z) = 0 \tag{2-161}$$

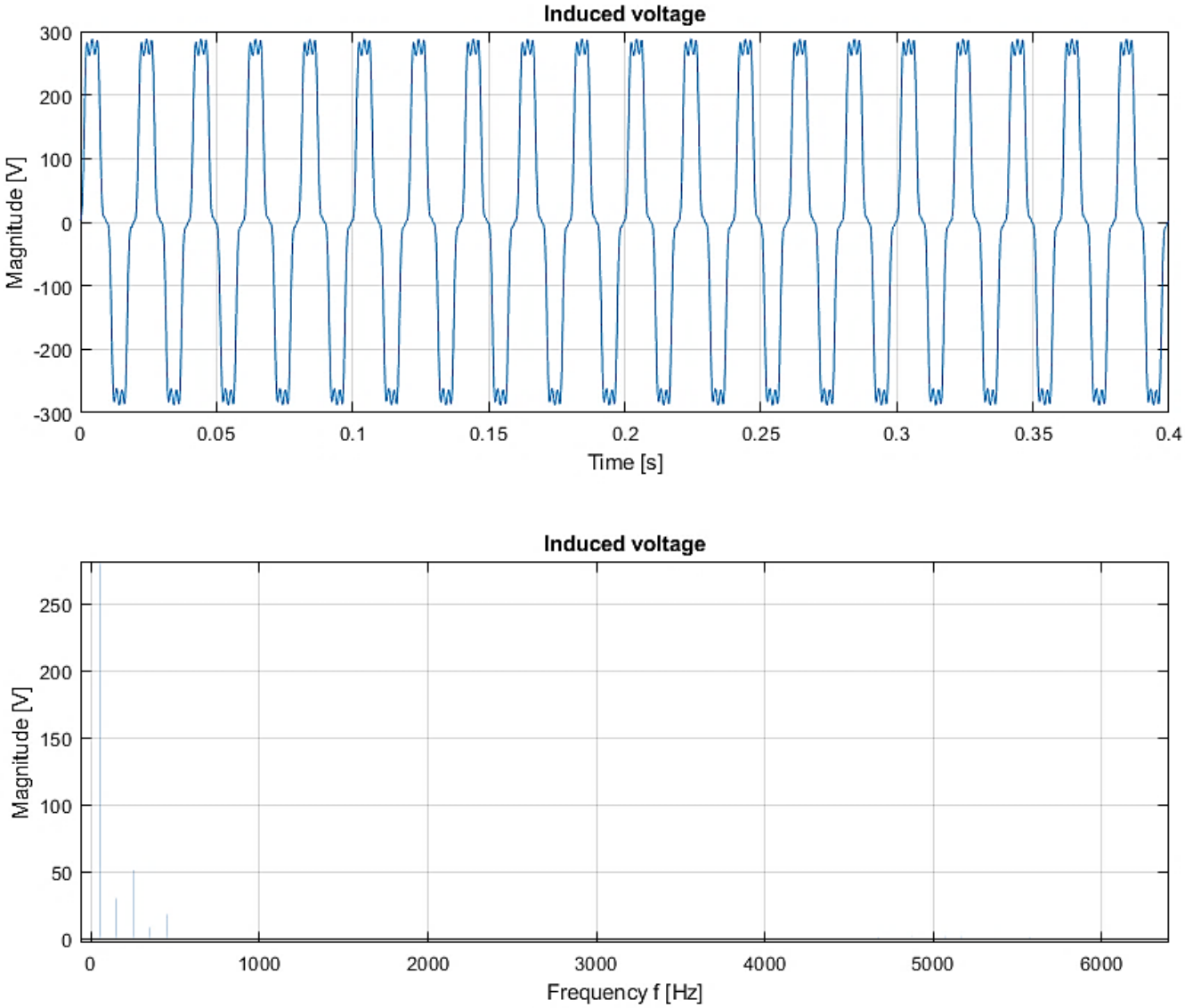

Fig. 2.4.4.3 The internal EMF or induced voltage as function of time along with its harmonic contents.

Essentially, Eq. (12-14) relies on the m and φ_z which define an assumption to ignore θ_x, Fig. 2.4.4.4 demonstrates the different operation modes, in which, Fig. 2.4.4.4-a, b, and c are representing 2/0, 2/3, and 3/3 operations, respectively [68].
The power delivered to the DC bus can be defined as given [68]:

$$P_0 = \frac{E_{pk}^2}{Z}(m - \frac{2V_D}{E_{pk}}).I_0^*(\theta_x, m, \varphi_Z) \tag{2-162}$$

The three-phase full rectifier load coupled with the PMSG defines the efficiency through iron and mechanical losses lumped in $P_{fe,\,mech}$ which can be calculated as [68]:

$$\eta = \frac{P_0 / E_{pk}^2 / z}{[P_0 / E_{pk}^2 / z] + [3.I_{rms}^{*2} \cos\phi z] + [2I_0^*(V_D / E_{pk}) + [P_{fe,mech.}(Z / E_{pk}^2)]} \tag{2-163}$$

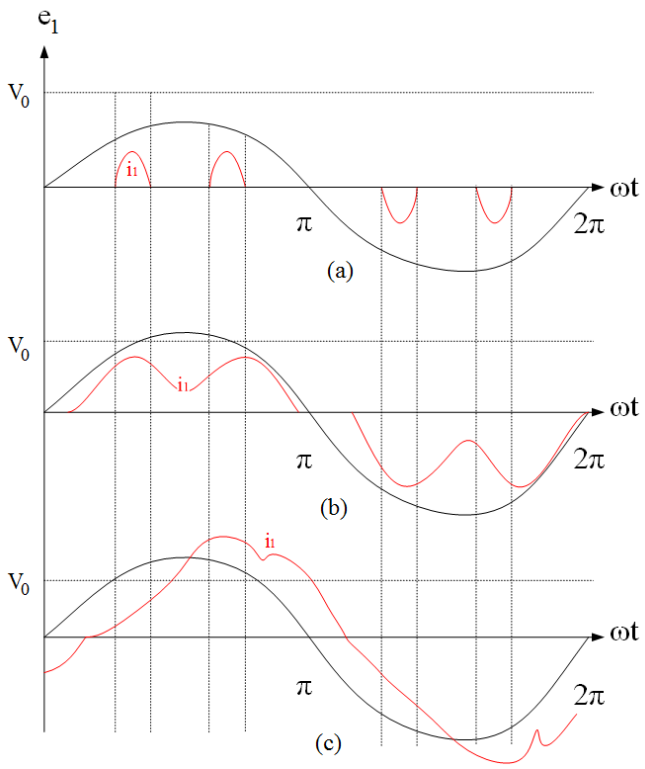

Fig. 2.4.4.4 The waveforms of various operation modes, in where, a) 2/0, b) 2/3, and c) 3/3 in the rectifier system.

The iron loss is approximated in $P_{fe,\ mech}$ [81] through the no-load iron losses, as well as also mechanical losses as given [68]:

$$P_{fe,mech.} = \omega(c_0 + c_1\omega) \tag{2-164}$$

c_0, and c_1 are lumped the frictional, mechanical, and hysteresis losses and mostly take into account the eddy current losses.

2.4.4.1 Load Electrical Performance Characteristics under Dynamic Condition

Respect to the previous section, the studied coupled-field-circuit FE model [37] [68] provides the following electrical major values, however, the no-load stator current from the generator has been shown (Fig. 2.4.4.1.1) an approximately no cogging or ripples performance in ABC plane with line-to-line magnitude of 12.6 A. Due to the effect of circuit under load operation there are a few harmonics distortion, and thus, the output of the load is always offering not ideal sinusoidal results. Fig. 2.4.4.1.2-a illustrates the line-to-line peak voltage $V_{\mathrm{LL(pk)}}$ and DC voltage V_{dc} curves as a function of time, in which peak values of 695 V have become into an agreement. Fig. 2.4.4.1.2-b represents the initial FE-initial model connected to the three-phase rectifier load, which had a rectified current I_r with an average value of 0.6 A. The considered value of d-inductance of the initial model has been used at the nominal current of 2.12 (A).

Fig. 2.4.4.1.3 depicts that time-depended evaluation of all load-depended output parameters such as rectified current and voltage, load current and voltage, nominal power performance and mechanical torque. The rectified and load currents I_{r} and I_{L} with a peak value of 2.12 A have shown a proper response to the circuit. Afterward, the rectified or DC voltage has been generated after a short time of 0.2s by 594 V with very small distortion, while the line-to-line voltage contains small harmonic distortions. The average nominal power of 1.174 kVA, where the average mechanical torque of 72.6 N.m has been recorded.

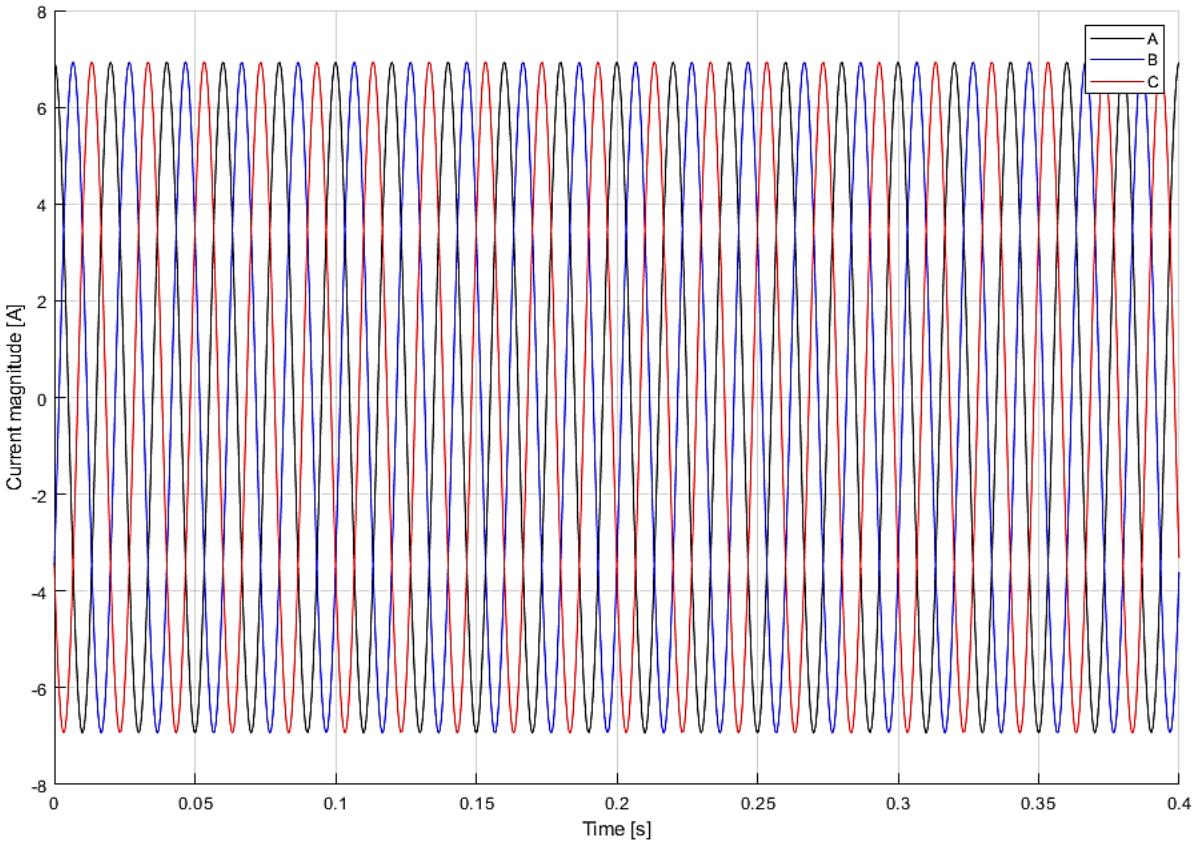

Fig. 2.4.4.1.1 No-load stator current waveforms as function of time in ABC plane.

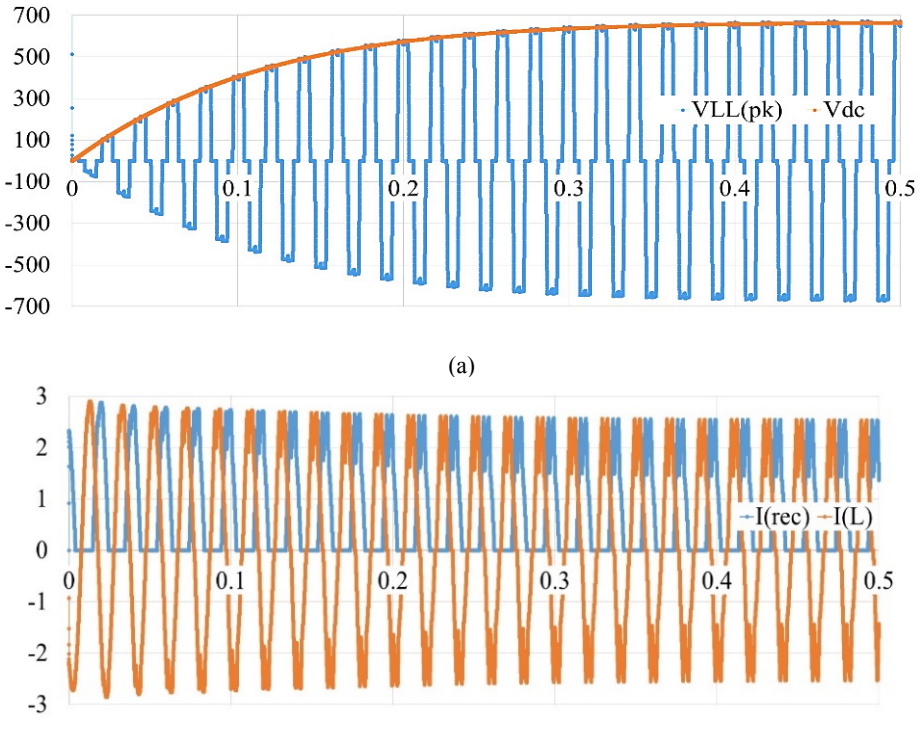

(a)

(b)

Fig. 2.4.4.1.2 Load identification of the studied PMSG as function of time, a) $V_{LL(pk)}$ and V_{dc}, and b) I_r and I_L.

The power factor (PF) calculation deals with the complexity of the mechanical structure and the magnet consumption in the PMSGs. For different machine designs, the structure and the operation principle of the PMSGs change, the relationship between the electrical parameters (such as power factor) can still be investigated through the classical synchronous machine theory.

Essentially, the PF is the ratio of the active and apparent power. If the fundamental harmonic components of the voltage and current are much higher than the higher harmonic components (low total harmonic distortion (THD) of the voltage and current), the PF is calculated simply as the cosine of the displacement between the voltage and current (phase angle) [69] which can be written as:

$$PF(NI) = \cos(\arctan(\frac{Q}{P})) = \frac{P}{P_s} \tag{2-165}$$

where P, Q, and P_s are the active, reactive, and apparent powers, respectively. The accuratly calculated power factors of the studied models are all 0.95 which represents that the width/pole pitch ratio and the length/pole pitch ratio are the same in the studied PMSG.

The reachable power factor calculation for the maximum output power, in which the graph represents that the maximum reachable output DC power at a current of 0.854 A.

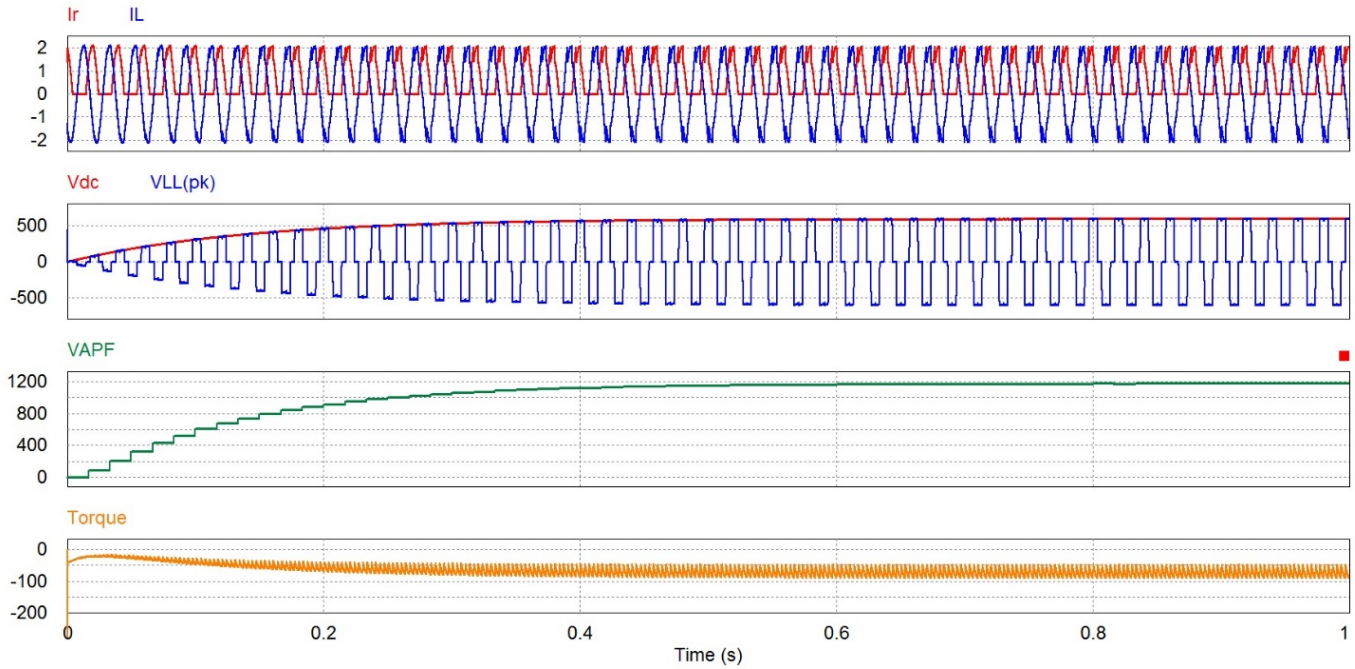

Fig. 2.4.4.1.3 Load identification of the studied PMSG as a function of time.

2.4.5 Electromagnetic Forces Distribution

The electromagnetic forces calculation methodology of a PMSG is investigated based on 3-D FEA. A force vectors schematic is presented in Fig. 2.4.5.1, where all the studied components, such as radial (F_r), tangential (F_t), and centrifugal (F_c) forces are considered. The green dashed line shows the path of magnetic flux density through the rotor core between windings of both stators. Both electromagnetic-based components, normal and tangential forces (B_n, B_t) are calculated using the Maxwell stress tensor equation [70] and the electromagnetic torque of the machine, respectively. Likewise, the centrifugal force is purely computed using the transient 3-D FEA (via Abaqus software) at the nominal rotational speed. The torque density production of the machine is independent of F_r and F_c; therefore, the torque density can be estimated directly from F_t Each of the force components is crucial for the deformation and mechanical stress issues regarding the machine's application. These force components are highly dependent on the electromagnetic behavior (forces distribution) and material used of the machine. For example, F_c increases while the rotor is rotating with a high angular momentum, not during constant speed operation.

The components of force can be computed [37] [83] through the following equations:

$$\vec{F}_r = \frac{1}{2\mu_0}\left((B_{n1}^2 - B_{t1}^2) - (B_{n2}^2 - B_{t2}^2)\right)$$
$$\vec{F}_t = \frac{1}{2\mu_0}\left((B_{n1}^2 \times B_{t1}^2) + (B_{n2}^2 \times B_{t2}^2)\right) \quad (2\text{-}166)$$
$$\vec{F}_C = m\omega^2 r$$

where μ_0 is the absolute permeability, B_n, and B_t are normal and tangential magnetic flux density. m is the mass of the rotational part (rotor), ω is the rotational speed, and r is the radius of the rotor. F_c, due to its mechanical essence, has a clockwise vector direction (based on the right's hand law) because of the body's inertia with a uniform distribution. Both the normal and centrifugal forces have a distribution with a radial vector direction have an overlapped influence on each other, where a summation of them, leading up to the resultant blue curve in Fig. 2.4.5.2, which indicates the total radial force on the rotor, where the peak value of 1.79 kN can be seen for the radial component and also the actual radial force which consists of both F_r and F_c shows the peak value of 3.3 kN.

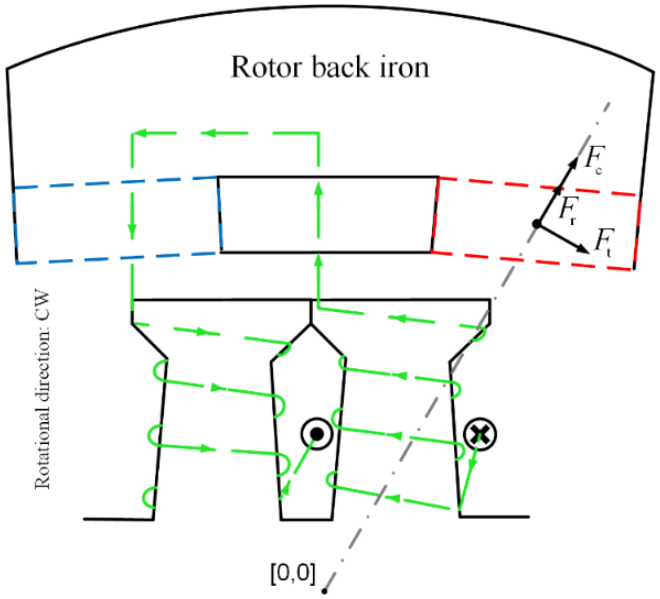

Fig. 2.4.5.1 Demonstration of radial F_r, tangential F_t, and centrifugal F_c force components in a two-dimensional PMSG.

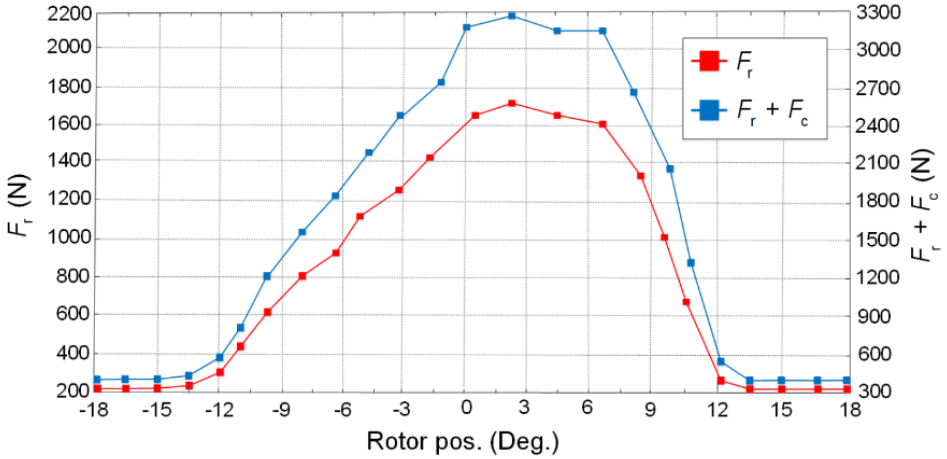

Fig. 2.4.5.2 Demonstration of radial force F_r, along with actual radial force which is corresponding to F_r+F_c.

Fig. 2.4.5.3-a-b illustrates the air-gap radial and tangential magnetic forces (F_r and F_t) as a function of time and frequency of the PMSG. The red curve (F_r) is aligned with the left-side vertical axis, and purple curve (F_t) is aligned with the right-side vertical axis. This computation is based on Maxwell tensor which directly affects the magnetic noise and related vibrations (studied in

Chapter 6). The average value of F_t is 600 N.m^{-2}. Additionally, the fundamental magnitude with the wavenumber of 64.064Hz produces 1190 and 896 N.m^{-2} (the largest FFT amplitude) for F_r and F_t, respectively.

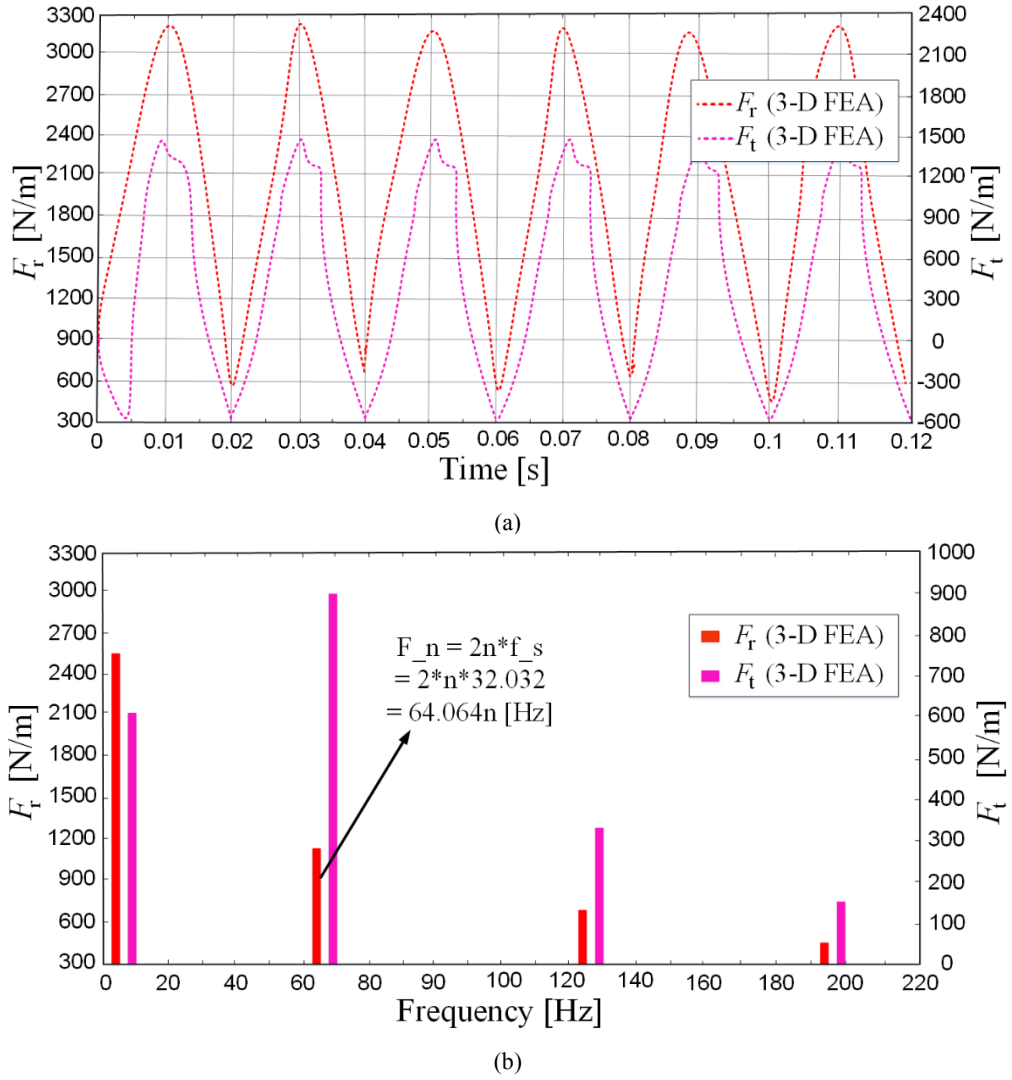

Fig. 2.4.5.3 Air-gap magnetic force components, a) F_r and F_t as function of time, and b) FFT magnitude of each force components as function of frequency.

2.5 Efficiency Map of the Proposed PMSG

Next to the torque, power capability as a function of speed in the studied PMSG, the efficiency is also an important parameter which requires speed range analysis. Through compiling the electromagnetic-based losses, the efficiency map can be generated. The efficiency can be calculated using the following equation [37]:

$$\%\eta = \frac{P_{out}}{P_{in}} = \frac{P_{out}}{P_{out} + P_{loss}} \times 100 \tag{2-167}$$

where P_{out} is the output power of the generator, P_{in} is the input power, and P_{loss} is the predicted iron and copper losses which are fully discussed in the next chapter. Moreover, the following assumptions are taken into account beforehand:

- The generator magnetic flux density is assumed to be sinusoidal as a function of time under different loading, where the amplitude of the magnetic flux density is set to 1.8 T for iron steel laminations.
- The iron losses are computed for the full model from the rotor to stator iron back.

- At the unaligned position, the magnetic flux travels perpendicularly to the plane of lamination, in which it is assumed that the losses produced via perpendicular fields under full load condition are impartial to the losses generated from the no-load condition.

Fig. 2.5.1 illustrates the total loss and efficiency maps of the studied PMSG under variable speed range analysis (from 0 to 1000 rpm), however, the rated speed of the PMSG is 150 rpm. During rated speed operation, the useful torque of 151 rpm and corresponding total loss of 639 W (shown in Fig. 2.5.1-a), and efficiency 96.8% [37] is reachable as presented in Fig. 2.5.1-b. Higher efficiency like 97.5% is possible to be reached between 200-1000 rpm, although, the risk of saturation increases for rotation speeds 200 rpm and higher. Respect to the calculations and illustrated graphs, the proposed PMSG offers a very high efficiency over a wide range of operational conditions. However, this high efficiency is possible to come out of the assumptions made when the predictions made, but yet we believe that the proposed optimized PMSG will deliver an excellent performance. It should be mentioned that the presented efficiency map belongs to the optimized model of the PMSG (not initial generator), in which all the optimization techniques used will be completely discussed in Chapter 5.

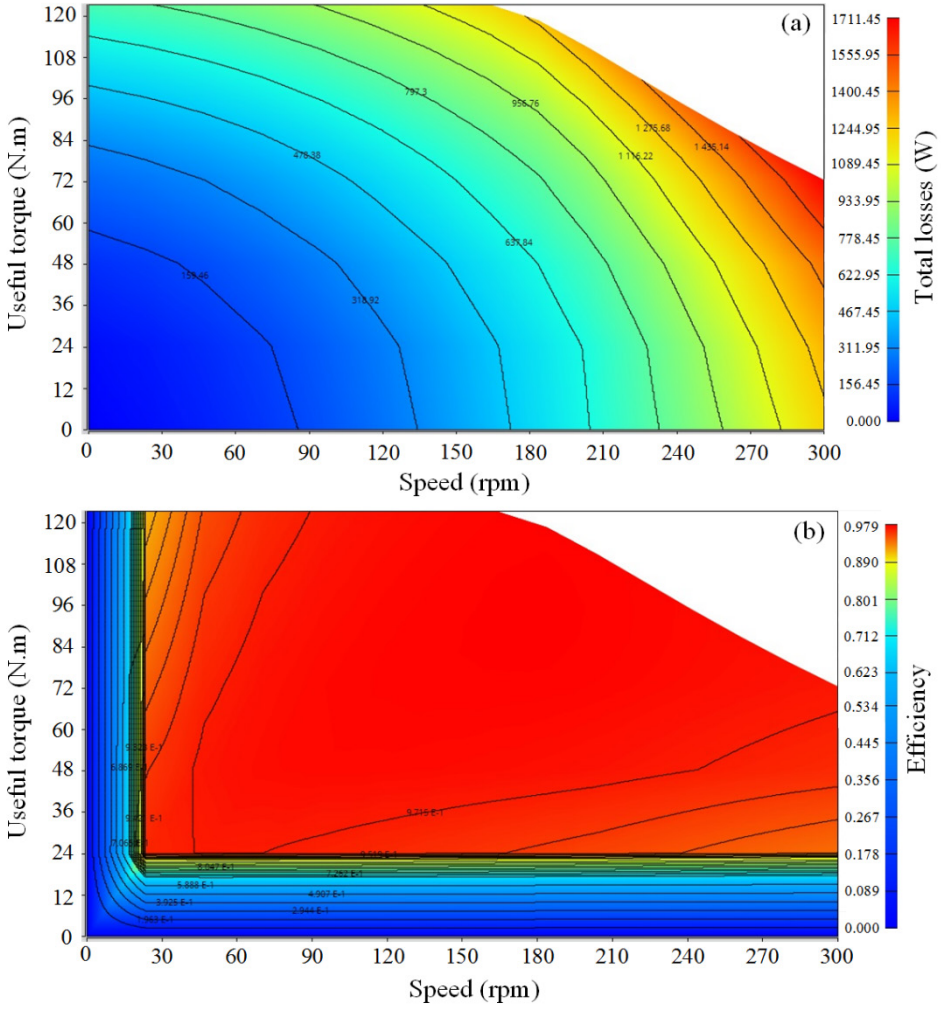

Fig. 2.5.1 Performance maps of the PMSG under variable speed analysis, a) torque vs. total losses, and b) torque vs. efficiency.

2.6 Magnetic Saturation Consideration of PMSG

To deal with magnetic saturation model, we have used the most accurate and fast technique based on transient FEA. In this method, an analytical function without any interpolation and extrapolation is carried out by the measured BH curve table. As illustrated in Fig. 2.6.1, depending on what level of frequency the designed PMSG is operating, the BH curve is different for any type of steel lamination, in which M400-50A. For instance, the rated speed of 150 rpm with 50 Hz frequency reinforces that how far the magnetic model is from being saturated. The maximum suggested frequency to avoid saturation effect is 100 Hz for this

model. Additionally, in the bottom graph, the red input curve presents the BH curve from the measured data, and the blue (saturated model) curve shows that the magnetic saturation consideration under defined ratings is operating with no risk.

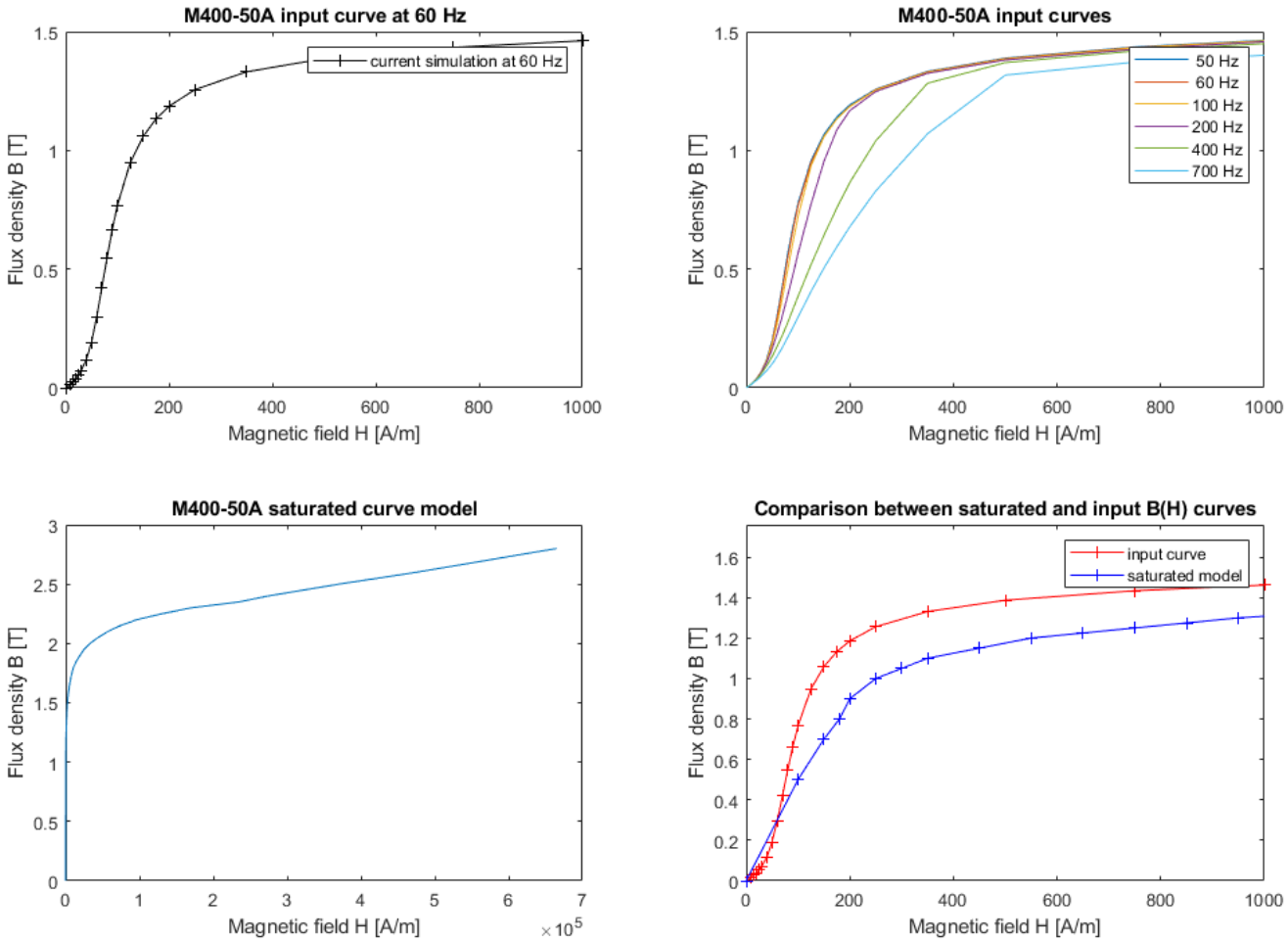

Fig. 2.6.1 Comparison of various perspective of saturation modeling as function of magnetic field intensity and frequency.

3. Iron Losses Investigation with Consideration of Resistance in PMSG

In the previous Chapter 2, the impact of the iron steel lamination in terms of dimensions and mass as 67% of the total mass of the studied PMSG was discussed. Basically, the iron losses include of Hysteresis and Eddy- current losses, where Hysteresis losses come from magnetizing and demagnetizing of the iron steel laminations through a magnetic flux route which highly depends on the MMF quality as discussed in Chapter 2. Eddy current losses appear when an alternating magnetic field (ideally sinusoidal) exist in a conductive material, afterward, based on the Ampere's law, a current will be induced in the material (known as Eddy-Currents); higher conductivity causes higher Eddy-current losses. In all machine's parts such as stator yoke, permanent magnets, coils (conductors), and rotor iron back due to conductivity and resistivity features of the material used, special attention is needed to accurately calculate them. While, they might be increased very much under different operation modes, for example, during the flux weakening condition which will be studied in this Chapter. In this Chapter, we have studied recent advanced methods in order to predict the iron losses in advance, in which the following remarkable studies are evaluated.

Wind power generation and development have been increasing during the past two decades worldwide [1], in which permanent magnet synchronous machines (PMSM)s are employed for their high energy production and efficiency in both geared-drive and direct-drive configurations [2–6]. However, achieving higher performance from conventional PMSMs requires notable attention to the design principles of electrical machines. The iron losses calculation itself takes a considerable share in the design process, where a number of considerations must be taken into account. The skin effect consideration for an accurate eddy-current loss calculation via 3-D modeling has been lately addressed [7–9] and has significantly developed the understanding of eddy-current behavior. Moreover, the use of the physical segmentation technique on the construction is another recent achievement to suppressing eddy-currents (particularly in the PMs); however, that comes always with a high manufacturing cost [10]. S. Steentjes *et al*. [11] presents an accurate prediction of iron losses in soft magnetic materials for various frequencies and magnetic flux densities that is important for an enhanced design of electrical machines. The IEM-Formula, which is used in this literature, resolves the limitation of the common iron-loss models by introducing a high order term of the magnetic flux density. Furthermore, the IEM-Formula was extended in order to include the influence of higher order harmonics and minor loops.

In another paper, D. Eggers *et al*. [12] describes IEM-Formula with semi-physically based parameters for non-linear material behavior in electrical machines. However, both studies focused on simulation without experimental tests.

The modeling of the iron losses based on Bertotti's approach has been classically studied in many references such as [13–15] via FEA. The models can be either carried out at the post-processing or nonlinear resolution stage in an electrical machine in order to increase the efficiency through an advanced estimation of iron losses distribution in the model.

M. Fratila *et al*. shows two iron loss models, based on Bertotti's decomposition method using FEA accounting for the eddy-currents in the damper bars of a turbo-generator. Moreover, the used methods have been validated experimentally for no-load condition [16].

P. Rasilo *et al*. investigated on the losses in the laminated core of a 150-kVA wound-field synchronous machine with calorimetric measurements and a numerical iron-loss model for steel laminations. The effect of rotor lamination material on total core losses has been studied through measuring and simulating the machine with three prototype rotors [17]. In another valuable work a comparison of frequency and time domain iron and magnet loss has been presented, where the focus is on recognizing the significance of including the analysis of higher harmonics in the electromagnetic loss calculation [18].

G. V. Pfingsten *et al*. [19] studied the global operating point dependent losses using a local transient loss formulation. In this work, the time and spatial distribution of flux density and the effect of choosing the best operating point has been included.

There are a number of well-known articles for iron loss calculations with skin effect considerations [20-25]; however, only a few have considered field weakening capability.

Z. Haisen, *et al*., studied a two-term piecewise variable parameter model for precise prediction of iron losses in induction motors. They used also eddy-current terms of IEM-Formula, in which also skin effect has been accounted. The iron loss model has been numerically and experimentally verified, however, the model is not valid during FWOT, while harmonic loss is not considered [26].

In ref. [27], S. H. Han *et al*. reported the influence of harmonic losses to increase and dominate the total iron loss during field weakening operation. A useful comparative study on the produced harmonics and eddy-current loss (in the stator-teeth) is presented. Although, lack of experimental verification afflicted the quality of the research.

Q. Li *et al*., investigated the rotor saliency of an interior permanent magnet (IPM) machine, large harmonic eddy current loss in the stator iron loss could be caused under field-weakening operation, conspicuously impairing the output performance of the IPM machine. They proposed a new stator teeth eddy-current loss analysis approach, in which the teeth eddy-current loss is divided to two parts, one part is caused by the synchronous air-gap field density rotating synchronously with rotor, while the other part is induced by the asynchronous air-gap field density [28]. There is a though-provoking consideration on the fractional-slot concentrated winding based on the eddy-current coefficients, however, an experimental test needs to be considered. In addition, the following works have been fully discussed the fractional-slot concentrated winding [29-30].

In [31], the iron loss resistance was calculated a priori from a finite-element analysis as functions of the d–q-axis currents. On the other hand, the effect of field-weakening current on the iron losses of the PMSM is presented in [32]. Further, FEA based iron loss calculation methods have been used to minimize the iron losses of the PMSM under field weakening condition in [34] and [34].

S. Kuttler *et al*. studied an original and mathematical model which has been developed and provides a fast and accurate estimation of iron losses, particularly in field weakening operation, even with the machine supplied by sinusoidal currents as described in this work. A polynomial form of iron losses as a function of fundamental electrical frequency and takes into account the filed density waveforms in the yoke and teeth by use of nonlinear iron coefficients linked to i_d–i_q currents. The paper has presented the complete method for calculating the iron coefficients from a nonlinear magnetic nodal network of the machine. A detailed study of the local field density waveform and harmonic content in the yoke and teeth was provided for two particular operating points: at maximal power without field weakening and at maximal power at maximal speed [35]. This article investigated mapping of local iron losses coefficients in yoke and teeth, and also the iron losses coefficients differences justified per unit volume between yoke and teeth. However, there was no experimental validation present in the article.

In ref. [36], a special design for a spoke-type IPM motor is presented to enhance motor field-weakening capability in operation over a wide speed range. Experimental results have been compared with analytical predictions showing satisfactory accordance. It can be concluded that calculation analysis with simulation and measurement results for motor operation through imposed voltage and torque profiles over the basic objectives is well presented.

In [37], the researchers dealt with the concept of winding switching for field weakening of PMSM. The study focused on the impact of harmonic contents on the field weakening capability of the machine. Afterward, a suitable drive topology for the winding switching technique under harmonic conditions is discussed. The technique as a field weakening solution was only investigated on the field and back-EMF. At last, the results are experimentally verified. Although, the iron loss consideration or influence of the proposed technique was not discussed, but the solution can be considerable for iron loss improvement during FWOT for further investigations. Moreover, ref. [38] proposed an improvement in the field weakening operation over a large speed range, in which power and torque have been raised.

In another research [39], the authors presented a special emphasis is placed on accurately representing core losses at variable frequency. The analytical model has been experimentally verified. Although, the lack of iron loss prediction namely during FWOT can be seen which can be considered to improve the accuracy during FWOT.

M. Basic *et al*. studied iron losses by means of an equivalent iron loss resistance which is connected in parallel with the stator inductance. Moreover, the iron loss resistance is modeled as variable with respect to both synchronous frequency and magnetizing field, whereas the magnetizing field influence is expressed by means of the corresponding iron loss current. Finally, a good achievement over the proposed model is carried out [40]. The research lacks filed weakening capability, and also experimental verifications.

The iron loss modeling development will introduce a quasi-FEA technique based on a theoretical segmentation in frequency domain, in which iron losses is evaluated locally, in each space point of the iron. Therefore, the eddy-current loss reduction is not aimed through segmentation in this paper. Although, theoretical segmentation allows the design procedure to provide a detailed iron losses calculation at each machine's part using 2D-FEA for the advanced iron losses distribution. The iron loss modeling is evaluated using accurate loss separation and identification of loss coefficients in the presence of skin effect at an Epstein frame (illustrated in Figure 3.1, respect to the IEC 60404-2 standard) [41].

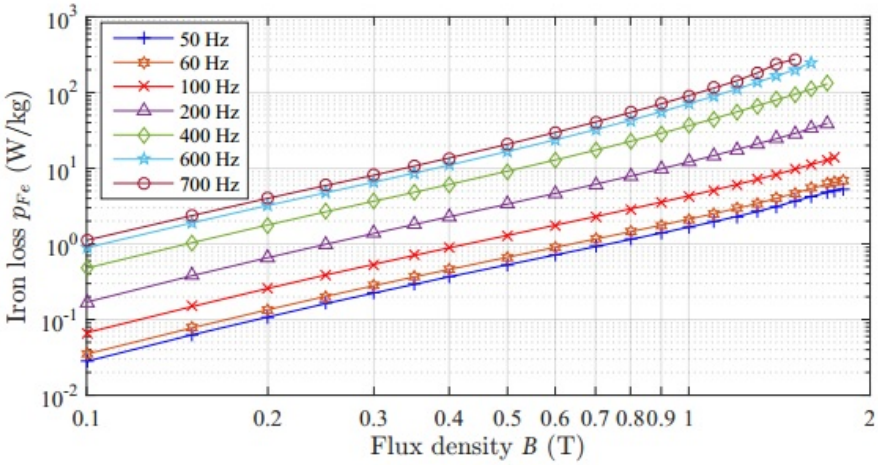

Fig. 3.1 Iron loss results obtained from Epstein test.

3.1 Classic Bertottie's Model

This model of iron loss is one of fastest and very commonly used among engineers to estimate the iron losses in the electrical machines for many years which can be split into several terms as following sub-sections.

3.1.1 Hysteresis Loss

The energy involved in continually reversing the molecular dipoles of the magnetic material, in which this type of iron loss is proportional to the area of the hysteresis loop of the materials (in this case, M400-50A steel lamination) times the number of times this area is traversed per second such as frequency [42]. In this thesis, we have used Bertotti's iron loss models which are based on the frequency domain. The most commonly used approach for iron loss calculation in electrical machines is decomposing the flux density waveform obtained from finite element models (FEM) into frequency components, then applying the Bertotti model. Mathematically, the approach is described as [41]:

$$W_{fe} = p_{fe,n}(B_n, f_1) \tag{3-1}$$

where B_n is the amplitude of nth harmonic component of flux density, f_1 is the fundamental frequency. $p_{fe,n}$ is the iron loss of nth harmonic calculated using the following equation (3-2). Usually, the calculation is carried during the post-processing of FEM, and the flux density is decomposed into the radial component B_{rn} and tangential component B_{tn} further, which is [42]:

$$W_{fe} = p_{fe,r,n}(B_{rn}, f_1) + p_{fe,t,n}(B_{tn}, f_1) \tag{3-2}$$

Based on empirical approach [23], the iron loss (P_{fe}) is separated into a hysteresis component (P_h), an Eddy current component (P_e) and an anomalous model (P_a) [13]. Under sinusoidal alternating excitation, hysteresis term us calculated as given:

$$P_h = k_h f . \widehat{B}^{\alpha} \tag{3-3}$$

k_h, and α, are loss coefficients, in which M-RGN approach will be carried out to calculate the best-fitted values. B is the peak value of the flux density in each segment.

3.1.2 Eddy-current Loss

When the magnetic flux density occurs in the iron core (M400-50A) under AC sinusoidal currents. The Eddy-current loss increases from precisely similar phenomena which result in the Eddy-current loss in the material with conductive feature. Basically, these losses account for the currents that circulate within the steel laminations of the stator and rotor, in which they are induced through the time-varying magnetic field. It is worthy to mention that the behavior of these currents is non-uniform and often tend to be largest in the surface of the laminations. Assuming that the steel lamination sheet with a length of L, and an axial length of D, and thickness of t which are presented in Fig. 3.1.2.1. If a sinusoidal flux density as $B_m \sin \omega t$ magnetizes the PMSG [42]. The produced flux density within the current path from a certain distance of x can be written:

$$\phi(x) = 2x[L - (t - 2x)]B_m \tag{3-4}$$

Therefore, the amplitude of the induced voltage for the corresponding path [42] can be given as:

$$E_m = B_m \omega 2x[L - (t - 2x)] \tag{3-5}$$

if the resistance to the current flow [42] can be defined as:

$$dR(x) = \rho_{Fe}\left(\frac{2[L - (t - 2x)]}{Ddx} + \frac{4x}{Ddx}\right) = \rho_{Fe}\left(\frac{2L - 2t + 8x}{Ddx}\right) \tag{3-6}$$

The corresponding Eddy-current loss [42] at the path is:

$$dP_e = \frac{E_m(x)^2}{2dR(x)} = \frac{\omega^2 B_m^2 \left(2x[L-(t-2x)]\right)^2 Ddx}{2\rho_{Fe}(2L-2t+8x)} \tag{3-7}$$

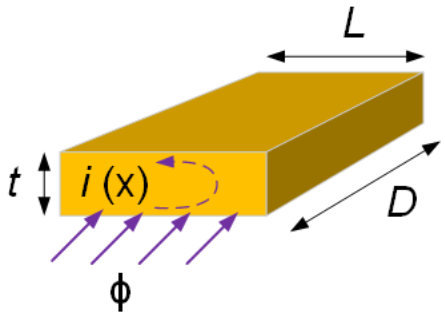

Fig. 3.1.2.1 Eddy-current path in a thin rectangular iron lamination sheet.

There are many remarkable studies which focused on the computation of Eddy-current loss with and without skin effect consideration [41] [7-9]. The eddy currents using the classic Bertotti's iron loss model in the rotor core are strongly influenced by the skin effect phenomena, especially under high excitation frequencies. The eddy current term can be improved as in the following equation to take skin effect into account [43]:

$$P_e = k_e f^2 . \hat{B}^\beta = k_e \left(\frac{\sinh(d\sqrt{f}) - \sin(d\sqrt{f})}{\cosh(d\sqrt{f}) - \cos(d\sqrt{f})} \right) . f^{1.5} \hat{B}^\beta \tag{3-8}$$

where d is another loss coefficient which depends on the steel sheet thickness.

It is well known that loss coefficient k_e and β exhibit a significant variation with the flux density B and the frequency f, as opposed to the conventional model [20]. Various models with variable coefficients have been proposed in the literature to improve the accuracy in wide frequency and flux density ranges [20-22].

3.1.3 Anomalous loss

In the magnetic circuit of the electrical machines, anomalous (or additional) term of iron loss which is produced by an alternating magnetic flux normal to the lamination plane. This type of iron loss is closely related to the magnetic anisotropy and the area of contacting surfaces between the exciting cores and the common magnetic circuit [44]. To model this type of iron loss, the classic Bertotti's iron loss model [2] is used as follows:

$$P_a = k_a f^{1.5} \hat{B}^\gamma \tag{3-9}$$

where k_a, and γ are loss coefficients, in which M-RGN approach will be carried out to calculate the best-fitted values. B is the peak value of the flux density in each segment [41].

3.1.4 Saturation loss

Saturation of the main-flux path has been considered individually in the models for synchronous machines [45-50]. In paper [51] saturation has been approached in a unified behavior for the general orthogonal-axis model and is valid for synchronous, induction and DC electric machines.

Through the conventional model of PMSG using constant d-q-plane inductances, we cannot accurately predict the electrical machine behavior, while the spatial harmonics and magnetic saturation effects in the stator and rotor cores are neglected [52].

Especially, during the field-weakening region, in which the phase voltage harmonics might result in distorted current waveforms due to the limited dc-link voltage. As the d-q-plane voltage and torque modeling of PMSMs can be defined as:

$$\begin{aligned} V_d &= L_d \frac{di_d}{dt} + R_s i_d - \omega_e L_q i_q \\ V_q &= L_q \frac{di_q}{dt} + R_s i_q + \omega_e \left(\Psi_m + L_d i_d \right) \\ T_e &= \frac{m}{2} p \left[\Psi_m i_q + \left(L_d - L_q \right) i_d i_q \right] \end{aligned} \tag{3-10}$$

where L_d is d-axis inductance, L_q is q-axis inductance, Ψ_m is the permanent magnet flux linkage which is a function of both d-q-axis currents i_d and i_q in order to consider magnetic saturation effect. Although, the conventional machine model only considers the influence of fundamental components, whereas the harmonic fields resulting from the combination of magnetic saturation, slotting, and permeance variation with the rotor position are neglected. Moreover, the separation of $L_d i_d$ and Ψ_m from the FE-estimated d-axis flux linkage cannot be accurately performed under saturation condition when the superposition principle is no longer valid.

To estimate the saturation iron loss effect on the machine, the classic Bertotti's iron loss model [41] is taken into account as:

$$P_{sat.} = k_e \hat{B}^{k_{sat}+2} f^2 \tag{3-11}$$

where k_e and k_{sat} are polynomials in f and B, the format of these functions:

$$k_e(\hat{B}) = k_{e0} + k_{e1}\hat{B} + k_{e2}\hat{B}^2 + k_{e3}\hat{B}^3 \tag{3-12}$$

$$k_{sat}(f, \hat{B}) = k_{sat0} + k_{sat1} f + k_{sat2} f^2 + k_{sat3}\hat{B} \tag{3-13}$$

Fig. 3.1.4.1 illustrates the computed nonlinear (saturation) loss saturation iron loss, where the magnetic flux density has been provided using 2-D FEA. A wide range of torque constant of over 120 Nm with peak saturation of 954 W.

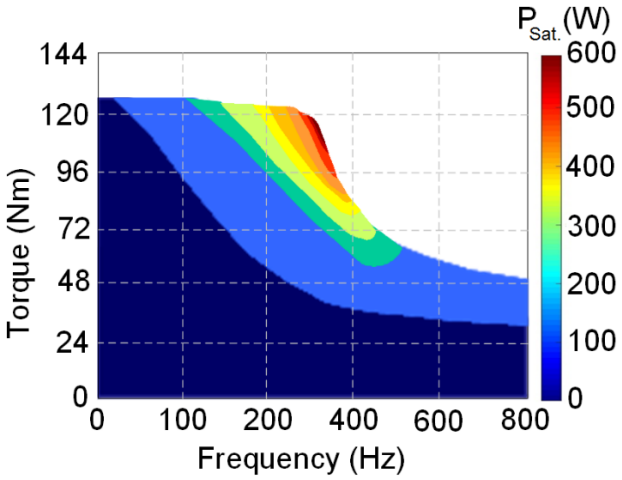

Fig. 3.1.4.1 The torque-frequency-saturation loss presentation based on the above equation (3-13).

3.2 Iron Loss Segmentation Modelling using Bertottie's Models

An advanced analysis from 50 to 700 Hz was performed to provide existing harmonics and the radial/ tangential components of the flux density at each machine's part, where each part has been theoretically segmented into four and eight segments for a more improved iron losses calculation on the PMSM [41].

The iron loss modeling development will introduce a quasi-FEA technique based on a theoretical segmentation in the frequency domain, in which iron losses is evaluated locally, in each space point of the iron. Therefore, the eddy-current loss reduction is not aimed through segmentation in this paper. Although, theoretical segmentation allows the design procedure to provide a detailed iron losses calculation at each machine's part using 2D-FEA for the advanced iron losses distribution [41].

In this thesis, the segmentation technique deals with the geometry, in which flux density calculation at each part (rotor yoke, tooth top, tooth, and stator yoke) will be subdivided into three types, 1, 4, and 8-segmented models (shown in Figure 3.2.1). The eight-segmented model has the highest number of segmentations as a limitation at each part due to mesh sizing [41]. Accordingly, the volume calculation at each iron part for each model is:

$$\begin{aligned} Vol_{1Sfe} &= \pi \sum_{i=0}^{n=1} (r_{n+1-i} - r_{n-1})^2 L \\ Vol_{4Sfe} &= \pi \sum_{i=1}^{n=4} (r_{n+1-i} - r_{n-1})^2 L \\ Vol_{8Sfe} &= \pi \sum_{i=1}^{n=8} (r_{n+1-i} - r_{n-1})^2 L \end{aligned} \tag{3-14}$$

where r_{n+1-i} is the outer radius of the segment, r_{n-1} is the inner radius of each iron segment, and L shows the axial length of the machine which is 100 mm. Thus, the volume of each segment is $\pi(r_{n+1-i} - r_{n-1})2.L$, in which n is the number of segmentation (can be seen in Figure 3.2.1-a, b, and c) has been considered based on equation (3-14).

Bertottie's iron loss equations based on various coefficients loss such as two-term is calculated using:

$$\begin{aligned} P_{fe} &= k_h(f,\hat{B}) f \hat{B}^{h(\hat{B})} + k_e \left(\frac{\sinh(d\sqrt{f} - \sin(d\sqrt{f})}{\cosh(d\sqrt{f}) - \cos(d\sqrt{f})} \right) f^{1.5} \hat{B}^{\beta} \\ &+ k_e k_{s1} \hat{B}^{k_{s2}+2} f^2 + k_e \hat{B}^{k_{sat}+2} f^2 \end{aligned} \tag{3-15}$$

where d is another loss coefficient which depends on the steel sheet thickness.

It is well known that loss coefficients k_h, α and k_e exhibit a significant variation with the flux density B and the frequency f, as opposed to the conventional model [20]. k_h, f, B, $h(B)$, k_{s1}, k_{s2}, k_{sat} and $k_e B$ are polynomials in f and B, the format of these functions differs to Eq. (3-15) as given:

$$\begin{aligned} k_h(f,\hat{B}) &= k_{h0} + k_{h1} f + k_{h2} f^2 + k_{h3} \hat{B} \\ h(\hat{B}) &= h_0 + h_1 \hat{B} \\ k_e(\hat{B}) &= k_{e0} + k_{e1} \hat{B} + k_{e2} \hat{B}^2 + k_{e3} \hat{B}^3 \\ k_{s1}(f,\hat{B}) &= k_{s10} + k_{s11} f + k_{s12} f^2 + k_{s13} \hat{B} \\ k_{s2}(f,\hat{B}) &= k_{s20} + k_{s21} f + k_{s22} f^2 + k_{s23} \hat{B} \\ k_{sat}(f,\hat{B}) &= k_{sat0} + k_{sat1} f + k_{sat2} f^2 + k_{sat3} \hat{B} \end{aligned} \tag{3-16}$$

The total iron losses for each segment using equation (3-14), and (3-15) can be defined for 1, 4, and 8-segmented models as followings:

$$P_{fe1S,total} = Vol_{1sfe}.P_{fe}$$
$$P_{fe4S,total} = Vol_{4sfe}\sum_{i=1}^{n=4} P_{fe(n+1-i)} \quad (3\text{-}17)$$
$$P_{fe8S,total} = Vol_{8sfe}\sum_{i=1}^{n=8} P_{fe(n+1-i)}$$

Loss coefficients in equations (3-16) is normally obtained from the measured loss data using curve fitting, in which the M-RGN was carried out to determine the best values with the lowest error. Iron losses of M400-50A iron sheet (with nonlinear *BH* curve) samples under various flux densities and frequencies measured from Epstein test. Equations (3-1), (3-2) and (3-15) are used for curve fittings. The three equations are referred to the three-term model, two-term model and variable coefficient model below. All the curve fittings are completed with sufficiently small residual, i.e. $r_2 > 0.999$.

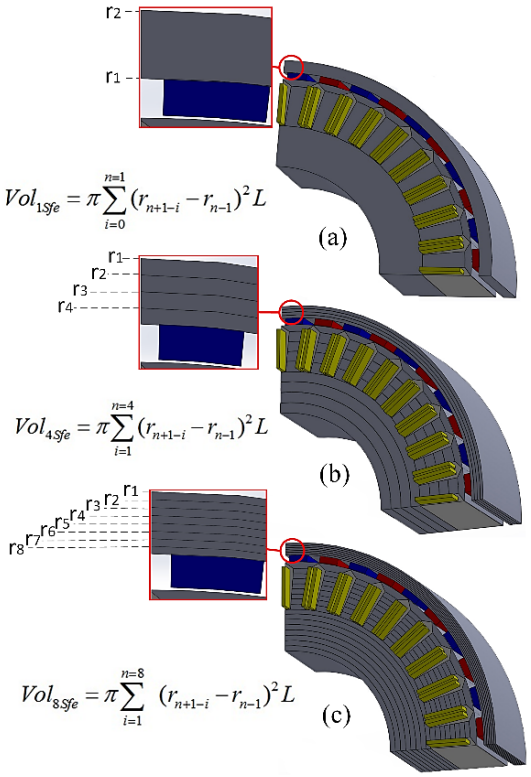

Fig. 3.2.1 3-D segmented FEM model of the 36/40 PM synchronous machine, a) 1-segmented, b) 4-segmented, and c) 8-segmented.

3.2.1 Iron Loss Segmentation Modelling using Bertottie's Models

The purpose of theoretical segmentation is to provide a distinct average value at each segment block. Iron losses are calculated at the measured flux density and frequency points using the obtained loss coefficients and three iron loss models respectively. Relative error distributions of the three models are compared with measured experimental data for different frequencies shown in Fig. 3.2.1.1 based on equations (3-14). Table 3.2.1.1 shows the obtained coefficients. All the three models predicted the iron losses with high accuracy under high flux densities and frequencies. However, both the three-term model and the two-term model result in significantly high errors under relatively low flux densities. Unsurprisingly, the best fit is achieved by the variable coefficient model, except for several points at very low flux density (0.1T), the relative errors are ±10%. The calculated results from the variable coefficient model and measured data at no load condition are compared in Figure 3.2.1.2, in which good curve fitting between calculated and measurement results exist based on material properties of steel M400-50A fully-processed non-oriented silicon with 0.36mm and 29 gauge, where a higher frequency causes a larger iron loss [41].

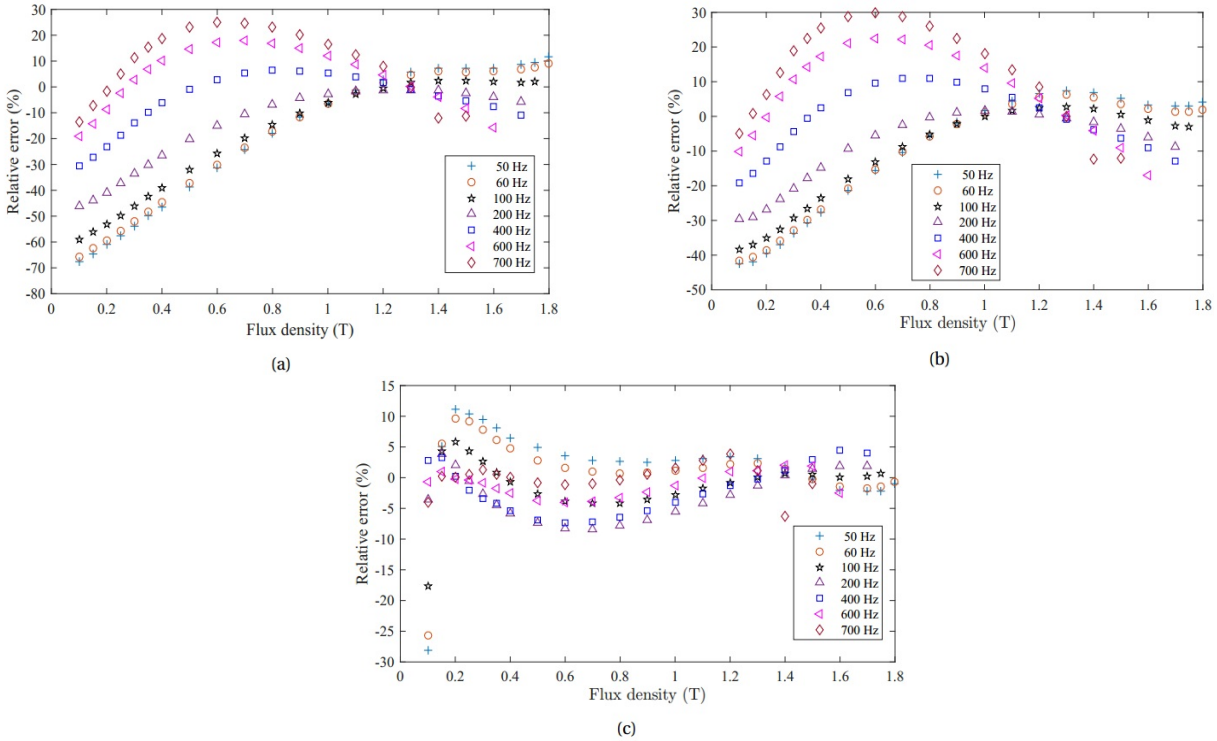

Fig. 3.2.1.1 Relative error distributions of the three iron loss models: a) three term model b) two term model c) variable coefficient model.

Table 3.2.1.1. Iron loss coefficient calculation using two, three, and variable coefficient models.

Coefficient	Three term model	Two term model	Variable coefficient model
h	2.386	2.03	NaN
k_h	0.02193	0.02193	NaN
k_e	1.845×10^{-4}	1.845×10^{-4}	NaN
k_a	3.152×10^{-9}	NaN	NaN
k_{s1}	25.7×10^{-7}	25.12×10^{-7}	26.2×10^{-7}
k_{s2}	3.6543	3.2313	3.9872
h_0	NaN	NaN	0.2936
h_1	NaN	NaN	0.07778
k_{h0}	NaN	NaN	−0.002409
k_{h1}	NaN	NaN	4.253×10^{-6}
h_{h3}	NaN	NaN	0.02895
d	NaN	NaN	0.01826
k_{e0}	NaN	NaN	0.02093
k_{e1}	NaN	NaN	−0.01927
k_{sat}	1.043×10^{-8}	1.001×10^{-8}	1.361×10^{-9}

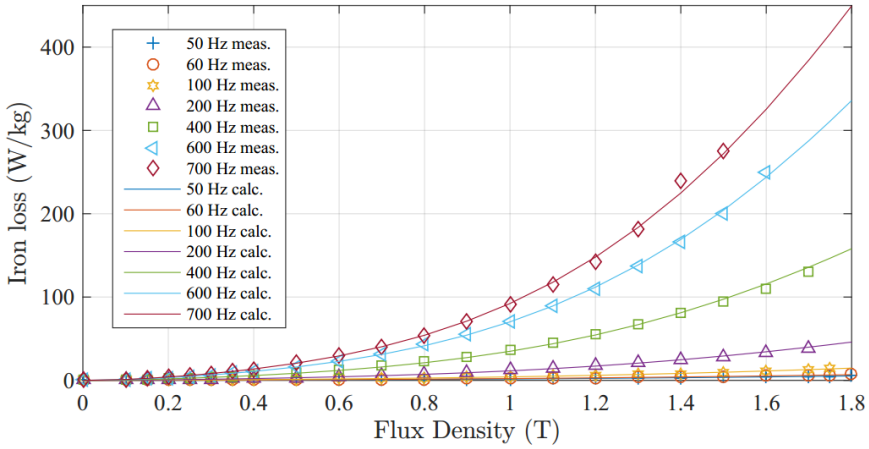

Fig. 3.2.1.2 Comparison between calculated results of the variable coefficient model and measured ones at a standard frame.

3.2.2 Results and Comparison

The 2-D FE models are calculated based on the proposed quasi-FE technique using equations (3-17) for each iron segment, where equation (3-14) is defined. The flux density distribution, as a significant variable of the study, is calculated through FEM for different number of axial segmentations in Figure 3.2.2.1. The preferred 2-D FE only due to the number of nodes that is 31258, which gains much lesser time-consuming simulation. The boundary setup used for each model considers each segment not physically separated [41].

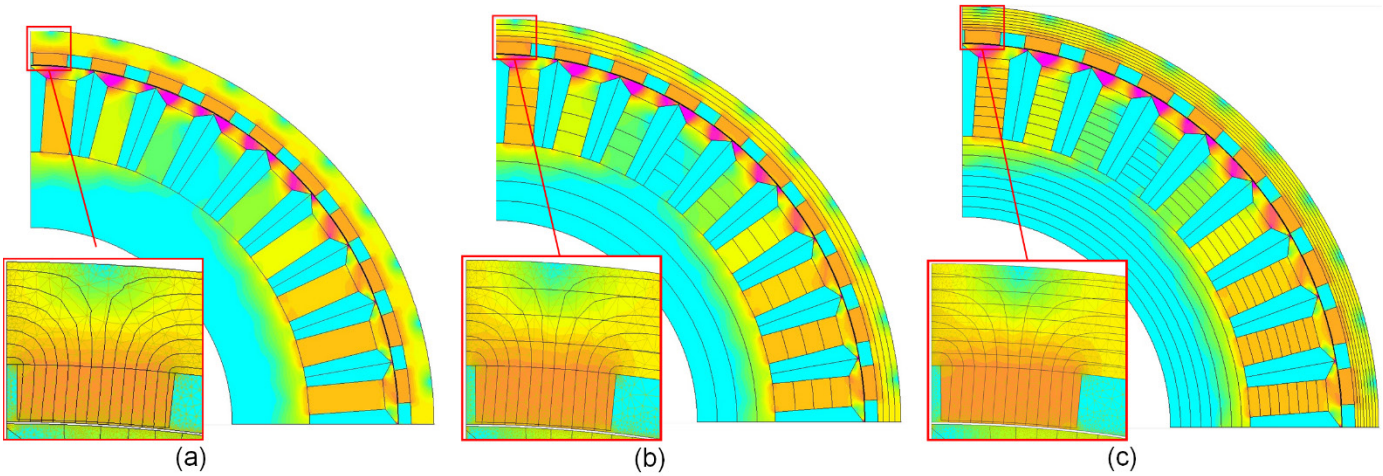

Fig. 3.2.2.1 2D flux density distribution on a) 1-segmented, b) 4-segmented, and c) 8-segmented FE models.

The saturation loss calculation in the laminated stator and rotor cores are predicted via the local waveforms of the magnetic flux densities. Single-valued magnetization curves are used to consider saturation effects originating from the non-linear material behavior. The magnetic material is utilized up to 2.1 T in the considered machine. Second-order effects, originating from hysteresis behavior, are neglected. The saturation term is specifically in the area around the transition point at high torques and high speeds with a large proportion [41].

The nonlinear (saturation) loss without segmentation consideration is shown as a smaller area of significant loss value of 290 W at 150rpm in Figure 3.2.2.2-a. However, through the four-segmented FE model, a slightly larger amount of saturation loss can be reported which is obviously presented via the color bar with a larger critical area by 306 W at 150 rpm seen in Figure 3.2.2.2-b. The eight- segmented FE model has a larger area of critical loss which is clearly represented in Figure 3.2.2.2-c by 350 W at speed of 150rpm. The quasi-FEA technique is limited to the eight segmented blocks due to mesh's size, where a single complete triangle mesh is required at each block [1].

The total iron losses calculation with skin effect consideration for stator and rotor cores is successfully done through equation (3-17) and based on the proposed quasi-FEA technique (in Figure 3.2.2.3), in which a larger amount of iron losses at low and high frequencies can be seen via the aid of a color bar at the four-, and eight-segmented models that are illustrated in Figure 3.2.2.3-a

and 3.2.2.3-b, respectively. The proposed eight-segmented model using the quasi-FEA technique has estimated a larger significant iron loss, in which the Figure 3.2.2.3 presented the peak total iron loss for a maximum torque of 122N.m, at 150rpm by 1.04, 1.21, and 1.538kW for conventional, four-segmented quasi-FEA, and the proposed eight-segmented quasi-FEA technique, respectively. The proposed eight-segmented quasi-FEA model predicts with a larger area of significant losses in comparison to the convent conventional (Figure 3.2.2.3-a) and four-segmented techniques due to a better mesh which is comparable to 3-D FEA [41].

Accurate calculation of the field harmonics at every single area (more specific by segmentation) of the iron parts is the main contribution of the work using a proposed quasi-FE technique. For example, through segmenting one tooth into eight, the tooth-top area is presented with much higher harmonics and related loss, whereas only considering the absolute value of a full tooth

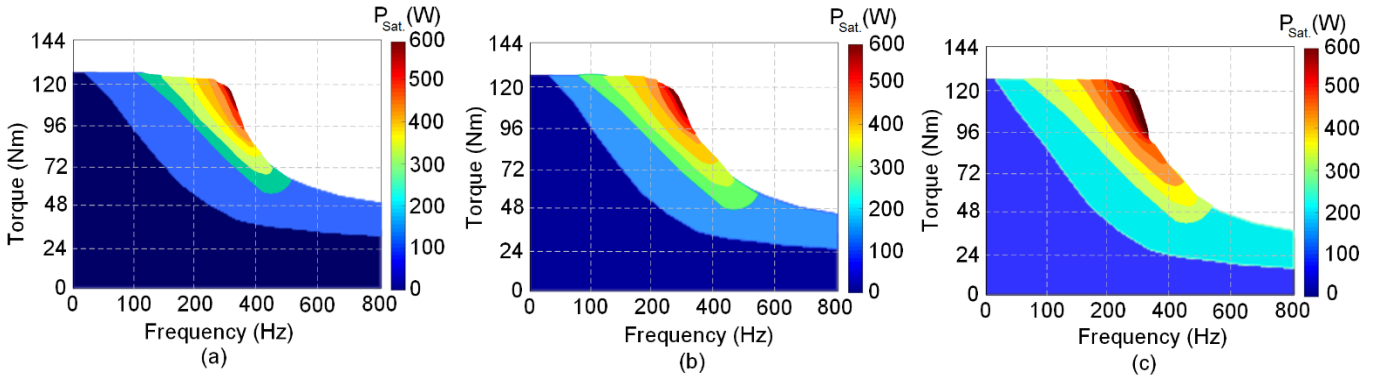

Fig. 3.2.2.2 The torque-frequency-saturation loss presentation through the last term of equation (3-11) for, a) the FE one-segmented, b) FE four-segmented, and c) eight-segmented techniques.

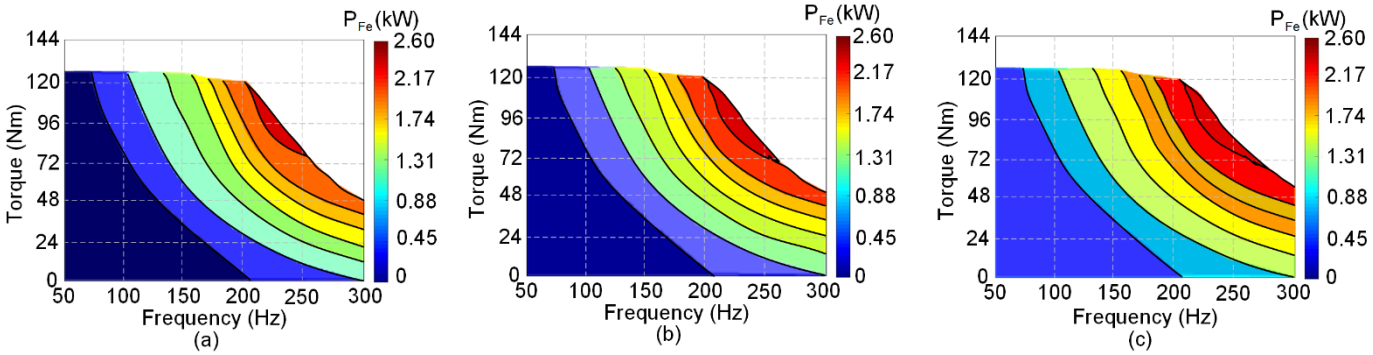

Fig. 3.2.2.3. Total predicted iron losses using variable coefficient model as function of torque and frequency, where a) the typical 2-D FE iron loss modeling, b) the quasi-2-D-FE technique with four segmented observation, and c) the proposed quasi-2-D-FE technique with eight-segmented observation.

shows lesser filed harmonics in the critical areas. Additionally, the proposed model (in Figure 3.2.2.3-c) illustrates a higher amount of iron loss at low frequencies between 0 to 350 Hz. Moreover, the quality of constancy in torque between 0 to 400 Hz is a perfect match with the goal of the machine's operation [41].

Field harmonic verification for various orders from fundamental to 15th order at each iron part is illustrated in Fig. 3.2.2.4. Using a typical technique, the magnetic field density and its corresponding harmonics are calculated for each iron part (rotor and stator yokes). Whereas, those data are calculated for smaller segments (4 or 8 times smaller) and a considerably higher number of mesh elements and nodes by the proposed eight-segmented quasi-FEA technique. Regarding the proposed technique the field harmonics that are calculated based on both the conventional models and the proposed model are employed to predict the iron loss on eight measured data points, and compared with the 3-D FEA and experiment results, the FEA results are calculated under sinusoidal three-phase current excitation.

As Fig. 3.2.2.5-a illustrates the comparison of iron loss obtained via eight-segmented technique presents a good agreement with the 3-D FEA and experiment results. The error between the proposed model and experiment results are due to neglecting the current the conventional model is obviously underestimated, particularly during flux weakening harmonic, slot opening effect and fringing effect. On the contrary, the iron loss predicted by range, because of ignoring the harmonic loss. Under flux weakening, the difference between the conventional model and the others two FE models (four- and eight-segmented) quickly increases as speed increases. Fig. 3.2.2.5-b presents the comparison of PMSM efficiency obtained via the proposed method. The PMSM efficiency of the proposed method is acceptable compared with the experiment measured machine efficiency and FEA results. The PMSM efficiency computed using the proposed method is slightly larger than experiment results, mainly due to neglecting the phase current harmonic. It should be accurate and fastest way to achieve the objectives of the study. Moreover, a significant in-crease of iron loss in the flux

weakening range, particularly in the range after passing via the transition point, is evident [41]. At the rated speed of 150 rpm, the iron loss is 1000 W, and the efficiency of 96% is reachable. Although, the error between each type of measurement is approximately 8.8%, the error between the proposed 8-segmented (2-D FEA) and 8-segmented (3-D FEA) is less than 1%.

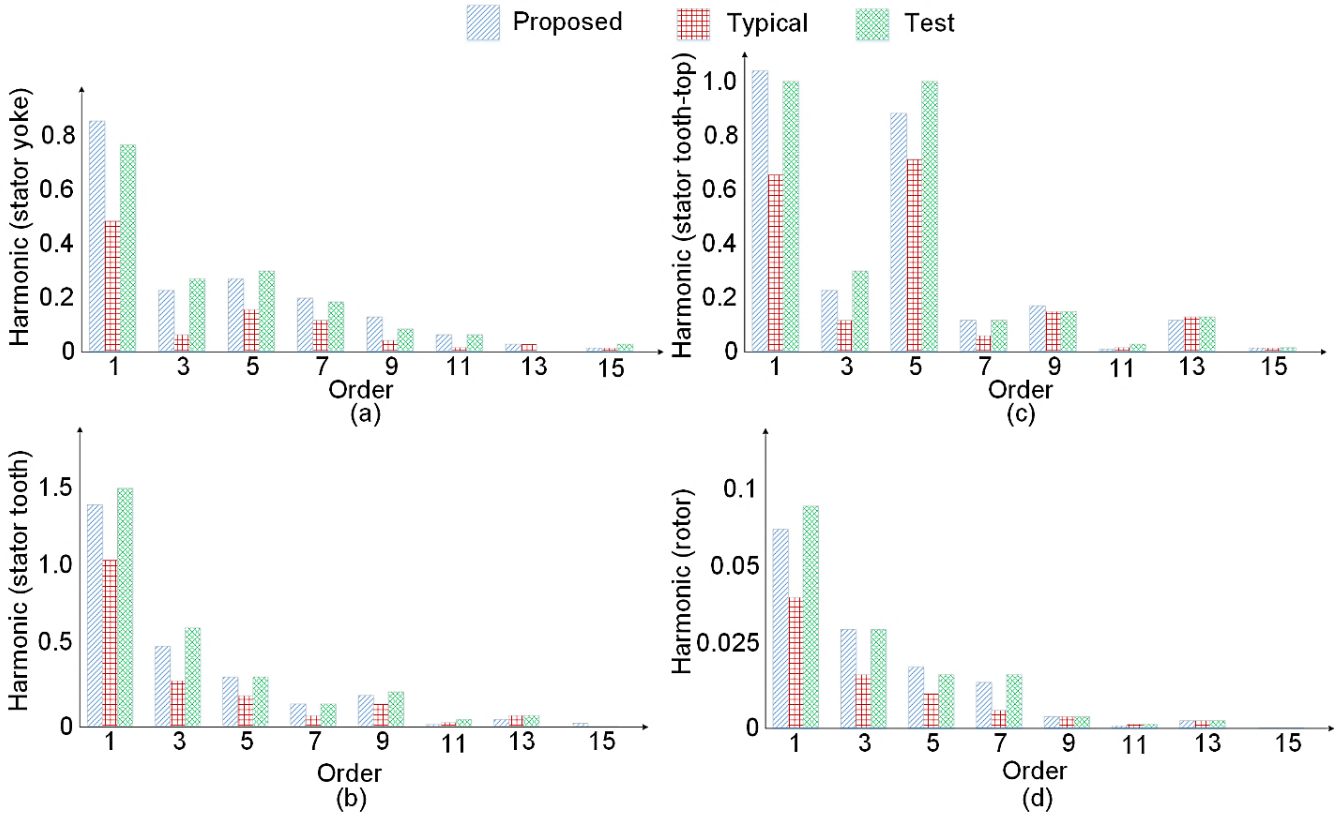

Fig. 3.2.2.4. Comparison of field harmonics in iron parts of the machine at a) stator yoke, b) stator tooth, c) stator tooth-top, and d) rotor yoke.

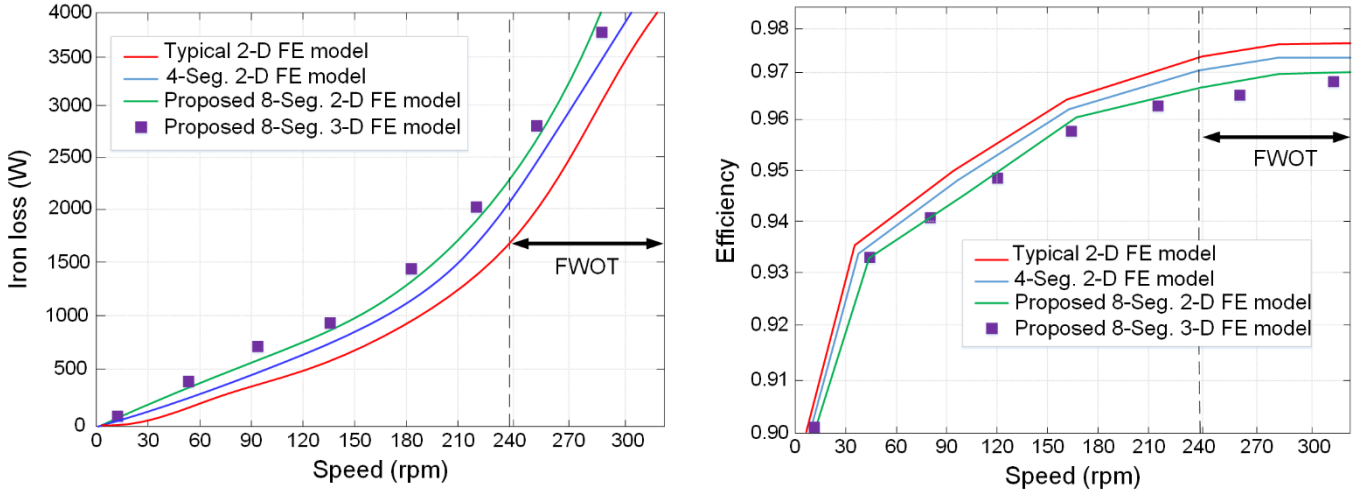

(a) (b)

Fig. 3.2.2.5 Comparison of the electromagnetic-based objectives for a wide speed operation, in which a) shows iron loss trend, and b) affected machines' efficiency because of losses computation.

3.3 IEM-Formula in Frequency Domain

Recently a modern distinguished iron loss formulation known as IEM-Formula by RWTH Aachen University in Germany has been proposed in order to deal with an advanced iron loss estimation on nonlinear materials such as soft magnetic materials for electrical machines [11-12] [53]. The proposed IEM-Formula needed to be evaluated under field weakening condition because the field weakening capability plays a significant role in the iron loss prediction of permanent magnet synchronous machines (PMSMs) over a wide range of speed, particularly at high speeds [54].

The classic IEM-Formula is introduced by D. Eggers [11-12] in 2012 in the following form:

$$P_{IEM}(B,f) = P_h + P_e + P_{exc} = a_1 B^{\alpha} f + a_2 B^2 f^2 (1 + a_3 B^{a4}) + a_5 B^{1.5} f^{1.5} \tag{3-18}$$

where a_1, a_2, a_3, a_4, and a_5 are the coefficients which will be estimated via nonlinear curve fitting. α is the fitted material parameter which is found using dc-measurements (quasi-static loss measurements using a field-meter) in a standard Epstein frame, finding the best parameter set describing the hysteresis losses as:

$$E_{DC} = a_1 . \hat{B}^{\alpha} \tag{3-19}$$

The classic formula is examined for M400-50A steel sheet between 50 to 700 Hz and is compared to a standard Epstein frame test.

Single-valued magnetization curves are employed to consider saturation effects (3) originating from the nonlinear material behavior. The magnetic material is utilized up to 2.1 T in the considered machine. Second-order effects, originating from hysteresis behavior, are neglected.

$$P_{sat.}(\hat{B}, f) = a_2 . a_3 \hat{B}^{a_4 + 2} . f^2 \tag{3-20}$$

To consider skin effect in the eddy-current term of the classic formula, we have:

$$P_e = a_2 B^2 f^2 (1 + a_3 B^{a_4}) \tag{3-21}$$

where the coefficient (a_2), which considers the skin effect by accounting for the thickness of the steel used, is:

$$a_2 = \frac{\pi^2 d^2}{6 \rho \rho_e} \tag{3-22}$$

with the sheet thickness (d), specific density (ρ) and specific electrical resistivity (ρ_e) of the soft magnetic material.

3.3.1 Modified IEM-Formula with Flux Weakening Consideration

In [27], Han *et al*. reported the influence of harmonic losses to increase and dominate the total iron loss during field weakening operation (FWOT). A useful comparative study on the produced harmonics and eddy-current loss (in the stator-teeth) is presented. However, lack of experimental verification afflicted the quality of the research.

Li *et al*. investigated the rotor saliency of an interior permanent magnet (IPM) machine, and large harmonic eddy-current loss in the stator iron loss could be caused under field-weakening operation, conspicuously impairing the output performance of the IPM machine. They proposed a new stator teeth eddy-current loss analysis approach, in which the teeth eddy-current loss is divided into two parts: one part is caused by the synchronous air-gap field density rotating synchronously with the rotor, while the other part is induced by the asynchronous air-gap field density [28]. There is a thought-provoking consideration on the fractional-slot concentrated winding based on the eddy-current coefficients; however, an experimental test needs to be considered. In addition, the following works have fully discussed the fractional-slot concentrated winding [29-30].

In [31], the iron loss resistance was calculated through a finite-element analysis as functions of the *d*–*q*-axis currents. On the other hand, the effect of field-weakening current on the iron losses of the PMSM is presented in [32]. Furthermore, FEA based iron loss calculation methods have been used to minimize the iron losses of the PMSM under field weakening conditions in [33-34].

The classic formula is examined for M400-50A steel sheet between 50 to 700 Hz, and is compared to a standard Epstein frame test, which is exhibited in Figure 3.3.1.1, where solid lines show the analytical data and measured data denoted by markers. The employed Epstein frame comprises a primary and a secondary winding. The sample is evaluated in a set of a number of strips cut from M400-50A steel sheet, in which each layer of the sample is double-lapped in corners and weighted down with a force of 1 N under the well-known International standard for the measurement configuration and conditions (IEC 60404-2:2008) magnetic materials. The iron loss prediction was predicted as acceptable on the steel sheet parts of the machine (approximately linear) for a various range of frequencies (50–700 Hz), and up to 2 T [54].

Single-valued magnetization curves are employed to consider saturation effects (3-11) originating from the nonlinear material behavior. The magnetic material is utilized up to 2.1 T in the considered machine. Second-order effects, originating from hysteresis behavior, are neglected:

During FWOT, the importance of stator and rotor cores' resistance, as well as its influence on the total iron loss, is orderly defined into the d–q-axis equivalent circuit to examine the iron loss evaluation in advance. The steady-state equivalent circuit of the PMSM is shown in Fig. 3.3.1.1 [39]. Moreover, the voltage drops $R_s I_d$ and $R_s I_q$ of the stator winding resistance are taken into account for the iron loss model based on the equivalent circuit, in which ref. [56] assumed the winding resistance negligible. However, its ohmic value can be large, especially under the field weakening condition. Therefore, a more accurate iron loss modeling is rooted from both core and winding resistance consideration. The following expressions can be extracted from the equivalent circuit:

$$
\begin{aligned}
&U_d = R_s I_d - \omega L_q I_{aq} \quad , \quad U_q = R_s I_q + \omega L_d I_{ad} + \omega \lambda_m \\
&I_d = I_{ad} + I_{cd} \quad , \quad I_q = I_{aq} + I_{cq} \\
&I_{cd} = -\frac{\omega L_q I_{aq}}{R_c} \quad , \quad I_{cq} = \frac{\omega L_d I_{ad} + \omega \lambda_m}{R_c} \\
&P_{fe} = \frac{\sqrt{\left(U_d - I_d R_s\right)^2 + \left(U_q - I_q R_s\right)^2}}{R_c} \\
&\textit{where} \quad U_s = \sqrt{U_d^2 + U_q^2}
\end{aligned}
\tag{3-23}
$$

During FWOT, the iron loss cannot be determined accurately using only the magnetic field density because the terminal voltage is steady, being limited with direct current (DC) link voltage. Regarding this issue, a harmonic loss and voltage are induced at the tooth and yoke of the stator core, which are analytically modeled (in Equation (3-23)) based on the iron loss resistance. Therefore, a large eddy-current loss will be generated, which critically decreases the efficiency, especially if a wide region of FWOT exists. Thus, the IEM-Formula model is adopted with a resistance model that considers harmonic loss. Harmonic loss is investigated through the air-gap magnetic field density harmonics from the elemental component and the machine's equivalent circuit parameters (shown in Figure 3.3.1.1), based on the air-gap field density analysis in [27] [39] [55]. Therefore, the iron loss decreases in a similar manner during FWOT. However, this predicted loss is far from the results from experiments and FEA computation. This is due to the fact that an important eddy-current loss will be generated at FWOT that significantly decreases the efficiency of the machine; this is also validated in [55-56]. The iron loss resistance model based on the IEM-Formula should be modified to consider harmonic loss during FWOT for the PMSM with closed-slot, double-layer fractional-slot concentrated winding [55-57].

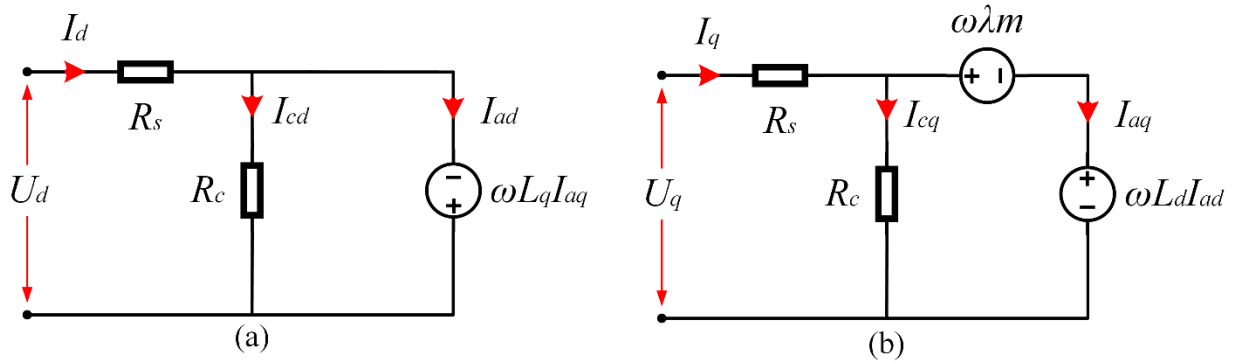

Fig. 3.3.1.1. Steady-state equivalent d–q circuits of permanent magnet synchronous machine (PMSM) with iron loss resistance, listed as: a) d-axis equivalent circuit; b) q-axis equivalent circuit.

It is required to wind search coils onto armature tooth tips of the tested generator to detect air-gap field. The d-axis pickup should also be installed at the generator to detect the number of revolutions and to synchronize the execution of a program with the revolutions. The d-axis pickup generates a pulse per electric cycle. In addition, the location of search coils at armature tooth tips and at various parts of the rotor and the location of the d-axis and the d-axis pickup in the tested generator. The used methodology is validated in [58].

By a sinusoidal three-phase current excitation, the total air-gap field density [59-60] is written:

$$B_g(\gamma,\omega.t) = B_{mg0}(\gamma,\omega.t) + B_{gr}(\gamma,\omega.t) \tag{3-24}$$

where B_{mg0} and B_{gr} are the sum of the no-load magnetic field density and the armature reaction air-gap magnetic field density. For non-sinusoidal waveforms, the eddy-current term can be modified (based on [56,40]) to give the following expression:

$$P_e = a_{2'}\left[\frac{dB}{dt}\right]^{\alpha} + (1 + a_3 B^{a4}) \tag{3-25}$$

α is a coefficient that depends on the type and thickness of the laminated magnetic material. In addition, $a_{2'} = a_2/(2\pi^2)$ is the new eddy-current coefficient, and dB/dt is the root mean square (RMS-value) of the rate of change of field density over one cycle of the fundamental frequency [61].

Consequently, the predicted iron loss produced in the flux weakening condition with the influence of the harmonic component on the hysteresis loss is found to be small (about 9% of total iron loss) under open-circuit condition; therefore, its effect on the hysteresis term is neglected. Hence, the modified eddy-current loss density in W/m^2 is proportional to the energy of the differential of the field density, which mainly originated via the eddy-currents behavior that is modelled by Equations (3-25), (3-26), and specific field density distribution over tooth (B_t) and yoke (B_y) shown in Equation (3-27), given as:

$$p_e = a_2 B^2 f^2 (1 + a_3 B^{a_4}) \tag{3-26}$$

$$B = B_t + B_y = \frac{1}{k_t \alpha_s}\int_{-\alpha_s/2}^{\alpha_s/2} B_g(\gamma)d\gamma + \frac{1}{2k_y\pi}\int_{-\pi/2}^{\pi/2} B_g(\gamma)d\gamma \tag{3-27}$$

The magnetic field density distribution over B_t and B_y is presented in Fig. 3.3.1.2, in which peak values are 1.98 T and 0.56 T, respectively. To simplify the above equation (3-27):

$$B = B_t + B_y = \sum_{h=1,3,5,7,\ldots}^{\infty} k_{tf}(h) B_g(h)\cos(\psi_h) + \sum_{h=1,3,5,7,\ldots}^{\infty} k_{yf}(h) B_g(h)\cos(\psi_h) \tag{3-28}$$

where B_g is the airgap magnetic induction between one tooth pitch. The teeth and yoke filter constants (k_{tf} and k_{yf}), which are dependent on harmonic order, can be calculated using IEM-Formula (3-18)-(3-22). B_t = 15 mm, and b_y = 81 mm in this study.

As a result of Equations (3-23)–(3-25), the following summed equation can be written to calculate the model-based parametric eddy-current loss equation, given as:

$$p_e = \frac{a_2}{2\pi^2 T}\int_0^T \left(\sum_{h\in 1,3,5,7}^{\infty} \frac{\partial B(\omega t)}{\partial t}\right)^{\alpha} dt + (1 + a_3 B^{a_4}) \tag{3-29}$$

As the generated synchronous air-gap magnetic field density (shown in Fig. 3.3.1.3, where Fig. 3.3.1.3-a presents fundamental no-load magnetic induction B_{m1}, and Fig. 3.3.1.3-b indicates no-load airgap magnetic induction B_m) is caused from the fundamental air-gap field density and harmonic component B_{syh},, it can be expressed as:

$$B_{syh}(\gamma,\omega t) = \frac{4B_{sym}}{\pi}\sum_{h=3,5,\ldots}^{\infty} \frac{k_{sw}(h)}{h}\cos(h(\gamma - \omega t)) \tag{3-30}$$

with fundamental form as [55]:

$$B_{sym} = B_m - \frac{\mu_0}{g} k_U k_{pe}(1)\cos(\psi_1) F_{s1} \tag{3-31}$$

Fig. 3.3.1.2 Magnetic flux density distribution using Equations (3-28) for tooth and yoke of stator.

where F_{s1} is the fundamental magnetic motive force (MMF) in the stator, k_{sw} constant is a unit square function and through Fourier series can be developed to:

$$k_{sw}(h) = \sin\left(\frac{\alpha_p \pi h}{2}\right) \tag{3-32}$$

where α_p is the pole-arc coefficient.

The ratio of the harmonic field density to the fundamental term can be given as:

$$P_h \propto \frac{4B_{sym}^2}{\pi} \sum_{h=3,5,\ldots}^{\infty} \left(k_{sw}^2(1)k_{tf}^2(1)\right)V_t + \left(k_{sw}^2(1)k_{yf}^2(1)\right)V_y \tag{3-33}$$

considering (h = 1) as fundamental, P_h can thus be rewritten in the following form:

$$P_h = \left(\frac{B_{sym}}{B_m}\right)^2 k_{ph} P_{h1} \tag{3-34}$$

$$k_{ph} = \sum_{h=3,5,7}^{\infty} \frac{\left(k_{tf}(h)^2 k_{sw}(h)\right)V_t + \left(k_{yf}(h)^2 k_{sw}(h)\right)^2 V_y}{\left(k_{tf}(1)^2 k_{sw}(1)\right)V_t + \left(k_{yf}(1)^2 k_{sw}(1)^2\right)V_y} \tag{3-35}$$

k_{ph} as a harmonic constant is employed to include the harmonic magnetic induction range, which can be known from the machine design parameters [55]. In addition, a harmonic voltage U_{ph} originated from Equations (3-23) and (3-36 and 3-37) is defined to model harmonic loss based on equivalent circuit parameters, which is:

$$U_{ph} = \omega\left[\sqrt{(\lambda_m - L_{ad}I_{ad})^2 + (L_{aq}I_{aq})^2}\right]\frac{B_{sym}}{B_m} \tag{3-36}$$

Regarding the armature reaction air-gap magnetic induction, the equivalent factors are affiliated with the machines' parameters like Equations (3-36 and 3-37), which are coupled with the d–q axis equivalent circuit as:

$$\begin{cases} B_{ad1} = \dfrac{\mu_0}{g}\left(1-\dfrac{4}{\pi}k_U k_{pe}(1)\right)F_{s1}\cos(\psi_1) \propto L_{ad} I_d \\ B_{m1} = \dfrac{4}{\pi}k_{sw}(1)B_m \propto \lambda_m \end{cases} \tag{3-37}$$

To simplify the harmonic voltage Equation (3-36), the combination of Equations (3-33) and (3-34) results in the new fundamental (h = 1) expression as given:

$$U_{ph} = \omega\left(\lambda_m - \frac{4}{\pi}k_{sw}(1)\right)\frac{k_U.k_{pe}(1)}{1-\dfrac{4}{\pi}k_U.k_{pe}(1)}L_{ad}(I_d - \omega I_{ad}) \tag{3-38}$$

By adopting the harmonic voltage U_{ph}, the harmonic loss P_{h} Equation (3-34) can be simplified into the formula of U_{ph} and k_{ph} as:

$$P_h = \frac{3}{2}\left(\frac{k_{ph}U_{ph}^2}{R_{ce}}\right) \tag{3-39}$$

The modified IEM-Formula based on the harmonic loss can be derived from the parametric machine modelling based on the machine's equivalent circuit parameters as:

$$P_{fe} = P_{IEM1} + P_h = \frac{3}{2}\left(\left(\frac{\sqrt{(\omega\lambda_m)^2 - (\omega L_{ad} I_{ad})^2 + (\omega L_{aq} I_{aq})^2}}{R_c}\right) + k_{ph}\frac{U_{ph}^2}{R_{ce}}\right) \tag{3-40}$$

where P_{IEM1} and P_{h} are the classic IEM-Formula and modified IEM-Formula (which considers iron loss resistance) and harmonic iron loss.

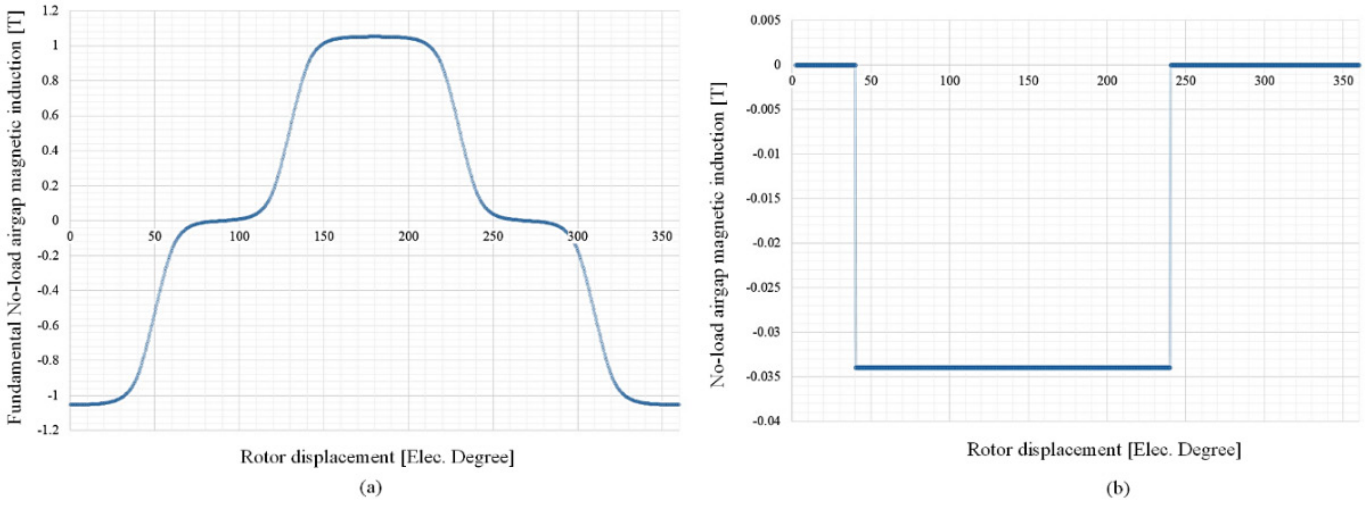

Fig. 3.3.1.3. Comparison of no-load air-gap magnetic field density waveforms using Equations (3-31) and (3-37), for a) fundamental no-load magnetic induction (B_{m1}), and b) no-load airgap magnetic induction (B_{m}).

A. Methodology

After the analytical and numerical modeling by the modified IEM-Formula, a wide region of FWOT is observed. Hence, a significant harmonic loss is produced, which causes a considerable increase in iron loss. Since a large deviation in iron loss prediction using the classic IEM-Formula can be seen in comparison with test results, an IEM- Formula-based modification on the equivalent circuit of the PMSM is proposed to consider harmonic losses.

Fig. 3.3.1.4 contains a flowchart illustrating the calculations on a fractional-slot concentrated winding, radial field permanent magnet machine with 5 kW rated power in generator-mode. The figure also shows the results of the analysis during FWOT. The total iron loss using classic IEM-Formula (red curve) sharply diverges; however, the modified IEM-Formula (green curve) along with the experimental results rapidly increases during FWOT. Table 3.3.1.2 illustrates the value of the coefficients.

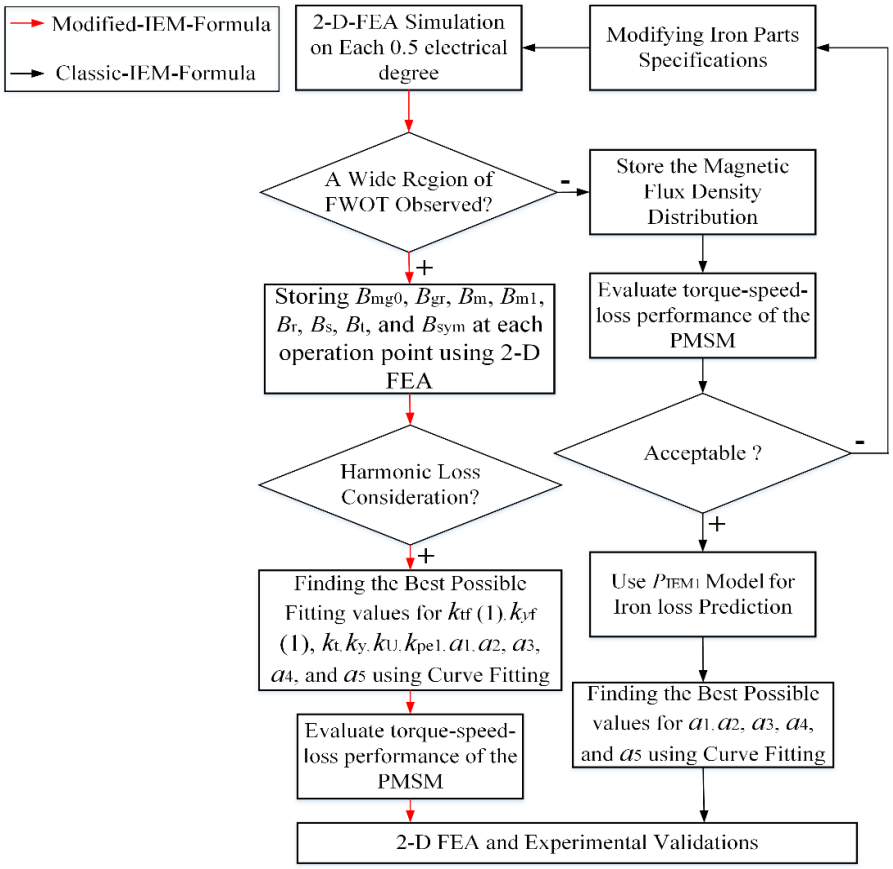

Fig. 3.3.1.4. Flowchart of the analysis dynamics.

First, a large range of FWOT is observed and the previously mentioned magnetic field density components are stored using 2D FEA for each 0.5 electrical degree. Second, the coefficients are calculated using a curve fitting technique based on the multi-generalized reduced gradient nonlinear (M-RGN) method [21].

Fig.3.3.1.5 illustrates the behavior of torque-frequency-loss of the machine, in which the terms of the iron loss such as hysteresis, eddy-current, excess, saturation, and harmonics are calculated from the modified IEM-Formula. The Hysteresis loss (Figure 3.3.1.5-a), eddy-current loss (Figure 3.3.1.5-b), excess loss (Figure 3.3.1.5-c), and saturation loss (Figure 3.3.1.5-d) are shown based on their constant torque and power range with a considerable field weakening region. Figure 3.3.1.5-a shows the generated harmonics perspective of eddy-current and total iron losses by the classic and modified-IEM-Formula. As expected, the maximum eddy-currents loss significantly increased to 1.5 kW during FWOT. The maximum eddy-current loss of 0.88 kW can be seen at the rated speed of 150 rpm, and 1.09 kW at 200 rpm. Also, hysteresis loss was increased to 820 W (during FWOT), hence as its value is not critically changed, and thus, having its terms modified is not going to be important in the total iron loss quantity. Excess and saturation losses by 145W and 0.84W at 150 rpm are remained approximately constant, and that is why the modified IEM-Formula did not update their terms in the total iron loss equation (3-40). A considerable difference in the total iron loss and also efficiency during FWOT can be seen between the two methods. In Fig. 3.3.1.6-a, the 7th harmonic order resulted in 0.90kW and 1.41kW for the eddy-current loss and the total iron loss, respectively. For 5th harmonic as the second largest, the eddy-current and total iron losses of 0.71kW and 1.08kW are reported for the modified IEM-Formula. The error between the classic and modified IEM-Formula during FWOT is approximately 15.7% for the total iron loss and 18.6% on the eddy-current

loss. Figure 3.3.1.6-b shows how the following terms in Figure 3.3.1.5-a are representing the total iron loss prediction based on torque-frequency-loss evaluation.

Table 3.3.1.2. Coefficients calculation using the modified institute of electrical machine formula (IEM-Formula) by curve fitting.

Coefficients	Values	Units
k_{tf} (1)	7.0439×10^{-1}	
k_{yf} (1)	7.7938×10^{-1}	
k_t	0.4567	
k_y	0.3031	
k_{pe} (1)	0.3991	
k_U	0.4586	
a_1	398.0363203	W/m^3
a_2	2.3821×10^{-2}	W/m^3
α	1.705944	
a_3	11.74239805	W/m^3
a_4	8.27×10^{-2}	
a_5	1.3617×10^{-9}	W/m^3

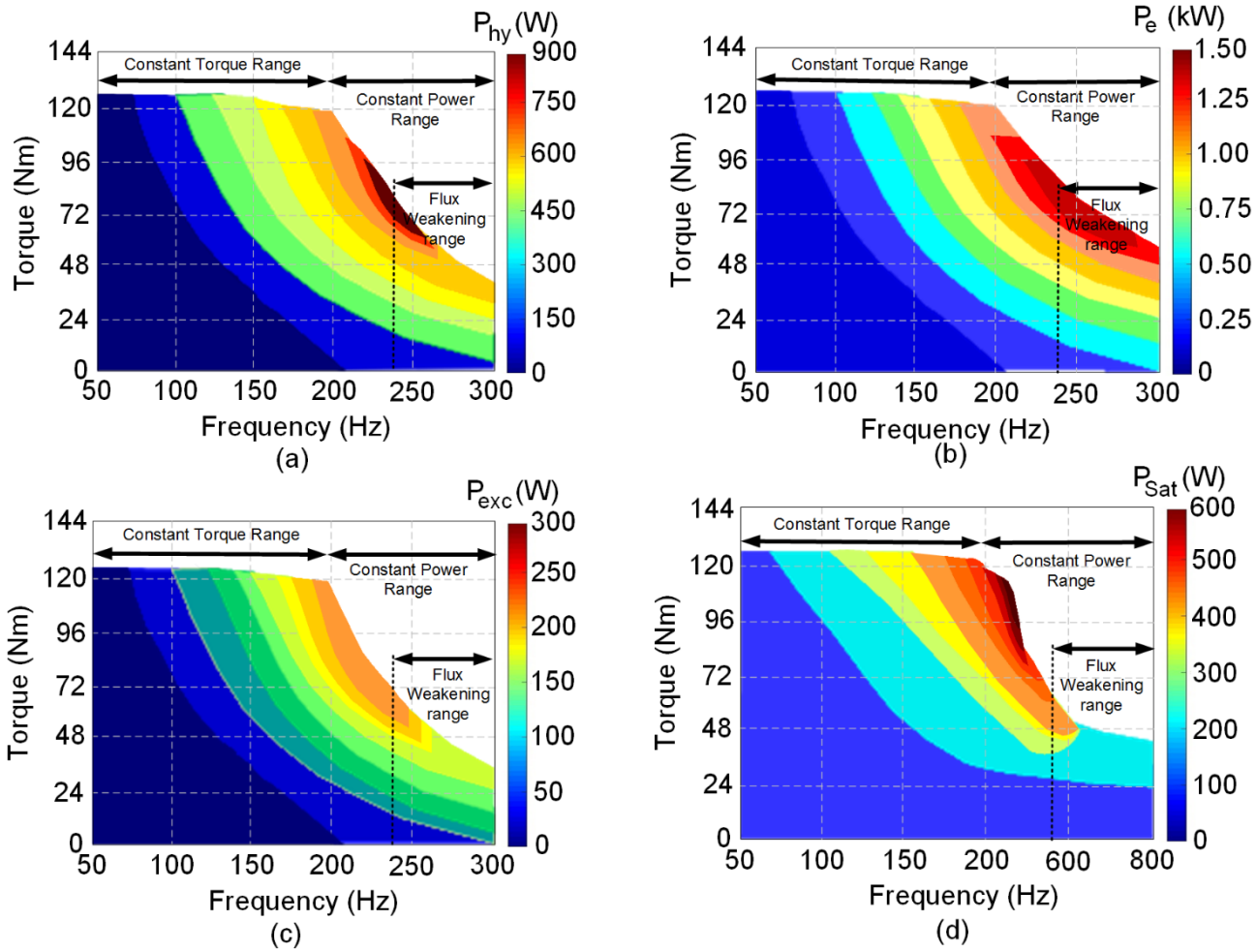

Fig. 3.3.1.5. Predicted iron losses using modified IEM-Formula as function of torque and frequency, where: a) the hysteresis loss; b) the eddy-current loss; c) excess loss contribution; and d) saturation loss.

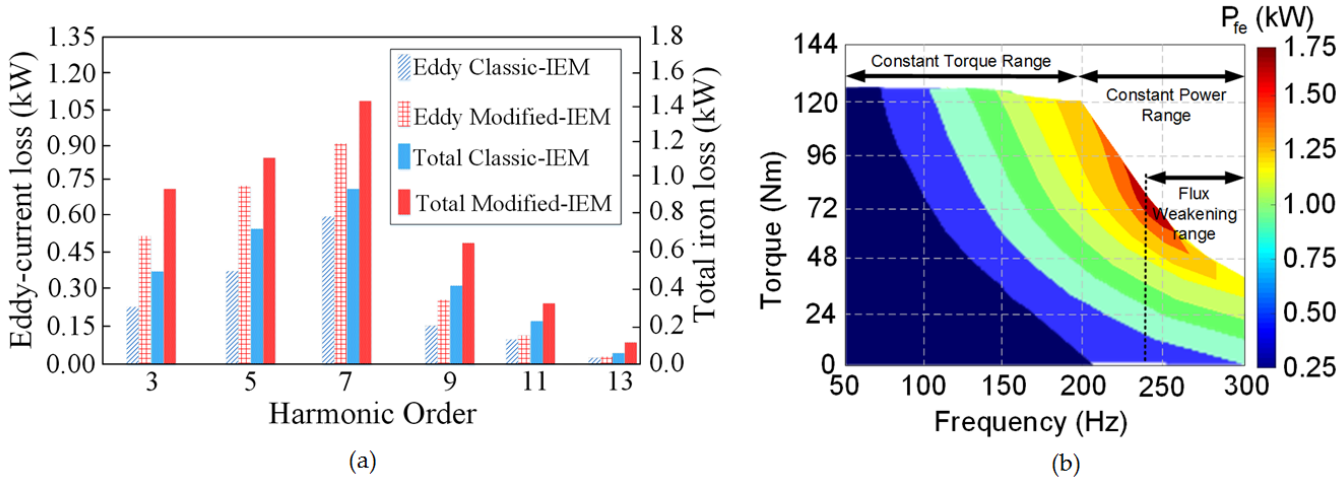

Fig. 3.3.1.6. Harmonic spectra and total iron loss prediction using classic and modified IEM-Formula during flux weakening operation time (FWOT), where: a) existing dominant harmonics on total iron loss and specially eddy current loss during FWOT; b) presentation of the torque-frequency-power loss by the modified IEM-Formula with FWOT concentration.

3.4 A Proposed Time-domain Advanced Iron Loss Computation Methodology

Iron loss prediction can be done in frequency and time domains, where the time domain computation considers the time and space harmonics which resulted in a better estimation. However, it is a way more time consuming and complex, but it offers an advanced estimation in comparison with the frequency domain.

Aramburo *et al*. [63] presents an accurate prediction of rotational iron losses with a purely alternating field and orthogonal components of the flux density on an induction machine. The authors have applied a correction factor based on the experimental results to improve the analytical calculation. In other research, Kowal *et al*. [18] presents an electromagnetic loss calculation by recognizing the significance of including an analysis of higher order harmonics. The article provides a comparison between frequency-domain and time-domain models for the iron loss calculation. The iron loss calculations have been presented for a 2.1-MW permanent magnet synchronous wind generator.

The iron loss model development introduces a FEA technique in the frequency and time domains. The eddy-current loss computation considers the rotational field and steel sheet magnetic reluctance. The proposed technique examines the geometry and space point of each iron segment and the flux density calculation for each part, rotor yoke, tooth top, tooth, and stator yoke as shown in Fig. 1(a). Each part has certain magnetic reluctance and volume features which affect the rotational iron losses. Fig. 1(b) presents a four-probe technique to compute the bulk conductivity, where black and red circuits belong to stator and rotor measurements, respectively. Vs and Vr are stator and rotor volt meters, As and Ar are the Ampere meters of stator and rotor cores. rso and rro are outer radius of the stator and rotor, rsi and rri are inner radius of stator and rotor. V_s and V_r volt meters have two probes each, which are connected to the both stator and rotor surfaces along z-axis. However, A_s and A_r Ampere meters with two probes each, will compute the current on the both cutoff surfaces of stator and rotor. To measure bulk resistivity, total eight probes for both stator and rotor is needed.

Regarding the d-axis equivalent circuit, which is based on the magnetic reluctance behavior of the system, the following expressions can be defined

$$U_d = R_w I_d - \omega L_q I_{aq} \quad , \quad I_d = I_{ad} + I_{cd}$$
$$P_{fe} = \frac{\left(U_d - I_d R_W\right)^2}{R_c} \tag{3-41}$$

where R_c and R_w are iron loss resistance in the stator core and winding, respectively. P_{fe}, based on equivalent circuit parameters, is given (1). The voltage drops $R_w I_d$ of the stator winding resistance are taken into account for the iron loss model based on the equivalent circuit.

To analytically compute the bulk conductivity of the machine's iron parts, the bulk resistivity calculation of each core is required, thus, if the area of stator and rotor cores is

$$A_{tot} = A_{st} + A_{rt} = \left[\left(\pi r_{so}^2 - \pi r_{si}^2\right) - \left(\frac{h_s}{2}\left(W_{s1} + W_{s2}\right)\right)Q_s\right] + \left(\pi r_{ro}^2 - \pi r_{ri}^2\right) \tag{3-42}$$

the term $h_s/2*(W_{s1}+W_{s2})*Q_s$ will subtract the stator slots area from the core, the geometrical parameters are presented in Fig.1(c). Then, the resistivity of the stator and rotor can be given

$$\begin{aligned} R_{tot} &= R_{st} + R_{rt} \\ &= \rho_{st}\frac{l_s}{A_{st}} + \rho_{rt}\frac{l_s}{A_{rt}} \end{aligned} \tag{3-43}$$

ρ_{st} and ρ_{rt} show the resistivity of the stator and rotor cores. In this study as both cores' materials (M400-50A) are the same, and thus $\rho_{st} = \rho_{rt} = 42$ μΩcm. Based on the Fig. 1(b), these values are possible to be calculated using

$$\rho_{st} = \frac{V}{I}2\pi S_{st}, \quad \rho_{rt} = \frac{V}{I}2\pi S_{rt} \tag{3-44}$$

where S_{st} and S_{rt} are the spacing (in mm) between each probes, total four probes for each core has used.

The conductivity of each core can be calculated by

$$\begin{aligned} \sigma_{tot} &= \sigma_{st} + \sigma_{rt} \\ &= \frac{l_s}{R_{st}A_{st}} + \frac{l_s}{R_{rt}A_{rt}} \end{aligned} \tag{3-45}$$

An accurate loss computation in electrical machines has to be based on time domain waveforms of the flux density. In this method of iron loss computation, a number of electrostatic simulations are run on each iron part's defined volume to find the radial flux density B_x and tangential flux density B_y values. These are stored to identify the time waveform of the induction. Afterwards, whilst considering the iron's resistance, the eddy-currents in the iron parts and eddy-current loss in W/cm^2 as a dominant term of the total loss is calculated by (validated [64] [67]):

$$P_{eddy} = \frac{1}{T}\int_T \left(\frac{1}{\sigma}\left[H(t)\right]^T [S][H(t)]\right)dt \tag{3-46}$$

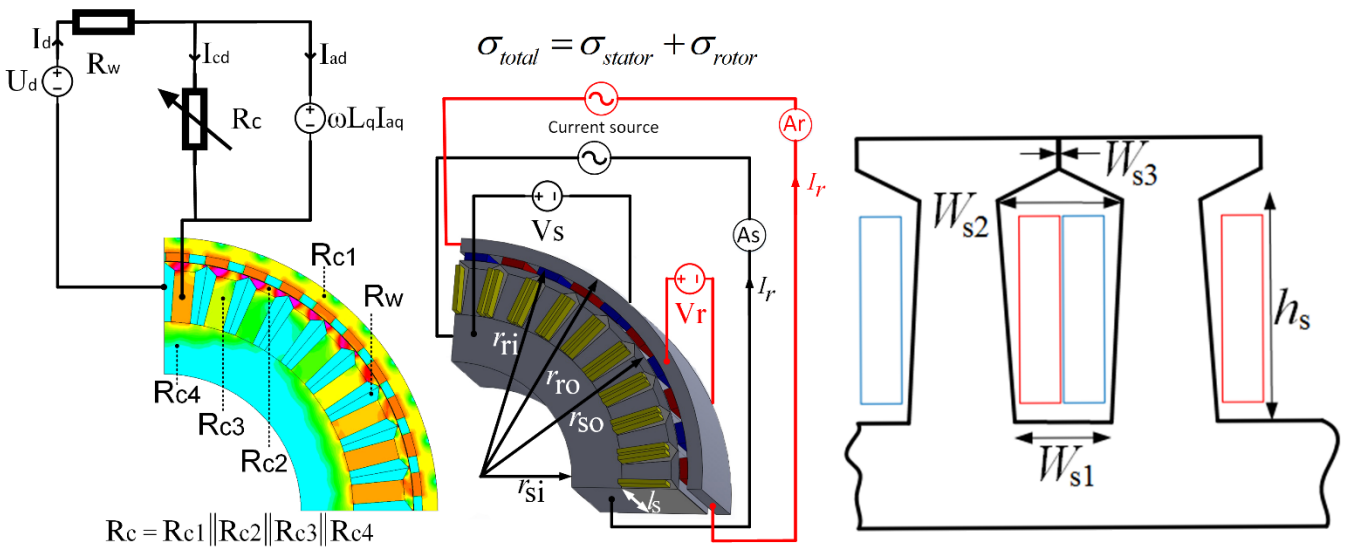

Fig. 3.4.1 A resistance-based FEM model of the 36/40 PM synchronous machine, a) static flux density by FEM, b) a 3D view with d-axis equivalent circuit, and c) a stator slot geometry.

The induced harmonic loss through the field density harmonic component is proportional to the square of the harmonic component order in the time domain computation. The hysteresis loss can be defined as (validated in [66-67]):

$$P_{hys} = \frac{1}{T}\int_0^T \left(\frac{1}{\Delta t}[H(t)]^T [G]\left([B(t)] - [B(t-\Delta t)]\right) \right) dt \tag{3-47}$$

where B and H are magnetic field and magnetic field strength. [S] has given by climbing the local equations. σ is the conductivity of the steel. P_{hys} depends on the time derivative of the flux density. The excess loss term is calculated by:

$$P_{exc} = \frac{n_0 V_0}{2}\left(\sqrt{1 + \frac{4\sigma GS}{n_0^2 V_0}\left|\frac{dB(\omega t)}{dt}\right|} - 1 \right)\left|\frac{dB(\omega t)}{dt}\right| \tag{3-48}$$

n_0 is the number of simultaneously active magnetic objects for $f \to 0$. V_0 is the statistics of the magnetic objects. Both parameters are functions of the peak flux density and determined by the excess field $n(H_{exc}) = n_0 + H_{exc}/V_0$. G is a dimensionless constant (G = 0.1277), and S is the lamination cross section which is calculated by the dimensions of steel samples [66-67].

According to [18], [64] and [67], harmonic losses, which are caused by the steel sheet material rotational iron losses, are written for the stator as:

$$\begin{aligned} P_{fe} &= \left(P_{hys0} + P_{eddy0} + P_{exe0}\right)V_t + \left(P_{hys} + P_{eddy} + P_{exe}\right)V_y = \\ &\left(\begin{array}{l} \frac{1}{T}\int_0^T \left(\frac{1}{\Delta t}[H_t(t)]^T [G]\left([B_t(t)] - [B_t(t-\Delta t)]\right) \right) dt \\ + \frac{1}{T}\int_T \left(\frac{1}{\sigma}\left[H_t(t)\right]^T [S][H_t(t)] \right) dt \\ + \frac{n_0 V_0}{2}\left(\sqrt{1 + \frac{4\sigma GS}{n_0^2 V_0}\left|\frac{dB_t(\omega t)}{dt}\right|} - 1 \right)\left|\frac{dB_t(\omega t)}{dt}\right| \end{array} \right) V_t \\ &+ \left(\begin{array}{l} \frac{1}{T}\int_0^T \left(\frac{1}{\Delta t}[H_y(t)]^T [G]\left([B_y(t)] - [B_y(t-\Delta t)]\right) \right) dt \\ + \frac{1}{T}\int_T \left(\frac{1}{\sigma}\left[H_t(t)\right]^T [S][H_t(t)] \right) dt \\ + \frac{n_0 V_0}{2}\left(\sqrt{1 + \frac{4\sigma GS}{n_0^2 V_0}\left|\frac{dB_y(\omega t)}{dt}\right|} - 1 \right)\left|\frac{dB_y(\omega t)}{dt}\right| \end{array} \right) V_y \end{aligned} \tag{3-49}$$

where k_e, B_{t} and B_{y} are the eddy-current constant and the flux density with time waveforms at the tooth and yoke of stator. V_{t} and V_{y} are the volume of the tooth and yoke of the stator core.

The harmonic iron loss is defined as:

$$P_h = \left(\frac{B_{syh}(\omega t)}{B(\omega t)} \right).k_{ph} P_{fe} \tag{3-50}$$

where B_{syh} is the harmonic component of the synchronous air-gap flux density that is calculated by:

$$B_{syh} = B(\omega t) - \frac{\mu_0}{g} k_U k_{pe}(1)\cos(\psi_1) F_{s1} \tag{3-51}$$

μ_0 is the vacuum permeability ($4\pi\times10^{-7}$ H). g is the air gap length, k_{U} and k_{pe} are the magnetic reluctance and the pole-cap constants. F_{s1} is the fundamental stator MMF. k_{ph} is the harmonic constant which is defined as:

$$k_{ph} = \sum_{h=3,5,7}^{\infty} \frac{k_{tf}(h)^2 k_{sw}(h)^2 V_t + k_{yf}(h)^2 k_{sw}(h)^2 V_y}{k_{tf}(1)^2 k_{sw}(1)^2 V_t + k_{yf}(1)^2 k_{sw}(1)^2 V_y} \tag{3-52}$$

where k_{sw} is the harmonic coefficient of the unit square wave expressed as:

$$k_{sw}(h) = \sin\left(h\frac{P_{arc}\pi}{2}\right) \tag{3-53}$$

To measure the magnetic flux density in XYZ orientations, we had to build up a multiple magnetic induction antennas modeling. The time domain magnetic flux density of the machine is simulated using a 3-D FE model of the machine and three magnetic antennae. From the simulation, the influence of the corresponding magnetic induction harmonics was recorded. The radiated magnetic induction is stored via magnetic coils shown in Fig. 3.4.5 which have been built using a 3-D printer. Two major parameters were considered to locate the antennae in the best location; distance d_1 and angle factor θ of the coil antennae. The magnetic field intensity, based on Maxwell's equation, is analytically calculated as:

$$H = -\frac{\beta I_0 dl \sin(\theta')}{4\pi r}.\sin(\omega t - \beta r)a_\theta \tag{3-54}$$

where β is the beam-width index, I_0 is the applied current at the coil, θ' is the angle between the coil current and the monitoring line. The optimum angle was found to be 45°, 135°, and 178° for phase A, B, and C, respectively. To achieve reliable accuracy, the model was meshed with 5.886 million degrees of freedom. The idea of using multiple magnetic antennae for a highly accurate measurement for condition monitoring was presented in [64], however no experimental verification was evident.

Fig. 3.4.2 presents a flowchart of the methodology used for the proposed computation in this study. This work investigates the rotational iron loss computation in the time domain based on independent orthogonal magnetic flux components. In the conventional frequency-domain iron loss calculation, a pure sinusoidal stator current is used. In this methodology, the magnetic flux density (via a 2-D electromagnetic model) is stored, based on peak values, to predict the defined coefficients for each term through conventional curve fitting approaches. Therefore, the effect of magnetic induction and proportional integral pulse width modulation (PI-PWM) controller harmonics are assumed to be zero.

The magnetic induction and controller harmonics are also considered, along with the harmonic losses which originate due to the resistivity of the steel sheets. A series of simulations with multiple magnetic antennae are modelled using a 3-D electromagnetic simulation.

These simulations are performed for the nonlinear M400-50A steel sheet for both the stator and rotor cores. For a rotating generator at 150 rpm, the time step for the static computation is 0.01 ms. The $dB(\omega t)/dt$ values are locally computed in the steel sheets via the recorded variation of the material induction in a time range. The *B*-loci graphs are developed for each iron part where $dB(\omega t)/dt$ is recorded by a computationally time consuming 3-D FEA. Then, all the iron loss terms are calculated, where resistance and skin effect considerations are taken into account for the eddy-current loss calculation in the steel sheets. Thus, the effect of eddy-currents on the inducing magnetic field is considered. In addition, the accuracy of the calculation is compared to the conventional frequency-domain iron loss calculation.

For the iron loss evaluation, curve fitting is employed for the coefficient calculation. The rotational iron loss is considered for both of the electrical machine's flux density vector spatial components. These are based on the independent major and minor axis components, Fig. 3.4.3.

Fig. 4.3.4 illustrates the 3-D time domain H-field simulation using a magnetic induction coil to capture the magnetic field intensity around the PMSM.

Fig. 3.4.4 shows the iron losses based on the induction variation of the variable coefficient model and the measured data for a no-load condition. A good fit is shown between the calculated and measured results for the M-400 fully-processed non-oriented silicon steel, where a higher frequency causes a larger iron losses.

Table 3.4.1 shows the constants of the equations which are presented in the previous section. Table 3.4.2 presents the variation of each iron loss term where the unidirectional and rotational field is simulated due to the changing direction of the magnetic flux density vector for each iron segment. For each individual volume, the dominant flux direction is determined for each time point. The Table presents a full load test at the rated speed of 150 rpm, where the purely alternating flux density method as well as the PI-PWM current method, which accounts the orthogonal components for the nominal current, are considered. The results show a rotational iron loss variation of 5.8% between a PI-PWM and pure sinusoidal current exists without considering the steel sheet resistance. Whereas, with the resistance consideration the difference is about 15.52%. The variation of eddy-current loss is the highest by approximately 4.62%. More significant are the variation of the total iron losses between the sinusoidal and PI-PWM current for the resistance consideration when compared with the non-resistance-based computation.

The 3-D model of PMSM along with the multiple magnetic antennae is modelled in ANSYS Emag. Although the most useful type of boundary known as periodic in the electrical machines, in which the advantage of repeating flux patterns is considerable when the magnetic vector potentials are computed. To calculate the induced magnetic flux density on all parts of the machine, this type of boundary condition is the most suitable one. However, it fails to consider the bulk conductivity including permittivity, surface, and interphase conductivities in practice. In this work, we proposed a new technique which is based on a multiple magnetic antenna to capture time domain magnetic flux density considering bulk conductivity. To do this, we have defined a far-field boundary condition in ANSYS Emag package. By this boundary setting, any unbounded field problem can be solved. To apply this setting, the node location and number are important to be determined for each element in order to provide accurate results, besides, the degree of freedom for magnetic vector potentials has been defined (1) = 0. The coefficient matrix of this boundary element is unsymmetrical. The advantage of using far-field boundary is to allow magnetic antennae to store magnetic flux generated by the PMSM.

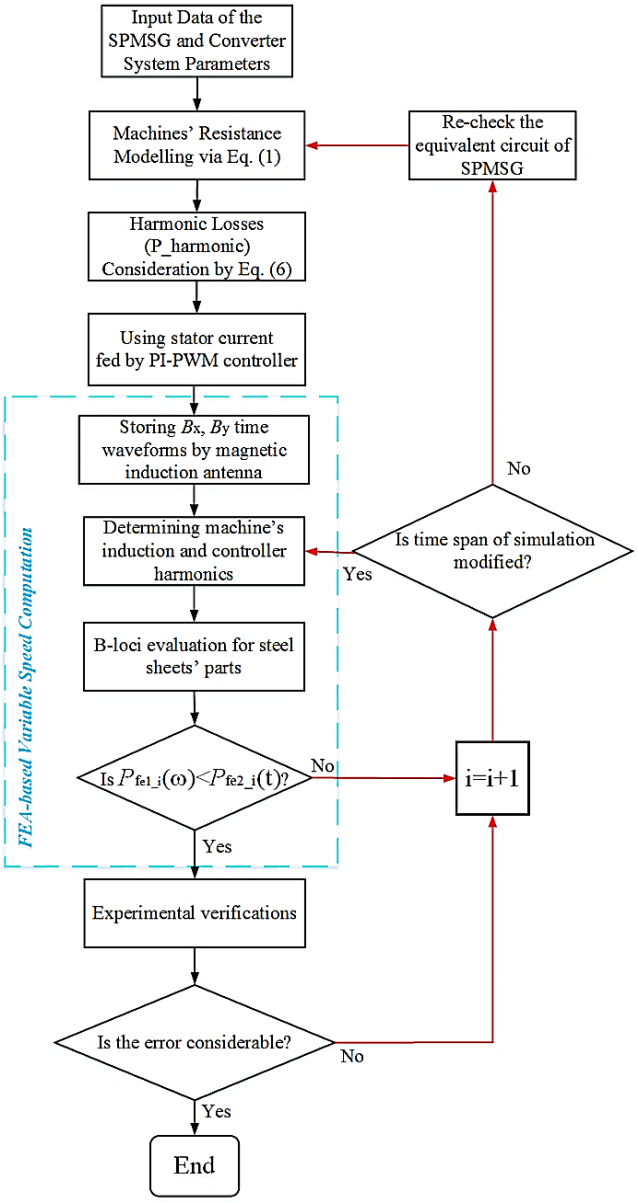

Fig. 3.4.2 The proposed methodology flowchart.

To enhance the accuracy of the rotational iron loss computation, we have considered the rotational magnetic flux density and its harmonics. The magnetic flux density vectors distribution varies due to the complex geometry, discontinuous configuration of the stator winding, and the non-sinusoidal current because of harmonics in the PMSMs. Although, the resulted magnetic flux density loci provides complex shapes, and thus, very difficult depending on the anisotropic characteristics of the material used. In this work, a non-oriented FeSi sheet with electrical conductivity $\sigma = 2.04.10^6$ S/m, and density of $\delta = 7650$ kg.m^{-3}, and average grain size of 92 μm were defined.

Table 3.4.2 presents the variation of each iron loss term where the unidirectional and rotational field is simulated due to the changing direction of the magnetic flux density vector for each iron segment at maximum speed of 400Hz. For each individual volume, the dominant flux direction is determined for each time point. The Table presents a full load test at the rated speed, where the purely alternating flux density method as well as the PI-PWM current method, which accounts the orthogonal components for the nominal current, are considered. The results show a rotational iron loss variation of 16.6% between a PI-PWM and pure sinusoidal current exists without considering the steel sheet resistance. Whereas, with the resistance consideration the difference is about 16.96%. The variation of eddy-current loss is the highest by approximately 14.62% with resistance consideration. More significant are the variation of the total iron losses between the sinusoidal and PI-PWM current for the resistance consideration when compared with the non-resistance-based computation.

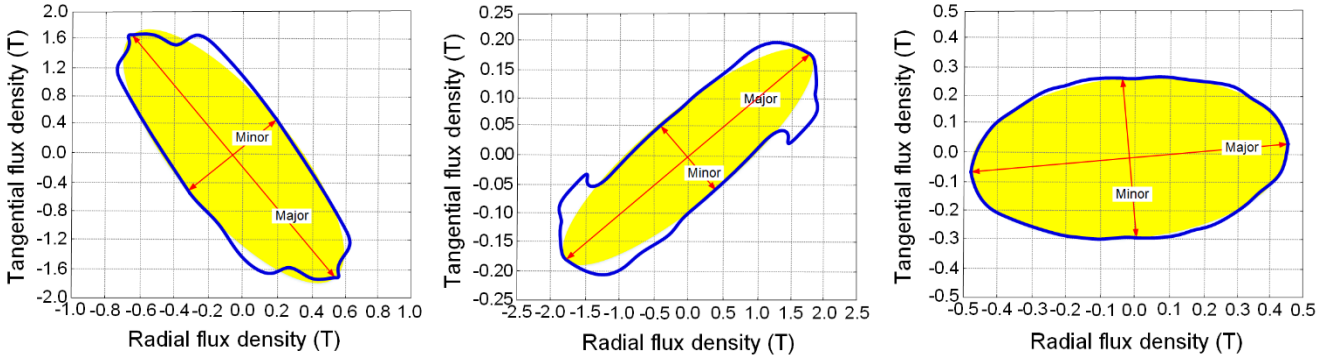

Fig. 3.4.3 Magnetic induction vector locus, where recorded point is set at a) the crossing point of the mean diameter of the yoke and the symmetry axis of the tooth, b) the center of a tooth, and c) rotor core.

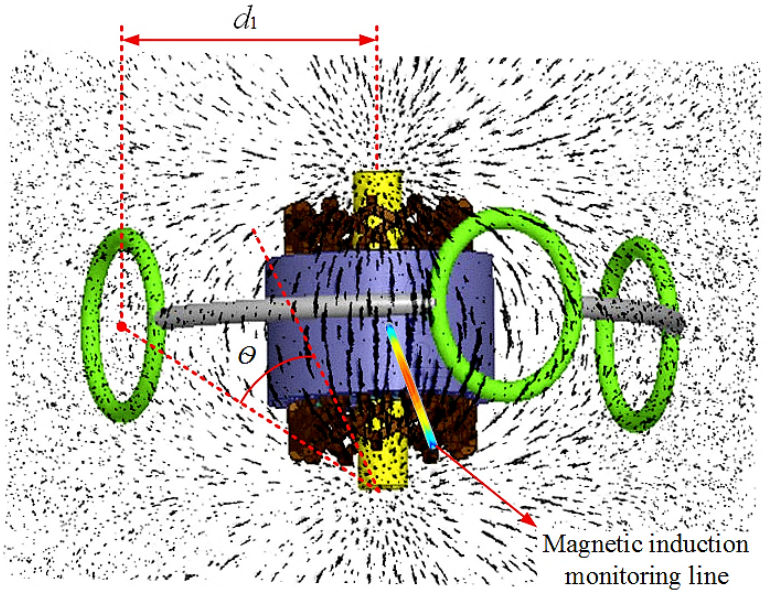

Fig. 3.4.4 3-D FE model of the SPMSG at *H*-field simulation equipped with a group of magnetic coil antennae.

Table 3.4.1 Constant values based on frequency domain iron losses computation.

Constants	***Definition***	***Values***	***Units***
k_e	Eddy-current constant	2.03	W/m^3
k_U	The magnetic reluctance constant	0.02193	
k_{pe}	The pole-cap constant	1.845×10^{-4}	
k_{tf}	The yoke filter constant	25.12×10^{-7}	
k_{yf}	The teeth filter constant	1.2654	
G	The dimensionless constant	0.1277	
d	The lamination thickness	0.5	mm
V_y	The volume of the stator yoke	3.79E-03	m^3
V_t	The volume of the stator teeth	3.34E-03	m^3

Table 3.4.2 Iron losses computation results with and without resistance consideration for sinusoidal and PI-PWM currents.

Iron losses type	***Sinusoidal current***	***PI-PWM current***
Iron losses computation without resistance consideration		
Hysteresis [kW]	0.357	0.478
Eddy-current [kW]	0.995	1.089
Excess [kW]	0.114	0.191
Total [kW]	1.466	1.758
Iron losses computation with resistance consideration		
Hysteresis [kW]	0.556	0.666
Eddy-current [kW]	1.232	1.443
Excess [kW]	0.210	0.297
Total [kW]	1.998	2.406

So far, the iron loss measurement testers are mostly based on an external equipment which measures the *B* and *H* from a certain distance from the prototype which considers the bulk conductivity of the iron materials. However, the engineers often do not model their measurement taster because the design complexity in FE environment, and thus, they store B and H values from different points. One, from the surface of the parts in the machine. Second, collected data from another location depending on where the measurement is located. When, two results (3-D FEA and experimental) are compared using (2), the possibility of having two different levels of error exist. In this work, the machine along with its measurement taster is modelled and the values are also collected from the same location to reduce this error.

Fig. 3.4.5 illustrates the computation of total iron losses with a wide torque constant (operation point) up to approximately 400Hz under four different analysis assumptions: 1) The stator current is fed by a pure sinusoidal. current, therefore with respect to a real system the harmonics which often originate from the controller (in this study, a PI-PWM) are neglected. The frequency domain iron loss computation is simulated with a maximum of 2.46 kW during the field weakening region (Fig. 3.4.5-a), where the steel sheet resistance is also neglected. The efficiency corresponding to each frequency also is represented by the dashed lines. 2) Using a similar stator current condition to Fig. 3.4.5-a while considering the resistance of the steel sheets for the harmonic loss calculation is shown in Fig. 3.4.5-b. The efficiency trend in the field weakening range decreases, while it increases in the constant torque operation range (up to 400 Hz). Additionally, larger iron losses are noted at various operation points in field weakening region with a maximum loss of 2.89 kW. 3) Fig. 3.4.5-c shows an iron loss computation where the flux density time waveform includes the influence of harmonics due to the PI-PWM controller. The resistance behavior of the steel sheets was considered to be zero. This graph is comparable to Fig. 3.4.5-a, where the influence of generated harmonics by the controller is ignored. The total iron losses have increased in both the operation and field weakening ranges (up to 2.67 kW). In addition, the calculated efficiency trend while ignoring the core's resistance is larger, particularly during the field weakening operation. 4) Employing a PI-PWM controller including its generated harmonics on the machine. The flux density time waveforms are considered along with the resistance of the steel sheet used. This time domain iron loss computation, shown in Fig. 3.4.5-d, is the most accurate because of both significant contributions to the losses which have not essentially been considered in previous research. The time domain rotational iron losses computation, under effect of current harmonics produced from the PI-PWM controller and the steel sheets' resistance is the major contribution of this study. The nominal output power is 5 kW at 200 Hz (carrier frequency), and the nominal current is 20 A.

Referring to the work presented in [65], which has been recently cited in other research, the rotational power, in which basically the variation of the flux direction in the laminations plane can be accounted for 50% of the loss in a rotating machine stator core with consideration of the steel resistance. However, in this research, a smaller variation of 15.52% (during full-load condition) was found with the resistance consideration [65]. Thus, a significant difference of approximately 44.2% remains as a share of the rotational iron losses between the existing work and [65]. Moreover, a variation of approximately 6% of the rotational iron losses was reported in another work [63] without controller and resistance considerations for an induction machine which is again larger than this researches' outcome of 5.8%.

Table 3.4.3 presents a comparison among three different rotational iron loss prediction methods and experimental data under constant torque range condition, in which method 1 shows iron losses prediction supplied with a pure sinusoidal current without resistance and bulk conductivity consideration. In addition, this method only considers the altering magnetic field. method 2 offers the iron loss prediction supplied with PWM controller, which considers iron resistance and harmonic loss. However, the rotational magnetic field was ignored (only altering *B* was considered). method 3 proposes a time-domain rotational iron loss supplied by PWM, considering both resistance and bulk conductivity of the iron parts. method 4 refers to experimental measurement data. Finally, the error percentage of each method in comparison to the test measurement data using the following expression for each part and methodology is discussed in the table:

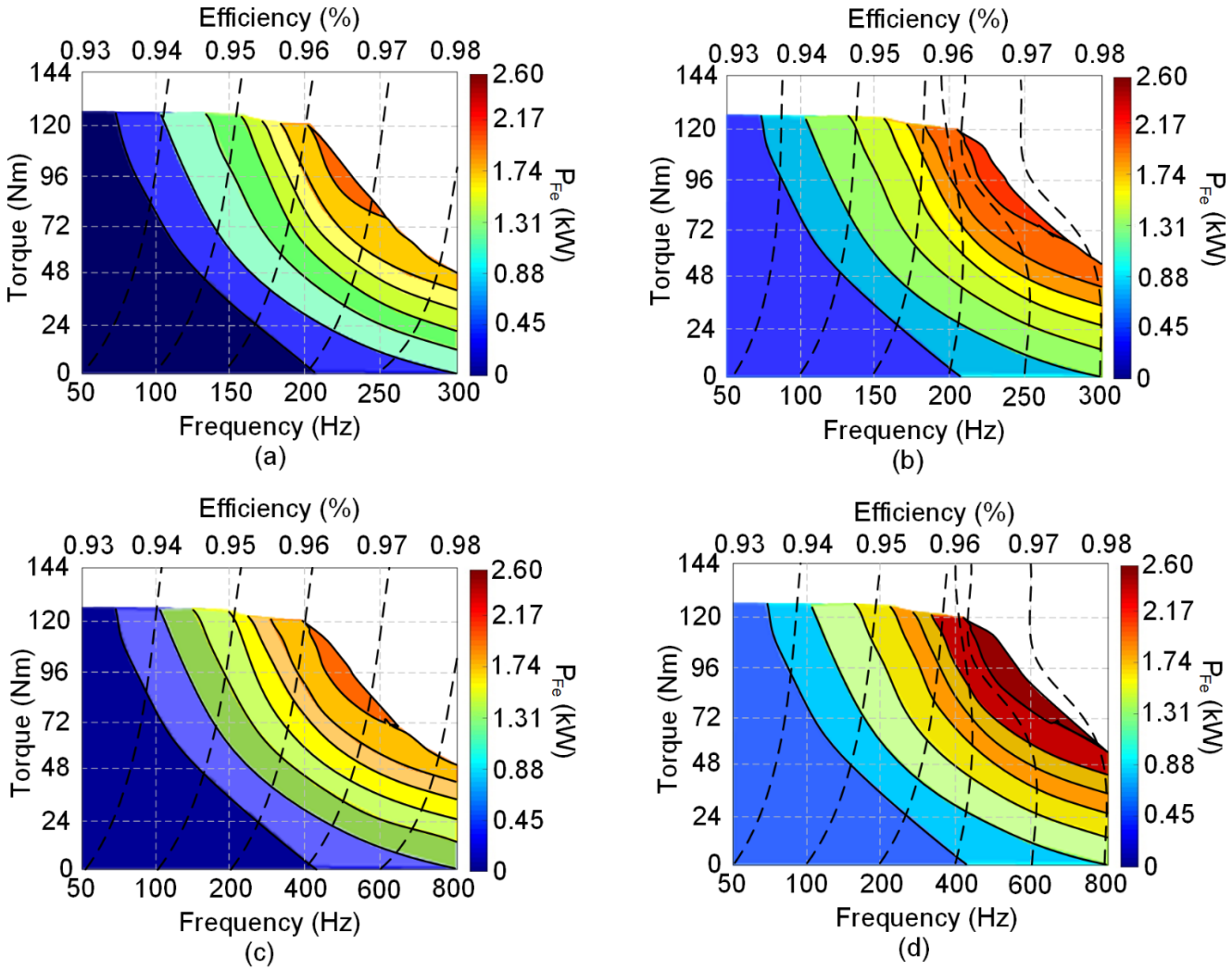

Fig. 3.4.5 Total iron losses evaluation based on FE simulation, in which torque-frequency (speed)-loss results including an efficiency trend for each frequency is shown with flowing conditions: a) using a pure sinusoidal stator current; without resistance consideration, b) using a pure sinusoidal stator current; with resistance consideration, c) using PI-PWM stator current without resistance consideration, d) using PI-PWM stator current with resistance consideration.

$$Error = \frac{P_{\exp} - P_{FEA}}{P_{\exp}} \times 100 \tag{3-55}$$

the error calculated is an average value of each presented method, it is shown that the method 1 as the fastest method of prediction results in a significant error of 17.03% in comparison with the measured data (method 4). To minimize the error, method 2 was studied, in which a good achievement of 11.31% prediction improvement was reported. The proposed method of iron loss prediction dealt with both altering and rotational magnetic field with consideration of bulk conductivity of the iron parts. To avoid idealistic results, the PMSM was supplied by PWM controller which contains harmonics current. As a result, the proposed method 3 decreased the error level to 1.7% as the best possible achievement.

Table 3.4.3 Comparison of different iron loss prediction methods with 550 V supply voltage under constant torque range.

Methods	**Method 1**	**Method 2**	**Method 3**	**Method 4**
P_{sh} [W]	640.32	674.29	699.23	728.33
P_{se} [W]	290.55	301.65	319.82	323.95
P_{rh} [W]	79.52	85.77	91.02	89.96
P_{re} [W]	219.81	269.05	279.06	280.12
Error [%]	17.03	5.72	1.7	-

To reduce the error between 3-D FEA and measurement, the *B* and *H* from both FEA and test bench were collected from the same location The proposed methodology is also experimentally verified, where the test results were found to be very similar to

the 3-D FE model with a very small error of 1% with 350 V supplied voltage and 1.7% with 550 V supplied voltage over a range of speed operation. The main advantage of this method is very high accuracy of the iron loss prediction. However, the complexity and time, along with cost could be highlighted as drawbacks of the methodology. Also, a fast prediction of iron loss cannot be achieved using the proposed methodology. The authors proposed the methodology for whom the prediction accuracy is very critical depending to the application.

4. Thermal and Mechanical Design Aspects of PMSG

In this Chapter, several key design considerations respect to thermal and mechanical design are studied. To ensure that temperature distribution due to magnetic forces and harmonics at variable speed analysis will be under the thermal characteristics of the material used unless the losses of the machine can be critically increased. Similarly, the mechanical design restrictions must be taken into account to avoid unacceptable deformation, stress, fatigue, static deflection, etc. Therefore, this chapter is discussed in two parts. First, the thermal modeling of PMSG will be studied, afterward, the mechanical considerations are provided.

4.1 Introduction of Thermal Modelling in Electrical Machines

As all electrical machines (particularly if permanent magnets are used) depicts temperature gradient, therefore, heat transfer appears. When this heat travels through various thermo-physics phenomena as followings:

- Conduction
- Convection
- Radiation (which is neglected in this study due to very small value)

1. Conduction

From the second principle of thermo-dynamics, we know that heat always flows from higher temperature to lower, where this whole travel happens because of conduction. Based on Fourier's law, the heat flow can be expressed as:

$$q_k = -k_k \times S \times \frac{dT}{dx} \tag{4-1}$$

S is the heat transfer area, k_k is the thermal conductivity of the material used (i.e. M400-50A, and Nd-Fe-B), x denotes the distance that the heat has been conducted, and T is the local temperature which is a function of x, in other words, the average temperature in distance x. As the heat flows in a solid material, thus, a heat resistance can be given as:

$$R_k = \frac{x}{S \times k_k} \tag{4-2}$$

As the heat transfer is often modeled using an equivalent circuit in electrical machines. Therefore, each part of the machine has the equivalent conduction resistance. However, not all the resistances are showing the conduction, but also a few of them belong to convection which is discussed below.

2. Convection

When there is a temperature gradient between the surface of a solid material and surrounding medium applied on the fluid, the heat can be transferred via either forced or natural, where the natural convention is originated by an external force. Based on Newton's law, the heat flow due to only convection can be defined as follow:

$$q_c = h_c \times S \times \Delta T \tag{4-3}$$

where h_c and ΔT are the convective heat transfer constant and the difference between surface and fluid temperature. The thermal equivalent resistance due to convective heat transfer can be defined as:

$$R_c = \frac{1}{S \times h_c} \tag{4-4}$$

The PMSMs are subject to a high thermal stress during their operation, if these stresses are observed, then that is possible to adapt the machine's control parameters such as current depending on the load and the supplying technique, in order to avoid overheating and a significant heat transfer problem. The conventional model observes with a considerable temperature-rise and related critical heat transfer at the stator core due to segmentation, in which closed-slot configuration is addressed for

electromagnetic improvement. In fact, there are many types of cooling systems [1] to overcome this challenge. Although, they can be costly for a number of applications. We studied an innovative airflow coolant for an application-oriented case, in which the cooling system is exempt from employing any external resources to remove the heat in the stator core.

The outer-rotor surface mounted PM synchronous machines (PMSMs), where two-layer fractional slot-concentrated stator winding is employed. The outer-rotor machines can reach a high torque at low speed, in which for the direct-drive small power generation applications with a low-speed operation as [1].

R. Wrobel, *et al*. [2] studied a thermal analysis of a segmented stator winding design. While the thermal performance played one of the major factors limiting a machine's output capability, a thermal test on a complete prototype machine is an essential part of the design process. The method was allowed for a rapid and inexpensive assessment of the thermal performance of the complete machine and early identification of design modifications needed. The research has been applied to the design of a highly efficient and compact permanent-magnet traction motor. A thermal model for a single-tooth was developed and supported by tests to identify key heat transfer coefficients.

Reference [3], discussed the problem of temperature-rise that influencing the operation performance and also the lifetime of the PMSM. Based on double Fourier series decomposition, the research established a 3-D analytical model of PM eddy-current loss in the PMSM that considers the effect of time and space harmonics. By applying the thermal network model, the influence of different speed and load on temperature-rise has been analyzed, and a steady-state thermal analysis of the motor has been performed using finite element analysis. The paper caters the theoretical basis for the design of the ventilation and cooling system of the PMSM.

M. Polikarpova, *et al*. [4] presented a direct liquid cooling system design for an 8 MW outer-rotor direct-drive permanent magnet synchronous motor (PMSG). The approach was novel for wind turbine generators, so its impact on the thermal behavior and reliability for the total electrical machine has been evaluated and reported. In addition, the article focused on dramatic cost savings that can be realized with the development of a more effective stator windings cooling systems.

In reference [6], the authors discussed a thermal analysis and cooling system design of a dual mechanical port (DMP) using inner wound rotor is surrounded by the stator and the permanent magnet (PM) outer-rotor prototype machine are investigated. To predict the heat sources in actual operation, a transient co-simulation method has been presented. Thermal parameters and the flow distribution at the cooling ducts are calculated in detail. Finite-element analysis of the thermal field is carried out to obtain the temperature distribution and two typical thermal contacts are considered. A robust fully forced-air cooling system with inner rotor teeth ducts is proposed for the DMP machine and a 10-kW DMP machine is prototyped.

Marco Tosetti *et al*. described a complete conjugate heat transfer analysis of a scaled-sized prototype of an integrated air-cooled surface-mounted permanent-magnet generator for the "more-electric engine" application. Additionally, to predict and prevent the critical working conditions of the prototype, the adopted cooling system has been investigated using a complete fluid–thermal analysis. Due to the capabilities of the computational fluid dynamic software, it has been possible to analyze the temperature and flow fields inside the machine, giving an idea about the distribution of the thermal quantities both inside the solid materials and above the surfaces [21].

The finite-element analysis (FEA), CFD, and lumped-parameter-based methodologies are employed for the entire study [7–12], [14-20], [24-28].

4.2 A Novel Natural Air-cooling System for Temperature-rise Suppression on PMSG

In this section, a speed-functional model with radial and circumferential airflow ducts under 3-D thermal transient analysis of three FE models with two innovative structures are studied using an in-core circular natural air-cooling system, regardless of any external sources (liquid and/ or air) at the stator yoke of an outer-rotor surface-mounted PM synchronous generator with closed-slot topology. Additionally, the proposed model is verified through its heat transfer calculation at each heat flux sensors, and along with the experimental investigation discussed in Chapter 6. The CFD analysis is evaluated the heat transfer at a number of specific positions of heat flux sensors on the rotor and stator cores. Heat transfer coefficients are measured at 9 key positions in the stator and rotor cores, and accordingly, a good performance of thermal analysis is also predicted. The natural airflow is assumed to vary over the range from 0 to 0.6 (m^3/s), and temperature between 18 to 35 ºC. Moreover, the rotor speed limited to 500 rpm due to malfunctioning in higher speeds of the data-loggers recording data from sensors on the machine. At last, the temperature-rise is suppressed by 11 ºC without fail in the efficiency. Whereas, the electromagnetic performance of the FE models is also examined numerically and experimentally.

During the operation time, a high temperature-rise is experimentally measured in the stator core of the conventional FE model due to a high mechanical and thermal stresses. Under test bench, the temperature-rise of 83.8 ºC, in which the direction of heat transfer is from the inner surface of the stator (with a higher temperature) to outer surface of the rotor (with lower temperature), that is governed by the second law of thermodynamics. The natural air-cooling system based on the robustness of the FE results depends on the fitness of the generated mesh at the pre-calculation stage. Thermal FE modeling should be taken into account free of any following errors at this stage (1) improper geometric description (if an axial symmetry and/ or rotational symmetry has

been accounted without considering that an anti-symmetric load), (2) a poor definition of the used materials, for instance the limit of Poisson's ratio at isotropic materials, (3) improper definition of the load that is not recommended to simplify a complex load states or a number of loads with one load, (4) a wrong boundary expresses, (5) choosing a wrong kind of analysis (depends on the case), (6) singularity concept existing in the model which leads the points in the model where values tend toward an infinite value; FE model, where the infinite density and gravity are equivalent to an infinite stress in a sharp corner [22]. Therefore, a good mesh can be successfully generated for all three FE models.

The design solution alternatively resolves the problem using an innovative airflow path, in which the radial ducts are perpendicular to the shaft and pushes the air into the ducts due to rotation of the shaft and its path to out of housing, where we expect the natural airflow to vary over the range from 0 to 0.6 (m^3/s). Fig. 4.2.1 illustrates the main air-flow path, in which the innovative models consist of circumferentially (circular at the stator yoke) and axially (from the circular path to the inner face of the ducts). Next, the heated air-flow goes out through the gap between the stator core and the shaft. Moreover, the position of heat flux sensors is shown, in which positions 1, and 3 are on a pole-pair. Position 2, in the center of the rotor yoke. Positions 4, and 5 on the stator centerlines of the coil front/ and bottom faces. Positions 6, 7, 8, and 9 at the different points of the stator core.

Fig. 4.2.2 shows that ducts are introduced to separate the machine axial segments for enhancing the thermal dissipation capability with relevant (r = 3.8mm) dimensions. Table. 2 represents the used materials for different parts of the models with their thermal specifications such as thermal conductivity and specific heat which greatly affect the accuracy of the thermal analysis. The problem of the conventional model is determined after a careful steady-state thermal analysis using lumped-circuit (LC) and FE methods that Fig.3 carries the results under a condition of 35 °C ambient temperature and 150 rpm rated speed of the shaft. The LC method which modeled similarly to an electrical circuit solves the steady-state temperatures at each node via solving a set of non-linear equations [23].

$$\Delta T = P \times R \tag{4-5}$$

where ΔT indicates the temperature-rise that corresponds to the voltage of the electrical circuit, P stands for a power source that corresponds to the current of the electrical circuit, as well as R shows thermal resistance that corresponds to electrical resistances of the electrical circuit. The FEA based on a 3-D model solves partial differential equations (PDEs) using ANSYS multi-physics engineering, where the heat transfer at the body of the model is controlled using below heat equation [24].

$$Q = \rho C\left(\frac{\partial T}{\partial t}\right) - \nabla.(k \nabla T) \tag{4-6}$$

where Q is the heat source, ρ is the density, C is the heat capacitance, and k shows the thermal conductivity. Additionally, extra transverse heat flux terms of the convection and with regarding Fig. 4.2.2, the stator core of the conventional model is the major challenge to cool up. However, the cost of this design process is highlighted, thus, the innovative FE models are accounted to adjust the temperature-rise of stator core cooling system.

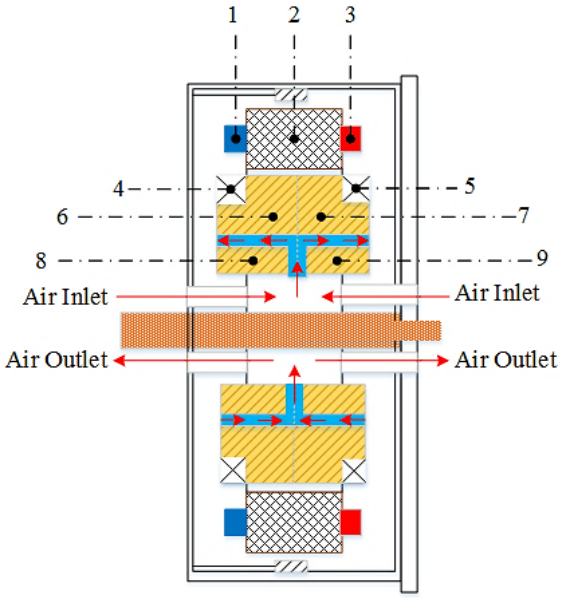

Fig. 4.2.1 The main heat transfer paths and position of heat flux sensors on the rotor and stator cores.

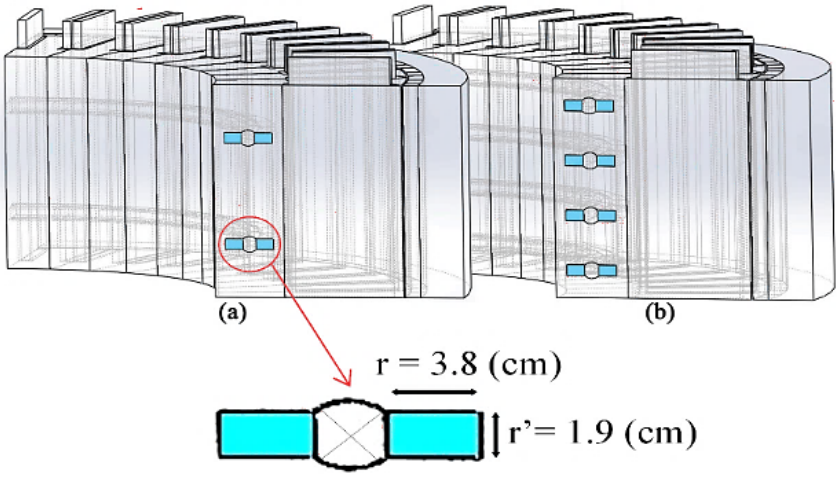

Fig. 4.2.2 3-D sketch of the innovative coolant models with, a) 2-ducts, and b) 4-ducts.

4.2.1 Steady-State Lumped Circuit Model

When a steady-state condition is taken into account, the energy storage term in the conservation of energy equation vanishes and the resulting balance between the heat transfer out of the system and the heat generated in the system forms the basis of the thermal model. However, the flow in a cooling channel (if available) around the stator is nearly uniform, the air-flow cooling the rotor is complex. The finite element computational fluid dynamics package of ANSYS was used to create the model. A 60° arc segment has been modeled which consists of one pole-pair (360 electrical degrees) of the machine. Because of the high number of nodes and current sources, the analytical resolution is more complicated that is why a Multiphysics FE-based software is recommended. Although, a matrix is presented to solve the problem. It is used here with some simplifications in combination with our specially developed slot and rotor local models. In a steady-state thermal analysis, n equations are necessary to define a thermal network with $n + 1$ nodes. The extremity of the shaft and the coolant for the stator are supposed to be at a constant temperature and are taken as reference equal to 40°C. Table 4.2.1 presents the thermal characteristics of the material used for this calculation [29].

This coolant technique can be complex and time-consuming but considering the thermal behavior of the PMSMs is very significant. Therefore, the increase of temperature may deteriorate the mechanical and electrical strength of the coil insulations and the stator core, raises the stator coil resistance, and strongly decreases the lifetime of involved parts (stator core including windings) which tends to a terrible traffic accident. In order to determine the temperate distribution at the electrical machines, following states are considered, (1) accurate calculation of the losses, (2) properties of the cooling fluid and thermal characteristic of the magnetic (in this case, the properties of ambient temperature is measured at the sea level due to location of the generator), (3) proper definition of conductive and insulating parts (in this study, class A insulation per IEEE 177 and 101 standards is selected), (4) accurate analysis of heat conduction and Internal heat generation since the core-loss distribution is completely different in various positions of the stator core [29].

A thermal modeling of the conventional, 2-ducts, and 4-ducts FE models using lumped-circuit can be addressed in Fig. 4.2.1.1. A steady-state temperature distribution and improvement trend throughout the models are shown, where convection, power sources, delta temperatures (trapezius blocks), and thermal resistance blocks are presented. It should be noted that the blocks with temperature and power tags are for steady-state temperature (or power) of conventional, 2-ducts, and 4-ducts models, respectively. For example, in thermal resistance block of the stator core that named by "Tooth/2 +Yoke", 81 °C / 8 W is reported for initial model, and 73.8°C/ 3.9 W stands for 4-ducts model [29].

Fig. 4.2.1.2 presents how the temperature distribution using steady-state analysis in the machine's parts using the lumped-circuit and FEA. The aim of natural air cooling is removing the heat in the stator core through the innovative models, in which the electromagnetic performance of the generator is included as a constraint of the technique's improvement. Fig. 4.2.1.2 presents the temperature-rise performance of the innovative models. This figure illustrates the results enclosed by less than 3% from 2-D FEA in compare to 3-D FEA, also a very good prediction among the models can be seen in where the temperature difference between the conventional model and 4-ducts model is approximately for 11.0 °C.

Table 4.2.1.1 Materials and thermal specification.

Name	Materials	Thermal Conductivity (W/m/°C)	Specific Heat (kJ/kg/°C)
Stator core	M4000-50A	38	0.45
Rotor core	M400-50A	38	0.45
Magnets	Nd-Fe-B	10	0.45
Winding	Copper	401	0.38
insulation	Kapton	0.2	1.7
Coil dividers	Nomex	0.14	1.3

4.2.2 Transient Thermal Computation Using FEA

3-D transient thermal FEA should be used to analyze the temperature distribution for the most accurate simulation. The heat transferred by radiation is ignored. The partial differential equation of the heat conduction and convection is expressed [8] as:

$$\rho.c(\frac{\partial T}{\partial t}+\{V\}^T.\{L\}T)=\{L\}^T.(|D|.\{L\}.T)+Q \tag{4-7}$$

where ρ is the mass density, c is the specific heat, T in K shows mass transport of heat; $\{L\}$ is the vector operator, |D| is the temperature, t stands for time, $\{V\}$ is the velocity vector for conductivity matrix, and Q is the heat source rate per unit volume. It should be mentioned that for steady-state thermal analysis, the first term on the left-hand side of Eq. 4-7 should be zero.

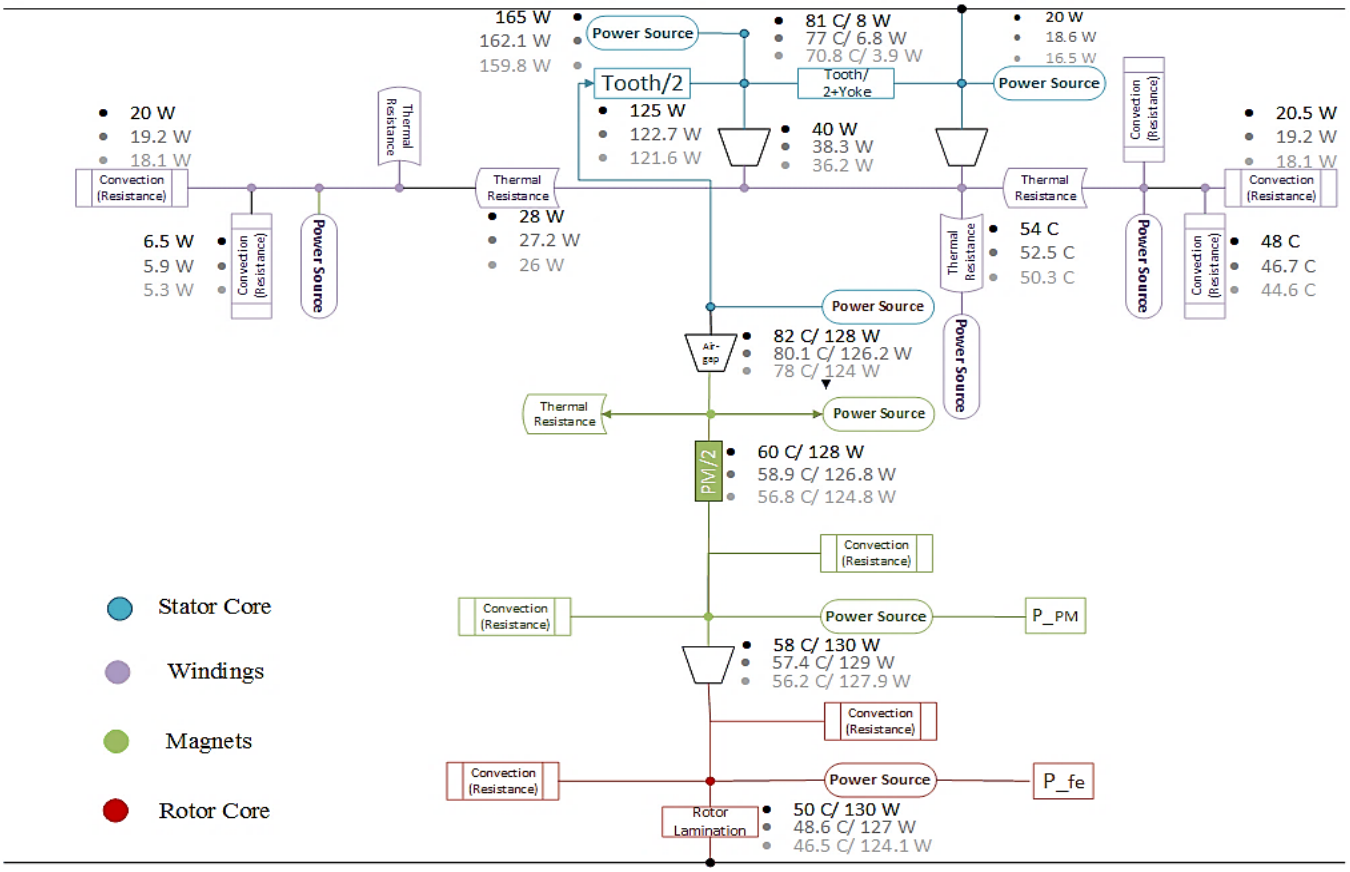

Fig. 4.2.1.1 Lumped-circuit modeling of the FE models ducts, 2-ducts, and 4-ducts models, respectively. For example, in thermal resistance block of stator core that named by "Tooth/2 +Yoke", 81 (ºC)/ 8 (W) is reported for initial model, and 73.8 (ºC)/ 3.9 (W) stands for 4-ducts model.

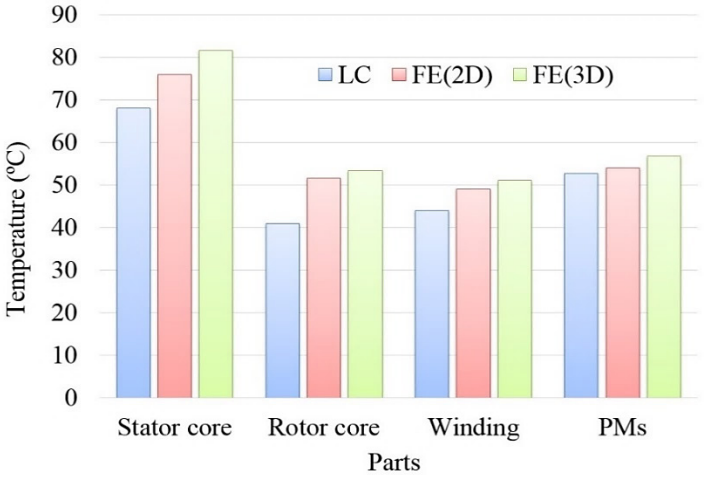

Fig. 4.2.1.2 Comparison of steady-state temperature distribution in the machine's parts of the initial model using LC and FE methods.

At this stage, the iron losses as the function of temperature is calculated using Bertotti's iron loss separation models [29-31], in which skin effect has been accounted through the following equation. The calculation results have been reported in Table 4.2.2.1.

$$P_{fe} = k_h(f,B) f B^{h(B)} + k_e \left(\frac{\sinh(d\sqrt{f} - \sin(d\sqrt{f})}{\cosh(d\sqrt{f}) - \cos(d\sqrt{f})} \right) f^{1.5} B^{\beta} \tag{4-8}$$

where $kh\,f$, B, $h(B)$ and keB are polynomials in f and B.

In the CFD modeling, 1.543 million volume cells are used, in which the typical cell edge size is 3 mm, and the axial length of the model is 100 mm. The symmetry and 90º periodic boundary conditions are applied. In addition, the commercial CFD code ANSYS is used for the related analysis [29].

Table 4.2.2.1 Losses calculation results at rated speed of 150rpm.

Losses/ model	Iron losses (W)	Joule losses (W)
FE-Conv.	220	40
Exp. Conv.	219	44
FE-2ducts	198	43
Exp.-2 ducts	201	42
FE-4-ducts	171	44
Exp.-4-ducts	170	43

The mesh generation is successfully generated (Fig. 4.2.2.1) for the conventional, two-ducts, and 4-ducts models with 367691 nodes and 146213 elements, 382517 nodes and 153400 elements, and 389945 nodes and 158988 elements, respectively [29].

This section is classified into two parts, one the results of the transient thermal analysis using 3-D FEA for all introduced FE models, and next, it will be a general comparison and discussion on the other aspects.

In Fig. 4.2.2.2, the temperature distribution of the first-cycle is shown, in which the conventional model varies between 24.941 up to 26.808 °C. Although, the two-ducts FE model with a segmented stator core (model Fig. 4.2.2.2-b) resulted in a better temperature distribution performance that varies between 21.852 up to 23.018 °C. At last, the best-achieved performance is clearly seen through the four-ducts innovative model with the segmented stator core, shown as the model (c) with temperature distribution performance from 21.88 up to 22.308 °C. Additionally, in this cycle, all the models have pointed the same parts by minimum and maximum probes in blue and red labels, respectively [29].

In the second cycle, models (Fig. 4.2.2.2-a-b-c are shown a temperature-rise in comparison with the corresponding models in the first-cycle of analysis. The conventional model (Fig. 4.2.2.2-a) is illustrated temperature distribution variation of 34.7 to 41.15 °C. The two-ducts model (Fig.7-b) resulted in a maximum temperature distribution at the stator yoke. In this model, the temperature varies from 30 to 38.8 °C. The four-ducts model (Fig. 4.2.2.2-c) with a better thermal performance, in which the temperature varies between 23.724 up to 32.246 °C, and the same parts for maximum and minimum temperature labels with other models in this cycle.

In the third-cycle, all models have carried out the maximum temperature label at the stator core due to segmentation. The conventional model (Fig. 4.2.2.2-a) is illustrated the peak temperature in comparison to the two-ducts model (Fig. 4.2.2.2-b) varies

from 47.822 up to 53.474 °C, and the four-ducts model (Fig. 4.2.2.2-c) with a better performance varies between 41.829 to 50.578 °C. At last, the four-ducts model has presented the best cooling performance to remove the heat [29].

In Fig. 4.2.2.3, the influence of the duct-width on the electromagnetic key parameters such as back-EMF and torque is shown in Fig. 4.2.2.3-a. Also, the temperature rise and power can be seen in Fig. 4.2.2.3-b, in which the duct width r =3.8 mm was chosen for the innovative models.

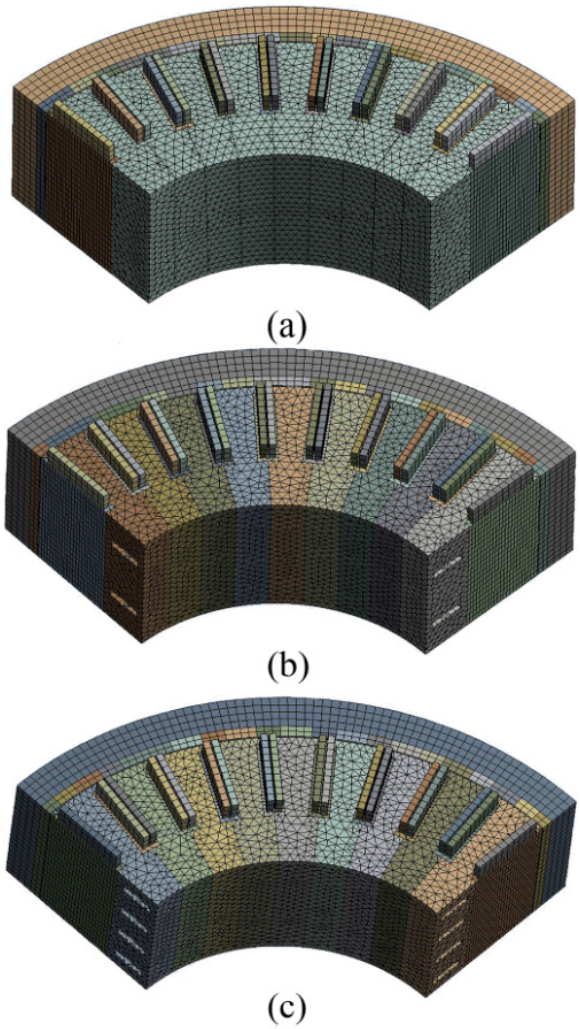

Fig. 4.2.2.1 3-D generated mesh for a) conventional, b) 2-ducts, and c) 4-ducts FE models.

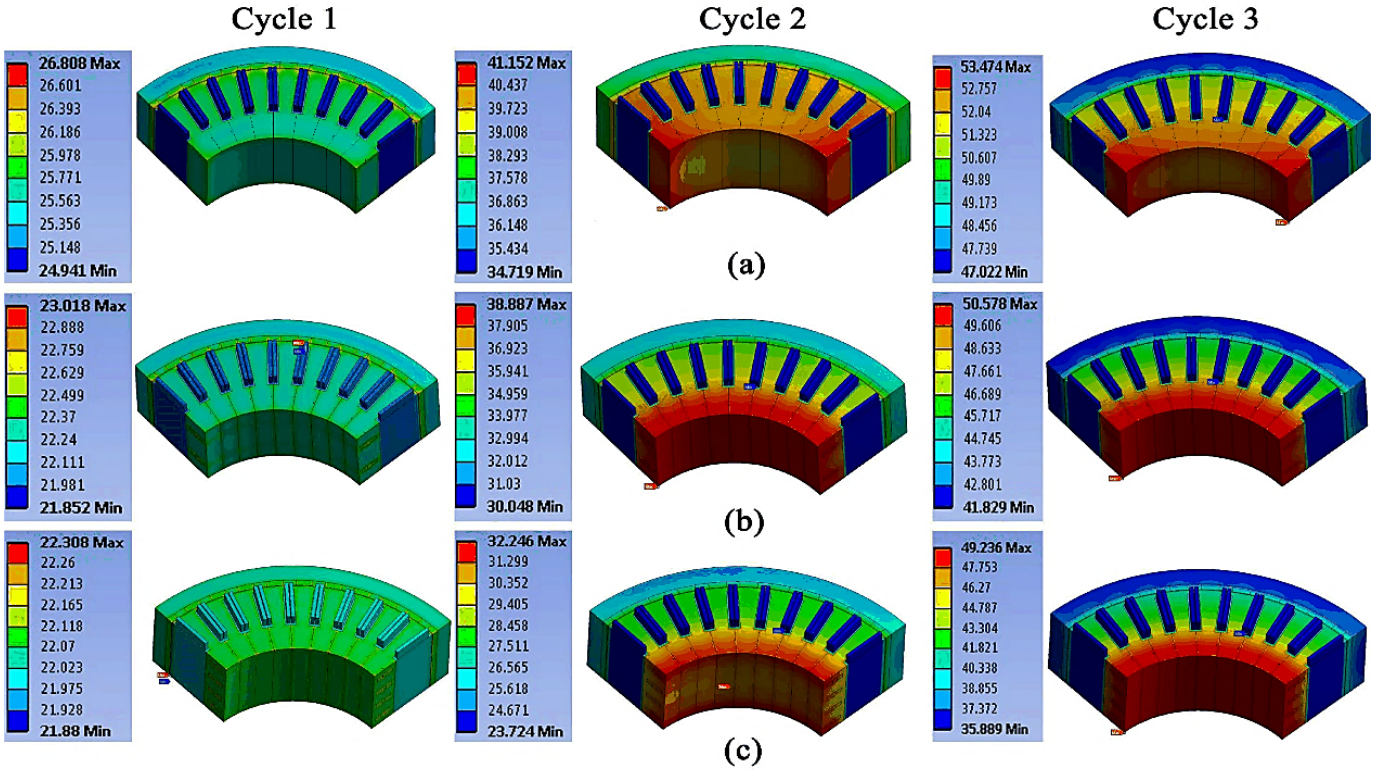

Fig. 4.2.2.2 3-D transient thermal FEA by three cycles, a) conventional model, b) 2-ducts model, and c) 4-ducts model at 1st, 2nd, and 3rd.

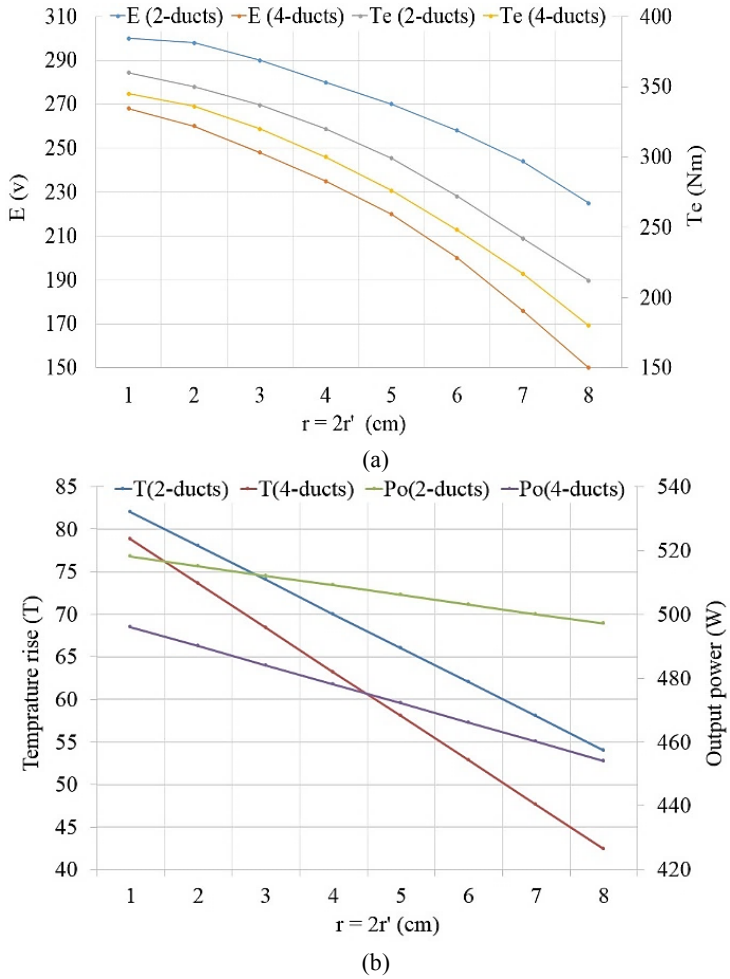

Fig. 4.2.2.3 Influence of duct-width on a) the back-EMF and torque, as well as b) temperature-rise and output power.

4.2.3 Heat Transfer Calculation

The heat transfer is known as one the most critical parameters in the thermal design of the PMSMs, thus, the most sensitive heat transfer coefficients are calculated and also experimentally reported in Fig. 4.2.3 under following conditions:

- The axial inlet velocity of the cooling air was defined between 0.5 to 3 (m/s)
- The rotor tip velocity is varied between 2 to 8 m/s
- The air approach angle is defined between 0 to 30º

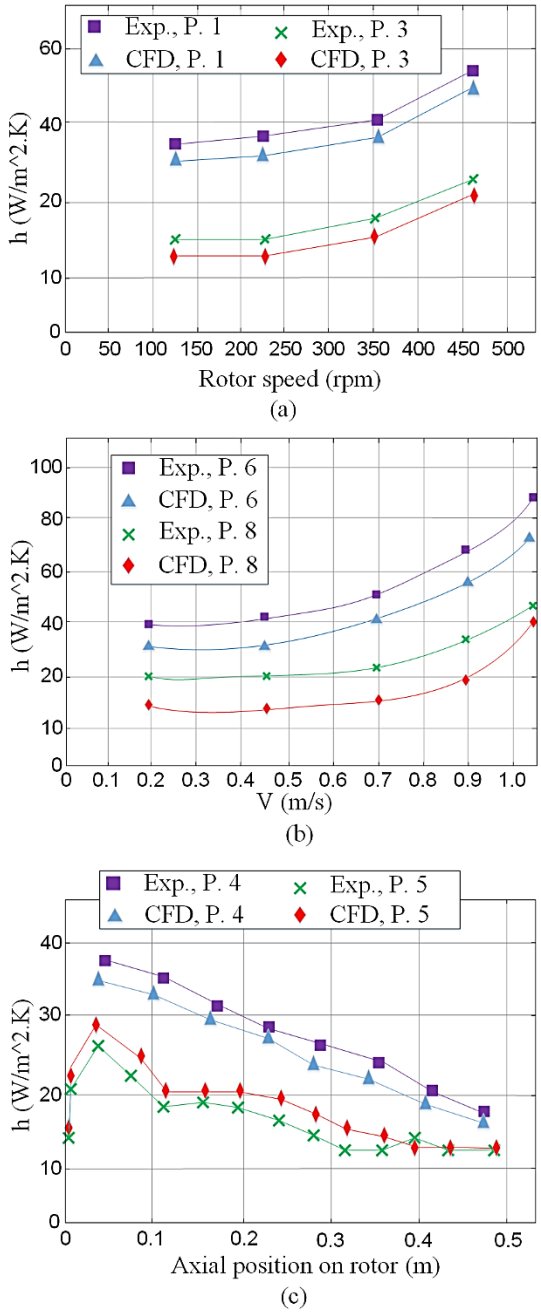

Fig. 4.2.3.1 Heat transfer coefficients verification for the FE models, a) at points 1 and 3 variable airflow rate, b) at points 6 and 8 for variable rotor speed, and c) at points 4 and 5 for variable rotor speed.

It should be mentioned that no significant difference is seen for the change of the air approach angle from 0 to 60º. Fig. 4.2.3.1(a) illustrates the change of heat transfer coefficients at the poles (points 1 and 3) at a variable speed condition. In Fig.

4.2.3.1(b), the heat transfer coefficients are at the stator core (points 6 and 8), in which the low-velocity ratio (axial inlet velocity/ rotor tip velocity) is variable. Fig. 4.2.3.1(c), presents the surface heat transfer coefficients around the bottom face of the field coil at the leading side of the magnet (points 4), and the bottom face of the field coil at trailing side of the pole (point 5) [29-30].

4.3 Mechanical Design Consideration

In this section, we present several mechanical-based design considerations under variable speed analysis. All computations are done on the studied PMSG with 36 slots and 40 poles, between 15-150 rpm (rated speed). However, a wider speed range is tested to find out where resonances will happen in order to be aware of them.

The methodology that we used is 3-D FEA, where we have stored magnetic flux density values as a function of time from ANSYS Maxwell and imported to MANATEE to predict mechanical parameters as following sections.

4.3.1 Radial Acceleration

If an infinite beam is hit in the middle, bending vibration waves will propagate on the left and right sides of the impact point. If the beam has a finite length, these vibration waves will reflect on the edges, creating two additional vibration waves which will interfere with previous waves, creating a particular vibration pattern. This vibration pattern is known as a modal shape or a structural mode, it occurs at a specific frequency called a natural frequency, due to it is the frequency at which the beam will naturally vibrate just after the external perturbation. In fact, a real mechanical system has generally several degrees of freedom (bending, torsion, etc), and thus, it indicates several structural modes. One can demonstrate that these modal shapes represent a mathematical basis when the mechanical structure behave linearly, which means that any deflection shape can be represented as a weighted sum of modal shapes (e.g. 90% of the first bending mode, 10% of the first torsional mode) [32].

The stator structural modes are generally characterized using the analogy with a cylindrical shell, whose structural modes can be labeled (*m, n*) where m is the rank of the circumferential deflection and n is the rank of the longitudinal deflection. There are presented in Fig. 4.3.1 respect to *m* and *n* values.

Fig. 4.3.1.2 presents radial acceleration of PMSG under variable speed analysis, where series resonance areas are displayed for each specific structure mode individually. It is mention that first resonance occurs 158 Hz, 356 rpm which beyond the ratings of the designed generator, and thus, the machine will not meet any resonance problems.

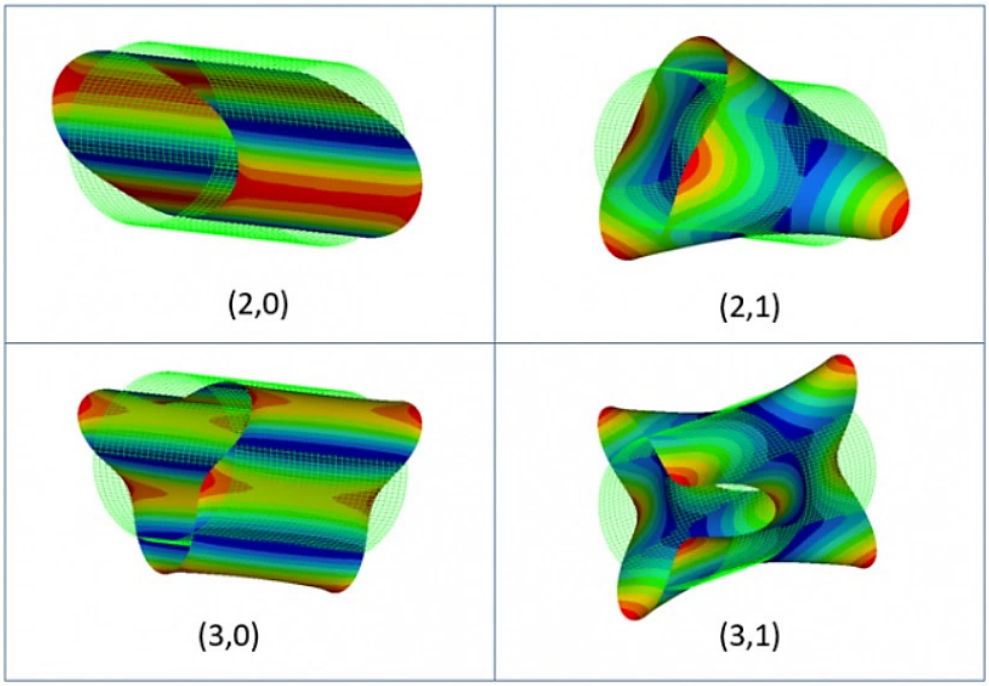

Fig. 4.3.1.1 Examples of structural modes of a cylindrical shell [1].

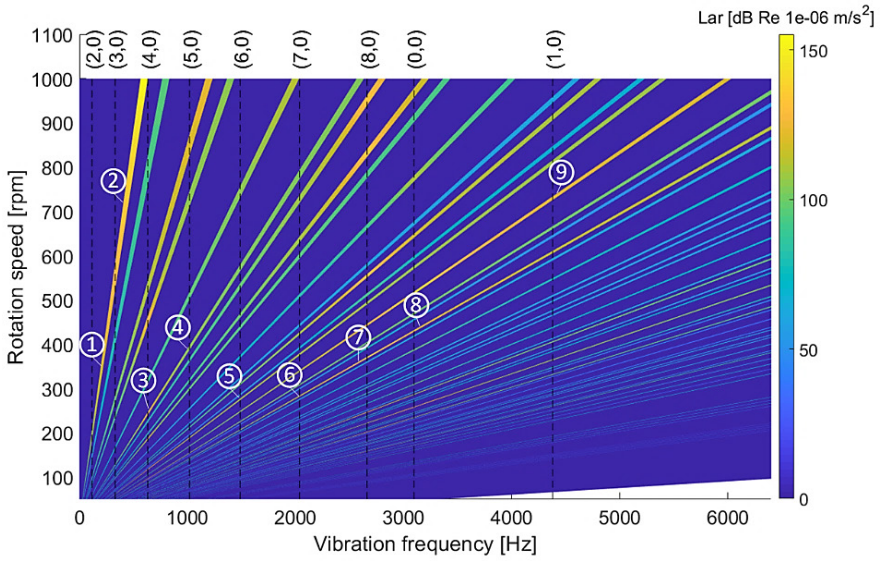

Fig. 4.3.1.2 Radial acceleration spectrogram under variable speed condition.

4.3.2 Dynamic Radial Vibrations Velocity

The magnetic flux density of the PMSG is imported in MANATEE tool to compute the electromagnetic-based forces which are proportional to the vibration production in electric machines [32].

Fig. 4.3.2.1 presents a radial velocity of PMSG under variable speed analysis, where impactful magnetic noise is marked for each specific structure mode individually. Using this graph helps to identify vibration resonances of variable speed electrical machines due to magnetic forces, where first resonance occurs 158 Hz, 356 rpm which beyond the ratings of the designed generator, and thus, the machine will not meet any resonance problems.

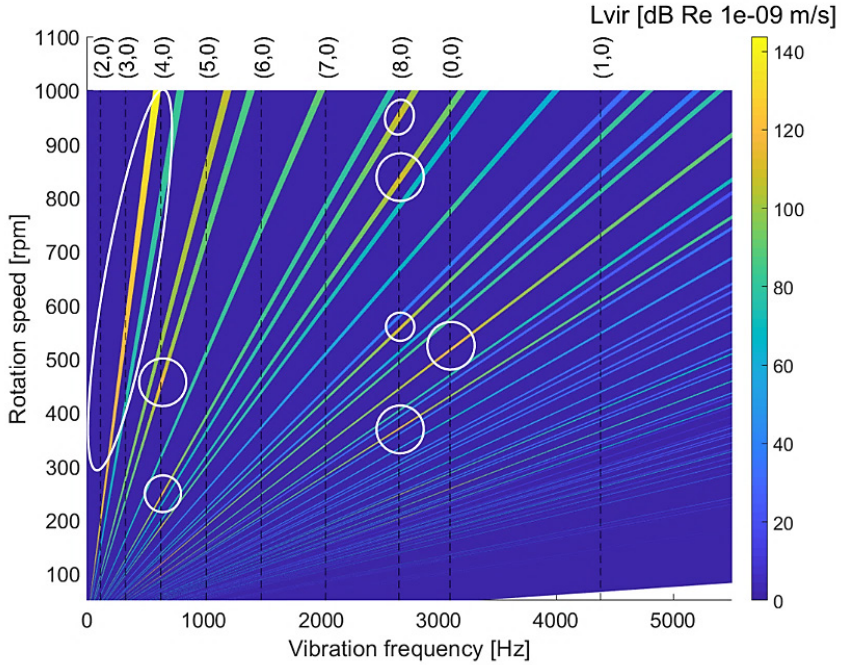

Fig. 4.3.2.1 Radial velocity spectrogram under variable speed condition.

4.3.3 Natural Frequencies of PMSG

Produced vibrations from the machine body are known as natural vibrations. Normally they occur when the PMSG tends to oscillate at the absence of any damping force. According to the equivalent circuit of the electric machines, as they have RLC circuit components, and thus, the produced natural frequency can be defined in a simplified form of:

$$\omega_0 = \frac{1}{\sqrt{LC}} \tag{4-9}$$

where L and C are inductance and capacitance of the equivalent circuit.

Fig. 4.3.3.1 shows the resonance phenomena at the various frequency as a function of structure modes (0,0) to (8,0). From the graph, we can see that the first resonance happens because of vibrations with the structure form of (2,0) which occurs at 120 Hz. Respect to the rated frequency of the PMSG by 50 Hz, therefore, while the machine operated under ratings there is no any risk of resonance.

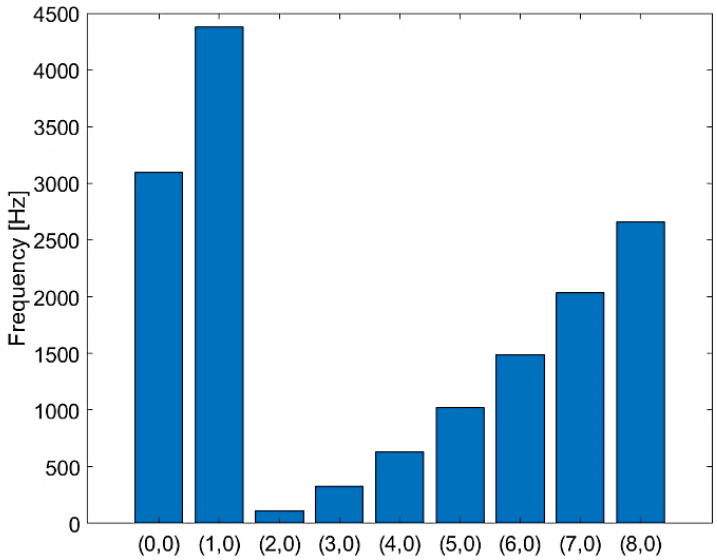

Fig. 4.3.3.1 Radial velocity spectrogram under variable speed condition.

4.4 Critical Speed Consideration

The critical speed of any electrical machines depends on mostly the mechanical characteristics of the defined geometry. In this section, we define all required equations, based on the primary presented data in Table 4.4.1. Also, three major parameters of the following calculations are presented in Fig. 4.4.1.

The mass of shaft can be calculated from:

$$m_{sh} = \rho_{sh} \frac{\pi . D_{sh}^2}{4} . L \tag{4-10}$$

The mass of rotor:

$$m_1 = \rho_1 \frac{\pi . D_1^2}{4} . w_1 \tag{4-11}$$

The mass of driven wheel:

$$m_2 = \rho_2 \frac{\pi . D_2^2}{4} . w_2 \tag{4-12}$$

Area moment of inertial of the shaft:

$$I_{sh} = \frac{\pi . D_{sh}^4}{64} \tag{4-13}$$

Table 4.4.1. Mechanical data used for the critical speed calculations.

Parameters	Definition	Unit	Value
E_1	Modulus of elasticity of the rotor (steel disc and PMs)	Pa	200×10^9
E_2	Modulus of elasticity of the driven wheel	Pa	200×10^9
E_{sh}	Modulus of elasticity of the shaft	Pa	210×10^9
ρ_1	Mean specific mass density of the rotor	$Kg.m^{-3}$	7600
ρ_2	Specific mass density of the driven wheel	$Kg.m^{-3}$	7650
ρ_{sh}	Specific mass density of shaft	kg	7700
D_1	Outer diameter of the rotor	m	0.46
D_2	Outer diameter of the driven wheel	m	0.05
D_{sh}	Outer diameter of the shaft	m	0.05
w_1	Width of the disk rotor	m	0.02
w_2	Width of the driven wheel	m	0.00001
a_1	Location of the rotor from the left end of shaft	m	0.1
a_2	Location of the driven wheel from the left end of shaft	m	0.35
L	Length of the shaft	m	0.5
g	Acceleration of gravity	$m.s^{-2}$	9.81

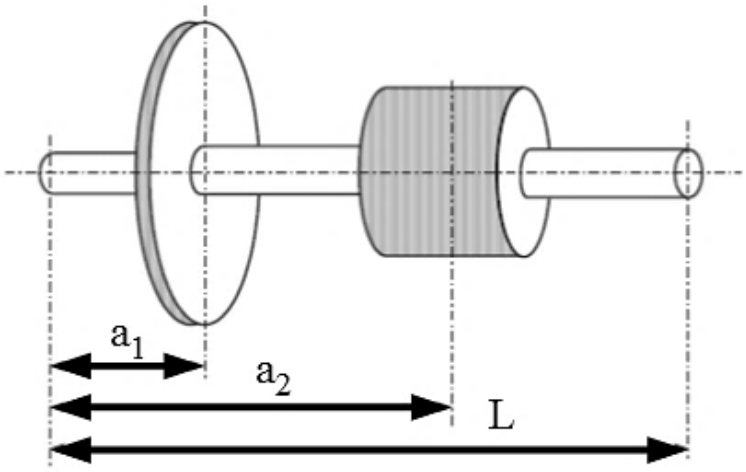

Fig. 4.4.1 Solid cylindrical shaft loaded with two masses m_1 and m_2.

Area of moment of inertia of the rotor:

$$I_1 = \frac{\pi . D_1^4}{64} \tag{4-14}$$

Area of moment of inertia wheel:

$$I_2 = \frac{\pi . D_2^4}{64} \tag{4-15}$$

Mid-point of the shaft:

$$a_{sh} = 0.5.L \tag{4-16}$$

Based on the above expressions, the static deflection of the shaft can be calculated as:

$$\delta_{sh} = \frac{m_{sh}.g.a_{sh}^2.(L-a_{sh})^2}{3.E_{sh}.I_{sh}.L} \tag{4-17}$$

Static deflection of the shaft at the position of the rotor due to the rotor core:

$$\delta_1 = \frac{m_1.g.a_1^2.(L-a_1)^2}{3.E_1.I_1.L} \tag{4-18}$$

Static deflection of the shaft at the position of a driven wheel due to the driven wheel as:

$$\delta_2 = \frac{m_2.g.a_2^2.(L-a_2)^2}{3.E_2.I_2.L} \tag{4-19}$$

Finally, the critical speed of the shaft can be given as:

$$n_{sh} = \frac{1}{2\pi}.\sqrt{\frac{g}{\delta_{sh}}} \tag{4-20}$$

Critical speed of the rotor as:

$$n_1 = \frac{1}{2\pi}.\sqrt{\frac{g}{\delta_1}} \tag{4-21}$$

Critical speed of the driven wheel as:

$$n_2 = \frac{1}{2\pi}.\sqrt{\frac{g}{\delta_2}} \tag{4-22}$$

Critical angular speed of the shaft as:

$$\Omega_{sh} = 2\pi n_{sh} \tag{4-23}$$

Critical angular speed of the rotor:

$$\Omega_1 = 2\pi n_1 \tag{4-24}$$

Critical angular of the driven wheel:

$$\Omega_2 = 2\pi n_2 \tag{4-25}$$

According to the Dunkerley equation, we have:

$$x = \frac{1}{\Omega_{sh}^2} + \frac{1}{\Omega_1^2} + \frac{1}{\Omega_2^2} \tag{4-26}$$

Critical angular speed of rotation of the system based on the Dunkerley equation:

$$\Omega_{cr} = \frac{1}{\sqrt{x}} \tag{4-27}$$

Critical angular speed of rotation of the system according to the Dunkerley equation [34]:

$$n_{cr} = \frac{\Omega_{cr}}{2\pi} \tag{4-28}$$

Critical speed of rotation of the system according to Rayleigh-Ritz method [34]:

$$n_{cr} = \frac{1}{2\pi}\sqrt{\frac{g(m_{sh}\delta_{sh} + m_1\delta_1 + m_2\delta_2)}{m_{sh}.\delta_{sh}^2 + m_1\delta_1^2 + m_2\delta_2^2}} \tag{4-29}$$

As the results from both methods, Dunkerley and Rayleigh-Ritz methods are similar, therefore, a good prediction is done.

Table 4.4.2 reports the numerical results of the above calculations based on the critical speed consideration of each component of the generator, in which the critical values of n_{sh}, n_1, n_2, and both n_{cr} values are 17275.33, 1219686.1, 4502482.2, 17273.47, and 17281.12 (in the minute), respectively. Two methods of Dunkerley and Rayleigh-Ritz methods are used to examine the calculations, as results the values are very close which indicates a good prediction of the critical speed of each part.

Table 4.4.2. Calculated critical speed-based parameters as given in above equations.

Parameters	Unit	Value
m_{sh}	kg	7.559
m_1	kg	25.261
m_2	kg	1.502×10^{-4}
I_{sh}	m^4	3.068×10^{-7}
I_1	m^4	2.198×10^{-3}
I_2	m^4	3.068×10^{-7}
a_{sh}	m	0.25
δ_{sh}	m	3.0×10^{-6}
δ_1	m	6.013×10^{-10}
δ_2	m	4.413×10^{-11}
n_{sh}	1. s^{-1}	287.922
n_1	1. s^{-1}	20328.1
n_2	1. s^{-1}	75041.37
Ω_{sh}	Rad. s^{-1}	1809.1
Ω_1	Rad. s^{-1}	127725.2
Ω_2	Rad. s^{-1}	471498.8
x	-	3.056×10^{-7}
Ω_{cr}	Rad. s^{-1}	1808.87
n_{cr} (Dunkerley)	1. s^{-1}	287.89
n_{cr} (Rayleigh-Ritz)	-	288.019

4.5 Weight Distribution

In many applications as wind power, there is always a weight restriction respect to the rated power and size of the turbine. The designed PMSG's weight can be summarized in the following Fig. 4.5.1. As presented the heaviest part of the machine is stator yoke made by iron lamination M400-50A by 52.38 kg (67%), afterward, the rotor core with 11.87 kg (15%), the copper mass used for the windings by 8.3 kg (excluding the insulation, 11%), and the smallest portion of the generator belongs to the permanent magnets which are actually the most expensive part by 5.6 kg, only 7%. The total mass of 78.22 kg which is desired for a wind generator with 5 kW rated power.

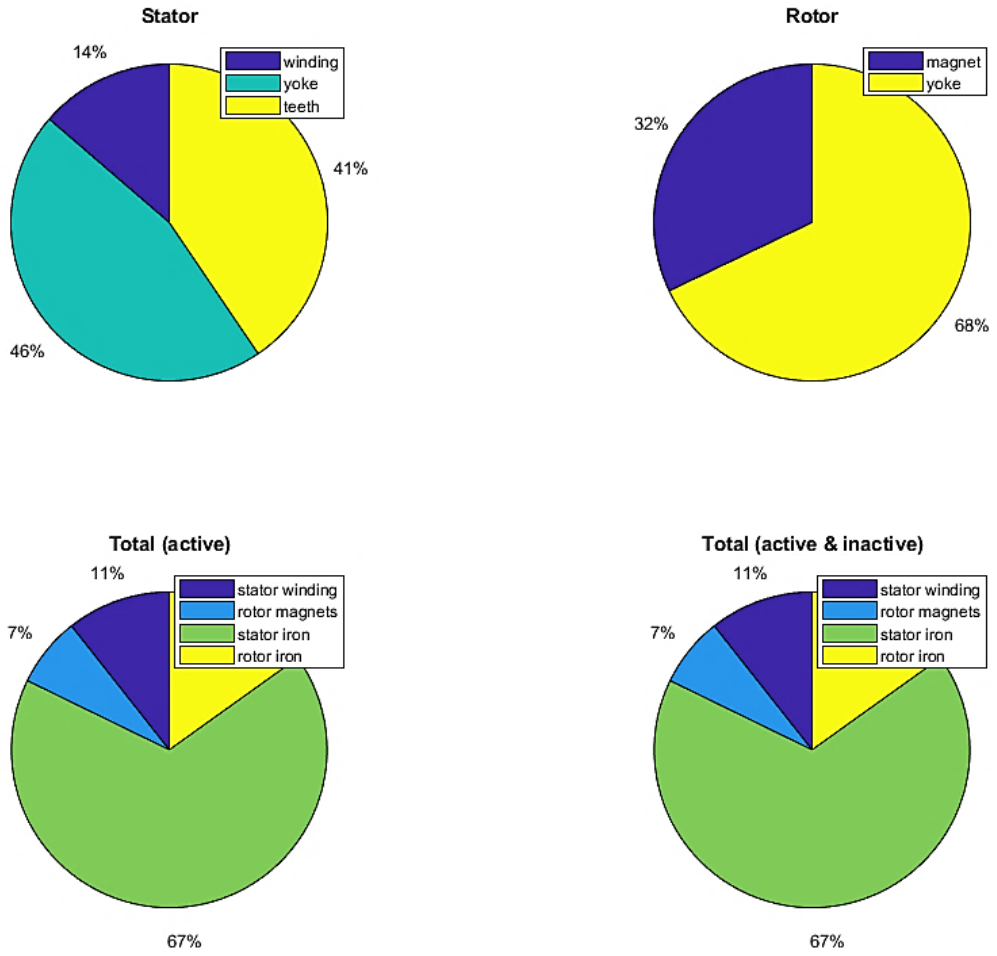

Fig. 4.5.1 Mass comparison of the generator parts in percentage.

4.6 Noise Sources in Electric Machines

Noise sources in electrical machines can be generally listed in three sources:

- Electromagnetic-based noise of electrical machines. For example, magnet/slot interactions due to Maxwell forces, the Pulse Width Modulation (PWM) harmonics, etc
- Aerodynamic noise of electrical machines (e.g. fans)
- Mechanical noise of electrical machines. For instance, bearings, shaft, etc

Electromagnetic noise is characterized by strong tonalities, its frequency content depends on the control law applied at variable speed analysis, and more in particular on PWM strategy. Depending on the type of PWM scheme, the harmonic contents are different to be considered. There are a number of ways to improve electromagnetic-based noise such as slot/ pole combination, skewing technique (which is fully studied in 4.13), harmonic current injection, winding topology, choice of machine topology, asymmetries, and etc. In this section, we will review several of them [32].

Aerodynamic noise is basically due to shaft-mounted fans, therefore it proportional to speed. Its frequency depends on the number of blades and it is characterized both harmonic tones at blade passing frequencies, and broadband noise because of turbulence.

Mechanical noise due to bearings increases with speed, however, its frequency is normally too low to create significant noise problems.

A. Choice of Machine Topology

There is not any special choice for a machine topology which delivers low noise & vibration, however, several topologies are more challenging. This also depends on the application constraints such as power density, fixed speed or variable speed application.

In this research, due to a number of benefits from outer rotor surface mounted topology. However, outer rotor topologies (also known outrunner motor if it is a brushless DC motor) can lead to higher noise & vibration because of rotor yoke lower stiffness compared to an outer stator topology. Fractional-slot winding or more particularly concentrated or tooth winding might lead to higher acoustic noise & vibrations compared to integral distributed winding due to a higher number of wavenumbers in the armature field and the possible presence of subharmonics. Hence, a special care must be taken into account when outer rotor topology with fractional-slot concentrated winding (FSCW) topology is used unless a critical noise and vibration can happen [32].

The best armature winding is the one creating the most sinusoidal MMF. Thus, the double-layer, shorted-pitch, distributed integral winding. For permanent magnet rotors, the best magnet architecture is also the one creating the most sinusoidal rotor MMF. Either Halbach configuration for surface magnets (which is studied with different magnetic orientation in Chapter 5), or multi-barriers V-shape interior magnets with bread-loaf pole shapes (also known as sinusoidal field poles) [32].

B. Choice of the Pole/ Slot Combination

Increasing the number of slots per pole per phase decreases the harmonic density of magnetic air-gap flux density and resulting in a cleaner magnetic force. Although, increasing the number of pole pairs provides a lower electromagnetic yoke height, and thus, higher vibration and noise. However, the lowest force wavenumber is also given by the greatest common divider between stator slots and poles numbers in PMSMs: increasing p also potentially increases GCD(Q,2p), and finally results in a lower electromagnetic vibration [32].

In case of induction machines, the number of rotor slots Q_r is a key design parameter as it influences both wavenumbers and frequencies of Maxwell harmonic forces. Pole/slot interactions in induction machines create exciting forces at multiples of the rotor slot passing frequency.

Some empirical rules to choose the slots/poles combination are given in many electrical engineering books such as [35-37]. However, these rules are continuous, they do not reflect correctly the discrete nature of the harmonic force wave and do not account for the stator natural frequencies nor the speed range of the machine. The use of such empirical rules should be avoided, and therefore numerical simulation is advised for instance with MANATEE software.

While both stator slot and rotor slot numbers Q_s and Q_r are even integers, Maxwell force harmonics only include even force wavenumbers for integral windings, thus avoiding unbalance magnetic pull/ force (UPM or UMF) which is the net electromagnetic force acting along X or Y axis in the stator frame. Similarly, to cogging torque, that is characterized through an average / DC value and a ripple / time-harmonic component. Its magnitude corresponds the magnitude of the Maxwell stress harmonic component of wavenumber r = 1. In magnetically-balanced electrical machines, this force is null [32].

The number of Q_s and Q_r should never be equal, otherwise strong pulsating radial and tangential force waves occur in the machine, creating high air-borne noise the stator breathing mode and potentially high structure-borne noise due to torque ripple.

In PMSMs, where several global rules on slots/poles combination can be relevant, the case of induction machines is more complex. Ideally one should avoid the presence of high magnitude (due to the first rank of permeance), "low" wavenumber so in particular one should be avoided. Relying upon only these rules of thumbs for the design of an electric machine is suboptimal and critical.

In case of synchronous machines, while Q_s is an even integer, Maxwell force harmonics only offers even force wavenumbers for integral windings, therefore avoiding unbalance magnetic pull. More precisely UMP only exists if $|Q_s - 2p|=1$. Maximization of LCM (Q_s ,2p) increases the frequency of open-circuit pulsating (wavenumber r = 0) radial and tangential force harmonics (mainly in cogging torque and average radial force). Minimization of GCD (Q_s ,2p) decreases the magnitude of open-circuit pulsating (wavenumber r = 0) radial and tangential force harmonics (in particular cogging torque and average radial force). Maximization of GCD (Q_s ,2p) increases the non-zero wavenumbers of open-circuit magnetic forces, therefore, potentially minimizing noise and vibration levels [32].

C. Choice of winding topology

The ideal winding offers a sinusoidal MMF waveform, it has an infinite number of phases (ideally without belt harmonics), an infinite number of slots (ideally free of slot harmonics or step harmonics) which makes airgap winding configuration an option. To avoid UMP, the winding-induced MMF should never have two harmonics separated of one.

Concentrated winding, tooth-winding, and fractional winding have the largest MMF distortion factor, however, if properly designed they do not generate noise & vibrations. As this research dealt with FSCW, therefore, a special care must be taken into account regarding the noise computation.

Shorted-pitch distributed windings provides the smoothest MMF. Short-pitching or chording technique consists of having several winding layers and shifting the winding pattern in each layer. The chording cannot reduce the largest MMF step harmonics at Q_s - p and Q_s + p space harmonics. The coil pitch Y (in slots, between 0 and Q_s /(2p)-1) can be chosen as (5/6) Q_s /(2p) to reduce the stator MMF space harmonics 5p and 7p [32].

4.7 A-Weighted Sound Pressure and Power Level Study

In acoustics, sound power level (SWL) characterizes the intrinsic acoustic power of an acoustic noise source, whereas sound pressure level (SPL) characterizes the acoustic noise level observed at a certain distance from the source (e.g. PMSG) in a certain acoustic environment [32].

The expression linking those two quantities in free-field can be given as [32] [38-39]:

$$L_p = L_w + 10 \times \log\left(\frac{D_f}{4\pi \times d^2}\right) \tag{4-30}$$

where L_p is the sound pressure level, L_w is the sound power level, D_f is the directivity factor, d is the distance between the observer to the center of the source, and *log* denotes logarithm in base 10 (which log10 is MATLAB).

In a reverberant field environment, the Eq. (4-29) can be defined as [38-39]:

$$L_p = L_w + 10 \times \log\left(\frac{D_f}{4\pi \times d^2} + \frac{4}{R_c}\right) \tag{4-31}$$

where R_c is the room constant which depends on the total surface area of the room and the average absorption coefficient in the room. This latter parameter can be obtained from reverberation time measurements inside the room. The directivity factor of a PMSG source placed on the floor equals $D_f = 2$; for a PMSG placed on the floor close to a wall, $D_f = 4$, and for a PMSG placed on the floor in a corner, $D_f = 8$ [32].

A-weighting concept is defined by IEC 61672-1:2013, in order to take into account, the average sensitivity of human's ear as a function of frequency. A-weighting is used to convert a physical quantity of acoustic pressure (in dB) in a psychoacoustic quantity (in dBA) which is supposed to better quantify how loud a noise can be perceived. As the ear is less sensitive to low frequencies (< 100 Hz), the A-weighting offers less weight to that part of the acoustic energy spectrum. The part of the spectrum near 2500 Hz has the highest sensitivity and electrical systems frequently whine in this frequency range, that's why the electromagnetically-excited noise of rotating machines can be so annoying [32].

Fig. 4.7.1 presents the variation of A-weighted sound pressure level (ASPL) under a variable speed analysis up to 1000 rpm. The maximum ASPL under the rated speed of 150 rpm occurs at 119 rpm by 82 dBA. It is important to mention that a microphone is radially placed by 100 cm distance (in simulation). The green line shows the speed above which field weakening is applied if relevant.

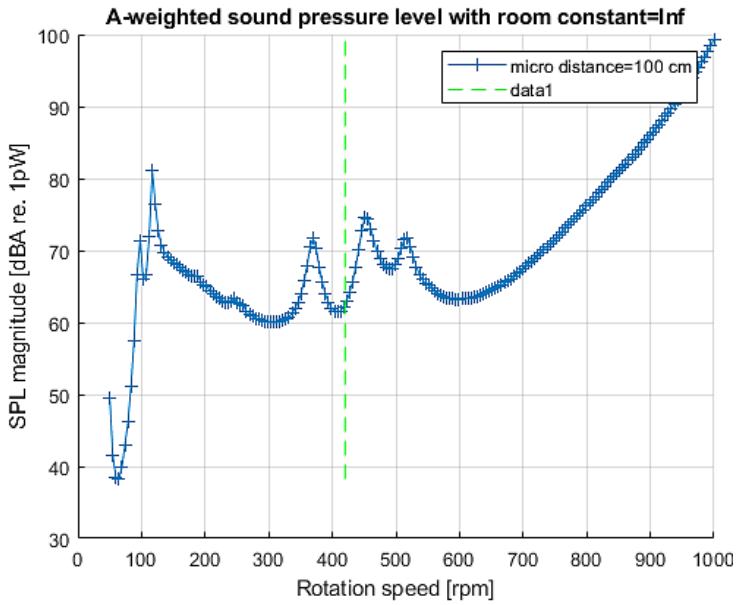

Fig. 4.7.1 A-weighted sound pressure level of the studied PMSG.

4.8 Modal Contribution at Variable Speed Range

Respect to the machine's structure, there is a unique post-processing variable speed analysis which allows evaluating A-weighting sound power (magnetic noise) by MANATEE software. The magnetic noise level when canceling the effect of a given structural mode to quantify the modal contribution to magnetic noise in electrical machines [32] [38].

Fig. 4.8.1 presents the structure mode contribution to the magnetic noise within a variable speed analysis. This modal calculation reinforces the idea of geometrical-based design and optimization improves the maximum sound power level as a function of speed. This figure helps in identifying which structural modes are involved in airborne acoustic noise radiation of the studied PMSGs. Additionally, the acoustic noise level enhancement through canceling the effect of a given structural mode to quantify the modal contribution to magnetic noise is targeted. The maximum radiated magnetic noise of 91 dBA can be seen at 124 rpm (up to the rated speed of 150rpm). However, the maximum sound power of 110 dBA can be reported for the initial model between 0-1000 rpm [32] [37-39].

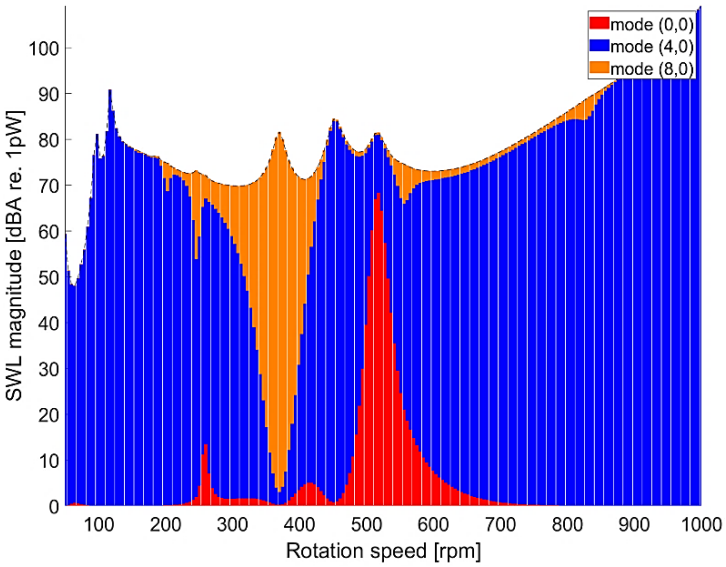

Fig. 4.8.1. Modal contribution of the machine's structure on the variable speed magnetic noise (sound power).

4.9 A-weighted Sound Power and Pressure Sonograms

The most accurate computation over magnetic noise is using FEA to calculate radial and tangential components of magnetic flux density and import them into MANATEE software to compute variable speed vibro-acoustic performance of the machine with considering natural frequencies. The maximum sound power radiated by the PMSG due to magnetic vibrations can be also written as [39]:

$$L_{p,\max}(f_{\max}) = \frac{1}{2} Z_0 S_c \sigma_m(f) \left\langle v_{m\omega}^2 \right\rangle v_{m\omega} \tag{4-32}$$

where Z_0 denotes the air acoustic impedance, S_c is the PMSG frame area, and σ_m is the modal radiation factor. The maximum sound power level $L_{\omega,\max}$ can be computed using [39]:

$$L_{\omega,\max}(f_{\max}) = 10\log_{10}\left(\sum_m \frac{L_{p,\max}(f_{\max})}{10^{-12}}\right) \tag{4-33}$$

The natural frequencies of the stator circumferential mode have been chosen only as even values due to the stator and rotor pole numbers both being even. Thus, the Maxwell exciting force harmonics are produced only as even spatial orders due to symmetry. By assimilating the stator to an equivalent ring has been considered. The breathing mode natural frequency f_0 can be defined as:

$$f_0 = \frac{1}{2\pi a}\sqrt{\frac{E_s}{K_{f_s}\Delta_m \rho_s}} \tag{4-34}$$

where a is the stator mean radius, which applies h_f as the frame width, K_{fs} is the stator stacking factor, ρ_s is the stator stack mass density, and Δ_m denotes the increasing mass because of the winding and teeth.

Fig. 4.9.1 presents an A-weighted maximum magnetic noise under a variable speed range. The spectrogram is evaluated in the post processing stage, in which the electromagnetically-excited radial vibration illustration identifies whether the vibration resonances of variable speed of the PMSG due to magnetic forces occur during the operation or not. The graph shows that the first resonance happens at 180 Hz and 354 rpm which is shown between the grey dashed line in the modal structural modes of (2,0) and (3,0). In addition, the PMSG rotates in the flux weakening condition at 430 rpm which is indicated by the red dashed line. Afterward, the largest 730 rpm, 480 Hz. Note that the first resonance at structural mode (2,0) happens when the electrical frequency of the traveling force wave of wavenumber r matches with the circumferential-mode natural frequency, where 2 is the rank of the circumferential deflection and 0 denotes the rank of the longitudinal deflection in the structural mode. To evaluate all the natural frequencies of the PMSG with the rated speed of 15-150 rpm (0 to 50 Hz), the radial velocity in unit of the dBA should be computed for over 5000 Hz.

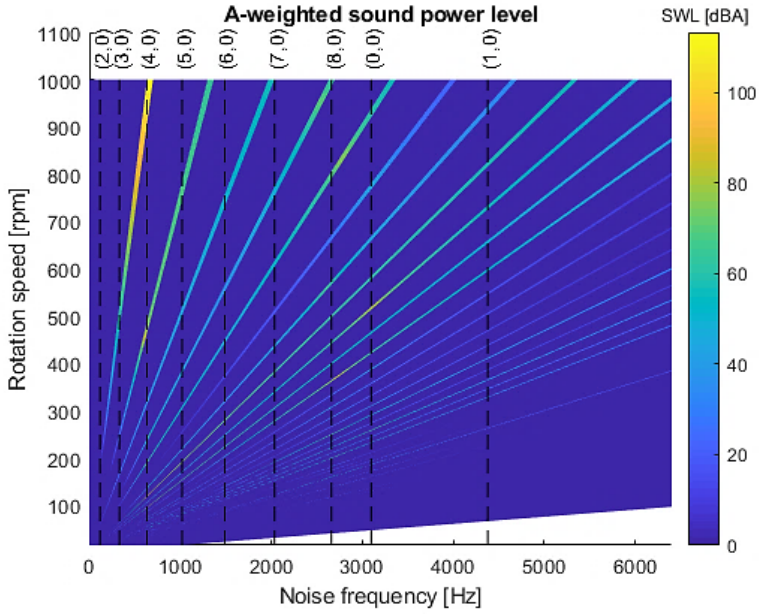

Fig. 4.9.1. A-weighted maximum magnetic noise sonogram of PMSG.

Fig. 4.9.2 illustrates a variable speed A-weighted sound pressure sonogram, in which the natural frequencies are considered (as mentioned in Fig. 4.9.1).

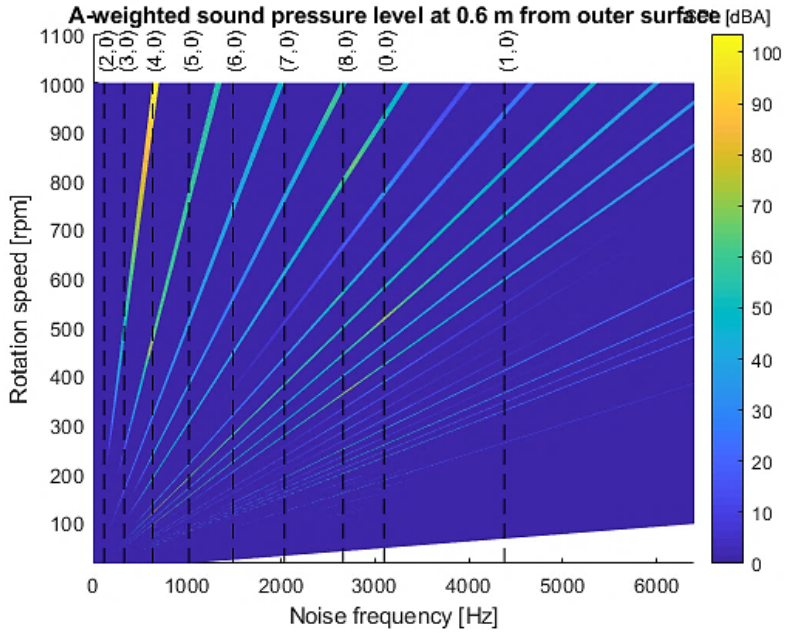

Fig. 4.9.2. A-weighted maximum sound pressure sonogram of PMSG.

In addition to the stator natural frequencies which are presented in Fig. 4.9.1, there are also rotor natural frequencies as a function of structure modes (Equivalent cylindrical mode (m, n)) which are indicated in Table 4.9.1. Where m is the rank of the circumferential deflection and n is the rank of the longitudinal deflection in the studied PMSGs that have produced three major deflection modes in common such as outer rotor structure mode (2,0), (3,0), and (4,0), in which each of these modes indicates different structure deflection. The natural frequencies are calculated using analytical modal damping coefficients method.

Table 4.9.1 Rotor natural frequency as function of structure mode with damping coefficient of ksi = 2%.

Rotor mode	Natural frequency	Unit
(0,0)	3096	Hz
(1,0)	4379	Hz
(2,0)	177	Hz
(3,0)	331	Hz
(4,0)	633	Hz
(5,0)	1019	Hz
(6,0)	1488	Hz
(7,0)	2036	Hz
(8,0)	2661	Hz

4.10 Vibro-acoustic Optimization Techniques

As mentioned in section 4.6, there are several techniques to deal with radiated vibrations and audible magnetic noise. One of these new techniques is skewing the stator and rotor cores of the machines which are studied in section 4.10.1 for the first time. It should be mentioned that there have been some attempts to tackle noise and vibration recently, however, the researchers did not consider two major considerations through their computations which make the outcome unreliable. One the machine, in fact, operates at variable speed, and thus, to examine acoustics of the machine it is mandatory to check magnetic noise and vibrations as the function of speed. Second, the importance of natural frequencies consideration is also very critical, because if resonance occurs when the machine runs, the whole system will be significantly affected and consequently the noise increases. This consideration helps engineers to see if the designed machine can operate under a defined range of speed with a standard range of vibration and noise. As a result, the stator and rotor natural frequencies must be calculated to provide trustable results. In this

thesis, we have minimized the vibrations and audible magnetic noise using the skewing technique, as well as optimal pole number. In the second optimization approach, increasing the number of slots per pole per phase mitigates the harmonic density of air-gap magnetic flux density which results in global magnetic forces reduction. By providing a larger number of pole-pairs, a lower electromagnetic yoke, and therefore higher vibration and magnetic noise occur. In this research, the influence of different pole-pairs number on vibro-acoustic design aspect of the machine is studied using a subdomain method (SDM) to challenge the final choice of the designer through with considering the natural frequencies. To find out the optimal number of pole-pairs for a low-speed, high-torque permanent magnet synchronous generator (PMSG) with the double-layer fractional-slot non-overlapping concentrated winding (FSCW) for wind turbine applications. First, all possible slots/ pole combinations which offer the use of double-layer FSCW are studied through magnetomotive force (MMF) harmonic analysis. Second, the analytical subdomain model of PMSG is discussed to deal with the vibro-acoustic performance under variable speed analysis. Finally, all affected major parameters are compared to gain the optimal pole number of the PMSG. To verify the analytical-based results from the SDM, 3-D time-stepping finite element analysis (FEA) is employed.

4.10.1 Skewing the Stator and Rotor

Among all main sources of acoustic noise such as mechanical, and aerodynamic, the magnetic source can be very critical in many applications (transport systems, aerospace, EV motors, etc.), particularly in low-speed, high-torque wind generators, where a large number of poles and a thinner stator yoke always result in a medium mechanical stiffness. This induces magnetic vibration due to magnetic forces which consist of Maxwell and magnetostrictive forces. Fractional-slot concentrated windings (FSCW) are very popular because of many remarkable enhancements during recent years in terms of manufacturability and modularity [40], increased flux weakening performance [41], fault tolerance features [42], and short-end windings [43-44]. However, the acoustic noise needs special attention because of the small number of slots per pole per phase q which causes large magnetomotive force (MMF) distortion due to low-order harmonics in the spatial distribution of the radial forces in comparison to other traditional PM machines [45-46].

The first attempt to reduce magnetic vibrations and acoustic noise produced in the electrical machines via Maxwell forces has been modeled in [47-49].

In recent research work, there are several studies to present the impact of various machine design considerations on magnetic noises with considering variable-speed and natural frequencies conditions as follows.

J. Le Besnerais *et al.*, studied a multi-objective optimization on a fastanalytical model of a variable-speed induction machine which calculates both motor performances and sound power level of electromagnetic origin. The model has been coupled to a Non-dominating Sorting Genetic Algorithm (NSGA-II) in order to perform global constrained optimizations with respect to several objectives (e.g. noise level, efficiency and material cost) [50]. In another work [51], the authors present a fast simulation tool for the variable-speed magnetic noise emitted by induction machines, based on fully analytical models. On the basis of these models, they derive and experimentally validate an analytical expression for magnetic vibrations due to slotting reluctance harmonics, confirming the prime importance of slot combination in magnetic noise radiation. Finally, a database that efficiently replaces the old empirical rules for slot combination numbers and helps in designing quiet induction motors has been proposed which can be built for other power ranges. In reference [52], the paper investigates the importance of the zeroth mode of vibration in low-speed high-torque surface-mounted permanent magnet (PM) machines with non-overlapping concentrated windings. Additionally, the impact of pole and slot combinations and the effect of rectifier load also have been discussed. In another study [53], the authors offer a fully analytical model of the electromagnetic and vibro-acoustic behavior of variable-speed squirrel-cage induction machines. The studied model has been integrated in a fast simulation tool that can be used to design motors with low magnetic noise levels on their whole speed range. Furthermore, the influence of vibration-based forces and noises due to PWM supply in induction machines have been studied in [54-55].

This paper investigates the impact of a skewing technique to minimize the vibration level power and audible magnetic noise on a permanent magnet synchronous generator (PMSG) using a subdomain model (SDM) with use of non-overlapping FSCW for a variable-speed-range analysis. With respect to the importance of MMF distortion of the FSCW used, the results of both initial and optimized PMSG have been presented. The skewing angle for a wide-range of skew rate has been expressed by stator slot pitch between 0.8-1.2. We investigate whether or not the skewing slice number is significant to the vibro-acoustic objectives in the studied PMSG. Although many empirical rules have been established for correctly carrying out the skewing of stator and rotor, as to limit the maximum audible magnetic noise level radiated from the PMSG, none of these empirical rules have considered the stator's natural frequencies or variable-speed-analysis. The literature contains many papers which have been recently published using empirical-based approaches to choose skewing angle [56-61], and also numerical-based studies to minimize vibration and noise [62-65] without considering the natural frequencies, as well as variable-speed analysis in some cases. This study demonstrates how these important considerations can change the choice of skewing angle. In addition to acoustic-based optimization, the electromagnetic performance of the wind generator such as torque, cogging torque, and back-EMF parameters are defined as optimization constraints. We have derived the best skewing rate and slice number in order to reduce the vibration

level power and maximum audible magnetic noise, while the electromagnetic performance remained constant. Finally, the SDM optimized PMSG has numerically (3D-FEA) and experimentally verified the achievements. This theoretical work is based on a series of analytical models that were implemented in simulation tools, MANATEE linked to MALAB, and ANSYS Maxwell. The reason of using ANSYS Maxwell is that MANATEE lacks 3D FEA simulations, however, a powerful SDM is defined.

A. Analytical Vibro-Acoustic Modelling

Magnetic noise phenomenon consists of magnetostrictive and Maxwell forces. To calculate magnetic noise natural frequencies, the Fourier development of the PM is necessary by a permeance/ MMF model. This study has to consider the stator and rotor MMF, however, the rotor MMF is much smaller. the Transient magnetic field for low frequency can be given by Maxwell's equation:

$$\begin{cases} \nabla \times \frac{1}{\sigma} \nabla \times H + \frac{\partial B}{\partial t} = 0 \\ \nabla .\ B = 0 \end{cases} \tag{4-35}$$

where H is magnetic field strength, B is magnetic flux density, E is electric field strength, σ is electric conductivity.

To compute the radial component of the force, F_x and F_y are defined based on the cylindrical coordinate system:

$$\begin{cases} F_x = \int_s p_r(\theta, z)\cos\theta - p_\theta(\theta, z)\sin\theta \\ F_y = \int_s p_r(\theta, z)\sin\theta + p_\theta(\theta, z)\cos\theta \end{cases} \tag{4-36}$$

where both radial forces, which are basically produced by the stator and rotor winding harmonic magnetic field, are:

$$\begin{cases} p_r(\theta, z) = \frac{1}{2\mu_0}\left(B_r^2(\theta, z) - B_\theta^2(\theta, z) - B_z^2(\theta, z)\right) \\ p_\theta(\theta, z) = \frac{B_\theta(\theta, z).B_r(\theta, z)}{\mu_0} \end{cases} \tag{4-37}$$

Regarding the Maxwell stress tensor (4-35), the radial magnetic force, a major source of magnetic vibration, and as a function of both space and time, can be defined as:

$$\begin{aligned} \vec{F}_r &= \frac{1}{2\mu_0}\left(B_r^2 - B_t^2\right) \\ \vec{F}_r(\theta, t) &= F_{r,\max}\cos(n\theta - k\omega t) \\ \vec{F}_c &= m\omega^2 r \end{aligned} \tag{4-38}$$

where F_r is the radial magnetic force, B_r and B_t are the radial and tangential components of magnetic flux density in the middle of air-gap, θ is the mechanical angular position, n is the spatial harmonic order, k is the time-harmonic order, ω is the angular velocity, r is the radius of the rotor, and m is the mass of rotor.

Assuming that the stiffness and mass of the model are constant; when the machine is considered as time invariant, all the displacement and deformation should be calculated at each node of the generated meshes. Thereupon, the non-linear vibration of the PMSG can be given as:

$$\{F(t)\} = [M]\{\ddot{x}(t)\} + [C]\{\dot{x}(t)\} + [K]\{x(t)\} \tag{4-39}$$

Hence, the sound wave of the PMSG with a small amplitude is propagating which is a simplistic but useful idealistic homogeneous medium as:

$$\frac{\partial^2 p}{\partial x^2} + \frac{\partial^2 p}{\partial y^2} + \frac{\partial^2 p}{\partial z^2} = \frac{1}{c^2}\frac{\partial^2 p}{\partial t^2} \tag{4-40}$$

The maximum sound power radiated by the PMSG due to magnetic vibrations can be also written as:

$$L_{p,\max}(f_{\max}) = \frac{1}{2} Z_0 S_c \sigma_m(f) \left\langle v_{m\omega}^2 \right\rangle v_{m\omega} \tag{4-41}$$

where Z_0 denotes the air acoustic impedance, S_c is the PMSG frame area, and σ_m is the modal radiation factor. The maximum sound power level $L_{\omega,\max}$ can be computed using:

$$L_{\omega,\max}(f_{\max}) = 10 \log_{10} \left(\sum_m \frac{L_{p,\max}(f_{\max})}{10^{-12}} \right) \tag{4-42}$$

The natural frequencies of the stator circumferential mode have been chosen only as even values due to the stator and rotor pole numbers both being even. Thus, the Maxwell exciting force harmonics are produced only as even spatial orders due to symmetry. By assimilating the stator to an equivalent ring has been taken into account. The breathing mode natural frequency f_0 can be defined as:

$$f_0 = \frac{1}{2\pi a} \sqrt{\frac{E_s}{K_{f_s} \Delta_m \rho_s}} \tag{4-43}$$

where a is the stator mean radius, which applies h_f as the frame width, K_{fs} is the stator stacking factor, ρ_s is the stator stack mass density, and Δ_m denotes the increasing mass because of the winding and teeth.

B. Results and Discussion

The results and discussion section include the electromagnetic impact of various skewing angles on the vibration and acoustic results with special attention on the audible magnetic noise and vibration computations. The input design data of the studied PMSG for the simulation is presented first. Table 4.10.1.1 indicates this data in four individual sections, geometrical, numerical (FE-based), electrical, and magnetic.

Each design case was simulated using nonlinear 3D FEA, ANSYS Maxwell and MANATEE. For both the initial and optimized designs, the PMs are made of NdFeB-N48 with a remanent flux density of 1.2 T, and the back irons are made of isotropic M400-50A non-orientated magnetic lamination steel; the mechanical properties of the material used can be seen in Table 4.10.1.1. All the following sections are based on 3D FEA unless specifically indicated otherwise.

Figs. 4.10.1.1 through 10 demonstrate several important electromagnetic-based behaviors of PMSG, in which the magnetic noise is targeted on the parametric FEA simulation study results. In particular, Figs. 4.10.1.1 and 4.10.1.2 depict the variation of the magnetic flux density as a function of time and space which produces the presented radial flux density (shown in Fig. 4.10.1.3). Fig. 4.10.1.4 reinforces the impact of various skew angles of the stator and rotor on both the x-axis magnetic force and maximum sound power. Additionally, the effect of the skewing technique on the magnitude of the maximum sound power level with respect to the impactful modal contribution of the PMSG's structure is presented in Fig. 4.10.1.5. Figs. 4.10.1.6 and 4.10.1.7 validate the outcome of the numerical variable speed noise results by a 1/3 octave, A-weighted acoustic noise spectrum, and spectrum where the resonances are considered. Figs. 4.10.1.8, 4.10.1.9. and 4.10.1.10 validate the numerical-based results by experimental tests.

C. Electromagnetic-based Variable Speed Analysis

The original design input parameters can be seen in Table 4.10.1. The stator contains 36 segmented teeth because of closed slot modulation in order to reduce the amplitude of cogging torque significantly. The proposed equations in the previous section

Table 4.10.1.1 Input data of the studied PMSG.

Parameters	Values	Units
Geometrical		
l_s	100	*mm*
R_{ri}/ R_{ro}	217/ 230	*mm*
R_{si}/ R_{so}	115/ 209.5	*mm*
S_w	15	*mm*
δ_g	0.6	*mm*
P_{arc}	100	$^o e$
S_d	50	*mm*
$Q_s/2P$	36/40	
α_p	0.55	
SP	0.9	
Numerical (FE-based)		
N	150	rpm
Total time steps	180	
Number of elements	544289	
Number of nodes	163013	
FEA Formulation	Potential vector	
Electrical		
m	3	
N_c	80	turns
J_{rms}	1.2206	
I_{rms}	4.899	A/mm^2
Number of parallel circuit per phase	2	
Slot/ pole/ phase	0.3	
λ_d	1703.9381	mVs
Line-to-line inductance (d-axis)	937.8789	mH
Magnetic		
μ_0	$4\pi\times10^{-7}$	H/m
μ_s	2500	
μ_{PM}	1.05	
μ_{air}	1	
B_{rm}	1.2	T
H_k	891×10^3	*A/m*
Magnet permeance per half pole	0.1437	μWb/At

explain how the resulting magnetic flux density distribution by an SDM and 3D FE model with variable range analysis can be demonstrated in Fig. 4.10.1.1(a), in which the maximum flux density is seen around the stator teeth and the outer surface of the stator. The radial air-gap flux density as a function of time and mechanical angle also is presented in Fig. 4.10.1.1(b).

Fig. 4.10.1.2 demonstrates a good agreement between SDM and 3D-FEA models, where the harmonics as a function of space (shown in Fig. 4.10.1.2(a)), and time (Fig. 4.10.1.2(b)) are compared. In Fig. 4.10.1.2(a), the largest harmonic exists on wavenumber 20 (as the PMSG has 20 poles). As the saturation effect on the magnetic field is not considered by SDM simulation (the model details can be found in [46 and 66]), thus, there are very small differences presented in Fig. 4.10.1.2 (a, b). The temporal harmonic contents on the flux are the same, however, the amplitude varies on the fundamental and the first harmonic. Indeed, the saturation is flattening the spatial distribution of magnetic flux such that the first harmonics are lower than the SDM results.

Fig. 4.10.1.3 illustrates the maximum radial magnetic force variation from Eq. 4.34 with and without centrifugal force consideration. As presented in the graph, the produced radial forces F_r from the inner stator excited coils, F_c, due to its mechanical essence, has a clockwise vector direction (based on the right's hand law) because of the body's inertia with a uniform distribution. Both the radial and centrifugal forces have a distribution with a radial vector direction and have an overlapped influence on each other. A summation of them, leading up to the resultant blue curve in this graph, indicates the total (or actual) radial force on the rotor.

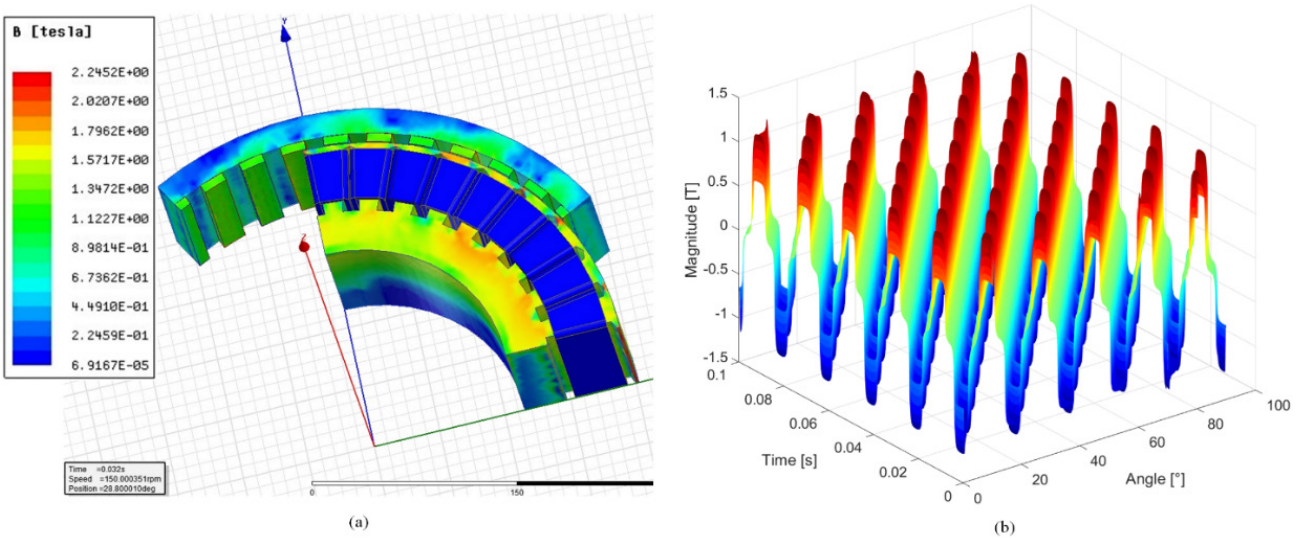

Fig. 4.10.1.1. Magnetic flux density using 3-D FEA, a) flux density distribution at $t = 0.032$s, and b) air-gap rotor radial flux density as function of time and angle.

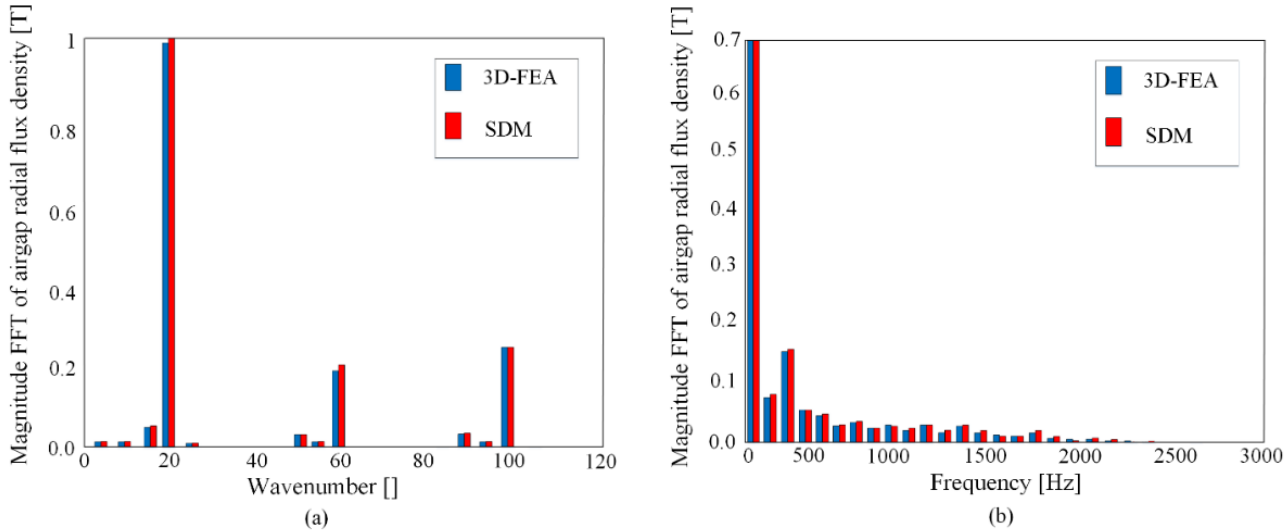

Fig. 4.10.1.2. Magnitude FFT of radial flux density using SDM and 3D-FEA, as function of a) space, and b) time.

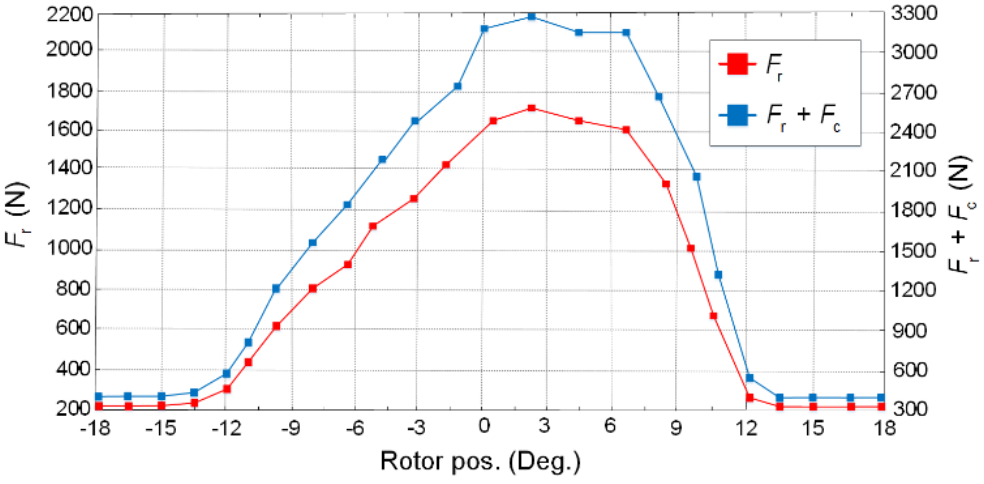

Fig. 4.10.1.3. Maximum radial force (normal and centrifugal components) of the DSPMBL under 4.9 A RMS excitation current with 30˚ rotation.

D. Vibro-Acoustic Optimization under Variable Speed Condition

To deal with vibro-acoustic behavior of the PMSG, the magnetic flux density values as a function of time computed by ANSYS Maxwell was imported to the MANATEE package for further investigation.

The influence of various skew angles (as variables) is studied in the stator/ rotor, slot/ magnet pitch factors unit. Each single slot pitch factor, equal to 10°, from 0.8-1.2 (due to electromagnetic capability of the studied PMSG) on the *x*-axis component of the magnetic force F_x and A-weighted maximum sound power level $L_{p,max}$ (shown in Fig. 4.10.1.4) was calculated at variable speeds from N_{min} = 15 rpm to N_{max} = 1000 rpm. To find the best possible angle for each part (stator and rotor), this computation evaluates the impact of each variable on the objectives with respect to each other. Each graph is also a function of the number of the skew slice. Fig. 4.10.1.4(a) presents two main regions (red and blue dashed areas) in which the red area is where the stator skew obtains the highest rate, between 1 to 1.2, whereas the rotor skew rate is lower. This area provides a higher level of $L_{p,max}$, between 92.4 to 92.5 dBA. The lowest $L_{p,max}$ (optimal area) is reached when the highest rate of rotor skew angle (including magnets), and smaller stator angle skew were chosen (92.2 dBA). Comparing to the initial skew angle, which is analytically calculated (black arrow), an enhancement of approximately 1 dBA has been achieved. The analytical method used is based on the average flux density in 2D along the axial direction, while the proposed method has computed the magnetic flux density using 3D FEA. Additionally, this graph (Fig. 4.10.1.4(a)) depicted the skew model by 5 slices. Fig. 4.10.1.4(b) illustrates the optimal area as the same as Fig. 4.10.1.4(a) with ratings of 1.2 and 0.8 for the rotor and stator. However, a larger F_x with a higher skew slice of 10, which produces consequently higher outputs such as torque. Fig. 4.10.1.4(c) demonstrates how the odd number (15) of the skew slots again decreases F_x by nearly 100 N. In this configuration, $L_{p,max}$ has been enhanced by 1.5 dBA when compared to the initial model. As presented in Fig. 4.10.1.4(d), higher F_x has been produced by the maximum value of 874 N, when an even number (20) of skew slice has been used. Therefore, the importance of the skew slice number on F_x and its harmonics are considerable with respect to the number of stator slots and rotor magnets (or slots, in case of other machine topologies) which can be an even or odd number proportionally, although, it could not directly reduce $L_{p,max}$.

Fig. 4.10.1.5 reinforces the idea that the structural contribution of the PMSG skewing technique, based on a various range of skew angles (which is basically a structural-based variable), has the significant influence on the sound power level as the function of speed. This figure helps in identifying which structural modes are involved in airborne acoustic noise radiation of the studied PMSGs. Additionally, the acoustic noise level enhancement through canceling the effect of a given structural mode to quantify the modal contribution to magnetic noise is targeted. Fig. 4.10.1.5(a) indicates the magnetic noise magnitude as a function of speed, where the maximum radiated magnetic noise of 91 dBA A-weighted, can be seen at 124 rpm, however, this quantity is reduced using the optimized model (shown in Fig. 4.10.1.5(b)) by 16 dBA re.1pW. The magnetic noise increases proportionally with the speed, and thus, the maximum sound power of 110 and 91.04 dBA can be reported for both the initial and optimized models.

Fig. 4.10.1.6 illustrates the one-third octave A-weighted acoustic noise spectrum for the initial (Fig. 4.10.1.6(a)) and optimized (Fig. 4.10.1.6(b)) models. As presented, the maximum sound power bars based on the human's normal audition for each range of frequencies are reduced using the skewing technique.

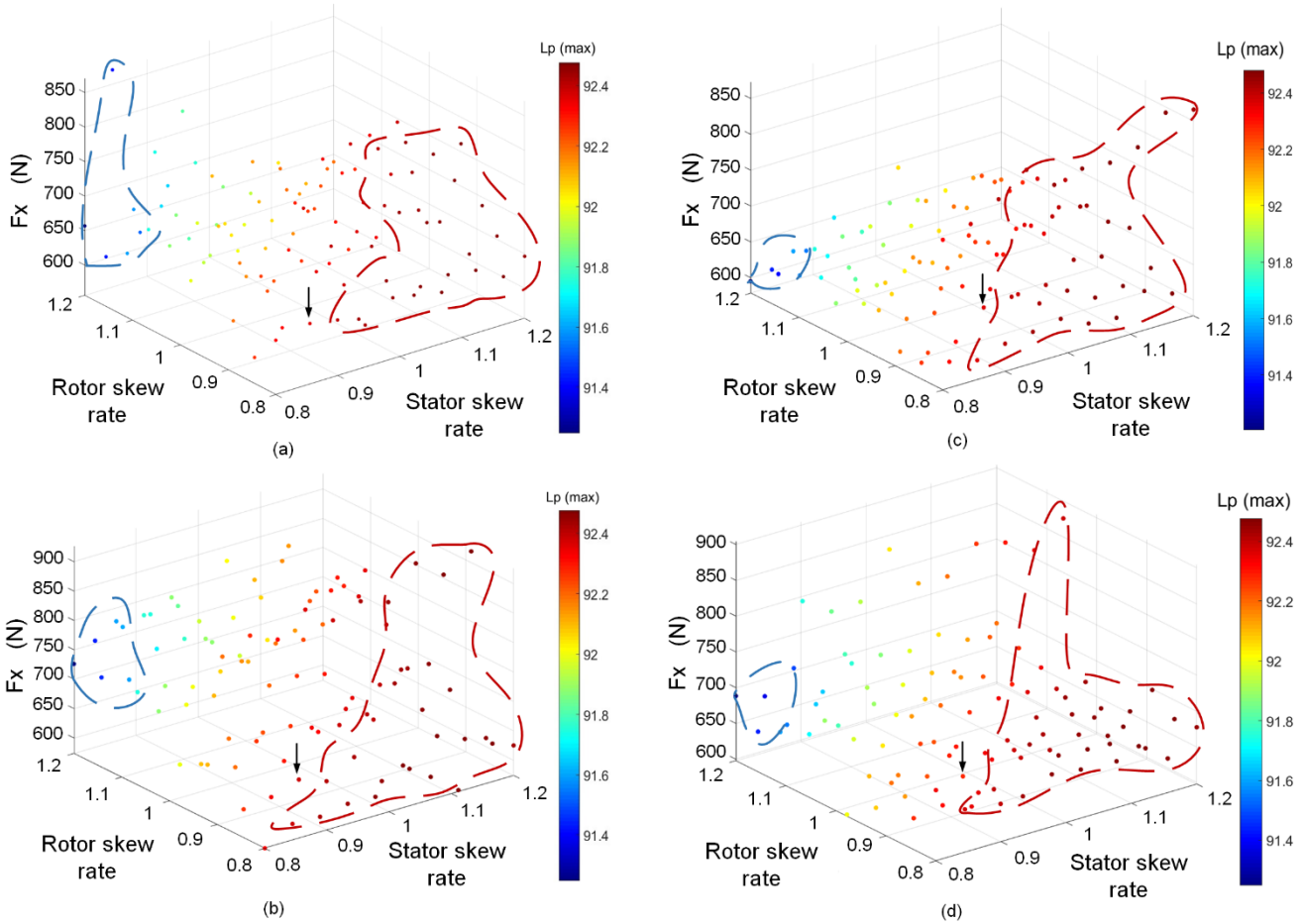

Fig. 4.10.1.4. Objective-variable-based variation of stator and rotor skew angle versus F_x and $L_{p,max}$ as function of skew slice number, where: a) 5 slices, b) 10 slices, c) 15 slices, and d) by 20 slices.

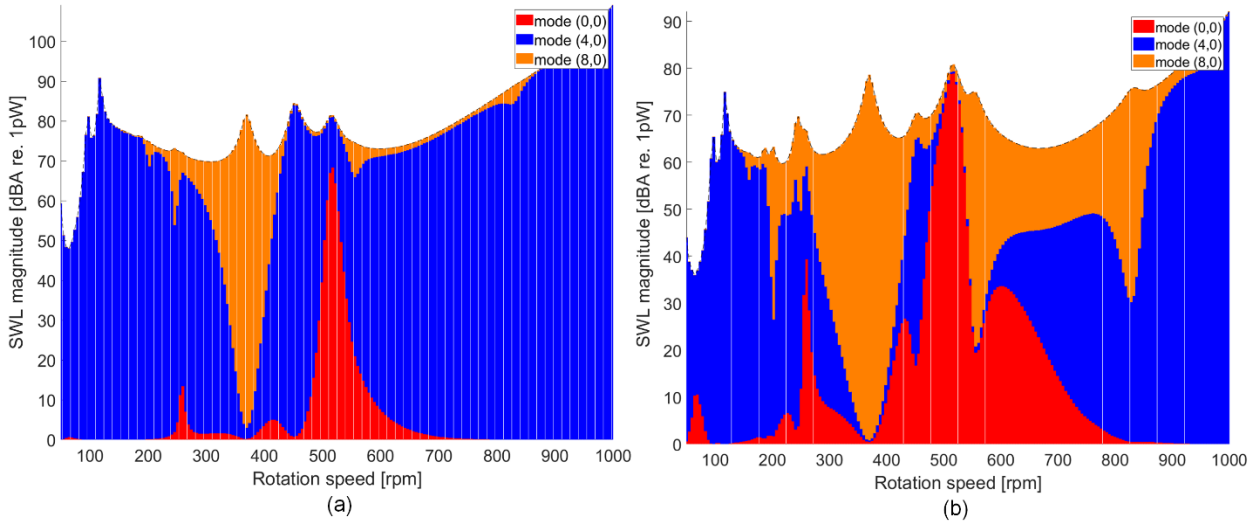

Fig. 4.10.1.5. Modal contribution of the machine's structure on the magnetic noise (sound power), a) initial, and b) optimized PMSGs.

noise at the rated speed of 150 rpm on both initial and optimized PMSGs has obtained 78.08 and 62.67 dBA, respectively. Note that A-weighting was defined by IEC 61672-1:2013, which enables one to convert a physical quantity of acoustic pressure (in dB) into a psychoacoustic quantity (in dBA) that is supposed to better quantify how loud a noise is perceived.

Fig. 4.10.1.7 presents an A-weighted maximum magnetic noise spectrogram of the optimum skew angles of rotor and stator 12˚ and 8˚ under a variable speed range. The spectrogram is evaluated in the post-processing stage, in which the electromagnetically-excited radial vibration illustration identifies whether

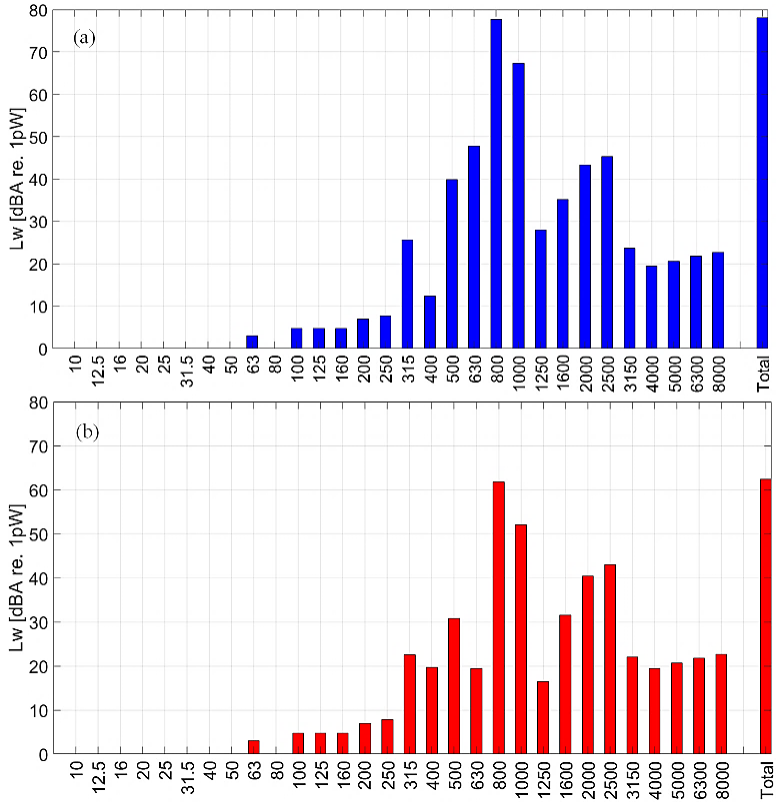

Fig. 4.10.1.6. 1/3 octave A-weighted acoustic noise spectrum for a) initial, b) optimized PMSG.

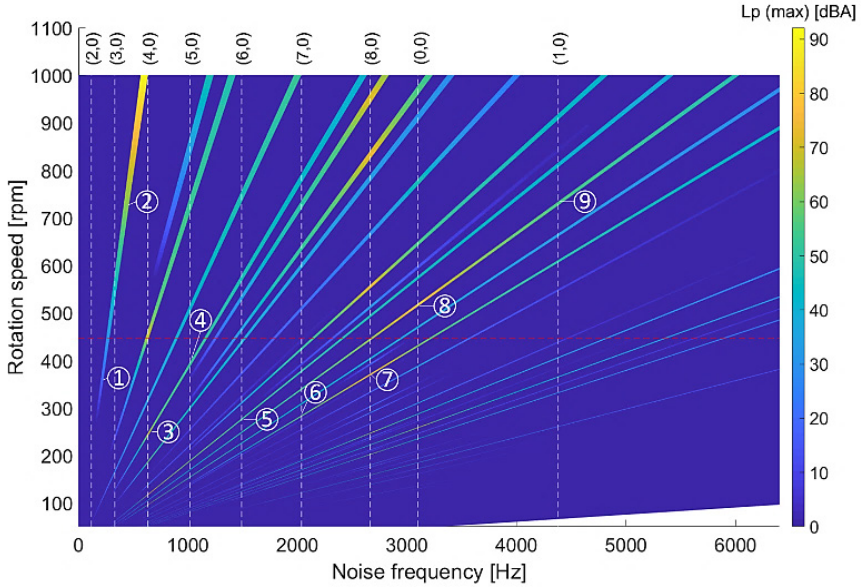

Fig. 4.10.1.7. A-weighted maximum magnetic noise spectrogram of PMSG.

the vibration resonances of variable speed of the PMSG due to magnetic forces occur during the operation or not. The designed PMSG allows operating under 150 rpm, 50 Hz, while it is a low-speed wind generator. Fig. 4.10.1.7 presents that the first resonance actually happens at 185 Hz and 356 rpm which is shown between the grey dashed line in the modal structural modes of (2,0) and (3,0). In addition, the PMSG rotates in the flux weakening condition at 430 rpm which is indicated by the red dashed line. Afterward, the largest 736 rpm, 488 Hz. Note that the first resonance at structural mode (2,0) happens when the electrical frequency of the traveling force wave of wavenumber *r* matches with the circumferential mode natural frequency, where 2 is the rank of the circumferential deflection and 0 denotes the rank of the longitudinal deflection in the structural mode. To evaluate all the natural frequencies of the PMSG with the rated speed of 15-150 rpm (0 to 50 Hz), the radial velocity in the unit of dBA should be computed for over 5000 Hz.

4.10.2 Optimal Pole Number of the Outer Rotor

In fact, there are many empirical-based studies for calculating the optimum pole number for restricting the magnetic noise radiated from electrical machines. However, these studies have never considered the behavior of the machine under a variable speed analysis, regardless of the fact that resonances and their effect on the choice of optimal pole number are occasionally critical. Several of these studies to reduce magnetic noise and vibrations using a generic slots per poles combination can be addressed in [67], where the first attempts to study an acoustic design perspective were presented by Kron. In 1989, some of these laws are listed in Timar's book [68], such as $0.75Z_s \leq Z_r < Z_s$. These empirical laws, not only in the 19th century but also in the 20th, are globally proposed by researchers [34-35] [71-50]. In addition, there are many recent publications [57] [62] [64] and [65] dealing with magnetic noise and vibration, where the designers have ignored the fact that electrical machines can run at variable speed. In addition to that, not considering natural frequencies can be critical when the operation point obtained by optimum parameters is nearby or inside the resonance regions [67].

During recent research developments in this field, the experts have found the importance of these considerations. Some of these studies can be addressed as follows.

In [72], an analytical subdomain model to compute the magnetic field distribution in surface-mounted permanent-magnet synchronous motors (PMSMs). The proposed model is sufficiently general to be applied with any number of slots per pole per phase (known as q) and any windings topology. The model accurately accounts for armature reaction magnetic field and mutual influence between the slots. The analytical method is based on the resolution of two-dimensional Laplace and Poisson equations in polar coordinates for each subdomain. In another work [46], the paper develops an analytical model for computing the radial vibration force of fractional-slot concentrated winding (FSCW) in PMSMs. In this work, the researchers present the impact of several important issues such as stator slotting, tangential field component, radius in the airgap for computation, and load condition on the vibration. All findings are analyzed using finite element analysis (FEA).

In research [51], the authors authors propose a fast simulation tool which is based on analytical models for the variable-speed magnetic noise emitted by induction machines. One of the major findings is the significance of q number in magnetic noise. Finally, they proposed a power range tool based on a dataset, where the former empirical criterions were modified. Furthermore, the influence of vibration-based forces and noises due to PWM supply in induction machines has been studied in [54-55], where they considered natural frequencies.

This research investigates the impact of optimal pole number, in which a double-layer fractional-slot concentrated winding (FSCW) is employed. Therefore, there are not many slots per pole per phase combinations which are investigated to reduce the audible magnetic noise and vibration level on a low-speed, high-torque permanent magnet synchronous generator (PMSG) for a variable-speed-range analysis. The vibro-acoustic modeling of the PMSG is based on a semi-analytical subdomain model (SDM), in which the machine is run at variable speed and the natural frequencies are considered. The results and improvements of each machine are studied in both the electromagnetic and vibro-acoustic design aspects. Finally, the optimum pole number is proposed to reduce magnetic noise and vibrations with respect to the electromagnetics consequences. The SDM results are verified using both 3-D FEA and experimental tests with a very good agreement. This theoretical work is based on a series of SDMs that were implemented in simulation tools, MANATEE linked to MATLAB, and ANSYS Maxwell as 3-D FEA package, is employed to validate the results.

A. Analytical MMF Harmonic Analysis of Each Machine with Double-Layer FSCWs

The stator winding factor of PMSMs is studied for the fractional-slot concentrated windings (FSCW) with $q < 1$ which depends on the slot/pole numbers. The fundamental winding factor (k_{w1}) is reported in Table I. The q value is a fraction of the number of slots per pole per phase, the periodic or antiperiodic indicates the winding distribution as well. As the electromagnetic torque is a significant product of PMSMs and is proportional to the value of k_{w1}, therefore, a higher fundamental k_{w1}, when other sub-harmonics are as low as possible is preferred. To enhance a small k_{w1} in special machines, a higher current or coil turns are required which makes the machine more expensive.

Table 4.10.2 illustrates that the study investigates five different pole-pairs which affect the stator winding distribution of each machine to offer benefits of the double-layer FSCWs. The winding factor of five different slot/pole combinations, where each of those machines (1-5) have shown various winding layouts and fundamental winding factors. Machine No. 4 with 36 slots, 40 poles has the highest $k_{w1} = 0.945214$, and apparently the best combination. The Highest k_{w1} brings the greatest electromotive forces (EMFs) and highest average electromagnetic torque. Machine No. 1 has the minimum k_{w1}, which meant the lowest production of EMFs and torque. All five machines have a periodic winding distribution, and also assumed to be equal in the winding turns and magnet volume for an identical comparison [67].

Fig. 4.10.2.1 illustrates the winding layout of each three-phase machine, where the double-layer non-overlapping FSCW pattern is considered. Fig. 4.10.2.1(a) presents the winding pattern of machine No.1 with a winding layout of 'CA'AB'BA'AB'BC'CB'BC', Fig. 4.10.2.1(b) shows the winding pattern of machine No.2 with winding layout of 'CA'AB'BC'. Fig. 4.10.2.1(c) indicates the machine No. 3 winding the stator winding pattern with the following layout

'AA'AB'BB'BC'CC'CA'. Fig. 4.10.2.1(d) represents the wind pattern of machine No. 4 with a layout of 'BA 'AA'AA'AC'CC'CC'CB'BB'BB'. Fig. 4.10.2.1(e) depicts the stator winding pattern of machine No. 5 with the layout of 'BA'AA'AC'CC'CB'BB'. Because of the discrete position of a coil within the slots, there are space harmonics in the MMF distribution. Let v be the order of the MMF harmonic according to the two-pole MMF harmonic, also called the fundamental harmonic. Thus, the order of the main harmonics is $v = p$, where p is the number of pole pairs [73-74]. The number v is considered without a sign. It can be the only positive integer. The main harmonic is that harmonic whose order is the same of the number of the pole-pairs p. Only this main harmonic is synchronous with respect to the rotor. Conversely, all harmonics of a different order are asynchronous with the rotor. Therefore, since they cause a time-varying magnetic field, they induce currents in the rotor, which is one of the most significant reasons that induced eddy-current losses (mostly in the rotor) can be increased along with a permeance variation and PWM harmonics [75]. Synthesis of different slots/pole combinations with respect to the dimensions and an acceptable winding factor can be chosen in the design of FSCWs [67]. Next, to harmonics of higher order (fundamental) there are also lower order harmonics, which are known as sub-harmonics.

Fig. 4.10.2.2 illustrates the MMF behavior in the air-gap, which is enlarged for a better understanding in this graph. The fundamental or main harmonics $v_3 = p$ are synchronous with the rotor speed, where the sub-harmonic $v_1 < p$ occurs when the speed is greater than rotor speed. Whereas, whem the speed is lower than the rotor speed, positive or negative harmonics of $v_2 > p$ can appear as shown in the figure. The MMF harmonics rotate in the air-gap with various speeds. The mechanical speed of the generic v-th MMF harmonic in the stator reference frame can be calculated from [75]:

$$\omega_{vs} = \frac{\omega}{sign \ . \ v} \tag{4-44}$$

where *sign* is the sign function, and *sign* = +1 if the v–th harmonic rotates in the same direction of the rotor, on the other hand, *sign* = −1 if the v–th harmonic rotates in the opposite direction. The sign function is defined in [75-76]; harmonics that correspond to the values of:

$$v = 1 + 3k, \qquad where: k = 0, 1, 2, ... \tag{4-45}$$

have the positive sign, while harmonics that correspond to the value of [16]:

$$v = 2 + 3k, \qquad where: k = 0, 1, 2, ... \tag{4-46}$$

have the negative sign, where k is always a positive integer.

Table 4.10.2.1 Double-layer FSCW characteristics.

Slot/ pole number		Slots/poles combination	q	Periodic number of winding	t	k_{wl} (pu)
1	36/20	9/5	3/5	12	2	0.735246
2	36/24	3/2	1/2	12	12	0.866025
3	36/30	6/5	2/5	6	3	0.933013
4	36/40	9/10	3/10	4	4	0.945214
5	36/42	6/7	2/7	6	3	0.933013

A positive sign is conventionally assigned to the series containing the main harmonic ($v = p$). The MMF speed with respect to the rotor is computed as [75-76]:

$$\omega_{rv} = 2\pi f \left(\frac{sign}{v} - \frac{1}{p} \right) \tag{4-47}$$

The rotating MMF harmonics induce in the rotor an EMF at the frequency f_{rv}. Such a frequency can be expressed as a function of the harmonic order ν as [75-76]:

$$f_{rv} = v \frac{\omega_{rv}}{2\pi} = f \left| sign - \frac{v}{p} \right| \tag{4-48}$$

Fig. 4.10.2.2 presents the total air-gap MMF waveforms of each machine with the double-layer non-over lapping FSCWs as a function of space, in addition, the harmonic content over the wavenumber of each studied PMSG is individually shown. Machine No. 1 with total harmonic distortion (THD) of 0.492736 is presented in Fig. 4.10.2.2(a). Machine No. 2 with a larger THD of 0.556982 over each wavenumber is seen in Fig. 4.10.2.2(b). Machine No. 3 with the largest THD of 0.764972 is indicated in Fig. 4.10.2.2(c). Machine No. 4 as the second largest THD, 0.731797 is reported in Fig. 4.10.2.2(d). Machine No. 5 (shown in Fig.

4.10.2.2(e)) with THD of 0.700293 reinforces that there is no linear relationship between the pole-pairs number and the THD of the total air-gap MMFs [67].

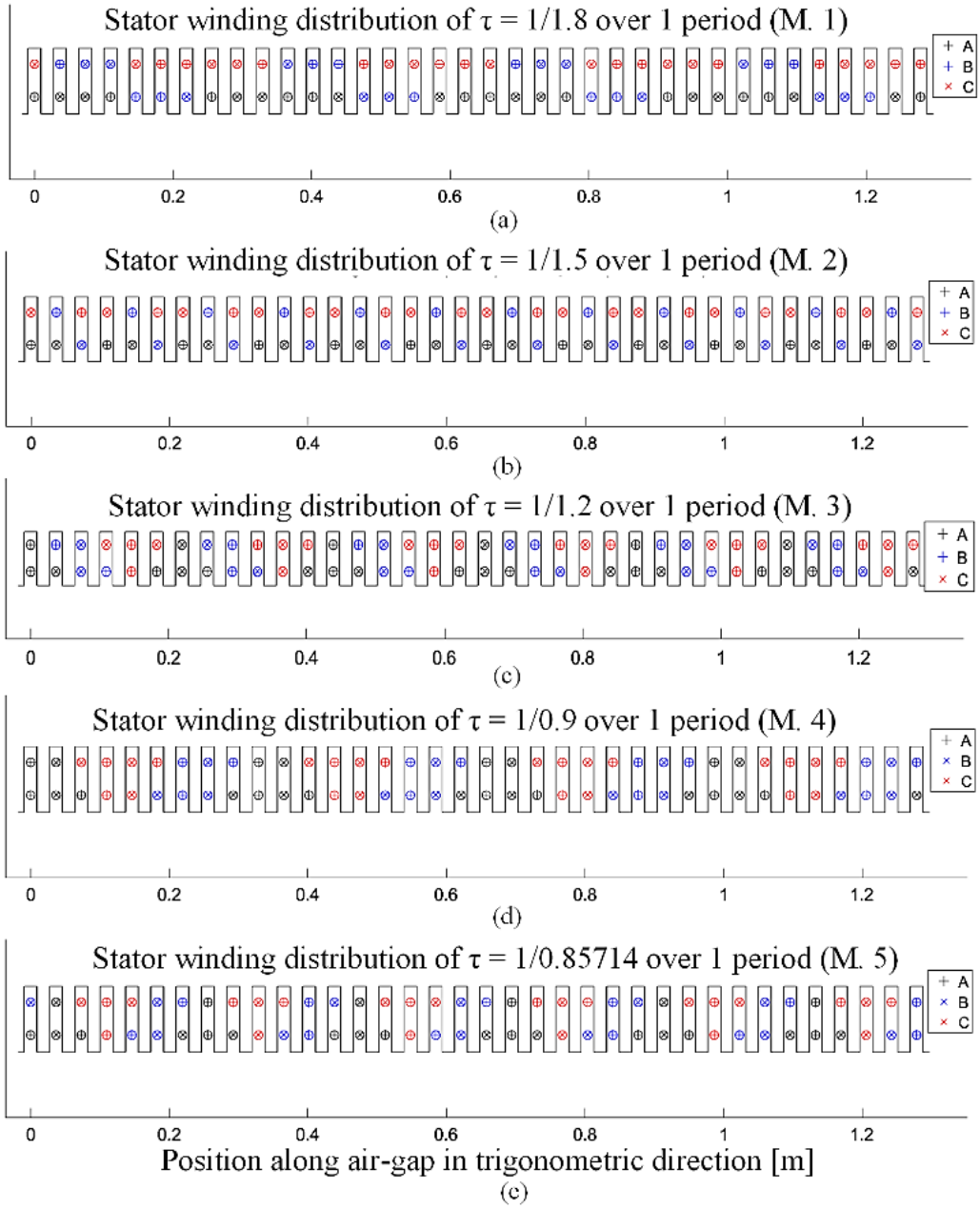

Fig. 4.10.2.1. Double-layer non-overlapping FSCW distribution of each studied machine, a) Machine No.1, b) Machine No. 2, c) Machine No. 3, d) Machine No. 4, and e) Machine No. 5.

B. Multi-slice Subdomain Method (SDM) Definition of PMSG

To compute the vibro-acoustic performance of all studied PMSGs, the semi-analytical SDM of the PMSG with an outer rotor and surface mounted topology is discussed in this section. The SDM is based on the analytical resolution of Maxwell equations, which is possible under several assumptions (details can be seen in [46] [66] and [74]). These assumptions are summarized as follows:

1. The problem is resolved into physical subdomains with polar or Cartesian geometry, with uniform magnetic relative permeability and including a magnetic source, either current density or magnet.
2. The problem is calculated using a 2-D Magnetic Vector Potential (MVP) formulation in each subdomain, meaning 3-D effects such as end-effect or skewing are ignored. The magnetic flux density B derives from the MVP A by $B = \mathrm{rot}(A)$, and thus, it is continuously known inside the subdomain (without mesh discretization).
3. The problem is calculated by a steady-state solver (rotor mechanical speed Ω is constant) for each independent and

successive time-step.

4. Stator and rotor iron cores are infinitely permeable. Regarding the continuity equations, the tangential field is null at each iron interface (flux lines are orthogonal to the surface), which enables to set the iron cores as external boundaries of the problem. The MVP and the flux density distributions are consequently not known in iron cores and magnetic saturation is ignored.

Fig. 4.10.2.3 depicts the semi-analytical SDM of the studied outer rotor surface mounted PMSG, in which the following expressions are defined.

$$\frac{\partial A_{slot}}{\partial r} = 0 \tag{4-49}$$

$$\begin{cases} A_{slot} = A_{gap} \\ \dfrac{\partial A_{slot}}{\partial r} = \dfrac{\partial A_{gap}}{\partial r} \end{cases} \tag{4-50}$$

$$\nabla^2 \vec{A}_{slot} = \mu_0 \vec{J}_{slot} \tag{4-51}$$

$$\frac{\partial A_{slot}}{\partial \theta} = 0 \tag{4-52}$$

$$\frac{\partial A_{gap}}{\partial r} = 0 \tag{4-53}$$

$$\nabla^2 \vec{A}_m = \mu_0 \vec{\nabla} \Lambda \vec{M} \tag{4-54}$$

$$\frac{\partial A_m}{\partial r} = 0 \tag{4-55}$$

$$\begin{cases} A_m = A_{gap} \\ \dfrac{\partial A_m}{\partial r} + \mu_0 M_\theta = \dfrac{\partial A_{gap}}{\partial r} \end{cases} \tag{4-56}$$

$$\nabla^2 \vec{A}_{gap} = \vec{0} \tag{4-57}$$

where A_{slot}, A_{gap}, and A_{m} are magnetic vectors potential on the r and θ coordinates due to the presence of current in the slot, air-gap, and magnet, respectively. Vector J_{slot} denotes the current density in the slot. Δ is the offset in the tangential direction, M is the magnetization vector, μ_0 is the permeability of vacuum. Λ is the air-gap permeance per unit area [46] [66] and [74].

By defining the transient magnetic field for low frequency based on Maxwell's equation as follow:

$$\begin{cases} \nabla \times \dfrac{1}{\sigma_j} \nabla \times H_j + \dfrac{\partial B_j}{\partial t} = 0 \\ \nabla .\ B_j = 0 \end{cases} \tag{4-58}$$

The resulting magnetic noise originates from magnetostrictive and Maxwell forces at jth subdomain slice which are essentially produced by the stator winding and rotor magnet's harmonic magnetic field which, can be defined as:

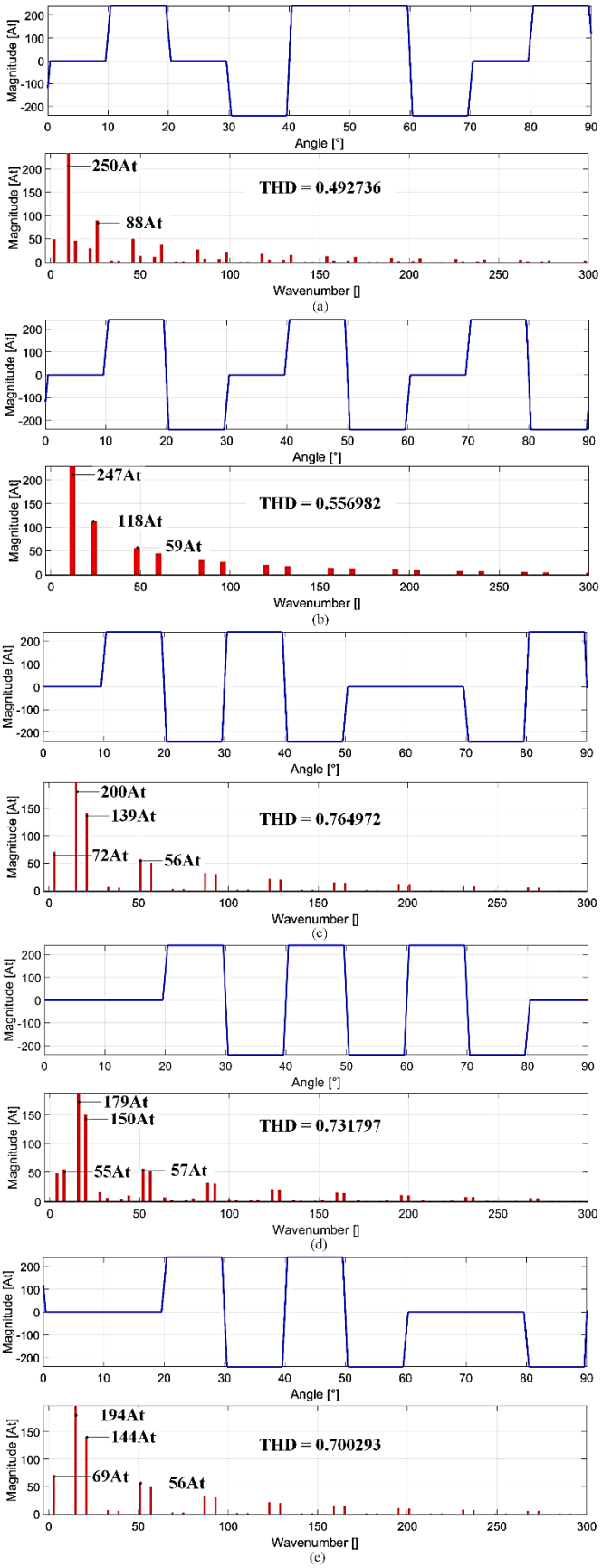

Fig. 4.10.2.2. Total air-gap MMF, and its harmonic content as function of space for different FSCWs pattern, a) Machine No.1, b) Machine No. 2, c) Machine No. 3, d) Machine No. 4, and e) Machine No. 5.

$$\begin{cases} p_{rj}(\theta,z)=\dfrac{1}{2\mu_0}\left(B_{rj}^2(\theta,z)-B_{\theta j}^2(\theta,z)-B_{zj}^2(\theta,z)\right) \\ p_{\theta j}(\theta,z)=\dfrac{B_{\theta j}(\theta,z).B_r(\theta,z)}{\mu_0} \end{cases} \tag{4-59}$$

Hence, the sound wave of a PMSG as a useful idealistic homogeneous medium can be given:

$$\frac{\partial^2 p}{\partial x^2}+\frac{\partial^2 p}{\partial y^2}+\frac{\partial^2 p}{\partial z^2}=\frac{1}{c^2}\frac{\partial^2 p}{\partial t^2} \tag{4-60}$$

The maximum sound power radiated by the PMSG due to magnetic vibrations can be also written as:

$$L_{pj}(f_{\max})=\frac{1}{2}Z_{0j}S_{cj}\sigma_{mj}(f)\left\langle v_{m\omega}^2\right\rangle v_{m\omega} \tag{4-61}$$

where Z_0 denotes the air acoustic impedance, S_c is the PMSG frame area, σ_m is the modal radiation factor. j denotes jth subdomain slice number. The maximum sound power level $L_{\omega j}$ can be computed using:

$$L_{\omega j}(f_{\max})=10\log_{10}\left(\sum_j\frac{W_{pj}(f_{\max})}{10^{-12}}\right) \tag{4-62}$$

The natural frequencies of the stator circumferential mode have been only chosen as an even value due to the even stator and rotor pole numbers, and thus, the Maxwell exciting force harmonics have been produced as only even spatial orders due to symmetry reasons by assimilating the stator to an equivalent ring. The breathing mode natural frequency f_0 can be defined:

$$f_0=\frac{1}{2\pi a}\sqrt{\frac{E_s}{K_{f_s}\Delta_m\rho_s}} \tag{4-63}$$

where a is the stator mean radius, K_{fs} is the stator stacking factor, ρ_s is the stator stack mass density, and Δ_m denotes the increasing mass because of the winding and teeth (details can be found in [55]).

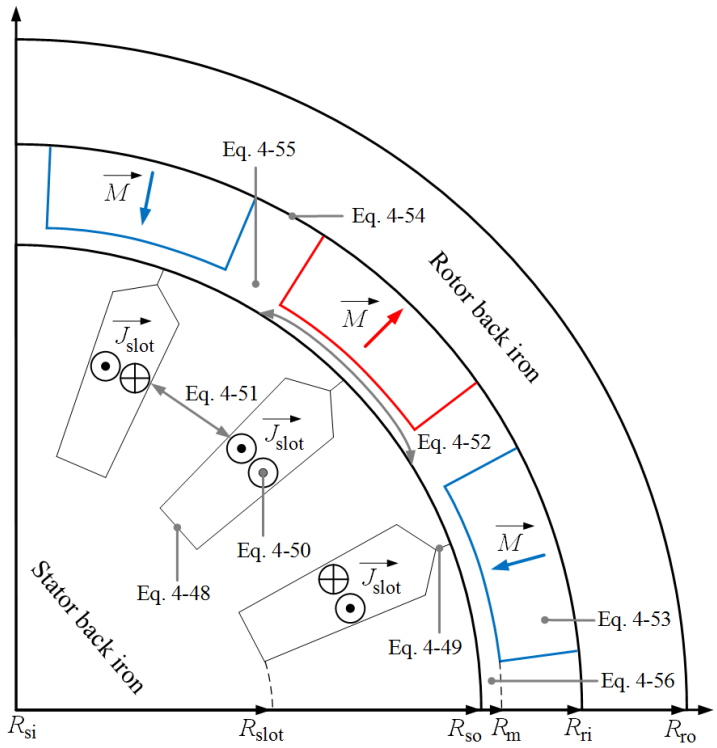

Fig. 4.10.2.3. The semi-analytical multi-slice SDM of the studied outer rotor PMSG.

C. Results and Discussion

In this section, the most impactful vibro-acoustic parameters which are influenced by each machine are discussed to determine the best possible pole-pairs number for this specific PMSG. The input data of the studied machine is presented in Table 4.10.2.2. The stator core contains 36 segmented teeth due to closed-slot modulation in order to reduce the amplitude of cogging torque significantly. The rotor consists of the different numbers of pole-pairs (20, 24, 30, 40, and 42) in each machine. These pole-pairs numbers are chosen based on the double-layer non-overlapping FSCWs patterns. This type of winding is selected because of numerous benefits and recent improvements such as manufacturability and modularity, increased flux weakening performance, and short-end windings. The number of stator slots is fixed to 36, because of weight and dimension restrictions. To obtain high performance non-overlapping FSCWs, 36 slots appears to be the best choice among other options. Regarding the outer and inner diameters of the generator, a larger number of slots than 36 could put the machine in a high risk of saturation, mainly in the teeth. Likewise, a smaller number of stator slots has weakened the electromagnetic performance of the PMSG with a low efficiency and power density. Moreover, other combination possibilities such as 24 slots resulted in zero mean EMF. The periodic or antiperiodic indicates the winding distribution. As the electromagnetic torque is a significant product of PMSMs and is proportional to the value of k_{w1}, therefore, a higher fundamental k_{w1}, when other sub-harmonics are as low as possible is preferred. To enhance a small k_{w1} in special machines, a higher current or coil turns are required which makes the machine more expensive.

The back irons are made of isotropic M400-50A non-orientated magnetic lamination steel with 7650 kg.m^{-3}. The elastic characteristics of the lamination is E_x = 215MPa, E_y = 215MPa, and E_z = 80 MPa, besides, shear modulus is G_{xy} = 82.7 MPa, G_{yz} = 2MPa, and G_{zx} = 2Mpa. The Poisson ratio is defined as V_{xy} = 0.3, V_{yz} =0.03, and V_{zx} = 0.03. Additionally, equivalent cylinder thickness/radius ratio equals 0.048998, and equivalent cylinder length/radius ratio is 0.44543.

Table 4.10.2.1 illustrates that the study investigates five different pole-pairs which affect the stator winding distribution of each machine to offer benefits of the double-layer FSCWs. The winding factor of five different slot/pole combinations, where each of those machines (1-5) have shown various winding layouts and fundamental winding factors. Machine No. 4 with 36 slots, 40 poles has the highest k_{w1} = 0.945214, and apparently the best combination. The highest k_{w1} brings the greatest electromotive forces (EMFs) and highest average electromagnetic torque. Machine No. 1 has the minimum k_{w1}, which meant the lowest production of EMFs and torque. All five machines have a periodic winding distribution, and also assumed to have equal winding turns and magnet volume for an identical comparison. These five machines are selected based on the defined optimization constraints for the design and experiment stage such as: a) satisfying q for only non-overlapping double-layer FSCW; b) electromagnetic capability, in which efficiency g_1 (x) = 0.90 - $\eta \leq 0$, output power g_2 (x) = 1200 - $P_o \leq 0$, current density g_3 (x) = J_c - 4 $\leq$ 0 (at rated speed of 150 rpm). From all possible pole numbers, only these five machines could successfully satisfy the design constraints.

Each design case was simulated using variable speed SDM, via MANATEE. For the all studied PMSGs, the PMs are made of NdFeB-N48 with a remanent flux density of 1.2 T, and the back irons are made of isotropic M400-50A non-orientated magnetic lamination steel [67].

Fig. 4.10.2.4 presents the structure-based influence of each machine with a various number of pole-pairs on the A-weighted sound power level $L_{p,max}$ magnitude in a variable speed analysis. The outer rotor structural modes are mostly characterized using the analogy with a cylindrical shell, whose structural modes can be labelled by (m,n), where m is the rank of the circumferential deflection and n is the rank of the longitudinal deflection All studied PMSGs have produced four deflection modes in common such as outer rotor structure mode (0,0), (4,0), (6,0) and (8,0), in which each of these modes indicates a different structure deflection. Machine No. 1 (Fig. 4.10.2.4(a)) has radiated a low $L_{p,max}$ by only 73.4 dBA via model (0,0), (4,0), and (8,0), if the machine operates under the ratings. At 435 rpm, the peak $L_{p,max}$ of 85 dBA can be seen. Fig. 4.10.2.4(b) shows how increasing the

Table 4.10.2.2. Geometrical input data of the studied PMSG.

Parameters	Description	Values	Units
l_s	Stack length	100	mm
R_{ri}/ R_{ro}	Rotor radiuses	217/ 230	mm
R_{si}/ R_{so}	Stator radiuses	115/ 209.5	mm
S_w	Slot width	15	mm
δ_g	Air-gap length	0.6	mm
S_d	Slot depth	50	mm
$Q_s/2P$	Stator slot/ poles	36/ 20, etc	
α_p	Pole pitch	0.55	
SP	Slot pitch	0.9	
μ_0	Vacuum permeability	$4\pi\times10^{-7}$	H/m
μ_s	Iron relative permeability	2500	
μ_{PM}	Magnet relative permeability	1.05	
μ_{air}	Air relative permeability	1	
B_{rm}	Magnet residual flux density	1.2	T

pole-pairs number affects the machine structure deflection by only mode (0,0). The maximum ASPL under the rated speed of 150 rpm is 38.7 dBA, which is a considerable increase of 34.7 dBA in comparison to the PMSG with 20 pole-pairs. A very high sensitivity of $L_{p,max}$ is apparent over the different pole-pairs number, even though this change is small. The $L_{p,max}$ radiated by machine No. 3 (Fig. 4.10.2.4(c)) is 53.4 dBA (under the rated speed of 150 rpm), from structure deflection modes (0,0), (4,0), and (8,0). Fig. 4.10.2.4(d) shows the maximum $L_{p,max}$ of 74.9 dBA originated by deflection modes (0,0),(4,0), and (8,0) for machine No. 4. Fig. 4.10.2.4(e) presents the modal contribution of deflection modes (0,0) and (0,6), in which the maximum ASPL under rated speed is 72.3 dBA.

Fig. 4.10.2.5 illustrates the operational deflection shape (ODS) based on the hammer method of each machine's outer rotor (a sinusoidally fed slotted PMSG without PWM time harmonics and rotor MMF space harmonics), only resulting from its structure deflection modes (m,n). To check the spatial order, the frequency and the propagation direction of pure slotting lines, the ODS analysis was run in a sinusoidal case (f_s = 52 Hz) on a 12-point mesh around the rotor frame median circumference. The accelerometer accuracy and the software features make it possible to visualize rotor structure movements at each frequency, even when it is subjected to an exciting force far from any resonance. Fig. 4.10.2.5(a) shows the ODS with counter-clockwise rotation (CCR) of machine No. 1 which is only caused by modes (0,0), (4,0), and (8,0), where the rotor and stator main slotting frequencies are Z_r*f_R = 60 Hz, and Z_s*f_R = 90 Hz. Fig. 4.10.2.5(b) presents the ODS with CCR originating from mode (0,0) on machine No. 2. The rotor and stator main slotting frequencies are 50 Hz, and 90 Hz. Fig. 4.10.2.5(c) represents the ODS with clockwise (CR) of machine No. 3 which is from mode (0,0) and (6,0), where the rotor and stator main slotting frequencies are 75 Hz, and 90 Hz. Fig. 4.10.2.5 (d) shows the ODSwith CCR of machine No. 4 originated by modes (0,0), (4,0), and (8,0), where the rotor and stator main slotting frequencies are 100 Hz, and 90 Hz. Fig. 4.10.2.5(e) depicts the ODS of machine No. 5 with CR by modes (0,0) and (6,0). The rotor and stator main slotting frequencies are 105 Hz and 90 Hz. It can be seen that each machine has its own specific ODS, regardless of the type of structure modes involved.

Fig. 4.10.2.6 presents the overall vibrations over variable speed of each PMSG model, in which the dashed line shows the rated speed of 150 rpm. As presented in the graph, machine No. 1 produces maximum vibration of 119.6 dB at 135 rpm. Machine No. 2 radiates the lowest vibration by 81.5 dB (max) at 150 rpm. Machine No. 3 with 30 poles radiates a maximum vibration of 100 dB at 150 rpm. The highest vibration is produced by machine No. 4 (40 poles) at 122 dB. A lower level of vibration is reported (108.6 dB at 130 rpm) by machine No. 5, where 42 poles are used. Above the rated speed, up to 1000rpm, the vibration level gradually increases, where machine No. 4 obtains 144 dB at 1000 rpm as the highest, while the lowest vibration of 115 dB at 573 rpm is radiated by machine No. 2.

Fig. 4.10.2.7 depicts A-weighted, maximum magnetic sound power level ($L_{p,max}$) sonograms of different numbers of pole-pairs under a variable speed range, evaluated in the post-processing stage. The electromagnetically- excited radial vibration illustration identifies whether, at variable speeds of the PMSG, the vibration resonances caused by magnetic forces occur during the operation or not. The designed PMSGs allow for operation under 150 rpm, 50 Hz, while it is a low-speed wind generator. In Fig. 4.10.2.7 (a), machine No. 1 with 20 pole-pairs has been simulated with 60.6 dBA at 150rpm, and 86.81 dBA (up to 1000rpm). The first major resonances occur around 48 Hz at 288 rpm (marked as 1), 95 Hz 563 rpm (marked as 2), 101 Hz at 605 Hz (marked as 3), and 115 Hz at 691 rpm, which are also shown by the red dashed lines. The while ellipsoids indicate the critical noisy areas (above 75 dBA). The main slotting magnetic forces wavenumbers of r = 0, 4, -4, 8, and -8 are produced in this machine. The noisy areas occur mostly under 1000 rpm. Fig. 4.10.2.7(b) presents the $L_{p,max}$ (or magnet noise) sonogram of machine No. 2 (36slots/ 24poles) as 40.62 dBA at 150 rpm and 76.89 dBA (up to 1000rpm), in which a considerably lower magnetic noise is radiated in comparison to machine No. 1. In addition, the main slotting magnetic forces wavenumber of r = 0 is generated in this machine. The main resonances are addressed by the red dashed lines at 111 Hz and 553 rpm (marked as 1), 138 Hz and 691 rpm (marked as 2), and 184 Hz and 921 rpm (marked as 3). As presented, the number of noisy spots are much lower than machine No.1. The noisiest areas are reported over 1200 rpm. Fig. 4.10.2.7(c) shows the variable speed magnetic noise sonogram of machine No. 3 (36slots/ 30poles) by with 58.5 dBA at 150rpm, and 70.55 dBA (up to 1000 rpm), in which the main resonances have occurred at 107 Hz and 295 rpm (marked as 1), 115 Hz and 446 rpm (marked as 2), 121 Hz and 535 rpm (marked as 3), and 143 Hz and 649 rpm (marked as 4). The main slotting magnetic forces wavenumbers of r = 0, 6, and -6 are involved in this machine. Fig. 4.10.2.7(d) indicates the $L_{p,max}$ sonogram of machine No. 4 (36slots/ 40poles) as 62.06 dBA at 150 rpm and 96.39 dBA (from 15 to 1000 rpm). The main slotting magnetic forces wavenumbers of r = 0, 4, and 8 are involved in this machine. There are two main resonances marked as 1 and 2, which have occurred at 172 Hz and 516 rpm, as well as 185 Hz and 554 rpm.

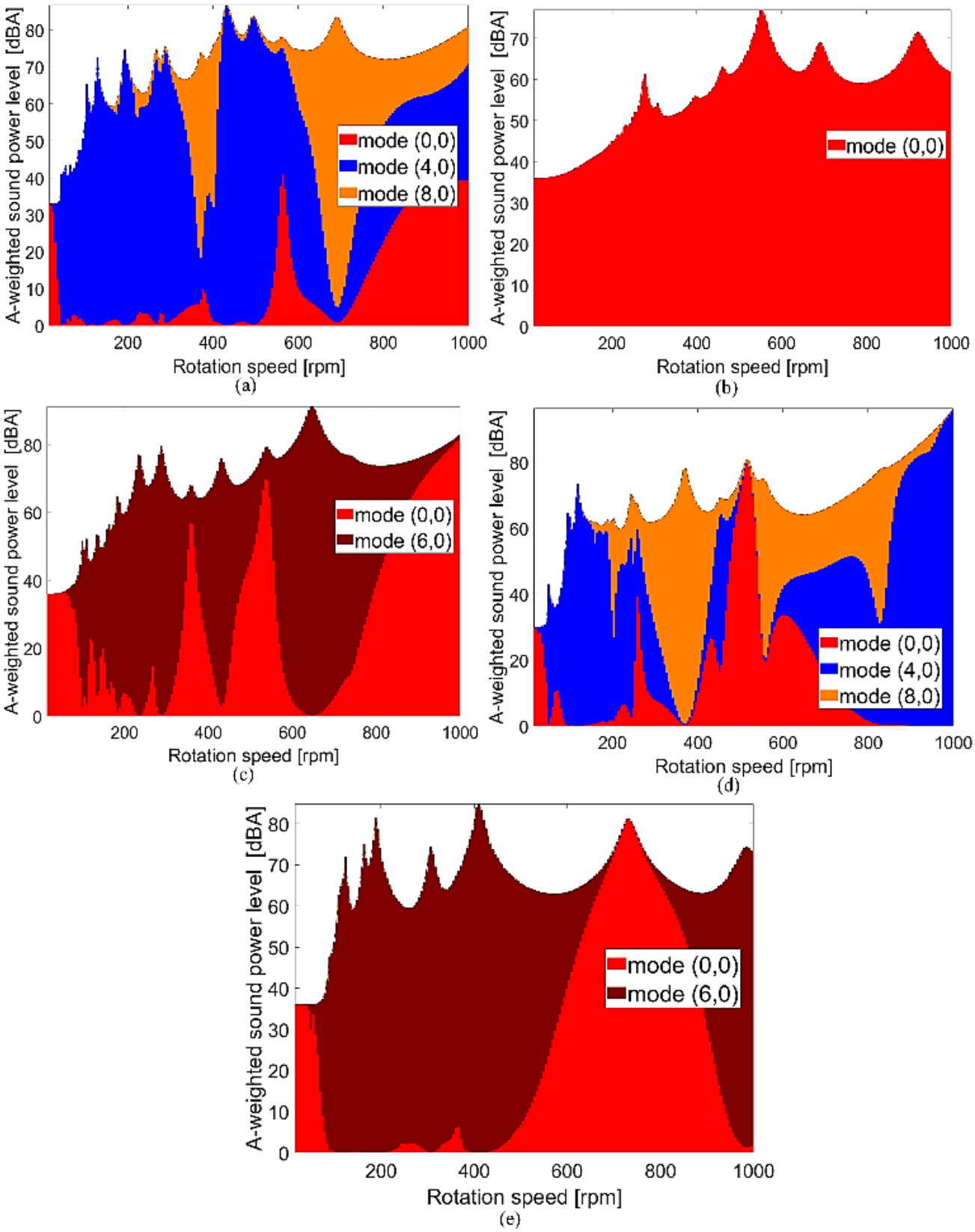

Fig. 4.10.2.4. Modal contribution of the machine structure on the sound power level radiation, a) Machine No.1, b) Machine No. 2, c) Machine No. 3, d) Machine No. 4, and e) Machine No. 5.

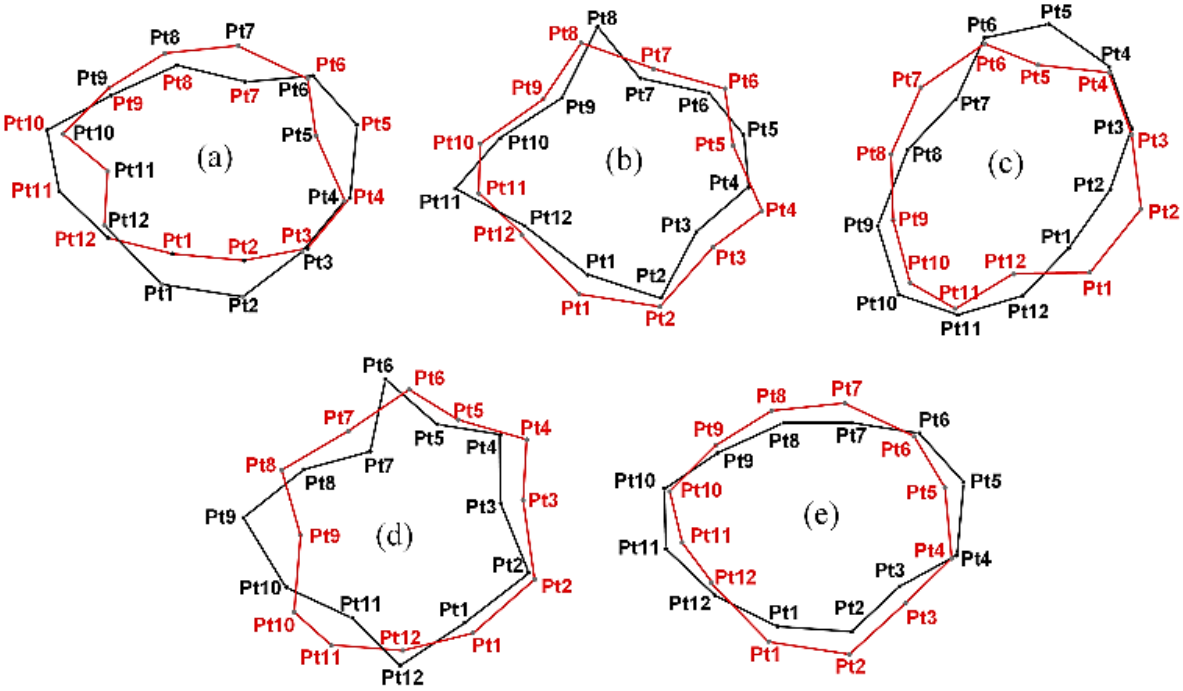

Fig. 4.10.2.5 Outer rotor ODSs of the outer rotor under slotting force waves, and their propagation direction (counter-clockwise rotation (CCR), and clockwise rotation (CR)), a) Machine No.1, b) Machine No. 2, c) Machine No. 3, d) Machine No. 4, and e) Machine No. 5.

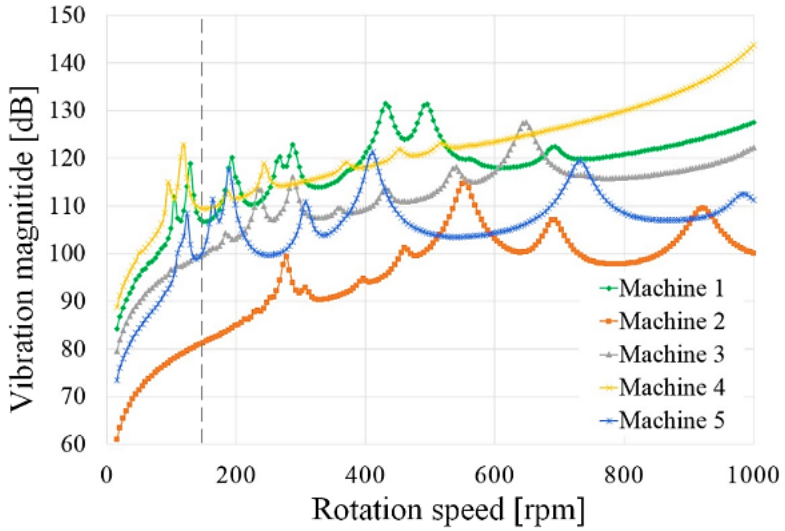

Fig. 4.10.2.6. Overall vibration under variable speed analysis, a) Machine No.1, b) Machine No. 2, c) Machine No. 3, d) Machine No. 4, and e) Machine No. 5.

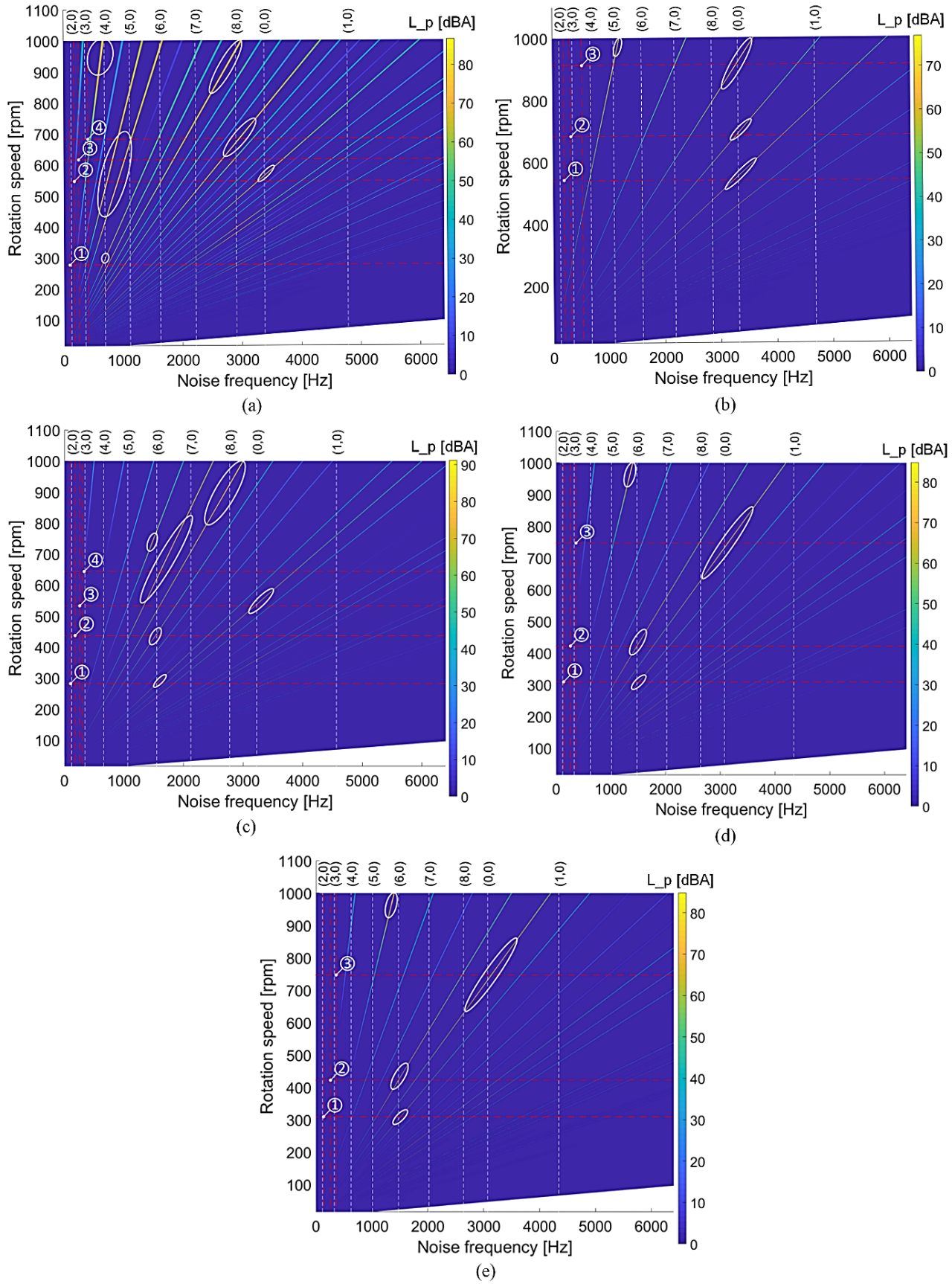

Fig. 4.10.2.7. A-weighted sound power level ($L_{p,max}$) sonograms of PMSGs under variable speed analysis and stator natural frequencies consideration, a) Machine No.1, b) Machine No. 2, c) Machine No. 3, d) Machine No. 4, and e) Machine No. 5.

Fig. 4.10.2.7(e) represents the magnetic noise of machine No. 5 (36 slots/ 42poles) as 62.24 dBA at 150 rpm and 84.85 dBA from 15-1000 rpm. The main slotting magnetic forces wavenumbers of r = 0, 6, and -6 are involved in this machine. The main resonances are addressed by the red dashed lines as a function of speed and frequency, which are 108 Hz and 308 rpm (marked as 1), 144 Hz and 410 rpm (marked as 2), and 256 Hz and 731 rpm (marked as 3). Also, major magnetic noises are radiated over 1000 rpm. The frequency response function of Maxwell stress wavenumbers (e.g. r = 2 meets the natural frequencies of the elliptical model (2,0)) of the PMSG.

Table 4.10.2.3 compares the outer rotor natural frequencies based on the modal damping coefficients approach of all the PMSG models (M.1 to M.5) with different pole numbers. The response of the outer rotor under magnetic forces has been quantified using the rotor (including magnets) excited through radial and tangential elementary forces. The rules of the switching frequency are based on [13, Eq. 10 and 11], these rules can either be applied prior to the PWM strategy setup. To reduce magnetic noise, the PMSG natural frequencies must be properly designed in terms of the switching strategy.

Table 4.10.2.4 presents a comparison of the three main vibro-acoustic and electromagnetic outputs of all the studied PMSG (M.1 to M.5). Among all the models, M. 1 has produced both the lowest electromagnetic (output power, torque, and efficiency) and above average vibro-acoustic outputs, 106.7 dB vibration and 60.5 dBA magnetic noise. M. 2 has radiated the lowest vibrations and magnetic noise (81.3 dB and 40.6 dBA), however, the output power, torque, and efficiency (91.6%) have been reduced. M. 3 has performed more reliable in both electromagnetic and vibro-acoustic outputs, where the magnetic noise is 58.5 dBA and efficiency of the PMSG, 94.7%. Therefore, the 30 pole-pairs number is a better choice than 20 and 24 pole-pairs. M. 4 has produced rather higher vibration and magnetic noise (109.44), but the electromagnetic outputs have a significantly very high efficiency of 97.1%. M. 5 shows still a very high electromagnetic performance, in which the efficiency of 96.408% is obtained. Also, the vibrations and magnetic noise radiations are lower than M. 1, and M. 4. In general, as the PMSG is not producing a critical level of vibrations and magnetic noise, M. 4 and M. 5 perhaps can be suitable because of the very high electromagnetic performance. The choice between these two machines (40 or 42 poles) is a tradeoff issue for the designer.

Table 4.10.2.3 Rotor natural frequencies of all the studied PMSGs.

m	**Unit**	**M. 1**	**M. 2**	**M. 3**	**M. 4**	**M. 5**
0	Hz	3379	3317	3188	3096	3072
1	Hz	4779	4690	4505	4379	4344
2	Hz	128	125	120	117	116
3	Hz	368	354	342	331	328
4	Hz	960	678	653	633	628
5	Hz	1112	1091	1018	1019	1011
6	Hz	1623	1593	1516	1488	1476
7	Hz	2221	2180	2109	2036	2020
8	Hz	2902	2849	2751	2661	2640

Table 4.10.2.3 Electromagnetic-vibro-acoustic results and comparison at rated speed.

Parameters	**M. 1**	**M. 2**	**M. 3**	**M. 4**	**M. 5**
Vibration [dB]	106.72	81.399	100	109.44	101.08
$L_{p,max}$ [dBA]	60.5	40.626	58.5	62.065	62.249
ASPL [dBA]	50.72	30.846	49.3	52.285	52.469
P_o [kW]	1.391	1.591	4.172	5.5159	4.9991
η [%]	90.6	91.6	94.71	97.163	96.408
T [N.m]	99	102	290.29	378.93	346.872

This work has studied a radial-flux surface mounted permanent magnet synchronous generator (PMSG) with outer rotor topology and an even integer slot number (in this case 36), which is wound with a double-layer non-overlapping FSCW. This slot number has produced even force wavenumbers (0, 2, 4, 6, and 8) of Maxwell force harmonics under a variable-speed computation of electromagnetically-excited noise to determine the predicted vibro-acoustic radiations. To find the optimal pole number, five PMSGs with double-layer non-overlapping FSCW and different pole numbers (such as 20, 24, 30, 40, and 42) were modeled. To compute the vibro-acoustic performance of each studied PMSG, all the simulations were completed using SDM. After a careful study on the MMF harmonic analysis, variable speed vibration spectrums and the magnetic noise while considering the natural frequencies; we have found the PMSG with 42 poles (M. 5) with a better performance in both electromagnetic and magnetic noise. Finally, the semi-analytical results from SDM on M. 5 have been validated using both 3-D FEA and experimental measurements.

5. Multi-Level-Objective Optimization for PMSG

In the process of optimizing electrical machines, the major objective is to define a set of key design parameters that include geometry, topology, and material choice. These appease specified design specifications and constraints, such as output power, which is observed as a major concern. In this paper, the research objectives focus on developing an application-oriented, design optimization method based on deterministic and optimal design methods due to their reliability, simplicity, and practicality. The robust design is investigated in different subject domains such as numerical analysis (FEA) and analytical models for the evaluation of performance. For decades, researchers are employing classic and modern optimization methodologies in the field of electrical machines and drive systems to improve efficiency [1-2]. To overcome this issue, various kinds of methods emphasize to find out the global optimum solely based on a typical torque/speed, or the flux weakening operation point [3]-[6]. However, it is difficult and accordingly rare to reinforce the sizing process optimization, considering the practical design details of permanent magnet synchronous generator (PMSG) and power electronic system for variable-speed applications such as wind generators [7], [8]. The application of response surface methodology (RSM) with different fashions has been recently carried out for electrical machines design optimizations [9]. In another paper, [10] presents design optimization for brushless dc permanent magnet motors for a hard disk driver to reduce cogging torque. This work is a good example of the feasibility of using RSM with typical central composite design (CCD) function to minimize the cogging torque. But, no other design functions were considered to challenge the accuracy of the fitting model. Moreover, the experimental verification was not considered.

Recently, surface-mounted PMSGs (SPMSG) have been employed for power generation to implement high-power, high-torque, high-efficiency, small-scale, and low-maintenance systems. The PM generator applied to conventional small-scale wind power generation has been designed with an exterior rotor topology because its structure has the desired advantage to generate power with higher output power density at low speeds which are often found in urban applications [11].

The DRSM, as a multi-level empirical modeling method, is investigated for the modeling and analysis of problems in which a number of variables (treatments) impact the observed result; and where the objective is to optimize the quantity of interest. This also avoids the time-consuming drawbacks of direct simulation which result in significant costs. The methodology is particularly applicable to the design of yields or processes, which can be sensitive to uncontrollable variables. A local and global sensitivity analysis is necessary to consider for the noise variables in the design. Then, a combination of settings can be applied to the control variables, which allows the process output to remain robust and flexible to changes in the noise variables.

In terms of the optimization process and yielded design, there are many approaches, which fit the robust design requirements. The mixed resolution robust design (known as MR-RD) has been observed to decrease the number of experimental runs and is compared to the FFD approach. A conceptual study of this surface methodology was reviewed by D. C. Montgomery [12]. G. Lei *et al.* [13] have studied how to apply multidisciplinary machine design optimization using RSM. A very good mathematical basic modeling of RSM in electrical machines has been presented in these references.

L. Jolly *et al.* [14] presented how the process of integrating a single level RSM with a genetic algorithm can be applied to a multi-objective optimization. This study dealt with a newer and common CCD function to estimate the optimum operation point at a PMSM. This work suffers a comparison among all design functions used, and also experimentally could be verified. Additionally, the coupled optimization design of permanent magnet motors using RSM and genetic algorithms (GAs) has been studied in order to optimize the torque and speed of the machine. However, we believe that a faster and accurate design procedure could be compared if different design functions were defined in the same dimensions. The lack of GA's contribution to the work and also experimental verification can be seen.

X. K. Gao *et al.* [15] investigated optimization using RSM with a zoom-in windows method and mixed-resolution CCD (MR-CCD) experiment design. A complex and modern design function, mixed-resolution CCD has been theoretically presented. The article lacks comparative results to show the advantages of the proposed robust optimization method.

In X. Liu and H. W. Fu's paper [16], a dynamic dual-RSM was studied to optimize copper losses, torque, and efficiency. All mentioned references were studies on PM synchronous machines. This article used also a complex model, where particle swarm and RSM (using radial basis function) methods are employed to improve torque and efficiency. Although, the work suffers an experimental investigation. In dual-RSM part, they used a radial basis function and a moving least-square approximation to improve the efficiency and decrease core and copper losses. In addition, the finding of the research was examined by goodness-of-fitting.

In this study, a novel approach is applied, where a modified Booth's multiplication algorithm utilizing simulated annealing (BA-SA) is used to develop the design optimization process of electrical machines. Simulated annealing (SA) is a methodology for solving unconstrained and bound-constrained optimization issues. SA results from statistical thermal physics and simulates the cooling process of a material from its melting-state at a high temperature to its crystallization-state at a low temperature. This physical process can be used to develop a new nonlinear optimization method, the SA algorithm, in which the model parameters are observed as state vectors and the objective function is observed as an energy function of the physical system. The nature of SA can be referred to as a heuristic Monte Carlo method with a higher efficiency and effectiveness [17-18].

In reference [19], Yang *et al*. investigates multi-objective optimisation design, and proposed a systematic process of a multi-objective sizing design of an axial-flux permanent-magnet motor for electric scooters. The preliminary design employed a zero-

dimensional (0D) model to determine the number of slots and poles and initial sizes of the motor according to the driving requirements of the scooter. The optimal design process used a 1D magnetic circuit model with an effective air-gap distribution function, where it's searching for a set of motor parameters that minimise or maximise motor electromagnetic performance such as back-EMF, torque, torque density and torque ripple. The research was finally verified through the 3D FEA along with experimental verifications.

G. Lei *et al.* proposes the system-level design optimisation method based on a robust approach, in which steady and dynamic performance achievements for the drive system and motor were reported. Additionally, the research was experimentally verified [20].

5.1 Sensitivity Analysis

Neglecting the fact that sensitivity analysis and optimizing the machine with all design parameters at a single level (at the same time) can result non-accurate with huge computing cost, while there are always some design parameters corresponding to the objectives weightier than others. In this study, we assumed that $f(x)$ will be the objective function, where η and P_{out} have to be targeted as objectives in different studies [20-21]. The sensitivity of the *i*th parameter, x_i in the point x_0 can be mathematically represented as follows:

$$S_i = \left.\frac{\partial f(x)}{\partial x_i}\right|_{x=x_0} \tag{5-1}$$

where S_i denotes the sensitivity of the objective function. Therefore, the bigger the $|S_i|$ is more sensitive objectives to the parameter x_i. The sensitivity of P_{out} and η have been evaluated by their defined equations with three variables A, B, C which are L_{PM} (length of PM), l_g (length of air-gap), and S_{width} (slot width) [20-21], respectively.

$$P_{out}(\gamma, I, A, B, C, N) = P_i - P_{Fe} - P_{Cu} - P_{mech} - P_{eddy} = 3.[E.I_q(\gamma) - (X_d(I) - X_q(I))I_d(\gamma)I_q(\gamma)] - 3RI^2 \tag{5-2}$$

And its sensitivity to each variable (for example L_{PM} should be calculated as given:

$$S(A) = \frac{d}{dA}P_{out}(\gamma, I, A, B, C, N) \times \frac{A}{P_{out}(\gamma, I, A, B, C, N)} \tag{5-3}$$

For the efficiency as the following:

$$\eta(\gamma, I, A, B, C, N) = \frac{|P_{out}(\gamma, I, A, B, C, N)|}{|P_{abs}(\gamma, I, A, B, C, N)|} \times 100 \tag{5-4}$$

where P_{abs} can be defined as:

$$P_{abs}(\gamma, I) = P_i + P_{Fe} + P_{Cu} + P_{mech} + P_{eddy} \tag{5-5}$$

Finally, we have:

$$S(A) = \frac{d}{dA}\eta(\gamma, I, A, B, C, N) \times \frac{A}{\eta(\gamma, I, A, B, C, N)} \tag{5-6}$$

Table 5.1.1 presents the local sensitivity of both objectives, as a brief conclusion from this table, the efficiency has obviously less sensitivity to treatments (A_1 to C_3), which stand for l_m, l_g, and S_{width}, respectively. the largest sensitivity on efficiency has been seen by $C = S_{width}$ treatment. On the other hand, S_{width} has been also reported as the largest effect on output power.

Additionally, the smallest effect of sensitivity on output power can be seen as approximately the same as the largest effect of sensitivity on efficiency.

Table. 5.1.1 Local sensitivity results.

Treatments	P_{out}	η
A_1	0.051	1.171×10^{-3}
A_2	0.056	1.277×10^{-3}
A_3	0.057	1.29×10^{-3}
B_1	-0.057	-1.449×10^{-3}
B_2	-0.155	-4.25×10^{-3}
B_3	-0.33	9.975×10^{-3}
C_1	1.06	0.02
C_2	1.614	0.019
C_3	1.84	0.014

Sensitivity analysis should be done as the first task prior to any optimization study. In another study, in which the controllable and noise variables are listed in Table 5.1.2, where x_1, x_2, and x_3 as controllable variables are magnetic thickness l_{m}, air-gap length l_{g}, as well as slot width S_{w}. z_1 and z_2 are uncontrollable variables or noises which because undesirable variability includes the under-cut angle of the stator tooth tip δ_{st} that varies between $25° \leq z_1 \leq 45°$ because of the tolerance of the manufacturing process, machining, as well as assembly. The second noise factor is screened due to its impact on the volume and magnetization distribution of magnets which are located in the air-gap between PMs ($L_{\text{a-pm}}$) that varies between $3° \leq z_2 \leq 5°$ [22].

Fig. 5.1.1 presents the local sensitivity (LS) of controllable and uncontrollable variables on the objectives of the optimization, where the most affected are efficiency, output power, iron loss, and back-EMF by design factors. The local sensitivity analysis benefits are noticed, such as good estimation similar to global sensitivity analysis due to the simplicity of the system (relationship of inputs and outputs), and considerably shorter time-consuming analysis [22].

Table 5.1.1 Design controllable variables.

Controllable design treatments		**Coded design treatments**		
All variables are normalized		-1	0	1
x_1	Magnet thickness (mm), l_{m}	5	6.5	8
x_2	Air-gap length (mm), l_{g}	0.5	1.17	2
x_3	Slot width (mm), S_{w}	8	12	15.5
z_1	Under-cut angle of the stator tooth tip (°), δ_{st}	25	35	45
z_2	Air-gap between PMs (°), $L_{\text{a-pm}}$	3	4	5

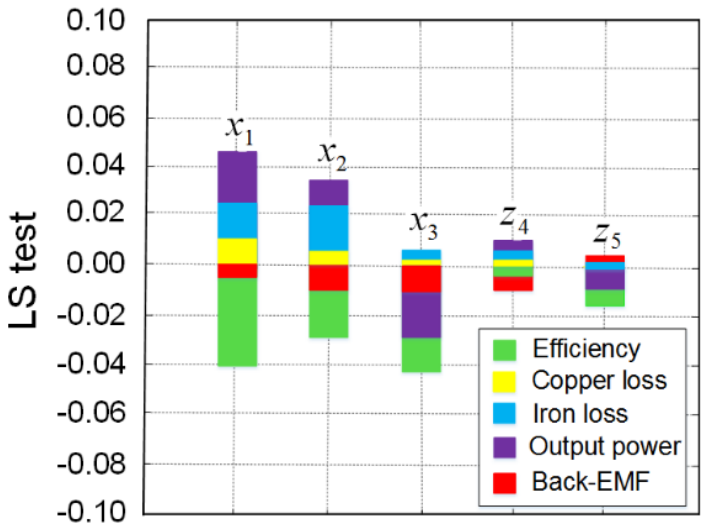

Fig. 5.1.1. Local sensitivity analysis of variables on the objectives.

In another study [24], the influence of the geometrical design parameters on the output power is examined by local/global sensitivity analysis (LSA/ GSA) in Table 5.1.2. To provide accurate results, each parameter is assumed to have four variations. The table presents the samples required for the data analysis of LSA.

In total, 33 samples are needed in this calculation, in which 32 points are for those four-variations of the initial sample "0" and the eight parameters. The sensitivity order can be obtained from the data as below:

$$|\rho| > |l_m| > |\delta_g| > |S_w| > |l_p| > |D_{si}| > |D_{ro}| > |N_c|$$

To set the optimization framework, the following four factors, ρ, l_{m}, δ_{g}, and S_{w} are considered significant factors.

Table 5.1.2 LSA and GSA results.

Par.	Amplitude variations of parameter					Sen.	Combined sen.
	-20%	-10%	0	10%	20%		
l_{m}	3.5	4.1	4.9	5.5	6.1	0.0995	0.1992
δ_{g}	1.2	1.4	1.6	1.8	2.0	0.0991	0.2017
ρ	3.8	4.3	4.8	5.4	6.2	0.1489	0.2081
S_{w}	2.3	2.7	3.2	3.6	4.0	0.0744	0.2055
D_{si}	19.6	21.4	23.7	24.5	27.6	0.0221	0.0791
D_{ro}	15.1	17.6	19.2	21.8	23.1	0.0115	0.0685
l_{P}	3.1	4.5	5.5	6.8	7.6	0.0498	0.2031
N_{c}	0.5	0.6	0.7	0.8	0.9	0.0093	0.0284

5.2 Analysis of Variance (ANOVA) for Un-Replicated Factorials

An assemblage of statistical models used to analyze the differences among group means and their associated procedures such as "variation" among and between groups which can be named as analysis of variance (ANOVA). In the ANOVA setting, the observed variance at a particular variable has to be partitioned into components attributable to different sources of variation [12] [22] [23].

In ANOVA, it is assumed that there is "a" treatment (a specific combination of factor levels) whose effect is to be compared with other treatments. The observed response (the output(s) of a process) from each of the "a" treatment is a random variable. A way to represent the observations from an experiment via a linear statistical model (called means model) [23] can be written as follows:

$$y_{ij} = \mu_i + \varepsilon_{ij} \begin{cases} i = 1, 2, \ldots, a \\ j = 1, 2, \ldots, n \end{cases} \tag{5-7}$$

where y_{ij}, μ_i, ϵ_{ij} are the *ij*th observation, the mean of the *ij*th treatment, and a random error component which integrates any other sources of variability in the experiment by consisting measurement, variability arising from un-controlled factors, differences between the experimental units to which the treatments have been applied, and the general background noise in the process [12] [23]. An alternative way to represent a model for the data is:

$$\mu_i = \mu + \Im_i \quad , i = 1, 2, \ldots, a \tag{5-8}$$

Despite to Eq. (5-7) and Eq. (5-8) will appear as effects model that is a linear statistical model [24] by:

$$y_{ij} = \mu + \Im_i + \varepsilon_{ij} \begin{cases} i = 1, 2, \ldots, a \\ j = 1, 2, \ldots, n \end{cases} \tag{5-9}$$

where μ denote a frequent parameter to any treatments (named as overall mean), and $\beth_i$ is an individualized parameter to the ith treatment [23] (which known as *i*th treatment effect). As long as $\beth_i$ is independent of ϵ_{ij}, therefore, the variance of any observation can be:

$$V(y_{ij}) = \sigma_{\Im}^2 + \sigma^2 \tag{5-10}$$

However, both forms of the model can be applicable, but the effect model has more widely involved in the experimental design literature.

The objectives of this study are to evaluate by hypotheses about the treatment means and to assess them. In hypothesis examining, the model errors have been assumed to be normally and independently distributed random variables with mean zero

and variance of σ^2 which is assumed to be constant for all levels of the factor. By indicating that all observations have mutually independent$y_{ij} \sim N(\mu + \text{ב}_i, \sigma^2)$.

In this study, all observations under the *i*th treatment can be defined [12] [23] through:

$$\begin{cases} \text{cov}(y_{ij}, y_{ij'}) = \sigma_{\text{ג}}^2 & j \neq j' \\ \text{cov}(y_{ij}, y_{ij'}) = 0 & i \neq i' \end{cases} \tag{5-11}$$

Therefore, the capable hypotheses can be defined as:

$$\begin{cases} H_0 : \sigma_{\text{ג}}^2 = 0 \\ H_1 : \sigma_{\text{ג}}^2 > 0 \end{cases} \tag{5-12}$$

As ANOVA derives through a partitioning of total variability to components, the total reformed sum of squares (SS_T) has been accounted as a measure of overall variability in the data [12] [15], by:

$$SST = \sum_{i=0}^{a}\sum_{j=0}^{n}(y_{ij} - \overline{y}_{..})^2 = \sum_{i=0}^{a}\sum_{j=0}^{n}[(\overline{y}_{i.} - \overline{y}_{..}) + (y_{ij} - \overline{y}_{i.})]^2 \tag{5-13}$$

The difference between the grand average and the observed treatment averages have known as the measure of the differences between treatment means. Although, this caused only random error as long as that error exist the total reformed sum of squares (*SST*) can be re-written [12] [20] like

$$SST = SS_{treatments} + SSE \tag{5-14}$$

where the random error sum of squares can be given as below:

$$SSE = \sum_{i=1}^{a}\sum_{j=1}^{n}(y_{ij} - \overline{y}_{i.})^2 = \sum_{i=1}^{a}[\sum_{j=1}^{n}[(y_{ij} - \overline{y}_{i.})^2] \tag{5-15}$$

whereas, the quantities of $SS_{Treatments}$ $(as\ MS_{Treatments})$ and SSE $(as\ MSE)$ are [12]:

$$MS_{treatments} = \frac{SS_{treatments}}{a-1} \tag{5-16}$$

$$MSE = \frac{SSE}{N-a} \tag{5-17}$$

Finally, the expected values of these mean squares *E*(*MSE*) and $E(MS_{Treatments})$ can be calculated by:

$$E(MSE) = \sigma^2 \tag{5-18}$$

$$E(MSE) = \frac{1}{a-1}E(SS_{treatment}) = \frac{1}{a-1}E\left[\frac{1}{n}\sum_{i=1}^{a}(\sum_{j=1}^{n}\mu + \Im_i + \varepsilon_{ij})^2 - \frac{1}{N}(\sum_{i=1}^{a}\sum_{j=1}^{n}\mu + \Im_i + \varepsilon_{ij})^2\right] \tag{5-19}$$

In this study, the definition of six treatments have been considered, in which main treatments consist of length of PM (known as *A* treatment), air-gap (known as *B*), and slot width (as *C*). Moreover, the effect of each treatment on the others as AB, AC, and BC will be addressed. In addition, the results from combination design of experiments (DOE) for this calculation can be seen in Table. 5.2.1. Now, the effect of treatments on observations will be presented in Fig. 5.2.1-a to -i, and 5.2.6 on y_{L_d}, y_{L_q}, y_T, $y_{P_{output}}$, y_{λ_m}, y_{Eff}, $y_{P_{Fe}}$, y_{k_s}, and $y_{I_{LR}}$.

As Fig. 5.2.1-a illustrates among all main treatments only treatment *B* and the second-order interactions involving *B* have been seen with smaller effect on the objective (y_{L_d}) in comparison to treatments *A*, and *C*. Therefore, treatment *B* has not significant effect on this objective. In addition, the same resulting effect is valid for objective (y_{L_q}) as expected because of the SPM topology

of the generator (where $L_d = L_q$). In Fig. 5.2.1-c, it can be seen that resulting effect by the main treatment *B* and the second-order interactions involving treatment *B* have the largest effect on the objective (y_T) in compare to other main treatments *A* and *C*. From Fig. 5.2.1-d, it can be reported that the main treatments are *A* and *B* and the second-order interactions involving *A* and *B* have the largest and the most significant resulting effect on the objective ($y_{P_{out}}$). In Fig. 5.2.1-e, all main treatments *A*, *B*, and *C* approximately have a significant effect on the objective (y_{λ_m}), however, the treatment *B* and its second-order interaction involving *B* in comparison to other treatments have the biggest effect on the objective.

As it can be seen in Fig. 5.2.1-f, the main treatment *C* and its second-order interactions have the largest effect on the (y_{Eff}) objective. Thus, treatment *C* in compare to treatments *A* and *B* has more significant effect on the efficiency objective. In Fig. 5.2.1-g, the main treatment *B* and its second-order interactions involving *B* have the largest effect on the objective ($y_{P_{Fe}}$) in comparison to other treatments. As reported in Fig. 5.2.1-h, the main treatment *C* and its second-order interactions involving *C* have the largest effect on the objective (y_{k_s}) in compare to other treatments. In Fig. 5.2.1-i, we can see that the main treatment *C* and its second-order interactions involving the largest effect on the objective ($y_{I_{LR}}$) in comparison to other treatments.

The main treatment *A* and its second-order interactions involving only a small effect on the objectives especially on the efficiency in compare to *B* and *C*. As this analysis returns and error because of objective (y_1) which is un-replicated. However, since treatment "*A*" also is not that significant, some runs are duplicates as far as treatments *B*, *C* are concerned. In fact, all three variables (*A*, *B*, *C)* with 2^3 design matrix contains a duplicate of the (*B*, *C*) 2^2 design matrix when *A* has been seen not significant. Now, by calling a full-factorial function to create a 2^2 design matrix, then the names of treatments will change to *A* and *B* from *A*, *B*, and *C* and the results from DOE will fit a 2^2 design matrix instead of 2^3 design matrix. Thus, from that calculation Table. 5.2.2 can be reported. Also, based on the random effects model in ANOVA, if $\sigma_\tau^2 = 0$, any treatments can be identical; but if $\sigma_\tau^2 = 0$, variability exists among treatments. As $SS_{residual}/\sigma^2$ has been distributed as chi-square with $N - a$ degrees of freedom (DF) and also under the null hypothesis ($SS_{regression}/\sigma^2$) has been distributed as chi-square with $a - 1$ DF. Base on the null hypothesis, the $F - value$ ratio [24] can be calculated by both DFs as:

$$F = \frac{\frac{SS_{regression}}{a-1}}{\frac{SS_{residual}}{N-a}} = \frac{MS_{regression}}{MS_{residual}} \tag{5-20}$$

In addition, an important statistic to expresses the proportion of the variation of y_i by fitted-model and FEA data for the mean of $\overline{y}$, given:

$$R^2 = \frac{SS_{regression}}{SST} = \frac{\sum_{i=1}^{n}(\hat{y}_i - \overline{y})^2}{\sum_{i=1}^{n}(y_i - \overline{y})^2} \tag{5-21}$$

As the initial treatments *A*, and *B* have been seen significant at the 5% level since their *F*-values are larger than their critical *F*-value for L_d, L_q, Eff, k_s, and I_{LR} objective. This analysis of variance reinforces the subjective conclusion derived from the effects plot. On the other hand, the initial treatments *A*, and *B* are no important as long as their *F*-values are smaller than their critical *F*-values (at 5% level) for T, P_{out}, $\boldsymbol{\lambda_m}$, and $P_{\boldsymbol{Fe}}$ objectives.

ANOVA has been performed to examine how good the fitted-model is able to predict the response in any observation points and for this purpose $SS_{treatments}$, F-value, and R^2-value which are belonged the variations of the response were calculated.

Table. 5.2.1 Coded DOE design results for ANOVA calculation.

A	B	C	coded			L_d (H)	L_q (H)	T (Nm)	P_{out} (W)	λ_m (Vs)	Eff (%)	P_{Fe} (W)	k_s	I_{LR} (A)
5	0.5	8	-1	-1	-1	0.4853	0.4852	343.407	460.8051	1.8685	85.4256	11.1114	0.1594	63.9943
5	0.5	15.5	-1	-1	1	0.4754	0.4753	305.5633	434.1385	1.6548	90.4497	12.0779	0.6063	127.9572
5	2	8	-1	1	-1	0.4816	0.4816	269.2391	348.5931	1.4709	82.4253	7.0071	0.1606	64.1715
5	2	15.5	-1	1	1	0.4717	0.4716	261.88	368.9583	1.4239	89.6923	8.7393	0.6139	128.3321
8	0.5	8	1	-1	-1	0.4787	0.4786	331.2973	442.7655	1.8044	85.0817	10.2119	0.1599	64.073
8	0.5	15.5	1	-1	1	0.4687	0.4687	305.1288	433.5903	1.6527	90.4642	11.9874	0.6096	128.1236
8	2	8	1	1	-1	0.4778	0.4778	302.7734	399.6545	1.6515	84.0325	8.6212	0.1606	64.1715
8	2	15.5	1	1	1	0.4678	0.4678	287.724	407.6715	1.5609	90.2016	10.6216	0.6139	128.3321

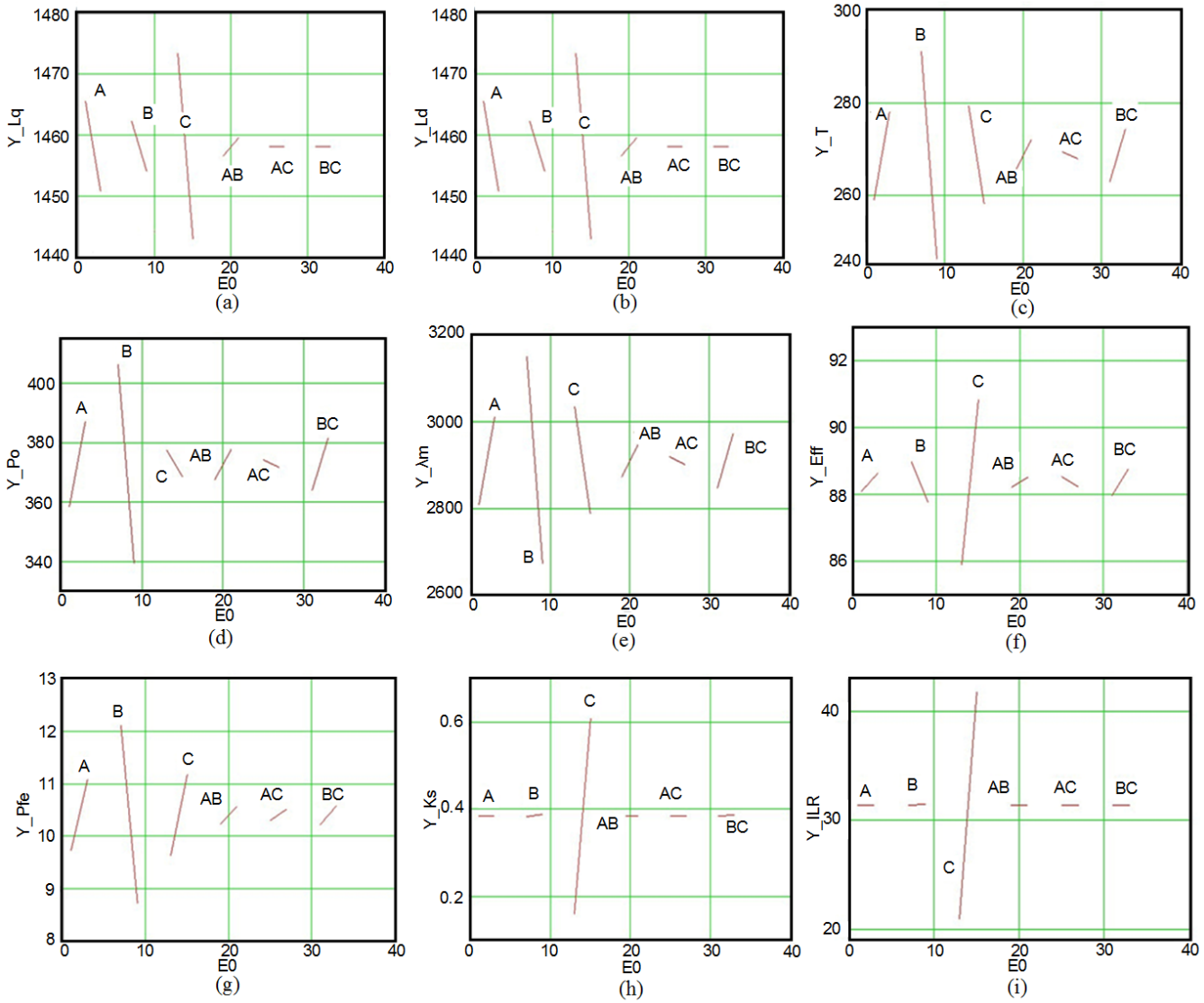

Fig. 5.2.1 Overall effect of each treatments on a specific objective, as a) L_d, b) L_q, c) T, d) P_{out}, e) λ_m, f) Eff., g) P_{Fe}, h) k_s, and i) I_{LR}.

Table. 5.2.2 ANOVA results for L_d objective with 5% level, and critical F-value 7.709.

Source	Sum of Squares	DF	Mean square	F-value	R^2-value
A	438.511	1	438.511	11.276	0.028
B	$1.857*10^3$	1	$1.857*10^3$	47.76	$2.3*10^{-3}$
AB	$3.725*10^{-9}$	1	$3.725*10^{-9}$	$9.58*10^{-11}$	1
Error	155.549	4	38.887	-	-
Total	$2.451*10^3$	7	-	-	-

Table. 5.2.3 ANOVA results for L_q objective with 5% level, and critical F-value 7.709.

Source	Sum of Squares	DF	Mean square	F-value	R^2-value
A	435.034	1	435.034	11.398	0.028
B	$1.857*10^3$	1	$1.857*10^3$	48.661	$2.221*10^{-3}$
AB	0	1	0	0	1
Error	152.667	4	38.167	-	-
Total	$\mathbf{2.445*10^3}$	**7**	**-**	**-**	**-**

Table. 5.2.4 ANOVA results for T objective with 5% level, and critical F-value 7.709.

Source	Sum of Squares	DF	Mean square	F-value	R^2-value
A	739.249	1	739.249	0.67	0.459
B	898.585	1	898.585	0.815	0.418
AB	4.668	1	4.668	$4.232*10^{-3}$	0.951
Error	$4.412*10^3$	4	$1.103*10^3$	-	-
Total	$6.054*10^3$	7	-	-	-

Table. 5.2.5 ANOVA results for P_{out} objective with 5% level, and critical F-value 7.709.

Source	Sum of Squares	DF	Mean square	F-value	R^2-value
A	$1.661*10^3$	1	$1.661*10^3$	0.672	0.458
B	162.605	1	162.605	0.066	0.81
AB	13.249	1	13.249	$5.36*10^{-3}$	0.945
Error	9.888	4	$2.472*10^3$	-	-
Total	$1.173*10^4$	7	-	-	-

Table. 5.2.6 ANOVA results for λ_m objective with 5% level, and critical F-value 7.709.

Source	Sum of Squares	DF	Mean square	F-value	R^2-value
A	$8.313*10^4$	1	$8.313*10^4$	0.67	0.459
B	$1.213*10^5$	1	$1.213*10^5$	0.978	0.379
AB	662.953	1	662.953	$5.343*10^{-3}$	0.945
Error	4.964	4	$1.241*10^5$	-	-
Total	$7.015*10^5$	7	-	-	-

Table. 5.2.7 ANOVA results for Eff objective with 5% level, and critical F-value 7.709.

Source	Sum of Squares	DF	Mean square	F-value	R^2-value
A	0.62	1	0.62	0.551	0.499
B	48.936	1	48.936	43.454	$2.743*10^{-3}$
AB	0.179	1	0.179	0.159	0.71
Error	4.505	4	1.126	-	-
Total	54.24	7	-	-	-

Table. 5.2.8 ANOVA results for k_s objective with 5% level, and critical F-value 7.709.

Source	Sum of Squares	DF	Mean square	F-value	R^2-value
A	0	1	0	0	1
B	0.405	1	0.405	$2.738*10^4$	$8.003*10^{-9}$
AB	0	1	0	0	1
Error	$5.92*10^{-5}$	4	$1.48*10^{-5}$	-	-
Total	0.405	7	-	-	-

Table. 5.2.9 ANOVA results for I_{LR} objective with 5% level, and critical F-value 7.709.

Source	Sum of Squares	DF	Mean square	F-value	R^2-value
A	$-1.819*10^{-12}$	1	$-1.819*10^{-12}$	$-3.963*10^{-10}$	1
B	875.134	1	875.134	$1.907*10^5$	$1.65*10^{-10}$
AB	$-1.819*10^{-12}$	1	$-1.819*10^{-12}$	$-3.963*10^{-10}$	1
Error	0.018	4	$4.59*10^{-3}$	-	-
Total	875.152	7	-	-	-

5.3 Response Surface Methodology (RSM)

Response surface methodology (RSM) has been defined as a collection of mathematical and statistical techniques practical to the modeling and analysis of issues, in which a response of interest has affected via a number of variables and the objective is always to optimize this response (quantity of interest), where a single or multi-level RSM (MRSM) with full factorial or any other design will be considered to achieve the most optimum response. In mathematical terms, a mathematical interaction between the response and the level of the factors has assumed to affect that is out of reach as long as the fundamental phenomena is too complex [12] [13] [19-20]. In this study, we have used new design functions to improve the accuracy of the model. There are two studies have done respect to response surface method. One to optimize output power and cost of the material used [20]. Another to maximize the efficiency of the PMSG [19]. In each individual study, we have used a new design function to deal with RSM.

An alternative technique by regarding to that the whole process named a black box in order to observe the response for the different level of the factors, where an estimation of the interaction between the response and the factors will be involved through a regression analysis of the data.

As the model will integrate a curvature in the system to approximate the response, this study requires the second-order polynomial models [12] [14] [19] as given:

$$y = \beta_0 + \sum_{i=1}^{k} \beta_i x_i + \sum_{i=1}^{k} \beta_{ii} x_i^2 + \sum_{i<j} \sum \beta_{ij} x_i x_j + \varepsilon \tag{5-22}$$

where ϵ stands for the noises (or errors) observed in the response y. Another matrix is shown as [12-14]:

$$x = \begin{bmatrix} x_1 \\ x_2 \\ \vdots \\ x_k \end{bmatrix}, \quad b = \begin{bmatrix} \hat{\beta}_1 \\ \hat{\beta}_2 \\ \vdots \\ \hat{\beta}_k \end{bmatrix}, \quad \& B = \begin{bmatrix} \hat{\beta}_{11} & \hat{\beta}_{12}/2 & \cdots & \hat{\beta}_{1k/2} \\ & \hat{\beta}_{22} & \cdots & \hat{\beta}_{2k/2} \\ & & & \vdots \\ sym. & & & \hat{\beta}_{kk} \end{bmatrix} \tag{5-23}$$

b represents a $(k \times 1)$ vector of the first-order regression coefficients and B shows a $(k \times k)$ symmetrical matrix that consists of pure quadratic coefficients ($\hat{\beta}_{ii}$) in main diagonal elements and for off-diagonal elements, one-half the mixed quadratic coefficients ($\hat{\beta}_{ij}, i \neq j$)[12-14] [22].

In continue, the use of fitted models for each treatment will be discussed to see how accurately relate the model of the SPMSG to the design variables. In this study, the experimental data used to fit the polynomials have merely been provided by FE analysis. The procedure of the first-level RSM can be reported by below general flowchart (as Fig. 5.3.1), where the efficiency is assumed to be the objective.

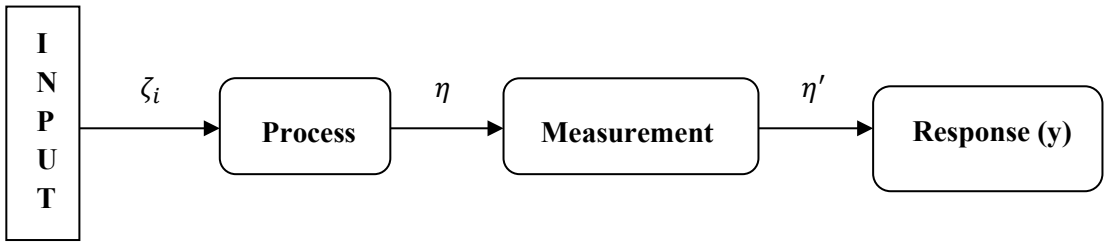

Fig. 5.3.1 General perspective of RSM flowchart.

where the yield of work relies on the response (as output), and the pure response can be achievable through η (the output of process block), in which this parameter has a few influences that have been donated via treatments ζ_i (input block), and base on the number of treatments, a n-dimensional space can be defined. The η is the pure response but not the true response. Thus, the true response η' consists of an experimental error (or noise) known as ε_{exp} which is given by the measurement block with a variance (σ^2) [14]. The observation of the response can be given as:

$$y = \eta' = \eta + \varepsilon_{\exp} = f(\zeta_1, \zeta_2, \zeta_3) + \varepsilon_{\exp}, \quad with \quad V(y) = \sigma^2 \tag{5-24}$$

However, many designers assumed that ε_{exp} is a random variable with zero mean and neglect it.

First, the choice of the region where the trend of the response is of interest. Second, a normalization on treatments is needed in order to eliminate unit's differences and stop creating rounding errors by next regression analysis. So, each treatment (ζ_i) can be coded with a variable (x_i) via its maximum and minimum [13-15] as follows:

$$x_i = \frac{\zeta_i - \overline{\zeta_i}}{\Delta\zeta_i} \tag{5-25}$$

And:

$$\overline{\zeta_i} = \frac{\zeta_{i_{\max}} + \zeta_{i_{\min}}}{2} \quad and \quad \Delta\zeta_i = \frac{\zeta_{i_{\max}} - \zeta_{i_{\min}}}{2} \tag{5-26}$$

Based on Eq. (5-22), the model of the observed response with three treatments (variables) is:

$$y = \beta_0 + \beta_1 x_1 + \beta_2 x_2 + \beta_3 x_3 + \beta_{12} x_1 x_2 + \beta_{13} x_1 x_3 + \beta_{23} x_2 x_3 + \beta_{11} x_1^2 + \beta_{22} x_2^2 + \beta_{33} x_3^2 + \varepsilon \tag{5-27}$$

where β_i, β_{ii}, and β_{ij} are constant coefficients which should be estimated by calculation. In terms of simplification of Eq. (5-27), the equation can be re-written as:

$$y = [x]^T.[\beta] + \varepsilon \tag{5-28}$$

$$[x]^T = \begin{bmatrix} 1 & x_1 & x_2 & x_3 & x_1x_2 & x_1x_3 & x_2x_3 & x_1^2 & x_2^2 & x_3^2 \end{bmatrix} \tag{5-29}$$

$$[\beta]^T = \begin{bmatrix} \beta_0 & \beta_1 & \beta_2 & \beta_3 & \beta_{12} & \beta_{13} & \beta_{23} & \beta_{11} & \beta_{22} & \beta_{33} \end{bmatrix} \tag{5-30}$$

where $[x]$, and $[\beta]$ are the point in which the response should be expected and the vector of coefficients, respectively. In this study coded value of treatments (variables) can be seen by Table. 5.3.1 and their points in 3-D space in where the response (optimum point) will be observed is shown in Fig. 5.3.2.

Table. 5.3.1 Coded treatments.

Coded values	l_m	l_g	S_{width}
-1	8	2	8
0	6.5	1.1667	12
1	5	0.5	15.5

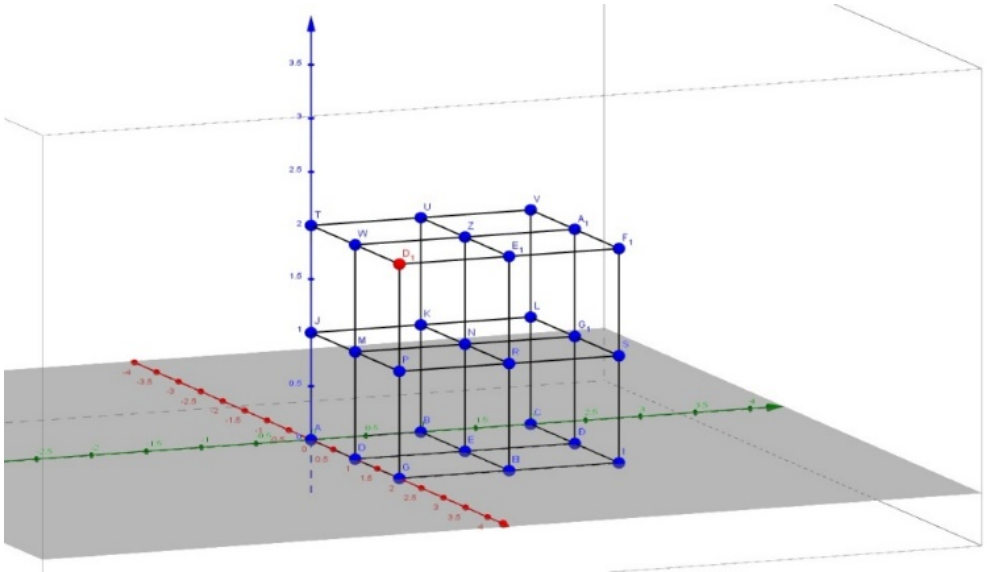

Fig. 5.3.2 Generated cube from first-level RSM, in which red point shows the second cube center point.

Base on Eq. (5-25), and (5-26), where $-1 \le x_i \le$, we have:

$$\begin{cases} x_1 = \dfrac{\zeta_1 - \overline{\zeta}_1}{\Delta\zeta_1} = \dfrac{\zeta_1 - 5}{1.5} \\ x_1 = \dfrac{\zeta_2 - \overline{\zeta}_2}{\Delta\zeta_2} = \dfrac{\zeta_2 - 1.25}{0.75} \\ x_1 = \dfrac{\zeta_3 - \overline{\zeta}_3}{\Delta\zeta_3} = \dfrac{\zeta_3 - 11.75}{3.75} \end{cases} \tag{5-31}$$

From:

$$\begin{cases} \overline{\zeta}_1 = \dfrac{\zeta_{1_{\max}} + \zeta_{1_{\min}}}{2} = \dfrac{8+5}{2} = 5 \quad \& \quad \Delta\zeta_1 = \dfrac{\zeta_{1_{\max}} - \zeta_{1_{\min}}}{2} = \dfrac{8-5}{2} = 1.5 \\ \overline{\zeta}_2 = \dfrac{\zeta_{2_{\max}} + \zeta_{2_{\min}}}{2} = \dfrac{2+0.5}{2} = 1.25 \quad \& \quad \Delta\zeta_2 = \dfrac{\zeta_{2_{\max}} - \zeta_{2_{\min}}}{2} = \dfrac{2-0.5}{2} = 0.75 \\ \overline{\zeta}_3 = \dfrac{\zeta_{3_{\max}} + \zeta_{3_{\min}}}{2} = \dfrac{15.5+8}{2} = 11.75 \quad \& \quad \Delta\zeta_3 = \dfrac{\zeta_{3_{\max}} - \zeta_{3_{\min}}}{2} = \dfrac{15.5-8}{2} = 3.75 \end{cases} \tag{5-32}$$

The average and maximum errors (in case full factorial design) can be calculated [13-14] to validate the fitted-model by [19-20]:

$$Error_{ave} = \frac{1}{27}\sum_{i=1}^{27}\left|\frac{y_i - \hat{y}_i}{y_i}\right| \tag{5-33}$$

$$Error_{\max} = \max\left\{\left|\frac{y_i - \hat{y}_i}{y_i}\right|\right\}_{i=1,\ldots,27} \tag{5-34}$$

5.3.1 Full Factorial Design (FFD) Function

This type of design is known as the most expensive experimental design. It consists of the largest number of experiments which consider only controllable treatments (3^3) =27 runs. FFD refers to the three levels of treatments as low, intermediate, and

$$X_{FFD} = \begin{bmatrix} 1 & -1 & -1 & -1 \\ 2 & -1 & -1 & 0 \\ 3 & -1 & -1 & 1 \\ 4 & -1 & 0 & -1 \\ 5 & -1 & 0 & 0 \\ 6 & -1 & 0 & 1 \\ 7 & -1 & 1 & -1 \\ 8 & -1 & 1 & 0 \\ 9 & -1 & 1 & 1 \\ 10 & 0 & -1 & -1 \\ 11 & 0 & -1 & 0 \\ 12 & 0 & -1 & 1 \\ 13 & 0 & 0 & -1 \\ 14 & 0 & 0 & 0 \\ 15 & 0 & 0 & 1 \\ 16 & 0 & 1 & -1 \\ 17 & 0 & 1 & 0 \\ 18 & 0 & 1 & 1 \\ 19 & 1 & -1 & -1 \\ 20 & 1 & -1 & 0 \\ 21 & 1 & -1 & 1 \\ 22 & 1 & 0 & -1 \\ 23 & 1 & 0 & 0 \\ 24 & 1 & 0 & 1 \\ 25 & 1 & 1 & -1 \\ 26 & 1 & 1 & 0 \\ 27 & 1 & 1 & 1 \end{bmatrix}$$

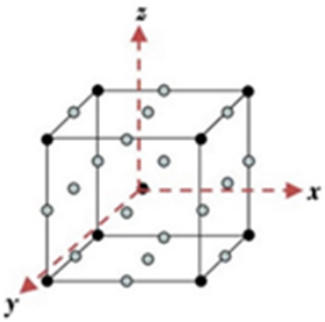

Fig. 5.3.1.1 Design of experiment cube of FFD function.

high (x_1, x_2, x_3) as needed to observe the true response η', which consists of an experimental error (or noise) known as ε_{exp}. This error is given by the measurement block with a variance (σ^2). In geometrical terms, the observations should be simulated on the vertex of a cube, in the middle of its faces and edges, and at the origin. The cube model of this design is illustrated in Fig. 5.3.1.1 [19-20].

5.3.2 Box-Behenken Design (BBD) Function

The BBD is well known as a subset of the FFD and is the most economical design due to only requiring 13 runs, which is less than other conventional designs such as FFD and CCD. Therefore, it is comparable to the design of MR-RD only if its error is as small as that of MR-RD. In terms of complexity, it can be called the simplest type of design in comparison to the others. This is considered when these experiments cannot be realized for practical reasons such as issues with physical constraints. The cube model of the design is illustrated in Fig. 5.3.2.1 [19-20].

$$X_{BBD} = \begin{bmatrix} 1 & -1 & -1 & 0 \\ 2 & 1 & -1 & 0 \\ 3 & -1 & 1 & 0 \\ 4 & 1 & 1 & 0 \\ 5 & -1 & 0 & -1 \\ 6 & 1 & 0 & -1 \\ 7 & -1 & 0 & 1 \\ 8 & 1 & 0 & 1 \\ 9 & 0 & -1 & -1 \\ 10 & 0 & 1 & -1 \\ 11 & 0 & -1 & 1 \\ 12 & 0 & 1 & 1 \\ 13 & 0 & 0 & 0 \\ 14 & 0 & 0 & 0 \\ 15 & 0 & 0 & 0 \end{bmatrix}$$

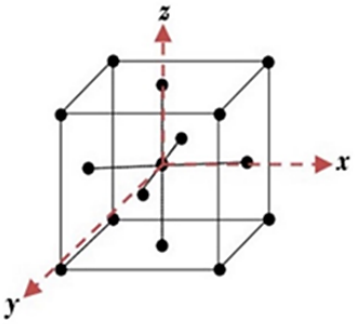

Fig. 5.3.2.1 Design of experiment cube of BBD function.

5.3.3 Central Composite Design (CCD) Function

A Box-Wilson central composite design generally referred to as a central composite design (CCD), is studied by many statisticians in the RSM. It is perhaps the most popular class of second order designs. The design involves 15 runs that consist of the eight vertices of the first cube at (±1, ±1, ±1) as cube points, and six-star points at (±1.682,0,0), (0, ±1.682,0), and (0, 0, ±1.682) plus the origin of the first cube (0, 0, 0). After the first-level optimization by the first cube, the origin of the second cube (second-level) is provided by the optimum points of the observation (y_1). The cube model of this design is illustrated in Fig. 5.3.3.1 [19-20].

$$X_{CCD} = \begin{bmatrix} 1 & -1 & -1 & -1 \\ 2 & -1 & -1 & 1 \\ 3 & -1 & 1 & -1 \\ 4 & -1 & 1 & 1 \\ 5 & 1 & -1 & -1 \\ 6 & 1 & -1 & 1 \\ 7 & 1 & 1 & -1 \\ 8 & 1 & 1 & 1 \\ 9 & 0 & 0 & 0 \\ 10 & 0 & 0 & 0 \\ 11 & 0 & 0 & 0 \\ 12 & 0 & 0 & 0 \\ 13 & 0 & 0 & 0 \\ 14 & 0 & 0 & 0 \\ 15 & 1.682 & 0 & 0 \\ 16 & -1.682 & 0 & 0 \\ 17 & 0 & 1.682 & 0 \\ 18 & 0 & -1.682 & 0 \\ 19 & 0 & 0 & 1.682 \\ 20 & 0 & 0 & -1.682 \end{bmatrix}$$

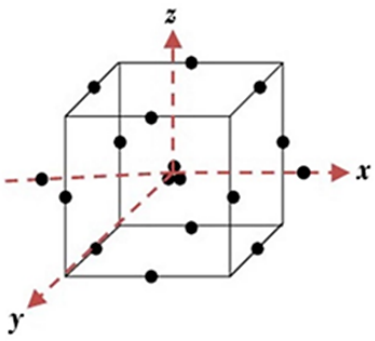

Fig. 5.3.2 Design of experiment cube of CCD function.

5.3.4 Mixed-Resolution Robust Design (MR-RD) Function

The MR-RD approach as a modern and new family of designs is used to improve the quality of yields and processes by 25 runs. Assuming a situation with three controllable variables, x_1, x_2, x_3, and three noise variables, z_1, z_2, and z_3. To estimate the linear terms of all control variables and all noise variables, the quadratic terms of the control variables, the interactions among the control variables, and the interactions between the control and noise variables and has as the defining relation $I = x_1x_2x_3z_1 = z_1z_2z_3 = x_1x_2x_3z_2z_3$. The quality of results is improved, whilst a higher level of performance is obtained via three controllable and three uncontrollable variables. The highest possible performance is obtained by determining the optimum combination of design treatments [23]. The consistency of performance can be improved by making the yield/process insensitive to uncontrollable treatments (known as noise). In this approach, the optimum design should be determined by using the design of experiment (DOE) principles. Also, performance consistency is achieved by carrying out the experiment under the influence of noise treatments. The DOE using the MR-RD approach can economically satisfy the needs of problem-solving and yield/process design optimization of electrical machines as long as the number of runs is significantly reduced. This results in a large emphasis on the size and cost of experiments. Additionally, the challenge arises in obtaining this response due to the influence of the uncontrollable noise factors.

Sets of noise factors, by adding variability to the system, affect the target response [24-25]. The function model of this design is validated in [25]. This design function is used for the very first time in power systems modeling application. A possible challenge with this design is there are several two-factor interactions of potential interest aliased with one another [19-20]. In particular, from the first term in the defining relation, $x_1x_2x_3z_1$, the aliases involving two-factor interactions are as:

$$\begin{aligned} x_1x_2 &= x_3z_1 \\ x_1x_3 &= x_2z_1 \\ x_2x_3 &= x_1z_1 \end{aligned} \tag{5-35}$$

Table 5.3.4 presents two alternative design functions from [23], in which a mixed-resolution robust design with 25 and 31 runs can be seen. In this study, we have used 25 runs due to lesser number of runs, a design with α = 2.38 and three center points is carried out as shown in the left-hand panel of the table. To predict all the two-factor interactions, we need the control-by-control and control-by-noise interactions to be dealiased which is carried out by adding additional runs. In addition, the sign changed on only one of the controllable variables which is x_2 in this design. Finally, the augmented mixed-resolution design with extra six runs (total 31 experimental runs) is illustrated in the right-hand panel with G-efficiency of 90% [23].

Table 5.3.4 Mixed resolution ronust design with two alternatives.

	Alternative 1						**Alternative 2**					
Run	x_1	x_2	x_3	z_1	z_2	z_3	x_1	x_2	x_3	z_1	z_2	z_3
1	-1	-1	-1	-1	-1	1	-1	-1	-1	-1	-1	1
2	1	-1	-1	1	-1	-1	1	-1	-1	1	-1	-1
3	-1	1	-1	1	-1	-1	-1	1	-1	1	-1	-1
4	1	1	-1	-1	-1	1	1	1	-1	-1	-1	1
5	-1	-1	1	1	-1	-1	-1	-1	1	1	-1	-1
6	1	-1	1	-1	-1	1	1	-1	1	-1	-1	1
7	-1	1	1	-1	-1	1	-1	1	1	-1	-1	1
8	1	1	1	1	-1	-1	1	1	1	1	-1	-1
9	-1	-1	-1	-1	1	-1	-1	-1	-1	-1	1	-1
10	1	-1	-1	1	1	1	1	-1	-1	1	1	1
11	-1	1	-1	1	1	1	-1	1	-1	1	1	1
12	1	1	-1	-1	1	-1	1	1	-1	-1	1	-1
13	-1	-1	1	1	1	1	-1	-1	1	1	1	1
14	1	-1	1	-1	1	-1	1	-1	1	-1	1	-1
15	-1	1	1	-1	1	-1	-1	1	1	-1	1	-1

16	1	1	1	1	1	1	1	1	1	1	1	1
17	-2.38	0	0	0	0	0	-1	-1	-1	-1	1	-1
18	2.38	0	0	0	0	0	1	-1	-1	1	1	1
19	0	-2.38	0	0	0	0	-1	1	-1	1	1	1
20	0	2.38	0	0	0	0	1	1	-1	-1	1	-1
21	0	0	-2.38	0	0	0	-1	-1	1	1	1	1
22	0	0	2.38	0	0	0	1	-1	1	-1	1	-1
23	0	0	0	0	0	0	-2.38	0	0	0	0	0
24	0	0	0	0	0	0	2.38	0	0	0	0	0
25	0	0	0	0	0	0	0	-2.38	0	0	0	0
26							0	2.38	0	0	0	0
27							0	0	-2.38	0	0	0
28							0	0	2.38	0	0	0
29							0	0	0	0	0	
30							0	0	0	0	0	0
31							0	0	0	0	0	0

5.3.5 Mixed-Resolution Central Composite Design (MR-CCD) Function

The MR-CCD design function is employed to improve the quality of yields and processes by 41 runs (based on [9]). The classic form of the response can be modeled as follows:

$$\widehat{Y}(x,z) = \beta_0 + x^T\beta + x^T Bx + z^T\gamma + x^T\Delta z + \varepsilon \tag{5-36}$$

where β_0, β, B, γ, and Δ are coefficients of the controllable variables (x), and uncontrollable variables (z) via a random error (ε). An improved quality has resulted while a higher level of performance has coherently obtained. The best possible performance is obtained by determining the optimal combination of design variables. In this approach, the global optimal operation point should be located using the DOE principles, and also the consistency of performance is performed by carrying out the experimental conditions under the influence of the uncontrollable variables. The MR-CCD function satisfies the needs of problem-solving economically and yield/process design optimisation of the electrical machines owing to the number of runs which is strongly reduced. This advantage brings a higher emphasis on the size and cost of experiments. Moreover, the experimental planning and problem formulation based on a modern work discipline of working as teams can be noted as another main advantage of using this approach [12] [26].

Regarding the below matrix, the three main design variables are defined based on sizing, in which there are controllable variables, and also two uncontrollable variables via a MR-CCD approach. The uncontrollable or noise variables cause undesirable variability which includes an under-cut angle of the stator tooth tip δ_{st} that varies between $25° \leq z_1 \leq 45°$ because of tolerance of the manufacturing process, machining, as well as assembly. The second noise factor is screened due to its impact on the volume and magnetization distribution of magnets which are located in the air-gap between PMs $L_{a\text{-}pm}$ that varies between $3° \leq z_2 \leq 5°$ [14]. The values of lower and upper boundaries of the noise factors are selected in a range to prevent any unwanted electromagnetic manner such as cogging and dynamic axial magnetic force. In coded form, the MR-CCD consists of:

- $2^{k\text{-}m}$, where k presents the number of total variables which is 5, and m=2 as the factor levels are -1, +1. Thus, $2^{5\text{-}2}$.
- Center points are:

  0 0 0 0 0

- Axial points can be matrixed as:

x_1	x_2	x_3	z_1	z_2
-α	0	0	0	0
α	0	0	0	0
0	-α	0	0	0
0	α	0	0	0
0	0	-α	0	0
0	0	α	0	0

α is the distance among each controllable design variable which can be calculated by $\alpha = \sqrt[3]{k}$, where three is the number of controllable variables and $k = 5$. Also, the axial points of noise variables are set zero because of quadratic components of the noise factors in the design [14] [20].

5.4 Multi-Objective Optimization using D-RSM and Booth's Algorithm using a Simulated Annealing Method

The objective of this study relies on a permanent magnet synchronous AC generator with exterior rotor topology applied to a wind turbine. The initial design parameters are given in Table 5.4.1. The stator contains 36 segmented teeth with closed slot modulation in order to reduce the amplitude of cogging torque significantly (Fig. 5.4.1). A 2D FE model is studied to examine magnetic flux distribution. The mesh is automatically generated (Fig. 5.4.1-a), and the magnetic field distribution is shown in Fig. 5.4.1-b.

The objective of the design is to maximize the output power while remaining cost-effective. Table 5.4.1 demonstrates the design parameters of a 1st-level RSM optimization, in which the current density fixed as 1.22 A/ mm^2. Also, the three noise variables for the MR-RD approach are considered, in which the under-cut angle of the stator tooth tip (δ_{st}) changes between 25º $\leq z_1 \leq$ 45 º, air-gap between PMs ($L_{a\text{-}pm}$) which varies between 3mm $\leq z_2 \leq$ 5mm, and the tooth width between 10mm $\leq z_3 \leq$ 20mm [19].

Fig. 5.4.2 shows how the pre-analysis and post-analysis are linked to provide the optimum operation point for output power maximization with an acceptable performance. The FEA uses LUA scripting to analyze the electromagnetic performance of the SPMSG. Afterward, finalized output data from the design block is integrated with the multi-objective optimization block (yellow block) to find the best set the treatment combinations through DRSM using the least squares method (LSM) with different design functions. Then, Booth's algorithm using SA is used to minimize the cost of the materials and maximize the output power.

Table 5.4.1 Initial geometrical dimension of the machine geometry.

Variable	Value	Unit
D_{ro}/ D_{ri}	460/430	*mm*
D_{so}/ D_{si}	419/228	*mm*
l_s	100	*mm*
A_{slot}	802.7	mm^2
L_m	8	*mm*
δ_g	0.6	*mm*
S_w	15	*mm*
P_{arc}	100	*°e*
S_d	50	*mm*
Q_s	36	
α_p	0.55	
2P	40	
m	3	

The BBD, CCD, MR-RD, and FFD approaches are calculated with 13, 15, 25, 27 runs, respectively.

DRSM is a multi-level collection of mathematical and statistical techniques used to detect the "best-fit" using the MR-RD, BBD, CCD, and FFD approaches. The analysis is performed in order to observe the effect of a number of chosen variables on a quantity of interest. The objective is always to optimize the response in the physical system. Since the model integrates a curvature in the system to approximate the response, this study requires the second-order polynomial model as given in Eq. (5-22) and (5-23) [19].

For the first level of RSM, the variables boundary restriction is given as 5mm$\leq x_1 \leq$8mm, 0.5mm$\leq x_2 \leq$2mm, 8mm$\leq x_3 \leq$15.5mm, 25°$\leq z_1 \leq$45°, 3mm$\leq z_2 \leq$5mm, 10mm$\leq z_3 \leq$20mm. While the optimal point is found (based on Fig. 5.4.4), then all controllable and

noise variables are one more time adjusted, in which the center point of each variable should be the optimal value of the first level of RSM. Therefore, the second level of RSM is designed by the following smaller boundaries (ranges), 7.5mm≤x_1≤9.5mm, 0.5mm≤x_2≤0.9mm, 15mm≤x_3≤17mm, 36°≤z_1≤40°, 3mm≤z_2≤5mm, 10mm≤z_3≤14mm. Only in case of x_2 the optimal value of first level of RSM is not centrized for the second level, because of manufacturing limitations x_2 cannot be smaller then 0.5. Thus, its value is shifted to a smaller range.

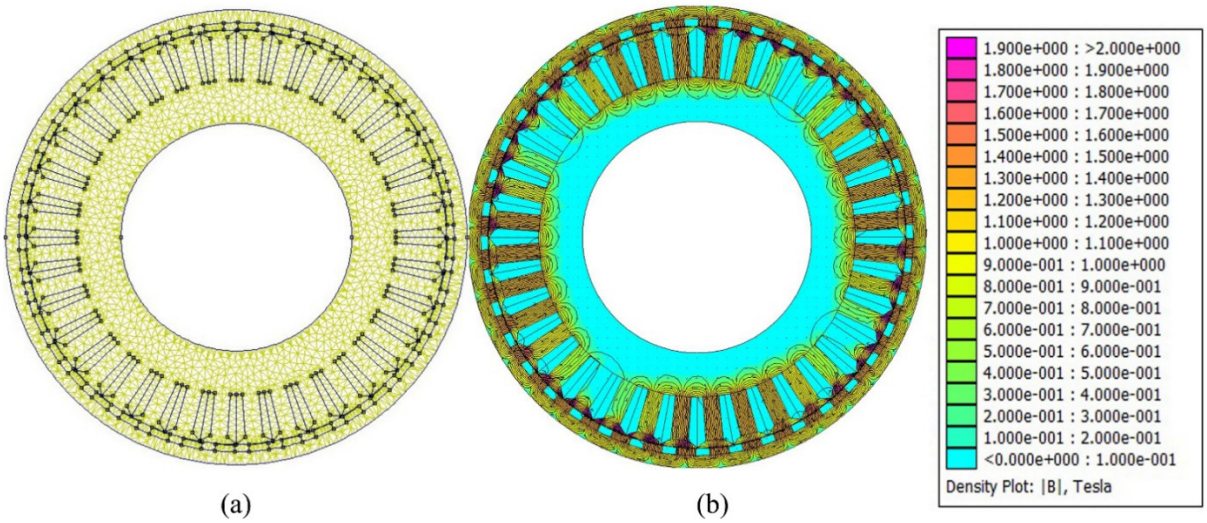

Fig. 5.4.1. Schematic of the SPMSG, a) generated mesh, and b) magnetic-field distribution using FEA.

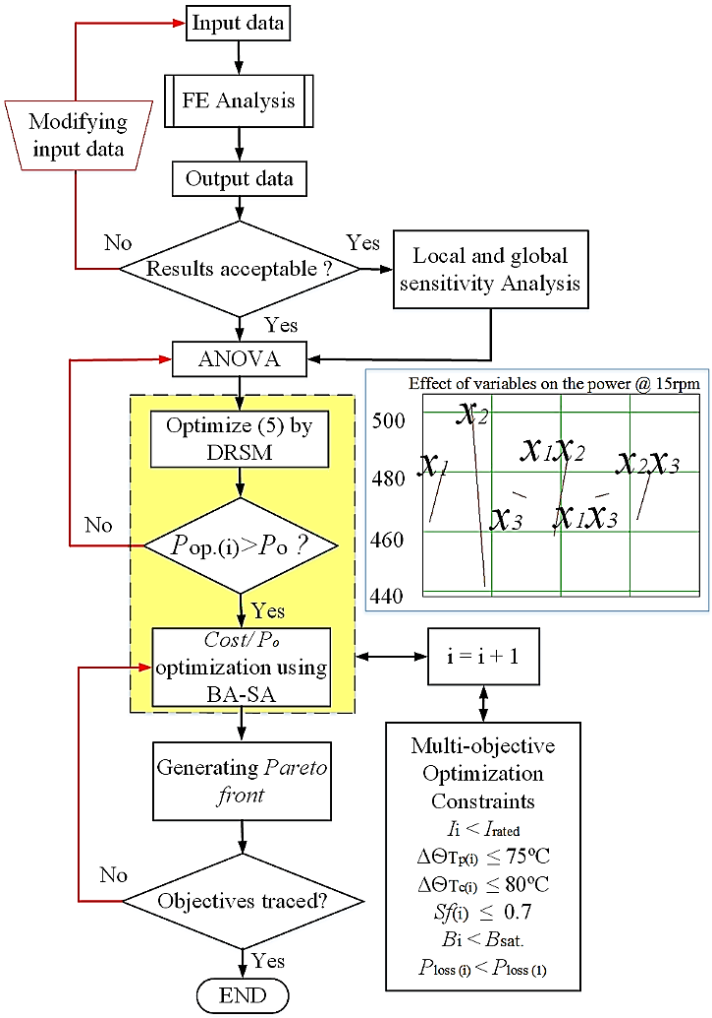

Fig. 5.4.2. Flowchart of the proposed multi-objective design optimization.

A. Booth's Algorithm using simulated annealing (SA)

Booth's Algorithm (BA), is a method particularly applicable for multiplying signed numbers integrated, in which here BA is mathematically coupled to simulated annealing (SA). The application of it is well-known in low power VLSI techniques for the digital filter for hearing aid applications. In this project, the use of BA-SA is carried out to solve electrical machine issues for the first time. SA is an effective and general form of optimization (an intelligent search function). It is useful in finding global optima in the presence of large numbers of local optima. "Annealing" refers to an analogy with thermodynamics, specifically with the way that metals cool and anneal. SA has four useful features such as 1) Iterative improvement. 2) Local random search. 3) Exploration. 4) Greed. This multi-objective method begins with the addition and subtraction of the signed-magnitudes in different configurations (Table 5.4.2), as there are multiple ways to compute a yield. BA is a well-known multiplication algorithm, which utilizes two complementary notations of signed binary numbers for multiplication. BA is also called a uniform shift method which examines multiple portions of the multiplier simultaneously to determine multiples of the multiplicand to be added to the partial yield. This algorithm requires no sign correction for the two complementary notation numbers and the decoding of the multiplier may initiate from either direction. The main drawback of the algorithm is that it still relies on a process which needs *n* shifts and an average of *n/2* additions for an *n*-bit multiplier. A boosted multiplication speed can be reached by evaluating more than two bits of the multiplier at a time as the process can be simply seen with an *n*-bit multiplier (Fig. 5.4.3). In this figure, B_0 to B_{n-1} stand for the multiplicand process (MP), *C*-block is a 1-bit register block, Q_0 to Q_{n-1} represent the multiplier process and the dashed lines show control signal orders [20] [27-28].

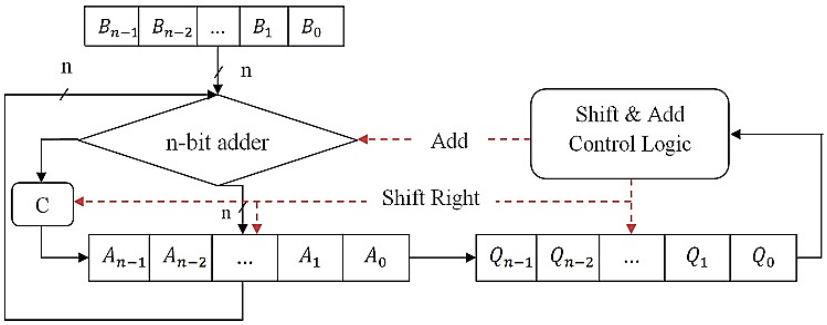

Fig. 5.4.3 The general flowchart of modified *N*-Bit bus Booth's algorithm.

Table 5.4.2 Add / subtract signed-magnitude generator.

Operation	**Add Magnitudes**	**Subtract Magnitudes** **A>B** **A<B** **A=B**
(+A) + (+B)	+ (A+B)	
(+A) + (-B)		+(A-B) - (B-A) +(A-B)
(-A) + (+B)		- (A-B) + (B-A) + (A-B)
(-A) + (-B)	- (A+B)	
(+A) - (+B)		+(A-B) - (B-A) + (A-B)
(+A) - (-B)	+ (A+B)	
(-A) - (+B)	- (A+B)	
(-A) - (-B)		-(A-B) + (B-A) + (A-B)

In this study, a novel method, known as Simulated Annealing (SA), was integrated with Booth's algorithm. SA is a method for solving unconstrained and bound-constrained optimization issues. The method models the physical process of heating a material and afterward slowly lowering the temperature to reduce defects, thus minimizing the system energy. At each iteration of the SA method, a new point is randomly generated. The distance of the new point from the current point, or the extent of the search, is based on a probability distribution with a scale proportional to the temperature. The algorithm accepts all new points which lower the objective, but also, with a certain probability, points which raise the objective. Through accepting points that raise the objective, the algorithm avoids being trapped at local minima, and is able to search globally for more possible solutions. An *Annealing schedule* is selected to systematically reduce the cost of the SPMSG as the algorithm proceeds. As the temperature decreases, the algorithm reduces the extent of its search to converge to a minimum cost of the SPMSG [20].

The objective function, validated in [29], is defined as:

$$s.t.\begin{cases} f(x)=\dfrac{C}{C_0}+\dfrac{P_0}{P} \\ g_1(x)=0.92-\eta\le 0 \\ g_2(x)=450-P_{out}\le 0 \\ g_3(x)=J_c-4\le 0 \\ g_4(x)=\Delta\theta T_p-75\le 0 \\ g_5(x)=\Delta\theta T_c-80\le 0 \\ g_6(x)=B_i-2.1\le 0 \\ g_7(x)=sf-0.7\le 0 \end{cases} \tag{5-37}$$

where C_0, and P_0 stand for the current cost of design and output power of the generator, and C and P are the optimum values of C_0 and P_0, respectively. Under these conditions, the efficiency is greater than 92%, the output power > 450 W at a minimum speed (15 rpm), and the current density (J_c) should not exceed 4 A/mm^2 [21]. The probability of acceptance by SA can be given by Equation (5-38) where Δ shows [new objective - previous objective], and T stands for the current temperature.

$$S_a = 1/1+exp\left(\Delta / \max(T)\right) \tag{5-38}$$

To employ the SA algorithm in MATLAB, the following piece of code helps, where the design function is defined in Eq. (5-37). The bound constrainted minimization is needed to be defined. Then. Simulated annealing mimics the annealing process to solve an optimization problem. It uses a temperature parameter that controls the search. The temperature parameter typically starts off high and is slowly "cooled" or lowered in every iteration. At each iteration, a new point is generated and its distance from the current point is proportional to the temperature. If the new point has a better function value it replaces the current point and iteration counter is incremented. It is possible to accept and move forward with a worse point. The probability of doing so is directly dependent on the temperature. This unintuitive step sometime helps identify a new search region in hope of finding a better minimum.

```
ObjectiveFunction = @multi_objective; % Objective function is stored in a separate m-file
X0 = [0.5 0.5]; Y0 = [2.0 2.0];   % Starting points of both objectives
[x, y, fval,exitFlag,output] = simulannealbnd(ObjectiveFunction,X0,g1,g2,g3,g4,g5,g6,g7);
```

B. Optimization and Analysis

In this section, a discussion is presented on how the multi-objective optimization, with an aim of maximization of output power in conjunction with a minimization of the generator's cost, will be investigated. This will be approached through a multi-disciplined study of the generator's cost where the results of optimization will be discussed.

- Optimization Constraints

To consider the local constrained optimization of the *d*-axis current at each operating point based on [30], for objective $P_{opt.(i)}$ in each operating point, the *d*-axis current $i_{d,i}$ should be evaluated. To complete the description of this optimization problem, a number of conditions are required to be defined. Some constraints must be satisfied at each operating point. They can be qualified as instantaneous constraints:

a) Rated current: $\forall i, \sqrt{i_{d,i}^2+i_{q,i}^2}\le\sqrt{3}.I_r$

b) Rated voltage: $\forall i, \sqrt{v_{d,i}^2+v_{q,i}^2}\le\sqrt{3}.V_{rated}$

c) EM saturation for each part of the machine as $\forall i, B_i(\max)\le B_{sat.}$

d) The losses evaluation by $\forall i, P_{loss,i} < P_{loss}$

e) Magnet and winding temperature-rise by

$$\max(\Delta\theta T_{PM})_i \le (\Delta\theta T_{PM})_{\max}$$
$$\max(\Delta\theta T_c)_i \le (\Delta\theta T_c)_{\max}$$

where maximum induction level B_i (max) is 1.9 T. Each operating point of the profile is treated independently, and current control is optimized at every operating point to not only minimize the PMSM's drive losses but also satisfy the conditions above. A current control strategy (direct and transverse axis current) is used to contribute to the extension of the constant speed power range, which is validated in [30]. This consideration takes the form of an (i_d, i_q) optimization to minimize losses at each operating point of the profile respecting other instantaneous constraints (a, b, c, and d) [28] [31]. Therefore, $i_{d,i}$ should be optimized, otherwise, the particular operating point cannot be reached. The instantaneous constraints c and d are satisfied at each operating point (T_i, Ω_i), where B_{sat} and also demagnetization, are subject to being smaller than 2.1 T and 891×10^3 A.m^{-1}, respectively. The thermal constraint requires additional consideration. The temperature rise of the hottest point relative to ambient temperature must be calculated accurately by means of a transient thermal model. The maximum value over the entire temperature-rise profile must, therefore, plateau below a threshold value, $\max(\Delta\theta T_P(t)) \le 75$ ºC, and $\max(\Delta\theta T_c(t)) \le 80$ ºC [32]. Although the thermal transient analysis is very time consuming, the following two definitions are considered based on thermal time constants (TCs) to allow the simulation run via steady-state thermal analysis:

a) While TCs is large: $\sum_i \Delta\theta_i d_i / \sum_i d_i$

b) While TCs is small: $Max(\Delta\theta(t))$

$\Delta\theta$ is calculated once in the winding, and another time in the magnet that corresponds to the temperature rise between the hottest point (of the slot or magnet) as well as the ambient temperature. The copper loss with respect to the armature resistance per phase (R_s) resolves through the set of geometrical parameters. The copper resistivity is chosen at the maximum temperature (80ºC) [32-33]. Hence, total copper losses per phase with a slot-filling factor of 0.4 can be calculated using:

$$P_{copper,i} = R_s(i_{d,i}^2 + i_{q,i}^2) \tag{5-39}$$

Based on [32-33] the first harmonic hypothesis, the iron loss can be predicted using:

$$P_{iron,i} = \left(\frac{2k_H}{\pi}\right)|\Omega_i|\,\widehat{B}_i^2 + \frac{(p.\Omega_i.\widehat{B}_i)^2}{2}.\alpha_p \tag{5-40}$$

where $\widehat{B}_i$ is the maximum local flux density for ith operating point k_H, and α_p are loss coefficients which are 0.045 A.m/V and 73 A.m /V.s respectively. Thus, the total iron loss consists of the iron loss from the machine parts (stator yoke, and teeth). Let us assume that the loss densities are considered to be homogeneous in each of these two parts, while through a static analysis, iron losses at the rotor yoke are nearly zero in the first harmonic.

Table 5.4.4 shows that R^2 values using FFD, MR-RD, CCD, and BBD are 0.9993, 0.9994, 0.9981, and 0.9989, respectively. As an example, the R^2 value using FFD represents 99.93% of the total variation of output power performance. Furthermore, the MR-RD approach results in the minimum error (0.77%), whereas the CCD approach results in the maximum value of the residual (error). Therefore, ANOVA is performed to examine how well the fitted-model is able to predict the response at any observation points. For this reason, the *SST, F*-value, and R^2, which resulted from the variation of the response, are calculated. The average errors of the fitted-models of the various design functions are reported as nearly the same across all functions but slightly larger for the model fitted with the CCD function. However, this design function explored a larger domain of the design treatment space than other design models during the observation-stage; it is worthy to mention that the accuracy of a model is not necessarily increased by increasing the number of experiments involved in the model fit. Fig. 5.4.6 indicates the current behavior, and best function values (of Eq. 5-37) which is analyzed using BA-SA to determine the best function value through 3000 sample iterations in which it was assumed that the efficiency, output power, and current density had to be greater than 92%, greater than 450 W, and less than 4 A/mm^2, respectively [20].

The second-level RSM plots, presented in Fig. 5.4.4, are used to check the variation of the treatments under objective tracking. Also, the counter plots of each surface plot are reported to summarize the results of the study. The RSM plots indicate the response surface based on the defined treatments through two different levels of rotation speed: minimum speed (15 rpm), which is used in the optimization process, and rated speed (150 rpm). The maximum output power that could be generated is 5.1 kW @ 150 rpm, and the minimum generated output power provided is 500 W @ 15 rpm, when the torque constant range condition exists.

Based on the fitted model for the RSM, the prediction of the output power can be compared to FEA data in order to check the error at 15 rpm as represented in Fig. 5.4.5. This demonstrates that the prediction of the fitted model has a small error and can be

incorporated into the DRSM. In the first and second-levels of RSM, the calculated second-order regression model can be reported (Table. 5.4.3) based on equation (5-22). Fig. 5.4.5 demonstrates how the fitted model is improved through the following equation:

$$\hat{y} = 460.235 + 5.878x_1 - 3.804x_2 - 10.8x_3 + 0.14x_1.x_2 + 0.76x_1.x_3 + 0.09x_2.x_3 - 0.286x_1^2 + 0.017x_2^2 - 0.247x_3^2 \quad (5\text{-}41)$$

The average error is decreased as can be seen in Fig. 5.4.4-d which uses (5-42).

$$Error_{ave} = \frac{1}{27}\sum_{i=1}^{27}\left|\frac{y_i - \hat{y}_i}{y_i}\right| \quad (5\text{-}42)$$

In Table 5.4.4, the error decreases from 1 to less than 0.04 on average by the 2nd level coefficients. Thus, a finalized fitted second-order regression model can be given by Equation (5-41). The fitted regression model is checked via the *F-value* to ascertain the validity under the null hypothesis as:

$$F = SSR(1-a)^{-1} / SSE(N-a)^{-1} \quad (5\text{-}43)$$

where a is the number of terms at the fitted-model. Additionally, R^2 is a significant statistic to express the proportion of the variation of the y_i by the fitted-model and FEA data for the mean of $\bar{y}$, as given:

$$R^2 = SSR \times (SST)^{-1} \quad (5\text{-}44)$$

The major design outputs such as L_d, L_q, λ_m, P_{opt}, $\eta\%$, *CPSR*, T_r, and C are calculated over two steps of analysis as pre-optimization and post-optimization analyzes using different design functions in which the improvements of multi-objective optimization using DRSM and BA-SA resulted in a minimum rotation speed (15rpm) in Table 5.4.5. Afterward, FEA method is verified with an insignificant error. In addition, the *CPSR* is highly sensitive to the machine key parameters. Furthermore, to further improve the accuracy of the optimization, the choice of materials can be studied while taking cost-effective design into consideration.

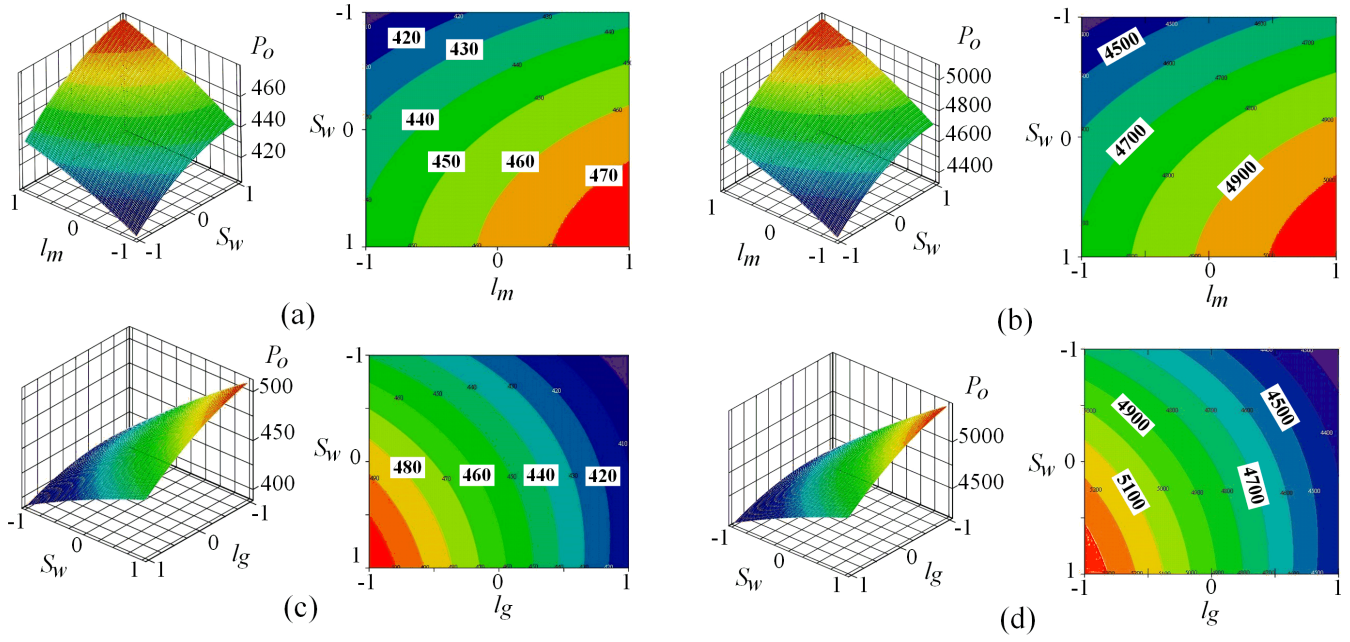

Fig. 5.4.4 Surface and counter plots of Multi-level RSM results on P_o objective at minimum and rated speeds (15 and 150rpm), a) thickness of magnet versus slot-width @15rpm, b) thickness of magnet versus slot-width @150rpm, c) slot-width versus length of magnet @15rpm, d) slot-width versus length of magnet @150rpm.

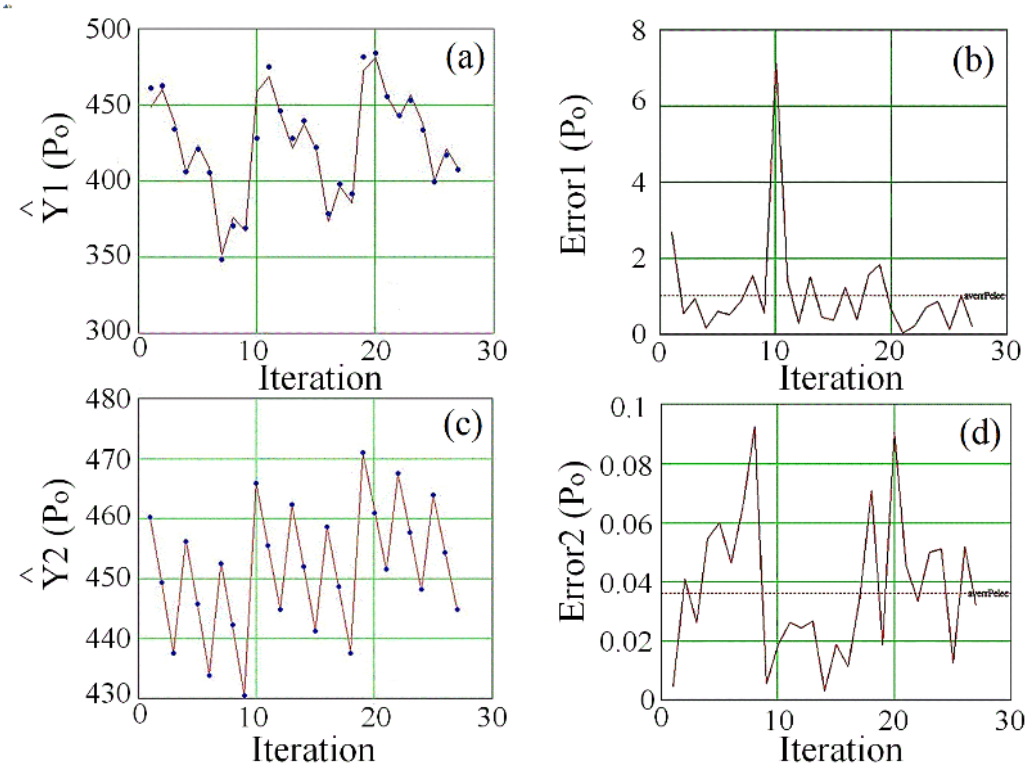

Fig. 5.4.5 Predicted objective (P_o) at minimum speed via a) 1st-leve fitted-model and FEA data, b) the error of the 1st-leve fitted-model, c) 2nd-leve fitted-model and FEA data, and d) the error of the 1st-leve fitted-model.

Table 5.4.3 ANOVA using different approaches with 5% level.

Approach	Source	Sum of Squares	DF	Mean square	*F*	R^2
FFD	A	$1.661*10^3$	-	$1.661*10^3$	0.672	-
	B	162.605	-	162.605	0.066	-
	AB	13.249	-	13.249	$5.36*10^{-3}$	-
	Error	0.8%	4	2.472	-	-
	Total	$1.173*10^4$	7	-	-	99.93%
MR-RD	A	$1.556*10^3$	-	$1.556*10^3$	0.788	-
	B	143.605	-	143.605	0.098	-
	AB	11.249	-	11.249	$6.79*10^{-3}$	-
	Error	0.77%	4	3.130	-	-
	Total	$1.453*10^4$	6	-	-	99.94%
CCD	A	$1.597*10^3$	-	$1.556*10^3$	0.799	-
	B	168.605	-	143.605	0.1	-
	AB	11.997	-	11.249	$6.98*10^{-3}$	-
	Error	0.91%	4	3.130	-	-
	Total	$1.503*10^4$	8	-	-	99.81%
BBD	A	$1.669*10^3$	-	$1.556*10^3$	0.799	-
	B	173.781	-	143.605	0.1	-
	AB	12.765	-	11.249	$6.98*10^{-3}$	-
	Error	0.88%	5	3.130	-	-
	Total	$1.803*10^4$	12	-	-	99.89%

Table 5.4.4 Calculated second-order regression model at 1st-level and 2nd-level RSM @15 rpm.

Coefficients	First-level RSM	Second-level RSM
β_0	448.484	460.235
β_1	7.633	5.878
β_2	-37.811	-3.804
β_3	28.387	-10.8
β_4	6.086	0.14
β_5	-1.714	0.76
β_6	6.355	0.09
β_7	2.235	-0.286
β_8	-5.305	0.017
β_9	-16.747	-0.247

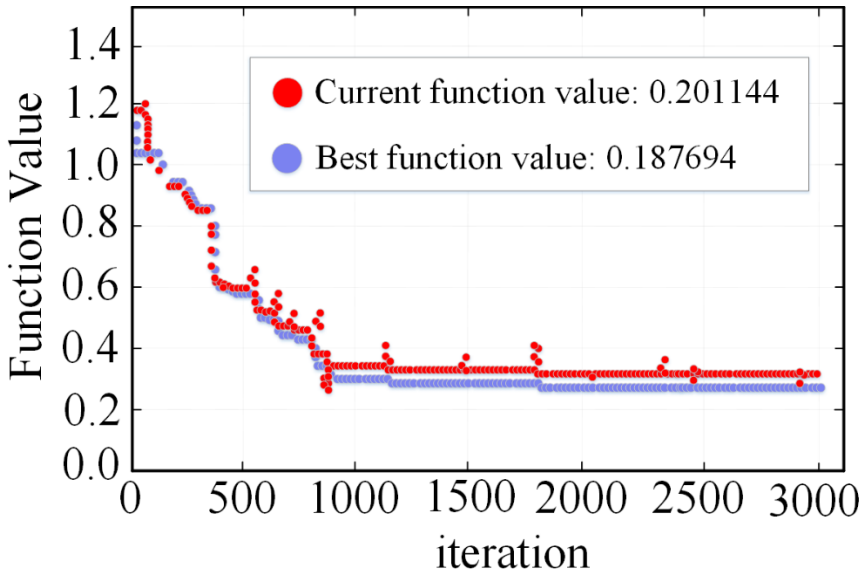

Fig. 5.4.6 Cost effective optimization analysis using BA-SA.

The procedure can be repeated on a smaller range of design treatments centered on the optimal design that was obtained in this work.

Fig. 5.4.7, demonstrates the multi-objective optimization for determining the optimum design point using Pareto front, in which the best optimum design point is marked at 15 rpm resulting in the maximum output power, and minimum cost of manufacturing that is all summarized in Table 5.4.7. Fig. 5.4.8 presents the values of the controllable and uncontrollable design variables on the initial model (Fig. 5.4.7-a), and the impact of these variables on the machine's structure after multi-objective optimization shown in Fig. 5.4.7-b.

Fig. 5.4.9 reinforces the impact of the optimization, in which Fig. 5.4.9-a presents the materials used minimization, particularly in NdFeB as the most expensive one. Fig. 5.4.9-b illustrates the output power maximization in compare to the initial model which has been experimentally validated.

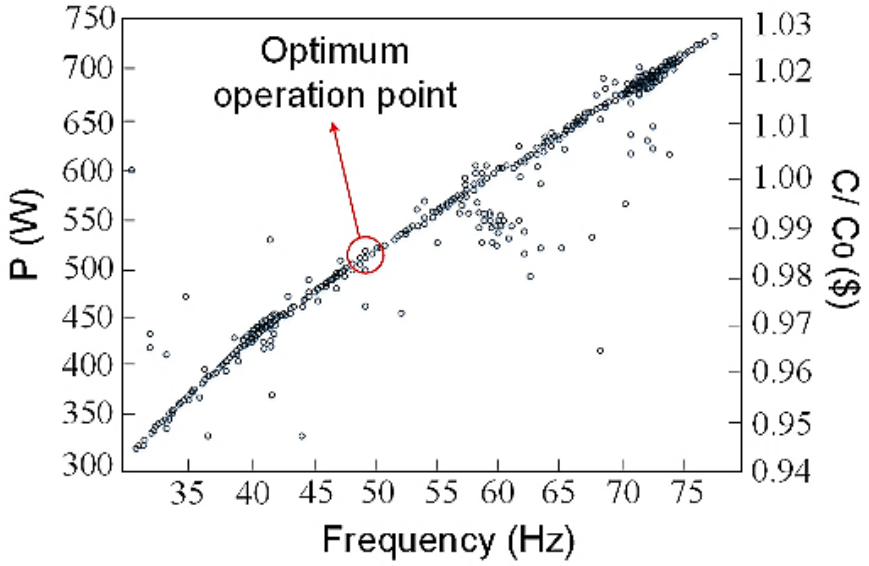

Fig. 5.4.7 Pareto front of the multi-objective optimization at various frequency.

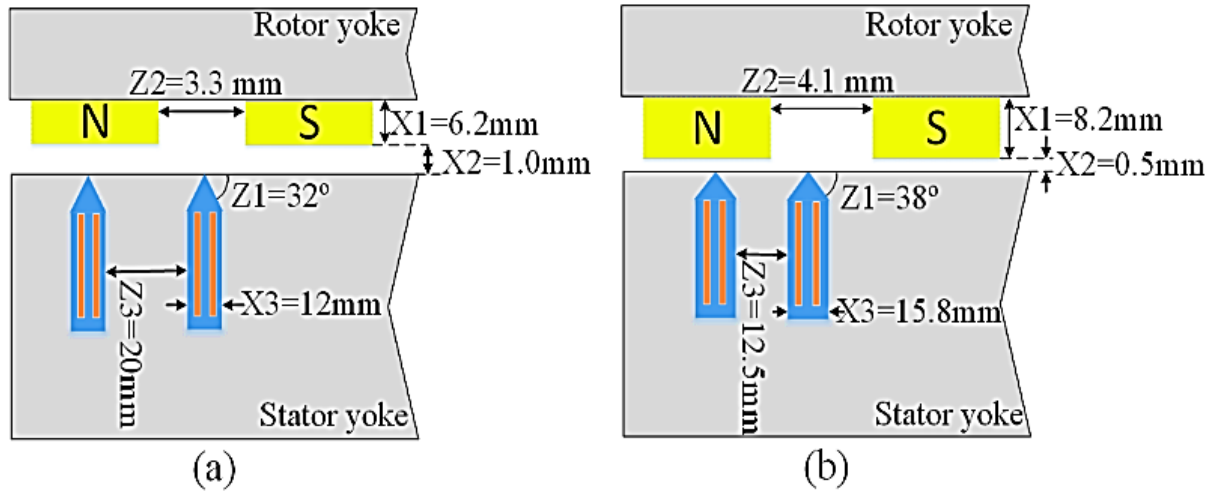

Fig. 5.4.8 Controllable and uncontrollable variables on a) the initial and b) optimized model.

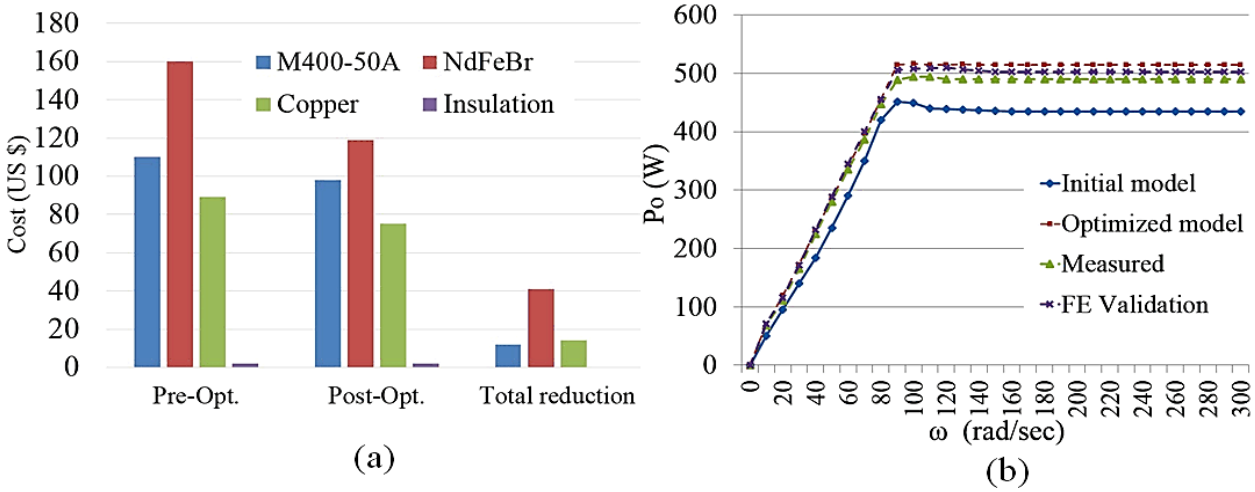

Fig. 5.4.9 A comparison over output power and cost objectives, a) cost, and b) output power with simulated and experimental data.

Table 5.4.5 Optimization results and verification.

Par.	Pre-Opti.	Opti-MR-RD	Opti-FFD	Opti-CCD	Opti-BBD	Test
L_d (mH)	468.2	470.7	471.6	468.5	469.8	473.2
L_q (mH)	468. 2	471	470.9	469.7	469.2	474.5
D_{si} (mm)	228	234	235.6	232	233	234
D_{si} (mm)	460	452	451.6	449.8	450.4	452
λ_m (mVs)	1691.8	1720.4	1714	1710	1713	1799.2
P_o (W)	440.7	514.8	507.2	488	498	511.6
η (%)	92.2	96.6	94.8	93.7	94.3	97
CPSR	434.7	497.8	477.3	469	470	505.7
l_g	1.0	0.9	0.88	0.8	0.95	0.9
N_c (turn)	120	80	98	111.8	110	80
ρ (g/m^3)	7.63	8.5	8.3	7.96	8.1	8.5
l_p (mm)	100	92	95	94.3	90	92
T_r	314.6	370.35	367.4	348	356.5	370
Cost ($)	2979.6	2904.6	2897	2912.8	2890.5	2906.5

5.5 Global Sizing Optimization using D-RSM under Variable Speed Analysis

The stator contains 36 segmented teeth because of closed slot modulation in order to reduce the amplitude of cogging torque significantly which can be seen in Fig. 5.5.1-a. This figure shows a 3D FE model coupled with a variable-speed field-circuit PMSG finite element time-stepped model. Fig. 5.5.1-b illustrates the design geometrical variables of the model. It should be noted that blue double arrows are representing the uncontrollable variables, and red double arrows stand for controllable variables in this graph. It supplies power for an uncontrolled three-phase full rectifier load system which is shown in Fig. 5.5.1-c as a whole in order to calculate the magnetic flux distribution and corresponding performance via a parameterized model [19] [34].

The global optimisation generally depends on the PMSG's design, and its electronic system to find out the best possible sizing optimisation in order to maximise the efficiency. The combination of 36 slots/ 40 poles with air-gap of 0.6 mm is chosen due to the acceptable electromagnetic outcome especially in cogging torque and back-EMF from double-layer fractional concentrated winding. Regarding Table 5.5.1, the three main design variables are defined based on sizing, in which there are controllable variables, and also two uncontrollable variables via the MR-CCD approach [19].

According to the nature of each individual design function, the design functions of BBD, CCD, and FFD without consideration of noise have 13, 15, 27 runs, respectively. However, MR-CCD has 41 runs [12].

Fig. 5.5.2 shows how the pre-analysis and post-analysis are shown to cater to a framework of the study to maximise the efficiency of an acceptable global optimal operation point. Regarding the flowchart, first, all input data (such as dimensions, constraints, i_{di} (d-axis control current), L_{di} (d-axis inductance), $\tilde{I}$ (moment of inertia), $V_{LL(pk)}$ (peak line to line voltage) of the machine and converter system as a whole analysis loop must be considered, where specifically the converter system is a three-phase full bridge rectifier load that is shown in Fig. 5.5.1-c. Through launching a linked-simulation of FE original model and LUA scripts, the acceptable electromagnetic (EM) performance with reachable operation point of the original PMSG is stored. Afterward, a local sensitivity (LS) analysis finalized the best geometrical variables which can be defined as two groups, controllable, and uncontrollable (noise) variables for the optimisation process. The chosen variables are evaluated via the ANOVA to validate the adequacy of fit that originated from a number of different methods of DOE such as (the MR-CCD, BBD, CCD, and FFD). Subsequently, the variables under a number of conditional factors for an optimal operation point globalization will be executed to optimize the original PMSG using the D-RSM with the window-zoom-in approach. After that, if only in case the optimized efficiency will be larger than original efficiency, the design optimisation completes via response surface and contour plots. Whereas, the LS analysis must be modified for further performs. Table 5.1.1 indicates the controllable design variables for all the DOE methods in this study.

A. Model of Machine-Converter System Losses

The copper losses based on the armature resistance per phase (R_s) resolves by the set of geometrical parameters, where the copper resistivity is chosen at the maximum temperature (90ºC). Thus, total copper losses per phase with a slot-filling factor of 0.4 can be calculated as:

$$P_{copper,i} = R_s(i_{d,i}^2 + i_{q,i}^2) \tag{5-45}$$

Based on the first harmonic hypothesis, the iron losses can be determined as follows:

$$P_{iron,i} = (\frac{2k_H}{\pi})|\Omega_i|\widehat{B}_i^2 + \frac{(p.\Omega_i.\widehat{B}_i)^2}{2}.\alpha_p \quad (5\text{-}46)$$

where $\widehat{B}_i$ is the maximum local flux density for the *i*th operating point. In addition, k_H, and α_p are loss coefficients that are 0.036 A.m /V and 66 A.m /V.s. The total iron losses include iron losses from machine parts (stator yoke, and teeth). The loss densities are considered to be homogeneous in each of these two parts, while through a static analysis, iron losses at the rotor yoke are nearly zero in the 1st harmonic.

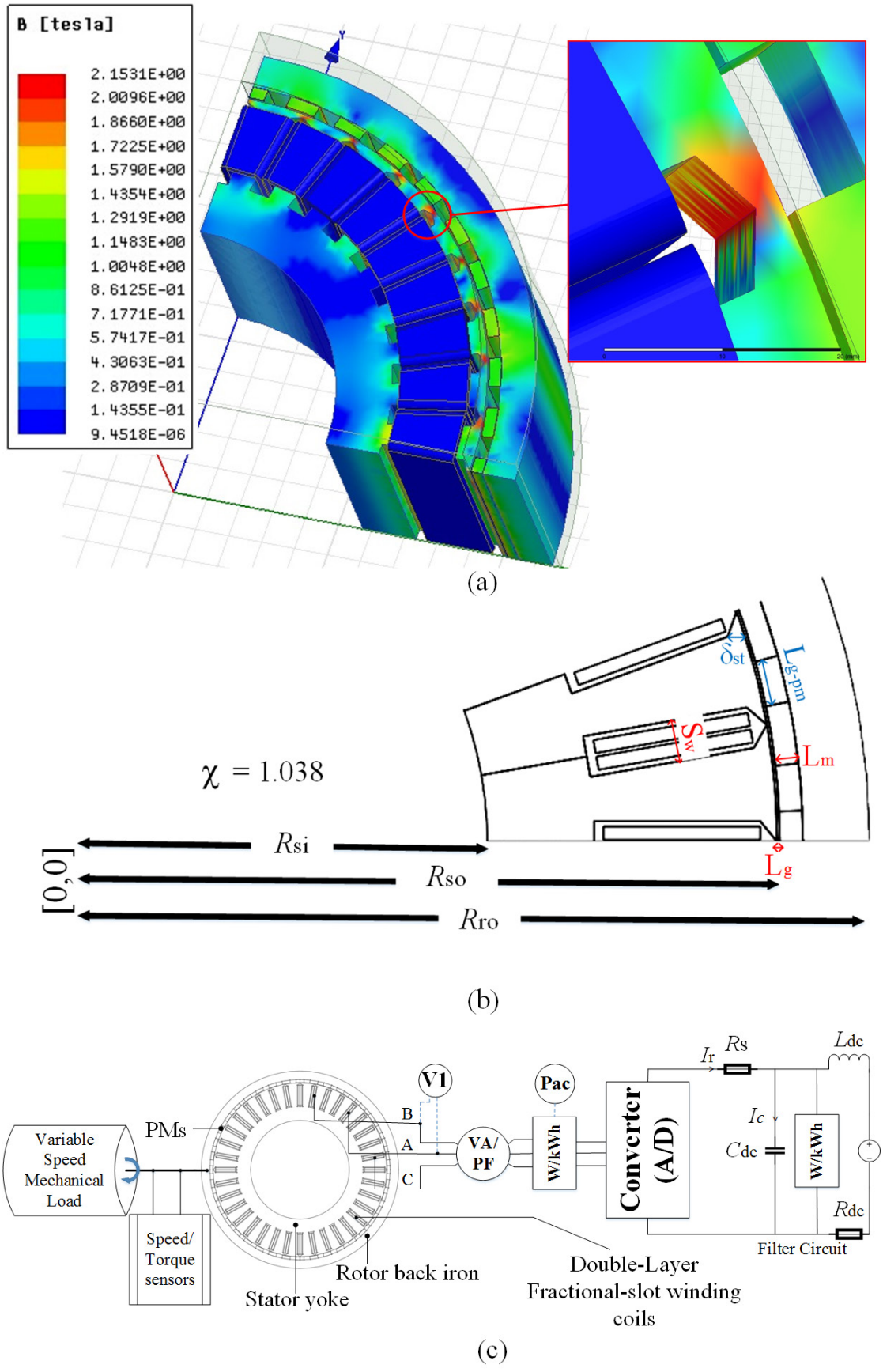

Fig. 5.5.1. Schematic of the original 3-D PMSG model at rated speed using FEA, a) magnetic flux density distribution, b) design geometrical variables of the PMSG, c) a coupled three-phase full rectifier load system during test bench.

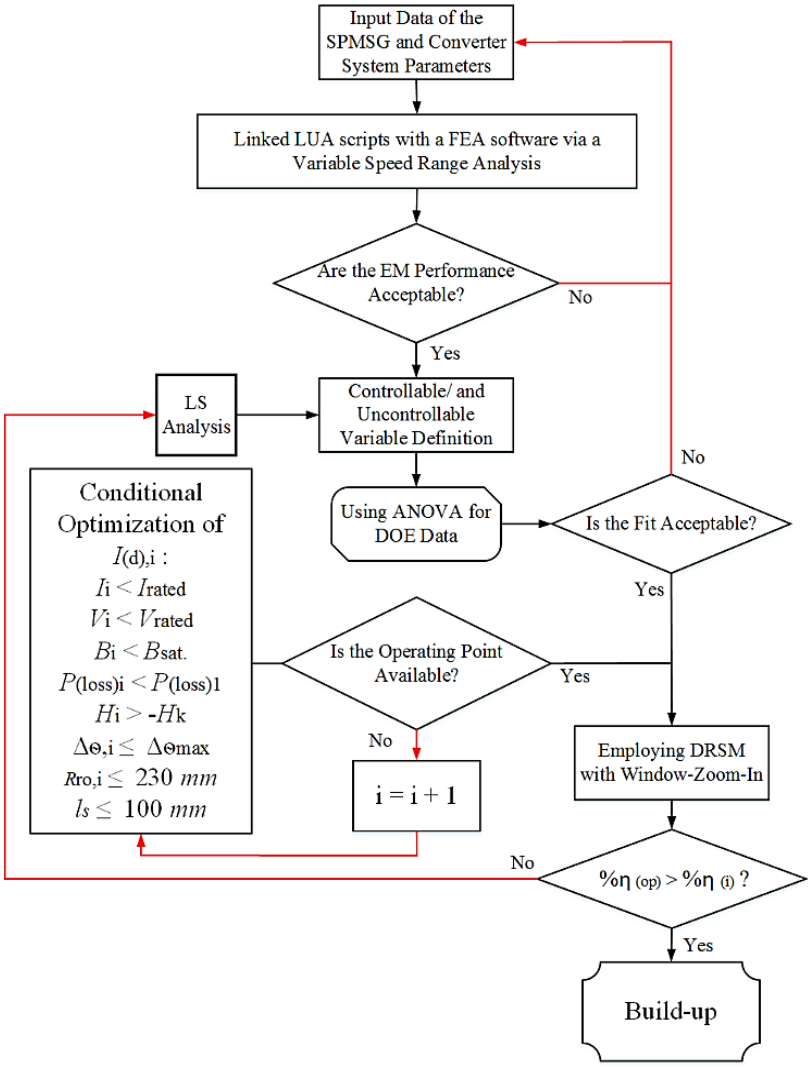

Fig. 5.5.2 Flowchart of the proposed objective design global optimization.

Dual-level optimization process mover is based on the window-zoom-in approach that is defined for all design functions (MR-CCD, FFD, CCD, and BBD). Each window defines the range of controllable and uncontrollable variables which should be scanned through a response surface of the prototype with an acceptable operation point in the boundary. Fig. 5.5.3 represents that how the movement of each window will approach the global optimal operation point using a steepest gradient between two controllable variables. The black curves find out the 1st –level optimal operation point of the original prototype in the boundary and blue curves ended up with the 2nd –level optimal operation point with a new range definition.

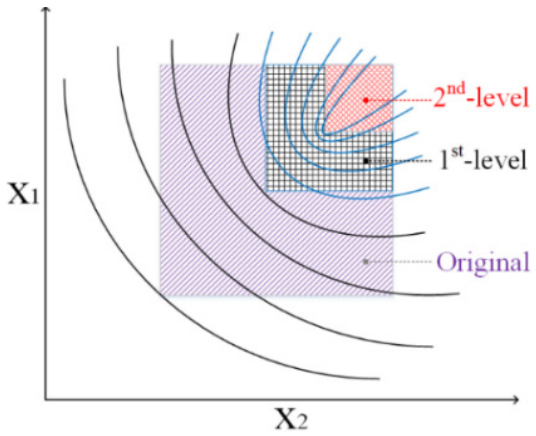

Fig. 5.5.3 Dual-level windows moving and zoom-in framework.

Fig. 5.5.3 demonstrates how the window mover works to reach the best optimal operation point from the original window to the final window which generates a new set of variables with a more specific range closer to optimal point at each level of optimization, that is 2nd –level plane in this study.

Regarding the eq. (5-22), the best optimal operation point through presented coefficients (in Table 5.5.1) using FFD is reachable in the boundary. However, the focus is obtaining the best optimal operation point through MR-CCD with reaching a higher number of the experiment (41) in comparison to the FFD with 27 experiments. Eventually, the above ANOVA using un-replicated factorials, uncontrollable variables z_1, and z_2 exceed the range of the boundary. Therefore, the true optimal point cannot be comparable with other used approaches. For further analysis, the boundary should be moved to the lower boundary ($15° \leq z_{1'} \leq 35°$, and $2° \leq z_{2'} \leq 4°$) of the original range on the MR-CCD. The variables regions are readjusted in Table 5.5.3. Regarding this fact, the modified MR-CCD is resulted as shown in Table 5.5.2 and compared with the initial MR-CCD. There is an improvement on the R^2 using the modified-MR-CCD with (0.02) and less error in comparison with the FFD in the same range due to the different boundary adjustment on the uncontrollable variables; however, the MR-CCD, in general, has the drawback of complexity. The FFD approach is fairly preferred for a further stage of design optimisation. Fig. 5.5.3 presents that how fitted-model is improved in Table 5.5.3 to decrease the error from 0.15 to less than 0.0015 in average. According to the fitted-model on the RSM, the prediction of the objective can be compared to FEA validation to check the error, which is suppressed by the window-zoom-in approach. Regarding the prediction of fitted-model, a very small error is strongly considered in the D-RSM. The finalized fitted second-order regression model can be given as:

$$\begin{aligned} Y = (x_1, x_2, x_3) = 96.345 + 0.054\mathrm{x}_1 - 0.029\mathrm{x}_2 + 0.269\mathrm{x}_3 + \\ 2.358\times10^{-3}\mathrm{x}_1.\mathrm{x}_2 + 3.583\times10^{-4}\mathrm{x}_1.\mathrm{x}_3 + 3.017\times10^{-3}\mathrm{x}_2.\mathrm{x}_3 - \\ 4.083\times10^{-3}\mathrm{x}_1^2 - 7.667\times10^{-4}\mathrm{x}_2^2 - 0.03\mathrm{x}_3^2 \end{aligned} \quad (5\text{-}47)$$

The first and second-levels of RSM with the calculated second-order regression model is reported in Table 5.5.1 based on equation (5-22), where the average error is:

$$Error_{ave} = \frac{1}{27}\sum_{i=1}^{27}\left|\frac{y_i - \hat{y}_i}{y_i}\right| \quad (5\text{-}48)$$

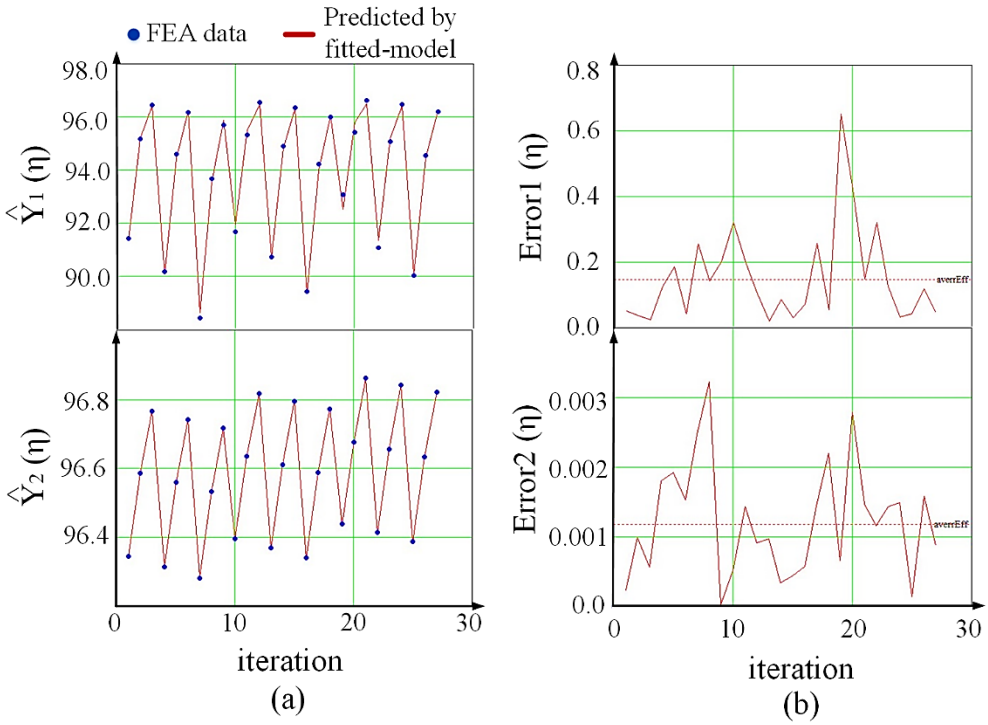

Fig. 5.5.4 Predicted efficiency by the fitted-model at minimum speed of 15 rpm via a) the 1st -level and 2nd –level fitted-models ($\hat{Y}_1(\eta)$, and $\hat{Y}_2(\eta)$), with b) their corresponding errors for each level.

The fitted regression model is checked via *F-value* statistic to ascertain the validity under the null hypothesis as:

$$F = SSR(a-1)^{-1} / SSE(N-a)^{-1} \tag{5-49}$$

where *SSR*, *SSE*, and *a* are random regression sum of squares, the random residual sum of squares, and the number of terms at the fitted-model, respectively. R^2 is an important statistic to express the proportion of the variation of the y_i by fitted-model and FEA data for the mean of $\bar{y}$ as:

$$R^2 = SSR(SST)^{-1} \tag{5-50}$$

for checking the adequacy of fit in the design region, the ANOVA is employed through developing a linear statistical model as:

$$y_{ij} = \mu + \tau_i + \epsilon_{ij} \begin{cases} i = 1,2,\ldots,a \\ j = 1,2,\ldots,n \end{cases} \tag{5-51}$$

The ANOVA is using un-replicated factorials, in which the total and error refer to regression, and residual, respectively. Based on the Table 5.4.2, R^2-*value* using MR-CCD, FFD, CCD, and BBD are 0.9998, 0.9992, 0.9987, and 0.9982, respectively. Among all design function, the efficiency of MR-CCD was increased to the maximum value of 99.98% during the rated-speed-operation.

Fig. 5.5.5 comprehensively presents the efficiency as objective function. Based on the framework, the optimal efficiency through the global sizing optimisation was drawn into the true responses, where Fig. 5.5.5-a indicates the response to the controllable variables (x_1, x_2) at the lowest shaft rotation of 15 rpm maximum reachable efficiency of %90.15. Fig. 5.5.5-a illustrates the 99.93% of the total variation in efficiency, in which the MR-CCD has a minimum error of 0.28% in the same boundary range, whereas BBD carries the maximum value of error with 0.97%. Thus, ANOVA is performed to examine how good the fitted-model is able to predict the response at any observation points, and for this target, *SST*, *F-value*, and R^2-*value* which belongs to the variations of the response were calculated. Fig. 5.5.5-b represents controllable variables of (x_1, x_3), in which maximizes the efficiency of %91.2. The response for the controllable variables (x_1, x_2) with a speed raise to 75 rpm is shown in Fig. 5.5.5-c, when a larger efficiency is obtained through controllable variables of (x_1, x_3) as presented in Fig. 5.5.4-d to analyze the effect of each controllable variable on the efficiency. Regarding the knowledge of the operation environment, the generator is compulsory to provide the best performance and also efficient at the rated speed which is 150 rpm. Fig. 5.5.5-e-f represents that the response based on the defined variables is significant with maximum efficiency of %98.13. Therefore, the fitted-model is successfully performed over the variable-speed-range analysis [19].

The optimisation process to achieve the global optimal operation point using the modified MR-CCD for the variable-speed-range application is reported through Table 5.5.3, where the optimal operation point deals with *dq*-plane inductances, - and also efficiency maximization, in which the output power is considered fixed in this study. The optimized efficiency is reported in Table 5.5.4 at the minimum speed of 150 rpm, where the maximum reachable efficiency of 98.13% was reached.

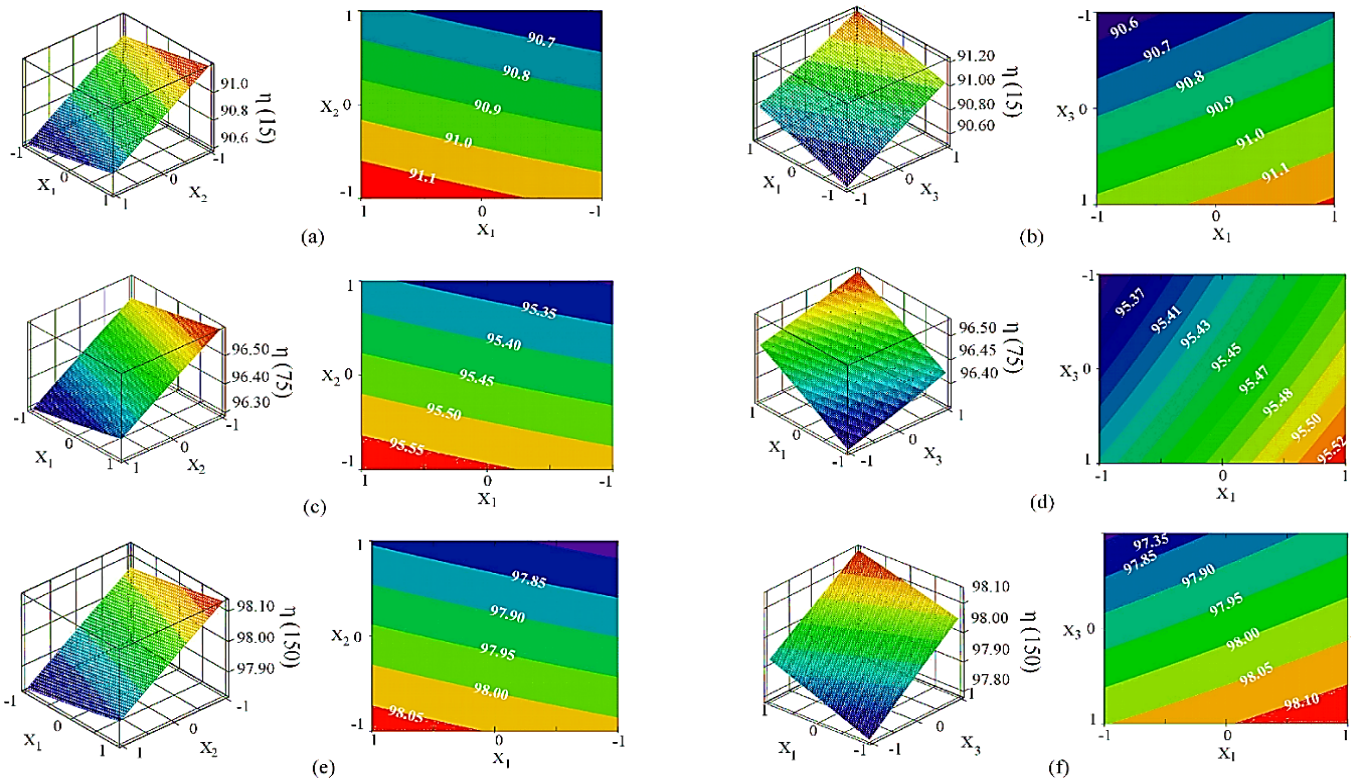

Fig. 5.5.5. Surface and counter plots of D-RSM results for variable-speed-range-objective from minimum speed of 15 up to the rated speed 150 (rpm), a) l_m versus l_g @15 (rpm), b) l_m versus S_w @15 (rpm), c) l_m versus l_g @75 (rpm), d) l_m versus S_w @75 (rpm), e) l_m versus l_g @150 (rpm), and f) l_m versus S_w @150 (rpm).

Fig. 5.5.6 illustrates torque-speed-loss and torque-speed-efficiency maps at the variable-speed-analysis of the optimised FE model with a vast range of 0-1000 rpm; however, the PMSG is designed to be operated under rated speed of 548 rpm. Fig. 5.5.6-a presents the variation of total losses (including iron and copper) at different speed and torque. Fig. 5.5.6-b indicates the variation of efficiency at different speed and torque. It is illustrated that PMSG operates by 0.98% higher efficiency during from 150 up to 1000 rpm. It is worthy to mention that the inverter losses are ignored to generate both maps.

Table 5.5.1 Coefficients of second-order regression model at 1st-level and 2nd-level RSM.

Coefficients	First-level	Second-level
β_0	91.382	96.345
β_1	0.568	0.054
β_2	-1.247	-0.029
β_3	5.115	0.269
β_4	0.075	2.358×10^-3
β_5	-0.265	3.583×10^-4
β_6	0.548	3.017×10^-3
β_7	-5.833×10^-4	-4.083×10^-3
β_8	-0.063	-7.667×10^-4
β_9	-1.296	-0.03

Table 5.5.2 ANOVA using different DOE's methods with 5% level.

Method	Source	Sum of Squares	DF	Mean square	*F*	R^2 (%)
MR-CCD	x_1	0.228	-	0.228	0.288	-
	x_2	69.06	-	69.06	50.54	-
	x_3	0.53	-	0.53	0.039	-
	Total	80.56	40	-	-	99.98
	Error	0.28%	11	1.544	-	-
FFD	x_1	0.399	-	0.399	0.297	-
	x_2	71.059	-	71.059	52.905	-
	x_3	0.068	-	0.068	0.051	-
	Total	71.526	7	-	-	99.92
	Error	0.53%	4	1.343	-	-
CCD	x_1	0.466	-	0.466	0.381	-
	x_2	81.005	-	81.005	53.37	-
	x_3	0.789	-	0.789	0.0831	-
	Total	82.26	8	-	-	99.87
	Error	0.6%	4	1.778	-	-
BBD	x_1	0.77	-	0.77	0.799	-
	x_2	84.92	-	84.92	0.1	-
	x_3	1.51	-	1.51	$6.98*10^{-3}$	-
	Total	86,2	12	-	-	99.82
	Error	0.97%	5	2.095	-	-

Table 5.5.3ANOVA Using mixed-resolution-CCD.

Method	Source	Sum of Squares	DF	Mean square	*F*	R^2 (%)
MR-CCD	x_1	0.228	-	0.228	0.288	-
	x_2	69.06	-	69.06	50.54	-
	x_3	0.53	-	0.53	0.039	-
	Total	80.56	40	-	-	99.96
	Error	0.574%	11	1.544	-	-
Modified-MR-CCD	x_1	0.393	-	0.399	0.297	-
	x_2	71	-	71.059	52.905	-
	x_3	0.066	-	0.068	0.051	-
	Total	71.459	40	-	-	99.98
	Error	0.457%	11	1.343	-	-

Table 5.5.4 Optimization results and verification.

Parameters at rated speed	Pre-optimization	Post-optimization	FEA verification
L_d (mH)	468.26	470.76	470.88
L_q (mH)	468. 21	471	470.96
E_p (V)	315	414	428
λ_m (mVs)	1691.88	1720.43	1719.72
P_o (W)	455.75	460.84	469.44
P_{copper} (W)	46.8	33.5	34.0
P_{iron} (W)	226.6	206.5	207.3
η (%)	94.23	97.13	97.10

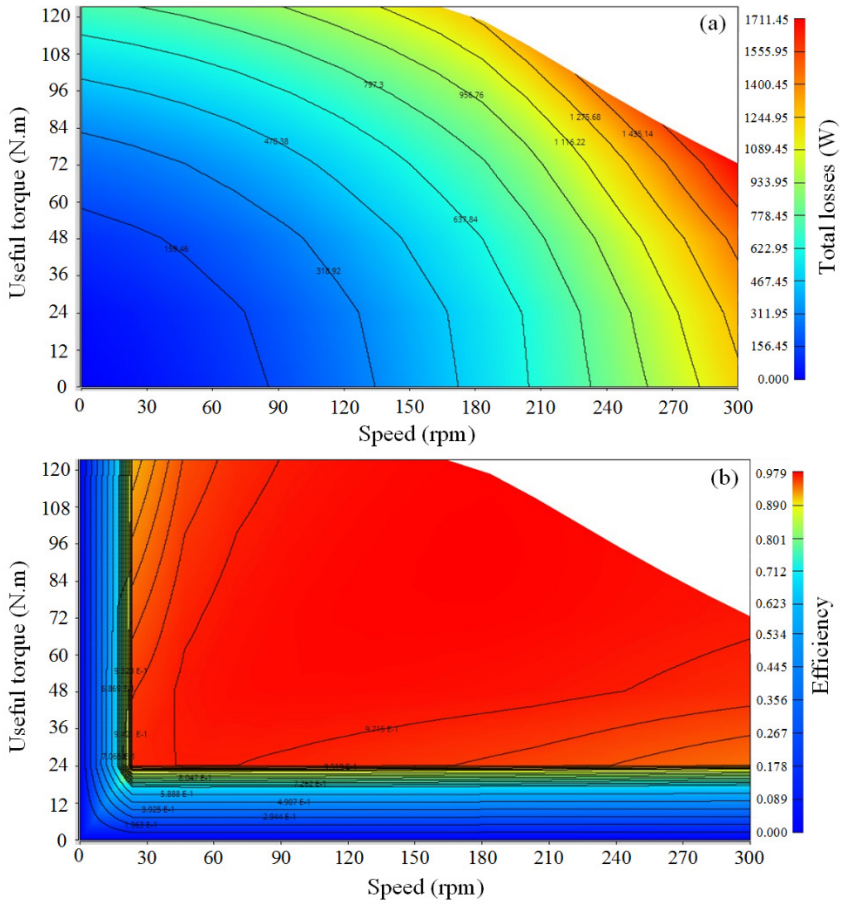

Fig. 5.5.6. Performance maps of the optimized PMSG at variable-speed-range analysis, a) Total losses, and b) efficiency maps.

5.6 Halbach Array Topologies and their Performance Improvements

Electromagnetic (EM) solutions possess many technical advantages contrary to conventional topologies in terms of performance of electrical machines using the Halbach array-based orientation (HABO) that results to improve and increase sinusoidal electromotive forces (EMFs) waveforms which originates from an increased sinusoidal airgap flux density distribution, and reduced machine's mass because of its self-shielding magnetization that allows the machine to operate without any back-iron [35-41]. The main objective is to determine the best possible magnetization orientation with the gap consideration between each magnetic segment particularly in the HABOs for the first time. Therefore, the influence of different segment numbers per pole for fundamental amplitude, waveform distortion factor, and all other fundamental EM aspects is studied by given objective design function (5-61) along with some analytics.

In 1973, the influence of installing magnetic blocks in a certain order was discovered by John C. Mallinson to achieve higher airgap flux density for the very first time [35]. Afterward, Klaus Halbach invented the HABO to focus particle accelerator beams in the 1980s [36]. Since then, many researchers studied analytical and numerical modeling of different HABO in electrical machines.

The outer rotor surface mounted PM synchronous machines (PMSMs), in which a double-layer 2nd grade fractional winding is employed due to a number of advantages such as short end-winding. The outer rotor machines can reach a high torque at a low speed for the direct-drive applications with a low-speed operation, such as small power generation [37].

Y. Shen, and Z. Zhu [38] discussed a general analytical model which is capable of predicting the electromagnetic performance of slotted/slotless brushless PMSMs with both even- and odd-segment Halbach array, having different magnet remanence, magnetization angle and arc for each single magnet segment. The emphasis has been on the magnetization which is the key in analytical modeling of PMSMs having a segmented Halbach array and its investigation.

Reference [39], investigated the differences between a segmented HABO PMSMs, and a single ring HABO PMSMs at airgap magnetic field distribution and back-EMF waveforms, where the gap between segments is ignored by FE model. Whereas, research has carried out the effects of the segment number per/pole on airgap magnetic field distribution and back-EMF waveforms.

In ref. [40], and [41], the established analytical models aimed on the Halbach array, in which it has two segments per/pole and the magnetized directions of two segments are radial and tangential, respectively. Additionally, influences of the width ratio of two segments per/pole on torque pulsation and maximum torque have been analyzed.

Ch. Xia, *el al*. [42] also studied analytical modeling of HABO in PMSMs with consideration of gap between each segment. Moreover, the effects of the parameters of the segmented Halbach array, enclosing gap between segments, segment number per/pole, and pole pair number on the fundamental amplitude, and waveform distortion factor of the radial component of airgap flux density are analyzed using the analytical model. Whereas, reference [43] presents a comparative study of torque analysis for PMSMs couplings with parallel and four segmented Halbach-array magnetized magnets, by analytical field calculations. On the basis of the magnetic vector potential, they derived analytical solutions for the magnetic field produced by the interaction between the inner and outer PMs for the parallel- and Halbach-array magnetized cases. Then, the magnetic torque calculation using the derived solutions and Maxwell stress tensor has been reported. This study inspired us to consider gap consideration for the most well-known HABO's topologies on PMSM.

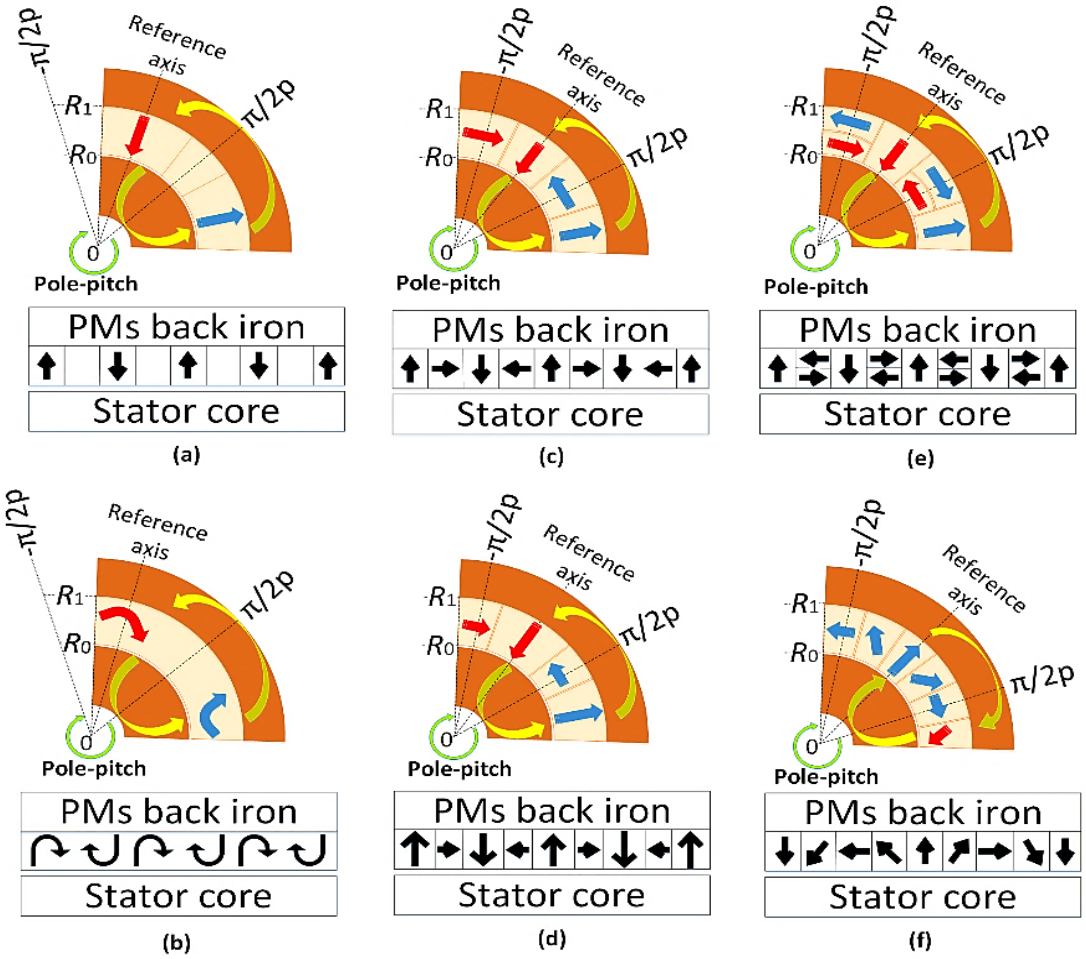

Fig. 5.6.1 A comparative schematic of different EM orientation topologies with equivalent pole-pitch, a) conventional parallel topology with considering airgap between each magnet, b) polar anisotropic topology, c) 2-segmented HABO with gap consideration between each magnet, d) 2-segmented unbalanced HABO with gap consideration between each magnet, e) modified 2-segmented HABO with gap consideration between magnets, and f) 4-segmented HABO with gap consideration between magnet.

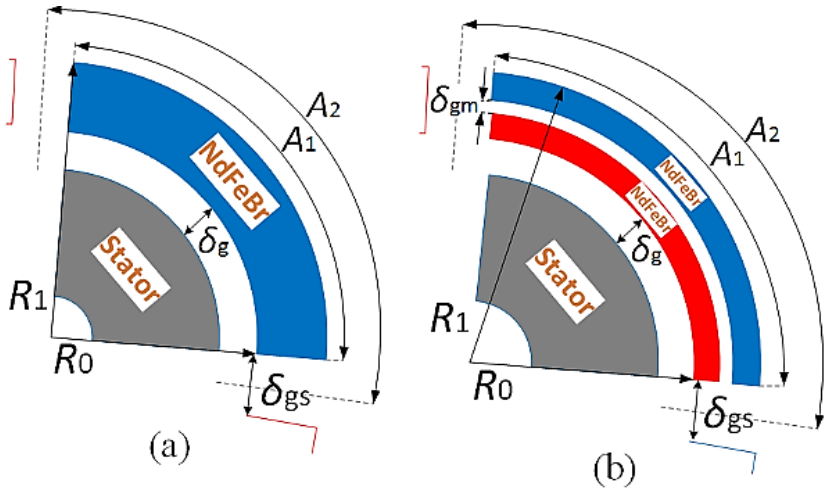

Fig. 5.6.2 Permanent magnet's geometrical design perspective with gap consideration.

N. Del-Valle, *et al*., investigated the levitation and guidance forces calculation and stability arising from both conventional arrangements and recently proposed Halbach-like arrangements. Afterward, a comparison was carefully made under similar conditions, in which conclude that not always complicated arrangements based on Halbach arrays bring significant improvements with respect to some simpler arrangements that also provide large force [48]. This section aims to gauge EM performance for six distinctive patterns of magnetization, five HABO FE-models, and one conventional parallel-based FE model. To study how modified 2-segmented Halbach array develops its performance in comparison with the classic 2-segmented Halbach array model for the outer rotor PMSMs with a double-layer, 2nd-grade fractional-slot winding [44-45]. All the significant EM perspectives are performed with the gap consideration among the FE models using a design function with a number of constraints. At last, the best magnetization topology is proposed for experimental investigation. Additionally, the proposed prototype is under operation for a standalone wind energy conversion system [46].

In EM design, it is always crucial to deal with various levels of performance and its complexity. However, based on the demand, the design topology and quality may change.

The key in the analytical modeling of PMSMs with segmented Halbach array is the magnetization with consideration of the gap, in order to deal with interaction force between each segment. The field vector in airgap and magnetic blocks (PMs) [38] can be calculated using:

$$B_g = \mu_0 . H_g \tag{5-52}$$

$$B_{PM} = \mu_0 . \mu_r . H_{PM} + \mu_0 . M \tag{5-53}$$

where the amplitude of magnetization vector M in polar-coordination for parallel topology can be defined in (5-54):

$$\begin{aligned} M_{parallel} &= M_r . r + M_\theta . \theta \\ &= \sum_{n=1,2,3,\ldots}^{\infty} M_{rn} . \cos(np\theta) . r \mp \sum_{n=1,2,3,\ldots}^{\infty} M_{\theta n} . \sin(np\theta) . \theta \end{aligned} \tag{5-54}$$

where '+' has to present while the PMSM operates with outer rotor topology, which is the case study of the paper. Also, '-' for interior rotor machines [38]. In Fig. 5.6.1, a proper view of the magnetization topologies, which are used in this study for PMSM based on magnetic orientations of the PMs, segmentation, and gap considerations can be seen. Fig. 5.6.1(a) shows a conventional parallel EM orientation topology (CPT) using 20 pole-pair NdFeBr magnets without any segmentation, in which gap consideration is neglected, therefore a higher demand of magnet volume needed in comparison to HABO-based models.

Fig. 5.6.1(b) illustrates with continuous HABO which is known as PA commercially, where no segmentation is needed to provide HABO. However, there is significant negligence that is addressed in the EM-based study results and discussion section. Fig. 5.6.1(c) presents a 2-segmented HABO with gap consideration between each segmented magnet. From the manufacturing process standpoint, the radial gaps between each magnet segment can be glued. Moreover, the interaction force between each segment can be considered. Afterward, an unbalanced-2-segmented HABO with the unequal area of magnet is studied which can be seen in Fig. 5.6.1(d). At last, a modified 2-segmented HABO with orientation with radiallly and axially segmentations for gap consideration is shown in Fig. 5.6.1 (e). To provide a comprehensive study over the most well know HABO's, a 4-segmented HABO with radial consideration of the gap between segments considered that is illustrated in Fig. 5.6.1(f). Fig. 5.6.2 represents the significant geometrical design parameters which are taken into account for the gap consideration.

In HABO each magnetic block has a specific magnetization orientation, where the orientation of each block can be given as:

$$\theta_{m,i} = \theta_i(1+p) \tag{5-55}$$

where θ_i represents the angle between the center of the ith segment in which $\theta = 0$ (the conditional angle of orientation). Thus, θ_i can be redefined as follows:

$$\theta_{i=1,2,3,\ldots,2pl} = \frac{(i-1)\pi}{p.l} \tag{5-56}$$

The HABO consists of three segments, side-magnet, mid-magnet, and end side-magnet. Each segment is magnetized in the parallel orientation, however with a different angle of orientation. Therefore, the ratio of the nth PM pole-are to the pole-pitch can be expressed as:

$$R_{pa/pp} = W_m / W_p \tag{5-57}$$

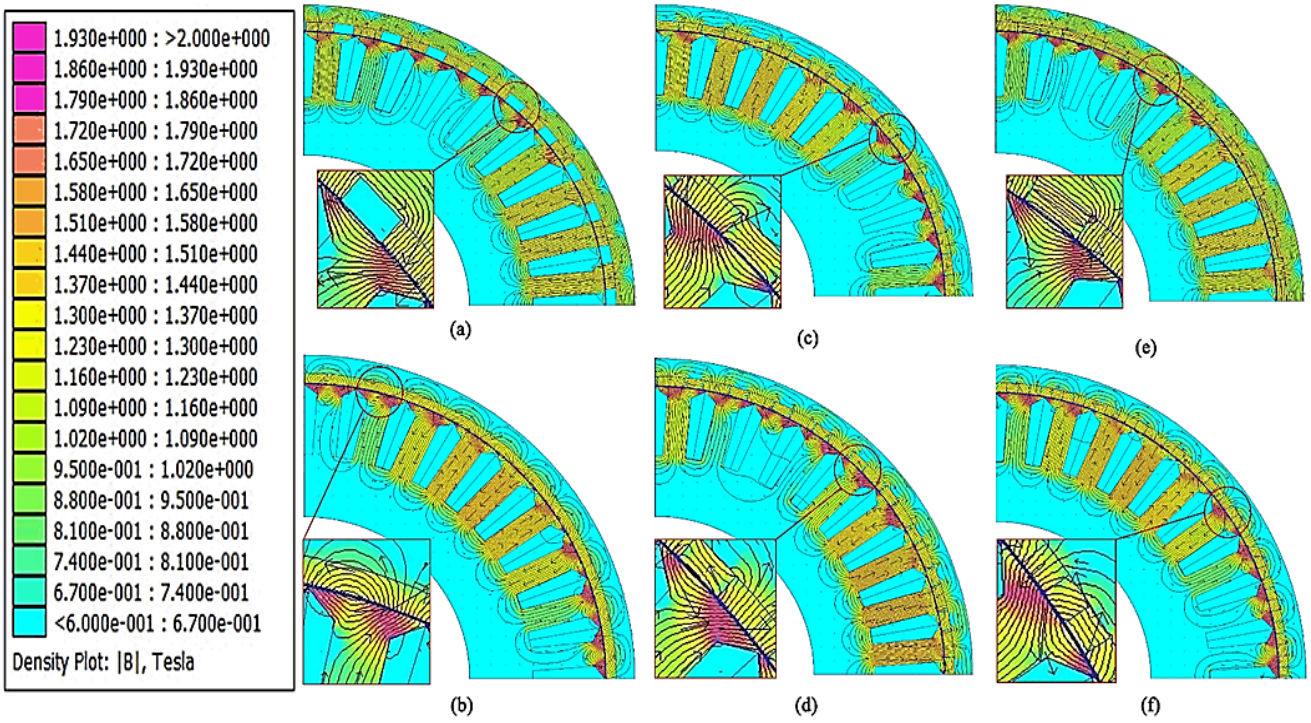

Fig. 5.6.3 Magnetic flux density distribution using FEA for different magnetized PM topologies with equivalent pole-pitch, a) conventional parallel topology with considering the airgap between each magnet, b) polar anisotropic topology, c) 2-segmented HABO with the gap consideration between each magnet, d) 2-segmented unbalanced HABO topology with the gap consideration between each magnet, e) modified 2-segmented HABO with the gap consideration between magnets, and f) 4-segmented HABO with the gap consideration between each magnet.

The ratio of *n*th PM pole-arc to the pole-pitch is given:

$$R_{n_{pa/pp}} = W_{n_{pa}} / W_p \tag{5-58}$$

The gap consideration as shown in Fig. 5.6.1 can be defined by the distance between magnets is presented as A_1, and the width of the segment is shown as A_2. Thus, the ratio of A_1 and A_2 is defined as the relative pole-arc coefficient using:

$$\alpha_{pa} = A_2 / A_1 \tag{5-59}$$

Accordingly, the gap between the PM segments in this paper is calculated by the relative pole-arc coefficient and the radius at the center of the PM [41], given by:

$$\Delta A = A_2 - A_1 = (1 - \alpha_{pa}).\frac{\pi(R_0 + R_1)}{2p.l} \tag{5-60}$$

Normally, in many papers, the consideration of gap between segments was neglected in order to reduce design complexity by setting to one. Consequently, the gap between each magnetic block will be zero.

To determine the best gap size between each magnet segment, the following objective design functions can be drowning into an optimization process:

$$s.t.\begin{cases} f_1(x) = (1-\alpha_{pa,i}).\dfrac{\pi(R_0(i)+R_1(i))}{2p.l} \\ g_1(x) = 450 - P_{out} \le 0 \\ g_2(x) = J_c - 4 \le 0 \\ g_3(x) = T_r(i) - T_{rn} \le 0 \\ g_4(x) = T_c(i) - T_{cn} \le 0 \\ g_5(x) = B_i - 2.1 \le 0 \\ g_6(x) = 0.92 - \eta \le 0 \\ g_7(x) = sf - 0.7 \le 0 \end{cases} \quad (5\text{-}61)$$

Through this section, the conceptual idea of the paper by introducing the magnetization topologies and its considerations was presented. Next, the EM comparative results are discussed in the following section.

A. EM-based Study Results and Discussion

According to the preceding sections, a significant emphasis lies on the magnetic flux density distribution (which can be seen in Fig. 5.6.2,) particularly in maximizing the airgap flux density of the models which causes preferably coming EM characterizes such as higher output torque, and EM power. In this section, analytical calculations will be validated through FEA and, in addition, both calculation methodologies are implemented with considerable accuracy. The airgap flux density [48] can be calculated as follows:

$$B_r = \sum_n \frac{q(M_n.H_n + N_n.K_n)}{\mu_r(q^2-1)}.[r^{q-1} + a^{2q}r^{-q-1}]c^{-q+1}H_n\cos(q\theta) \quad (5\text{-}62)$$

where $q = np$; M_n and N_n are the nth harmonic component of the radial and tangential components of magnetization; H_n and k_n are functions of q, μ_r and the different radii given in Rasmussen's paper [14]. The back-EMF as an open-circuit concept is defined with [51]:

$$e = \frac{\partial\psi}{\partial t} = \omega.\frac{\partial\psi}{\partial\theta} \quad (5\text{-}63)$$

Accordingly, the fundamental EMF/phase is calculated using:

$$E_{q1} = (\frac{p.k_{w1}.T_{ph}.\Phi_{m1}}{\sqrt{2}}).\omega_m \quad (5\text{-}64)$$

The flux-linkage is [50-51]:

$$\psi = \int edt \quad (5\text{-}65)$$

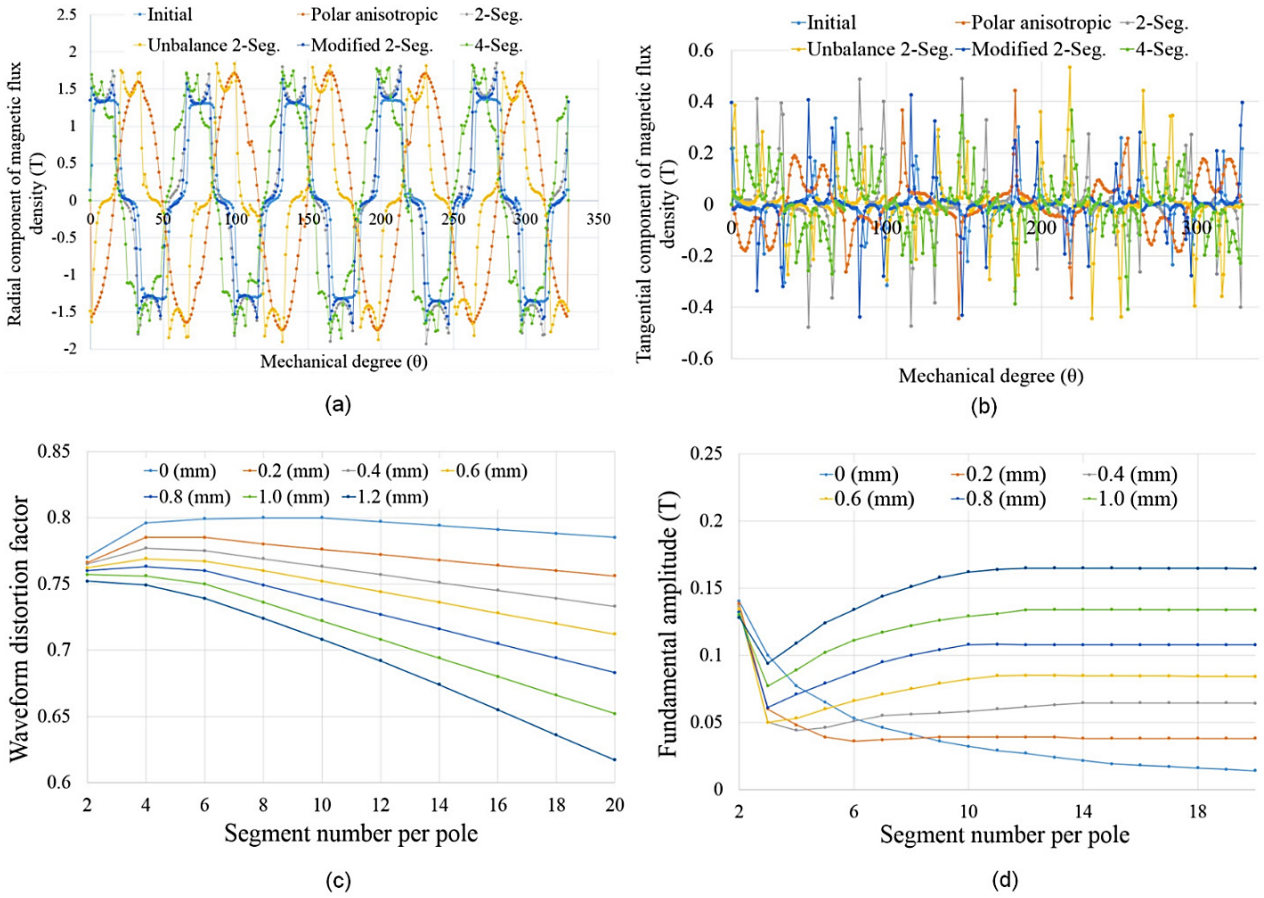

Fig. 5.6.4 FE comparison of the magnetic airgap flux density capability with gap consideration, a) radial component of the magnetic flux density, b) tangential component of the magnetic flux density, c) effect of segmentation on waveform distortion factor, and d) effect of segmentation on fundamental amplitude.

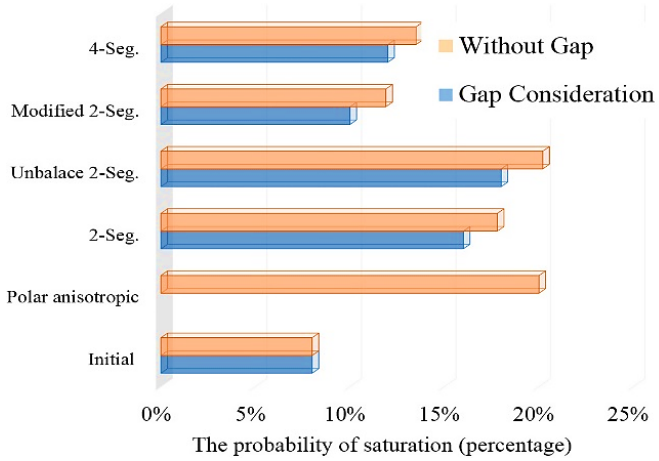

Fig. 5.6.5 The probability of magnetic flux density saturation.

Based on Fig. 5.6.3, it is obvious that by implementing various magnetization topologies, the pole pair of the machine yet remained unchanged. The veracity of magnetic fields with maximum 1.8 (T) somewhere around magnetic blocks can be seen in purple color. In Fig. 5.6.4(a), it can be seen that PA is provided such a great sinusoidal radial component which is utilized

in order to model HABO without considering segmentation and gaps with a significant error in comparison with the other real case of HABOs. Furthermore, the error also can be seen in the tangential component of the magnetic airgap flux density.

According to the results, it should be mentioned that the modified 2-segmented and 4-segmented models are presented a better probity among all HABOs. Although, unbalance 2-segmented and 4-segmented models have recorded a bigger radial and tangential component of the airgap flux density. The waveform distortion factor of the radial component of airgap flux density [41] is achieved by:

$$K_{dB} = \sqrt{\sum_{i \neq 1} \left(\frac{\left|B^{1}_{radial}\right|}{B^{h}_{radial}}\right)^{2}} \tag{5-66}$$

The gap between segments should not be changed to study the effect of the segment number per pole on the radial component of airgap flux. In the above equation, if only the gap between segments is unchangeable under the condition for the radius of the magnet, and pole pair number will be constant. Therefore, the relative pole-arc coefficient [41] will change with the segment number per pole through below expression:

$$\alpha_{pa} = 1 - \frac{l}{l_i}(1 - \alpha^{i}_{pa}) \tag{5-67}$$

Fig. 5.6.4(c) demonstrates that the fundamental amplitude of the radial component of airgap flux density is risen slowly and ended to be stable through the rise of the segment number per pole, while the gap between segments is chosen to zero. Whereas, the fundamental amplitude of the radial component of airgap flux density reaches the maximum value at the beginning and subsequently a gradual reduction via the increased of the segment number per pole when the gap between segments sets involving a value other than zero and the consideration of the gap between segments is accounted. In addition, when a larger gap between segments is involved, the lesser segment number per pole causes the maximum fundamental amplitude, and accordingly a larger change rate of the fundamental amplitude will be carried out. Fig. 5.6.4(d) illustrates that having the gap between segments set to zero, the waveform distortion factor of the radial component of airgap flux density is decreased slowly and ended to be stable by the increasing of the segment number per pole. In contrast, while the gap between segments is involving a value other than zero. Thereafter, the radial component of airgap flux density gains a smaller value first, and after that, it fluctuates through the increase of the segment number per pole. Nonetheless, the larger the gap between segments will be, the less the segment number per pole is required.

Table 5.6.1 Coenergy calculation in Joules.

Models/Methods	CPT	PA	2-Seg.	Un.2-Seg.	Modified 2-Seg.	4-Seg.
Analytical	91.1	144.7	145.9	151	159.4	143.4
FEA	90.33	143.66	145.2	150.4	158.8	142.8

The waveform distortion factor gains a smaller value, also a larger the change rate of the waveform distortion factor causes the waveform distortion factor to be the minimum. The likelihood of the saturation (from Fig. 5.6.3 data) based on percentage is represented in Fig. 5.6.5. The CPT model has the minimum probability of magnetic saturation in comparison with the HABO models, due to use of fewer magnets. Among the HABO models, the modified 2-segmented model has the least likelihood of saturation. However, the conventional parallel orientation with fewer magnetics blocks has even less probability. Therefore, the modified 2-segmented is proposed, while the PA magnetization even by neglecting segmentation and the gap

between each block is observed as the highest likelihood of the EM saturation. Fig. 5.6.6(a) shows the flux linkage waveforms from different models, in which the flux passes by the surface S to link the flux linkage of the counter integral through using Stoke's Theorem, where the expression [49-50] can be given:

$$\psi = \int_S (\nabla \times A) dS = \oint A.dl \tag{5-68}$$

From Fig. 5.6.6(a), in addition, it can be seen that the PA and 4-segmented models are produced and passed more flux in comparison with other models. However, all Halbach-array-based models have the largest amplitude of flux linkage, which

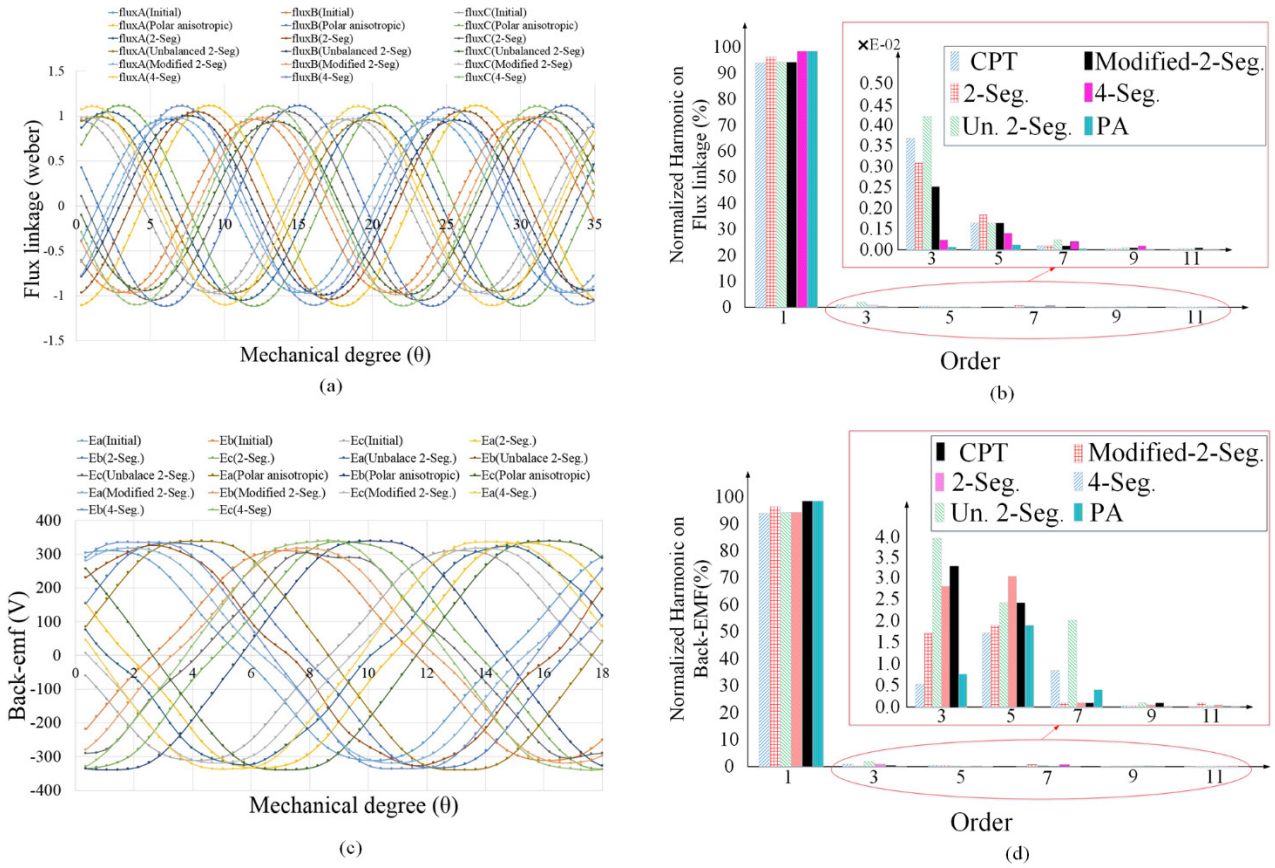

Fig. 5.6.6 FE comparison of all discussed models with gap consideration in terms of, a) flux linkage waveforms, b) harmonics on the flux linkage waveforms, c) back-EMF waveform, d) harmonics on the back-EMF waveforms.

caused by involving larger coenergy because of having more magnetic blocks (NdFeBr). The generated coenergy of the different model is analytically and numerically verified in Table. 5.6.1, based on the following [48] [51] expression:

$$W_c = \int_0^i \psi di \tag{5-69}$$

While the self-inductance remains changeless, ψ is completely produced by only the PMs. Hence, the additional ψ of the winding is out of consideration. Involving Fourier series on the waveform, gives the accurate harmonics calculations on the

flux linkage by Fig. 5.6.6(b). The fundamental has the largest normalized value (approximately 100%), and after for having a better understanding of the major harmonics such as 3rd and 5th, a zoom-in used. Again, it can be seen that the PA model provided a better picture by having the smallest major harmonics, although out of reality that tends to the error. The 4-segmented model presented a good real-case performance with having smallest 3rd and 5th. However, modified 2-segmented brought almost less amplitude on the 7th order. Fig. 5.6.6(c), after the largest sinusoidal back-EMF of the PA, and 4-segmented models have presented the most sinusoidal back-EMF waveforms, respectively. Thus far, the 4-segmented and modified 2-segmented brought the minimum 3rd and 5th harmonic orders, and by 7th harmonic order, the CPT, modified 2-segmented, and 2-segmented with almost the same value (about 0.1%), after the PA with 0.37%, and also 4-segmented by 0.85%. Moreover, the unbalance 2-segmented model carries the highest 7th harmonic by 2.0%. Thereupon, the minimum back-EMF harmonics are obtained by the proposed models of 4-segmented and modified 2-segmented. Furthermore, the minimum amplitude of harmonic orders can be seen in the PA model with a thinkable difference with other HABO models. Fig. 5.6.7(a) shows the cogging torque waveforms which originate from the variation of the magnetic reluctance of the stator teeth as seen through the PMs, while the rotor rotates between all models with different magnetization topologies, the modified 2- segmented model with less than 2 (N.m) is greatly simulated. However, the 4-segmented and PA topologies are placed as the maximum value of torque turning. The Table. 5.6.2 shows the comparison of the ripple torque and average torque which is calculated analytically and numerically with consideration of gap between segments M_p (gap) and without consideration M_p (no gap). Among the results, the 4-segmented with 390.8 (N.m), and 7.15% ripple torque is the most practical one. However, the unbalance 2-segmented topology with the minimum ripple torque (M_p) with 6.46% can be named as the most polished waveform. By the differences in the torque ripples, the influence of gap consideration is also obviously shown approximately 1% larger than non-gap consideration. The PA topology remains exceptional as long as this type of topology meets only theoretical issues and without any practical justification. Thus, the maximum practical average torque belongs to the 4-segmented model. The maximum EM output power with consideration of gap for all magnetization topologies is presented in Table 5.6.3, in which the largest calculated power with the value of 601.4 (W) belongs to the theoretical PA model. Although, the proposed topology relied on the 4-segmented design which takes the largest practical value with consideration of the gap.

Table 5.6.4 presents the iron loss prediction comparison, where the most considerable changes belonged to the eddy-current loss due to the various type of magnetization and used active magnet material. As result, the 4-segmented model brought a minimum total iron loss of 182 (W), whereas the unbalance 2-segmented draw on the maximum total iron loss by 241.4 (W). The calculation methodology is validated in [18-21].

Table 5.6.5 illustrates the THD over each single phase of back-EMF waveform, where it can be mentioned that mostly the highest percentage of THD is produced in phase C in all the models. Moreover, the lowest THD is reported in the proposed 4-segmented model. Additionally, all the HABO-based models have lower THD except unbalanced 2-segmented model.

Table 5.6.2 Torque ripple calculation [N.m].

Topology	Ave. Torque	Analytical M_p (gap)	FEA M_p (gap)	Analytical M_p (no gap)	FEA M_p (no gap)
CPT	349.1	8.29%	8. 35%	6.55%	7.18%
P.A.	394	None	None	5.11%	5.87%
2-Seg.	376.8	7.22%	8.99%	6.31%	7.22%
Unbalance 2-Seg.	353.4	4.88%	6.46%	3.62%	5.87%
Modified 2-Seg.	358.7	7.12%	7.89%	5.97%	6.94%
4-Seg.	390.8	6.71%	7.15%	5.66%	6.32%

Table 5.6.3 Rated EM output power [W].

Models/ Methods	CPT	P.A.	2-Seg.	Un. 2-Seg.	Modified 2-Seg.	4-Seg.
Analytical	495.9	600.4	574.6	539.5	542	598.7
FEA	496.2	601.4	575.1	541.8	543.3	600

Table 5.6.4 Iron loss prediction comparison.

Model	P_{hy} [W]	P_{eddy} [W]	P_{exe} [W]
CPT	73.5	124.3	19.4
P.A.	60.4	115	18.3
2-Seg.	66	129.2	17.8
Un.-2-Seg.	75.6	143.8	22
Modified-2-Seg.	65.8	113.4	14
4-Seg.	61	105.3	15.7

Table 5.6.5 THD on back-EMF per phase [%].

Back-EMF/ models	CPT	P.A.	2-Seg.	Un. 2-Seg.	Modified 2-Seg.	4-Seg.
A	8.2	3.5	7.8	8.8	3.4	2.9
B	8.5	3.7	8.0	8.9	3.5	3.0
C	8.8	3.8	8.1	9.2	3.6	3.2

5.6.1 Load Identification of Halbach Array Topologies with Gap Consideration

Distributed generation and electric vehicles normally employ permanent magnet synchronous generators (PMSGs) due to their high efficiency and power density characteristics, where the load is often supplied through a diode rectifier connected across the armature terminals. For this purpose, the electromagnetic (EM) and mechanical machine parameters should be accurately calculated. The most significant electromagnetic parameters are permanent magnet flux linkage, d-axis, and q-axis inductances, the line to line peak voltage, and rotor electromagnetic torque. The mechanical parameters are prevailing with

respect to the load characteristics, which is preferred in real applications where the commercial machine drive has the capability to estimate these parameters online or offline. Accordingly, many investigations have been reported recently.

Basically, the estimation of the mechanical parameters requires the electromagnetic torque and rotor speed as the inputs to the estimation model [58]–[65]. In reality, the rotor speed can be measured directly by the position sensor, while the electromagnetic torque needs to be calculated via the torque-constant and measured current. A typical solution is to use the nominal value of torque-constant of the generator to nearly calculate the electromagnetic torque [58].

Moreover, to reduce the design costs, the inverter can be replaced by a full-bridge diode rectifier followed by a DC–DC single switch converter [58]–[61] instead of using a pulse width modulation (PWM) converter acting as a controlled rectifier.

The main motivation is to take the gap consideration between each magnetic segment into account and evaluate its influence on the load side for the different type of magnetization orientations.

Lacchetti *et al.* [66], analyzes some operational issues of three-phase PMSG connected to a diode rectifier. This configuration coupled to a single-switch DC–DC converter has been used in small-scale wind energy conversion systems, and in energy harvesting systems to reduce costs.

Weiming *et. al* [67], discusses an equivalent circuit model of a synchronous generator with a diode-bridge rectifier and back-electromotive force (EMF) load has been presented in the paper. The principle of harmonic balance has been

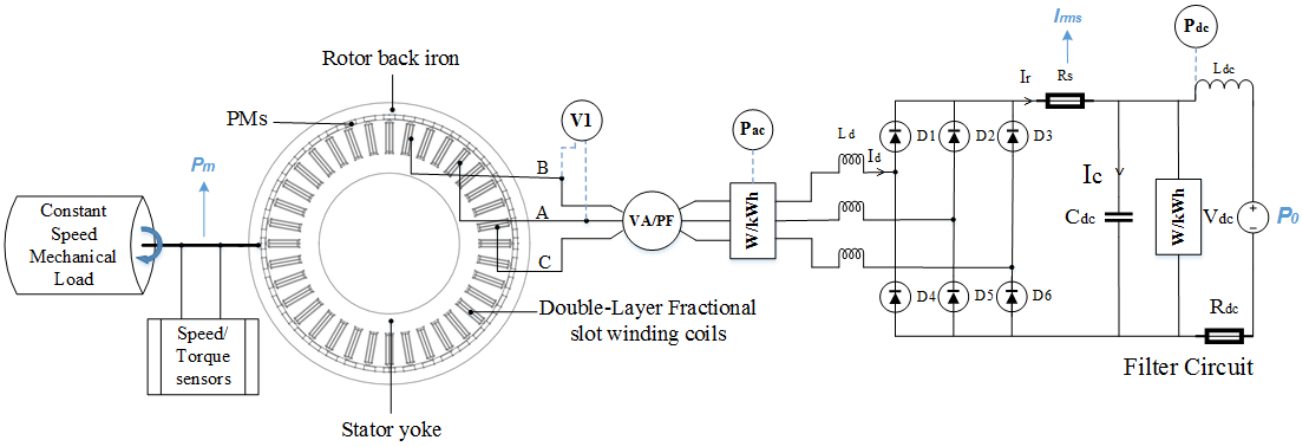

Fig. 5.6.1.1 The experimental setup of the coupled field-circuit PMSG finite element model feeding an uncontrolled three-phase full rectifier load.

applied, which makes it possible to construct a state-space mathematical model for the system. The criterion of stability is obtained for the system under small disturbances. Additionally, it is shown that the system's stability can effectively be improved by installing a short-circuited quadrature-axis winding on the machine rotor.

Wang *et al.* [68], the performance of an axial flux (PMSG) feeding an isolated rectifier load is studied using a coupled-circuit, time-stepping, 2-D finite-element analysis. The short- circuit performance has also been investigated. The second-order serendipity quadrilateral elements have been used in the analysis to obtain the accurate results of the analysis. Non-linearities in the field and electric circuit are taken into consideration. With the strong nonlinear diode parts existing in the external circuit, the special interpolating algorithm has been used for the motion interface between the stator and rotor to overcome the non-convergence problem in the computation. The algorithm has been validated by comparison with a conventional algorithm for an AFPMSG feeding with a rectifier resistive load.

In most of the recent design developments, where HABOs have been employed, such as [69-75]. The researchers have been neglected a fully realistic design consideration, the gap between each magnetic block which might affects the output load results. Therefore, we introduced an analytical and numerical modeling to overcome this challenge and finally presented the normalized error with and without the gap consideration.

This study challenges the mentioned electromagnetic and mechanical key designs of the machine via the coupled field-circuit SPMSG finite element (FE) models under a dynamic load analysis while the machine is feeding a diode rectifier load. Correspondingly, an evaluation is conducted on the influence of the different HABOs on the following EM parameters "L_d" axis inductance in (mH), "L_q" q-axis inductance (mH), "VLL(pk)" the peak line to line voltage in (V), in which the gap between each magnet segment is under consideration. In addition, various geometric models are studied in the mechanical perspective of the design due to a different combined moment of inertia This comparative study is using an uncontrolled three-phase full rectifier load (Fig. 5.6.1.1) that is provided a comprehensive comparison through the load mechanical torque, its torque ripples, the output load power, the power factor, combined moment of inertia calculation by the given experimental layout. Where, the "blue" parameters will be calculated in the following sections. All other mentioned design parameters with and without the gap consideration are also traced.

Through the schematic (in Fig. 5.6.1.1), it should be mentioned that the constant speed via a prime mover has been adjusted to the rated speed of 150 (rpm) coupled with the cross-sectional SPMSG. Also, the three output phases are measured for the power factor at the voltage.ampere/ power factor (VA/PF). Therefore, the coupled field-circuit SPMSG finite element (FE) time-stepped model under the dynamic analysis will be performed differently and reported in the following. The following section will discuss the analytical issues in the study along with notable considerations and assumptions. Following this, the section of comparison and investigation will represent the comparative results through a comprehensive discussion. Finally, the conclusion will summarize the highlights and outcomes of the research. The conclusion as the last section ends up with an overview of the work with outcomes. Also, the electromagnetic performance of the novel models is verified numerically and experimentally. The analytical definitions of how to consider gaps between each magnet segment are presented in Eq. 5-55 to 5-60 in the previous section. The gap consideration as shown [76] in Fig. 5.6.1.2 can define the distance between magnets as presented by A1, and A2.

A. The Combined Moment of Inertia of PMSG Models

The combined moment of inertia (also known as combined angular mass) is a mechanical design parameter that has to be calculated accurately. It is necessary for the load identification which determines the required torque for a desired angular acceleration about a rotational axis. This depends on the body's mass distribution as well as the axis chosen, with larger moments needing more torque to transform the body's rotation. Basically, the moment of inertia

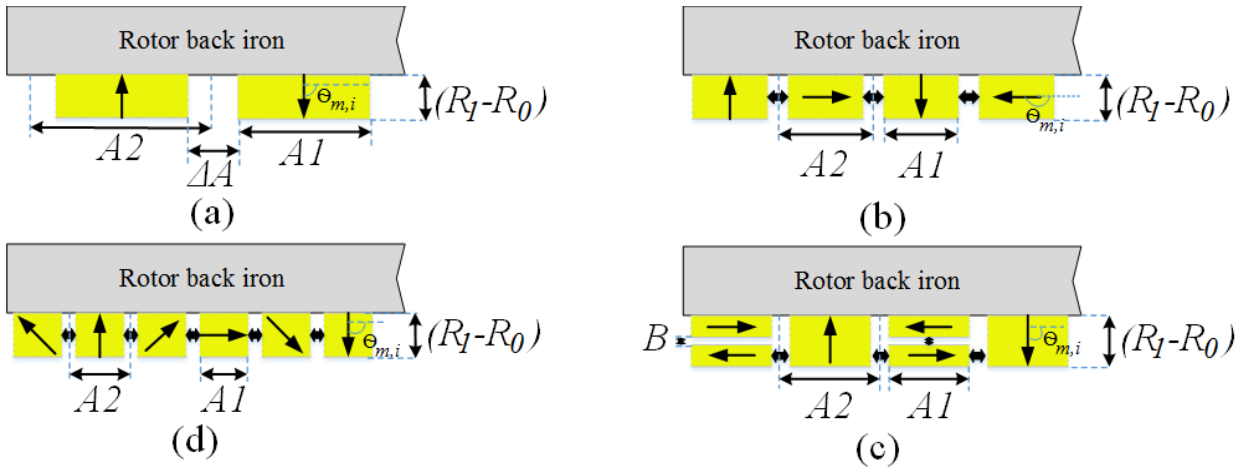

Fig. 5.6.1.2 The scheme of different EM orientation topologies with the gap consideration between each segment, a) conventional parallel topology (CPT), b) 2-segmented unbalanced HABO, c) modified 2-segmented HABO with gap consideration between magnets, and d) 4-segmented HABO.

relies on the radiuses, used material, and related density [77]. Therefore, the combined moment of inertia is calculated based on Fig. 3 for each individual geometry and corresponding regions through the below equation:

$$\tilde{I} = \sum_{n=1}^{3}\left(\int_{Q} r^2 dm\right) \tag{5-70}$$

where $\tilde{I}$ is integrated over the entire mass (Q) of the machine that consists of three regions of the SPMSG. The rotor back iron, the PMs, and the stator yoke are region 1, 2, and 3, respectively. The conventional parallel topology (CPT), 2-segmented, modified-2-segmented, and 4-segmented are 0.786, 0.8185, 0.8157, and 0.8146 (kg.m^2), respectively.

B. The Three-phase Uncontrolled full Rectifier Load Behavior

Based on the steady-state analytical model that is developed in [8], and [24], the behavior of the rectifier in Fig. 5.6.1.1 can be studied through a constant voltage (V_0), and series of connected resistances and inductances as:

$$e_k(t) = \hat{V}.\sin(\omega t - (k-1).\frac{2\pi}{3}), k = 1,2,3 \tag{5-71}$$

where $\hat{V}$ stands for the amplitude of the phase voltage and ω is the angular frequency.

Table 5.6.1.1 The density of used materials.

Parts	**Rotor back iron**	**PMs**	**EPOXY-KLEBER 8601**	**Stator yoke**	**Coils**
Density	7800	7600	1.31	7800	8890
Unit	kg/m^3	kg/m^3	g/cm^3	kg/m^3	kg/m^3

The diode forward voltage drop is v_D due to the diode current i_D, which is modeled via a threshold voltage V_D, and a resistance R_D:

$$v_D(i_D) = V_D + R_D i_D \tag{5-72}$$

where $i_D > 0$. Since the DC load caters an adequate inductance, the load DC current I_{dc} will remain ripple-free and constant. The rectified voltage that is the yield of three-phase diode rectifier includes the generated ripples by the rectifier [78].

In this modeling system, two key parameters referred to as the m-ratio and φ_z can be addressed as follows:

$$m = \frac{V_0 + 2V_D}{E_{pk}}, \cos(\varphi_z) = \frac{R + R_D}{Z} \tag{5-73}$$

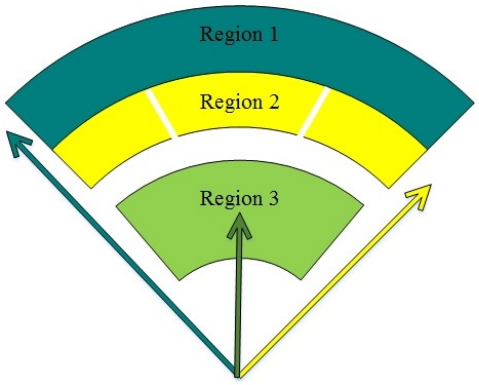

Fig. 5.6.1.3 The region definition with the related radiuses.

where Z stands for the modulus of the internal impedance that consists of R_D which further consists of the incremental resistance of the diodes by:

$$Z = \sqrt{(R + R_D)^2 + (\omega L)^2} \tag{5-74}$$

The peak value of the internal EMF (E_{pk}) is:

$$E_{pk} = \omega k_\omega N \varphi \tag{5-75}$$

where k_ω, N, and φ are the winding factor for the fundamental harmonic, the number of turns in series per phase, the peak magnet flux, and ω is the stator angular frequency. Additionally, the average DC current as well as the AC RMS current can be expressed as:

$$I_0 = \frac{E_{pk}}{Z} I_0^*(\theta_x, m, \varphi_z) \tag{5-76}$$

$$I_{rms} = \frac{E_{pk}}{Z} I_{rms}^*(\theta_x, m, \varphi_z) \tag{5-77}$$

Eq. (5-76 and 5-77), θ_x is an auxiliary variable angle that is integrated via an additional constraint equation that is:

$$F(\theta_x, m, \varphi_z) = 0 \tag{5-78}$$

Essentially, Eq. (12-14) relies on the m and φ_z which define an assumption to ignore θ_x, Fig. 5.6.1.4 demonstrates the different operation modes, in which, Fig. 5.6.1.4(a), (b), and (c) are representing 2/0, 2/3, and 3/3 operations, respectively.

The power delivered to the DC bus can be defined as given:

$$P_0 = \frac{E_{pk}^2}{Z}(m - \frac{2V_D}{E_{pk}}).I_0^*(\theta_x, m, \varphi_Z) \tag{5-79}$$

The three-phase full rectifier load coupled with the PMSG defines the efficiency through iron and mechanical losses lumped in $P_{fe,\,mech}$ which can be calculated as:

$$\eta = \frac{P_0 / E_{pk}^2 / z}{[P_0 / E_{pk}^2 / z] + [3.I_{rms}^{*2} \cos\phi z] + [2I_0^*(V_D / E_{pk}) + [P_{fe,mech.}(Z / E_{pk}^2)]} \tag{5-80}$$

The iron losses are approximated in $P_{fe,\,mech}$ which are approximated [66] through the no-load iron losses, as well as also mechanical losses as given:

$$P_{fe,mech.} = \omega(c_0 + c_1\omega) \tag{5-81}$$

c_0, and c_1 are lumped the frictional, mechanical, and hysteresis losses and mostly take into account the eddy current losses.

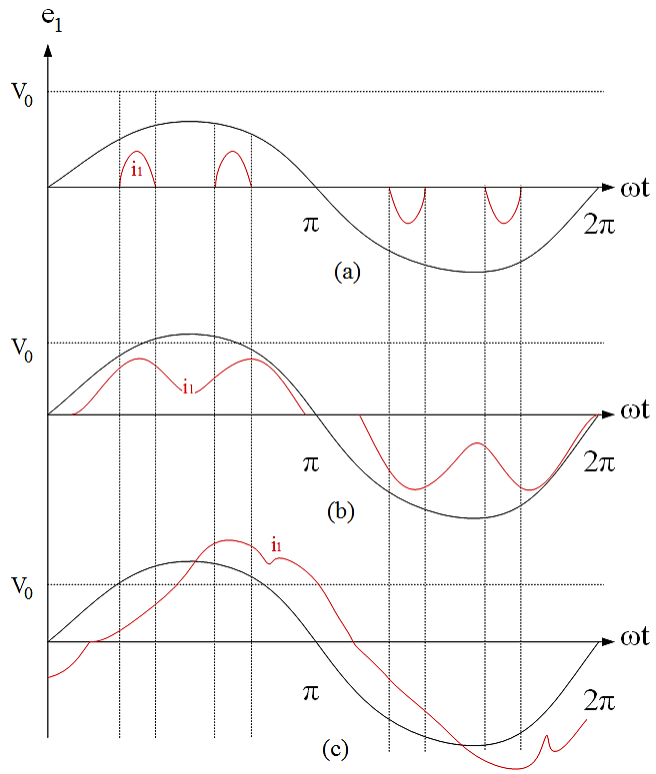

Fig. 5.6.1.4 The waveforms of various operation modes, in where, a) 2/0, b) 2/3, and 3/3 in the rectifier system.

C. The Eddy Currents Effects

According to [66], the important harmonic derived from the stator current necessitates that the eddy-current losses are taken into account. As resistance increases due to the eddy currents, a coefficient ($k_R > 1$) is employed for the calculation of Joule losses through increasing the windings DC resistance. Essentially, the k_R factor is a function of the square of the frequency and normal to the slot leakage flux direction. Thus, the winding losses can be expressed as:

$$\begin{cases} P_w = 3I_{rms}^2.k_R.R \\ P_w = 3I_{rms}^2.\tilde{k}_R.R \rightarrow if: I_2 = distorted \end{cases} \quad (5\text{-}82)$$

where I_2, and R are the stator winding current and the resistance of the winding. Additionally, when the current is distorted, a new resistance factor should be defined as follows:

$$\tilde{k}_R = 1 + (k_R - 1)\sum_k k^2 \left(\frac{I_k^2}{I_{rms}^2}\right) \quad (5\text{-}83)$$

$\tilde{k}_R$ factor is a function of the defined key parameters m-ratio and φ_z, on the operation point of the rectifier system that is derived by the eddy-currents. The k_R is based on the various characteristic angles of the impedance Z (φ_z) that are π/2, π/4, and π/6 results in the new resistance factors of 1.30986, 1.22891, and 1.19621 (rad). The lower φ_z results in higher eddy current losses due to the distorted current waveforms. It should be mentioned that fundamental k_R is bounded by 1.15 which

indicates that through a proper division and transportation of the conductors in the stator slots, the contribution of eddy-current losses can be more than 23% due to the distortion [66], [83].

As a simplified outcome of the previous sections, a flowchart based on the proceedings of the paper has been presented as Fig. 5.6.1.5. This demonstrates how the entire study has been developed from the initial input design data (such as slot/ pole number, the pole thickness of the magnet, pole-width, slot type and dimension, stack length, air-gap length, and etc.) of each model which was then defined in the algorithm. Following this, the calculation of coordinate points and geometry modeling was performed by the LUA program with automatic handling of boundary conditions, required key parameters have been computed by the 2-D FEA solver. Additionally, the time-stepped (transient) analysis was performed using the FE field analysis data and the circuit data (including external and the rectifier load) [83-84] simultaneously in order to calculate the P_0 and η. The larger d-q axis inductances are caused by the larger coercivity (in A/m) produced by the magnets in each model. Thus, the d-q plane inductances of each model have been presented in Fig. 5.6.1.6. Accordingly, the figure has mentioned that how the consideration of gap for the HABOs will affect the value of the produced inductances.

For instance, due to an increased number of involved gaps (instead of high coercivity in comparison with other models), the segmented model has been ranked with the lowest d-axis inductance among all the HABO models. Additionally, the polar anisotropic (continuous distribution) of the non-segmented model produced the greatest number of inductances. The considered value of d-inductance of each model (included the CPT model) has been used at the nominal current of 2.12 (A). Fig. 5.6.1.7(a) represents the initial FE-CPT model connected to the three-phase rectifier load, which had a rectified current (I_r) with an average value of 0.6 A. Additionally, for the 2-segmented HABO model shown in Fig. 8(b), there are considerable increases in VDC, and I_r. The modified-2-segmented HABO model seen by Fig. 8(c) that has improved the behavior of the classic-2-segmented model through maximizing V_{DC}, I_r. However, the 4-segmented HABO model responded with the greatest maximization of the mentioned calculated parameters V_{DC}, I_r.

The power factor (PF) calculation deals with the complexity of the mechanical structure and the magnet consumption in the SPMSGs. Although the structure and the operation principle of the SPMSGs are different based on the magnet consumption and the related geometrical changes, the relationship between the electrical parameters (such as power factor) can still be investigated through the classical synchronous machine theory. Essentially, the PF is the ratio of the active and apparent power. If the fundamental harmonic components of the voltage and current are much higher than the higher harmonic components (low total harmonic distortion (THD) of the voltage and current), the PF is calculated simply as the cosine of the displacement between the voltage and current (phase angle) [84-86] which can be written as:

$$PF(NI) = \cos(\arctan(\frac{Q}{P})) = \frac{P}{P_s} \tag{5-84}$$

where P, Q, and P_s (shown in Fig. 5.6.1.8) are the active, reactive, and apparent powers, respectively. The accurately calculated power factors of the studied models are all 0.95 which represents that the width/pole pitch ratio and the length/pole pitch ratio are the same in both the CPT and HABO-based models. However, the achieved MP for the different model has been seen through Fig. 5.6.1.8, and 5.6.1.9. The Fig. 5.6.1.9(a) represents that the maximum reachable output DC power at a current of 0.854 A, and PF=0.95. Fig. 5.6.1.9 (b) presents that the maximum P_0 *(I, cosφ)* of the 2-segmented HABO model as the function of the current and the PF will be achievable at the current of 1.037 A. In Fig. 5.6.1.9 (c), the maximum P_0 *(I, cosφ)* of the modified-2-segmented HABO can be generated at the current of 1.038 A, and PF=0.95. In Fig. 5.6.1.9 (d), the 4-segmented HABO model with maximum P_0 *(I, cosφ)* can be generated at a current of 1.107 (A), and PF=0.95. In addition,

the FE time-stepped behavior of the power P_0 *(I, cosφ)* can be seen in Fig. 5.6.1.9, in which the studied models of 4-segmented, modified-2-segmented, 2- segmented HABO models and the CPT model are 1.1 kW, respectively. Additionally, the Fig. 5.6.1.7, 5.6.1.8, and 5.6.1.9 have been summarized in Table 5.6.1.3. This improvement of the HABO-based models has been carried out due to several circumstances as [86]:

1) Higher flux linkage waveforms that are better suited to the studied geometries
2) More sinusoidal radial magnetic flux density
3) Fewer space and time harmonics
4) Increased fit of the sinusoidal back-EMF waveforms

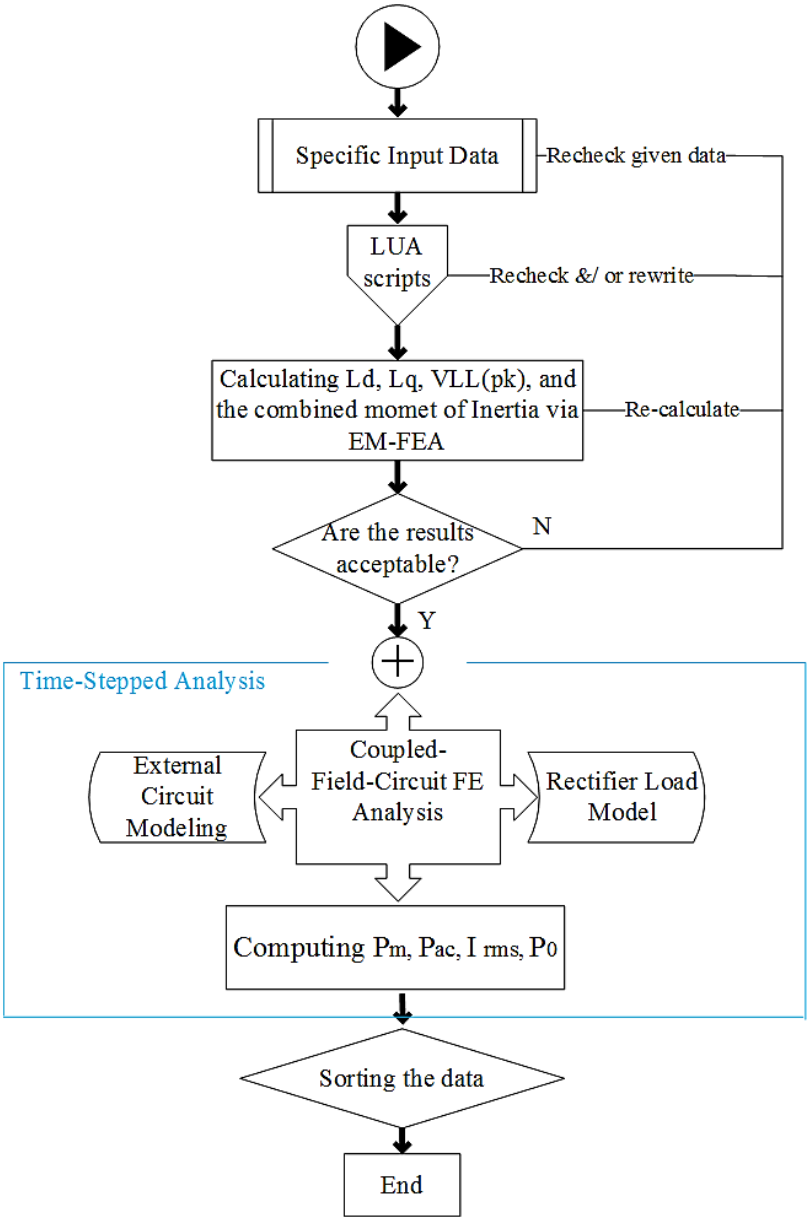

Fig. 5.6.1.5 The simplified procedure of the used methodology.

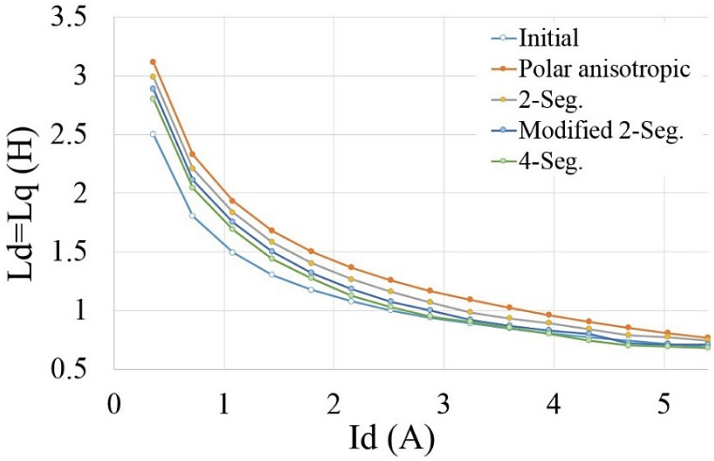

Fig. 5.6.1.6 The DQ-axis inductances FE computations via different models.

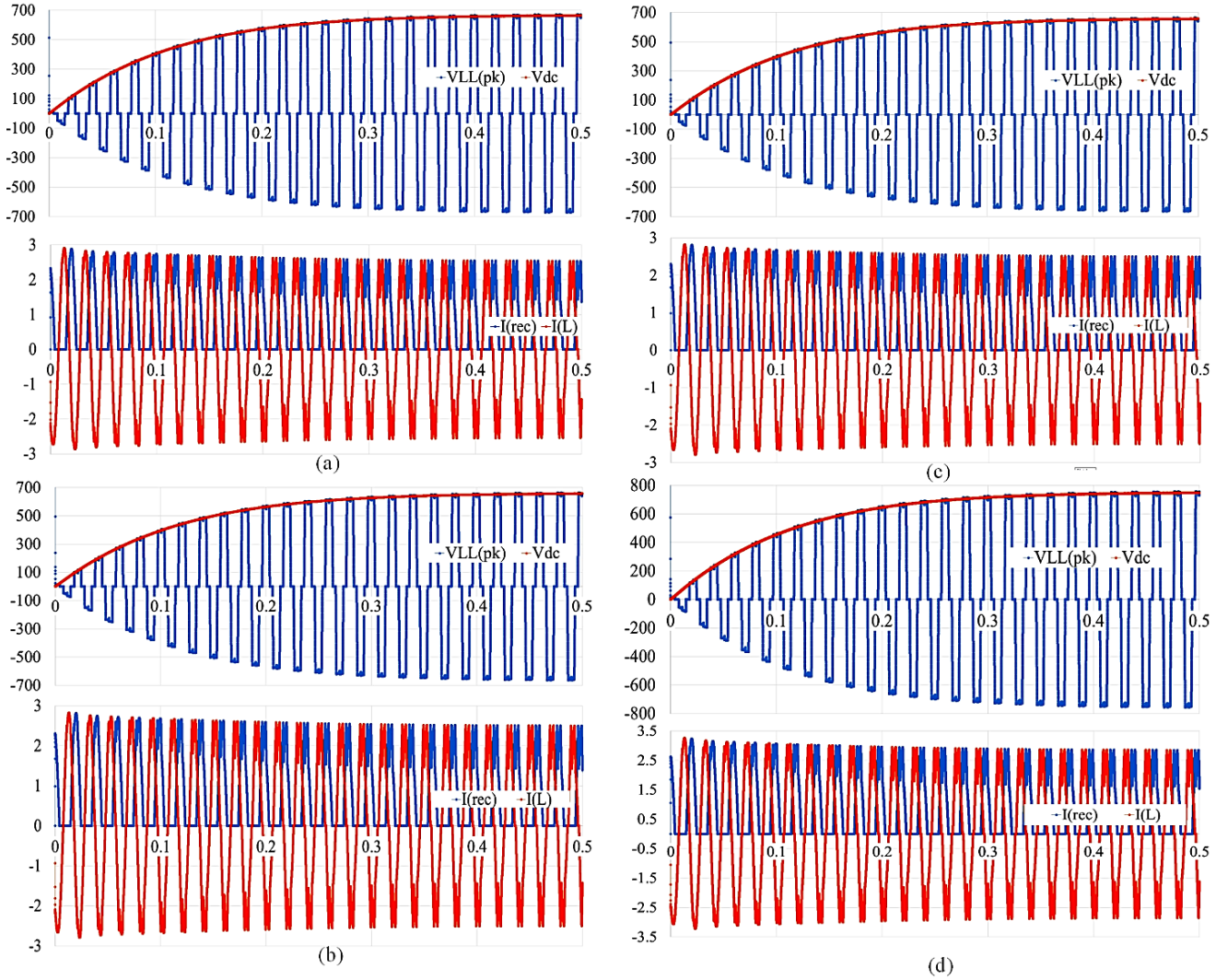

Fig. 5.6.1.7 The scheme of different HABO with the gap consideration between each segment, a) the CPT, b) the 2-segmented HABO, c) modified 2-segmented HABO, and d) the 4-segmented HABO.

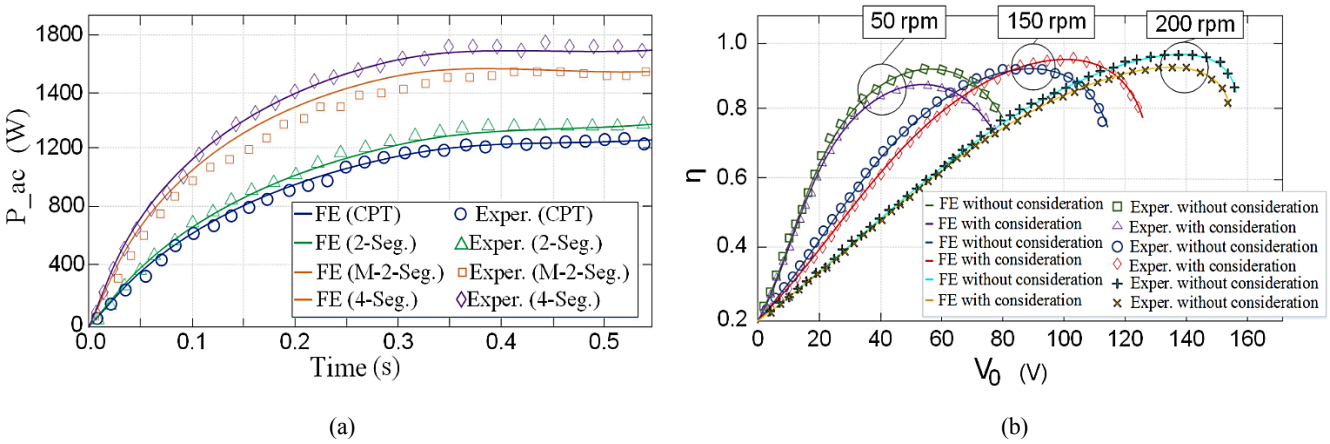

(a) (b)

Fig. 5.6.1.8 Numerical and experimental P_{ac} and efficiency of different HABOs, in comparison with gap consideration. a) P_{ac} variation, b) efficiency variation.

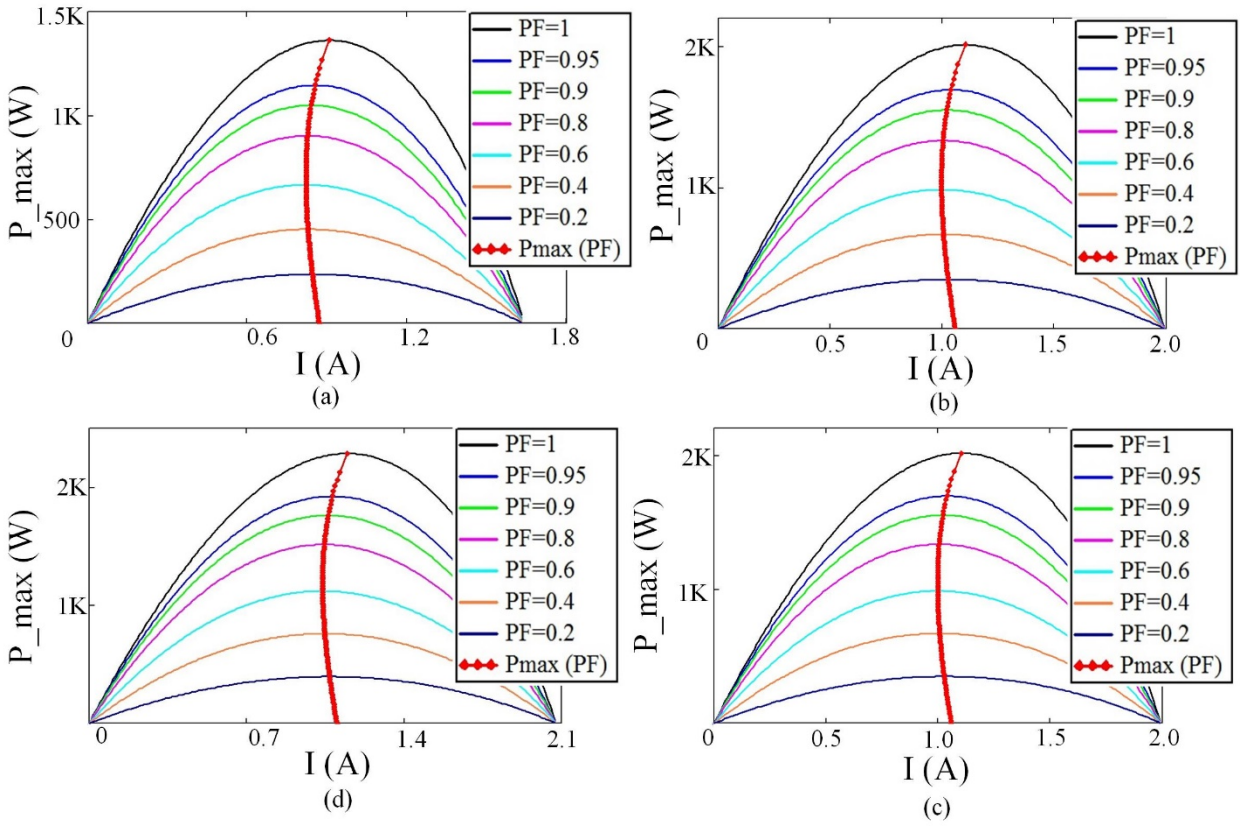

Fig. 5.6.1.9 The maximum output power of different EM orientation topologies with the gap consideration between each segment, a) the CPT, b) the 2-segmented HABO, c) modified 2-segmented HABO, and d) the 4-segmented HABO.

Table 5.6.1.2 Maximum power calculation with PF=0.95.

MP	CPT	2-Seg.	M-2-Seg.	4-Seg.
I_L (A)	0.96	1.037	1.038	1.107
I_{rec} (A)	0.60	0.61	0.61	0.63
P_{ac} (kVA)	1.16	1.37	1.44	1.66
P_0 (kW)	1.17	1.65	1.67	1.93

Similarly, the Table. 5.6.1 shows the produced co-energy [71] of the different models that is directly related to the EM output power of the SPMSGs. It can thus be observed that having more magnetic parts does not necessarily increase the co-energy production.

For example, the polar anisotropic model neglects the segmentation and the gap considerations which can be compared with other HABO-based models and is approximately equal in production. Additionally, the Table. 5.6.1 illustrates the diode rectifier load average results in comparison with all the studied models with the gap consideration. With respect to this Table, the output DC voltage, torque, and output DC power are raised, hence the efficiency is also increased. The 4-segmented model is reached 709 V (as the highest) among HABO-based models. It should be also mentioned that the output voltage by the proposed 4-segmented model is namely 115 V increased in comparison with the CPT model. The variation of maximum DC output power using HABO models is increased, in which 4-segmented, modified-2-segmented, 2-segmented, and CPT obtained 1.92, 1.39, 1.3, as well as 1.1 kW, respectively. Thus, a significant efficiency improvement could be finally presented, where the proposed 4-segmneted with gap consideration brought 96.8% which means 4.2% enhancement to the primarily CPT's efficiency (92.6%).

Table 5.6.1.3 The summarized calculated results.

Model	I_{rms} [A]	V_{dc} [V]	S [kW]	T_m [Nm]	P_{DC} [kW]
CPT	0.6	594	1.174	-72.6	1.1
2-Sg	0.7	644	1.377	-83.7	1.3
M2Sg	0.68	661	1.447	-89.3	1.39
4Seg	0.71	709	1.975	-103	1.92

6. Experimental Investigations of Optimal PMSG

In chapters 2, 3, 4, and 5, the nonlinear steady-state and transient finite element analysis (FEA) in 2-D and 3-D were developed for several individual targets. Even though there are some analytical studies done in the thesis, but they are verified using FEA. Transient FEA model was employed by rotor motion in order to check the magnetic flux density distribution in the PMSG in chapter 2. In chapter 3, mostly steady-state FEA was used to predict iron loss computation of the model, and the 2-D model was sufficient to bring accurate results due to the type of PMSG (which is radial-flux). As 3-D FEA performance is a reference of the machine's behavior, yet experimental investigations are required to validate the numerical-based models. To ensure that we have considered every single design aspect such as magnetic noise. By comparing analytical, FEA-based simulation and experimental results, the PMSG model can be verified. To avoid large cost of active materials and manufacturing, only the optimum PMSG is considered to be experimentally manufactured and being under measurements tests in this thesis.

Table 6.1 Input data for the optimal PMSG.

Parameters	Values	Units
Geometrical		
l_s	100	mm
R_{ri}/ R_{ro}	217/ 230	mm
R_{si}/ R_{so}	115/ 209.5	mm
S_w	15	mm
δ_g	0.6	mm
P_{arc}	100	ºe
S_d	50	mm
$Q_s/2P$	36/40	
l_m	8	mm
α_p	0.55	
A_{slot}	802.7	mm^2
SP	0.9	
Numerical (FE-based)		
N	150	rpm
Total time steps	180	
Number of elements	544289	
Number of nodes	163013	
FEA Formulation	Potential vector	
Electrical		
m	3	
P_{out}	5	kW
N_c	80	turns
J_{rms}	1.2206	
I_{rms}	4.899	A/ mm^2
Number of parallel circuit per phase	2	
Slots/ pole/ phase	0.3	
λ_d	1703.9381	mVs
Line-to-line inductance (d-axis)	937.8789	mH
Magnetic		
μ_0	$4\pi\times10^{-7}$	H/m
μ_s	2500	
μ_{PM}	1.05	
μ_{air}	1	
B_{rm}	1.2	T
H_k	891×10^3	A/m
Magnet permeance per half pole	0.1437	μWb/At

The prototype PMSG is a radial-flux surface mounted permanent magnet generator with outer rotor topology and closed-slot (stator) configuration. The stator is operating electrically in star connection. The rated power of 5 kW and rated rotational speed of 150 rpm are defined. The magnets are built by Neodymium-Iron-Boron (Nd-Fe-B), type N48. The stator and rotor cores materials are fully-processed electrical steel laminations sheets of M400-25A, where the stator core is radially segmented for facile wounding on the closed-slot configuration. The winding topology is based on double-layer, non-overlapping, fractional-slot, concentrated winding which are recently very popular because of many remarkable enhancements during recent years in terms of manufacturability and modularity [1], increased flux weakening performance [2], fault tolerance features [3], and short-end windings [4-5]. Table 6.1 presents the main design parameters of the PMSG prototype.

It should be mentioned that the experimental tests are done for each individual study in this thesis which are discussed in the next sections of the chapter under variable speed no-load, and load conditions.

The manufactured prototype is tested for the case of small power generation (5kW) via wind energy along the coast of Barcelona in Spain. Fig. 6.1 illustrates the manufactured PMSG. Fig. 6.1(a) with a segmented stator core for improving slot fill factor, simpler winding, and closed-slot topology, the rotor included the magnets. This prototype is used for wind energy production using a vertical-axis twisted savonius type wind turbine (VAWT) is installed on the PMSG, shown in Fig. 6.1(b), and under operation is shown in Fig. 6.1(c).

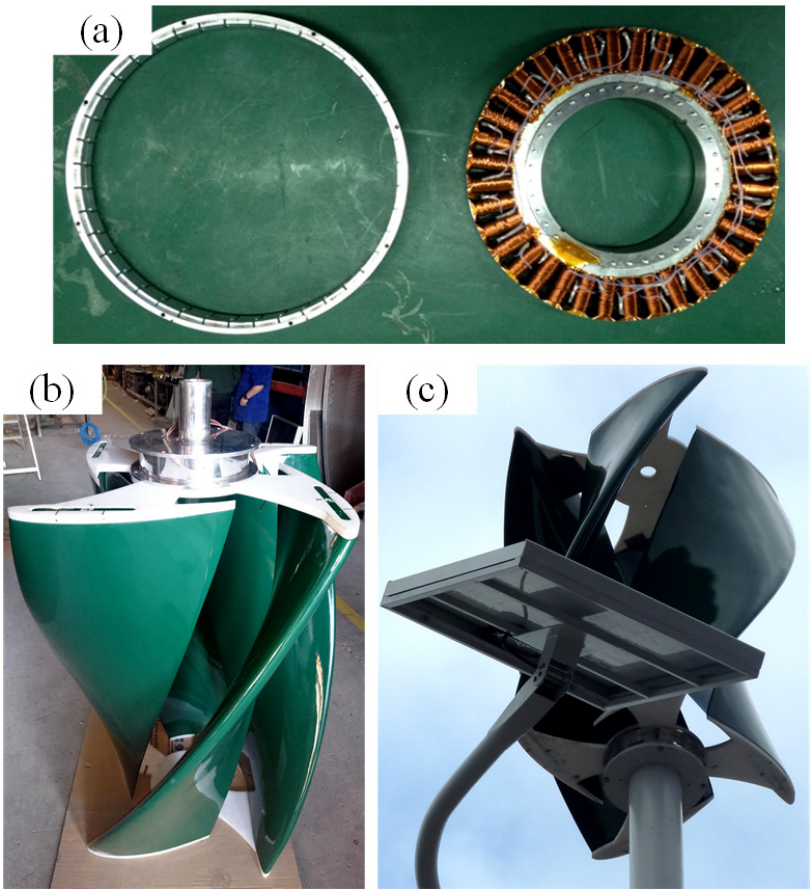

Fig. 6.1. The manufactured analyzed PMSG model, a) the SPMSG with segmented stator and rotor cores, b) installed VAWT on the generator, c) PMSG under operation.

To measure only the mechanical loss, the no-load measurement without considering the stator because the whole PMSG with stator measures the internal voltage, no-load torque, as well as no-load loss under no-load test. Hence, the iron loss during no-load is the difference between the values with stator consideration and the mechanical loss without stator. During the load test, voltage, current, torque, and speed are measured to provide the total loss and efficiency. Moreover, the mean electromagnetic torque is measured as the difference between the mean measured torque under load test (which is resistive) and mean torque under no-load test.

6.1 Back-EMF

The setup arranged for the PMSG under test has been fed by a variable speed frequency converter (ABB ACS600) and loaded by a DC machine. The shaft torque has been measured by a torque transducer (Vibro-meter, model: TORQUEMASTER TM-214) with 0.2% accuracy. The torque transducer is connected through a reading unit (Vibrometer, model: DCU 280) to a PC, which collects the data from a power analyzer and from the temperature sensors. The electrical power has been measured by a power analyzer (Yokogawa PZ4000) with 0.1% accuracy. The 6-µs offset gives adequate time to measure all terminal voltages, when maximizing the settling time after the last transient edge. Obtaining all software tasks can complete within 25 µs of the 50-µs PWM cycle, the sudden ADC advance or delay by 25 µs has no effect on operation of the drive. To measure the average offset, all inverter phases are driven to the dc link ground. Then, all values were in real units using floating point representation. Flux linkage was calculated via numerically integrating the back EMF.

By the bearing nuts the rotor position can be fixed, where the amplitude of the fundamentals is equal. Fig. 6.1.1 presents the experimental validations of induced back-EMF for the optimal 3-D FEA-based (blue curve). The comparison indicates that the curvatures are in a good agreement, however, the experimental data is flattened within peak values (which is because of the manufacturing technique for the magnets).

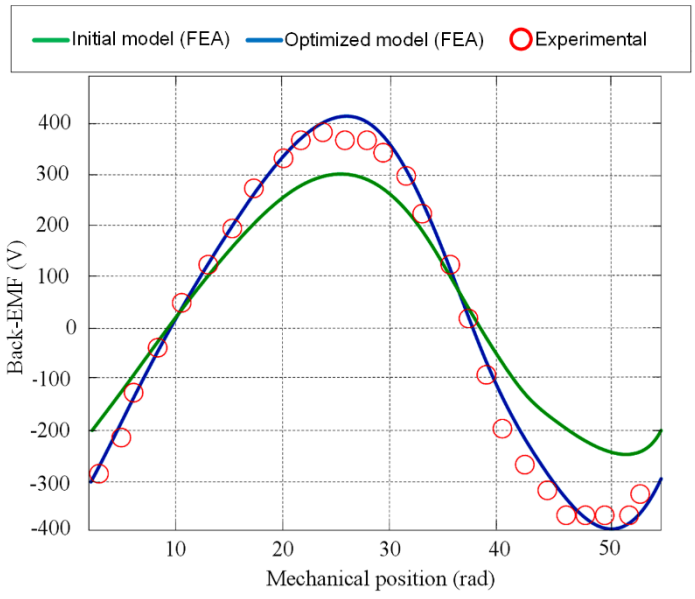

Fig. 6.1.1 Measured phase A voltage in comparison with numerical-based (3-D FEA) data.

6.2 Cogging Torque

The torque has been measured by using 50 N.m torque transducer, the prototype PMSG being rotated at a 10 rpm speed, in addition, the speed-controlled DC machine being operated as a motor. The rotation speed corresponds to the electrical frequency of 1 Hz for the prototype PMSG. Fig. 6.2.1 the numerical-based (3-D FEA) calculated and the experimental measured cogging torque are compared. The amplitude of the measured cogging torque is approximately 10% larger compared to the result obtained by the 3-D FEA. Fig. 6.2.1 also shows that the major contribution to the cogging torque is by the 3rd and 5th harmonics. This is an obvious result since for the prototype machine the number of slots per pole and phase is equal to 0.3.

The procedure to provide the cogging torque from the back-EMF differs according to whether a slotted stator is employed for the measurement of the back-EMF. The following steps were taken: 1) record the value of the EMF, $e(\alpha)$ when the PMSG rotates at constant speed. 2) FFT analysis is applied to the back-EMF to offer its harmonic content spectrum. 3) multiply harmonic contents by the dimensional constant k_{emf} = 0.06729 V/ rad^{-1}, angular velocity of the rotor, and by the Fourier coefficients of its derivative, to approximate magnetic induction. 4) the magnetic induction spectrum can be provided along with the cogging torque spectrum. Finally, 5) by the inverse fast Fourier transform, the spectrum providing the spatial content is obtained.

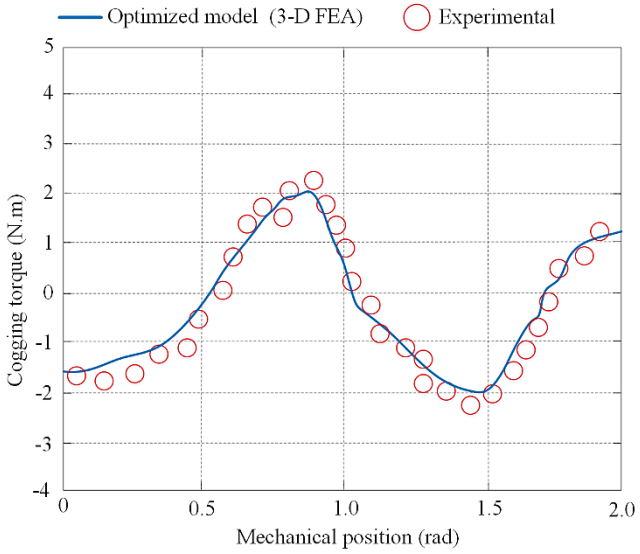

Fig. 6.2.1 Measured cogging torque in comparison with numerical-based (3-D FEA) data.

6.3 Shaft Torque

To measure the shaft torque (output) test, while the period of the torque pulsation is 6◦ (mechanical degree) because of the PMSG symmetry as presented in Fig. 6.3.1, therefore, to provide 12 static torque measurements over a period of 6◦ by exciting the three-phase winding by DC currents with respect to the rotor positions. The average torque of the proposed PMSG configurations with different phase angles and rated current (6A) excitation from experiments are compared with the 3-D

FEA results in Fig. 6.3.1. Moreover, there are further measurement uncertainties in the DC currents in the machine windings, and more significantly the machines have 40 rotor poles which would amplify any rotor position errors by 40 times when conducting the measurements. These factors potentially attribute to more considerable experimental faults. Nevertheless, the experimental results further confirm the superiority of the rotor for its smallest torque pulsations. The average torque output of the machines with different current excitations and 0◦ phase angle from both 3-D FEA and experimental tests are illustrated in Figure 6.3.1, which presents good agreements are reached between the predicted and experimental measured results.

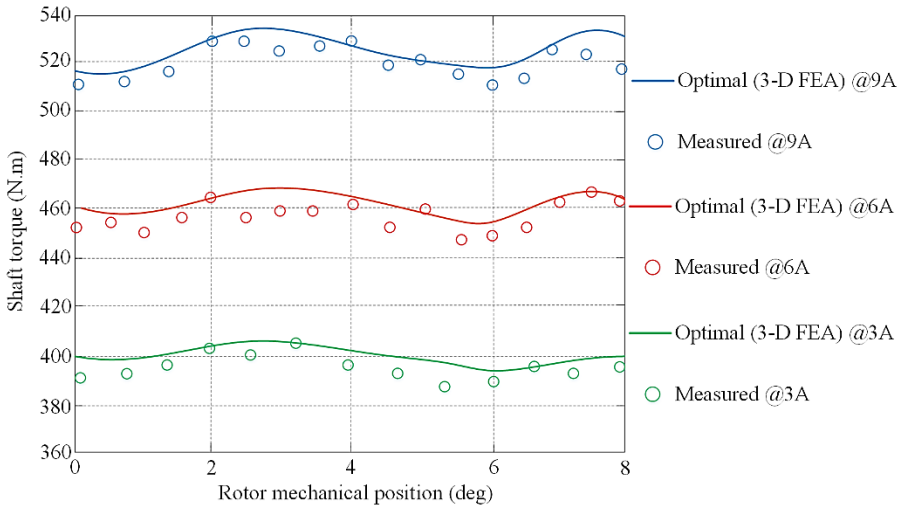

Fig. 6.3.1 Measured output torque in comparison with numerical-based (3-D FEA) data at different level of rated currents.

6.4 Output Power and Efficiency Measurements

The measured input and output power of the proposed PMSG as a function of the speed with a constant pure resistive load of about 100 Ω is illustrated in Fig. 6.4.1. The difference between them represents the power losses of the PMSG, which arises as a function of speed. As the speed (frequency) increases, the iron and copper losses increase consequently.

The PMSG efficiency has been calculated based on the measured electrical and mechanical powers. Fig. 6.4.2 presents the behavior of the machine efficiency as a function of time under a test run. The efficiency is calculated according to Eq. (2-167) and its value is at steady-state 97.1% whereas the measured efficiency is 95.2%. A reasonable agreement between the results is thus found. The measured efficiency is determined from the measured electrical power and from the measured mechanical power. In this comparison, the parameters of the numerical computation model are fixed to the design values of the prototype machine. Fig. 3.9 shows also that a rapid reduction in the efficiency is obtained when the output power exceeds 5.5 kW. This may be explained by the typical behavior of the PMSGs. As the permanent magnet temperature arises, the remanence flux density of the permanent magnet decreases. Thereby, if the original stator flux linkage is maintained, more magnetizing current in the stator is needed causing more copper losses. While the copper loss increases, the temperature begins to go up, causing further reduction in a permanent magnet remanence as well as an increment in the phase winding resistance. These phenomena further increase the power losses in the stator winding. As a certain output power is exceeded, the described self-feeding phenomenon happens very rapidly and only a little percent change in the output power may cause

tens of percent's increment in the temperature rise. For the prototype machine, this is the case at an output power of approximately 5 kW without any cooling system.

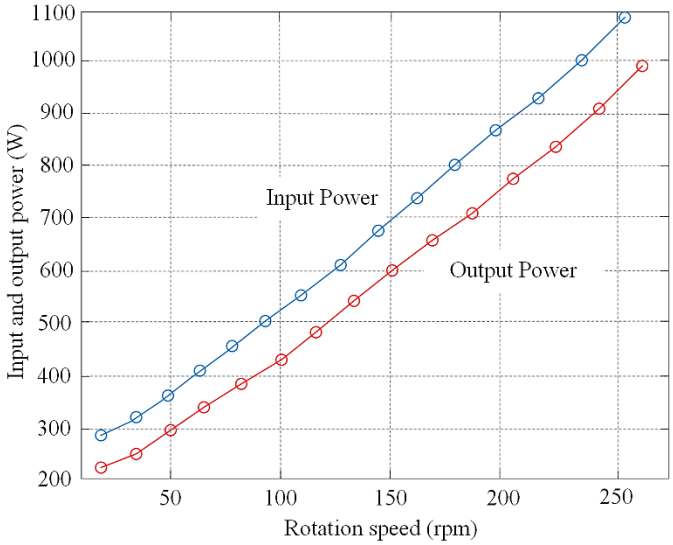

Fig. 6.4.1 Measured input and output power as function of speed under 100 Ω resistive load.

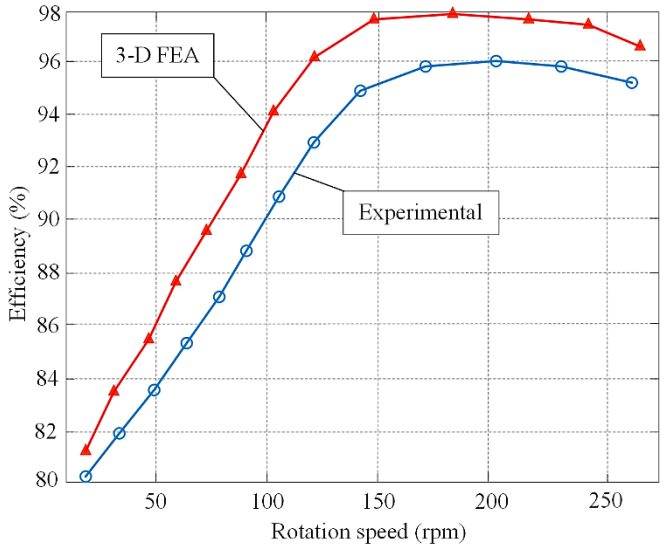

Fig. 6.4.2 Measured efficiency as function of speed under 100 Ω resistive load in comparison with 3-D FEA prediction.

6.5 Iron Losses Measurement

The modeling and computation of iron loss were successfully done using different approaches in Chapter 3. A comparison of predicated (simulation) and measured (experimental) results of iron loss during no-load condition is discussed in this section [6-7].

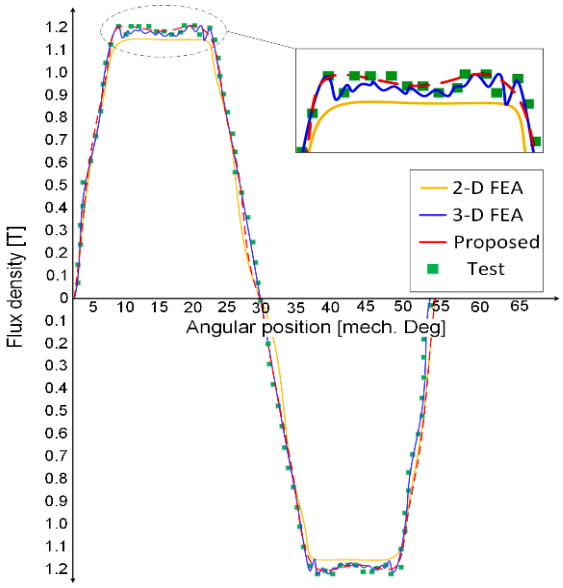

Fig. 6.5.1 Airgap flux density verification.

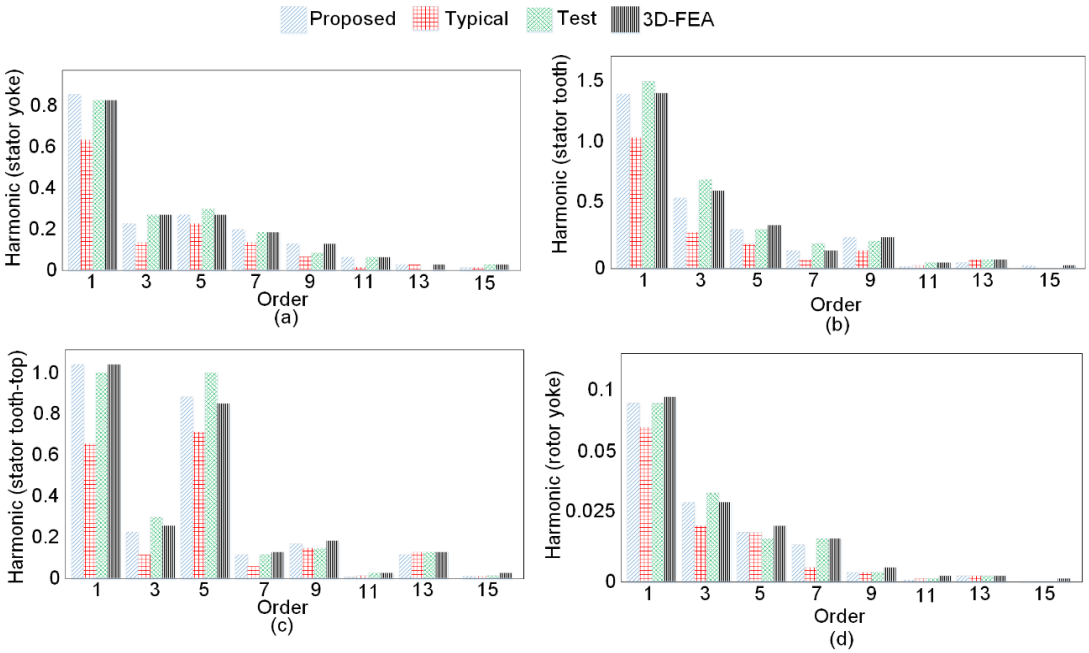

Fig. 6.5.2 Comparison of field harmonics in iron parts of the machine at a) stator yoke, b) stator tooth, c) stator tooth-top, and d) rotor yoke.

The proposed quasi-FE technique using 2-D FE model is verified with a 3-D FE model, in which the mesh is generated with a high quality with 544289 elements, 163013 nodes as shown in Figure 8, and its 3-D FE magnetic flux density distribution (as shown in Fig. 6.5.1). The course, the proposed technique results in a faster and cheaper simulation analysis in comparison with the 3-D FEA and has comparable accuracy. The stored airgap flux density through the proposed quasi-FEA technique is verified by the 3-D FEA and also experimental data (test), in which a good agreement can be seen between them in Fig. 6.5.1 [7].

Field harmonic verification for various orders from fundamental to 15th order at each iron part is illustrated in Fig. 6.5.2. Using a typical technique, the magnetic field density and its corresponding harmonics are calculated for each iron part (rotor and stator yokes). Whereas, those data are calculated for smaller segments (4 or 8 times smaller) and a considerably higher number of mesh elements and nodes by the proposed eight-segmented quasi-FEA technique. Regarding the proposed technique the field harmonics that are calculated based on both the conventional models and the proposed model are employed to predict the iron loss on eight measured data points, and compared with the 3-D FEA and experiment results, the FEA results are calculated under sinusoidal three-phase current excitation. The generator is coupled to an asynchronous machine employed to drive it at different speeds. Moreover, the studied generator was instrumented with several magnetic flux sensors at each segment in order to compare the measured waveforms with the simulated ones [8]. The iron loss is determined by the tests with the sinusoidal and PWM supplies and also performed with the rotor in a standstill condition, all the stator and rotor iron losses are measured, besides, the technique can be applied. Considering all the iron loss that are active in only iron parts of the PMSM in order to remove certain uncertainties in the iron-loss measurement. This method allows the use of (the international standards, such as the IEEE 112 method B) with a good accuracy [9].

The optimized PMSG with 36 slots for a vast operating range of 5.5 kW (nominal power) is manufactured with the listed sizeable dimensions and specifications. The stator and rotor cores both are made of M400-50A steel sheets. The modified IEM-Formulas' coefficients are extracted by numerically fitting the no-load experiment results combined with FEA results. The no-load iron loss is measured through the difference between the total no-load loss and mechanical loss. First, the prototype PMSM is dragged under the no-load condition and tested the total no-load loss curve versus the speed. This total no-load loss P_{fe} (total) consists of the no-load iron loss P_{fe} and the mechanical loss P_{mech}. The PMSG under testing is fed by a variable-speed frequency converter (ABB ACS600) and loaded by a DC machine (prime mover). The shaft torque is measured by a torque transducer (TORQUEMASTER TM-214). The electrical power (input and output) is measured by a power analyzer (Yokogawa PZ4000). Afterward, all the data (such as voltage, torque, power, and efficiency) were stored by a reading unit to the laboratories' computer. The prototype machine is designed particularly for laboratory test use. As the output power is stored by a dynamometer. Thus, the total loss (consists of copper, iron, and mechanical losses) has been obtained by a simple subtraction between input and output powers. The copper loss has been calculated via the measured phase current and resistance, as well as the mechanical loss being provided in the coefficient extracting experiment.

Fig. 6.5.3 illustrates the influence of the modified IEM-Formula on the total iron loss and efficiency with 3-D FEA and experimental verifications for the studied PMSG. From the standpoint of the classic IEM-Formula model, the iron loss resistance is the parallel connection of the hysteresis losses and the eddy-current losses. This is examined through the air-gap field density with the motor speed as the operation parameter. While the PMSM operates in the field weakening region, the terminal voltage remains changeless because it is diminished by the DC link voltage. As predicted by the classic IEM-Formula model, the iron loss resistance rises with the speed, shown in Chapter 3, section 3.3. Thus, the iron loss decreases in a similar

manner during field weakening operation. However, this predicted result is far from the results from the experiments and FEA calculation. This is due to the fact that large eddy-current loss is generated during the field weakening, rapidly decreasing the efficiency of the machine. Figure 6.5.3(a) shows the comparison of iron loss obtained by the proposed PMSM for the classic IEM-Formula, the proposed modified IEM-Formula, 3-D FEA and experimental measurement. The classic IEM-Formula shows significant deviation during FWOT from the modified formula, which shows worthy agreement with experimental and 3-D FEA results. This result presents that the harmonic loss must be considered if a wide FWOT exists. Fig. 6.5.3(b) presents how the efficiency calculation might create a considerable error during FWOT. The error between the proposed model and experiment results is due to neglecting the slot opening effect and fringing effect. However, the iron loss predicted by the classic IEM-Formula is obviously underestimated, particularly during the field weakening region, due to ignoring the harmonic loss [6].

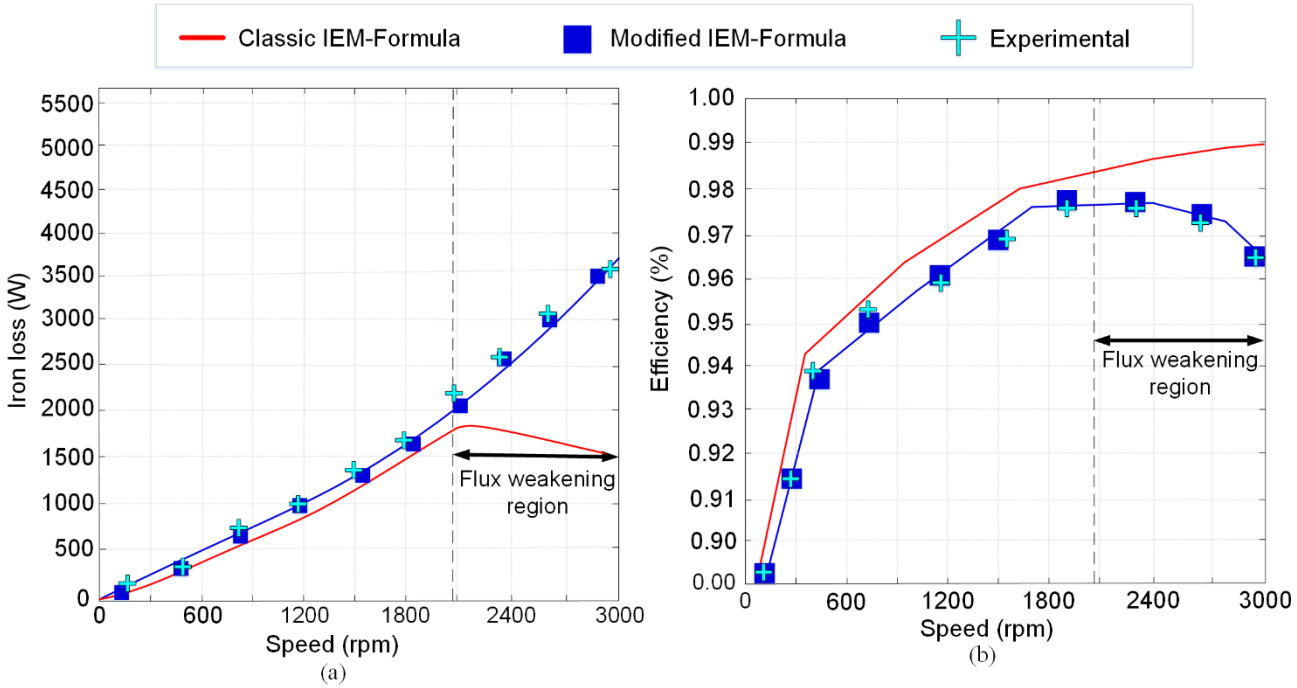

Fig. 6.5.3. Comparison of classic IEM-Formula with modified IEM-Formula during FWOT, where: a) shows total iron loss evaluation; and b) presents efficiency computation.

6.6 Magnetic Field Measurement Using a Novel Technique by Multiple Magnetic Antennae

In this section, the numerical-based results are compared to experimental data to verify the research achievement.

Fig. 6.6.1 presents the computed magnetic flux density time waveforms by the purely sinusoidal and PI regulator and PWM controller stator current methods where the analyzed harmonics consist of those resulting from the use of PWM of the voltage of the generator. This computation has been completed over 2.5 s at two different locations in the stator core, where Fig. 6.6.1(a) is computed in the center of the stator tooth and Fig. 6.6.1(b) at the center of stator yoke. The difference between frequency and time domains can be observed in these two figures where the pure sinusoidal waveform (simulation only) shows the frequency domain iron losses method, and the PWM real-time waveform represents the real-time waveform iron loss calculation (in simulation and measured experimental data). As test conditions, the classical no-load test as imposed by the international standards, such as the IEEE 112 method B which has been taken into account. The no-load tests at a synchronous speed have indicated that the additional losses because of the rotor harmonic currents are not negligible with respect to the actual iron losses. As a result, to offer more accurate values for the iron loss, all the experimental tests used for the validation of the proposed time-domain method have been performed using this 5 kW PMSG prototype. All the elements needed for the iron loss evaluation with the arbitrary voltage supply are given. To avoid any resulted slip in the no-load test at a synchronous speed, the supply frequency required to be the same for both the motor under test and the PMSG. This condition was set during the tests with the sinusoidal supply [10]. Whereas, this condition cannot be replicated for the inverter supply because of the impossibility of synchronizing the fundamental frequency of the used inverter with the sinusoidal supply of PMSG.

The PWM control scheme details can be found in [11], in which the minimum harmonic distortion is assumed. The PWM control has been utilized in the rotor flux-oriented reference frame. To enable a suitable comparison, the PWM control scheme is complemented with the standard stator voltage decoupling terms for enhancing its dynamic response. The output of the PWM controller includes both planes' synchronous voltage references, which are rotationally transformed back into the stationary reference frame. The proportional and integral coefficients of the four PI controllers are tuned via simulation (MATLAB *Simulink*) and next fine-tuned experimentally. Each pair of the PI controllers used the same values to control the current in the simulations and experiments [12-13]. The PWM controller and its effects have been modeled using a dSpace module.

The magnetic antennae are assembled with two polymer 3-D printed rods, which have been located a distance of 268 mm from the origin point of the shaft (0, 0, 0). The data was collected through a number of sensors such as a torque transducer and magnetic antenna and were transferred to a Yakogawa WT 3000 module to monitor the major parameters via a laboratory computer. Additionally, the requested speed was sent through the PC block to adjust the

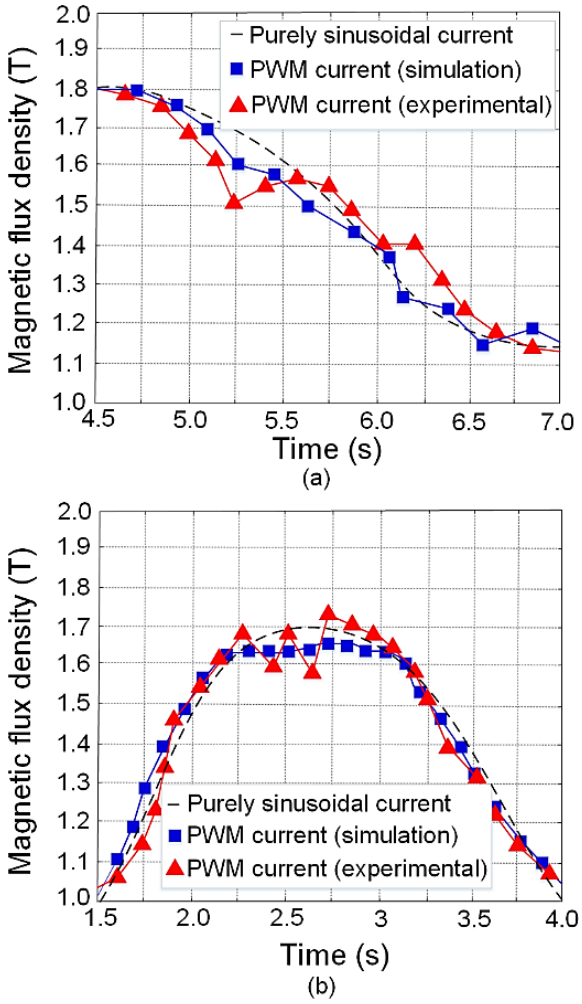

Fig. 6.6.1. Magnetic flux density time waveforms using a pure sinusoidal and PWM stator current (experimental), where the computation is done for, a) the center of stator tooth, and b) the center of stator yoke.

level of the load. The simulation time for solving the model at each frequency was 146 minutes with the modified solution settings due to the size of the model [10].

Fig. 6.6.2 indicates the novel polymer-based structure which is printed in five parts (unassembled) and glued through their designed slits. The assembled structure carries the multiple magnetic antennae [13].

A set of simulations are completed to determine the total harmonics by a PWM controller on the radial magnetic induction of the machine. Fig. 6.6.3(a) presents the radial magnetic flux density time waveforms at the airgap which are resulted from the simulation and experimental measurement. Fig. 6.6.3(b) shows the amplitude of the magnetic induction harmonics due to the effects of reluctance where the 36th order harmonic has the largest amplitude (0.502 (T)) which is due to the reluctance effect. The experimental data is compared (red bars) with the simulation results (blue bars).

Fig. 6.6.4 illustrates the experimental setup at our laboratory. A three-phase permanent magnet synchronous generator has been designed for the simulations of this work. The generator is connected through a PWM controller (via a dSPACE 1104 module).

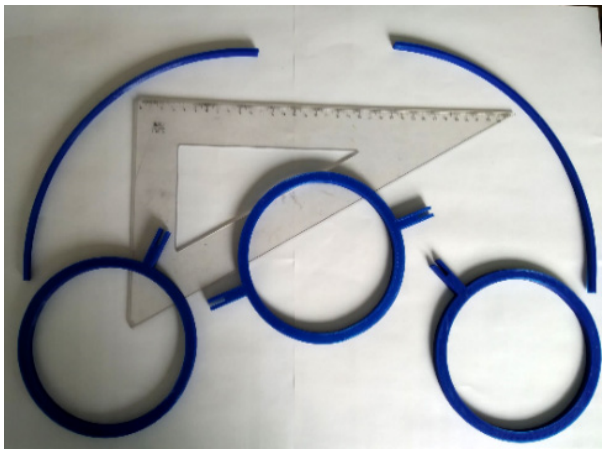

Fig. 6.2.2. The experimental printed structure (not-assembled) of the multiple magnetic antennae using a 3-D printer.

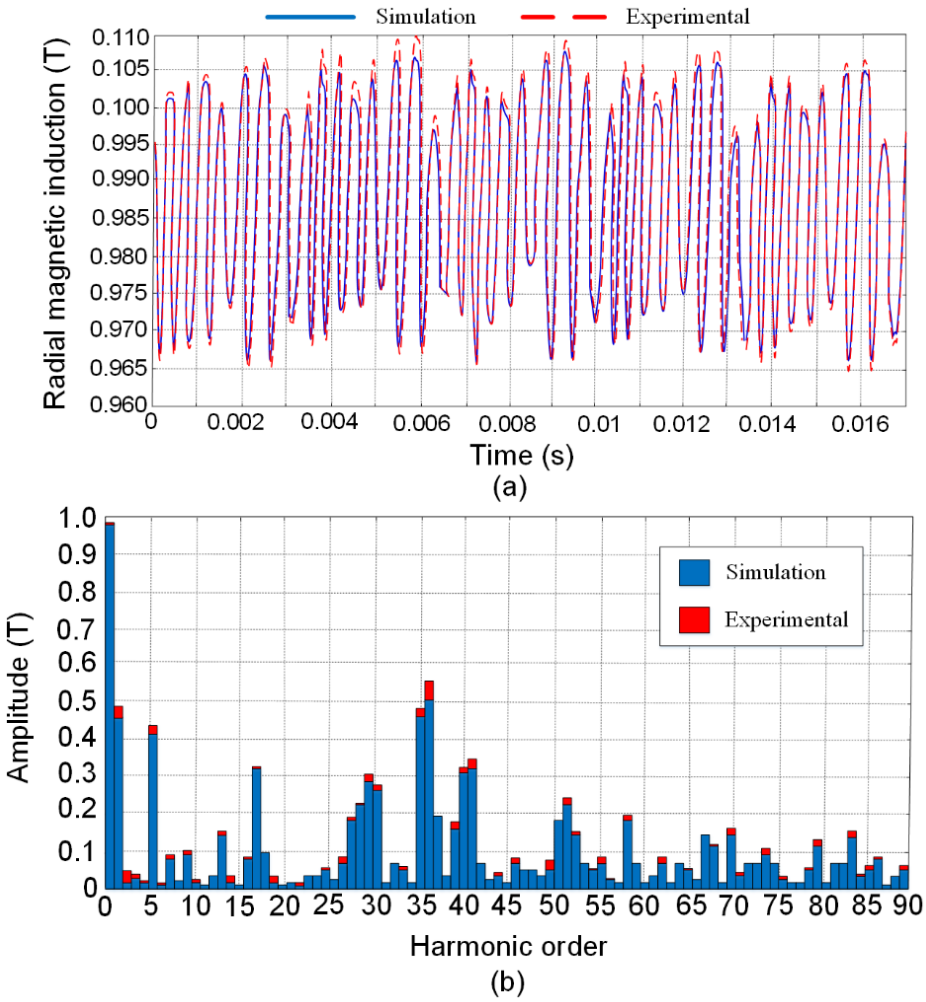

Fig. 6.6.3. The experimental total harmonics by a PWM controller on the radial magnetic induction of the PMSM where, a) the radial magnetic flux density time domain waveform in the airgap, and b) the amplitude of the magnetic induction harmonics due to the effects of bulk conductivity.

Fig. 6.6.5 illustrates the variation of the stator and rotor iron losses, where P_{sh}, P_{se}, P_{rh}, and P_{re} are the stator core hysteresis loss, the stator core eddy-current loss, the rotor core hysteresis loss, and the rotor core eddy-current loss, respectively. As reported, the major stator core iron loss accounts for the hysteresis loss, when the rotor core has mostly the eddy current loss. At the supply voltage of 350 V, the stator core hysteresis loss of 375.4 W has approximately 34.01% of the total stator iron loss. While the eddy-current loss of the rotor core by 145.8 has 23.58% of the total rotor core iron loss.

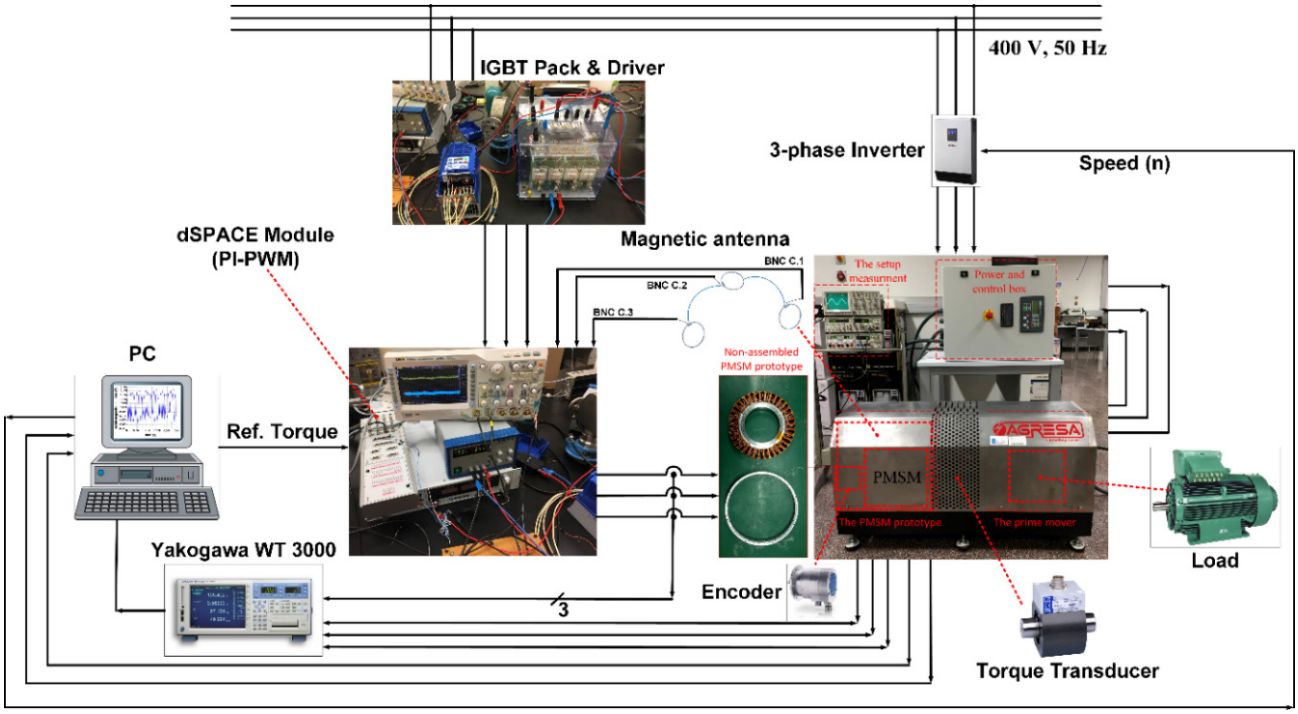

Fig. 6.6.4. Implementation setup of the bench test.

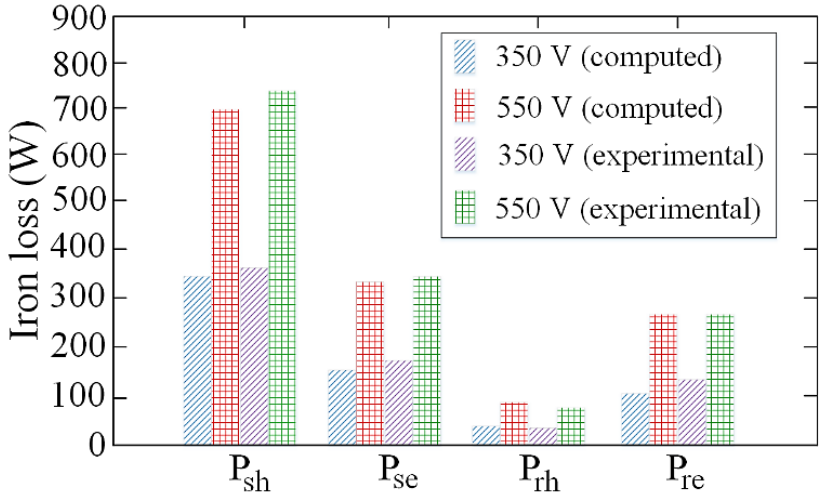

Fig. 6.6.5 Variation of the total iron loss with the supply voltage in 5 kW PMSM.

6.7 Temperature Distribution of the PMSG using Infrared (IR) Thermo-Camera

The manufactured generator (cf., Fig. 6.7.1) with 1.5 kW (@40 rpm) is applied for the small power generation through wind energy along the coast of Barcelona city in Spain. The manufactured PMSG is shown in Fig. 6.7.1 uses the segmented stator-teeth core for improving slot fill factor, simpler winding, and providing closed-slot topology which is illustrated in Fig. 6.7.1(a), (b). The optimised thickness of the magnets was manufactured with 7.8 mm, shown in Fig. 6.7.1(c). In fact, this graph shows the optimal PMSG, in which global sizing was studied in [14] with considering slot width S_w, airgap length l_g and magnet thickness l_m as design variables.

Lastly, the infrared thermal imaging is done by FLIR E60bx–SERIES, shown in Fig. 6.7.2, that has the thermal sensitivity of <0.045°C, and accuracy of ±2%. Based on the applied thermal constraint of 90°C, the temperature distribution at the optimized model was recorded under 65°C.

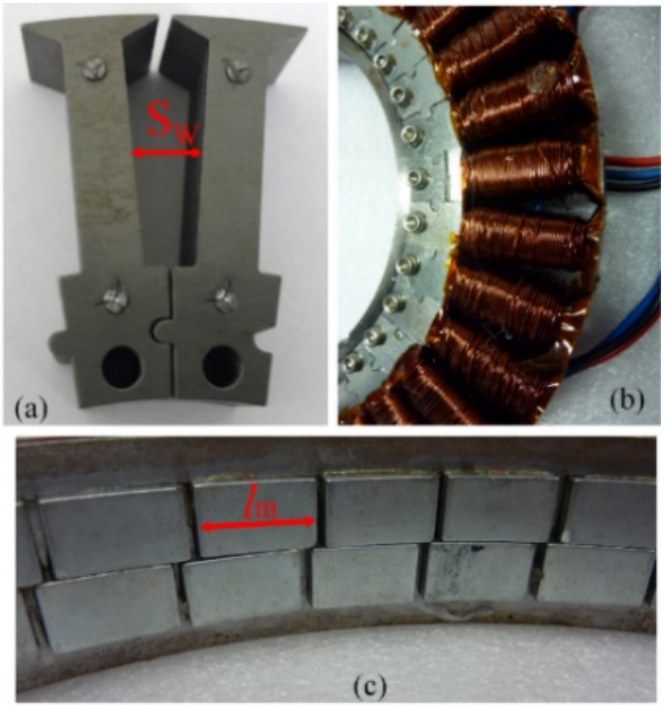

Fig. 6.7.1. Manufactured optimised generator, a) the tooth, b) mounted stator core, and c) permanent magnets on the rotor.

Table 6.7.1 Optimisation results and verification.

Parameters at 15 rpm speed	Pre-optimisation	Post-optimisation	FEA verification
L_d (mH)	468.26	470.76	470.88
L_q (mH)	468. 21	471	470.96
E_p (V)	315	414	428
λ_m (mVs)	1691.88	1720.43	1719.72
P_o (W)	455.75	460.84	469.44
P_{copper} (W)	46.8	33.5	34.0
P_{iron} (W)	226.6	206.5	207.3
η (%)	94.23	97.13	97.10

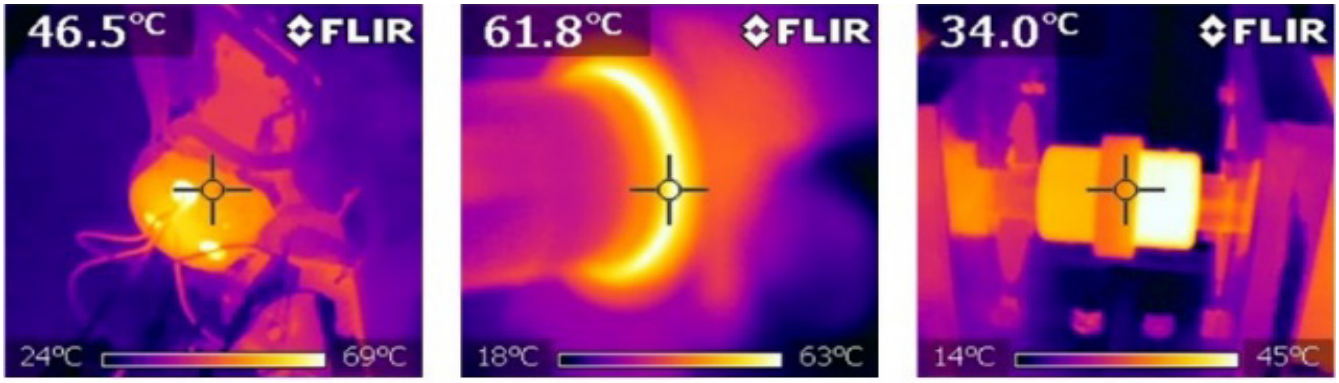

(a) (b) (c)

Fig. 6.7.2. Use of infrared thermal imaging measurement on the test bench at rated speed, a) the stator core, b) the rotor core, and c) the housing.

6.7.1 Heat Transfer Measurement

Essentially, the heat transfer is known as one the most critical parameters in the thermal design of the PMSMs, thus, the most sensitive heat transfer coefficients are calculated and experimentally reported in Fig 6.7.1.1 under following conditions:

- The axial inlet velocity of the cooling air was defined between 0.5 to 3 m/s
- The rotor tip velocity is varied between 2 to 8 m/s
- The air approach angle is defined between 0 to 30º

it should be mentioned that not significant difference is seen for the change of the air approach angle from 0 to 60º. Fig. 6.7.1.1(a) illustrates the change of heat transfer coefficients at the poles (points 1 and 3) at a variable speed condition. In Fig. 6.7.1.1(b), the heat transfer coefficients are at the stator core (points 6 and 8), in which the low-velocity ratio (axial inlet velocity/ rotor tip velocity) is variable. Fig. 6.7.1.1(c), presents the surface heat transfer coefficients around the bottom face of the field coil at the leading side of the magnet (points 4), and the bottom face of the field coil at trailing side of the pole (point 5) [15].

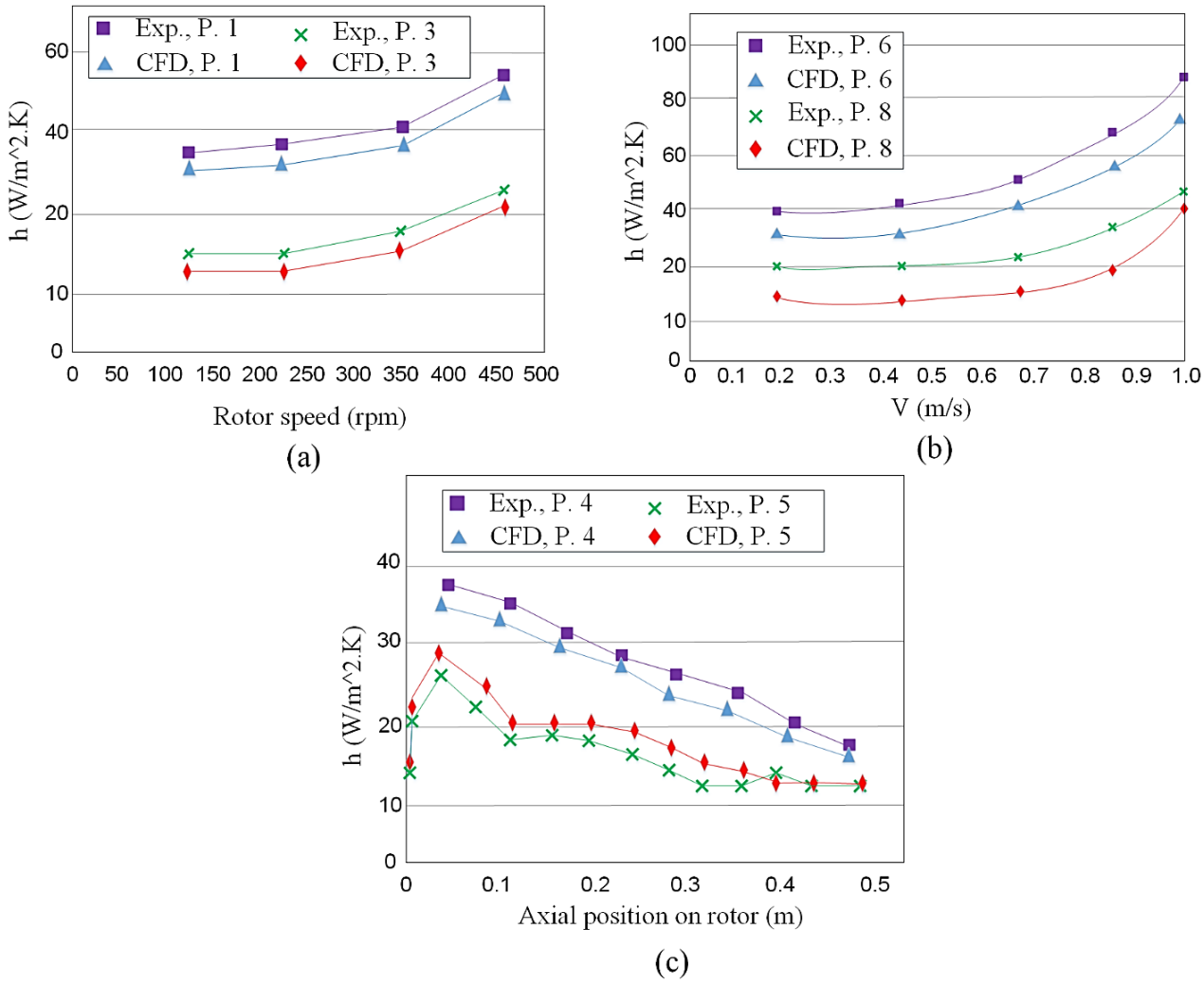

Fig. 6.7.1.1. Heat transfer coefficients verification for the FE models, a) at points 1 and 3 variable airflow rate, b) at points 6 and 8 for variable rotor speed, and c) at points 4 and 5 for variable rotor speed.

6.8 Vibro-acoustic Performance Tests

Respect to references [16-17], where we have used a semi-analytical subdomain model (SDM) of PMSG to predict the variable speed vibrations and magnetic noise of the generator with considering natural frequencies. The methodology has been verified using 2-D and 3-D FEA in those studies. During the load condition, we have noticed that the first main mechanical resonance occurs at the rotation speed of 365 rpm (185 Hz) in [16], where we used the skewing technique by optimal skew angles of rotor and stator 12º and 10º in order to minimize the magnetic noise. Therefore, a vibration and magnetic noise measurements have been done.

In another study [17], we have studied the optimal slots per pole per phase number for the PMSG, once again to minimize the magnetic noise. In this study, the first main resonance as a function of speed and frequency happens 108 Hz and 308 rpm.

In the vibro-acoustic bench test, we have measured the parameters in two different environments. One, the whole prototype was located in an anechoic chamber room to cancel external sources of noise in the laboratory. Also, in this test, the measurement equipment's were very advanced in terms of accuracy. Second, the measurement was done using portable measurement equipment's to store online data without using the anechoic chamber room. In the next sub-sections, the differences will be presented.

6.8.1 PMSG Prototype with Optimal Skew Angles

The manufactured prototype with the optimum skew angles was tested for the case of small power generation (5 kW), low-speed, via wind energy along the coast of Barcelona in Spain under EU directive 2010/30/EU sound power level regulation. The generator was electromagnetically optimized in another recent study which can be found in [16].
A modular system of Brüel & Kjær's sound power kit which is detailed in Table II, in which all component models are given.

To gather noise data of the PMSG under 150 rpm (rated speed), the PMSG was placed, based on ISO 6396. The microphone has been placed in the radial direction of the rotor by 60 cm away from the PMSG to reduce the effect from the airflow, which is induced by the rotating rotor in an anechoic environment which is shown in Fig. 6.8.1.1. This device allows for measuring sounds and noises with various frequency filters. In this assessment, one third octave band filters are used because of the following advantage, higher accuracy due to lower sensitivity to the ambient sounds and those noises which are known as external sources to the main noise source being measured. In addition, the vibration meter provides the needed data by FFT analysis. A high-performance vector control module (PI-PWM) from OMRON with CIMR-A model is used for this experiment.

Table 6.8.1.1 Modules of Brüel & Kjær's sound power kit.

Component	Model	Range
PULSE Empty C-Size Front End (5In)- Dyn-X	3560-C-E12	-
Microphone of ½ (free field)	4188	8 to 12,5 kHz, prepolarized
preamplifier microphone ½	2669B	-
Microphone Cable LEMO	AO-0419-d-150	0 B to 1 B connector 15m
windscreen of ½ mod. UA0459	EG-9999	-
PULSE Sound Power, Node-locked License	7799-N	-
license CPB analysis program and overall of 1 channel	7771-N1	-
program analysis of FFT and Overall of 1 channel	7770-N1	-
Sound level calibrator	4231	-

A key feature is the Dyn-X technology, which avoids the need for input ranging via dual A/D converters to ensure you get the data the first time – when reaching an effective dynamic range of over 160 dB. This equipment operates as sample-synchronous phase alignment between all channels using IEEE 1588v2 precision time protocol (PTP) and GPS time synchronization. The measurement has been made in an anechoic room in order to avoid any external source of the noise.

During the vibration test, the following physical-based magnitudes are measures for the studied PMSG, where depending on what the aim of the measurement is, some may be more appropriate to be considered:

- Displacement (frequency range of below 100 Hz).
- Speed (frequency range of 10 Hz to 1 kHz).
- Acceleration (high frequency measurement > 1 kHz).

The Rion vibration analyzer VA-12 allows precise vibration measurement by a piezoelectric accelerometer attached to a magnet. The meter provides an FFT analyzer measuring mode with both spectrum and time waveforms.
During the vibration test, the measuring instrument was set to provide an FFT analysis via acceleration measurements. The frequency span measured is over 5000 Hz to include high pass and low pass filters of 3 Hz and 20 kHz, respectively. Three measurement are done due to the x-axis, y-axis, and z-axis directions of vibration waves.
The presence of the magnetic noise produced in form of sound pressure level as a function of frequency is obtained at 15, 32, and 50 Hz.

The experimental measurement was conducted in the laboratory of Electrical Machines and Drives at the Polytechnic University of Catalonia-BarcelonaTech. The environmental impact was carefully considered. In fact, noise pollution persistency in any form of vibrations and audible noise in residential or industrial ranges are harmful and can even cause health issues to anyone who is near the sources.

Fig. 6.8.1.1 illustrates A-weighted sound pressure level (ASPL) as a function of rotating speed (up to 1000 rpm). The blue curve presents the proposed PMSG model with peak value 65.8 dBA for speed range between 15-150 rpm, which has been experimentally verified by 78.6 dBA which is shown in the red color for the optimum skew angles and slice. In addition to the predicted and measured optimized model, the predicated initial model (in orange color) based on the empirical model is presented to highlight the improvement, where the peak radiated ASPL is 79.7 dBA under the defined ratings of the system operation (such as voltage, current, speed, etc.). Note that the maximum ASPL over rating speed is above 10 dBA approximately.

Table 6.8.1.2 reports the influence of the different models with various values of skew angle and slice number on the electromagnetic capability of the PMSG at 15 rpm rotation speed. $L_{vib,max}$ shows the maximum magnitude of vibration in the defined speed range of 15-150 rpm, in which the vibration has been reduced in the optimized model by 7.2 dB in comparison to the initial model. Furthermore, small improvements can be reported for output power P_o, electromagnetic torque T, efficiency η, and constant power speed range $CPSR$. Also, the fundamental d-axis phase flux linkage λ_m remains almost constant.

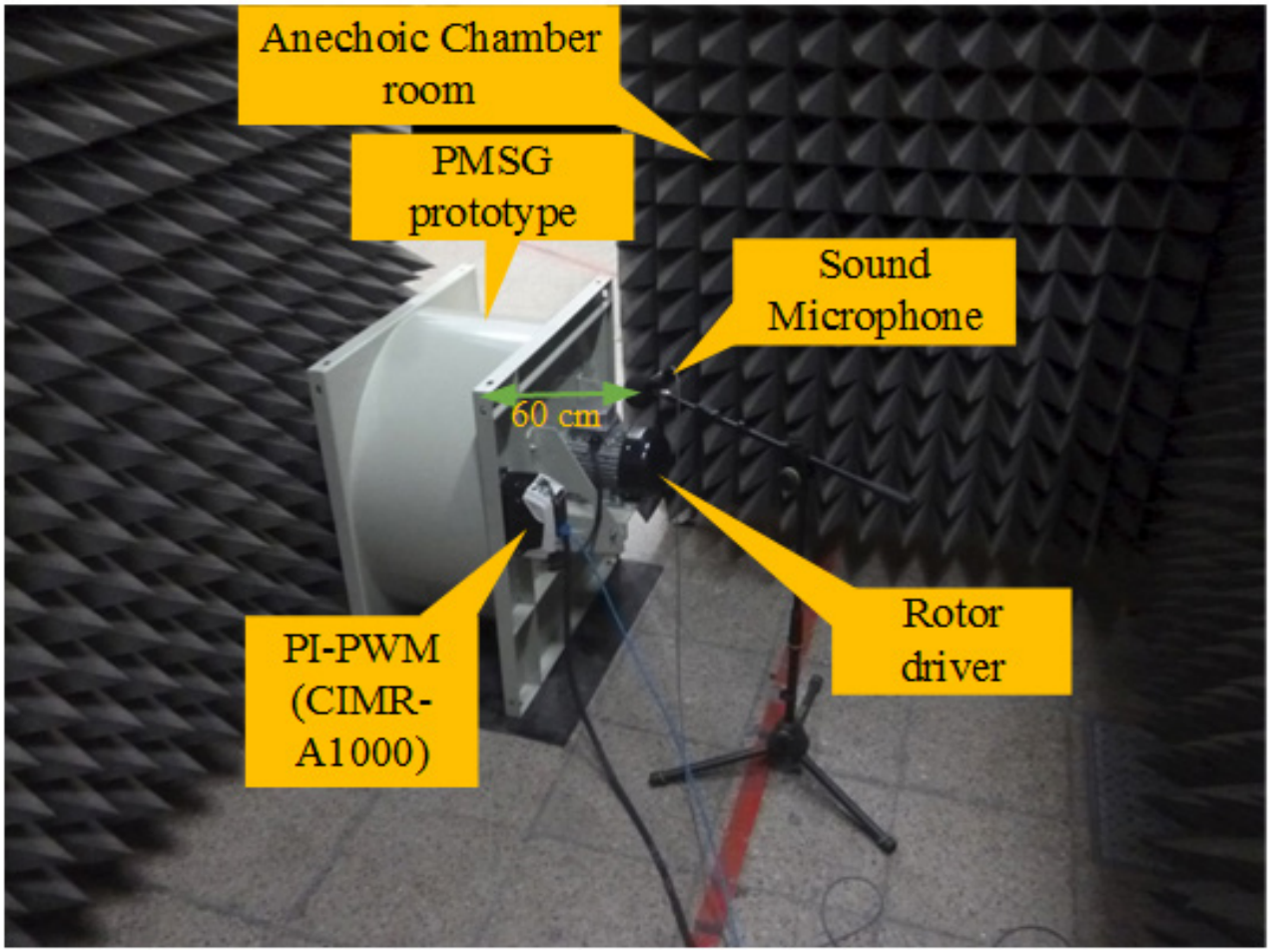

Fig. 6.8.1.1. The maximum magnetic noise spectrogram of the optimum PMSG.

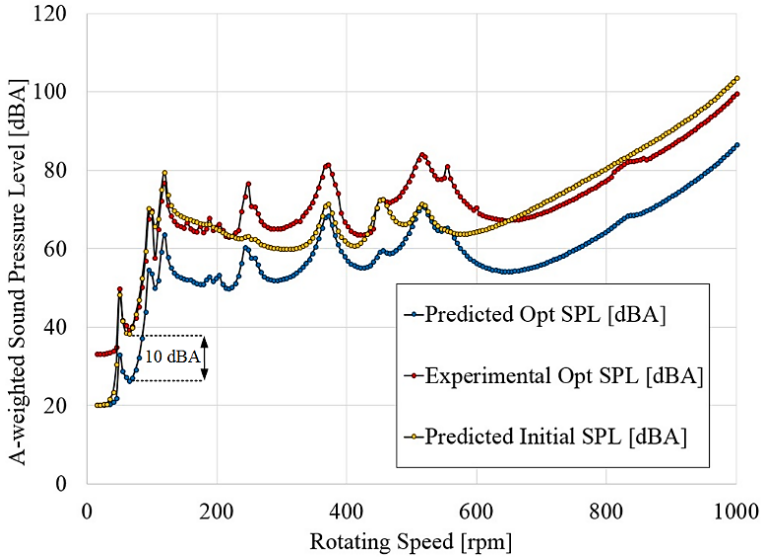

Fig. 6.8.1.2. A-weighted sound pressure as function of variable speed analysis.

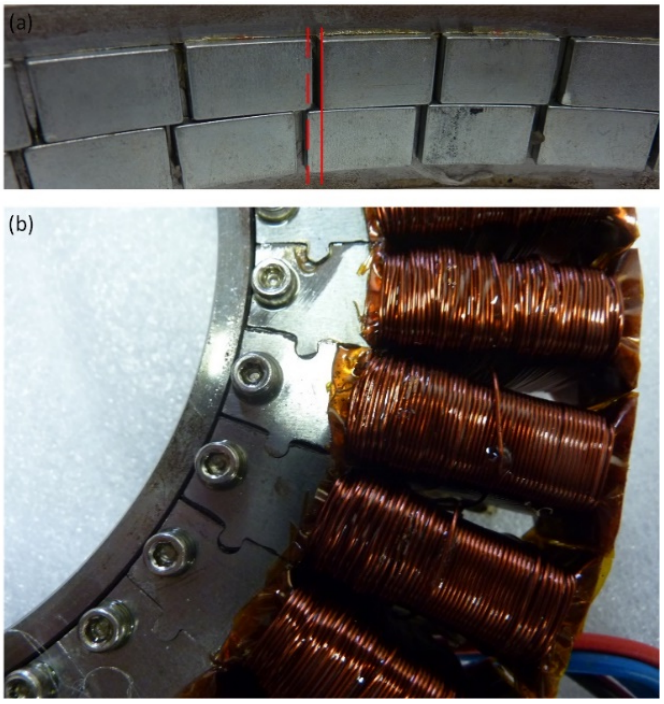

Fig. 6.8.1.3. Manufactured PMSG based on optimized skew angles, a) Permanent magnets including rotor iron back, b) Stator slots.

Table 6.8.1.2 Electromagnetic results and verification.

Parameters/ model	No Skew	Initial	Optimized	Test
λ_m (mVs)	1691.5	1714	1721.3	1718
P_o (W)	449.2	503.2	514.7	511.7
η (%)	92.1	95.8	97	96.9
CPSR	434.5	477.3	487.9	505.8
T	314.6	367.4	370.2	369.8
$L_{vib,\ max}$ (dB)	118.7	110.6	102.8	105.6

6.8.2 Optimal Pole Number Prototype Test

The manufactured second prototype with the optimum pole numbers of 42 is tested for the case of small power generation (5 kW), low-speed, via wind energy along the coast of Barcelona in Spain under EU directive 2010/30/EU sound power level regulation. First, the air-gap magnetic flux density B_r and its harmonics as the function of space are calculated by SDM and verified via 3-D FEA (shown in Fig. 6.8.2.1) with a reasonable agreement. Second, through the following measurement instruments, the vibration and $L_{p,max}$ are verified experimentally. The sound meter used to gather noise data is the model SC-420 from CESVA. This device allows measuring sounds and noises in different frequency filters. For this project, the option used allows for the reduction of ambient sounds and those noises that are external to the noise source being measured [17].

Fig. 6.8.2.2 illustrates the test bench setup at the Machine Lab of the EEBE school of Universitat Politècnica de Catalunya. The two main measurement kits are used, CESVA SC-420 (magnetic noise), and Rion AV-12 for the

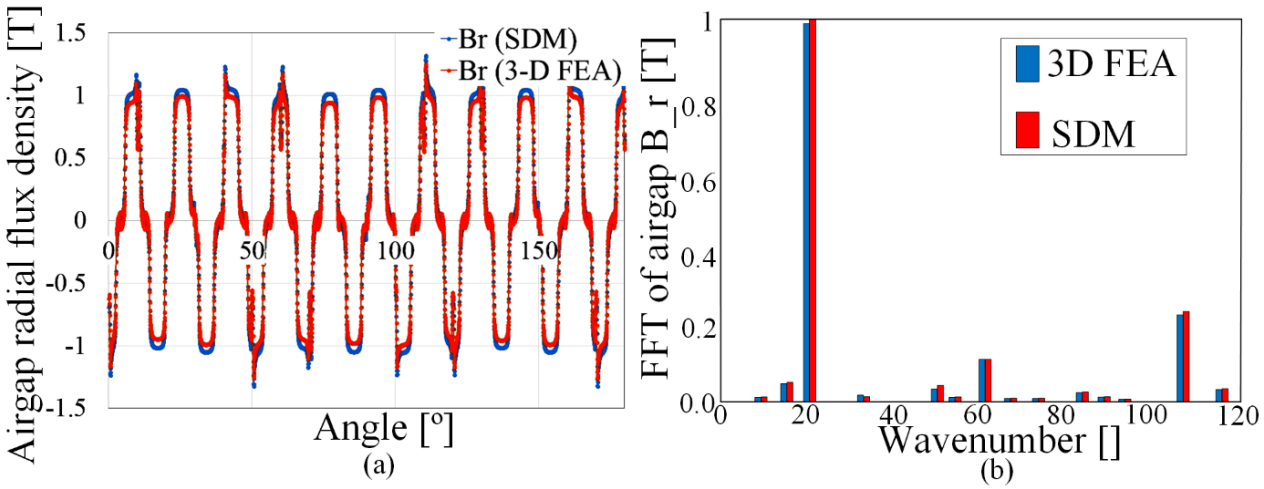

Fig. 6.8.2.1. The radial component of air-gap flux density calculated by multi-slice SDM and 3-D FEA as function of space, (a) waveforms, (b) magnitude FFT.

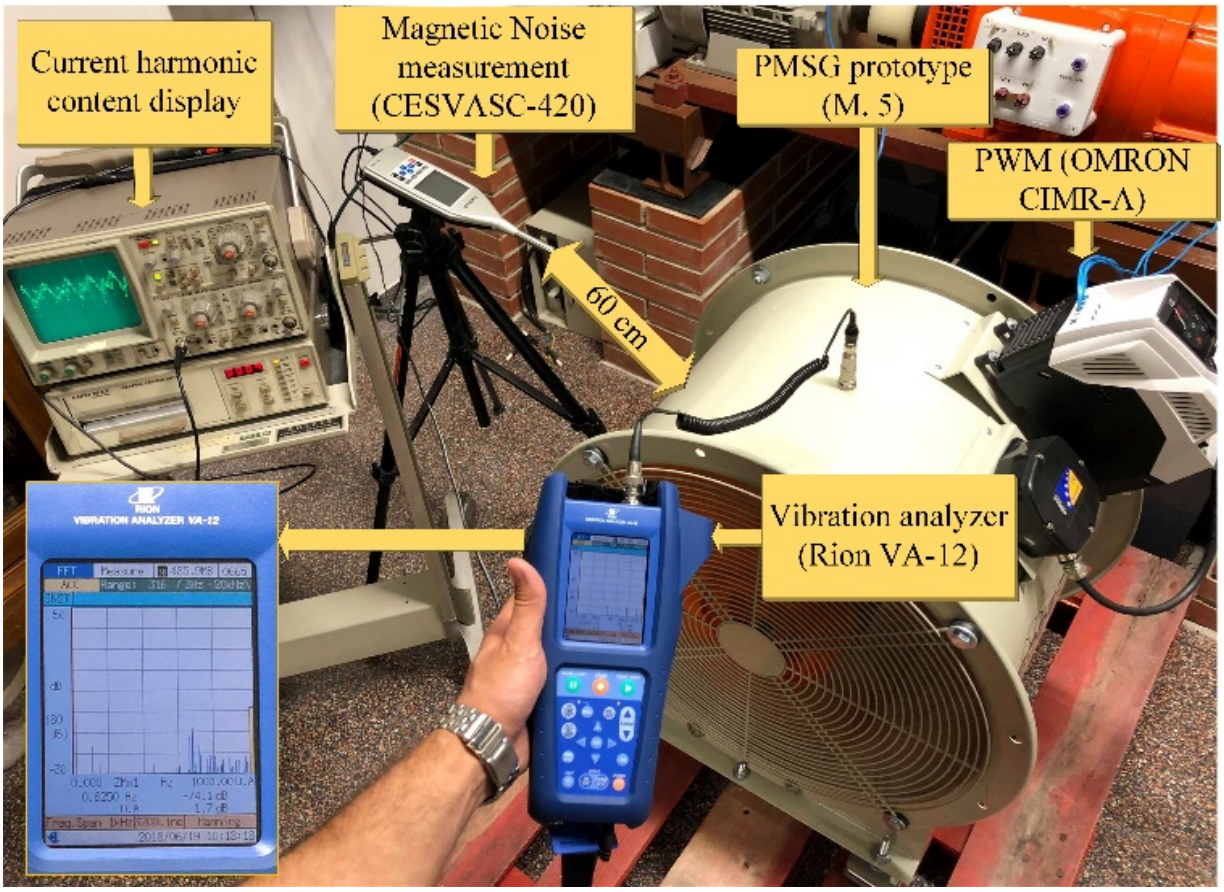

Fig. 6.8.2.2. The experimental bench setup.

vibrations. To gather noise data of the PMSG under the rated speed, the PMSG was placed, based on ISO 6396. The microphone has been placed in the radial direction of the rotor 60 cm away (as the same as simulation setup) from the PMSG to reduce the effect from the airflow, which is induced by the rotating rotor [17].

Fig. 6.8.2.3 validates the optimal PMSG noise with 42 poles (instead of 40) as the function of rotation speed with peak value 73.8 dBA (blue curve) for speed range between 15-150 rpm, which has been experimentally verified as 88.6 dBA for the optimal PMSG with 42 poles. During the test, the rotor of the studied PMSG was coupled to an induction motor for deriving purpose, the induction motor itself produced between 5 to 15 dBA (these values are measured when the induction motor was operating without coupling with other machines) between 0-1000 rpm. As presented, the grey curve shows the experimental maximum noise measurement when the machine driver (induction motor) noise is canceled. The difference between MS-SDM method and experimental measurement (grey curve) is less than 5 dBA (the only source of this emitted noise is environmental sounds) under rotation speed of 200 rpm.

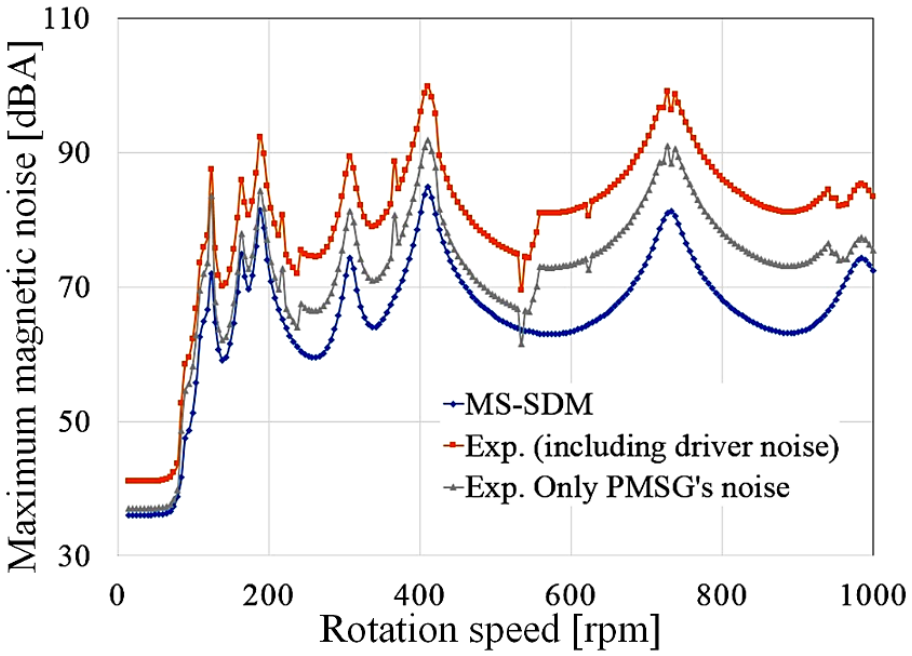

Fig. 6.8.2.3. Variable speed A-weighted sound power level validation.

7. Photovoltaic System Design Optimization for an Urban Environment

Sustainable energy and technology development play a significant role in power generation today. Photovoltaic (PV) system design and development have been combined with advanced shading analysis, to predict and enhance the output power and losses resulting from complete and partial shadings. The shading effect evaluation, with any level of variation, is essentially a mechanical design aspect but directly affects the main electrical factors. A PV module depends on a photovoltaic cell which generates an electrical current when solar radiation strikes its surface. The operation and performance of a PV module are affected by various factors such as; solar radiation, ambient temperature, PV array configuration, and shading, which may be either complete or partial. A partial shadow can be caused by clouds, trees, neighboring buildings, and utilities. The shadow effect causes the output power and efficiency to decrease and high-power loss in the shaded cells producing a hotspot [1-2].

In this chapter, we have studied how to deal with solar PV challenges when there is an urban application, such as a smart tree (as shown in Fig. 7.1), where the PV panels prediction and measurement must be carried out carefully. Due to complete (in this application mainly by wind turbine, the branches, and the tower, in addition, the buildings shading is also another concern for urban applications but not for smart tree application as it is located in the Barcelona coast) and partial shadings during the whole year, and also nominal operating cell temperature (NOCT) consideration must be considered. In this research, we investigate the influence of complete and partial shading on an annual basis using 3-D dynamic shading analysis

Fig. 7.1 Smart tree illustration with focus of eight solar PV panels as an innovative urban application.

for an application-oriented design in a new urban environment. An analysis of variance (ANOVA) method using un-replicated factorials via a dual-level window-zoom-in approach was used to determine the dominant design factors over three design variables while under various rates of shading. The focus is on the input data (i.e. NOCT, weather and sky condition data, and

ambient temperature) that have a direct effect on the module's outputs. The aim is to minimize the number of shaded cells and consequently maximize the output power of the system as a whole. A maximum power point tracking (MPPT) method, enhanced by a Perturb and Observe Algorithm (P&O) was, employed to reach the maximum possible output power. The proposed technique uses Pareto optimization, which relies on the input weather data.

A paper by Zhen *et al.* [3] presents valuable research on the nominal operation cell temperature (NOCT) under the IEC61215 standard for building-integrated photovoltaic (BIPV) modules. The authors found that the measurement error on a simulated BIPV house was about 15 °C higher than that of modules on an open rack. This is a considerable difference and more accurately resembles the conditions under which the modules would be used. It is important to determine the NOCT of BIPV modules by measuring it in the simulated BIPV house. A 7 °C temperature difference was found between grid-connected and open-circuit modules. Thus, the NOCT has to be tested under a closed-circuit condition to better mimic the real operating conditions of the modules. We have tested the PV module in both grid-connected and open-circuit experiments to evaluate and verify this fact.

N. Belhaouas *et al.* [4] presents three new physical PV array arrangements which are proposed to mitigate partial shading effects. The arrangements are based on maximizing the distance between adjacent PV modules within a PV array by appropriately arranging modules in different rows and columns without changing the electrical connections. A systematic analysis is performed to assess the proposed PV array arrangements. The new configurations simplify operation and improve performance significantly compared to the reference Series-Parallel (SP) and Total Cross Tied (TCT) configurations. The characteristic P-V curves exhibit a single peak allowing tracking of the maximum power point with a simple controller removing the need for complex controller algorithms and costly hardware, and the power output gains range from 19 to 140% compared to SP, and 13 to 68% compared to TCT.

R. Rachchh *et al.* [5] proposes a novel approach to maximize the total number of solar panels in a given area with an enhanced energy output without compromising the overall efficiency of the system. The number of solar panels can be maximized in a solar PV energy generation system by optimizing installation parameters such as tilt angle, pitch, gain factor, altitude angle and shading to improve the energy yield. In this paper, a mathematical analysis is performed to prove that the capacity and generated energy can be enhanced by more than 25% for a given land area through optimization of various parameters under different shading patterns and scenarios, and to compare the performance with existing configurations.

In another paper [6], the authors introduce a Pareto-based design-optimization problem solver for designing new energy-efficient static daylight devices that surround the external windows of a residential building in Madrid. The study identified, via a multi-objective optimization methodology, the set of optimal shading devices that allow low energy consumption of the dwelling while maintaining high levels of thermal and lighting comfort for the inhabitants.

In [7], A. J. Hanson, *et al.* demonstrate the measured performance data at the module level for 542 PV systems to estimate lost system performance due to partial shade. They have improved an average of 36% of the power lost due to partial shading via use of module-level dc power electronics.

7.1 Weather Data Observation and Acquisition

In this original study, the horizon shading is modeled as a broken line superimposed onto the sun path diagram, which can hold any number of height/azimuth points. The horizon profile is designed using *PVsyst* and *PV*Sol* software for a specific location on the Barcelona coast in Spain. Also, the meteorological data regarding at the location of the project is considered. Fig. 7.1.1 illustrates the simulated annual horizon line of the targeted location where the PV modules are installed. During azimuth = 0˚, approximately 13:00, the height of the sun can be between 74˚ to 79˚ in the peak days of the year (May, June, and July). Fig. 7.1.1 illustrates the simulated annual horizon line of the targeted location where the PV modules are installed. During azimuth = 0˚ approximately at 13:00, the height of the sun can be between 74 to 79 in the peak days of the year (May, June, and July).

This study uses two major parameters for the output power prediction. First, the nominal operating cell temperature (NOCT) found using the method studied in [8]. Then, the solar irradiance to the tilted surface of the PV generator is predicted while considering complete or partial shading of the module.

The active solar surface gives the radiation to the horizontal plane (in watts/m^2). According to the DIN5034-2 standard, the tilted global irradiance onto the PV modules, based on geometric principles is calculated [9] using:

$$E_{G,t} = E_{Dir,t} + E_{Diff,t} + E_{Ref,t} \tag{7-1}$$

where $E_{Dir,t}$, $E_{Diff,t}$, and $E_{Ref,t}$ are the tilted parameters of the direct and diffuse components of the solar irradiance onto the horizontal plane, and the reflected radiation from the ground, respectively.

Fig. 7.1.2 represents carpet plots with consideration of radiation and temperature distribution on the PV module area, where Fig. 7.1.2(a) shows how the global radiation appears on the module, and Fig. 7.1.2(b) illustrates the deviation from the nominal module temperature. The boundary of radiation onto tilted active PV surface varies between 8:00 to 16:00 (shown in Fig. 7.1.2(b)) is slightly smaller than the global radiation on the module (06:00 to 19:00) shown in Fig. 7.1.2(a). In Fig. 7.1.2(b), the deviation exists mainly during the night, during fully cloudy hours between -25 to 18 W/m^2, and much less during the daytime (09:00 to 16:00) with the variation of -60 to -280 W/m^2.

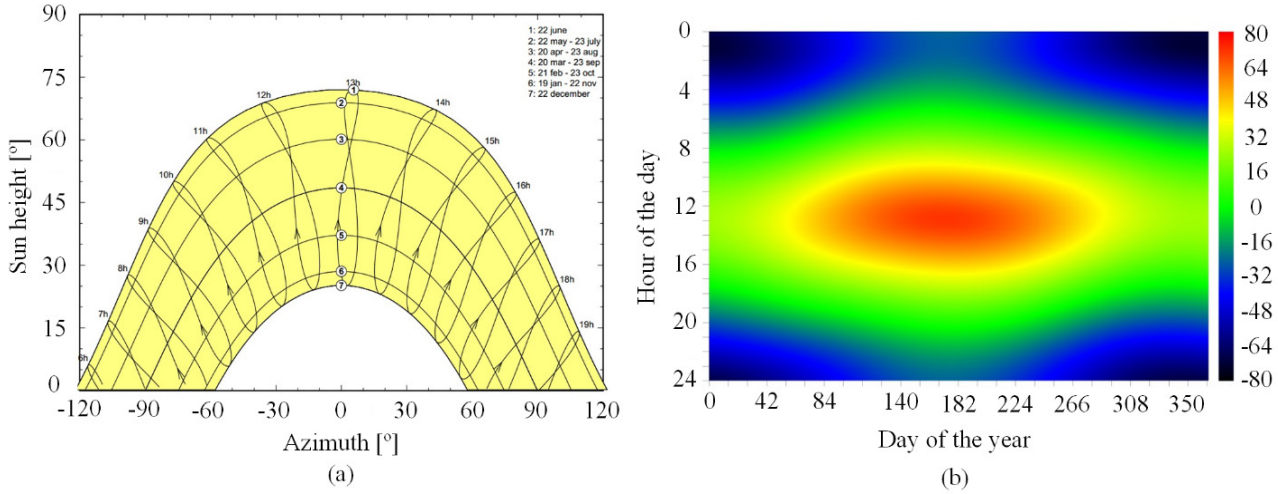

Fig. 7.1.1. Annual horizon condition in the targeted area based on horizon line.

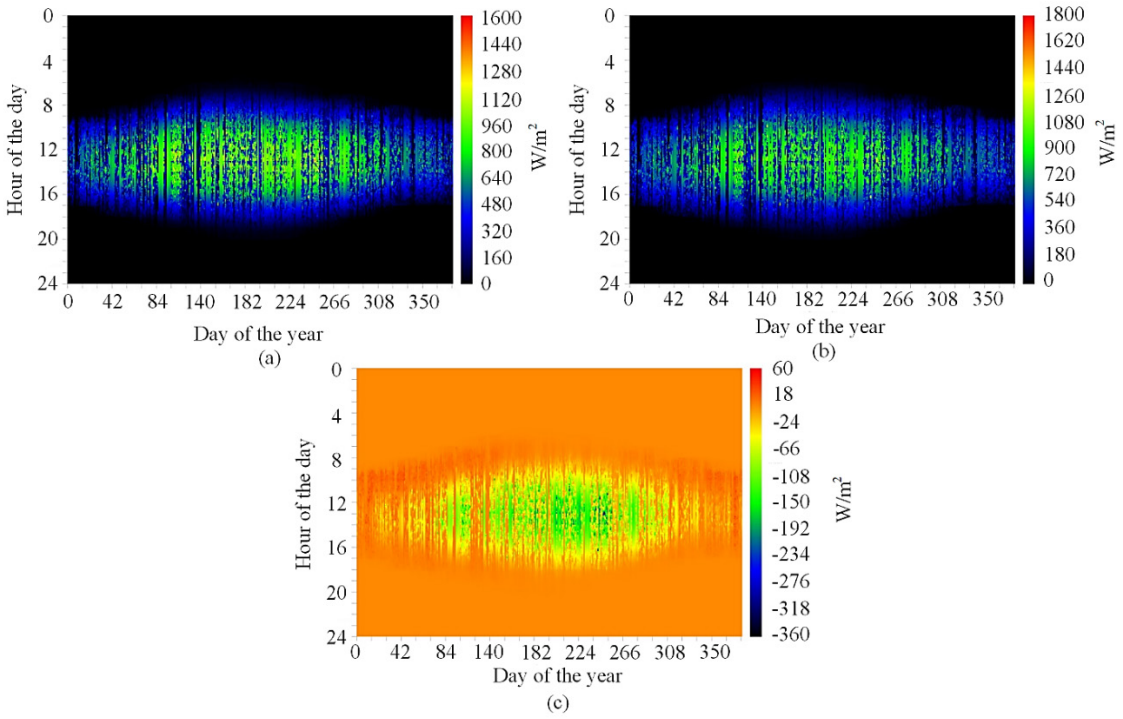

Fig. 7.1.2. Annual simulation of PV module's observation for: a) the global radiation onto the module, and b) deviation from the nominal module temperature.

Fig. 7.1.3. The daily experimental weather condition data in Barcelona city, Spain, for a) month of January, and b) month of June.

Fig. 7.1.3 presents the experimental input data of weather condition, partial shading, the average temperature of the PV module's surface, and the module losses during January and June. These experimental databases were stored through a daily observation throughout these two months in the specific location in the coast of Barcelona city in Spain. Fig. 7.1.3 (a) illustrates the stored data in June, where the red curve shows the daily average temperature of module' surface variation with the total average of 26 ˚C. The blue and green bars represent complete and partial shading losses with 10% average value for June. Fig. 7.1.3 (b) indicates the stored weather condition data in January, where the average temperature of the module's surface is 10 ˚C. In addition, the total average shading losses caused by complete and partial effects is about 20% [9].

7.2 Electrical Circuit Modeling for a Novel Application

Fig. 7.2.1(a) shows that the tower, as a part of an application-oriented renewable energy system design for power generation, consists of eight branches in the direction of suns' track where the *x*-axis and *y*-axis present the east and north directions, respectively. A total area of 30 m^2 is reserved for the PV cells, where each PV module (Fig. 7.2.1(b)) is presented as module $m1$ in series with module $m1'$. The PV system is designed with four series and parallel connections. An equivalent circuit of a PV module is simplified into three cells in series with three bypass diodes. V_{pT} is the total terminal voltage of the shaded cells, which is acquired via summation of V_{p1}, V_{p2} and V_{p3}. These voltages are across R_{p1}, R_{p2}, and R_{p3} due to shaded cells. The shading analysis is studied for one of the branches, which has approximately 60 cells. The S1, S2, and S3 areas have 24 cells each for the top, middle, and bottom sections of the module, respectively. The parameters of these three cells' areas and diodes are assumed variable due to shading. In addition, the bypass diodes are shut down only if the three cells are receiving equal irradiation. Based on the commonly employed single diode solar cell model, the output current *I* by the load is given through Eq. (7-2) [9-13]:

$$I = I_{ph} - I_0\left(\exp\left[\frac{q.(V + IR_s + I_{RP1}R_{p1} + I_{RP2}R_{p2} + I_{RP3}R_{p3}}{A.k.T}\right] - 1\right) \tag{7-2}$$

I_{ph} and I_0 are the photocurrent and the inverse saturation current, respectively. R_s is the total series resistance (which is summed by $R_s = R_{s1} + R_{s2} + R_{s3}$). A is the ideality factor of the diode. T shows the ideality factor of the temperature in Kelvin. q is electron charge 1.6×10^{-19} C and k is Boltzmann's constant 1.38×10^{-23} J/K. The partial shading causes voltage drops of V_{p1}, V_{p2}, and V_{p3} which originate from R_{p1}, R_{p2}, and R_{p3}. Hence, each area of the module (S1, S2, and S3) passes the currents of $I_{R_{P1}}$, $I_{R_{P2}}$, and $I_{R_{P3}}$, respectively.

The current I_b that passes the bypass diode can be calculated from:

$$I = I_{ob}\left(\exp\left[-\frac{q.V}{A_b.k.T_b}\right] - 1\right) - \frac{q - V}{R_p} \tag{7-3}$$

For example, I_{ob} is calculated by (photo current I_{ph} – saturation current I_{Sat}) of each S1, S2, and S3 areas, in which I_{ph} is linearly dependent on the irradiance and increases with increasing cell temperature [9-13]:

$$I_{ph}(n) = \sum_{n=1}^{3} (C_1 + C_2.T_n) E_n \tag{7-4}$$

In this study, I_{ph} is calculated for $n = 1$, 2, and 3 due to the module cells segmentation (S1, S2, S3). C_1 and C_2 are cell-dependent parameters, T_n is the temperature measured on each segment by an infrared thermal camera for different conditions, E_n is the global radiation onto the segment area.

The saturation current is defined in this research as:

$$I_{Sat}(n) = \sum_{n=1}^{3} C_s T^{k_n} \exp\left(-\frac{E_{gap}(n)}{m.k_n.T_n} \right) \tag{7-5}$$

where C_s is a material and technology-dependent constant ($C_s = 10^2$), k is the exponent of the temperature which is normally defined as $k = 3$ in the literature $E_{gap}(n)$ is the band gap of the cell material which is functional to each segment temperature. For instance, $E_{gap}(3)$ at a measured temperature of 26˚C is approximately equal to 1.13 eV for silicon [13].

The parallel resistances (R_{p1}, R_{p2}, and R_{p3}) are inversely proportional to the irradiance which is computed for various shading levels, while the series resistances (R_{s1}, R_{s2}, and R_{s3}) are negligible for irradiance and temperature changes. Consequently, the influence of shading on R_p is significant and one of the major factors to be considered in this research.

$$R_p(E_n) = \sum_{n=1}^{3} R_p \frac{E}{E_n} \tag{7-6}$$

under short circuit condition, R_p and E have been specified, however, E_n is the segment-dependent radiation in the PV module. With respect to Fig. 7.2.1, a shadow falls on cell number 1 which results in an energy input reduction to the cell. The energy loss at the partially shaded cell is increased when cell number 2 is connected and completely under illumination (i.e. no shadow). The photocurrent, I_{ph2}, is seen to be higher than that of the shaded cell, I_{ph1}.

The output characteristics of the partially shaded PV module are different from those of the completely illuminated module due to the decreased luminous energy input. In addition, because of the existence of a bypass diode, as illustrated in Fig. 7.2.1, the shaded cell is protected from damage by hot spots. The I-V curve of the partially shaded PV module is defined through a piecewise function (Eq. 7-7) that breaks at the state switching point of the bypass diode. Three states are defined to predict the voltage drops (V_i, V_j, and V_k) based on the current variation due to the various shading factors on each section of the module.

$$\begin{aligned}
&if \quad I_{ph1} < I < I_{ph2}: \\
&V_i = \frac{AkT}{q} \ln\left(\frac{I_{ph2} - I}{I_0} + 1 \right) - \frac{A_b.k.T_b}{q} \ln\left(\frac{I - I_{ph1}}{I_{ob}} + 1 \right) - IR_s - IR_p \\
&if \quad I_{ph2} < I < I_{ph3}: \\
&V_j = \frac{AkT}{q} \ln\left(\frac{I_{ph3} - I}{I_0} + 1 \right) - \frac{A_c.k.T_c}{q} \ln\left(\frac{I - I_{ph2}}{I_{oc}} + 1 \right) - IR_s - IR_p \\
&if \quad 0 < I < I_{ph1}: \\
&V_k = \frac{AkT}{q} \ln\left(\frac{I_{ph1} - I}{I_0} + 1 \right) - \frac{A.k.T}{q} \ln\left(\frac{I_{ph2} - I}{I_0} + 1 \right) - 2.IR_s - IR_p
\end{aligned} \tag{7-7}$$

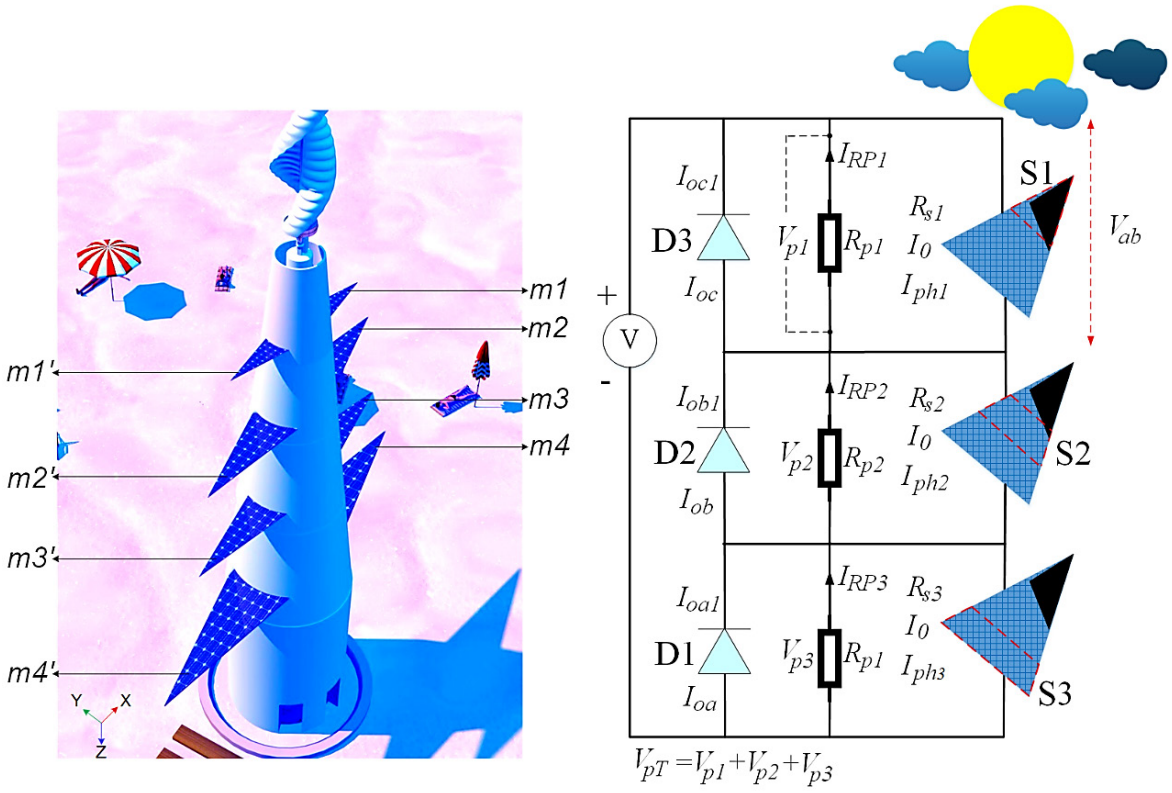

(a) (b)

Fig. 7.2.1. Partial shading modeling, a) 3-D modeling, and b) equivalent circuit of a PV module with shading.

Using the equivalent model in Fig. 7.2.1(b), the shading analysis of the PV module is theoretically acquired where a PV module containing N solar cells is divided into K groups via connecting K bypass diodes in parallel ($N \geq K$, not overlapping). If shadows fall on the solar cells at various proportions for each group, a voltage drop will affect the *I-V* curve and consequently output power of the PV module, which is presented in K steps [12-12].

In PV systems, data acquisition plays a major role due to different weather dependent factors such as the sun's height based on the azimuthal map, the modules' temperature, and shading obstacles. These databases are stored using numerical and experimental methods for high accuracy computation.

7.2.1 Electrical Circuit Modeling

The influence of the shading analysis with respect to the input data (sky) has a direct effect on the R_p which correlates to the shaded cell's rate, and thus any voltage drops over R_p results in the I-V and P-V variations shown in Fig. 7.2.1.1.

The simulation was done on one PV module of 60 cells using two databases under open-circuit conditions. First, the weather and sky data are simulated using *PVsyst* and *PV*Sol* software as input data to the power system part of the analysis, simulated with *Simulink*. Fig. 7.2.1.1(a) presents the variation of I-V curves where the shading cells factors are 20%, 40%, 60%, 80%, and 100% (normal) for the months of January and June with average ambient temperatures of 10 and 24 ˚C,

respectively. The uniform and dashed lines show the results during January and June, where a higher ambient temperature translates into a higher power loss in the hotter month with the same shading factor. During ideal conditions with 0% shading factor, a maximum current and voltage of 8.9 A and 23 V were acquired. The voltage and current dropped significantly with a shading factor of 20%, with 1.3 A and 21.5 V. Fig. 7.2.1.1(b) illustrates the P-V variation with similar simulation settings; under 20 V, the maximum power of 124, 76, 60, 45, and 30 W are reported in the month of January for shading factors of 100%, 80%, 60%, 40%, and 20%, respectively. A power reduction of up to 10 W between the two months can be seen due to the power loss from the ambient temperature.

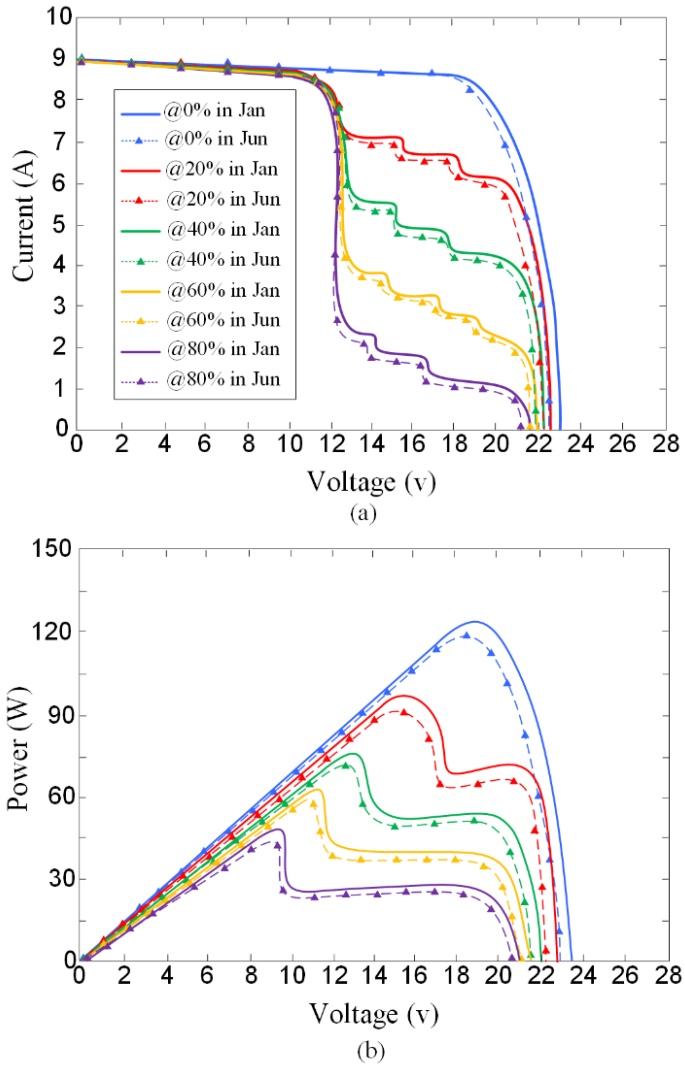

Fig. 7.2.1.1 The monthly PV module's outputs for different shading factors with respect to T_{amb} and rate of shaded cells: a) I-V variation, and b) P-V spectrum.

7.3 Maximum Power Point Tracking (MPPT) Architectures

Because of the increasing demand of electricity, and therefore larger investments on PV energy due to many advantages, maximum power point tracking (MPPT) methods used in solar photovoltaic (PV) power systems are deeply studied and implemented during last decade due to their significant role in the power systems. In references [13] and [14], the researchers studied a full review of the MPPT methods applied to PV systems.

The most used MPPT methods on PV application during the last years can be summarized as follow:

1. Curve-Fitting Method
2. Fractional Short-Circuit Current (FSCI) Method
3. Fractional Open-Circuit Voltage (FOCV) Method
4. Look-up Table Method
5. One-Cycle Control (OCC) Method
6. Differentiation Method
7. Feedback Voltage or Current Method
8. Feedback of Power Variation with Voltage Method
9. Feedback of Power Variation with Current Method
10. Perturbation and Observation (P&O) and/ Hill-Climbing Method
11. Incremental Conductance Method
12. Forced Oscillation Method
13. Ripple Correlation Control Method
14. Current Sweep Method
15. Estimated-Perturb-Perturb (EPP) Method
16. Parasitic Capacitance Method
17. Load Current/Load Voltage Maximization Method
18. DC Link Capacitor Droop Control Method
19. Linearization-Based MPPT Method
20. Intelligence MPPT Method
21. Artificial Neural Network (ANN)-Based MPPT Method
22. Sliding-Mode-Based MPPT Method
23. Gauss-Newton Technique Method

24. Analytic-Based MPPT Method
25. Hybrid MPPT (HMPPT) Method
26. Particle Swarm Optimization-Based MPPT Method

Among all the mentioned methodologies, the control strategy (indirect, direct, and probabilistic), type of control variable, type of circuit (analog or digital), option of parameter tuning, level of cost, technical complexity, type of application (stand-alone or grid-connected), are converter topology (DC/DC or DC/AC) are different which leaves the choice of MPPT method to engineers regarding the data, skill, and resources that they have from each of these methods. In this thesis, we have studied typical P&O and/ hill-climbing along with the modified P&O, FOCV, and incremental conductance methods which are very well known for this application. The reason to modify conventional P&O (which is known as an extended P&O method) is faster convergence time and more accuracy rate than conventional P&O method [15], in addition, the following features and advantages can be addressed for PV application:

1. Very fast convergence
2. Sampling type of control strategy
3. Control variables are V and I
4. Type of circuit is both analog and digital
5. There is no need for parameter tuning
6. Model complexity is high
7. Stand-alone applications (not grid-connected)
8. DC/DC converter
9. Very high accuracy

The only disadvantage of this model is the cost which is can be labeled as expensive. Also, the features and advantages of FOCV is listed as:

1. Fast convergence
2. Indirect type of control strategy
3. Control variables are V and I
4. Type of circuit is both analog and digital
5. Parameter tuning is required
6. The method is inexpensive to be implemented
7. Simple level of complexity
8. Stand-alone applications

9. DC/DC converter

This method is not accurate as the modified P&O method, however is inexpensive and easy to use. The incremental conductance method is tied with the following advantages and disadvantages:

1. Fast convergence
2. Sampling type of control strategy
3. Control variables are V and I
4. Digital type of circuit
5. No parameter tuning is needed
6. The method implementation is expensive
7. Complex
8. Stand-alone
9. High accuracy
10. DC/DC converter

In this thesis, we have used al above three methods in order to find the most suitable one. To do this, MATLAB/ Simulink R2017 is used. More detail regarding each of the methods can be found in the next sub-sections.

7.3.1 Modified Perturbation and Observation (P&O) Method

In the conventional P&O method, the PV variables (voltage and current) should be measured, afterward, the generated output power P_1 is calculated. By defining a small perturbation of voltage ΔV or perturbation of duty cycle Δd (from the DC/DC converter used) in one direction produced power P_2 can be computed. Then, they both resulted output powers will be examined under an if-loop as follow:

- If P_2 is larger than P_1, in this case, the perturbation is assumed to be in the right direction.
- Otherwise, the direction must be reversed.

Under such a correct direction of perturbation, the maximum power point P_{mpp} is determined, and thus the maximum voltage V_{mpp} can be computed. Additionally, there are a few disadvantages of the P&O and hill-climbing which should be taken into account in order to provide a proper steady-state and dynamic performance such as occasional deviation from the maximum operating point due to quick weather changes (clouds), perturbation size, perturbation step size [9] [13-15].

The conventional algorithm of perturb and observe (P&O) has been widely applied because of its simplicity, low cost and easy implementation [16-19]. However, it suffers from instabilities during rapid changes of weather and/or oscillation around the maximum power point (MPP) under a steady-state condition which is a major concern of this research. Hence, a modified-P&O algorithm, which has been validated in [17] is used for the following improvements: (1) convergence time reduction, (2) continuous perturbation, and (3) tradeoff between step sizes.

The formulation of the MPPT used, based on the DC- DC buck converter, is given as:

$$V_{out}(d) = V_{pv} \times d \tag{7-8}$$

$$I_{out}(d) = \frac{I_{pv}}{d} \tag{7-9}$$

$$d = \frac{1}{(1-d')} \tag{7-10}$$

$$S_L(d) = d^2\left(\frac{I_{out}(d)}{V_{out}(d)}\right) = \frac{d^2}{R_L} \tag{7-11}$$

$$R_L(d) = d^2\left(\frac{V_{pv}}{I_{pv}}\right) \tag{7-12}$$

where V_{out} and I_{out} are the output voltage and current of the DC-DC converter as a function of d which is a linear control variable between V_{out} and V_{pv}. d' is the duty cycle of the converter. S_{L} is the slope of the load line, and R_{L} is the output load resistance of DC-DC converter [9] [20].

This section details the methodology used, and simulation results, for the PV modeling and power electronic software based on sorting of data via a design of experiment (DOE) utilizing a full factorial function [21]. The following procedure is used to verify the whole dynamic performance, annual weather observation, complete and partial shadings, P&O algorithm for MPPT, and power electronics:

Step 1 : Storing weather condition data such as module temperature and defining the presence of the clouds for 0%, 20%, 40%, 60%, 80% and 100% (normal) during months of January (minimum power generation) and June (maximum power generation).

Step 2 : Initialize major design parameters such as pitch, and tilt for a variation of the capture beam, sailing, and optical losses. Afterward, the zoom-in-window approach based on ANOVA, is employed to find the optimum values to minimize the losses and shading rate over a single 60 cell module.

Step 3 : A conventional P&O algorithm is also simulated and compared to the proposed one (shown in Fig. 7.3.1.1 and Fig. 7.3.1.2) in order to highlight improvements. Moreover, model the shading rate of a module in a Simulink environment utilizing *Step* (*1*) data for maximizing the power through the MPPT method. The MPPT uses the proposed P&O method due to several advantages for this study.

Step 4 : Execute the whole system and store the output data for each day of the targeted months.

For the simulation studies, the parameters of the PV module are given as: P_{max} = 150 W, V_{mp} = 18.2 V, I_{mp} = 8.34 A, V_{oc} = 21.6 V, I_{sc} = 9.17 A with a power tolerance of 3%.

Fig. 7.3.1.2 illustrates the PV system which includes a three-part PV cell, DC-DC converter, MPPT controller and a load. The electronic-based model has the solar irradiance and temperature rates of each cell defined separately based on the weather acquisition data. Each cell's group is under individual control with respect to its V_{pv} and I_{pv} amplitudes. In addition, R_{p} (which is in parallel with each cell's group and diode) models the partial shading. The chosen P&O algorithm satisfies the objectives

of power maximization, fastest convergence, and continuous perturbation. Also, each cell's group is supplied with a bypass diode to minimize the hot-spot effect [19]. Finally, in view of achieving a faster convergence to the global peak, a few patterns were evaluated. V_{ref} (pu) was set from 0.8 to 0.98 V.

Fig. 7.3.1.3 illustrates the output power behavior using the optimum values of x_1, x_2, and x_3 under different radiation rates to evaluate unexpected fluctuating zones through sudden changes in the input data (solar radiation). At the radiation rates of 400, 600, and 1000 kW/m^2, the output power of 56, 65, and 129 W were achieved with an acceptable performance by the modern P&O algorithm. The conventional P&O algorithm contained much higher fluctuations especially under the 1000 kW/m^2 simulation condition. Fig. 7.3.1.3(a) zone (1) show how the modern MPPT controller has improved the output power with a faster convergence. In zone (2), a significant voltage drop exists which leads the power to a 15 W peak to peak non-stabilized variation (shown in Fig. 7.3.1.3(b)). In zone (3), the power achieved steady-state after 1 second of oscillations. The modern P&O algorithm performs well during any unexpected and quick weather condition changes compared to the conventional type.

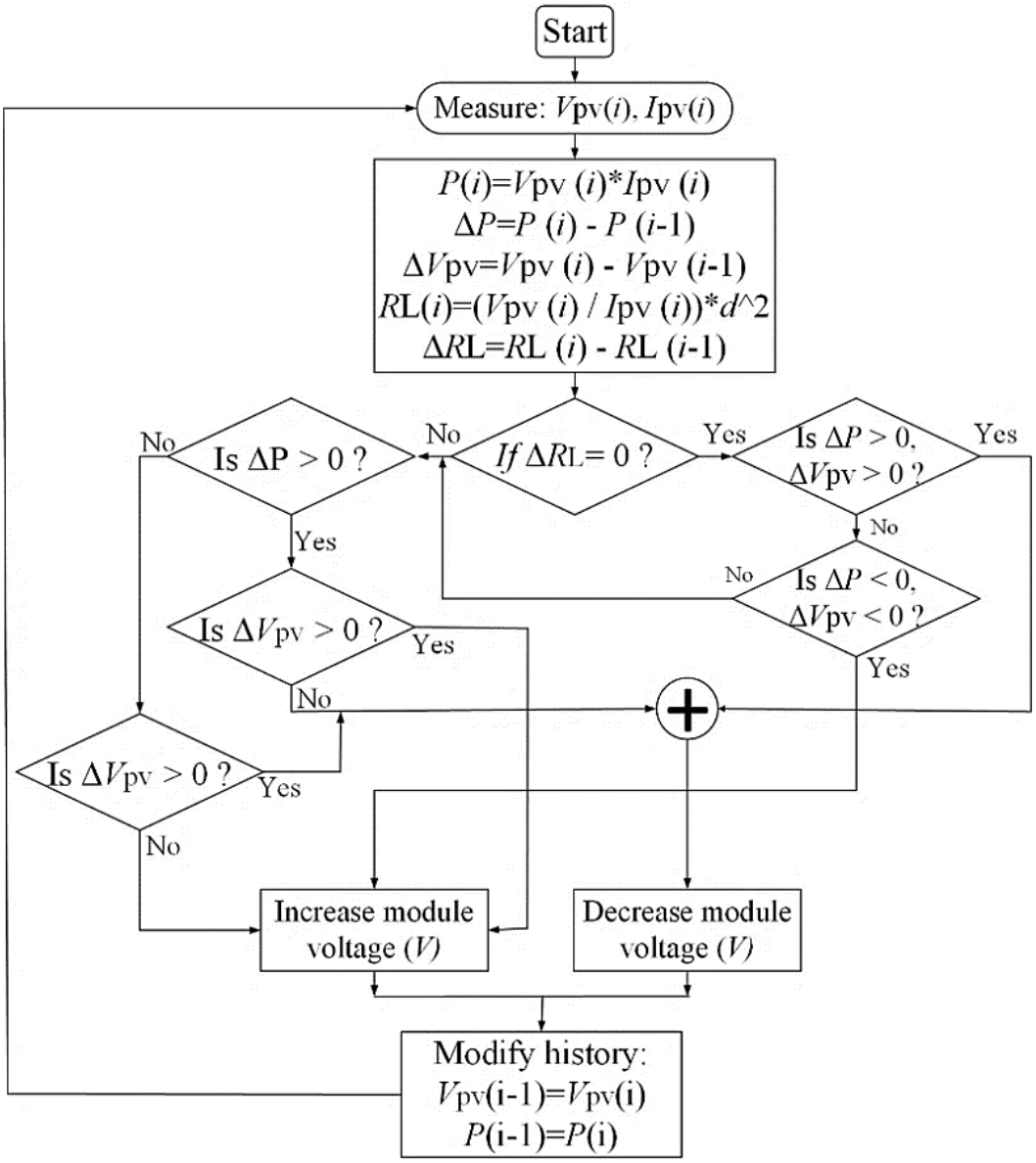

Fig. 7.3.1.1 The modified P&O method used for the maximum power point tracking.

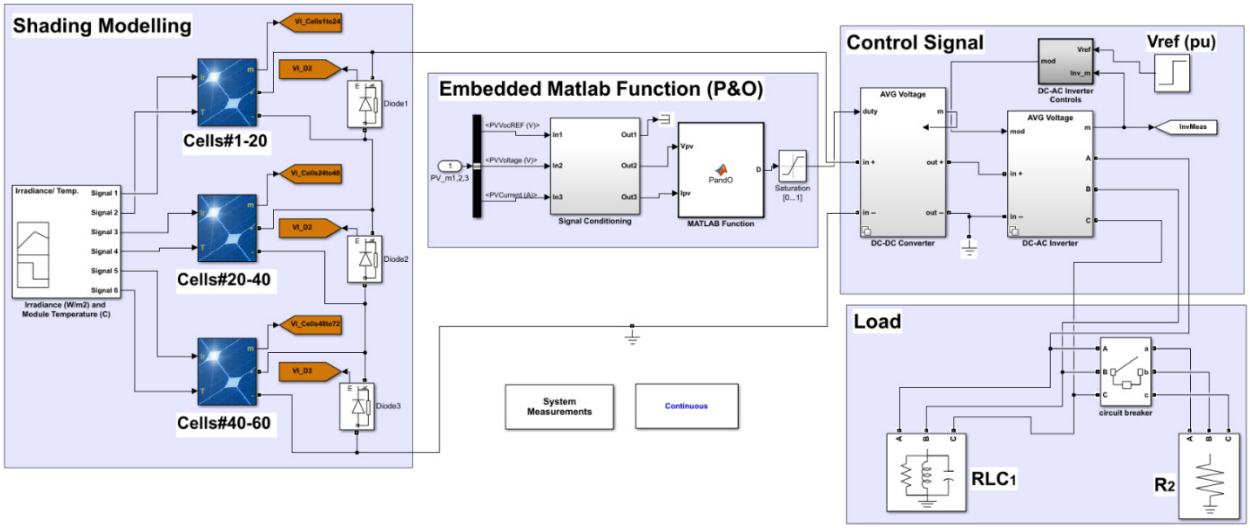

Fig. 7.3.1.2 Simplified PV-system shading analysis model in MATLAB/*Simulink*.

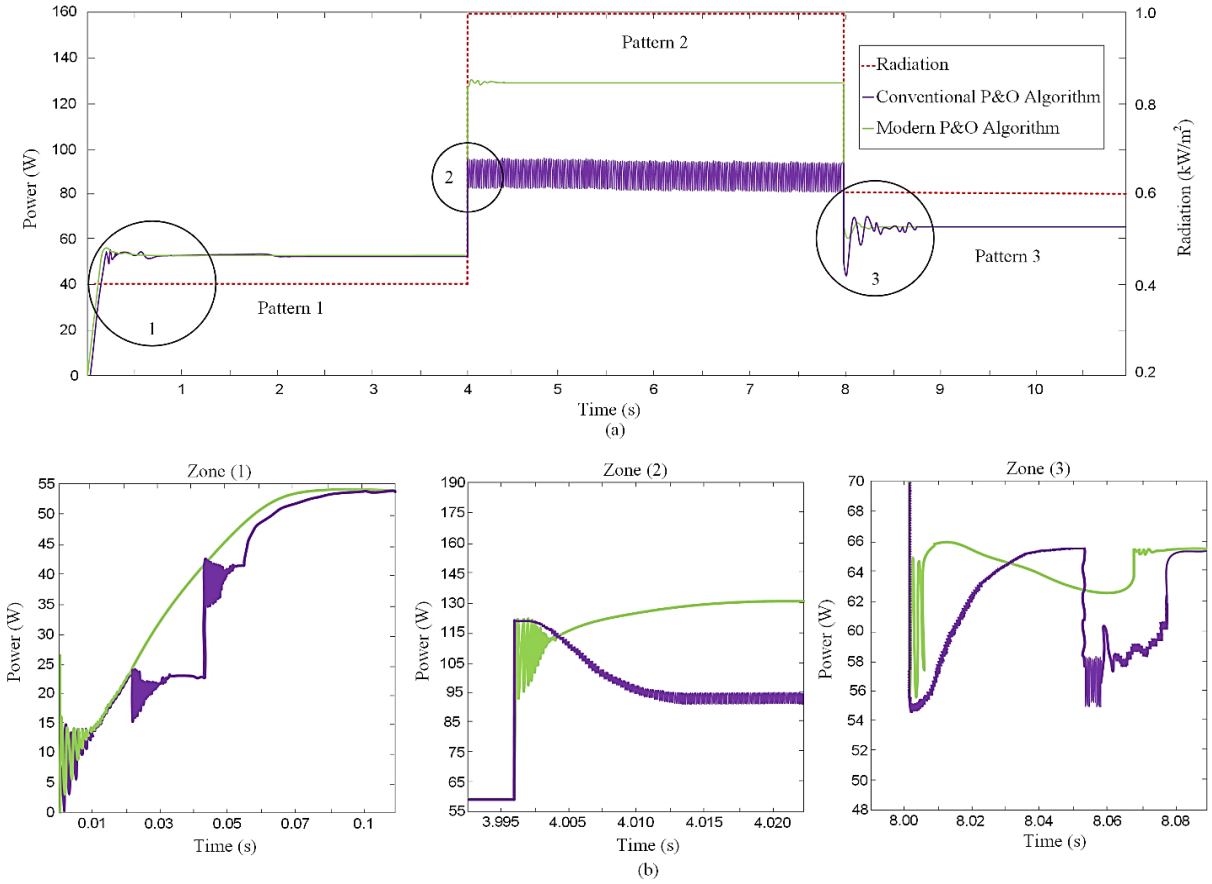

Fig. 7.3.1.3 The maximized output power using conventional and modern P&O methods for different radiation condition in the simulation, where a) presents the resilient spectrum of a complete 10s simulation, in which three patterns are considered with 400, 600, and 1000 kW/m^2, b) represents a zoomed in view during condition switching period of time.

7.3.2 Incremental Conductance (INC) Method

Basically, this type of MPPT detects the harmonic components of a solar PV module's variables (V and I) for tracking the maximum power accurately, where the PV operates under random variations in insolation (broken clouds). The typical P&O method fails to detect the maximum operating point when faces rapid changes by the broken clouds, but INC method allows the system to precisely track MPP under such a condition. As results, there have been numerous recent developments to enhance its performance. For instance, the researchers [22] studied a two-phased tracking that forms a photovoltaic (PV) power-increment-aided incremental conductance (PI-INC) maximum power point tracking (MPPT) to improve the tracking behavior of the conventional INC MPPT. The PI-INC MPPT performs, using either variable-frequency constant duty control (VFCD) or constant-frequency variable-duty control (CFVD), with reference to a collectively called threshold-tracking zone (TTZ), beyond which a power-increment (PI) tracking along the $P_{pv}-V_{pv}$ curve executes and within which an INC tracking along the $I_{pv}-V_{pv}$ curve toward maximum power point (MPP) does. Delay tracking due to ambiguous conductance-increment detection in the flat portion of the left-hand side of the MPP along the $I_{pv}-V_{pv}$ curve will not appear in the PI-INC MPPT by using the PI tracking with clear and correct power-increment detection along the $P_{pv}-V_{pv}$ curve. The research has successfully improved the performance of the conventional INC, in addition, it was experimentally validated.

In reference [23], the authors presented a modified INC algorithm which faces real challenges such as partial shading and load variations. While the system operates under such conditions, multiple peaks are observed in the power–voltage (P –V) characteristic curve of a photovoltaic (PV) array and the conventional maximum power point tracking (MPPT) algorithms may fail to track the global maximum power point (GMPP). Therefore, the paper proposed a modified incremental conductance (Inc. Cond.) algorithm that is able to track the GMPP under partial shading conditions and load variation. A novel algorithm is introduced to modulate the duty cycle of the DC–DC converter in order to ensure fast MPPT process. Simulation and hardware implementation are carried out to evaluate the effectiveness of the proposed algorithm under partial shading and load variation. The results show that the proposed algorithm is able to track the GMPP accurately under different types of partial shading conditions, and the response during variation of load and solar irradiation are faster than the conventional Inc Cond algorithm. Hence, the effectiveness of the proposed algorithm under partial shading condition and load variation is validated in this paper.

In another work [24], an enhancement has been introduced to INC algorithm in order to entirely eliminate the division calculations involved in its structure. Hence, algorithm implementation complexity has been minimized enabling the utilization of low-cost microcontrollers to cut down system cost. Moreover, the required real processing time has been reduced, thus the sampling rate can be improved to fasten system response during sudden changes. Regarding the applied step-size, a modified variable-step size, which depends solely on PV power, has been proposed. The latter achieves enhanced transient performance with minimal steady-state power oscillations around the MPP even under partial shading. For proposed technique's validation, simulation work has been carried out and an experimental set up has been implemented in which ARDUINO Uno board, based on a low-cost Atmega328 microcontroller, has been employed.

In theory, the derivative of the PV module's output power can be expressed as follow:

$$\frac{dP}{dV}=\frac{d(IV)}{dV}=I+V\frac{dI}{dV}=I+V\frac{\Delta I}{\Delta V} \tag{7-13}$$

While under MPP condition, we have:

$$\frac{dP}{dV} = 0 \tag{7-14}$$

Therefore, Eq. 7-15 would be zero at MPP, positive and negative on the left and right of MPP, respectively. This behavior can be formulated as given:

$$\begin{cases} \Delta I/\Delta V = -I/V & at \quad MPP \\ \Delta I/\Delta V > -I/V & at \quad left-side\ of\ MPP \\ \Delta I/\Delta V < -I/V & at \quad right-side\ of\ MPP \end{cases} \tag{7-15}$$

In this thesis, the common INC strategy which is shown in Fig 7.3.2.1 is used for the MATLAB/ Simulink model which presented in Fig. 7.3.2.2, however, The INC method was simulated for two series of 512 cells (the whole PV system), under 1000 kW/m^2. In fact, the INC strategy is built is DC/DC converter block shown in Fig. 7.3.2.2.

Fig. 7.3.2.2 presents the MATLAB/ Simulink modeling of the PV array system (a parallel PV module which consists of two 512 series cells), where a DC/DC Buck converter, and a DC/AC inverter are employed, in which the MPPT strategy is built-in DC/DC Buck control black right after PV module. There are two resistive loads with 4 and 1 kW (380 V_{rms} and 50 Hz), in which a circuit breaker connects the 1 kW load each 0.8s. It should be mentioned that the dynamic simulation has been successfully done for the different rate of irradiance.

Fig. 7.3.2.3 illustrates the dynamic performance of the MPPT as the function of time, under full load condition of two resistive loads with total power consumption of 5 kW. The PV system's performance under 1000 kW.m^{-2} solar irradiance is presented, where the orange curves are the maximized outputs by the MPPT used, and the blue curves are showing the system's behavior without MPPT implementation.

7.3.3 Fractional Open-Circuit Voltage (FOCV) Method

The methodology deals with the maximum power point voltage V_{mpp} calculation based on an empirical relationship which is expressed as:

$$V_{mpp} \approx K_{oc} V_{oc} \tag{7-16}$$

K_{oc} is an open-circuit coefficient which often varies between 0.78-0.92 [15] [25-26], this value is calculated as a function of the wide range of solar radiations and temperatures. This analysis of the PV system is done under the no-load condition for a fraction of second, afterward, the open-circuit voltage V_{oc} is measured. Then, V_{mpp} is calculated by using Eq. 7-17. The strategy works by sampling V_{oc} continuously in every second and updates V_{mpp} value. This type of MPPT is very popular because of being cost-effective, and simplicity of the system implementation.

The MPPT strategy can be improved in order to gain accuracy and faster MPP tracking. There are some studies which have been addressed as follow to enhance FOCV's performance for the solar PV application.

In [27], the researchers developed a hybrid MPPT method with variable step size for PV systems. The proposed MPPT method combines a new modified FOCV method and the current sensorless method with auto-modulation (CSAM) to achieve

fast and accurate tracking. This method not only has fast tracking but also automatically adjusts the step size according to the conditions of PV array. A modified FOCV has been designed to move the operating points fast to approach the maximum power points. Afterward, the CSAM has been used for fine-tuning, thus the PV system with the proposed MPPT can produce a stable and maximum possible output power. The theoretical analysis of the proposed MPPT is provided, and the laboratory prototype was constructed based on a boost converter with only a single voltage sensor.

In another remarkable study [28], they monitored and measured the maximum power of solar modules in real time for evaluating the performance of a solar electric system. In order to monitor the rapidly fluctuating output power of high-concentration photovoltaic (HCPV) modules, a simplified maximum power point (MPP) estimation and measuring system have been presented. The FOCV technique and a controllable electronic load circuit were proposed to estimate and measure the MPP. The feasibility of using the FOCV technique on HCPV modules was evaluated, the results of which demonstrate the maximum voltage and power estimation accuracy of the experimental modules. The main advantages of this simplified HCPV MPP measurement system are rapid response time, low complexity, and ease of implementation.

A. Omairi, *et al.* [29], studied wireless sensor networks (WSNs) is one of the most effective tools in collecting data autonomously going as recently as 5–10 years ago. A low deployment and maintenance cost WSN have highly recognized as one of the more advanced Internet of Things networks that can be deployed for a series of purposes namely environmental and industrial monitoring due to most of such systems run on an expendable power source that offers WSN with a limited lifetime service. The aim of the research was to review existing renewable energy and prospective approaches in energy harvesting strategy as a means of having a sustainable and low maintenance operation of WSN. Additionally, recent MPPT of solar energy harvesting is thoroughly discussed in a new perspective of the WSN framework. Semi-pilot cell fractional open-circuit voltage (SPCFOCV) MPPT is a fairly new concept in WSN application that features less complicated configuration with reduced hardware requirements and lower cost.

Recent research findings are evaluated throughout this paper leading to the SPC-FOCV MPPT materialization.
In this section, we have set similar simulation conditions such as loads, converters, etc. (as shown in Fig. 7.3.2.2), however, the DC/DC Buck control strategy is based on the following Fig. 7.3.3.1. As presented the MATLAB/

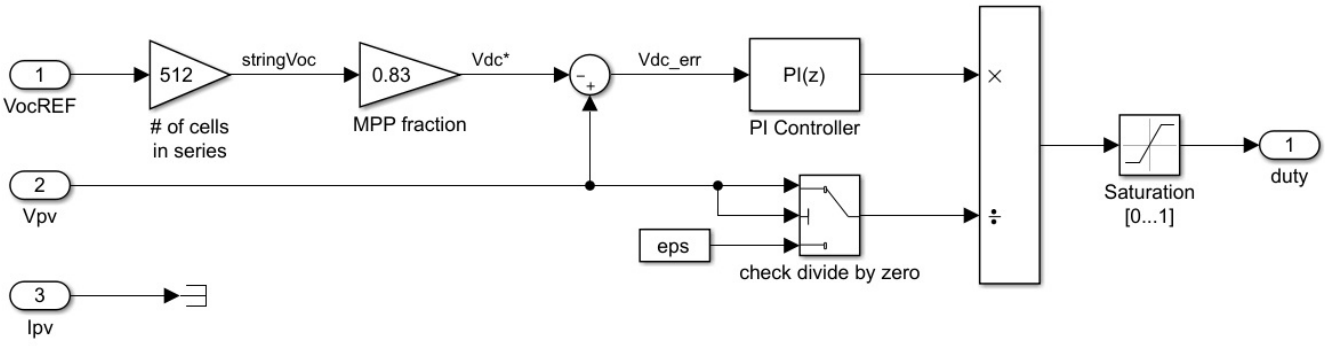

Fig. 7.3.3.1 The architecture of FOCV**.**

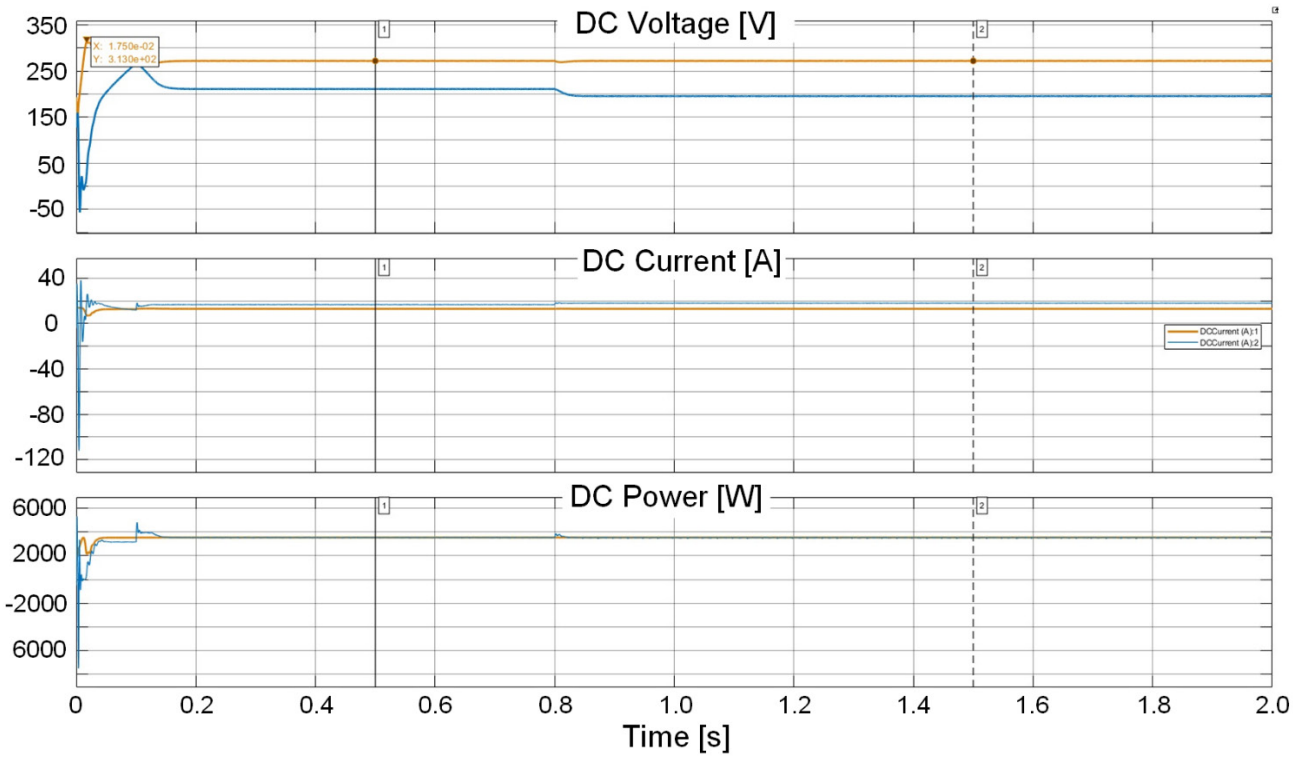

Fig. 7.3.3.2 The dynamic performance of FOCV method over voltage, current, and power as function of time.

Simulink model of the FOCV method, the open-circuit reference voltage V_{ocREF} after multiplication by K_{oc} = 0.83 (which is found as the best possible) is subtracted with the measured PV voltage in order to determine the error as shown by $V_{dc\text{-}err}$, then the PI controller will try to update its MPP value based on the given data.

Fig.7.3.3.2 illustrates the key performance of the FOCV method as the function of time, the performance shows a very smooth and fast which is also cost-effective is achieved. In particular, the output power has reached the steady-state at 0.15s by the maximum value of 3.5 kW, and V_{mpp} = 313 v (at 0.018s). The convergence time of 0.15s is nearly the same as the INC method, however, the modified P&O method could reach MPP at 0.08s which is a way better than other methods used.

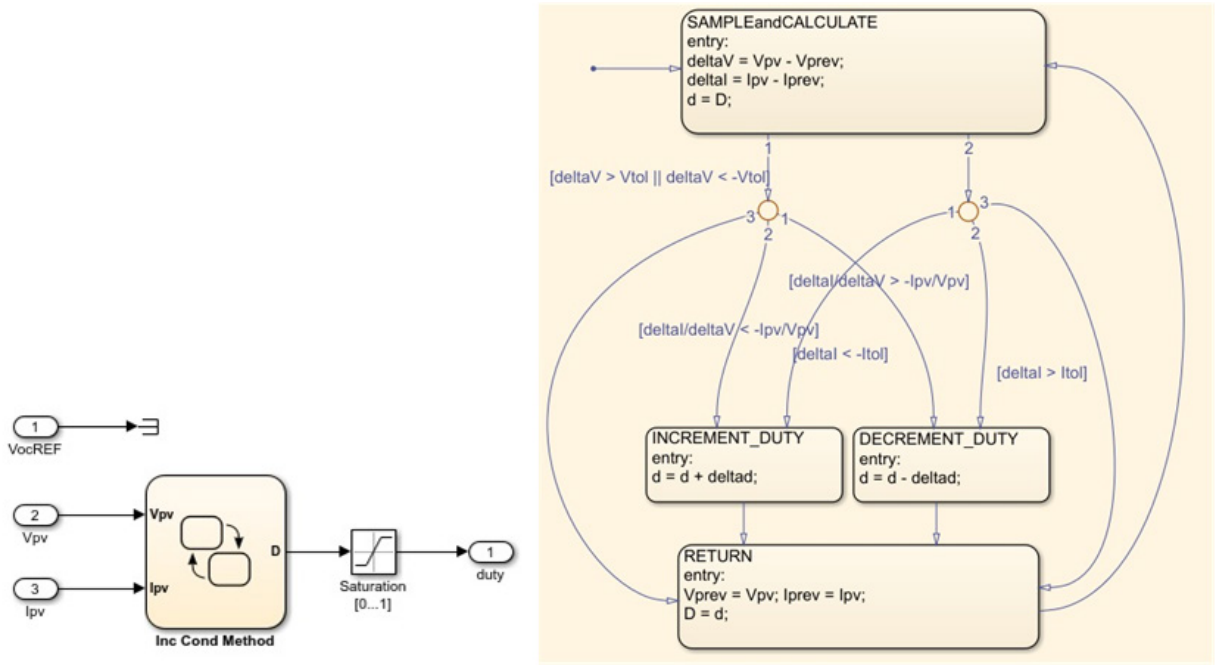

Fig. 7.3.2.1 INC methodology representation, a) Simulink block, and b) flowchart.

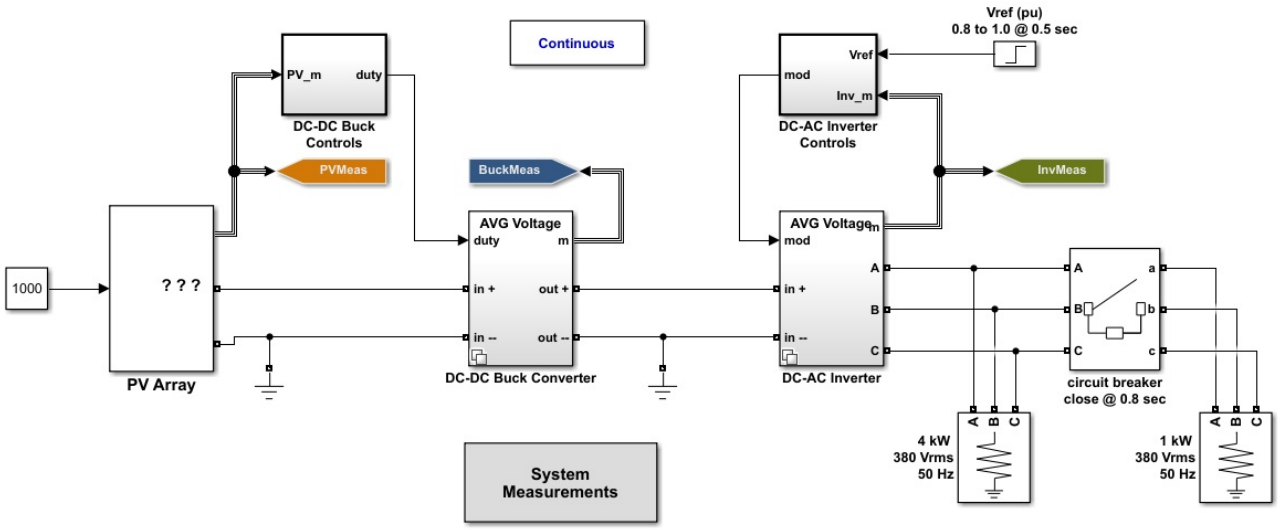

Fig. 7.3.2.2 INC methodology representation under 1000 kW.m^{-2}, a) simulink block, and b) flowchart.

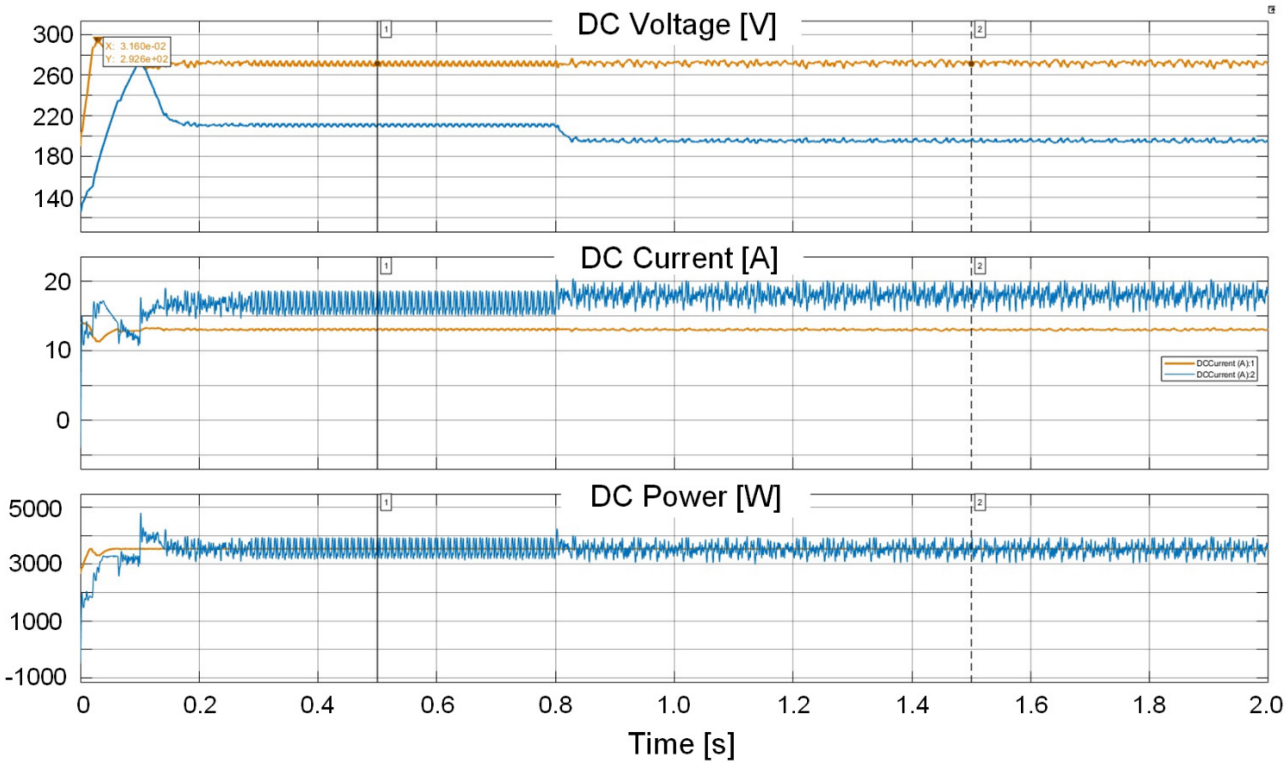

Fig. 7.3.2.3 Dynamic performance of MPPT-INC method through voltages, currents, and power waveforms.

7.4 A Novel 3-D Pareto Optimization on Complete and Partial Shading Analysis

For the 3-D structure of the project, *Google sketchUp 8* was used to analyze the three-dimensional model environment geometry and to read information such as latitude, longitude, date and time. This information and the sky condition data, when introduced in the *PVsyst*, allows for the estimation of the effective irradiation and the shading factor for a selected surface in the three-dimensional model, shown in Fig. 7.4.1 in which each branch holds PV modules. *PVsyst* software evaluated the shading analysis for a whole year.

The design and optimization procedure of the study is presented in Fig. 7.4.2. The flowchart is presented in two parts. Firstly, with the pre-calculation procedure which is shown on the left side. The right side of the flowchart represents the optimization process which is linked to the stored output data. ANOVA for un-replicated factorials based on a DOE is employed to check the accuracy where x_1, x_2, x_3 are the controllable variables pitch P, tilt angle β, and NOCT of the PV module. The main objective of the study is the maximization of the output power which depends on a number of design factors, particularly the shading analysis to decrease the total shading factor (S_t), where $S_t = S_c$ (complete shading) + S_p (Partial shading). Eq. 7-17 can be maximized when the optimum values for the variables (shown in Table 7.4.1) are found in the original design region. A modified P&O algorithm (MPPT) was used to trace the peak values for voltage, current, and power under a number of conditional terms defined as the design region (conditional optimization in Fig. 7.4.2). The optimization loop continues until the minimum total shading is achieved, and consequently, the $P_{eff}(z)$ value is maximized. For this target, the window-zoom-in approach was utilized for a more accurate design using a 2^{nd} -level design region for the variables. This

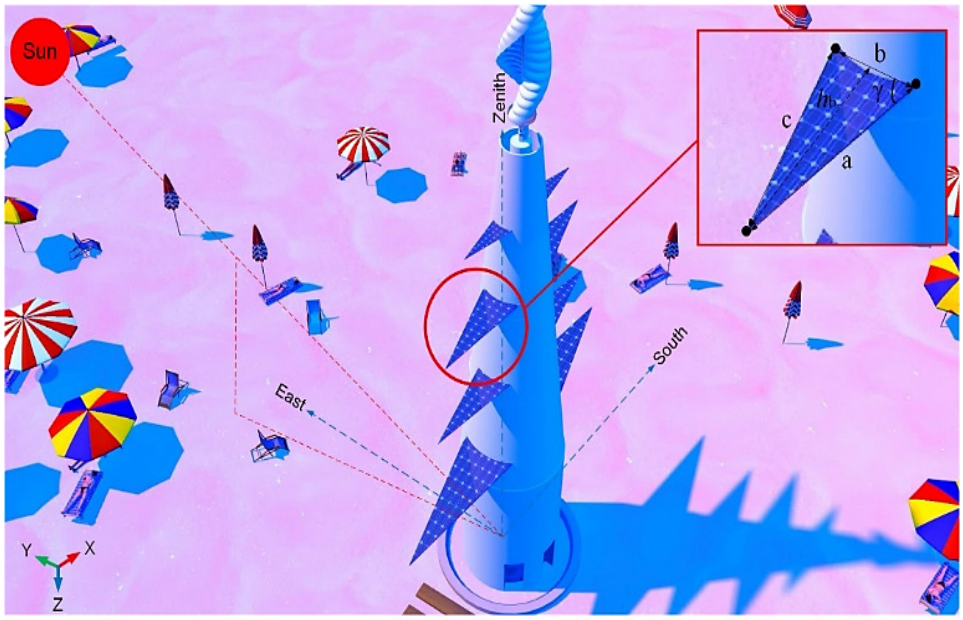

Fig. 7.4.1 The three-dimensional model environment for shading analysis.

graph indicates that the optimum point at each plane is provided until the 2^{nd} –level region. 24 variable data were analyzed, and the optimum operation point was achieved in the second level plane where the output power is maximized, and beam and shading losses are minimized.

There are several studies on PV module optimization using different methods (such as [30-32]). Regarding the above equations between the input and output variables of the DC-DC buck converter, the following problem formulation can be

studied for the Pareto Front optimization:

$$\begin{cases} Maximize: P_{eff}(z) \\ Subjected: \quad z_{\min} \le z \le z_{\max} \\ z_i = z_{i-1} \pm \phi \quad if \quad P_o > P_{o,i-1} \end{cases} \tag{7-17}$$

$P_{eff}(z)$ shows the PV array effective output energy where z is duty ratio of the DC-DC converter. The lower (z_{min}) and upper (z_{max}) limits of the duty ratio are from 5% to 95%, respectively. Under the perturbation setting of the optimization, the new duty ratio (z_i) has to provide a faster convergence and higher steady-state oscillation, only if the perturbed duty cycle (ϕ) has a large value. Whereas, smaller ϕ costs the system's convergence with slower performance. Hence, the new and larger output power P_o is considered to be larger than those last tracked points ($P_{o,i-1}$) [9].

The Pareto Front optimization determines noninferior solutions, in which an improvement in one objective needs a degradation in another. Solutions have found with either a direct (pattern) search solver or any evolutionary algorithms such as the genetic algorithm. In this study, a smooth problem with the nonlinear constraints has been defined. To build MATLAB code to maximize Eq. (7-17). First, write the function which returns z variable of the multi-objective function. Then, call it as below:

```
function P_eff(z) = pickindex(x,k) % Objective m-file function based on Eq. (7-17)
z = simple_mult(x); % evaluate both objectives
z = z(k); % return objective k
```

then, to find the maximum of the subjected variable using fminunc function for high-dimensional problems, as given:

```
k = 1;
[maxn1,maxfn] = fminbnd(@(x)pickindex(x,k),-1,2);
```

after that, set the target which are unconstrained optima for the variable, like `goal = [maxfn];` To compute the Pareto front, take weight vectors for a from 0 through 1. Solve the target attainment problem by different values for the weights.

```
nf = 1; % number of objective functions
N = 100; % number of points for plotting
onen = 1/N;
x = zeros(N+1,1);
f = zeros(N+1,nf);
fun = @simple_mult;
x0 = 0.5;
options = optimoptions('fgoalattain','Display','off');
for r = 0:N
    t = onen*r; % 0 through 1
    weight = [t,1-t];
    [x(r+1,:),f(r+1,:)] = fgoalattain(fun,x0,target,weight,...
        [],[],[],[],[],[],[],options);
end
figure
plot(f(:,1),f(:,2),'k.');
```

```
xlabel('f_n')
ylabel('iterations')
```

To develop the proposed methodology, the following software has been referenced, *Google SketchUp 8*, *PV*Sol Pre.2017*, *PVsyst Ver*. 6.66, and MATLAB *Simulink R17a* to perform the three-dimensional model [9].

In this study, two main simplifications are used which do not affect the concept and performance accuracy. To reduce the data's volume, the results are considered only for two months, June (peak operation time) and January (minimum operation time) in order to decrease the volume of data. The complete and partial shading analysis were simulated and verified only for one branch (all the other branches could be analyzed by the same computation procedure and optimization methodology used). The shading analysis on the branch marked in Fig. 7.4.2 was modeled.

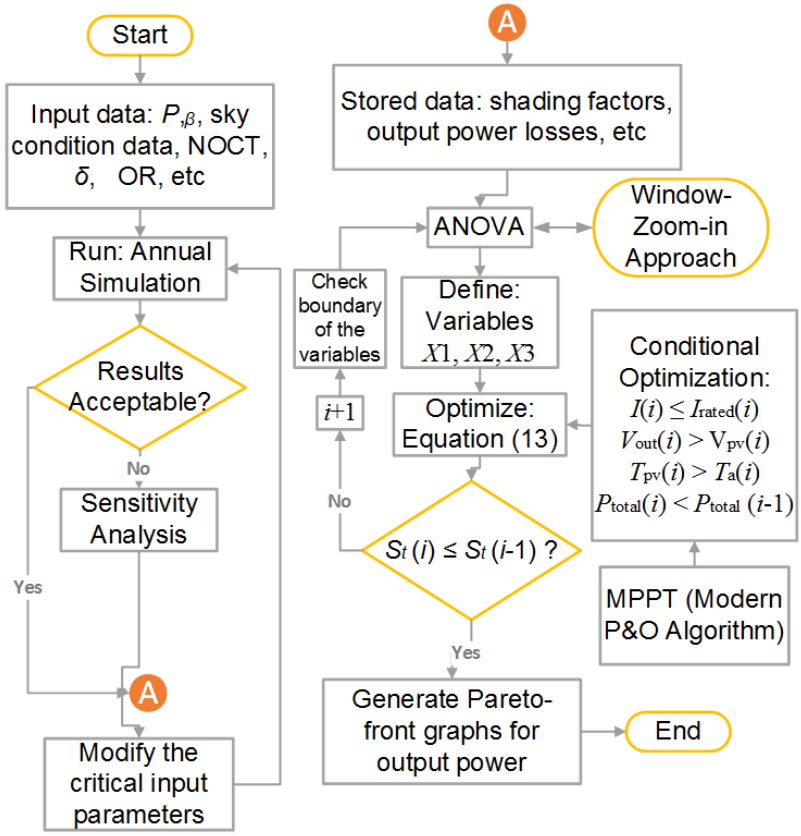

Fig. 7.4.2 The numerical-based methodology scheme.

Table 7.4.1 Original design controllable variables.

Controllable design treatments		Coded design treatments		
All variables are normalized		-1	0	1
x_1	Pitch length (m), P	0.5	1.5	2.5
x_2	Tilt angle (°), β	10	30	50
x_3	Height of the branch (m), h_b	1	4	7

Table 7.4.2 presents the second-level variation of responses y_i for the optimum variable values as x_1=1.51 (pitch length), x_2=31 (tilt angle), and x_3=5.6 (height of branch), where *DF* is the degree of freedom, *SS* is the sum of squares, *MS* is mean square. The fitted regression model was checked via an *F*-value statistic to ascertain the validity of the null hypothesis. Also, the *P*-value is a significant non-zero value, which is the probability of rejecting the factor, interaction, or blocking based on its *F*-value statistic. It should be mentioned that the input data of this table is provided by Fig. 7.3.1.3 [9].

Table 7.4.2 The second level ANOVA of DOE with 5% level.

Source of Variation	***y_i***	***DF***	***SS***	***MS***	***F-value***	***P-value***
Regression	P_o [W]	3	33.285	33.285	5.194	0.097
Residual		4	25.631	6.408	-	-
Total		7	58.917	-	-	-
Regression	P_{sn} [W]	3	0.313	0.313	0.304	2.31
Residual		4	4.125	1.031	-	-
Total		7	4.439	-	-	-
Regression	P_b [W]	3	1.103	1.103	1.446	1.662
Residual		4	3.055	0.764	-	-
Total		7	4.159	-	-	-
Regression	GlobEff [kWh/m^2]	3	161.506	161.506	7.336	0.865
Residual		4	88.059	22.015	-	-
Total		7	249.565	-	-	-
Regression	E_{array} [kWh]	3	1.583	1.583	3.993	1.633
Residual		4	1.586	0.397	-	-
Total		7	3.17	-	-	-

Fig. 7.4.3(a) presents the variation of *I-V* curves where the shading cells factors are 20%, 40%, 60%, 80%, and 100% (normal) for the months of January and June with average ambient temperatures of 10 and 24˚C, respectively. The uniform and dashed lines show the results during January and June, where for shading factors of 100%, 80%, 60%, 40%, and 20%, respectively. A power reduction of up to 10 W between the two months can be seen due to the power loss from the ambient temperature [9].

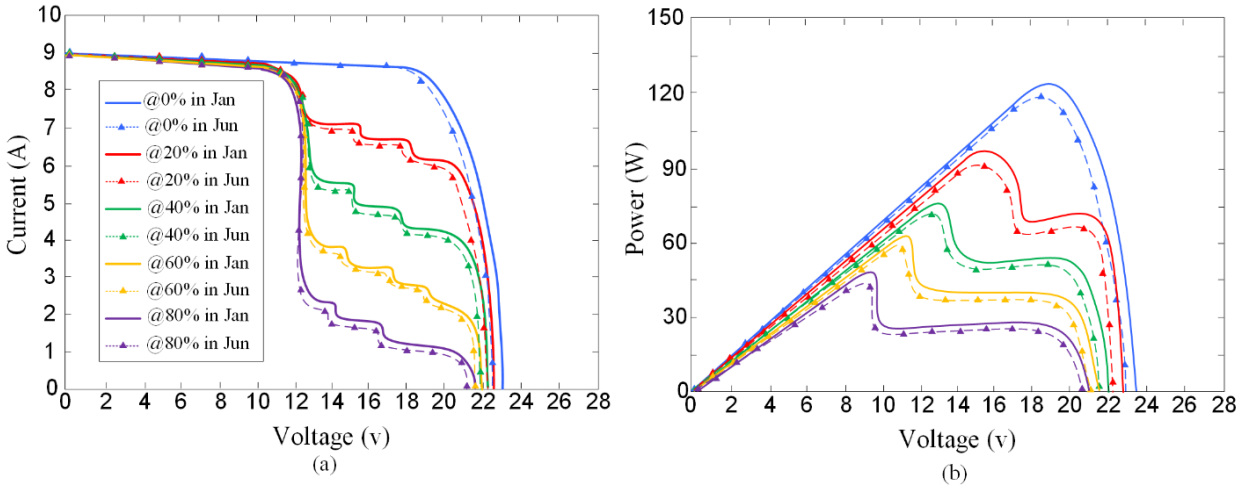

Fig. 7.4.3 The monthly PV module's outputs for different shading factors with respect to T_{amb} and rate of shaded cells: a) *I-V* variation, and b) *P-V* spectrum.

The influence of the shading analysis with respect to the input data (sky) has a direct effect on the R_p which correlates to the shaded cell's rate, and thus any voltage drops over R_p results in the I-V and P-V variations shown in Fig. 7.4.3. The simulation was done on one PV module of 60 cells using two databases under open-circuit conditions. First, the weather and sky data are simulated using *PVsyst* and *PV*Sol* software as input data to the power system part of the analysis, simulated with *Simulink* [9].

7.4.1 Pareto-front Optimization Achievements with Considering Module Losses

Fig. 7.4.1.1 presents generated Pareto-front graphs for the effective energy at the output of the array during two months (winter/ and summer). The values spectrum shown in Fig. 7.4.1.1(a) during the month of January indicated an average available energy of 2.7 kWh/day, in which the extracted output power and its relative module power losses are compared for different shading factors in Fig. 7.4.1.1(b). Under partial shading conditions, the relative module power losses (including beam loss) are defined as $\%\Delta P_{RL} = [P_o\text{-}P_s/P_o]*100$, in which P_o is the maximized output power of the PV array, and P_s is the maximized output power of the partially shaded PV array. $\%\Delta P_{RL}$ was reduced while the highest possible power is reached with the G = 1000W/m^2 condition. Fig. 7.4.1.1(c) illustrates the values of effective energy of the array for June where an average of 3.3 kWh/day was noted. For similar conditions, the extracted output power and relative power losses are computed

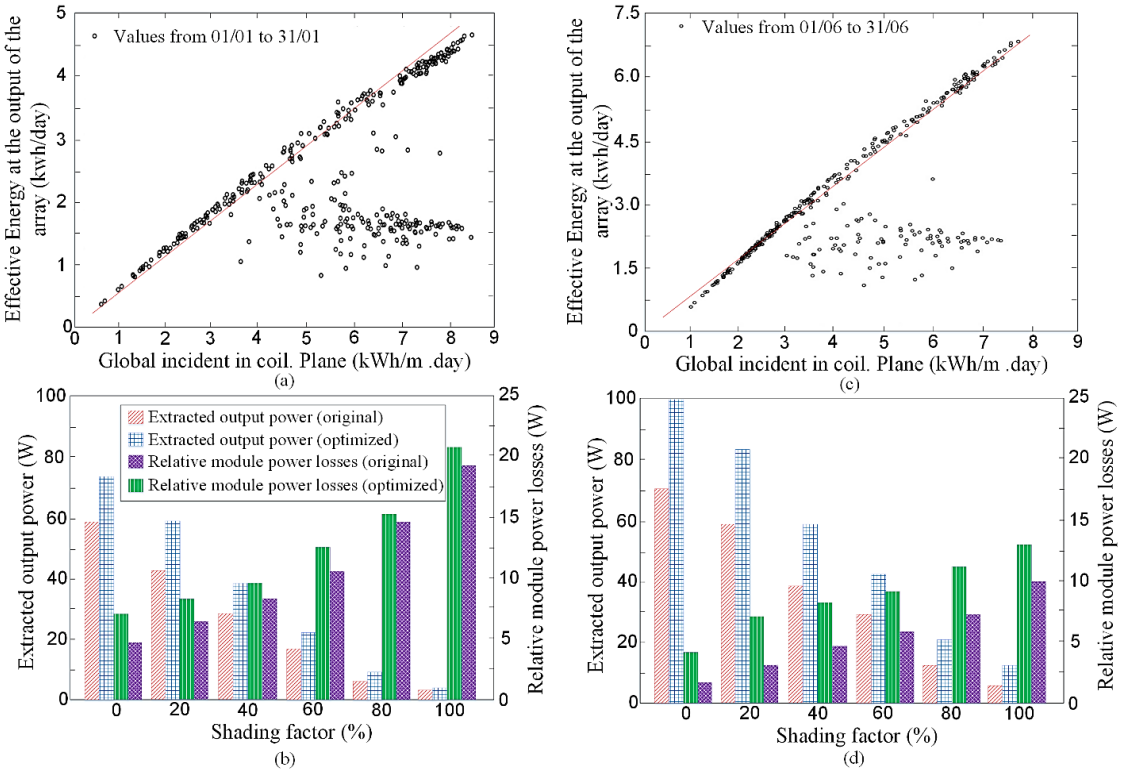

Fig. 7.4.1.1 Pareto-front monthly computation on the output energy of the array and its relative losses: a) effective energy at the output of the array in January, b) the extracted output power with its relative power losses in January, c) effective energy at the output of the array in June, and d) the extracted output power with its relative power losses in June.

and shown in Fig. 7.4.1.1(d). Much lower losses and higher output power resulted were delivered in June compared with January [9].

Table 7.7.1.1 depicts the major design parameters of a 30 m^2 cell area before (original plane) and after the optimization (second level plane) in January and June, where the shading factor is considered. The simulation is carried out with a grid-connected (closed-circuit) condition, instead of only using open-circuit NOCT values. Thus, the NOCT are accurately calculated and are slightly reduced post-optimization. Under partial shading conditions, the first affected parameter is V_{pT} which increases when R_{p1}, R_{p2}, and/or R_{p3} (total value of R_{pT}) have risen. The parameter was calculated for different shading factors and has been considerably mitigated. Under each shading factor, V_{pT} is optimized at approximately 0.045 V. The GlobEff (or effective global irradiation of the collectors), which also has a direct relation with shading, was significantly raised by an average value of 25 kWh/m2 through the proposed optimization. E_{array} (energy produced by the PV array) is another significant parameter which is influenced immediately after shading occurs. The produced energy has been maximized with an average of 5.5 kWh. P_{lossm} is the total minimum power losses caused by the shading and beam losses, for instance (in June), P_{lossm} (100%) = 0.2952 W is optimized to 0.2935 W. Finally, the objective defined in Eq. (7-7) is sufficiently satisfied where about P_o = 30 W maximization is apparent at various levels of shading [9].

Table 7.4.3 The simulation of 30 m^2 cell area with G = 1000 $W.m^{-2}$.

Parameters	Pre-optimization						Post-optimization					
Average values in month of June												
Shading factors	0%	20%	40%	60%	80%	100%	0%	20%	40%	60%	80%	100%
V_{pT} [v]	0	0.197	0.252	0.622	0.832	1.038	0	0.161	0.209	0.578	0.788	0.973
GlobEff [kWh/m^2]	220.5	209.3	196.4	179.7	151.7	126.8	245.8	235.4	221.9	204.1	174.5	159.4
E_{array} [kWh]	19.72	16.55	12.87	9.91	5.65	1.32	25.97	21.43	17.51	14.13	9.77	5.52
P_{lossm} [W]	0	0.0086	0.0335	0.756	0.2199	0.2952	0	0.0069	0.0321	0.0738	0.2179	0.2935
P_o [W]	99.656	80.332	59.881	38.974	17.558	5.217	125.066	108.554	91.995	73.649	59.772	41.713
NOCT [˚C]	51.6	42.2	31.7	24.7	18.3	16.6	51.9	42.4	32.9	25.1	18.8	16.1
Average values in month of January												
V_{pT} [v]	0	0.239	0.296	0.668	0.884	1.083	0	0.177	0.227	0.596	0.806	0.994
GlobEff [kWh/m^2]	129.5	119.5	110.7	99.2	76.9	50.5	148.7	138.9	127.2	111.6	99.4	71.9
E_{array} [kWh]	14.87	12.45	10.89	9.01	7.98	5.76	25.97	21.43	17.51	14.13	9.77	5.52
P_{loss} [W]	0	0.0108	0.0354	0.781	0.2221	0.2975	0	0.0091	0.034	0.0757	0.2197	0.295
P_o [W]	74.678	58.881	37.932	21.663	6.765	2.543	98.332	79.555	59.931	44.883	21.767	13.694
NOCT [˚C]	36.8	28.7	18.8	13.8	9.8	7.5	37.2	29.2	19.5	14.2	11.1	9.4

7.5 Conventional versus Proposed Measurement Technique

Nowadays the pace of research is very coherent among researchers for predicting the solar photovoltaic (PV) module's output power under various conditions [33]. Solar irradiance is the most significant factor for characterizing the magnitude of power generated in the cell and cell temperatures are the second most significant factor [34-35]. These factors are dependent on a number of data such as cell temperature, partial shading effect, wind speed etc.

Most of the applications corresponding to the field of PV need to evaluate the temperature of the PV cells as well as the solar radiation incident on them with adequate precision and reliability [36]. This is because the *I-V* curve of the photovoltaic module depends on the temperature and incident solar irradiation [37-38].

There is valuable research in the literature that has been reported in recent years to enhance the solar PV performance prediction [39-50]. Among them, some methods include the basis of the module operating temperature measurement techniques [39-40], the uncertainty performance loss-rate estimation measurement via indoor [41] and outdoor [42] techniques, and partial shading effect assessment approaches are also widely discussed [51-52].

G. Farivar and B. Asaei [53] presented an effective new method for estimating the operating temperature of a PV module with the simple diode model. The researchers have proposed the methodology, which is based on an analytical formula, in order to derive the temperature from the maximum power point, voltage and current. The work has been experimentally verified. In addition, other research by G. Mangeni, *et al*. [54], discussed a photovoltaic module's cell temperature measurement and an 81-point heat distribution mapping technique using only 9 temperature sensors. They used these 9 negative temperature coefficients thermistor-based temperature sensors (NTC thermistor) attached at the back of photovoltaic panel equally spaced in a 3 by 3 manner, a microcontroller, a data acquisition and visualization software with interpolation technique developed in MATLAB.

Malte Ruben Vogt, *et al*. [55] studied the reduced operating temperature of modules made from passivated emitter rear cells (PERCs) compared with modules made from cells featuring an "unpassivated fullarea screen-printed aluminum rear side metallization aluminum back surface field (Al-BSF)". Additionally, they increased the yield of modules using PERC instead of Al-BSF solar cells. The research offers a valuable experimental investigation.

In P. Ingenhoven*, et al*. [56] paper, the researchers have compared statistical and deterministic smoothing methods to reduce the uncertainty of performance loss rate (PLR) predictions.

Based on the addressed references, the main reasons for solar PV material degradation are continuous cycles of temperature, humidity, irradiation, mechanical stress, spotted soiling that can induce corrosion of the metallic connections, hot spots, bubbles, and other failures [56–58]. In addition to material degradation, there are other considerable outdoor operating conditions, such as partial shading analysis, which must be considered when a true output estimation is required. The following listed studies have allowed many researchers to evaluate their own Solar PV system under partial shading conditions [51-52].

The scope of this research is to introduce a new fast technique to estimate the performance metrics (output) of a solar PV module under a partial shading condition. In addition to this outdoor operating condition, the nominal operating cell temperature (NOCT) must be accounted for to avoid an incorrect prognosis during cell temperature measurement. In particular, this fact motivated us to experimentally test the cell temperature distribution during open/close circuits, as the PV module temperature settings have a significant impact on the output prediction. This research offers correlations to reduce the difference between predicted values and experiments.

To find an accurate estimate of the output, it is necessary to follow the simple procedure shown in Fig. 7.5.1, where the flowchart (Fig. 7.5.1(a)) illustrates the conventional way to predict the module temperature, which is based on either the ambient temperature of the PV module or the open-circuit module temperature distribution. The captured PV characteristics under a closed-circuit condition are derived in a different manner, in which the measurement restrictions is depicted in Fig. 7.5.1(b), for a high-efficiency crystalline PV module with a maximum output of 150 W, 7.6 A. The cells temperature is studied cell by cell based on the presented cells coding in Fig. 7.5.1(c).

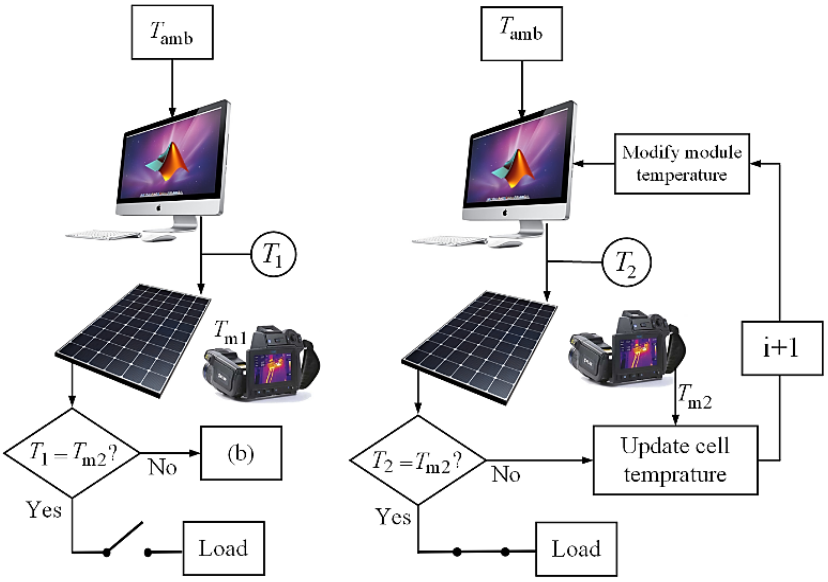

T_{11}	T_{12}	T_{13}	T_{14}	T_{15}	T_{16}	T_{17}	T_{18}	T_{19}
T_{21}	T_{22}	T_{23}	T_{24}	T_{25}	T_{26}	T_{27}	T_{28}	T_{29}
T_{31}	T_{32}	T_{33}	T_{34}	T_{35}	T_{36}	T_{37}	T_{38}	T_{39}
T_{41}	T_{42}	T_{43}	T_{44}	T_{45}	T_{46}	T_{47}	T_{48}	T_{49}
T_{51}	T_{52}	T_{53}	T_{54}	T_{55}	T_{56}	T_{57}	T_{58}	T_{59}

(c)

Fig. 7.5.1. Solar PV cells temperature measurement using a) conventional, b) proposed technique.

7.5.1 Methodology and Mathematical Definition

Based on the proposed schematic illustrated in Fig. 7.5.1(b), the procedure to manage the cell temperature relies on a NOCT consideration. In addition to the load's impact, the effect of partial shading at different levels has been considered. In this section, we describe the method used to compute the cell temperature, namely:

1. Define the PV module in MATLAB Simulink based on the ambient temperature using an average value of each month.

2. After storing the first estimations of the module's temperature (T_1) and output. Then the experimental cell temperature (online) can be measured under load (closed-circuit) conditions.
3. The measured cells temperature (T_2) can be seen to be considerably higher than T_1, therefore the output prediction has been affected due to the error of the PV module temperature as an input).
4. To avoid this defect, the input PV module temperature is updated monthly in Simulink. This back and forth measurement process come with a cost, which has solved by step 5.
5. All the data from both models (*a* and *b*) are stored within different shading-levels. Afterward, pairwise and Spearman's ρ statistical methods are applied to find out the best possible correlations with minimum error.
6. The proposed correlations as a function of NOCT and partial shading effects have resulted in a faster and more accurate estimation of the output.

- *Mathematical Definitions*

The total solar irradiance that strikes the surface of the PV module ϕ_{total} can be defined by the harvested power P_{E} and wasted energy P_{L}, where P_{L} is due to the light reflected or emitted through the module ϕ_{o}, and the power converted into heat ϕ_{h}. Thus, the effective power is calculated by:

$$P_E = \phi_{total} - P_L = \phi_{total} - \phi_o - \phi_h \tag{7-18}$$

For the simulation studies, the parameter ϕ_{total} is set by 800 W.m^{-2} in ambient temperature $T_{\text{amb}} = 20^{\circ}$C, wind speed $v = 1$ m.s^{-1}, in addition, an optical density of luminescent down shifting (LDS) layers at dye peak absorption equals 2. There is valuable research done regarding the impact of LDS over NOCT in [35].

The cell temperature measurements, either IR-Infrared-based (T_{m1} and T_{m2}) or linear interpolation technique (T_1 and T_2), have considered the module's cell coding or matrix (see Fig. 7.5.1(c)) [54]. In particular, to compare the outcome of both measurement techniques, the average string-based module temperature was calculated from:

$$T_1 = T_2 = \sum_{i=1}^{9} T_{1i} + T_{2i} + T_{3i} \cdots T_{5i} \tag{7-19}$$

Boundary conditions at the front surface of the glass and the back surface of the plastic are convection and radiation heat transfers which entirely discussed in [36]. Thus, the boundary conditions for the average PV module temperature (T_1 or T_2) can be defined, for instance, when the model (a) operates (see Fig. 7.5.1(a)) as:

$$\begin{aligned} k_1 \frac{\partial T_1}{\partial x} &= h_{FS}(T_1 - T_{amb}) + q_1 \\ k_2 \frac{\partial T_1}{\partial x} &= h_{BS}(T_{amb} - T_1) - q_2 \end{aligned} \tag{7-20}$$

The relative efficiency deviation $\Delta\eta_{\text{rel}}$ as function of solar irradiance G and cell temperature T_2 can be defined as:

$$\Delta\eta_{rel}(G, T_2) = \frac{P_{2,\max}(G,T)}{P_{2,\max}} \times \frac{G_{STC}}{G} - 1 \tag{7-21}$$

Based on the self-reference method [59-61], using the short-circuit current I_{sc} as a function of G can be written as:

$$\frac{G_{STC}}{G} = \frac{I_{sc}(G_{STC}, T_2)}{I_{sc}(G, T_2)} \tag{7-22}$$

The module's temperature dependency during the partial shading phenomenon can be modeled through heat equations over each individual layer of crystalline silicon (C-Si) in the solar modules. In this study, it is assumed that the temperature diffusion is uniform at the horizontal plane. The heat equations are given for each layer by Eq. (7-23), in which the suffix i varies between 20-100% depending on the shading rate.

$$\begin{aligned}
\frac{\partial T_1}{\partial t} &= \alpha_1 \frac{\partial^2 T_1}{\partial x^2} + G_i \frac{\alpha_1}{\kappa_1} \frac{a_1}{X_1} \quad (Glass) \\
\frac{\partial T_2}{\partial t} &= \alpha_2 \frac{\partial^2 T_2}{\partial x^2} + G_i \frac{\alpha_2}{\kappa_2} \frac{a_2 - P_{C-Si}}{X_2 - X_1} \quad (Silicon) \\
\frac{\partial T_3}{\partial t} &= \alpha_3 \frac{\partial^2 T_3}{\partial x^2} + G_i \frac{\alpha_3}{\kappa_3} \frac{a_3}{X_3 - X_2} \quad (Plastic)
\end{aligned} \tag{7-23}$$

where T_1, T_2, and T_3 are the uniformed temperature of the glass, silicon, and plastic parts, respectively. α_1, α_2, and α_3 are the thermal diffusion constants which are 3.77×10^{-7}, 7.65×10^{-6}, and 1.86×10^{-7} ($m^2.s^{-1}$), respectively. P is the generated power in the silicon layer given as:

$$P_{C-Si} = I_s \frac{V_s + 0.75}{m \times 60S} \tag{7-24}$$

where I_s and V_s are the current and voltage of the string (including the cell). m is the number of solar PV modules in series, as we tested the measurement for only a single module, thus, $m = 1$. $60S$ represents the number of cells, which is 60 in this study. Finally, S is the total active area of the cell in m^2.

Fig. 7.5.1.1-a presents a cross-sectional model of the C-Si solar PV cells, in which the PV module has been implemented at Barcelona in Spain. The thickness of glass, silicon, and plastic back sheet have been measured and are $X_1 = 3.5$, $X_2 - X_1 = 0.28$, $X_3 - X_2 = 0.6$ (mm), respectively. There are also two ethylene vinyl acetate copolymer (EVA) layers encapsulating the C-Si layer, which are considered in the model. The EVA layers over the C-Si layer are transparent and considerably thinner than the glass layer.

- *C-Si Photovoltaic Module Characteristics*

The 60 cells, C-Si, PV module with a nominal output power of 150 W, 7.6 A, under different partial shading rates (S = 0-80%), and open circuit test conditions has the *I-V* and *P-V* curves presented in Fig. 7.5.1.2(a) and (b).

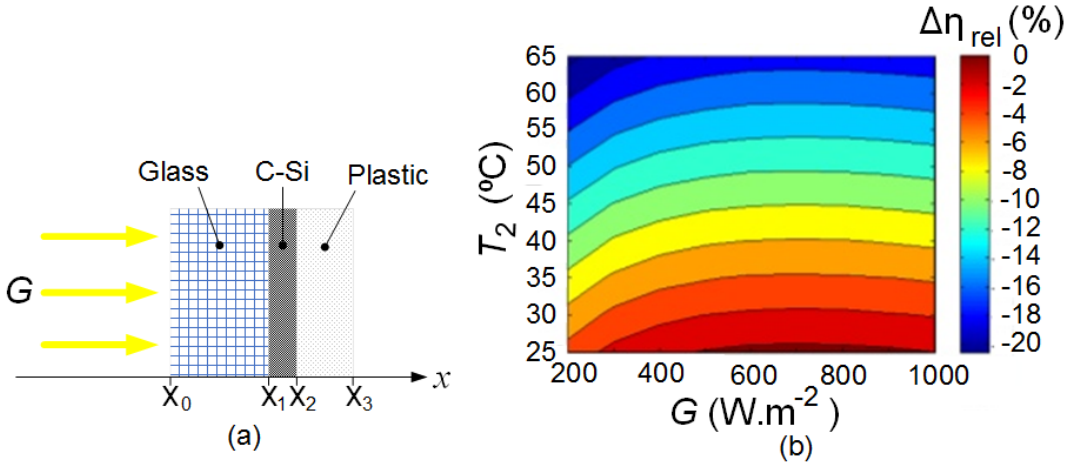

Fig. 7.5.1.1. Cross-sectional model of used C-Si solar module, a) Indicates the solar irradiance versus module partitions, b) Irradiance and temperature dependence of C-Si PV module.

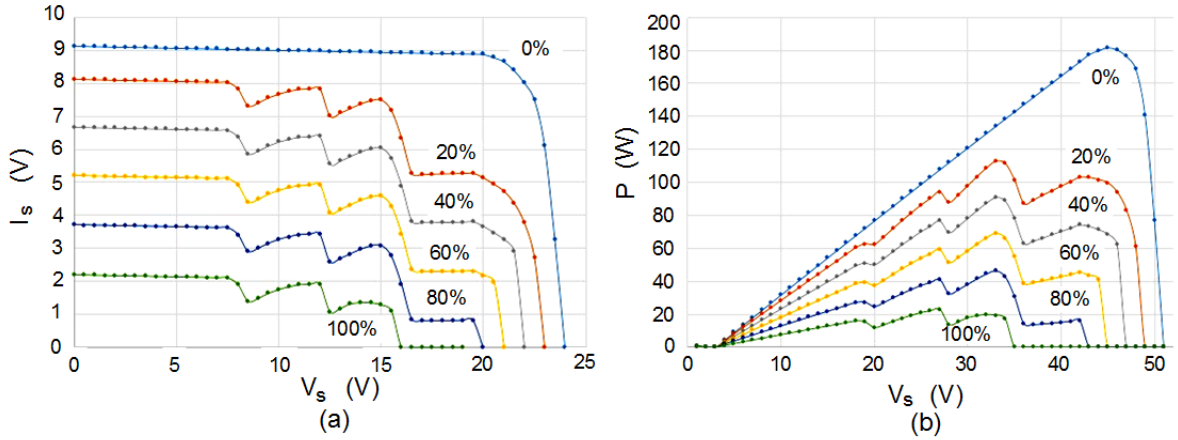

Fig. 7.5.1.2. Solar C-Si 60 cells PV module characteristics based on partial shading effect a) *I-V* curves, b) *P-V* curves.

7.5.2 Behavior of PV Module Considering NOCT and Shading

In this section, the behavior of the C-Si module under all defined considerations and assumptions have been collated and analyzed where the results have determined a significant estimation error. Afterward, a table of calculated correlations has been offered for engineers in order to be used to prevent such unreliability [62].

Fig. 7.5.2.1 illustrates the monthly variation maps of I_s as a function of V_s and cell temperature, where the influence of NOCT in comparison to a NON-NOCT consideration based on the seasonal horizon has been studied. Fig. 7.5.2.1(a),(b), (c), and (d) present the autumn, winter, spring, and summer seasons, respectively. When the difference between NOCT and NON-NOCT currents at higher voltages (14-22 V) can be seen on the September and October months. The sharp color map curvatures describe more voltage drop, mainly at the highest V_s when the NOCT is considered. In contrast, the variation of I_s appears more linear in the month of January, approximately similar to the NON-NOCT condition. Fig. 7.5.2.1(b), indicates

the winter, where insignificant errors of estimation are observed due to the lower I_s. The curvature range is between 18-22 V in this season. In spring (Fig. 7.5.2.1(c), a larger estimation error exists in comparison with autumn and winter, in which more nonlinear curves can be seen, especially in the range of 15-22 V. With respect to spring's maps, the most critical error occurs in the month of May within 14-22 V operation. During the summer, the current's maps have tended significantly towards the NOCT consideration, where the largest ramped curves occur at a different level of I_s (0.5-9 A), and V_s (12-22 V). The highlights of the presented current maps (Fig. 7.5.2.1) are; more estimation error exists when V_s is approaching the rated value V_m of the solar module, which mostly affects the peak operation months (Jun, Jul, and Aug). If the difference between the currents with and without the NOCT consideration defines the error of the I_s calculation, then the most critical error occurs during the widest range of V_s as well as a higher gradient. Therefore, the current prediction highly depends on the cell temperature and nominal voltage especially during peak operation times such as the summer season [62].

Fig. 7.5.2.2 presents the variation of maximum output power and voltage as the function of ambient temperature for conventional and NOCT cases. For various rates of partial shading (0-80%), the predicted values based on conventional measurement have a significant estimation error. The study proofs that the maximum error of power prediction occurred at the higher rate of partial shading S. In other words, a larger rate of S and V_s led to power prediction inaccuracy (error). Hence,

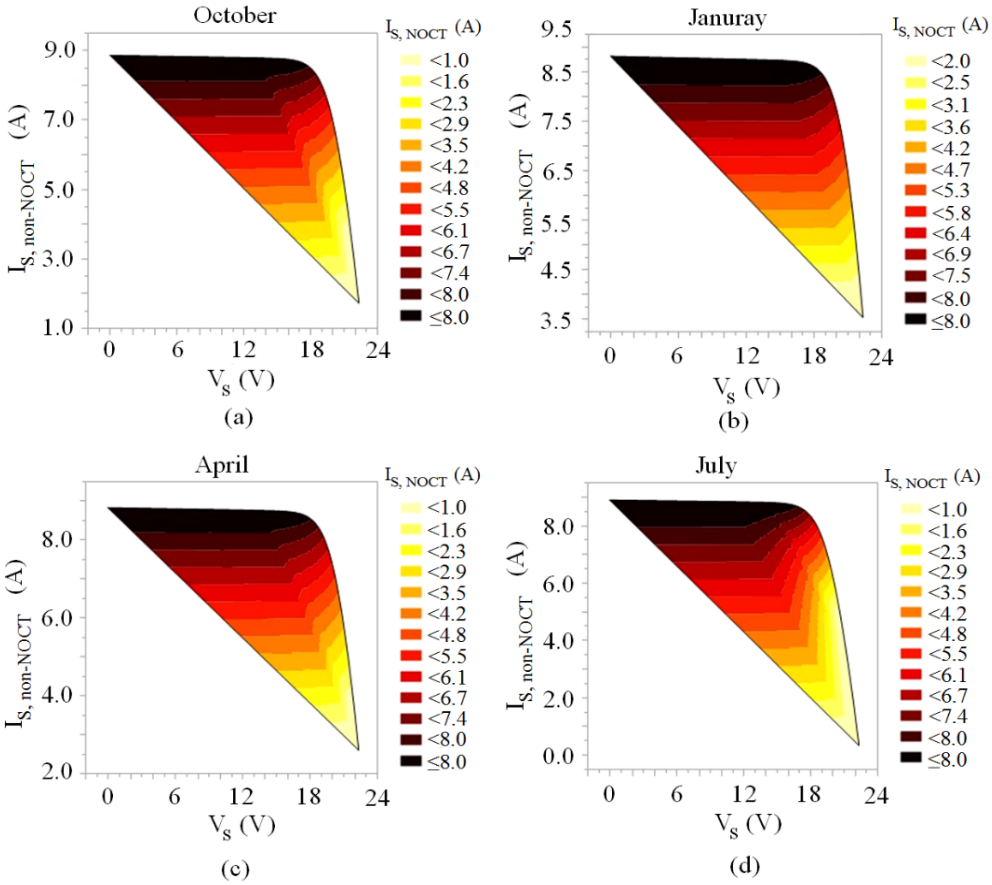

Fig. 7.5.2.1 Nominal output characteristic maps of the used solar C-Si module with and without nominal operating cell temperature (NOCT) consideration for month a) October, b) January, c) April, d) July.

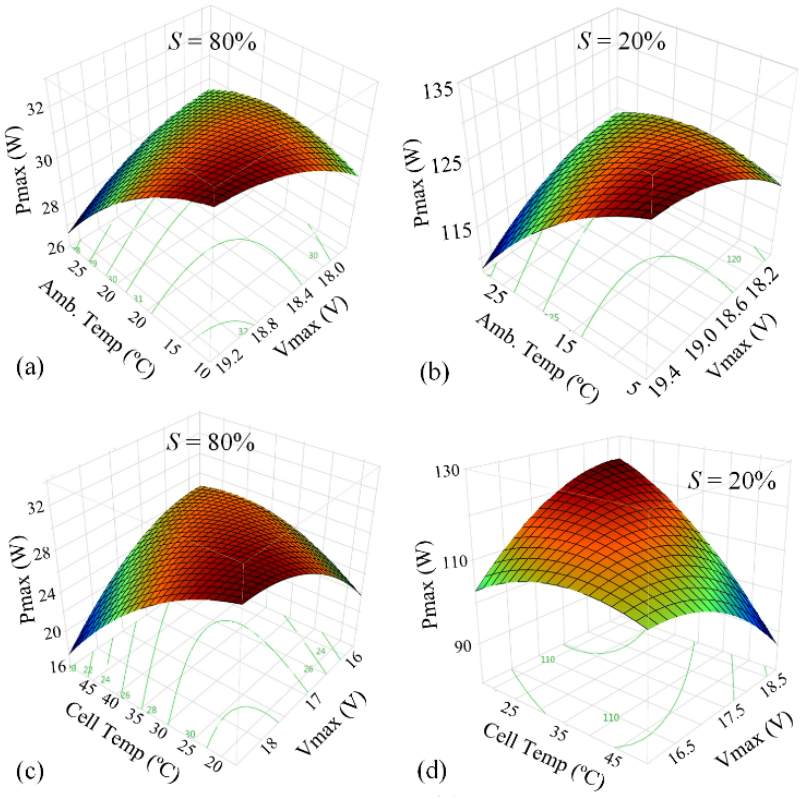

Fig. 7.5.2.2 Maximum output power based on partial shading range evaluation under conventional (non-NOCT) and NOCT computations a) S = 80% and non-NOCT, b) S = 20% and non-NOCT, c) S = 80% and NOCT, d) S = 20% and NOCT.

more nonlinearity in the prediction error has been presented. For instance, on cloudy days (S = 80%), the variation of the maximum output power shown in Fig. 7.5.2.2(a) and (c) have resulted in a negligible estimation error ⩽3% because of a lower voltage drop of V_s, where maximum power of 32.8 W has been reported in Fig. 7.5.2.2(a) (non-NOCT), and 30.5 W under NOCT consideration, as presented in Fig. 7.5.2.1(c). During partial cloudy days (S = 60%), the maximum extracted output power of 65 W during the partial shading condition without a NOCT consideration. Whereas, the maximum achieved power with the NOCT consideration is 62 W. On average, an estimation error about 4.5% has been noted. Under a partial shading of S = 40%, a maximum power of 98 W (non-NOCT), and 94 W (NOCT) could be seen with an error of 6.5%, respectively. During S = 20%, the maximum power based on the non-NOCT case was recorded as 131 W (Fig. 7.5.2.2(b)), while more heat loss for the NOCT consideration shows a maximum power of 126 W (Fig. 7.5.2.2(d)). In addition to a higher rate of G, larger heat loss has been observed, thus, the estimation error has slightly increased to 8.8% which can be seen in Fig. 7.5.3.2(b and d). The highest rate of estimation error occurs when the maximum possible rate of G = 1000 W.m-2, S = 0% (no shading) strikes the C-Si module. Then, the cell temperature raises, and accordingly the heat loss in each cell, which only can be modeled if the NOCT is considered. In a fully sunny day (S = 0%), the maximum available output power (158 W) through C-Si PV module used under the ideal conditions of highest rate of solar irradiance and no partial shading. Whereas, the true value of output power is recorded as 154 W under the NOCT consideration. A significant error estimation of 9.7% (annual average) was noted [62].

Fig. 7.5.2.3 illustrates the estimation error trend for the whole year, if using the non-NOCT technique and not the proposed measurement method described in this research. The estimation error increases when less partial shading and a higher rate of solar irradiance (G) hits the PV cells. The worst-case estimation error occurs in August, and generally during the summer season [62].

Fig. 7.5.2.4 depicts the temperature distribution over the module tested in August, in which the impact of NOCT has been highlighted. Fig. 7.5.3.4(a) presents the module with an open-circuit load connected. In contrast, the module under the proposed measurement with a NOCT consideration is shown in Fig. 7.5.3.4(b), where an average temperature of 3.6 ˚C is the difference (error). Temperature predictions through an infrared thermometer and NTC sensors at an irradiance of 800 W.m-2 are set for the simulation. The peak temperatures for both heat measurements are 53 °C and 52 °C respectively. All the 45 NTC sensors have been calibrated to 60 °C prior to the experiment [62].

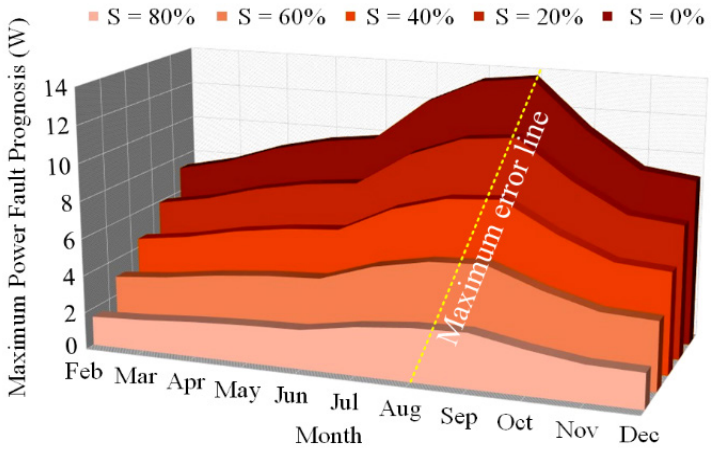

Fig. 7.5.2.3. Monthly spectrum of the estimation error.

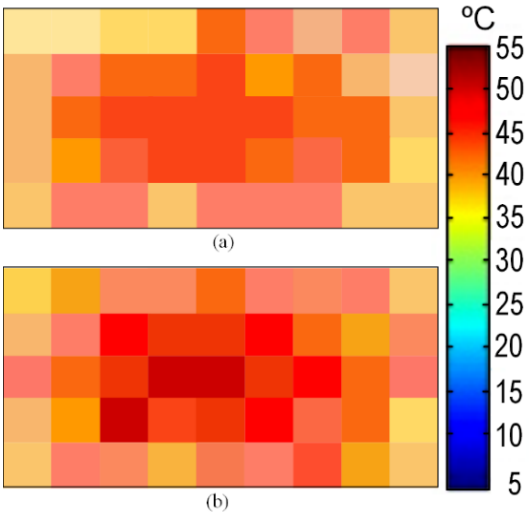

Fig. 7.5.2.4. 5 by 9 interpolated heat distribution during peak time with solar irradiance of 1000 W.m-2, under S = 0%, a) non-NOCT, b) NOCT Considerations.

7.5.3 Correlation of Power Prediction Considering NOCT and Shading

This section aims to bring simplicity along with accuracy for predicting the output power. To do this, A set of non-parametric correlations are calculated using Spearman's ρ and Kendall τ rank statistical methods in order to provide a fast and true estimation, as well as avoid experimental measurement difficulties and cost for an advanced output power prediction. To avoid such estimation error, this study has provided a set of non-parametric and parametric correlations with minimum error to simplify the process of measurement and importantly reduce the cost in both primary and post-processing predictions for engineers. Spearman's ρ (r_s) and Kendall τ rank correlation coefficients methodologies have been computed. Unlike the Pearson's method, the Spearman's ρ does not need an assumption of linearity in the relationship of the defined variables [62-63], which can be calculated using non-parametric model for a sample of *n* size:

$$r_s = \rho_{rg_X, rg_Y} = \frac{\mathrm{cov}(rg_X, rg_Y)}{\sigma_{rg_X} . \sigma_{rg_Y}} \tag{7-25}$$

where ρ is the Pearson correlation coefficient, cov (r_{gX},r_{gY}) is the covariance of the rank variables, and σ_{rgX} and σ_{rgY} are the standard deviations of the rank variables.

The Kendall τ rank correlation also identifies monotonic relationships, which can be defined as:

$$\tau(X,Y) = \frac{(number\ \ of\ \ concordant\ \ \ pairs) - (number\ \ of\ \ discordant\ \ \ pairs)}{0.5n(n-1)} \tag{7-26}$$

where concordant means the ranks for both elements agree, that is, if both $x_i > x_j$ and $y_i > y_j$ or if both $x_i < x_j$ and $y_i < y_j$. On the other hand, discordant means, if $x_i > x_j$ and $y_i < y_j$ or if $x_i < x_j$ and $y_i > y_j$. In an exceptional case, if $x_i = x_j$ or $y_i = y_j$, the pair is neither concordant nor discordant. Both correlation methods vary between fully opposed (-1) to identical (+1) for a correlation, and the interpretations are the same for the Spearman's correlation [63].

Table 7.5.3.1 presents the non-parametric correlations using Spearman's ρ, and Kendall τ rank with a very high significant probability of <0.0001. As illustrated, a correlation of 0.9859 can be injected to the output power estimated values in order to extract the true values, which are tested through the proposed technique (shown in Fig. 7.5.1(b)). As the variation is nearly linear during various partial shading rate, therefore, the correlations are independent of *S*.

Table 7.5.3.1 Output power correlation based on *S* rate.

Partial shading	Spearman's ρ	Kendall's τ	Signi. probability
S = 80%	0.9859	0.9458	<0.0001*
S = 60%	0.9859	0.9458	<0.0001*
S = 40%	0.9859	0.9458	<0.0001*
S = 20%	0.9859	0.9458	<0.0001*
S = 0%	0.9859	0.9458	<0.0001*

7.6 Experimental Verifications

Experimental measurements and tests are presented to verify the validity of the proposed technique of prediction in the coast of Barcelona city (Spain). The experimental results have been provided using actual total cell temperature estimation and maximum power point tracking (MPPT), where a DC-DC converter and variable DC load have been employed in a designed Hardware-in-the-loop configuration shown in Fig. 7.6.1.

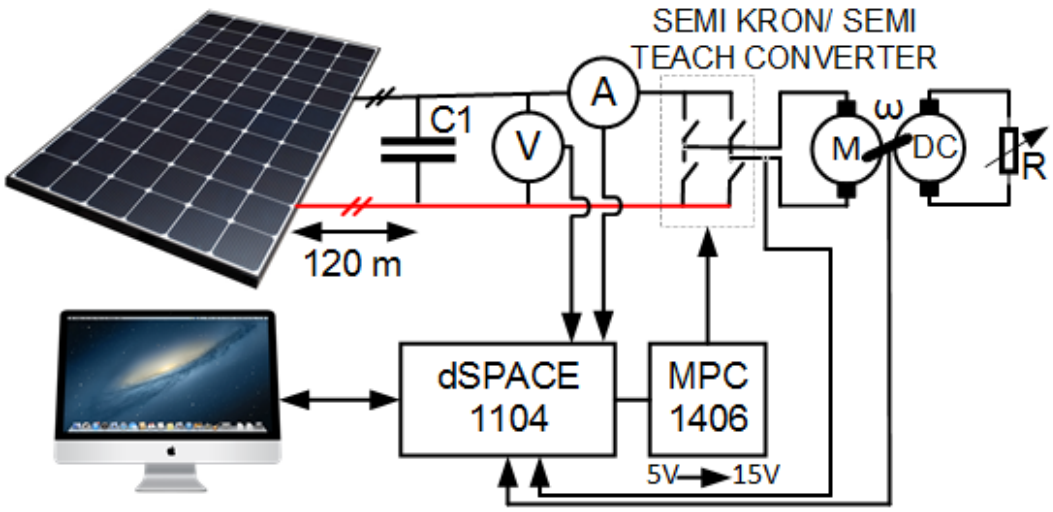

Fig. 7.6.1. The hardware-in-the-loop configuration designed for experimental validation.

The implemented experimental setup is represented in Fig. 7.6.2. The Solar PV module with parameters as listed in Table 7.6.1, has been installed out of the laboratory through approximately 120 m of cables. A 100 μF filter capacitor which is further connected to the SEMITEACH B6U+E1CIF+B6CI converter with IGBT switches is used as the interface between the PV module and the DC load. A brushless DC motor (MotorSolver DCMOT8077), with parameters as listed in Table 7.6.2, coupled with a DC generator with the same parameters are utilized as the DC load. By changing the variable resistor connected at the DC generator's terminal, the mechanical load on the DC motor's shaft changes and different loading scenarios can be achieved during the cell temperature measurements. The MPPT system with an average switching frequency of 5kHz is implemented in a MATLAB/Simulink environment and the obtained pulses have been sent to the converter through dSPACE1104. Load voltage and current are measured with LEM LV25-P and LEM LA25- NP voltage and current transducers, respectively and they have been sent to the MPPT algorithm. A Microchip MCP1406 IC is also utilized at the dSPACE 1104 output to regulate the pulse amplitude.

Table 7.6.3 shows the monthly maximum output power which was acquired by the utilized MPPT. The values have been experimentally supplied via a resistive load through the 250W DC motor-generator setup described earlier. Fig. 7.6.4 illustrates the total cell temperature estimation under non-NOCT (conventional) and NOCT setup considerations (drawn in Fig. 7.5.1(a)-(b)). The graphics show infrared thermography of the tested glass/glass PV module under grid (closed-circuit) and open-rack conditions. The experiment shows that there is a considerable difference in the module's surface when the module is connected to the grid as shown in Fig. 7.6.4(a). The difference varies between 5 to 10˚C ($G = 1000$ W/m^2) depending on the experiment test type, module characteristics and weather condition. Fig. 7.6.4(b) presents a 5˚C lower temperature due to having an open-circuit test, in contrast with the grid- connected temperature distribution (in Fig. 7.6.4(a)).

On August 20th, 2017 (peak time, sunny day), the cell temperature measurement was recorded through the 45 NTC sensors technique reported in [1-2] (as graphed in Fig. 7.6.3). The impact of this graph relies on error predicting of both the measurement techniques, $T_2 > T_1$, where T_2 deals with the true temperature under a condition of the full load. The T_1 trend (conventional) accounts only for the temperature of the module's surface due to the no-load measurement. The accuracy of each measurement test is approximately less than 0.1%.

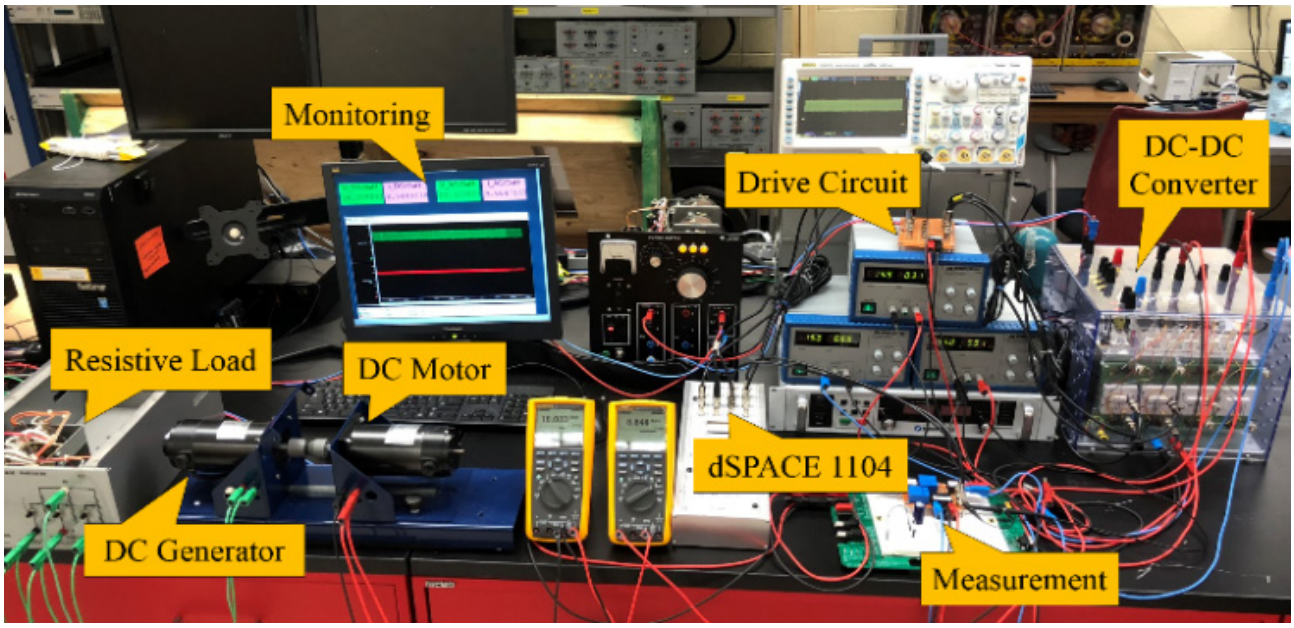

Fig. 7.6.2. Experimental setup for proposed technique validation.

Table 7.6.1 PV module parameters.

Parameter	Value
open circuit voltage (V_{oc})	21.06 V
short circuit current (I_{SC})	8.62 A
MPP voltage (V_{MPP})	17.09 V
MPP current (I_{MPP})	7.62 A
number of cells	36 (4×9)

Table 7.6.2 DC load parameters.

Parameter	Value
Rated Power	250 W
Maximum Voltage	42 V
Maximum Speed	4000 rpm
No-load Current	0.97 A
Voltage Constant (K_e)	0.0087 V/rpm
Armature Resistance (R_a)	3.9 Ω
Armature Inductance (L_a)	0.665 mH

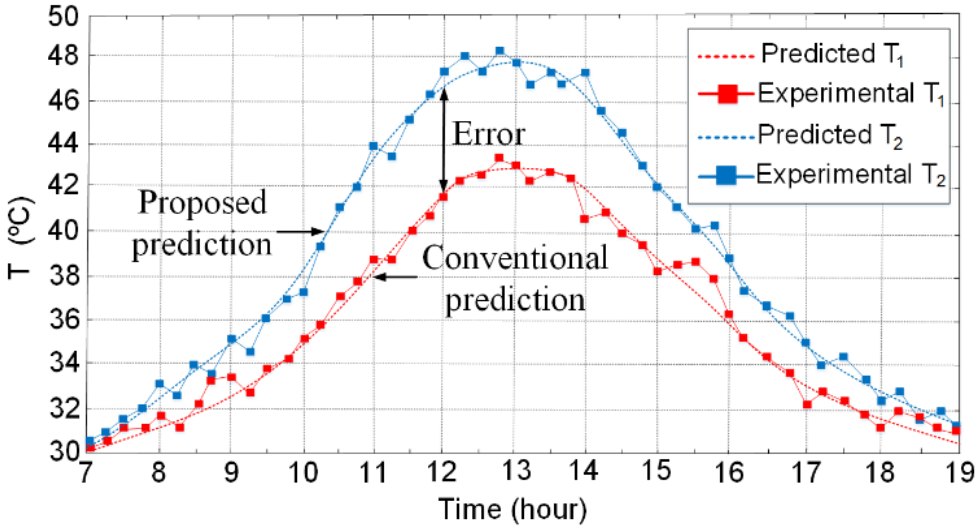

Fig. 7.6.3. Experimental cell temperature using non-NOCT and NOCT considerations during the peak operation time (20th of August 2017).

Table 7.6.3 Measured maximum output power under different rate of *S*, and *G*=1000W.m^{-2}.

Month	Unit	*S* = 80%	*S* = 60%	*S* = 40%	*S* = 20%	*S* = 0%
Jan	W	30.372	61.584	92.355	122.420	151.653
Feb	W	30.176	61.202	91.791	121.675	150.729
Mar	W	29.717	60.309	90.471	119.932	148.566
Apr	W	29.322	59.540	89.335	118.432	146.705
May	W	28.727	58.382	87.624	116.173	143.902
Jun	W	27.863	56.698	85.136	112.890	139.829
Jul	W	27.193	55.395	83.210	110.349	136.677
Aug	W	26.992	55.002	82.631	109.584	135.728
Sep	W	27.930	56.828	85.328	113.143	140.143
Oct	W	28.860	58.640	88.005	116.676	144.526
Nov	W	29.520	59.925	89.904	119.183	147.636
Dec	W	30.372	61.584	92.355	122.420	151.653

In the following section, not only verifies the numerical analysis, but also provides the input data such as ambient temperature, sky data (clouds), and NOCT. The PV system which was tested is summarized in Table 7.6.4.

Fig. 7.6.5 illustrates an experimental verification of the optimized values calculated in the previous section under the various shading factors of 0%, 20%, 60%, and 100% (which is observed during the whole month of June regarding Fig. 7.6.5) for G = 1000 W/m^2. During 0% shading, the blue solid curve shows the simulation results with an average value of 125.12 W, and the markers show the measured values. The blue dashed line indicates the simulation result before optimization to highlight the power improvement. At a 20% shading rate, there was a 16.53 W power reduction, shown by the solid red curve along with the experimental values (red markers) with an average of 108.56 W. The simulated values before optimization action are given by the dashed red line. For 60% shading, the green solid curve (simulated), and green markers (experimental) represent the average value of 73.55 W. In addition, a significant power

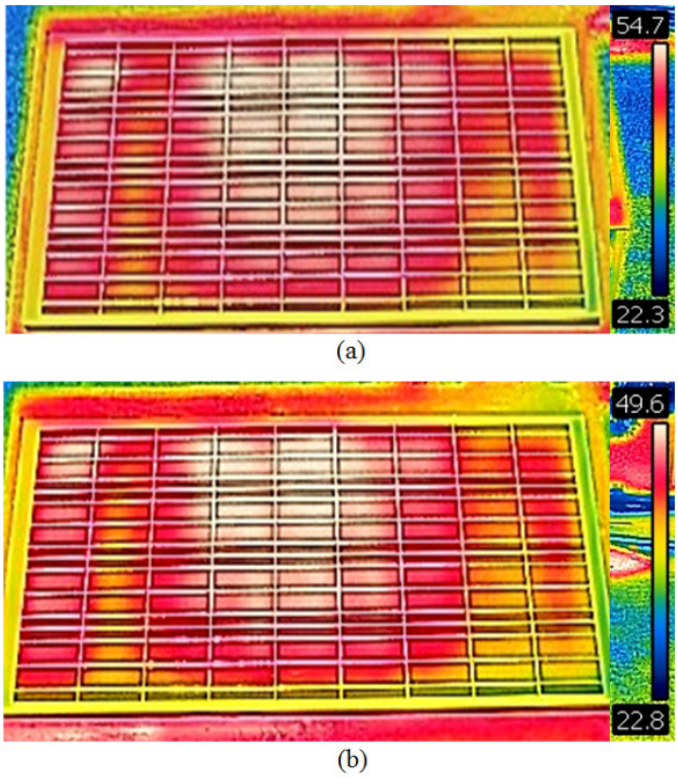

Fig. 7.6.4. IR thermo-graphs of C-Si PV module under grid-connected condition in the open rack; a**)** IR thermo-graphs of module under grid-connected (NOCT), b**)** the open-circuit (non-NOCT).

maximization has been observed (nearly 35.5 W) in comparison to the green dashed line (pre-optimization) which shows 38.87 W average. Around the sunset times (18:00), when full shading condition (100%) occurs, the purple solid line (post-optimization) is verified by the purple markers. The purple dashed line presents the values (pre-optimization). A very good agreement can be seen between simulation and experimental values which highlights that the proposed optimization methodology in this research is appropriate.

Table 7.6.4 PV system input data in Barcelona, Spain.

Parameters	***Value***	***Unit***
Latitude	41.42	˚N
Longitude	2.13	˚E
Altitude	273	m
Orientation	SE	
Albedo	0.247	
Surface dimension	62/32	mm
Occupation ratio	89	%
Tilt angle	31	˚
Pitch length	1.51	m
Attenuation for diffuse	0.138	
Number of tested PV module	1	
Nominal output power	150	W
Maximum PV module voltage	600	V_{dc}

Fig. 7.6.6 illustrates the experimental and simulation variation of PV module energy conversion efficiencies under different shading rates from 20-100%. Theoretically, the single-crystalline single-junction Si technology, the conversion efficiency is lower than 30%. However, the measured values at the peak operation under the irradiations of 1000 W/m^2 (during 0% shading) indicates 11.67%. During peak operation, the efficiency varies from 2.1-11.67% between 0-100% shading.

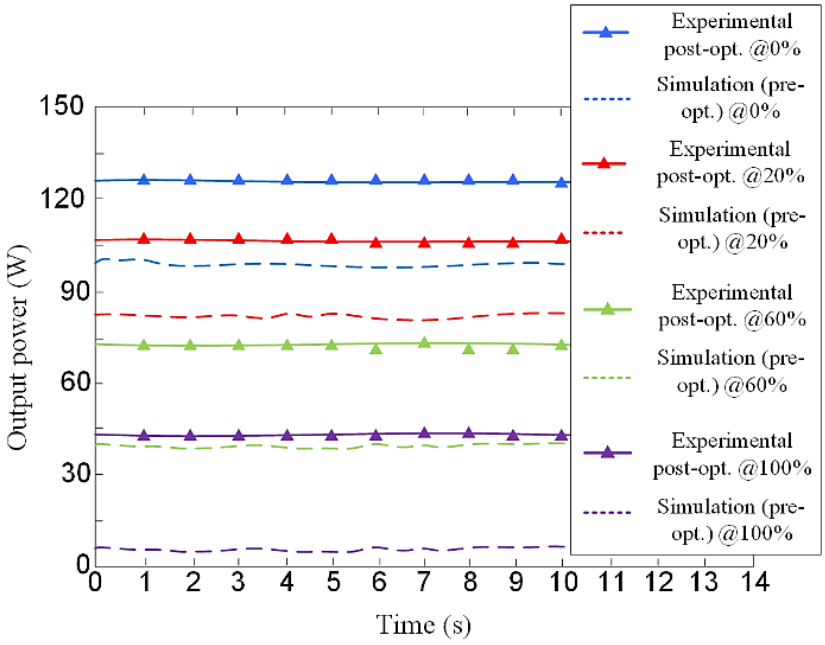

Fig. 7.6.5 The experimental output power measurement within different shading factor in June (peak time of operation).

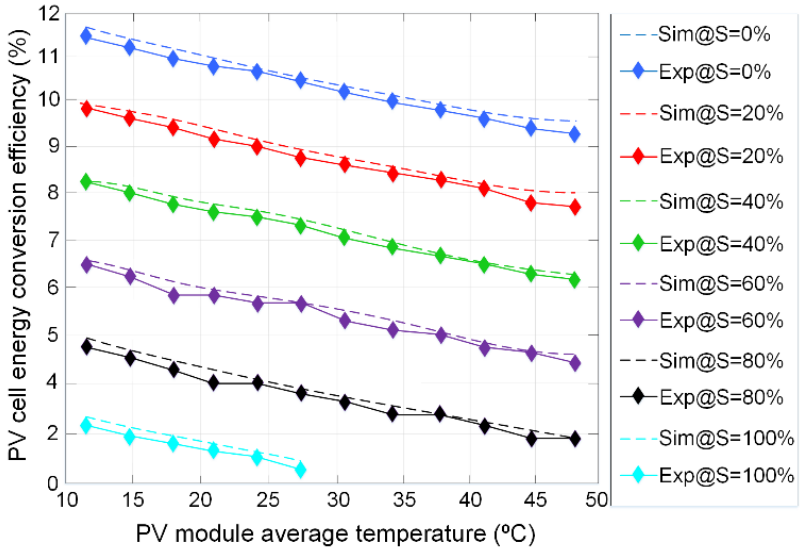

Fig. 7.6.6 Measured PV cell efficiencies under different shading rates.

Table 7.6.5 presents the annual impact of the solar PV system optimization over different shading rates from 0% (no shading) to 100% with an average of 3 kg/ year CO_2 emissions reduction which means the cost of 84,000 $ (USD) per ton CO_2. Based on the table, the environmental issues of the project have been highly considered to reduce CO_2 emissions as a

part of green power generation projects.

Table 7.6.5 Reduced CO_2 / each 100 W power generation.

Shading rate/ model	Unit	Pre-opt	Post-opt
0%	kg	29.8	32.7
20%	kg	24.6	27.8
40%	kg	17.6	20.5
60%	kg	12.2	15.5
80%	kg	8.8	11.3
100%	kg	3.6	6.4

8. Conclusions and Future Work

As covered in the previous chapters, this research mainly studies the design and optimization of a PMSG with double-layer, non-overlapping FSCW configuration for a small (up to 5 kW) wind power application. The design challenges in electromagnetic, thermal, and mechanical aspects were thoroughly investigated and resulted in several research contributions. Additionally, the research has provided considerable data analytics and a novel multi-level-objective optimization methodology based on dual-level RSM and Booth's algorithm to optimize the power, efficiency, and cost of the manufacturing materials such as permanent magnets. The stand-alone wind generator was intended to work along with some solar photovoltaic modules for enhancing the power output. Therefore, this research briefly studied the design and optimization of a PV system based on the area availability and the level of output power while considering shading effects. In addition, an advance consideration was given to factors such as NOCT to provide a reliable prediction. Finally, a 3-D pareto optimization was employed to deal with the most sensitive design variables for power maximization. The corresponding conclusions of this thesis and possible future direction for the research are given hereafter.

8.1 Conclusions

The following conclusions can be drawn based on the research accomplished in this thesis:

- Radial-flux PMSG electromagnetic-based design with outer rotor topology, laminated steel cores, and FSCW configuration with very short end windings for small wind power generation

    i. There was a suitable outcome among all studied slot per pole per phase cases using MMF harmonic analysis, and the main machine dimensions such as stack length, airgap length, etc which affected the main output parameters such as power, and efficiency.

    ii. A significant deviation between the 1-D analytical model, 2-D, and 3-D FEA models exist because of the considerations and assumptions. This error mostly originates from the complex geometry used, whereas, it is important to mention that these analytical methods are very useful for pre-design stage. The deviation between the 3-D prediction and experimental measurement can be enhanced by 1%. Also, as the PMSG operates as a radial-flux machine, and thus, the error between 2-D and 3-D FEA was negligible due to 3-D design difficulties and cost.

    iii. The Halbach array topologies on the magnet's orientation helped to significantly improve the output electromagnetic torque, Back-EMF, and cogging torque. In this study, five different electromagnetic orientation topologies were evaluated where the modified 2-segmented and 4-segmentaed HABOs have offered the best possible machine performance. Moreover, the influence of the gap consideration on the load identification under various HABOs was investigated while the system is on-duty for the first time. The load characteristics of a radial flux generator with closed-slots and the outer rotor topology was discussed, where the effect of eddy-currents is observed. The comparative study considers the combined moment of inertia calculation that demonstrates how electromagnetic-based post processing calculations are estimated without the aid of nominal machine parameter values. The analysis was performed using a 2-

D finite-element simulation of different HABOs with the gap consideration between the segments. Additionally, a comprehensive comparison with no gap was considered. Also, a dynamic analysis using an uncontrolled conventional rectifier model was used to derive effected key output parameters such a torque, output power, power factor, and line-to-line voltage. The major objective of the study was to determine corresponding load results in order to employ the most suitable and capable magnetization topology from the load perspective in the PM synchronous generator (PMSGs). Accordingly, the maximum power (MP) point was implemented to maximize the output DC power. With respect to the combined moment of inertia estimation, the load parameter estimation was verified experimentally on a surface-mounted PMSG using different magnetization topologies. Furthermore, commercial and environmental issues of the project were considered to reduce CO_2 emissions as part of green power generation development.

iv. A 3-D FEA model should be investigated with proper meshing and boundary conditions for providing a reliable and realistic estimation of the electromagnetic behaviour of the optimized PMSG especially when considerable end effects exist. In addition, to check the magnetic flux density distribution, cogging forces, etc.

v. Iron loss was computed using different Bertottie's models for both stator and rotor cores, in which Hysteresis, Eddy-current, Anomalous, and saturation losses are considered on segmented and non-segmented parts. In addition, the results of those approaches have been compared with a new iron loss model known as IEM-Formula. The main contribution of this work is to modify an analytical iron loss model which uses the classic IEM-Formula for an accurate iron loss and efficiency prediction during the field weakening operation. Harmonic losses were modelled in addition to the other terms and the outcome interpreted how significantly the behaviour of the PMSM was influenced during this wide FWOT. A large error can remain in the analysis process, if the classic IEM-Formula is used, due to phase current harmonics. The proposed modified IEM-Formula was also experimentally tested on a permanent magnet synchronous generator with a double-layer fractional-slot concentrated winding for a small power wind energy harvesting in the coast of Barcelona city. A qualified agreement is achieved between proposed analytical iron loss, numerical models and experimental results. Additionally, this research has ignored the effects of slot opening and fringing with minimal effect on the predicted losses. In addition, a method based on multiple magnetic antennae for the iron loss computation was proposed with bulk conductivity consideration. The objective of this practical study was to develop a time domain rotational iron loss computation using a packed FEA program for a PMSG with maximum power. To achieve this, the computation accuracy requires consideration of the bulk conductivity of the active iron parts, as well as the effect of generated harmonics by a PI regulator and PWM controller. A group of magnetic antennae were designed in 3-D FE (which include three magnetic coils) at various angles to compute the magnetic induction by storing the H-field between 0˚ and 180˚. Through a number of simulations, the optimum distance and angle were found for the final stage of computation. After an electromagnetic evaluation over the used methodology, it was found that a variation of 15.52% in the rotational iron losses exists when the magnetic reluctance is taken into account. In addition, a variation of 5.8% occurs when the magnetic reluctance consideration is neglected compared to the same conditions. Although, a much larger variation (about 50%) has been reported in that

study. Also, the variation of the rotational iron losses was reported to be about 6% for an induction machine which is closer to the findings of this research. The proposed methodology is also experimentally verified, where the test results were found to be very similar to the 3-D FE model with a very small error of 1% over a range of speed operation.

vi. By the help of 2-D FEA data based on several DOE's functions (e.g. FFD, MR-CDD, MR-RD, etc), a new multi-level-objective-optimization platform was developed, in which a dual-level response surface method (D-RSM) is coupled with a Booth's algorithm in order to maximize the output power and at the same time, minimize the cost of materials used. In another words, two different optimization methods are employed to deal with a multi-objective design function, a mathematical and statistical technique (DRSM using zoom-in- window approach), and a multiplication-algorithm-based (BA-SA). The objective is to maximize the output power and minimize manufacturing cost under a number of optimization constraints. This comparative study applied various types of design functions to find the best-fit parametric model, in which the influence of chosen design parameters is evaluated by local and global sensitivity analysis along with ANOVA. MR-RD with a minimum error (0.77%) is proposed, which is used for the very first time in the machine's design. The objectives of the research were achieved, where pre-optimization and post-optimization results were compared and FEA validation, with an error less than 0.5%, corresponded with analytical and mathematical calculations. Measured experimental results were additionally reported that support the improvement of the design optimization. As a comparative study, the outcomes of five various DOE's functions were compared within D-RSM computation, where the design function MR-RD with noise consideration was used for the first time in the field of power systems modelling. Also, a global design optimization framework was proposed, in which the 3-D FEA and D-RSM are used for a machine-converter system design optimisation with a strong coupling between the machine and the power electronic converter. The D-RSM is used with a moving least-squares approach by using various design functions such as MR-CCD, FFD, CCD, and BBD with a number of constraints to the optimisation as a function of $i_{d,i}$,.The values of currents $i_{d,i}$ at each operating point have to constitute significant optimisation parameters to the same extent as machine-converter system sizing parameters. The window-zoom-in approach is carried out as a mover from the original plane to the second-level plane to find out the global optimal operation point. Considering all sets of parameters and assumptions, it was found that the modified MR-CCD originates from a different set of boundaries to complete the use of MR-CCD, yet, the adequacy of fit in the design region using FFD is significant and cost-efficient. The influence of the sizing optimisation methodology satisfies the objective improvement considerably. The outcome is the sizing optimisation, in which the pre-optimisation and post-optimisation results are compared and verified by FEA with an error below 0.5%. Finally, the experimental verifications proved the sizing design optimisation through a high-quality prestige. Moreover, the influence of flux weakening on the model is highly recommended for further study.

vii. After careful electromagnetic design optimization of the PMSG, thermal, mechanical, and acoustic perspectives of the electromagnetically optimized PMSG were also studied. In the thermal design, an alternative natural cooling system was proposed. Moreover, two techniques based on optimal skewing angle and slot per pole per phase (pole) number were developed to minimize the vibro-acoustic performance of

the optimized PMSG under a variable speed analysis while considering natural frequencies for the first time. Both the FEA and experimental results have exhibited that the rotor and stator skewed, and optimal pole number techniques can minimize the sound power (magnetic noise) of the proposed machine effectively.

- Solar photovoltaic system design optimization for an urban environment application

  i. After a careful PV module design in a complex area for a stand-alone urban environment, the research proposes a 3-D Pareto optimization methodology using a Window-Zoom-in approach to maximize a PV array's effective energy output while considering complete and partial shading. The proposed methodology ensures special attention to the input data of the PV module as it has a considerable effect on the outputs. Therefore, a number of significant input parameters such as NOCT, weather, and sky condition (clouds) were carefully considered. The photovoltaic system was coupled with an enhanced MPPT controller which uses a P&O algorithm. The design variables were modified by the dual-level ANOVA method to find the optimized values over tens of simulations. The simulation results are presented for the original and optimized variables to highlight the design improvement particularly the output power. The analytical and numerical parts of the study have been successfully verified and show a good agreement with an experimental investigation where a smaller scale of the whole system (60 cells) was tested in Barcelona city, Spain. The proposed methodology was employed for the photovoltaic system design and optimization, where the nominal power generation of 6 kW was targeted for a complex structure in the urban environment. In addition, commercial and environmental issues of the project have been highly considered to reduce CO_2 emissions as a part of green power generation projects.

  ii. A new technique of measurement has been studied without any assumptions, in which a NOCT consideration was accounted for under different ranges of partial shading effects during the whole year. To minimize the error of the output power prediction, both techniques of measurements, conventional and proposed were examined through equal conditions to present the difference (error) between them. Afterwards, the impact of the proposed technique has been modified into the output results of the conventional technique via non-parametric correlations, known as the Spearman's ρ, and Kendall τ rank methods. This paper offers these correlations under different rates of partial shading to reduce the cost and complexity in design. The contribution of this investigation can be used by engineers in prediction studies with less than 0.1% error, regardless of the assumptions and considerations of which they applied for their measurements. The measurements data including current, voltage, and output power have been experimentally verified where the proposed measurement technique brought the true estimation because of full environmental considerations such as cell temperature, and partial shading.

8.2 Proposed Future Works

Some recommendations on practicable future research are listed as given:

i. Within this research, we have deeply studied the losses of the PMSG using different methods, in addition, the losses and efficiency maps have been presented to reinforc*es the improvements of the study. Although, we have proposed

a time-domain methodology with considering bulk conductivity as the most advanced technique to predict the iron loss during the machine test, but lack of analytical modelling and practical setup in the field of electrical machines exist. For this reason, the researchers still use classic approach which are not very accurate, but fast.

ii. The thermal model of the PMSG was also evaluated by network and FEA computations. The estimated critical parts could be studied significantly in order to reduce the temperature rise. Although, we have verified experimentally the temperature distribution of the model by infrared thermal camera, but there are several hot spots which were not easy to catch by this measurement technique. Therefore, we highly propose use of thermocouples/ sensors at each critical location of the machine for monitoring the temperature distribution while the machine is on-duty. As result of this investigation, the shape and/or material of targeted parts might change. Otherwise, the thermal restrictions should be modified.

iii. While the prototype PMSG built in this study is completely optimized (in fact, the objectives of the optimizations done in this thesis are geometrical-based or global sizing for the best possible output with being cost-effective) which means that there are many other aspects for optimizing such as: thermal behaviour, mechanical performance, cogging force minimizations, aerodynamics, etc. To achieve these objectives, multi-objective methods such as particle swarm, genetics, and also artificial intelligence like neural networks are highly suggested.

iv. This research was based on a well-known machine topology, outer rotor because of many advantages for wind power applications. However, there are several new topologies (such as double stator, double rotor, double stator and rotor, etc) which have been recently developed by the researcher for a better performance. These topologies bring complexity and cost. As being cost-effective was one of the goals of this research, we did not focus on them. However, depending to the goals of any future possible projects, they can be chosen. As a part of future work of this project, we have developed (development still going on) a novel machine topology known triple-rotor, double-stator PMSM, in which the structure in comparison to existing types is presented in Fig. 8.2.1 with details regarding the patent numbers and date. We have proposed this topology due to a better electromagnetic performance. This machine topology is under US patent registration by one of our academic partners in the USA. Additionally, we highly recommend researchers to work on thermal and mechanical development of this new structure for a more reliable behaviour.

v. Although the vibro-acoustic performance of the PMSG is computed with a very advanced technique, in which the machine is variable speed analysis, natural frequencies are considered. The software package of MANATEE was unable to compute in 3-D FEA. Thus, we have only computed the PMSG model through recommended SDM and 2-D FEA. We highly recommend the engineering to model the machine in another software or later versions of MANATEE which allows 3-D FEA analysis to verify the model. The techniques to minimize vibro-acoustic performance of the machine are known as choice of topology, asymmetries, number of slots per pole per phase, winding configuration, harmonic current injection, skewing, magnetization orientation, magnet shaping, damping, pole width and position, notches, slot and tooth shape and position, stator slot opening, magnetic wedges, flux barriers, control strategy, and etc. In this thesis, we could minimize using only two of mentioned approaches, however, we recommend the researchers to use other techniques in order to provide a more significant noise reduction. Since the noise of the electrical machines have three sources as electromagnetic, aerodynamic, and mechanical. Due to the

importance of electromagnetic source of noise in comparison to other two, we only considered this source of noise. However, the aerodynamic, and mechanical sources can be critical in some cases particularly when a complex geometry exists. We highly recommend you study them to ensure the design.

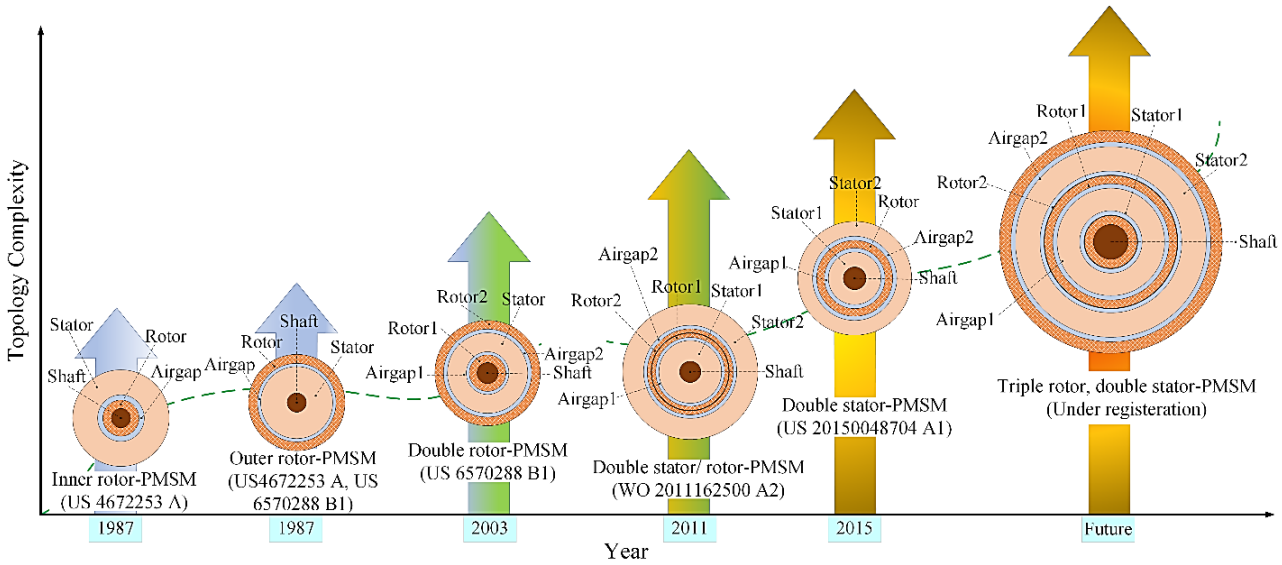

Fig. 8.2.1 Permanent magnet synchronous machine topologies overview.

vi. The impact of using various type of materials for both iron and magnetic parts could be investigated with respect to saturation effect to either maximize the performance or minimize the material cost of the machine.

vii. The solar PV system studied in this thesis uses a very popular modified P&O algorithm to find the maximum operation point, however, there are many more advanced methods which could be employed for a better and reliable performance. For instance, hybrid MPPT (where P&O and ANN are coupled), steepest-descent, Gauss-Newton, fuzzy logic-based techniques.

viii. The control system which is designed for the PV system can be enhanced in many aspects. For being cost-effective, we have used a buck converter and one inverter, however, to offer a more reliable and fast control strategy, we believe that there are many other new components and circuity which could improve the test bench. Furthermore, a non-intrusive condition monitoring technology could be used. For instance, this monitoring system for the urban application of this thesis can be presented as Fig. 8.2.2. In this diagram, the project is assumed as grid-connected while the level of power cannot be guaranteed for the electric vehicle station. In case of stand-alone power generation, the generated power is only consumed by the users of the base, and the electricity needed for the project.

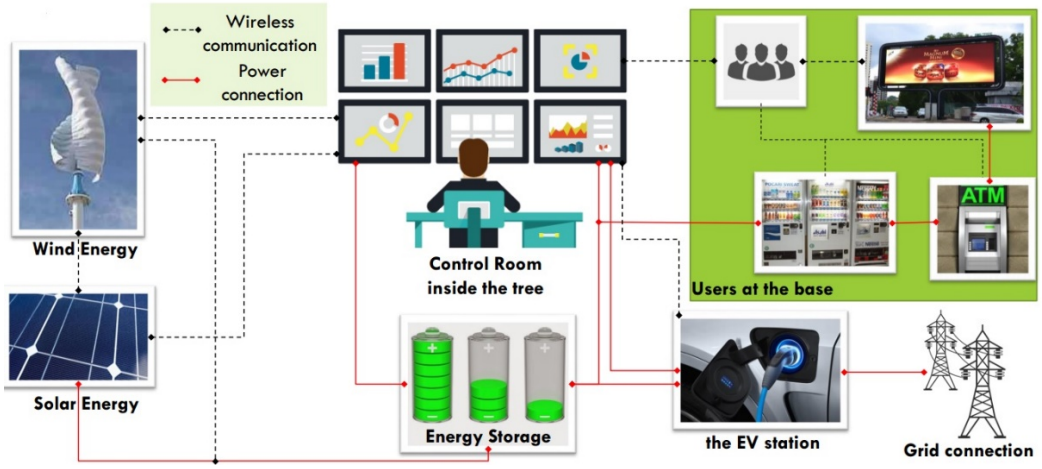

Fig. 8.2.2 Non-intrusive condition monitoring of the power generated by wind and solar resources.

9. Bibliography

• Chapter 1

[1] G. Caniot, M. B. Gracia, S. S. S. Naya, and E. Pozo, "Wind Resource Assessment of the Metropolitan Area of Barcelona," online link: http://www.meteodyn.com/wp-content/uploads/2015/11/SGCS2015-Wind-Resource-Assessment-of-theMetropolitan-Area-of-Barcelona.pdf, pp. 1-9, 2012.

[2] European Environment Agency, "Europe's onshore and offshore wind energy potential," EEA Technical report, ISBN 978-92-9213-000-8, DOI 10.2800/11373, pp. 19-59, 2009.

[3] L. Jolly, "Design optimization of Permanent Magnet Synchronous Motors using Response Surface Analysis and Genetic Algorithms," IEEE TRANSACTIONS ON MAGNETICS, VOL. 41, NO. 10, DOI: 10.1109/INTMAG.2005.1463474, pp. 3928-39-30, 2005.

[4] T. D. Strous, "Design of a permanent magnet radial flux concentrated coil generator for a range extender application," Submitted thesis at EEC-Delft University of Technology, 2010.

[5] H. A. Toliyat, and G. B. Kliman, "Handbook of Electric Motors," CRC press/ Taylor & Francis Group, ISBN: 0-8247-4105-6, 2004.

[6] F. Meier, "Permanent-Magnet Synchronous Machines with Non-Overlapping Concentrated Windings for Low-Speed Direct-Drive Applications," Submitted thesis at Royal Institute of Technology (KTH-Stockholm), ISBN: 978-91-7415-089-6, pp.5-100, 2008.

[7] M. R. J. Dubios, "Optimized Permanent Magnet Generator Topologies for Direct-Drive Wind Turbines," Submitted thesis to TU-Delft, ISBN: 0-9734585-0-X, pp. 9-100, 2004.

[8] P. Salminen, "Fractional Slot Permanent Magnet Synchronous Motors for Low Speed Applications," Submitted thesis at Acta Universitatis Lappeenrantaensis 198, ISBN: 951-764-983-5, pp. 13-120, 2004.

[9] G. Pellegrino, T. M. Jahns, N. Bianchi, W. L. Soong, and F. Cupertino, " The Rediscovery of Synchronous Reluctance and Ferrite Permanent Magnet Motors," Springer, ISBN: 978-3-319-32200-1, DOI: 10.1007/978-3-319-32202-5, pp. 1-22, 2016.

[10] T. D. Strous, "Design of a permanent magnet radial flux concentrated coil generator for a range extender application," Submitted thesis at EEC-Delft University of Technology, 2010.

[11] H. V. Xuan, "Modeling of Exterior Rotor Permanent Magnet Machines with concentrated windings," Submitted thesis to Hanoi University of Science and Technology, ISBN: 9789088914690, pp. 19-97, 2012.

[12] F. Meier, "Permanent-Magnet Synchronous Machines with Non-Overlapping Concentrated Windings for Low-Speed Direct-Drive Applications," Submitted thesis at Royal Institute of Technology (KTH-Stockholm), ISBN: 978-91-7415-089-6, pp.5-100, 2008.

[13] G. N. Tiwari, A. Tiwari, and Shyam, "Handbook of Solar Energy", Springer, DOI: 10.1007/978-981-10-0807-8, 2016.

[14] A. Goetzberger, and V. U. Hoffmann, "Photovoltaic Solar Energy Generation", Springer, DOI: 10.1007/b137803, 2005.

• Chapter 2

[1] H. A. Toliyat, and G. B. Kliman, "Handbook of Electric Motors," CRC press/ Taylor & Francis Group, ISBN: 0-8247-4105-6, 2004.

[2] J. Perho, "Reluctance Network for Analysing Induction Machines," Submitted thesis to Helsinki University of Technology, Finland, p. 147, 2002.

[3] C. B. Rasmussen, and E. Ritchie, "A magnetic Equivalent Circuit Approach for Predicting PM Motor Performance," Proceedings of IEEE Industry Applications Conference, IAS Annual Meeting. pp. 10-17, 1997.

[4] G. Perllegrino, T. M. Jahns, N. Bianchi, W. L. Soong, and F. Cupertino, “The Rediscovery of Synchronous Reluctance and Ferrite Permanent Magnet Motors,” Springer, DOI 10.1007/978-3-319-32202-5, pp. 1-142, 2016.

[5] EL-Refaie, A.M.: Fractional-slot concentrated-winding synchronous permanent magnet machines: opportunities and challenges. IEEE Trans. on Ind. Electro. 57(1), 107–121 (2010).

[6] EL-Refaie, A.M., Jahns, T.M.: Optimal flux weakening in surface PM machines with fractional-slot concentrated windings. IEEE Trans. Ind. Appl. 41(3), 790–799 (2005).

[7] P. Salminen, "Fractional Slot Permanent Magnet Synchronous Motors for Low Speed Applications," Submitted thesis at Acta Universitatis Lappeenrantaensis 198, ISBN: 951-764-983-5, pp. 13-120, 2004.

[8] F. Meier, "Permanent-Magnet Synchronous Machines with Non-Overlapping Concentrated Windings for Low-Speed Direct-Drive Applications," Submitted thesis at Royal Institute of Technology (KTH-Stockholm), ISBN: 978-91-7415-089-6, pp.5-100, 2008.

[9] C. C. Mi, " Analytical Design of Permanent-Magnet Traction-Drive Motors," IEEE TRANSACTIONS ON MAGNETICS, Vol. 42, No. 7, DOI: 10.1109/TMAG.2006.874511, pp. 1862-1864, 2006.

[10] T. D. Strous, "Design of a permanent magnet radial flux concentrated coil generator for a range extender application," Submitted thesis at EEC-Delft University of Technology, 2010.

[11] H. V. Xuan, "Modeling of Exterior Rotor Permanent Magnet Machines with concentrated windings," Submitted thesis to Hanoi University of Science and Technology, ISBN: 9789088914690, pp. 19-97, 2012.

[12] E. Fornasiero, "Advanced Designof Direct Drive PM Machines," Submitted thesis at University of Padova- Dept. of Electrical Engineering, pp. 7-48, 2010.

[13] V. X. Hung, “Modeling of Exterior Rotor Permanent Magnet Machines with Concentrated Windings”, Delft University of Technology, ISBN: 9789088914690, 2012.

[14] T. A. Lipo, “Introduction to AC Machines Design”, Wisconsin Power Electronics Research Center, University of Wisconsin, Madison, 1996.

[15] D. C. Hanselman, “Brushless Permanent Magnet Motor Design”, McGraw-Hill, New York, 1994.

[16] F. Sahin, “Design and Development of A high-Speed Axial-Flux Permanent-Magnet Machine”, Eindhoven University of Technology, 2001.

[17] A. M. El-Refaie, T. M. Jahns, and D. W. Novotny, “Analysis of Surface Permanent Magnet Machines with Fractional-Slot concentrated windings,” IEEE Trans. Energy Conversion, Vol. 21, No.1, pp. 34-43, Mar. 2006.

[18] A. M. El-Refaie, and T. M. Jahns, “Comparison of Synchronous PM Machine Types for Wide Constant-Power Speed Range Operation,” COMPEL: The Int. Journal for Computation and Mathematics in Electrical and Electronic Engineering, Vol. 27, No. 5, pp. 967-984, 2008.

[19] R. Richter, “Electrische Maschinen,” Band IV, Die Inductionsmachinen, Zweite Auflage. Birkhauser Verlag, Basel und Stuttgart, 707 p., 1963, (in German).

[20] R. Richter, “Electrische Maschinen,” Band II, Die Inductionsmachinen, Zweite Auflage. Birkhauser Verlag, Basel und Stuttgart, 440 p., 1954, (in German).

[21] M. S. Widyan, "Design, Optimization, Construction and Test of Rare-Earth Permanent-Magnet Electrical Machines with New Topology for Wind Energy Applications," Submitted thesis at TU-Berlin, link: http://dx.doi.org/10.14279/depositonce-1403, pp. 2-82, 2006.

[22] N. Madani, "Design of a Permanent Magnet Synchronous Generator for a Vertical Axis Wind Turbine," Submitted thesis at Royal Institute of Technology (KTH-Stockholm), pp. 5-66, 2011.

[23] L. Boldea, "Variable Speed Generators," CRC press/ Taylor & Francis Group, ISBN: 0-8493-5715-2, pp. 10-1 to 10-84, 2006.

[24] J. Cros, and P. Viarouge, "Synthesis of High Performance PM motors with Concentrated Windings," IEEE Trans. Energy Conversion, Vol. 17, No.2, pp. 248-253, Jun. 2002.

[25] T. Koch, A. Binder, "Permanent Magnet Machines with Fractional Slot winding for Electric Traction," Proceedings of the international Conference on Electrical Machines (ICEM), 2002.

[26] K. Vogt, "Berechnung elektrischer Maschinen," VCH Verlagsgesellschaft mbH Weinheim, ISBN 3-627-28391-9, 524p., 1996, (In German).

[27] T. D. Strous, "Design of a permanent magnet radial flux concentrated coil generator for a range extender application," Submitted thesis at EEC-Delft University of Technology, 2010.

[28] E. Fornasiero, "Advanced Designof Direct Drive PM Machines," Submitted thesis at University of Padova- Dept. of Electrical Engineering, pp. 7-48, 2010.

[29] M. Liwschitz-Garik and C. C. Whipple, Electric Machinery, vol.II, A–C Machines. New York: D. Van Nostrand Company Inc., 1960.

[30] N. Bianchi and M. D. Pré, "Use of the star of slots in designing fractional–slot single–layer synchronous motors," IEE Proc. – Electr. Power Appl., vol. 153, no. 3, pp. 459–466, May 2006, (online no. 20050284).

[31] Emanuele Fornasiero, "Advanced Design of Direct Drive PM Machines," Submitted Ph.D. thesis, University of Padova, 2010.

[32] J. Li, Da-W. Choi, D-H. Son, and Y-Hyun Cho, "Effects of MMF Harmonics on Rotor Eddy-Current Losses for Inner-Rotor Fractional Slot Axial Flux Permanent Magnet Synchronous Machines," IEEE Trans. Magnetics, Vol. 48, No. 2, Feb. 2012.

[33] M. Liwschitz-Garik and C. C. Whipple, Electric Machinery, vol.II, A–C Machines. New York: D. Van Nostrand Company Inc., 1960.

[34] P. G. Huray, "Maxwell's Equations," Wiley-IEEE Press, ISBN: 978-0-470-54276-7, 2009.

[35] P. Asef, R. Bargallo, and M. R. Barzegaran, "An innovative natural air-cooling system technique for temperature-rise suppression on the permanent magnet synchronous machines," Electric Power Systems Research, Vol. 154,

[36] L. Qinghua, "Analysis, Design and Control of Permanent Magnet Synchronous Motors for Wide-Speed Operation," Submitted Ph.D. thesis, National University Of Singapore, 2005.

[37] P. Asef, R. Bargallo, and M. R. Barzegaran, "Global sizing optimisation using dual-level response surface method based on mixed-resolution central composite design for permanent magnet synchronous generators," IET Electric Power Application, Vol. 12, No. 5, 2018.

[38] T. J. E. Miller, Brushless permanent-magnet and reluctance motor drive. Oxford, London: Claredon Press, 1989.

[39] P. C. Sen, Principles of electric machines and power electronics. New York: J. Wiley and Sons, second ed., 1997.

[40] R. F. Schiferl and T. A. Lipo, "Power capability of salient pole permanent magnet synchronous motors in variable speed drive applications," IEEE Transactions on Industry Applications, vol. 26, pp. 115–123, January/February 1990.

[41] L. Jolly, "Design Optimization of Permanent magnet Synchronous Motors Using Response Surface Analysis and Genetic Algorithms," Submitted thesis, National University of Singapore, 2005.

[42] M. Liwschitz-Garik and C. C. Whipple, Electric Machinery, vol.II, A–C Machines. New York: D. Van Nostrand Company Inc., 1960.

[43] J. Li, K. Wang, and F. Li, "Analytical prediction of optimal split ratio of consequent-pole permanent magnet machines," IET Electric Power Application, Vol. 12, No. 13, pp. 365-372, 2017.

[44] P. Asef, R. Bargallo, M. R. Barzegaran, and T. Agarwal, "Electromagnetic-based evaluation of different Halbach array topologies with gap consideration for the permanent magnet synchronous machines," Springer Journal of Electrical Engineering, DOI: 10.1007/s00202-017-0656-6, Vol. 99, No. 1, Nov. 2017.

[45] K. Liu, J. Feng, S. Guo, L. Xiao, and Z. Zhu, "Identification of Flux Linkage Map of Permanent Magnet Synchronous Machines Under Uncertain Circuit Resistance and Inverter Nonlinearity," IEEE Trans. Ind. Informatics., vol. 14, no. 2, pp. 556–568, Feb. 2018.

[46] S. Lee, Y. S. Jeong, Y. J. Kim, and S. Y. Jung, "Novel Analysis and Design Methodology of Interior Permanent-Magnet Synchronous Motor Using Newly Adopted Synthetic Flux Linkage," IEEE Trans. Ind. Appl., vol. 58, no. 9, pp. 3806–3814, Sep. 2011.

[47] J. D. M. De Kooning, J. V. Vyver, T. L. Vandoorn, B. Meersman, and L. Vandevelde, "Impact of speed ripple on the back-emf waveform of permanent magnet synchronous machines," IET Electr. Power App., Vol. 7, No. 5, pp. 400-407, 2013.

[48] H. C. Liu, I. G. Kim, Y. J. Oh, J. Lee, and S. C. Go, "Design of Permanent Magnet-Assisted Synchronous Reluctance Motor for Maximized Back-EMF and Torque Ripple Reduction," IEEE Trans. Magn., Vol. 53, No. 6, pp. 1-4, Jun. 2017.

[49] K. Kang, J. Song, C. Kang, S. Sung, and G. Jang, "Real-Time Detection of the Dynamic Eccentricity in Permanent-Magnet Synchronous Motors by Monitoring Speed and Back EMF Induced in an Additional Winding," IEEE Trans. Ind. Appl., vol. 64, no. 9, pp. 7191–7200, Sep. 2017.

[50] J. H. Kuhlman, " Design of Electrical Apparatus", John Wiley and Sons, Inc. New York, 2nd Edition, 1940.

[51] S. J. Sung, S. J. Park, and G. H. Jang, "Cogging torque of brushless DC motors due to the interaction between the uneven magnetization of a permanent magnet and teeth curvature," IEEE Trans. Magn., vol. 47, no. 7, pp. 1923–1928, Jul. 2011.

[52] Z. Q. Zhu and D. Howe, "Instantaneous magnetic field distribution in brushless permanent magnet DC motors. III. Effect of stator slotting," IEEE Trans. Magn., vol. 29, no. 1, pp. 143–151, Jan. 1993.

[53] Z. Q. Zhu, S. Ruangsinchaiwanich, and D. Howe, "Synthesis of cogging torque waveform from analysis of a single stator slot," IEEE Trans. Ind. Appl., vol. 42, no. 3, pp. 650–657, May/Jun. 2006.

[54] P. Jin, S. Fang, H. Lin, Z. Q. Zhu, Y. Huang, and X. Wang, "Analytical magnetic field analysis and prediction of cogging force and torque of a linear and rotary permanent magnet actuator," IEEE Trans. Magn., vol. 47, no. 10, pp. 3004–3007, Oct. 2011.

[55] W. Xhang, J. Gao, L. Dai, and S. Huang, "Analysis of Magnetic Field and Torque for All-Harmonic-Torque Motor with Surface-Mounted Permanent Magnets," IEEE CES Trans. Electrical Machines and Sys., Vol 2, No. 1, pp. 175-180, March 2018.

[56] K. Wang, et. al.. "Average torque improvement of interior permanent-magnet machine using third harmonic in rotor shape," IEEE Trans. Ind. Electron. vol. 61, no. 9, pp. 5047-5057. Sept. 2014.

[57] Jung Moo Seo, et. al.. "Novel hybrid radial and axial flux permanent-magnet machine using integrated windings for high-power density," Magnetics IEEE Transactions on. vol. 51, no. 3, pp. 8100804. Mar. 2015.

[58] Wenliang Zhao, et. al.. "Optimal design of a novel V-type interior permanent magnet motor with assisted barriers for the improvement of torque characteristics," Magnetics IEEE Transactions on. vol. 50, no. 11, pp. 8104504. Nov. 2014.

[59] K. Wang, Z.Q Zhu and G Ombach. "Torque enhancement of surface-mounted permanent magnet machine using third-order harmonic," Magnetics IEEE Transactions on. vol. 50, no. 3, pp. 8100210. Mar. 2014.

[60] Kai Wang, Z.Q Zhu and G Ombach. “Torque improvement of Five-phase surface-mounted permanent magnet machined suing third-order harmonic,” presented at the Int. Conf. PESGM, Boston, MA, USA, July 7-21, 2016.

[61] Gieras, J.F., Wing, M., “Permanent Magnet Motor Technology – Design and Applications,” New York: Marcel Dekker Inc, p. 444, 1997.

[62] Hanselman, D. C., “Brushless Permanent Magnet Motor Design,” New York: Elsevier Scientific Publishing Company, p. 330, 2003.

[63] P. Asef, R. Bargallo, M. R. Barzegaran, A. Lapthorn, and D. Mewes, “Multi-objective Design Optimization Using Dual-Level Response Surface Methodology and Booth's Algorithm for Permanent Magnet Synchronous Generators,” IEEE Trans. On Energy Conversion, Vol. 33, No. 2, pp. 652-659, Jun. 2018.

[64] C. Cavallaro, A. Oscar D. Tommaso, R. Miceli, A. Raciti, G. R. Galluzzo, and M. Trapanese, “Efficiency Enhancement of Permanent-Magnet Synchronous Motor Drives by Online Loss Minimization Approaches,” IEEE Trans. On Industrial Electronics Conversion, Vol. 52, No. 4, pp. 1153-1160, Aug. 2005.

[65] L. Fang, J. W. Jumg, J. P. Hong, and J. H. Lee, “Study on High-Efficiency Performance in Interior Permanent-Magnet

[66] Synchronous Motor With Double-Layer PM Design,” IEEE Trans. On Industrial Electronics Conversion, Vol. 44, No. 11, pp. 4393-4396, Nov. 2008.

[67] P. Wriggers, “Nonlinear Finite Element Methods,” Springer book. ISBN: 978-3-540-71001-1, 2008.

[68] D. V. Hutton, “Fundamental of Finite Element Analysis,” McGraw-Hill Science/Engineering/Math; 1 edition, ISBN-13: 978-0072395365, 2003.

[69] P. Asef, R. Bargallo, M. R. Barzegaran, A. Lapthorn, and D. Mewes, “Load identification of different Halbach-array topologies on permanent magnet synchronous generators using the coupled field-circuit FE methodology,” Electric Power Systems Research, Elsevier, Vol. 154, pp. 484-492, Jan. 2018.

[70] E.G. Shehata, “A comparative study of current control schemes for a direct-driven PMSG wind energy generation system,” Electric Power Systems Research, vol. 143, pp. 197–205, 2017.

[71] Ansys Maxwell, FEM software, 2017.

[72] M. A. Jabbar, et al,, “Modeling and Numerical Simulation of a Brushless Permanent-Magnet DC Motor in Dynamic Conditions by Time-Stepping Technique,” IEEE Trans. Ind. App., Vol. 40, No. 3, pp. 763-770, May 2004.

[73] Y. Zhilichev, “Three-dimensional analytic model of permanent magnet axial flux machine,” IEEE Trans. on Magnetics, Vol. 34, No. 6, pp. 3897-3901, 1998.

[74] G. Male, S. Mezani, T. Lubin, anf J. Leeveque, “A Fast Analytical Method to Compute the Radial Flux Density Distribution in the Airgap of a Superconducting Inductor,” IEEE Transaction on Applied Superconductivity, Vol. 21, No. 3, Jun. 2011.

[75] Y. Feng, X. H. Yu, and F. L. Han, “High-order terminal sliding-modenobserver for parameter estimation of a permanent-magnet synchronous motor,” IEEE Trans. Ind. Electron., vol. 60, no. 10, pp. 4272–4280, Oct. 2013.

[76] W. M. Lin, T. J. Su, and R. C. Wu, “Parameter identification of induction machine with a starting no-load low-voltage test,” IEEE Trans. Ind. Electron., vol. 59, no. 1, pp. 352–360, Jan. 2012.

[77] R. Babau, I. Boldea, T. J. E. Miller, and N. Muntean, “Complete parameter identification of large induction machines from no-load acceleration-deceleration tests,” IEEE Trans. Ind. Electron., vol. 54, no. 4, pp. 1962–1972, Aug. 2007.

[78] Matteo F. Iacchetti, Giovanni Maria Foglia, Antonino Di Gerlando, and Andrew J. Forsyth, “Analytical Evaluation of Surface-Mounted PMSG Performances Connected to a Diode Rectifier,” IEEE Trans. Energy Convers.,vol. 30, no. 4, pp. 1367–1374, Dec. 2015.

[79] Ma Weiming, Hu An, Liu Dezhi, and Zhang Gaifan "Stability of a Synchronous Generator with Diode-Bridge Rectifier and Back-EMF Load," IEEE Trans. Energy Convers., vol. 15, no. 4, pp. 458–463, Dec. 2000.

[80] Weimin Wang, K. W. E. Cheng, K. Ding, and L. C. Meng, "A Novel Approach to the Analysis of the Axial-Flux Permanent-Magnet Generator With Coreless Stator Supplying a Rectifier Load," IEEE Trans. Magnetics.,vol. 47, no. 10, pp. 2391–2394, Dec. 2011.

[81] T. F. Chan, L. L. Lai and L. T. Yan, "Analysis of a stand-alone permanent-magnet synchronous generator using a time-stepping coupled field-circuit method," IEE Proc.−Electric Power Applications. Vol. 152, No. 6, pp. 1459-1467, Nov. 4, 2005.

[82] A. Di Gerlando, G. M. Foglia, M. F. Iacchetti, and R. Perini, "Comprehensive steady-state analytical model of a three-phase diode rectifier connected to a constant DC voltage source," IET Power Electron., vol. 6, no. 9, pp. 1927–1938, Nov. 2013.

[83] J. R. Hendershot, and T. J. E. Miller, "Design of Brushless Permanent Magnet Machines." Oxford University Press, pp.185-465, 2010.

[84] P. Asef, R. Bargallo, S. Moazemie, and A. Lapthorn, "Rotor Shape Multi-Level Design Optimization for Double-Stator Permanent Magnet Synchronous Motors," IEEE Tran. On Energy Conversion, Status: under review, 2018.

- ## Chapter 3

[1] P. Asef., "Design, characteristic analysis of PM wind generator based on SMC material for small direct-drive wind energy conversion system," International Conference on Renewable Energy Research and Application (ICRERA), 41, DOI: 10.1109/ICRERA.2014.7016437, USA, 2014.

[2] Harrison, R., E. Hau, and H. Snel, *Large Wind Turbines Design and Economics*, Wiley, New York, 2000 (ISBN 0471-494569).

[3] Dubois, M. R., "Optimized permanent magnet generator topologies for direct-drive wind tur-bines," Ph.D. dissertation, Delft Univ. Technol., Delft, The Netherlands, 2004.

[4] Grauers, A., "Design of direct-driven permanent-magnet generators for wind turbines," Ph.D. dissertation, Chalmers Univ. Technol., Goteborg, Sweden, 1996.

[5] Poore, R. and T. Lettenmaier, "Alternative design study report: Wind PACT advanced wind tur-bine drive train designs study," *NREL, Golden, CO*, Rep. NREL/SR-500-33196, Aug. 2003.

[6] Cotrell, J. R., "A preliminary evaluation of a multiple-generator drive train configuration for wind turbines," presented at *the 2002 ASME Wind Energy Symp., 40th AIAA Aerosp. Sci. Meeting Exhibit*, Collection Tech. Papers, Reno, NV, Jan. 14–17, 2002.

[7] Martin, F., et al., "Improved analytical determination of eddy current losses in surface mounted permanent magnets of synchronous machine," *IEEE Trans. Magn.*, Vol. 50, No. 6, 1–8, Jun. 2014.

[8] Hemeida, A., et al., "Comparison of methods for permanent magnet eddy-current loss computations with and without reaction field considerations in axial flux PMSM," *IEEE Trans. Magn.*, Vol. 51, No. 9, 1–8, Sep. 2015.

[9] Kakhki, M. T., et al., "New approach for accurate prediction of eddy current losses in laminated material in the presence of skin effect with 2-D FEA," *IEEE Trans. Magn.*, Vol. 52, No. 3, 1–4, Mar. 2016.

[10] Huang, W. Y., et al., "Optimization of magnet segmentation for reduction of eddy-current losses in permanent magnet synchronous machine," *IEEE Trans. Energy Conv.*, Vol. 25, No. 2, 381–386, 2010.

[11] Steentjes, S., et al., "Iron-loss model with consideration of minor loops applied to FE-simulations of electrical machines," *IEEE Trans. Magn.*, Vol. 49, No. 7, 3945–3948, Jul. 2013.

[12] Eggers, D., et al., "Advanced iron-loss estimation for nonlinear material behavior," *IEEE Trans. Magn.*, Vol. 48, No. 11, 3021–3024, Nov. 2012.

[13] Bertotti, G., "General properties of power losses in soft ferromagnetic materials," *IEEE Trans. Magn.*, Vol. 24, No. 1, Jan., 1988.

[14] Bertotti, G. and M. Pasquale "Physical interpretation of induction and frequency dependence of power losses in soft magnetic materials," *IEEE Trans. Magn.*, Vol. 28, No. 5, Sep. 1992.

[15] Bertotti, G., et al., "An improved estimation of iron losses in rotating electrical machineS," *IEEE Trans. Magn.*, Vol. 27, No. 6, Nov. 1991.

[16] Fratila, M., et al., "Iron loss calculation in a synchronous generator using finite element analysis," *IEEE Tran. Energy Conv.*, Vol. PP, No. 99, 1–8, doi: 10.1109/TEC.2017.2648512, 2017.

[17] Rasilo, P., et al., "Experimental determination and numerical evaluation of core losses in a 150- kVA wound-field synchronous machine," *IET Electric Power App.*, Vol. 7, No. 2, 97–105, doi: 10.1049/iet-epa.2012.02422013.

[18] Kowal, D., et al., "Comparison of frequency and time-domain iron and magnet loss modeling including PWM harmonics in a PMSG for a wind energy application," *IEEE Trans. Energy Conversion*, Vol. 30, No. 2, 476–486, 2015.

[19] Pfingsten, G. V., et al., "Operating point resolved loss calculation approach in saturated induction machines," *IEEE Trans. Ind. Electr.*, Vol. 64, No. 3, 2538–2546, 2017.

[20] A. Krings; and J. Soulard. Overview and comparison of iron loss models for electrical machines. *Journal of Electrical Engineering*, vol. 10, no. 3, pp. 162–169, 2010.

[21] D. M. Ionel; M. Popescu; S. J. Dellinger; T. J. E. Miller; R. J. Heideman; and M. I. McGilp. On the variation with flux and frequency of the core loss coefficients in electrical machines. *IEEE Trans. Ind. Appl*., vol. 42, no. 3, pp. 658–667, May 2006.

[22] D. M. Ionel; M. Popescu; M. I. McGilp; T. J. E. Miller; S. J. Dellinger; and R. J. Heideman. Computation of Core Losses in Electrical Machines Using Improved Models for Laminated Steel," *IEEE Trans. Ind. Appl*., vol. 43, no. 6, pp. 1554–1564, Nov. 2007.

[23] A. D. Gerlando; and R. Perini. Evaluation of the Effects of the Voltage Harmonics on the Extra Iron Losses in the Inverter Fed Electromagnetic Devices. *IEEE Trans. on Energy Conversion*, Vol. 14, No. 1, pp. 57-62, March 1999.

[24] J. Kim; I. Jeong; K. Nam; J. Yang; and T. Hwang. Sensorless control of PMSM in a high-speed region considering iron loss. *IEEE Trans. Ind. Electron*., vol. 62, no. 10, pp. 6151–6159, Oct. 2015.

[25] P. Rasilo; et al.. Experimental determination and numerical evaluation of core losses in a 150-kVA wound-field synchronous machine. *IET Electric Power App*., doi: 10.1049/iet-epa.2012.0242, vol. 7, no. 2, pp. 97–105, 2013.

[26] Z. Haisen; et al.. Piecewise variable parameter model for precise analysis of iron losses in induction motors. *IET Electric Power App*., doi: 10.1049/iet-epa.2016.0009, vol. 11, no. 3, pp. 361–368, 2017.

[27] S.-H. Han; W. L. Soong; T. M. Jahns; M. K. Guven; and M. S. Illindala. Reducing harmonic eddy-current loss in the stator teeth of interior permanent magnet synchronous machines during flux weakening. *IEEE Trans. Energy Conver*sion, vol. 25, no. 2, pp. 441–449, Jun. 2010.

[28] L. Qi; et al.. Stator teeth eddy-current loss analysis of interior permanent magnet machine during flux weakening. *IEEE International Conference on Electrical Machines and Systems (ICEMS)*, DOI: 10.1109/ICEMS.2013.6713370, pp. 1226–1230, 2013.

[29] Y. Yokoi; et al.. General formulation of winding factor for fractional-slot concentrated winding design. *IET Electric Power App*., doi: 10.1049/iet-epa.2014.0336, vol. 10, no. 4, pp. 231–239, 2015.

[30] L. Yue, *et al*.. Increasing the saliency ratio of fractional slot concentrated winding interior permanent magnet synchronous motors. *IET Electric Power App*., doi: 10.1049/iet-epa.2015.0092, vol. 9, no. 7, pp. 439–448, 2015.

[31] K. Yamazaki. Torque and efficiency calculation of an interior permanent magnet motor considering harmonic iron losses of both the stator and rotor. *IEEE Trans. Magn*., vol. 39, no. 3, pp. 1460–1463, May 2003.

[32] K. Akatsu; K. Narita; Y. Sakashita; and T. Yamada. .Impact of flux weakening current to the iron loss in an IPMSM including PWM carrier effect. *in Proc. IEEE Energy Conversion. Congr. Expo*., San Jose, CA, USA, Sep. 2009, pp. 1927–1932.

[33] K. Yamazaki; and H. Ishigami. Rotor-shape optimization of interior permanent-magnet motors to reduce harmonic iron losses. *IEEE Trans. Ind. Electron*., vol. 57, no. 1, pp. 61–69, Jan. 2010.

[34] K. Yamazaki; M. Kumagai; T. Ikemi; and S. Ohki. A novel rotor design of interior permanent-magnet synchronous motors to cope with both maximum torque and iron-loss reduction. *IEEE Trans. Ind. Appl*., vol. 49, no. 6, pp. 2478–2486, Nov/Dec. 2013.

[35] S. Kuttler; et al.. Fast iron losses model of stator taking into account the flux weakening mode for the optimal sizing of high speed permanent internal magnet synchronous machine. *Elsevier Journal*, *Mathematics and Computers in Simulation*, 131 (2017) 328-343, pp. 1–15, 2017.

[36] A. Tessarolo; et al.. Modeling, Analysis, and Testing of a Novel Spoke-Type Interior Permanent Magnet Motor With Improved Flux Weakening Capability. *IEEE Trans. on Magnetics*, VOL. 51, NO. 4, MAY 2017, pp.1-9, 2015.

[37] S. Atiq; and B. Kwon. Susceptibility of the winding switching technique for flux weakening to harmonics and the choice of a suitable drive topology. *International journal of electrical power and energy systems (Elsevier Journal)*, https://doi.org/10.1016/j.ijepes.2016.07.001, VOL. 85, pp.22-31, 2017.

[38] M. Rekik; et al.. Improvement in the field-weakening performance of switched reluctance machine with continuous mode. *IET Electric Power App*., doi: 10.1049/iet-epa.2015.0092, vol. 9, no. 7, pp. 439–448, 2015.

[39] S. Vaez-Zadeh; and B. Zahedi. Modeling and analysis of variable speed single phase induction motors with iron loss. *Energy Conversion and Management (Elsevier Journal)*, doi:10.1016/j.enconman.2009.06.031, VOL. 50, No. 11, pp. 2747-2753, 2009.

[40] M. Basic; et al.. Dynamic and pole-zero analysis of self-excited induction generator using a novel model with iron losses. *International journal of electrical power and energy systems (Elsevier Journal)*, https://doi.org/10.1016/j.ijepes.2012.03.003, VOL. 42, pp.105-118, 2015.

[41] P. Asef, R. Bargallo, M. R. Barzegaran, A. Lapthorn, J. Dong, O. A. Mohammed, "A Comparative Study of Quasi-FEA Technique on Iron Losses Prediction for Permanent Magnet Synchronous Machines," *Progress In Electromagnetics Research*, Vol. 81, pp. 101-113, 2018.

[42] T. A. Lipo, "Introduction to AC Machine Design," University of Wisconsin-Madison, ISBN: 978-0-9745470-5-3, 2011.

[43] A. Boglietti, A. Cavagnino, M. Lazzari, and M. Pastorelli, "Predicting iron losses in soft mag-netic materials with arbitrary voltage supply: an engineering approach," IEEE Trans. Magn., vol. 39, no. 2, pp. 981–989, 2003.

[44] Y. Sakamoto, M. Natsusaka, K. Murakami, and N. Abe, "Anomalous iron loss observed in a parametric induction motor," *IEEE Transactions on Magnetics*, Vol. 29, No. 6, pp. 3156-3158, 1993.

[45] KILGORE, I.A.: 'Effect of saturation on machine reactances', Trans. Amer. Inst. Electr. Eng., 1935, pp. 545-549.

[46] VOIPIO, E.: 'The influence of magnetic saturation on transients and voltage properties of synchronous alternators, with special reference to large capacitive loads', Trans. R. Inst. Technol. Stockholm, 1955, 93, pp. 1-125.

[47] HARLEY, R.G., LIMEBEER, D.J.N., and CHIRRICOZZI, E.: 'Comparative study of saturation in synchronous machine models', IEE Proc. B, Electr. Power AppL, 1980,127, (1), pp. 1-7.

[48] FAUCHER, I, ANVARI, H.A., and TRANNOY, B.: 'Modeling and simulation of a converter fed synchronous motor drive with considering cross coupling effect'. IEEE IAS Annual Meeting, Chicago, USA, pp. 432-438, 1986.

[49] KERKMAN, R.K.: 'Steady state and transient analysis of an induction machine with saturation of the magnetizing branch', *IEEE Trans.,* 1985, IA-21, (1), pp. 226-234.

[50] CHEN, GU, and QISHAN, GU: 'A new method of predicting the performance of saturated synchronous inductor motor'. *IEE Conf. Publ. 254,* 198.

[51] BOLDEA, I., and NASAR, S.A.: 'Upon unitary treatment of magnetic saturation in orthogonal axis models of electrical machines', Paper presented at ICEM-1986, Munich, West Germany.

[52] L. Di Leonardo, F. Parasiliti, M. Tursini, and M. Villani, "Transient analysis of PM synchronous motor drives by finite element model cosimulation," in *Proc. IEEE IECON*, 2013, pp. 6834–6840.

[53] N. Alatawneh; et al.. Accuracy of time domain extension formulae of core losses in non-oriented electrical steel laminations under non-sinusoidal excitation. *IET Electric Power App*., doi: 10.1049/iet-epa.2016.0737, vol. 11, no. 6, pp. 1131– 1139, Nov. 2017.

[54] P. Asef, R. Bargallo, and A. Lapthorn, "Iron Loss Prediction Using Modified IEM-Formula during the Field Weakening for Permanent Magnet Synchronous Machines," *MDPI Journal of Machines*, Vol. 5, No. 4, pp. 1-15, 2017.

[55] Li, Q.; Fan, T.; Wen, X. Characterization of Iron Loss for Integral-Slot Interior Permanent Magnet Synchronous Machine during Flux Weakening. *IEEE Trans. Magn.* 2017, *53*, 1–7.

[56] Li, Q.; Fan, T.; Wen, X. Armature-reaction magnetic field analysis for interior permanent magnet motor based on winding function theory. *IEEE Trans. Magn*. 2013, *49*, 1193–1201.

[57] Saavedra, H.; Urresty, J.; Riba, J.; Romeral, L.; Detection of inter turn faults in PMSMs with different winding configurations. *Energy Convers. Manag.* 2014, *79*, 534–542, doi:10.1016/j.enconman.2013.12.059.

[58] Donolo, P.; Bossio, G.; Angelo, C. Analysis of voltage unbalance effects on induction motors with open and closed slots. *Energy Convers. Manag*. 2011, *52*, 2024–2030, doi:10.1016/j.enconman.2010.10.045.

[59] Ueda, Y.; Ohta, H.; Uenosono, C. Instrument for real-time measurements of airgap flux distribution of on-load synchronous generators. *IEE Proc. A Phys.* 1987, *134*, 331–334, doi:10.1049/ip-a-1:19870047.

[60] Hendershot, J.R.; Miller, T.J.E. *Design and Performance of Brushless Permanent-Magnet Motors*; Oxford University Press: London, UK, USA, 1994.

[61] Hendershot, J.R.; Miller, T.J.E. *Design and Performance of Brushless Permanent-Magnet Motors*; Oxford University Press: London, UK, USA, 1994.

[62] Zivotic-Kukolj, V.; Soong, W.L.; Ertugrul, N. Iron loss reduction in an interior PM automotive alternator. *IEEE Trans. Ind. Appl.* 2006, *42*, 1478–1486.

[63] C. A. H-Aramburo and *et al.*, "Estimating Rotational Iron Losses in an Induction Machine," *IEEE Trans. Magn.*,vol. 39, no. 6, pp. 3527–3533, 2010.

[64] I. Zaman, and *et. al.*, "Condition Monitoring of Electric Components Using 3-D Printed Multiple Magnetic Coil Antennas," *IEEE Trans. Magn*, vol. 53, no. 6, pp. 1–4, June 2017.

[65] A. J. Moses, "Electrical steels: past, present and future developments," *Proc. Inst. Elect. Eng.*, vol. 137, pp. 233–245, Sept. 1990.

[66] P. Asef, R. Bargallo, and A. Lapthorn, "A Time Domain Computation of Rotational Iron Losses with Resistance Consideration for Permanent Magnet Synchronous Machines," Status: under review.

- **Chapter 4**

[1] W. Chu, Z. Zhu, and Y. Shen: 'Analytical optimisation of external rotor permanent magnet machines', *IET Electrical Systems in Transportation*, doi: 10.1049/iet-est.2012.0045, pp.41-49, 2013.

[2] R. Wrobel, P. H. Mellor, and D. Holliday: 'Thermal Modeling of a Segmented Stator Winding Design', *IEEE Trans. on INDUSTRY APPLICATIONS*, VOL. 47, NO. 5, pp.2023-2025, 2011.

[3] H. Li, and Y. Shen: 'Thermal Analysis of the Permanent-Magnet Spherical Motor', *IEEE Trans. on ENERGY CONVERSION*, Vol. 30, No. 3 pp. 1-2, 2015.

[4] M. Polikarpova, P. Ponomarev, P. Röyttä,: 'Direct liquid cooling for an outer-rotor direct drive permanent-magnet synchronous generator for wind farm applications', *Journal of IET Electric Power Applications*, ISSN. 1751-8660, pp. 523-526, doi: 10.1049/iet-epa.2014.0342, 2015.

[5] Xikai Sun, and Ming Cheng: 'Thermal Analysis and Cooling System Design of Dual Mechanical Port Machine for Wind Power Application', *IEEE Trans. on Industrial Elec*., Vol. 60, no. 5, doi: 10.1109/TIE.2012.2190958, pp.1724-1732, 2013.

[6] G. Lei, and et al.: 'Techniques for Multilevel Design Optimization of Permanent Magnet Motors', *IEEE TRANSACTIONS ON ENERGY CONVERSION*, VOL. 30, NO. 4, DECEMBER 2015, pp. 1574-1582, DOI: 10.1109/TEC.2015.2444434, 2015.

[7] P. Asef, R. Bargallo, M. R. Barzegaran, A. Lapthorn, D. Mewes, "Multi-objective Design Optimization Using Dual-Level Response Surface Methodology and Booth's Algorithm for Permanent Magnet Synchronous Generators," *IEEE Trans. Energy Conversion*, Vol. 33, No. 2, pp. 652-659, June 2018.

[8] M. Tursini., and et al., "A switched-reluctance motor for aerospace application: Design, analysis and results." Electric Power Systems Research 142 (2017): 74-83.

[9] Adrian Pleşca. "Thermal analysis of a traction system with double conducting points in steady state conditions." Electric Power Systems Research 97 (2013): 126-132.

[10] Staudt, Tiago, et al. "An optimization-oriented sizing model for brushless doubly fed reluctance machines: Development and experimental validation." Electric Power Systems Research 132 (2016): 125-131.

[11] D. A. Staton, A. Boglietti, and A. Cavagnino,: 'Solving the more difficult aspects of electric motor thermal analysis in small and medium size industrial induction motors', IEEE Trans. Energy Convers., vol. 20, no. 3, pp. 620–628, Sep. 2005.

[12] D. A. Staton and A. Cavagnino,: 'Convection heat transfer and flow calculations suitable for electric machines thermal models', IEEE Trans. Ind. Electron., vol. 55, no. 10, pp. 3509–3516.

[13] A. Boglietti, A. Cavagnino, and D. Staton,: 'Determination of critical parameters in electrical machine thermal models', IEEE Trans. Ind. Appl., vol. 44, no. 4, pp. 1150–1159, Jul./Aug. 2008.

[14] A. Boglietti, A. Cavagnino, D. Staton, and et al.: 'Evolution and modern approaches for thermal analysis of electrical machines', IEEE Trans. Ind. Electron., vol. 56, no. 3, pp. 871–882, 2009.

[15] Gómez, D. J., et al. 'Experimental validation of an enhanced permeance network model for embedded magnet synchronous machines. 'Electric Power Systems Research 140,2016: 836-845.

[16] G. J. Li, J. Ojeda, E. Hoang, and et al.: 'Comparative studies between classical and mutually coupled switched reluctance motors using thermal-electromagnetic analysis for driving cycles', IEEE Trans. Magn., vol. 47, no. 4, pp. 839–847, Apr. 2011.

[17] Yusuf Yasa, Sincar, E., Ertugrul, B. T., & Mese, E. "A multidisciplinary design approach for electromagnetic brakes." Electric Power Systems Research 141 (2016): 165-178.

[18] A. Tenconi, F. Profumo, S. E. Bauer, and .: 'Temperatures evaluation in an integrated motor drive for traction applications', IEEE Trans. Ind. Electron., vol. 55, no. 10, pp. 3619–3626.

[19] Y. Huang, J. Zhu, and Y. Guo,: 'Thermal analysis of high-speed SMC motor based on thermal network and 3-D FEA with rotational core loss included' IEEE Trans. Magn., vol. 45, no. 10, pp. 4680–4683, Oct. 2009.

[20] T. A. Jankowski, F. C. Prenger, D. D. Hill, and et al.: 'Development and validation of a thermal model for electric induction motors," IEEE Trans.Ind. Electron, vol. 57, no. 12, pp. 4043–4054, Dec. 2010.

[21] Marco Tosetti, and et al.: 'Conjugate Heat Transfer Analysis of Integrated Brushless Generators for More Electric Engines', IEEE Trans. Industry Applications, Vol. 50, No. 4, pp. 2467-2474, July.

[22] N. S. Ottosen, and H. Petersson, "Introduction to the Finite Element Method," ISBN-13: 978-0134738772, Chapter. 20.3, Prentice Hall, October 1992.

[23] N. Zhao, Z. Q. Zhu, W. Liu, "Thermal Analysis and Comparison of Permanent Magnet Motor and Generator," IEEE International Conference on Electrical Machines and Systems (ICEMS), DOI: 10.1109/ICEMS.2011.6073482, pp, pp.1-3, 2011.

[24] Y. K. Chin, and D. A. Staton "Transient thermal analysis using both lumped-circuit approach and finite element method of a permanent magnet traction motor," IEEE 7th AFRICON Conference in Africa, 1027- 1035 Vol.2, doi: 10.1109/AFRICON.2004.1406847, 2004.

[25] A. M. Knight, Y. Zhan, D. A. Staton, and et al.: 'Influence of stator slot shape on temperature in surface mounted permanent magnet machines', in Proc. IEEE-ECCE, Sep. 2010, pp. 1753–1759.

[26] D. G. Dorrell, A. M. Knight, M. Popescu, and et al. 'Comparison of different motor design drives for hybrid electric vehicles', in Proc. IEEE ECCE, Sep. 2010, pp. 3352–3359.

[27] C. Mejuto, M. Mueller, M. Shanel, and et al.: 'Improved synchronous machine thermal modelling', in Proc. XVIII ICEM, Sep. 6–9, pp. 1–6, 2008.

[28] A. Boglietti, A. Cavagnino, D. A. Staton, and et al.: 'End space heat transfer coefficient determination for different induction motor enclosure types', in Conf. Rec. 43rd IEEE IAS Annu. Meeting, Oct. 2008, pp. 1–8.

[29] P. Asef, R. Bargallo, and M. R. Barzegaran, "An innovative natural air-cooling system technique for temperature-rise suppression on the permanent magnet synchronous machines," Electric Power Systems Research, Vol. 154, pp.174-181, Sept. 2017.

[30] D. M. Ionel, M. Popescu, M. I. McGilp, T. J. E. Miller, S. J. Dellinger, and R. J. Heideman, "Computation of Core Losses in Electrical Machines Using Improved Models for Laminated Steel," IEEE Trans. Ind. Appl., vol. 43, no. 6, pp. 1554 –1564, 2007.

[31] P. Asef, R. B. Perpina, M. R. Barzegaran, J. Dong, A. Lapthorn, and O. A. Mohammed.: 'An advanced quasi-FEA technique on iron losses prediction for permanent magnet synchronous machines', IEEE Trans on Mgn., id: TMAG-17-06-0445, pp. 1–8.

[32] MANATEE software, www.eomys.com53tutorials, 2018.

[33] G. Schofield, J. R. Chelikowsky, and Y. Saad, "A spectrum slicing method for the Kohn–Sham problem," *Computer Physics Communications*. **183** (3): 497 505. DOI53 10.1016/j.cpc.2011.11.005, ISSN53 0010-4655. 2012.

[34] J.F. Gieras, C. Wang and J.C. Lai, Noise of polyphase electric motors, CRC Press, 2005.

[35] P.L. Timar, Noise and vibration of electrical machines, Elsevier, 1989.

[36] S.J. Yang, Low noise electrical motors, Clarendon Press, Oxford, 1981.

[37] PYRHONEN Juha, Tapani Jokinen, Valéria Hrabovcova, Design of Rotating Electrical Machines (2nd Ed.), Wiley, 2013.

[38] P. Asef, R. Bargallo, and A. Lapthorn, "Audible Magnetic Noise Minimization using Skewing Technique for Fractional-slot Concentrated Permanent Magnet Synchronous Wind Generators," *IEEE Trans. on Magnetics*, under review, 2018.

[39] J. L. Besnerais, V. Lanfranchi, M. Hecquet, P. Brochet, and G. Friedrich, "Prediction of Audible Magnetic Noise Radiated by Adjustable-Speed Drive Induction Machines," *IEEE Trans. on Industry Application*, Vol. 46, No. 4, Aug. 2010.

[40] A.M. El-Refaie, "Fractional-slot concentrated-windings synchronous permanent magnet machines: Opportunities and challenges," *IEEE Trans. Ind. Electron.*, vol. 57, no. 1, pp. 107–121, Jan. 2010.

[41] A. Tessarolo, F. Luise, S. Pieri, A. Benedetti, M. Bortolozzi, and M. De Martin, "Design for manufacturability of an Off-Shore Direct-Drive wind generator: An insight into additional loss prediction and mitigation," *IEEE Trans. Ind. Appl.*, Vol. 53, No. 5, pp. 4831-4842, Sept. 2017.

[42] A. M. El-Refaie and T. M. Jahns, "Scalability of surface PM Machines with concentrated windings designed to achieve wide speed ranges of constant-power operation," *IEEE Trans. Energy Convers.*, vol. 21, no. 2, pp. 362–369, Jun. 2006.

[43] K. Ahsanullah, R. Dutta, M. F. Rahaman and T. M. Jahns, "Analysis of Low-Speed IPMMs With Distributed and Fractional Slot Concentrated Windings for Wind Energy Applications," *IEEE Trans. Magn.*, vol. 53, no. 11, pp. 1–10, Nov. 2017.

[44] L. Wu, R. Qu, and D. Li, "Reduction of Rotor Eddy-Current Losses for Surface PM Machines With Fractional Slot Concentrated Windings and Retaining Sleeve," *IEEE Trans. Magn.,* Vol. 50, No. 11, Nov. 2014.

[45] M. Valavi, A. Nysveen, R. Nilssen, R. D. Lorenz, and T. Rølvåg, "Influence of pole and slot combinations on magnetic forces and vibration in low-speed PM wind generators," *IEEE Trans. Magn.*, vol. 50, no. 5, May 2014.

[46] Z. Q. Zhu, Z. P. Xia, L. J. Wu, and G. W. Jewell, "Analytical modeling and finite-element computation of radial vibration force in fractional-slot permanent-magnet brushless machines," *IEEE Trans. Ind. Appl.*, vol. 46, no. 5, pp. 1908–1918, Sep./Oct. 2010.

[47] Y. S. Chen, Z. Q. Zhu, and D. Howe, "Vibration of PM brushless machines having a fractional number of slots per pole," *IEEE Trans. Magn.*, vol. 42, no. 10, pp. 3395–3397, Oct. 2006.

[48] Y. Okuyama, and S. Moriyasu, "Electromagnetic noise of induction motors driven by PWM inverters," *Electr. Eng. Japan*, Vol. 133, No. 3, pp. 55-62, 2000.

[49] A. Hubert, and G. Frienrich, "Influence of power converter on induction motor acoustic noise: interaction between control strategy and mechanical structure," *IEE Proc. Electr. Power App.,* Vol 149, pp. 93-100, 2002.

[50] J. Le Bensnerais, V. Lanfranchi, M. Hecquet, and P. Brochet, "Multiobjective Optimization of Induction Machines Including Mixed Variables and Noise Minimization," *IEEE Trans. Magn.*, vol. 44, no. 6, pp. 1102–1105, Jun. 2008.

[51] J. Le Bensnerais, V. Lanfranchi, M. Hecquet, and P. Brochet, "Optimal Slot Numbers for Magnetic Noise Reduction in Variable-Speed Induction Motors," *IEEE Trans. Magn.*, vol. 45, no. 8, pp. 3131–3136, Aug. 2009.

[52] M. Valavi, J. Le Besnerais, and A. Nysveen, "An Investigation of Zeroth-Order Radial Magnetic Forces in Low-Speed Surface-Mounted Permanent Magnet Machines," *IEEE Trans. Magn.*, vol. 52, no. 8, pp. 1–6, Aug. 2016.

[53] J. Le Bensnerais, V. Lanfranchi, M. Hecquet, P. Brochet, and G. Friedrich, "Prediction of Audible Magnetic Noise Radiated by Adjustable-Speed Drive Induction Machines," *IEEE Trans. Magn.*, vol. 46, no. 4, pp. 1367–1373, Aug. 2010.

[54] J. Le Bensnerais, V. Lanfranchi, M. Hecquet, and P. Brochet, "Characterization and Reduction of Audible Magnetic Noise Due to PWM Supply in Induction Machines," *IEEE Trans. Ind. Electron.*, vol. 57, no. 4, pp. 1288–1295, Apr. 2010.

[55] J. Le Bensnerais, V. Lanfranchi, M. Hecquet, G. Friedrich, and P. Brochet, "Characterisation of radial vibration force and vibration behaviour of a pulse-width modulation-fed fractional-slot induction machine," *IET Electr. Power App.*, vol. 3, no. 3, pp. 197–208, May. 2009.

[56] A. Nobahari, A. Darabi, and A. Hassannia, "Various skewing arrangements and relative position of dual rotor of an axial flux induction motor, modelling and performance evaluation," *IET Electric Power Appl.*, vol. 12, no. 4, pp. 575–580, Jan. 2018.

[57] C-Min Lee, H-Soo Seol, J-y. Lee, S-H. Lee, and D-Woo Kang, "Optimization of Vibration and Noise Characteristics of Skewed Permanent Brushless Direct Current Motor," *IEEE Trans. Magn*. Vol. 53, No. 11, pp. 1-5, 2017.

[58] W. Xu, X. Bao, C. Di, L. Wang, and Y. Chen, "Optimal Angle Combination for Improving Electromagnetic Torque in Induction Motor with Double-Skewed Rotor," *IEEE Trans. Magn*. Vol. 53, No. 11, pp. 1-5, Nov. 2017.

[59] C. Ho Kang, K. Jin Kang, J. Yong Song, Y. Jin Cho, and G. Hee Jang, "Axial Unbalanced Magnetic Force in a Permanent Magnet Motor Due to a Skewed Magnet and Rotor Eccentricities," *IEEE Trans. Magn*. Vol. 53, No. 11, pp. 1-5, Nov. 2017.

[60] L. Wang, X. Bao, C. Di, and J. Li, "Effects of Novel Skewed Rotor in Squirrel-Cage Induction Motor on Electromagnetic Force," *IEEE Trans. Magn*. Vol. 51, No. 11, pp. 1-5, Nov. 2015.

[61] C. Wang, X. Bao, S. Xu, Y. Zhou, W. Xu, and Y. Chen, "Effects of Novel Skewed Rotor in Squirrel-Cage Induction Motor on Electromagnetic Force," *IEEE Trans. Magn*. Vol. 53, No. 11, pp. 1-5, Nov. 2017.

[62] S. Guy Min, and B. Sarlioglu, "Modeling and Investigation on Electromagnetic Noise in PM Motors With Single- and Double-Layer Concentrated Winding for EV and HEV Application," *IEEE Trans. Transportation Elect*rification, Vol. 4, No. 1, pp. 292-302, Mar. 2018.

[63] C-Min Lee, H-Soo Seol, J-yong Lee, S-Hwan Lee, and D-Woo Kang, "Optimization of Vibration and Noise Characteristics of Skewed Permanent Brushless Direct Current Motor," *IEEE Trans. Magn*. Vol. 53, No. 11, pp. 1-5, Nov. 2017.

[64] W. Deng, S. Zuo, F. Lin, S. Wu, "Influence of pole and slot combinations on vibration and noise in external rotor axial flux in-wheel motors," *IET Electr. Power Appl.,* Vol. 11, No. 4, pp. 586-594, 2017.

[65] G-Yu Zhou and J-Xin Shen, "Rotor Notching for Electromagnetic Noise Reduction of Induction Motors," *IEEE Trans. Ind. Appl*. Vol. 53, No. 4, pp. 3361-3370, Nov. 2017.

[66] E. Devillers, J. Le Besnerais, T. Lubin, M. Hecquet, and J. P. Lecointe, "A review of subdomain modeling techniques in electrical machines: performances and applications," in ICEM International Conference on Electrical Machines, 2016.

[67] P. Asef, R. Bargallo, and A. Lapthorn, "Optimal Pole Number for Magnetic Noise Reduction in Variable Speed Permanent Magnet Synchronous Machines with Fractional-Slot Concentrated Windings," *IEEE Trans. Energy Conversion.*, under review, 2018.

[68] G. Kron, "Induction motor slot combinations: Rules to predetermine crawling vibration, noise and hooks in the speed-torque curve," *AIEE Trans.*, vol. 50, 1931.

[69] P. Juha, Tapani Jokinen, Valéria Hrabovcova, Design of Rotating Electrical Machines (2nd Ed.), Wiley, 2013.

[70] W. Deng, S. Zuo, F. Lin, S. Wu, "Influence of pole and slot combinations on vibration and noise in external rotor axial flux in-wheel motors," *IET Electr. Power Appl.,* Vol. 11, No. 4, pp. 586-594, 2017.

[71] G-Yu Zhou and J-Xin Shen, "Rotor Notching for Electromagnetic Noise Reduction of Induction Motors," *IEEE Trans. Ind. Appl*. Vol. 53, No. 4, pp. 3361-3370, Nov. 2017.

[72] T. Lubin, S. Mezani, and A. Rezzoug, "2-D exact analytical model for surface-mounted permanent-magnet motors with semi-closed slots," *IEEE Trans. Magn*., vol. 47, no. part 2, pp. 479–492, 2011.

[73] M. Liwschitz-Garik and C. C. Whipple, Electric Machinery, vol. II, A–C Machines. New York: D. Van Nostrand Company Inc., 1960.

[74] N. Bianchi and M. D. Pré, "Use of the star of slots in designing fractional–slot single–layer synchronous motors," *IEE Proc. – Electr. Power Appl*., vol. 153, no. 3, pp. 459–466, May 2006, (online no. 20050284).

[75] H. A. Toliyat, and G. B. Kliman, "Handbook of Electric Motors," CRC press/ *Taylor & Francis* Group, ISBN: 0-8247-4105-6, 2004.

[76] J. Li, Da-W. Choi, D-H. Son, and Y-Hyun Cho, "Effects of MMF Harmonics on Rotor Eddy-Current Losses for Inner-Rotor Fractional Slot Axial Flux Permanent Magnet Synchronous Machines," *IEEE Trans. Magnetics*, Vol. 48, No. 2, Feb. 2012.

- **Chapter 5**

[1] S. Carrie`re S. Caux, and M. Fadel, "Optimised speed control in state space for PMSM direct drives," *IET Electric Power Applications*, vol. 4, No. 3, pp. 158–168, 2010.

[2] M. Sreejeth, M. Singh, and P. Kumar, "Particle swarm optimisation in efficiency improvement of vector controlled surface mounted permanent magnet synchronous motor drive," *IET Electric Power Electronics*, vol. 8, No. 5, pp. 760–769, 2015.

[3] N. Boules, "Design optimization of permanent magnet dc motors," *IEEE Trans. Ind. Appl.*, vol. 26, no. 4, pp. 786–792, Jul. 1990.

[4] G. Slemon and X. Liu, "Modeling and design optimization of permanent magnet motors," *Elect. Power Compon. Syst.*, v.20, n.2, pp.71–92, 1992.

[5] J.-L. Shi, T.-H. Liu and S.-H. Yang, "Nonlinear-controller design for an interior-permanent-magnet synchronous motor including field-weakening operation," *IET Elctrc Pwr Applications*, vol. 1, no. 1, pp. 119–126, 2007.

[6] K. Laskaris and A. G. Kladas, "Internal permanent magnet motor design for electric vehicle drive," *IEEE Trans. Ind. Elctrns.*, v. 57, n. 1, pp. 138–145, Jan. 2010.

[7] Dorrell, *et al*., "A review of the design issues and techniques for radial-flux brushless surface and internal rare-earth permanent magnet motors," *IEEE Trans. Ind. Electron.*, v. 58, n. 9, pp. 3741–3757, 2011.

[8] J. Aubry, *et al*., "Sizing Optimization Methodology of a Surface Permanent Magnet Machine-Converter System Over a Torque-Speed Operating Profile: Application to a Wave Energy Converter," *IEEE Trans. Ind. Elctrns.*, v. 59, n. 5, pp. 2116–2124, 2012.

[9] H. Terrab, and A. Kara, "Parameters design optimization of 230 kV corona ring based on electric field analysis and response surface methodology," *Electric Power Systems Research*, pp. 1–7, 2017.

[10] J. T. Li, *et al*., "Design Optimization for Cogging Torque Minimization Using Response Surface Methodology," *IEEE Trans. Magn.*, vol. 40, no. 2, pp. 1176–1179, March. 2004.

[11] H. Fang, and D. Wang, "A Novel Design Method of Permanent Magnet Synchronous Generator From Perspective of Permanent Magnet Material Saving,"*IEEE* Trans. Energy Conv., V.32, N.1, pp.48-53, 2017.

[12] C. Montgomery, "Design and Analysis of Experiments" *John Wiley & Sons Singapore*, pp.65-544, 2013.

[13] L. Jolly, *et al.*, "Design Optimization of Permanent Magnet Motors Using Response Surface Methodology and Genetic Algorithms," IEEE Trans. *Mgn*., V. 41, N. 10, OCTOBER 2005, pp.3928-3930.

[14] X. K. Gao, T. S. Low, Z. J. Liu, S. X. Chen, "Robust design for torque optimization using response surface methodology," *IEEE Transactions on Magnetics*, Vol. 38, DOI: 10.1109/20.996292, No. 2, pp. 1141-1143, March 2002.

[15] X. Liu, and W. N. Fu, "A Dynamic Dual-Response-Surface Methodology for Optimal Design of a Permanent-Magnet Motor Using Finite-Element Method," IEEE Trans. *Mgn*, V. 52, N. 3, pp. 1-4, 2016.

[16] L. P. Rubinfield, "A Proof of the Modified Booth's Algorithm for Multiplication,"*IEEE Trans. Computers*, V.C-24, N.10, pp. 14-15, 1975.

[17] Bertsimas, J. Tsitsiklis, "Simulated annealing," *Journal of Statistical Science*, V. 8, N. 1 pp, pp.10-15, 1993.

[18] Yee-Pien Yang, Chung-Han Lee, and Po-Chang Hung, "Multi-objective optimal design of an axial-flux permanent-magnet wheel motor for electric scooters," *IET Elctrc Pwr Applctns*, Vol. 8, No. 1, pp. 1-12, 2014.

[19] P. Asef, R. Bargallo, and M. R. Barzegaran, "Global sizing optimisation using dual-level response surface method based on mixed-resolution central composite design for permanent magnet synchronous generators," *IET Electric Power Application*, Vol. 12, No. 5, May 2018.

[20] P. Asef, R. Bargallo, M. R. Barzegaran, A. Lapthorn, and D. Mewes "Multi-objective Design Optimization Using Dual-Level Response Surface Methodology and Booth's Algorithm for Permanent Magnet Synchronous Generators," *IEEE Trans. On Energy Conversion*, Application, Vol. 33, No. 2, Jun 2018.

[21] Lei, J. Zhu, and Y. Guo, "Multidisciplinary Design Optimization Methods for Electrical Machines and Drive Systems," Springer-Verlag Berlin Heidelberg, ISSN: 1612-1287, DOI: 10.1007/978-3-662-49271-0, pp. 9-170, 2016.

[22] X. Zhu, B, Yan, L. Chen, R. Chang, L. Quan, and L. Mo, "Multi-Objective Optimization Design of a Magnetic Planetary Geared Permanent Magnet Brushless Machine by Combined Design of Experiments and Response Surface Methods," *IEEE TRANSACTIONS ON MAGNETICS*, VOL. 50, NO. 11, pp. 1-3, 2014.

[23] T. J. Robinson, *et al.*, "Robust Parameter Design: A Review," *John Wiley & Sons*, Ltd, DOI: 10.1002/qre.602, V. 39, N. 1, pp. 90-98, 2004.

[24] J. J. Borkowski, J. M. Lucas, "Designs of Mixed Resolution for Process Robustness Studies," *TECHNOMETRICS*, V. 39, N. 1, pp. 1-8, 1997.

[25] M. Borror, and D. C. Montgomery, "Mixed Resolution Designs As Alternatives To Taguchi Inner/Outer Array Designs For Robust Design Problems," *John Wiley & Sons*, Ltd, Quality And Reliability Engineering International, *Qual. Reliab. Engng. Int.*, pp.117–127, 2000.

[26] Lei, *et al*., "System-Level Design Optimization Method for Electrical Drive Systems—Robust Approach," *IEEE Trans. Ind. Elec.*, VOL. 62, NO. 8, pp.4702-4712, 2015.

[27] Jin-Hua Hong, and Chen-Weng Wu, "Cellular-Array Modular Multiplier for Fast RSA Public-Key Cryptosystem Based on Modified Booth's Algorithm," *IEEE Trans. VLSI Sys.*, V. 11, N. 3, pp. 474-481, 2003.

[28] E. Ambikairajah, and M. J. Carery, "Technique For Performing Multiplication On A 16-Bit Microprocessor Using An Extension Of Booth's Algorithm," *IEEE Electronics Letters*, V.16, N. 2, 1980.

[29] Lei, C. Liu, J. Zhu, and Y. Guo, "Techniques for Multilevel Design Optimization of Permanent Magnet Motors," IEEE Trans. energy Conv., V. 30, N. 4, pp. 1574-1582, 2015.

[30] L. Chedot, *et al*., "Integrated starter generator: The need for an optimal design and control approach. Application to a permanent magnet machine," *IEEE Trans. Ind. Appl.*, vol. 43, no. 2, pp. 552–559, 2007.

[31] S. Morimoto, *et al*., "Expansion of operating limits for permanent magnet motor by current vector control considering inverter capacity," *IEEE Trans. Ind. Appl.*, vol. 26, no. 5, pp. 866–871, Sep. 1990.

[32] Mademlis, J. Xypteras, and N. Margaris, "Loss minimization in surface permanent-magnet synchronous motor drives," *IEEE Trans. Ind. Electron.*, vol. 47, no. 1, pp. 115–122, Feb. 2000.

[33] Cavallaro, A. O. DiTommaso, R. Miceli, A. Raciti, G. Galluzzo, and M. Trapanese, "Efficiency enhancement of permanent-magnet synchronous motor drives by online loss minimization approaches," *IEEE Trans. Ind. Electron.*, vol. 52, no. 4, pp. 1154–1160, Aug. 2005.

[34] E.G. Shehata, "A comparative study of current control schemes for a direct-driven PMSG wind energy generation system," *Electric Power Systems Research*, vol. 143, pp. 197–205, 2017.

[35] C. MALLINSON, "One-sided Fluxes - A Magnetic Curiosity?" *IEEE Tran. Magn.*, VOL. 9, NO. 4, pp.678-682, 1973.

[36] Klaus Halbach, "Design of permanent multipole magnets with oriented rare earth cobalt material"," Nuclear Instruments and Methods. 169 (1), doi:10.1016/0029-554X(80)90094-4 pp. 1-10, 1979.

[37] W. Chu, Z. Zhu, and Y. Shen: 'Analytical optimisation of external rotor permanent magnet machines', IET Electrical Systems in Transportation, doi: 10.1049/iet-est.2012.0045, pp.41-49, 2013.

[38] Yang Shen, Zi-Qiang Zhu "General analytical model for calculating electromagnetic performance of permanent magnet brushless machines having segmented Halbach array," Journal of IET Electric Systems in Transportation, ISSN. 1751-8660, pp. 57-66, doi: 10.1049/iet-est.2012.0055, 2013.

[39] Z. Q. Zhu, Z. P. Xia, and D. Howe, "Comparison of Halbach magnetized brushless machines based on discrete magnet segments or a single ring magnet," *IEEE Trans. Magn*., vol. 38, no. 5, pp. 2997–2999, Sep. 2002.

[40] P. H. Mellor and R. Wrobel, "Optimization of a multipolar permanent magnet rotor comprising two arc segments per pole," *IEEE Trans. Ind. Appl.*, vol. 43, no. 4, pp. 942–951, Jul./Aug. 2007.

[41] Y. Shen, G. Y. Liu, Z. P. Xia, and Z. Q. Zhu, "Determination of maximum electromagnetic torque in PM brushless machines having 2-segment Halbach array," *IEEE Trans. Ind. Electron.*, vol. 61, no. 2, pp. 718–729, Feb. 2014.

[42] Ch. Xia, L. Guo, and H. Wang, "Modeling and Analyzing of Magnetic Field of Segmented Halbach Array Permanent Magnet Machine Considering Gap Between Segments," *IEEE Trans. Magn*., vol. 50, no. 12, pp. 2–8, Sep. 2014.

[43] Han-Bit Kang, J. Choi, H. Cho, and J. Kim, "Comparative Study of Torque Analysis for Synchronous Permanent Magnet Coupling With Parallel and Halbach Magnetized Magnets Based on Analytical Field Calculations," *IEEE Trans. Magn*., Vol. 50, no. 11, DOI: 10.1109/TMAG.2014.2329010, pp.1-3, 2014.

[44] A. G. Pristup, and *et. al* "A Study of Cogging Torque in Permanent Magnet Synchronous Machines with Fractional Slot Windings," Springer journals, ISSN: 1068-3712, No. 12, pp. 36-40, Nov-2014.

[45] Schmidt OVE, and M. Susic, "Finite element analysis of permanent magnet synchronous machines with fractional slot tooth coil windings," Springer journals, DOI: 10.1007/s00502-011-0812-z, No. 128/3, pp. 86-94, 2011.

[46] Louar FATEH, and *et. al*, "Modeling and control of a permanent magnet synchronous generator dedicated to standalone wind energy conversion

[47] system," Springer journals, DOI: 10.1007/s11708-016-0410-1, No. 10(2), pp. 155-163, 2016.

[48] Nuria Del-Valle, and *et. al*, "Magnet Guideways for Superconducting Maglevs: Comparison Between Halbach-Type and Conventional Arrangements of Permanent Magnets," Springer journals, DOI: 10.1007/s10909-010-0225-0, No. 162, pp. 62-71, 2011.

[49] Y. K. Chin, and D. A. Staton "Transient thermal analysis using both lumped-circuit approach and finite element method of a permanent magnet traction motor," IEEE 7th AFRICON Conference in Africa, 1027 - 1035 Vol.2, DOI: 10.1109/AFRICON.2004.1406847, 2004.

[50] Y. Huang, J. Zhu, and Y. Guo, "Thermal Analysis of High-Speed SMC Motor Based on Thermal Network and 3-D FEA With Rotational Core Loss Included," IEEE TRANSACTIONS ON MAGNETICS, VOL. 45, NO. 10, pp. 4680-4682, 2009.

[51] R. Hendershot, and T. J. E. Miller, "Design of Brushless Permanent-Magnet Machines." Oxford University Press, ISBN: 1-88155-03-1, pp. 157-193, 2010.

[52] Lipo, T. A. 2011. "Introduction to AC Machine Design." In *Library of Congress Cataloging in Publication Data.* Madison, WI: University of Wisconsin-Madison, 120-7.

[53] A. Krings and J. Soulard, "Overview and comparison of iron loss models for electrical machines," Journal of Electrical Engineering, vol. 10, no. 3, pp. 162–169, 2010.

[54] D. M. Ionel, M. Popescu, S. J. Dellinger, T. J. E. Miller, R. J. Heideman, and M. I. McGilp, "On the variation with flux and frequency of the core loss coefficients in electrical machines," IEEE Trans. Ind. Appl., vol. 42, no. 3, pp. 658–667, May 2006.

[55] D. M. Ionel, M. Popescu, M. I. McGilp, T. J. E. Miller, S. J. Dellinger, and R. J. Heideman, "Computation of Core Losses in Electrical Machines Using Improved Models for Laminated Steel," IEEE Trans. Ind. Appl., vol. 43, no. 6, pp. 1554–1564, Nov. 2007.

[56] Y. Huang, J. Dong, J. G. Zhu, and Y. Guo, "Core Loss Modeling for Permanent-Magnet Motor Based on Flux Variation Locus and FiniteElement Method," IEEE Trans. Magn., vol. 48, no. 2, pp. 1023–1026, 2012.

D. C. Meeker, Finite Element Method Magnetics, Version 4.2 (23June2016 Build), http://www.femm.info53

[58] Y. Feng, X. H. Yu, and F. L. Han, "High-order terminal sliding-mode observer for parameter estimation of a permanent-magnet synchronous motor," *IEEE Trans. Ind. Electron.*, vol. 60, no. 10, pp. 4272–4280, Oct. 2013.

[59] W. M. Lin, T. J. Su, and R. C. Wu, "Parameter identification of induction machine with a starting no-load low-voltage test," *IEEE Trans. Ind. Electron.*, vol. 59, no. 1, pp. 352–360, Jan. 2012.

[60] R. Babau, I. Boldea, T. J. E. Miller, and N. Muntean, "Complete parameter identification of large induction machines from no-load acceleration-deceleration tests," *IEEE Trans. Ind. Electron.*, vol. 54, no. 4, pp. 1962–1972, Aug. 2007.

[61] N. J. Kim, H. S. Moon, and D. S. Hyun, "Inertia identification for the speed observer of the low speed control of induction machines," *IEEE Trans. Ind. Appl.*, vol. 32, no. 6, pp. 1371–1379, Sep./Oct. 1996.

[62] S. H. Li and Z. G. Liu, "Adaptive speed control for permanent-magnet synchronous motor system with variations of load inertia," *IEEE Trans. Ind. Electron.*, vol. 56, no. 8, pp. 3050–3059, Aug. 2009.

[63] F. J. Lin and H. M. Su, "A high-performance induction motor drive with on-line rotor time-constant estimation," *IEEE Trans. Energy Convers.*, vol. 12, no. 4, pp. 297–303, Dec. 1997.

[64] F. Andoh, "Moment of inertia identification using the time average of the product of torque reference input and motor position," *IEEE Trans. Power Electron.*, vol. 22, no. 6, pp. 2534–2542, Nov. 2007.

[65] Matteo F. Iacchetti, Giovanni Maria Foglia, Antonino Di Gerlando, and Andrew J. Forsyth, "Analytical Evaluation of Surface-Mounted PMSG Performances Connected to a Diode Rectifier," *IEEE Trans. Energy Convers.,*vol. 30, no. 4, pp. 1367–1374, Dec. 2015.

[66] Ma Weiming, Hu An, Liu Dezhi, and Zhang Gaifan "Stability of a Synchronous Generator with Diode-Bridge Rectifier and Back-EMF Load," *IEEE Trans. Energy Convers.,* vol. 15, no. 4, pp. 458–463, Dec. 2000.

[67] Weimin Wang, K. W. E. Cheng, K. Ding, and L. C. Meng, "A Novel Approach to the Analysis of the Axial-Flux Permanent-Magnet Generator With Coreless Stator Supplying a Rectifier Load," *IEEE Trans. Magnetics.,*vol. 47, no. 10, pp. 2391–2394, Dec. 2011.

[68] J. C. MALLINSON, "One-sided Fluxes - A Magnetic Curiosity?" *IEEE Tran. Magn.*, VOL. 9, NO. 4, pp.678-682, 1973.

[69] Klaus Halbach, "Design of permanent multipole magnets with oriented rare earth cobalt material"," Nuclear Instruments and Methods. 169 (1), doi:10.1016/0029-554X(80)90094-4 pp. 1-10, 1979.

[70] Yang Shen, Zi-Qiang Zhu "General analytical model for calculating electromagnetic performance of permanent magnet brushless machines having segmented Halbach array," Journal of IET Electric Systems in Transportation, ISSN. 1751-8660, pp. 57-66, doi: 10.1049/iet-est.2012.0055, 2013.

[71] Z. Q. Zhu, Z. P. Xia, and D. Howe, "Comparison of Halbach magnetized brushless machines based on discrete magnet segments or a single ring magnet," *IEEE Trans. Magn*., vol. 38, no. 5, pp. 2997–2999, Sep. 2002.

[72] Y. Shen, G. Y. Liu, Z. P. Xia, and Z. Q. Zhu, "Determination of maximum electromagnetic torque in PM brushless machines having 2-segment Halbach array," *IEEE Trans. Ind. Electron.*, vol. 61, no. 2, pp. 718–729, Feb. 2014.

[73] Ch. Xia, L. Guo, and H. Wang, "Modeling and Analyzing of Magnetic Field of Segmented Halbach Array Permanent Magnet Machine Considering Gap Between Segments," *IEEE Trans. Magn*., vol. 50, no. 12, pp. 2–8, Sep. 2014

[74] Han-Bit Kang, J. Choi, H. Cho, and J. Kim, "Comparative Study of Torque Analysis for Synchronous Permanent Magnet Coupling With Parallel and Halbach Magnetized Magnets Based on Analytical Field Calculations," *IEEE Trans. Magn*., Vol. 50, no. 11, DOI: 10.1109/TMAG.2014.2329010, pp.1-3, 2014.

[75] Pedram Asef, R. B. Perpina, and M. R. Barzegaran "Electromagnetic-based Evaluation of Different Halbach-Array topologies on the Exterior Rotor PM Synchronous Machines." *Springer Journal, Electrical Engineering.*, status: accepted, June. 2017.

[76] W. Will, "Introduction to Understandable Physics," *Chapter book*, Vol. 1- Mechanics. AuthorHouse. p. 10.10. ISBN 1449063330, 2010.

[77] J. R. Hendershot, and T. J. E. Miller, "Design of Brushless Permanent Magnet Machines." Oxford University Press, pp.185-465, 2010.

[78] Tze-Fun Chan, W. Wang, and L. Lei Lai, "Design of Brushless Permanent Magnet Machines." *IEEE International Electric Machines and Drives Conference*, pp. 1600-1604, 2009.

[79] M. C. McCalla, *Fundamentals of Computer-Aided Circuit Simulation,* Kluwer Academic, (1988).

[80] W. N. Fu, and S. L. Ho, "Enhanced Nonlinear Algorithm for the Transient Analysis of Magnetic Field and Electric Circuit Coupled Problems," *IEEE Trans. Magnetics.,*vol. 45, no. 2, pp. 701–705, Feb. 2009.

[81] A. Di Gerlando, G. M. Foglia, M. F. Iacchetti, and R. Perini, "Comprehensive steady-state analytical model of a three-phase diode rectifier connected to a constant DC voltage source," *IET Power Electron.*, vol. 6, no. 9, pp. 1927–1938, Nov. 2013.

[82] J. Pyrhonen, T. Jokinen, and V. Hrabvocova, *Design of Rotating Electrical Machines*. Hoboken, NJ USA: Wiley, 2008, pp. 259–261.

[83] T. F. Chan, L. L. Lai and L. T. Yan, "Analysis of a stand-alone permanent-magnet synchronous generator using a time-stepping coupled
field-circuit method," *IEE Proc.−Electric Power Applications.* vol. 152, no. 6, pp. 1459-1467, Nov. 4, 2005.

[84] Xiaoxu Zhang, Xiao Liu, Jinglin Liu, and Zhe Chen, "Analytical Investigation on the Power Factor of a Flux-Modulated Permanent-Magnet Synchronous Machine," *IEEE Trans. Magnetics.,*vol. 51, no. 11, pp. 1–3, Feb. 2015.

[85] M. Vukotic, and D. Miljavec, "Design of a permanent-magnet fluxmodulated machine with a high torque density and high power factor," *IET Electric Power Applications,* Volume: 10, Issue*:* 1*,* DOI: 10.1049/iet-epa.2015.0143, 201.

[86] P. Asef, R. Bargallo, M. R. Barzegaran, A. Lapthorn, and D. Mewes, "Load identification of different Halbach-array topologies on permanent magnet synchronous generators using the coupled field-circuit FE methodology," Electric Power Systems Research, Vol. 154, pp. 484-492, 2018.

- **Chapter 6**

[1] A.M. El-Refaie, "Fractional-slot concentrated-windings synchronous permanent magnet machines: Opportunities and challenges," *IEEE Trans. Ind. Electron.*, vol. 57, no. 1, pp. 107–121, Jan. 2010.

[2] A. Tessarolo, F. Luise, S. Pieri, A. Benedetti, M. Bortolozzi, and M. De Martin, "Design for manufacturability of an Off-Shore Direct-Drive wind generator: An insight into additional loss prediction and mitigation," *IEEE Trans. Ind. Appl.*, Vol. 53, No. 5, pp. 4831-4842, Sept. 2017.

[3] A. M. El-Refaie and T. M. Jahns, "Scalability of surface PM Machines with concentrated windings designed to achieve wide speed ranges of constant-power operation," *IEEE Trans. Energy Convers.*, vol. 21, no. 2, pp. 362–369, Jun. 2006.

[4] K. Ahsanullah, R. Dutta, M. F. Rahaman and T. M. Jahns, "Analysis of Low-Speed IPMMs With Distributed and Fractional Slot Concentrated Windings for Wind Energy Applications," *IEEE Trans. Magn.*, vol. 53, no. 11, pp. 1–10, Nov. 2017.

[5] L. Wu, R. Qu, and D. Li, "Reduction of Rotor Eddy-Current Losses for Surface PM Machines With Fractional Slot Concentrated Windings and Retaining Sleeve," *IEEE Trans. Magn.,* Vol. 50, No. 11, Nov. 2014.

[6] P. Asef, R. Bargallo, and A. Lapthorn, "Iron Loss Prediction Using Modified IEM-Formula during the Field Weakening for Permanent Magnet Synchronous Machines," *Machines Journal,* Vol. 5, No. 4, pp.1-15, 2017.

[7] P. Asef, R. Bargallo, M. R. Barzegaran, Andrew Lapthorn, J. Dong, and O. S. Mohammed, "A Comparative Study of Quasi-FEA Technique on Iron Losses Prediction for Permanent Magnet Synchronous Machines," *Progress in Electromagnetics Research*, Vol. 81, pp. 101-113, Feb 2018.

[8] Y. Huang, J. Dong, J. G. Zhu, and Y. Guo, "Core Loss Modeling for Permanent-Magnet Motor Based on Flux Variation Locus and Finite-Element Method," IEEE Trans. Magn., vol. 48, no. 2, pp. 1023–1026, 2012.

[9] A. D. Gerlando, and R. Perini, "Evaluation of the Effects of the Voltage Harmonics on the Extra Iron Losses in the Inverter Fed Electromagnetic Devices," IEEE Trans. on Energy Conv., Vol. 14, No. 1, pp. 57-62, March 1999.

[10] P. Asef, R. Bargallo, and A. Lapthorn, "A Time Domain Computation of Rotational Iron Losses Considering the Bulk Conductivity for Permanent Magnet Synchronous Machines*," IET Electric Power Applications*, under review, 2018.

[11] C. Zhou, G. Yang, and J. Su, "PWM Strategy with Minimum Harmonic Distortion for Dual Three-Phase Permanent-Magnet Synchronous Motor Drives Operating in the Overmodulation Region," *IEEE Trans. Power Electronics*, Vol. 31, No. 2, Feb. 2016.

[12] M. Jones, S. N. Vukosavic, D. Dujic, and E. Levi, "A synchronous current control scheme for multiphase induction motor drives," *IEEE Trans. Energy Convers.*, vol. 24, no. 4, pp. 860–868, Dec. 2009.

[13] C. S. Lim, E. Levi, M. Jones, N. A. Rahim, W. P. Hew, "FCS-MPC-Based Current Control of a Five-Phase Induction Motor and its Comparison with PI-PWM Control," *IEEE Trans. Indu. Elec.*,Vol. 61, No. 10, pp. 149-163. January 2014.

[14] P. Asef, R. Bargallo, and M. R. Barzegaran, "Global Sizing Optimisation Using Dual-Level Response Surface Method based on Mixed-resolution Central Composite Design for Permanent Magnet Synchronous Generators*," IET Electric Power Applications*, Vol. 12, /no. 5, pp. 684-6922, May 2018.

[15] P. Asef, R. Bargallo, M. R. Barzegaran, "An innovative natural air-cooling system technique for temperature-rise suppression on the permanent magnet synchronous machines," Electric Power Systems Research, Vol. 154, pp. 174-181, Jan 2018.

[16] P. Asef, R. Bargallo, and A. Lapthorn, "Audible Magnetic Noise Minimization using Skewing Technique for Fractional-slot Concentrated Permanent Magnet Synchronous Wind Generators," *IEEE Trans. on Magnetics*, under review, 2018.

[17] P. Asef, R. Bargallo, and A. Lapthorn, "Optimal Pole Number for Magnetic Noise Reduction in Variable Speed Permanent Magnet Synchronous Machines with Fractional-Slot Concentrated Windings," *IEEE Trans. on Energy Conversion*, under review, 2018.

- **Chapter 7**

[1] T. S. Babu, and *et al*., "Particle Swarm Optimization Based Solar PV Array Reconfiguration of the Maximum Power Extraction under Partial Shading Conditions," *IEEE Trans. on Sustainable. Energy*, Vol. 9, No. 1 pp.74-85, Jan. 2018.

[2] A. Xenophontos, and A. M. Bazzi, "Model-Based Maximum Power Curves of Solar Photovoltaic Panels under Partial Shading Conditions," *IEEE Trans. Of Photovoltaics*, Vol. 8, No. 1, pp. 223-229, Jan. 2018.

[3] Z. Zhen, X. Taoyun, S. Yanping, L. Wang, P. Jia and J. Yu, "A Method to Test Operating Cell Temperature for BIPV Modules," *IEEE Trans. Of Photovoltaics*, Vol. 6, No. 1 pp.272-277, Jan. 2016.

[4] N. Belhaouas, M.-S. A. Cheikh, P. Agathoklis, M.-R. Oularbi, B. Amrouche, K. Sedraoui, and N. Djilali, "PV array power output maximization under partial shading using new shifted PV array arrangements," *Applied Energy Journal*, Vol. 187, pp. 326-337, Feb. 2017.

[5] R. Rachchh, M. Kumar, and B. Tripathi, "Solar photovoltaic system design optimization by shading analysis to maximize energy generation from limited urban area," *Energy Conversion and Management, Journal*, Vol. 115, pp. 244-252, May 2016.

[6] M. Khoroshiltseva, D. Slanzi, and I. Poli, "A Pareto-based multi-objective optimization algorithm to design energy-efficient shading devices," *Applied Energy Journal*, Vol. 184, pp. 1400-1410, Dec. 2016.

[7] A. J. Hanson, and et al., "Partial-Shading Assessment of Photovoltaic Installations via Module-Level Monitoring," *IEEE Trans. Of Photovoltaics*, Vol. 4, No. 6, pp. 1618-1624, Nov. 2014.

[8] Z. Zhen, X. Taoyun, S. Yanping, L. Wang, P. Jia and J. Yu, "A Method to Test Operating Cell Temperature for BIPV Modules," *IEEE Trans. Of Photovoltaics*, Vol. 6, No. 1 pp.272-277, Jan. 2016.

[9] P. Asef, R. Bargallo, M. R. Barzegaran, and A. Lapthorn, "A 3-D Pareto-Based Shading Analysis on Solar Photovoltaic System Design Optimization," IEEE Trans. Sustainable Energy, DOI: 10.1109/TSTE.2018.2849370, Jun 2018.

[10] F. Belhachat, and C. Larbes, "Modeling, analysis and comparison of solar photovoltaic array configurations under partial shading conditions," *Solar Energy, Elsevier Journal*, DOI: https://doi.org/10.1016/j.solener.2015.07.039, Vol. 120, pp. 399-418, Aug. 2015.

[11] A. Fathy, "Reliable and efficient approach for mitigating the shading effect on photovoltaic module based on Modified Artificial Bee Colony algorithm," *Renewable Energy, Elsevier Journal*, DOI: https://doi.org/10.1016/j.renene.2015.03.017, Vol. 81, pp. 78-88, Sep. 2015.

[12] M Holt, "NEC REQUIREMENTS FOR SOLAR PHOTOVOLTAIC SYSTEMS," *Chapter book*, ISBN: 9780986353444, pp. 1-608, 2017.

[13] V. Salas, E. Olias, A. Barrado, and A. Lazaro, "Review of themaximum power point tracking algorithm for stand-alone photovoltaic system," *Solar Energy Mater. Solar Cells*, vol. 90, no. 11, pp. 1555–1578, 2006.

[14] T. Esram and P. L. Chapman, "Comparison of photovoltaic array maximum power point tracking techniques," *IEEE Trans. Energy Conv.*,
vol. 22, no. 2, pp. 439–449, Jun. 2007.

[15] B. Subudhi, and R. Pradhan "A Comparative Study on Maximum Power Point Tracking Techniques for Photovoltaic Power Systems," *IEEE Sustainable Energy*, Vol. 4, No. 1, Jan. 2013.

[16] S. Mohanty, B. Subudhi, and P. Kumar Ray, "A Grey Wolf-Assisted Perturb & Observe MPPT Algorithm for a PV System," *IEEE Trans. on Energy Conversion*, Vol. 32, No. 1 pp.272-277, March. 2017.

[17] A. A. Elbaset, H. Ali, M. Abd-El Sattar, and M. Khaled, "Implementation of a modified perturb and observe maximum power point tracking algorithm for photovoltaic system using an embedded microcontroller," *IET Renewable Power Generation*, Vol. 10, No. 4, pp. 551–560, 2016.

[18] X. Li, and et al., "Modified Beta Algorithm for GMPPT and Partial Shading Detection in Photovoltaic Systems," *IEEE Trans. On Power Electronics*, Vol. 33, No. 3, pp. 2172-2182, March. 2018.

[19] J. Ahmed, and Z. Salam, "An Accurate Method for MPPT to Detect the Partial Shading Occurrence in a PV System," *IEEE Trans. On Ind. Informatics*, Vol. 13, pp. 2151-2161, Oct. 2017.

[20] A. M. S. Furtado, and *et al*., "A Reduced Voltage Range Global Maximum
Power Point Tracking Algorithm for Photovoltaic Systems under Partial Shading Conditions," *IEEE Trans. On Ind. Informatics*, Vol. 65, No. 4, pp. 3252-3253, Apr. 2018.

[21] P. Asef, R. Bargallo, M. R. Barzegaran, A. Lapthorn, and D. Mewes, "Multi-objective Design Optimization Using Dual-Level Response Surface Methodology and Booth's Algorithm for Permanent Magnet Synchronous Generators," *IEEE Trans. on Energy Conversion*, Vol. 33, No. 2, pp.652-659, Jun. 2018.

[22] G. C. Hsieh, H-I. Hsieh, C-Y. Tsai, and C-H. Wang, "Photovoltaic Power-Increment-Aided Incremental-Conductance MPPT With Two-Phased Tracking," IEEE Trans. Power Electronics, Vol. 28, No. 6, Jun. 2013.

[23] K. S. Tey, and S. Mekhilef, "Modified Incremental Conductance Algorithm for Photovoltaic System Under Partial Shading Conditions and Load Variation," IEEE Trans. Industrial Electronics, Vol. 61, No. 10, Oct. 2014.

[24] N. E. Zakzouk, M. A. Elsaharty, A. K. Abdelsalam, and A. A. Helal, "Improved performance low-cost incremental conductance PV MPPT technique," IET Renewable Power Generation, Vol. 10, No. 4, pp. 561-574, 2016.

[25] M. A. S. Masoum, H. Dehbonei, and E. F. Fuchs, "Theoretical and experimental analyses of photovoltaic systems with voltage and current based maximum power point tracking," *IEEE Trans. Energy Conv.*, vol. 17, no. 4, pp. 514–522, Dec. 2002.

[26] B. Subudhi and R. Pradhan, "Characteristics evaluation and parameter extraction of a solar array based on experimental analysis," in *Proc. 9th IEEE Power Electron. Drives Syst.*, Singapore, Dec. 5–8, 2011.

[27] C-C. Hua, Y-H. Fang, W-T. Chen, "Hybrid maximum power point tracking method with variable step size for photovoltaic systems," *IET Renewable Power Generation*, Vol. 10, No. 2, pp. 127-132, 2016.

[28] Y-P. Huang, "A Rapid Maximum Power Measurement System for High-Concentration Photovoltaic Modules Using the Fractional Open-Circuit Voltage Technique and Controllable Electronic Load," *IEEE Journal of Photovoltaics*, Vol. 4, No. 6, pp. 1610-1617, Nov. 2014.

[29] A. Omairi, Z. H. Ismail, K. A. Danapalasingam, and M. Ibrahim, "Power Harvesting in Wireless Sensor Networks and Its Adaptation with Maximum Power Point Tracking: Current Technology and Future Directions," IEEE Internet of Things Journal, Vol 4, No. 6, pp. 2104-2115, Dec. 2017.

[30] K. Ishaque, Z. Salam, A. Shamsudin, M. Amjad, "A direct control based maximum power point tracking method for photovoltaic system under partial shading conditions using particle swarm optimization algorithm," *Applied Energy Journal*, Vol. 99, pp. 414-422, Nov. 2012.

[31] K. Wang, Y-L. He, X-D. Xue, B-C. Du, "Multi-objective optimization of the aiming strategy for the solar power tower with a cavity receiver by using the non-dominated sorting genetic algorithm," *Applied Energy, Journal*, Vol. 205, pp. 399-416, Nov. 2017.

[32] N. N. Castellano, J. Antonio G. Parra, J. V-Guirado, and F. M-Agugliaro, "Optimal displacement of photovoltaic array's rows using a novel shading model," *Applied Energy Journal*, Vol. 144, pp. 1-9, April. 2015.

[33] O. Dupre, R. Vaillon, and M. A. Green "Experimental Assessment of Temperature Coefficient Theories for Silicon Solar Cells," IEEE J. Photovolt., V.6, N.1, pp.56-60, 2016.

[34] W-C. Yang, C. Lo, C-Y. Wei, and W-S. Lour "Cell-Temperature Determination in InGaP–(In) GaAs–Ge Triple-Junction Solar Cells," IEEE Electron Device Letters, V.32, N.10, pp.1412-1414, 2011.

[35] D. A-Alvarez, E. Klamaftis, D. Ross, and B. S. Richards "External Thermalization of Carriers With Luminescent Down Shifting for Lower Operating Solar Cell Temperature," IEEE J. Photovolt., V.4, N.6, pp.1532-1537, 2014.

[36] S. Hara, M. Kasu, and N. Matsui "Estimation Method of Solar Cell Temperature Using Meteorological Data in Mega Solar Power Plant," IEEE J. Photovolt., V.6, N.5, pp.1255-1260, 2016.

[37] J. J. Wysocki and P. Rappaport, "Effect of temperature on photovoltaic solar energy conversion," J. Appl. Phys., vol. 31, no. 3, pp. 571–578, 1960.

[38] M. A. Green, Solar Cells: Operating Principles, Technology, and System Applications. Englewood Cliffs, NJ, USA: Prentice-Hall, 1982.

[39] D. S. H. Chan and J. C. H. Phang, "Analytical methods for the extraction of solar-cell single- and double-diode model parameters from I-V characteristics," IEEE Trans. Electron Devices, vol. ED-34, no. 2, pp. 286–293, Feb. 1987.

[40] M. Itoh, H. Takahashi, T. Fujii, H. Takakura, Y. Hamakawa, and Y. Matsumoto "Evaluation of electric energy performance by democratic module PV system field test," Solar Energy Mater. Solar Cells, vol. 67, nos. 1–4, pp. 435–440, 2001.

[41] M. D'Orazio, C. Di Perna, and E. Di Giuseppe, "Experimental operating cell temperature assessment of BIPV with different installation configurations on roofs under Mediterranean climate," Renewable Energy, vol. 68, pp. 378–396, 2014.

[42] D. Polverini, M. Field, E. Dunlop, and W. Zaaiman, "Polycrystalline silicon PV modules performance and degradation over 20 years," Prog. Photovoltaics, Res. Appl., vol. 21, no. 5, pp. 1004–1015, 2013.

[43] G. Makrides, B. Zinsser, M. Schubert, and G. E. Georghiou, "Performance loss rate of twelve photovoltaic technologies under field conditions using statistical techniques," Sol. Energy, vol. 103, pp. 28–42, 2014.

[44] M. A. Green, "General temperature dependence of solar cell performance and implications for device modelling," Prog. Photovoltaics, Res. Appl., vol. 11, no. 5, pp. 333–340, 2003.

[45] K. J. Sauer, T. Roessler, and C. W. Hansen, “Modeling the irradiance and temperature dependence of photovoltaic modules in pvsys,” IEEE

[46] J. Photovolt., vol. 5, no. 1, pp. 152–158, Jan. 2015.

[47] V. D. Rumyntsev et al., “Evaluation of the pv cell operation temperature in the process of fast switching to open-circuit mode,” IEEE J. Photovolt., vol. 5, no. 6, pp. 1715–1721, Nov. 2015.

[48] S. De Wolf, A. Descoeudres, Z. C. Holman, and C. Ballif, “High-efficiency silicon heterojunction solar cells: A review,” Green, vol. 2, pp. 7–24, 2012.

[49] K. Masuko et al., “Achievement of more than 25% conversion efficiency with crystalline silicon heterojunction solar cell,” IEEE J. Photovoltaics, vol. 4, no. 6, pp. 1433–1435, Nov. 2014.

[50] C. Ballif, S. De Wolf, A. Descoeudres, and Z. C. Holman,“Amorphous silicon/crystalline silicon heterojunction solar cells,”Semicond. Semimetals, vol. 90, pp. 73–120, 2014.

[51] T. Sen, N. Pragallapati, V. Agarwal, and R. Kumar “Global maximum power point tracking of PV arrays under partial shading conditions using a modified particle velocity-based PSO technique,” IET Renewable Power Gen., V.12, N.5, pp.555-563, 2018.

[52] E. I. Batzelis, P. S. Georgilakis, and S. A. Papathanassiou, “Energy models for photovoltaic systems under partial shading conditions: a comprehensive review,” IET Renewable Power Gen., V.9, N.4, pp.340-349, 2015.

[53] G. Farivar, and B. Asaei “A New Approach for Solar Module Temperature Estimation Using the Simple Diode Model,” IEEE Trans. Energy Conv., V.26, N.4, pp.1118-1126, 2011.

[54] G. Mangeni, R. H. G. Tan, T. H. Tan, S. K. Cheo, V. H. Mok, and J. Y. Pang “Photovoltaic Module Cell Temperature Measurements using Linear Interpolation Technique,” IEEE Int. Conf. Inst. and Measurement (I2MTC), DOI: 10.1109/I2MTC.2017.7969759, pp.1-6, 2017.

[55] M. R. Vogt, H. S-Huxel, M. Offer, S. Blankemeyer, R. Witteck, M. Kontges, K. Bothe, and R. Brendel “Reduced Module Operating Temperature and Increased Yield of Modules With PERC Instead of Al-BSF Solar Cells,” IEEE J. Photovolt.., V.7, N.1, pp.44-50, 2017.

[56] P. Ingenhoven, G. Belluardo, and D. Moser “Comparison of Statistical and Deterministic Smoothing Methods to Reduce the Uncertainty of Performance Loss Rate Estimates,” IEEE J. Photovolt., V.8, N.1, pp.224-232, 2018.

[57] V. Sharma and S. S. Chandel, “Performance and degradation analysis for long term reliability of solar photovoltaic systems: A review,” Renewable Sustain. Energy Rev., vol. 27, pp. 753–767, 2013.

[58] A. Ndiaye et al., “Degradations of silicon photovoltaic modules: A literature review,” Sol. Energy, vol. 96, pp. 140–151, 2013.

[59] S. Zhang, H. Wang, X. Zou, Y. Zhang, R. Lu, H. Li, and Y. Liu, “Optical Frequency-Detuned Heterodyne for Self-Referenced Measurement of Photodetectors,” IEEE Photonics Tech. Letter., V.27, N.9, pp.1014-1017, 2015.

[60] C. Iaconis, and I. A. Walmsley, “Self-Referencing Spectral Interferometry for Measuring Ultrashort Optical Pulses,” IEEE Journal of Quantum, V.35, N.4, pp.501-509, 1999.

[61] J. Yin, T. Liu, J. Jiang, K. Liu, S. Wang, S. Zou, Z. Qin, and Z. Ding “Self-Referenced Residual Pressure Measurement Method for Fiber-Optic Pressure Sensor Chip,” IEEE Photonics Tech. Letter., V.26, N.10, pp.272-277, 2014.

[62] P. Asef, P. Niknejad, M. R. Barzegaran, R. Bargallo, and A. Lapthorn, “Correlation of Power Prediction Considering the Nominal Operating Cell Temperature under Partial Shading Effect,” IET Renewable Power Generation, under review, 2018.

[63] S. S. Santos, D. Y. Takahashi, A. Nakata, and A. Fujita, “A comparative study of statistical methods used to identify dependencies between gene expression signals,” Briefings in Bioinformatics, DOI:10.1093/bib/bbt051, pp. 1–13, 2013.